MATHEMATICAL TREATMENT OF NANOMATERIALS AND NEURAL NETWORKS

EDITED BY: Jia-Bao Liu, Muhammad Javaid, Shaohui Wang and Jinde Cao
PUBLISHED IN: Frontiers in Physics and Frontiers in Computational Neuroscience

frontiers Research Topics

frontiers

ISSN 1664-8714
ISBN 978-2-88971-797-2
DOI 10.3389/978-2-88971-797-2

About Frontiers

Frontiers is more than just an open-access publisher of scholarly articles: it is a pioneering approach to the world of academia, radically improving the way scholarly research is managed. The grand vision of Frontiers is a world where all people have an equal opportunity to seek, share and generate knowledge. Frontiers provides immediate and permanent online open access to all its publications, but this alone is not enough to realize our grand goals.

Frontiers Journal Series

The Frontiers Journal Series is a multi-tier and interdisciplinary set of open-access, online journals, promising a paradigm shift from the current review, selection and dissemination processes in academic publishing. All Frontiers journals are driven by researchers for researchers; therefore, they constitute a service to the scholarly community. At the same time, the Frontiers Journal Series operates on a revolutionary invention, the tiered publishing system, initially addressing specific communities of scholars, and gradually climbing up to broader public understanding, thus serving the interests of the lay society, too.

Dedication to Quality

Each Frontiers article is a landmark of the highest quality, thanks to genuinely collaborative interactions between authors and review editors, who include some of the world's best academicians. Research must be certified by peers before entering a stream of knowledge that may eventually reach the public - and shape society; therefore, Frontiers only applies the most rigorous and unbiased reviews.
Frontiers revolutionizes research publishing by freely delivering the most outstanding research, evaluated with no bias from both the academic and social point of view. By applying the most advanced information technologies, Frontiers is catapulting scholarly publishing into a new generation.

What are Frontiers Research Topics?

Frontiers Research Topics are very popular trademarks of the Frontiers Journals Series: they are collections of at least ten articles, all centered on a particular subject. With their unique mix of varied contributions from Original Research to Review Articles, Frontiers Research Topics unify the most influential researchers, the latest key findings and historical advances in a hot research area! Find out more on how to host your own Frontiers Research Topic or contribute to one as an author by contacting the Frontiers Editorial Office: frontiersin.org/about/contact

MATHEMATICAL TREATMENT OF NANOMATERIALS AND NEURAL NETWORKS

Topic Editors:
Jia-Bao Liu, Anhui Jianzhu University, China
Muhammad Javaid, University of Management and Technology, Pakistan
Shaohui Wang, Louisiana College, United States
Jinde Cao, Southeast University, China

Citation: Liu, J.-B., Javaid, M., Wang, S., Cao, J., eds. (2021). Mathematical Treatment of Nanomaterials and Neural Networks. Lausanne: Frontiers Media SA. doi: 10.3389/978-2-88971-797-2

Table of Contents

frontiers in Physics

BRIEF RESEARCH REPORT
published: 21 April 2020
doi: 10.3389/fphy.2020.00106

Adaptive Neural Network Control of Chaotic Fractional-Order Permanent Magnet Synchronous Motors Using Backstepping Technique

Guangming Xue[1], *Funing Lin*[1]* *and Bin Qin*[1,2,3]

[1] College of Information and Statistics, Guangxi University of Finance and Economics, Nanning, China, [2] Guangxi Key Laboratory Cultivation Base of Cross-Border E-Commerce Intelligent Information Processing, Nanning, China, [3] Guangxi (ASEAN) Research Center of Finance and Economics, Guangxi University of Finance and Economics, Nanning, China

The backstepping technique is greatly effective for the integer-order triangular non-linear systems. Nevertheless, it is dramatically challenging to implement backstepping technique in the manipulation of fractional-order permanent magnet synchronous motors (FOPMSMs), since the fractional derivatives of the composite functions are deeply complex. In this paper, adaptive neural network (NN) backstepping-based control scheme for FOPMSMs on the basis of fractional Lyapunov stability criterion is established. First, we propose a novel adaptive synchronous controller for FOPMSMs by coupling with NNs and backstepping technique. Then, we present a detailed stability analysis in terms of FOPMSMs via the proposed controller. Finally, a simulation example is given to reveal that the proposed controller can effectively eliminate or restrain the chaos of FOPMSMs, and keep the tracking signals synchronous with the reference signals.

Keywords: adaptive control, backstepping technique, neural network, fractional-order chaotic system, permanent magnet synchronous motor

OPEN ACCESS

Edited by:
Muhammad Javaid,
University of Management and Technology, Pakistan

Reviewed by:
Mohd Ariffanan Mohd Basri,
Universiti Teknologi Malaysia, Malaysia
Shengda Zeng,
Jagiellonian University, Poland
Xianghu Liu,
Guizhou University, China

***Correspondence:**
Funing Lin
toplin518@126.com

Specialty section:
This article was submitted to Mathematical Physics, a section of the journal Frontiers in Physics

Received: *18 February 2020*
Accepted: *20 March 2020*
Published: *21 April 2020*

Citation:
Xue G, Lin F and Qin B (2020) Adaptive Neural Network Control of Chaotic Fractional-Order Permanent Magnet Synchronous Motors Using Backstepping Technique. Front. Phys. 8:106. doi: 10.3389/fphy.2020.00106

1. INTRODUCTION

In late decades, fractional-order non-linear systems (FONSs) [1] have been widely studied, not only owing to their accurate performance in modeling physical phenomena (e.g., chaos, oscillations, impulses, diffusions, see [2–5]), but also owing to their successful applications in a variety of fields, such as chemistry, medicine, biology, electronics, robotics, fuel cells, and so on [6–11]. Stability analysis [12] is regarded as a fundamental and crucial task in the development of cybernetics. Recently, more and more scholars have paid attention to stability analysis of fractional-order non-linear systems [13–16]. It is not exaggerated to say that stability analysis of FONSs along with their robust control have become a hot and promising research topic.

The researches on the control of chaotic systems are widely concerned due to its valuable significance in both theoretical and practical aspects [17, 18]. Since Kuroe and Hayashi [19] originally discovered chaotic phenomenon from the motor drive system in the late 1980's, chaos control has been one of the most popular research topics in cybernetics. There are several types of chaotic motor drivers that capture widespread interests. For instance, DC motor drivers [20], step motor drivers [21], single-phase induction motor drivers [22], synchronous reluctance motor drivers [23], switched reluctance motor drivers [24] and so on. The extensive utilization of permanent magnet synchronous motors (PMSMs) in industries mainly benefits from their merits

of high speed, high efficiency, high power, low loss and low temperature rise. Chaotic non-linear systems are very complex due to the irregular and unpredictable behaviors. A remarkable feature of chaotic systems is that they are very sensitive to the initial conditions. The small change of initial state will lead to great distinction. On the other hand, they have many other desired properties, such as information processing, secure communication and mechanical system. However, it may cause unexpected oscillations and even destroy the system stability. Therefore, such oscillations should be effectively suppressed. For this reason, various methods have been developed to stabilize non-linear chaotic systems, in which fractional order chaos control has also been focused, such as OGY type [25], feedback type [26–28], dynamic surface type [29], sliding mode type [30–33], backstepping type [34, 35], etc.

Neural network (NN) control technique [36, 37] is an intelligent method for controlling non-linear systems with uncertainties. Analogizing to fuzzy control approach [38, 39], the idea of NN control technique is to approximate unknown non-linear functions by using radial basis function neural networks (RBFNNs), which is a type of neuron-modeled structure formed by the computation of some adjustable parameter vectors and some specific continuous functions. As one of the most powerful tools to realizing approximation of functions, NN control technique is popular because it facilitates to control most of many non-linear systems in which the data are too imprecise or too complex to construct mathematical modeling. It provides an available way for the control designs, and it is considerably applicable in the field of control engineering.

Backstepping technique has engaged much attention due to its efficient performance in handling mismatched uncertainties of integer-order non-linear systems [40, 41]. Unfortunately, this control method has an inherent drawback, namely "explosion of complexity," triggered by iteratively differentiating virtual control inputs [42]. Additionally, it requires complicated analysis to compute a so-called "regression matrix" [43]. Dawson et al. [44] pointed out that the size of the regression matrix displays too large when backstepping technique was applied to manipulate DC motors in a conventional manner. Such complexities might be augmented remarkably for fractional-order non-linear systems.

It is well-known that the design of NN control is rarely systematic, which is difficult to work for the control of complex systems. It is also challenging to establish a systematic NN control theory to solve a series of problems, such as the mechanism of NN control, stability analysis, systematic design, etc. Backstepping control usually leads to the problem of "complexity explosion" when it is applied in the processing of unknown functions, so the methods of adaptive NN control [36], adaptive fuzzy control [45] and adaptive NN backstepping control [35] are put forward to address such a problem. These techniques enable systems to be greatly adaptive and robust obeying the required performance criteria for the control. However, the control performance is not desired for the non-linear systems with triangular structures, and the problem of "complexity explosion" will occur during the control proceeding. Based on the above discussion, this paper proposes an adaptive neural network control method of chaotic fractional-order permanent magnet synchronous motors using backstepping technique, which can improve the control performance of non-linear systems.

To deal with the synchronization issue of fractional-order permanent magnet synchronous motor (FOPMSM) with triangular structure, we expect to construct an adaptive NN controller combined with backstepping technique. This enables every uncertain complex non-linear functions being approximated by a radial basis function neural network (RBFNN) during each control step. The main contributions of this work can be summarized as follows:

The synchronization control scheme design and the stability analysis of FOPMSMs are investigated. In order to analyze the stability of the controlled systems, firstly, some basic results related to fractional calculus and RBFNN are recalled, including a fractional differential inequality, which lays the foundation for the application of the fractional Lyapunov function method. Meanwhile, it lays a foundation for the stability analysis of other types of FONSs. Secondly, an adaptive NN backstepping recursive control method is proposed for a class of uncertain FOPMSMs. The stability of FOPMSMs is analyzed based on fractional Lyapunov criterion. NN control technique is employed when dealing with the approximation of uncertain functions of FOPMSMs, and the fractional adaptive law is designed to update the parameters of NNs. The relevant properties of Mittag-Leffler function and Laplace transform are applied when the fractional Lyapunov function is defined to implement the system control. Our proposed control method fully averts the superfluous terms which are aroused by repeated derivation on virtual control inputs, and facilitates to overcome the so-called "complexity explosion" inherent drawback of the traditional backstepping technique. Finally, we present a numerical example to verify the main results. The simulation results show that our method embodies a perfect control effect. This also reveals the effectiveness of our control algorithm in another way.

The remainder of this work is arranged as below: In section 2, we recall several fundamental preliminaries of fractional calculus and RBFNN. Then, a brief overview of a class of FOPMSMs is provided. In section 3, we propose a RBFNN-based control scheme in three steps and present stability analysis. In section 4, we illustrate the effectiveness of the proposed synchronous controller via a simulation example. Finally, in section 5, we summarize the results of this work and put forward the prospect for our further investigation.

2. PRELIMINARIES AND MODEL DESCRIPTION

Some basic concepts, notations and lemmas, involved with fractional calculus and radial basis function neural network (RBFNN), need to be stated in this section before used. For convenience, we adopt the symbol $\mathbb{R}$ (resp. $\mathbb{R}^n$, $\mathbb{C}$) to represent the collection of all real numbers (resp. n-dimensional real vectors, complex numbers). $\Omega \subseteq \mathbb{R}^n$ is always assumed to be compact. $T = [0, +\infty)$ means the time-variable domain. The notation $C^1(T, \Omega)$ stands for the collection of all continuous

functions from T to Ω with continuous derivatives. Given a vector $x \in \mathbb{R}^n$, x^T denotes its transpose, $\| x \|$ denotes its Euclidean norm.

Definition 1 ([8]). Let $\alpha \geq 0$. For a given function $f:[0,\infty) \to \mathbb{R}$, its α-th order integral is written as

$$ {}_0\mathcal{I}_{\psi}^{\alpha} f(\psi) = \frac{1}{\Gamma(\alpha)} \int_0^{\psi} \frac{f(\eta)}{(\psi-\eta)^{1-\alpha}} \mathrm{d}\eta, \quad \psi > 0 \tag{1} $$

where $\Gamma(\alpha) = \int_0^{+\infty} s^{\alpha-1} e^{-s} \mathrm{d}s$.

Definition 2 ([8]). Let $\alpha \geq 0$. For a given function $f:[0,\infty) \to \mathbb{R}$, its α-th order Caputo derivative is expressed by

$$ {}_0^C\mathcal{D}_{\psi}^{\alpha} f(\psi) = \frac{1}{\Gamma(n-\alpha)} \int_0^{t} \frac{f^{(n)}(\eta)}{(\psi-\eta)^{\alpha+1-n}} \mathrm{d}\eta, \quad \alpha \geq 0, \quad \psi > 0 \tag{2} $$

where $\alpha \in [n-1, n)$, $n = 1, 2, \cdots$.

Definition 3 ([8]). Let $\alpha, \gamma > 0$. The Mittag-Leffler function $E_{\alpha,\gamma}$ on $\mathbb{C}$ is expressed as

$$ E_{\alpha,\gamma}(\zeta) = \sum_{k=0}^{\infty} \frac{\zeta^k}{\Gamma(\alpha k + \gamma)}. \tag{3} $$

Moreover, taking the Laplace transform on $E_{\alpha,\gamma}$ generates

$$ \mathcal{L}\{t^{\gamma-1} E_{\alpha,\gamma}(-at^{\alpha})\} = \frac{s^{\alpha-\gamma}}{s^{\alpha}+a}. \tag{4} $$

Lemma 1 ([1]). *Let $0 < \alpha < 1$, $\gamma \in \mathbb{C}$ and $\nu \in \mathbb{R}$ fulfilling the following:*

$$ \frac{\pi\alpha}{2} < \nu < \min\{\pi, \pi\alpha\} \tag{5} $$

If $|\zeta| \to \infty, \nu \leq |\arg(\zeta)| \leq \pi$, then the following statement holds:

$$ E_{\alpha,\gamma}(\zeta) = -\sum_{j=1}^{n} \frac{1}{\Gamma(\gamma - \alpha j)\zeta^j} + o\left(|\zeta|^{-n-1}\right), \tag{6} $$

where n is a non-zero natural number.

Lemma 2 ([1]). *Let $\alpha \in (0,2)$, $\beta \in \mathbb{R}$. If μ is a constant fulfilling*

$$ \frac{\pi\alpha}{2} < \mu \leq \min\{\pi, \pi\alpha\}, \tag{7} $$

then there exists $C > 0$ such that

$$ |E_{\alpha,\beta}(\zeta)| \leq \frac{C}{1+|\zeta|}, \quad \forall \zeta \in \mathbb{C} \tag{8} $$

with $|\arg(\zeta)| \in [\mu, \pi]$.

Lemma 3 ([35]). *Let $z(t)$ be a smooth function. Then*

$$ \frac{1}{2} {}_0^C\mathcal{D}_t^{\alpha}(z^T(t)z(t)) \leq z^T(t) {}_0^C\mathcal{D}_t^{\alpha} z(t) \ \ (\forall t \in T). \tag{9} $$

Lemma 4 ([34, 46]). *Let $z = 0$ be the equilibrium point of a FONS, which is given by*

$$ {}_0^C\mathcal{D}_t^{\alpha} z(t) = f(t, z(t)), \tag{10} $$

where $f: T \times \Omega \longrightarrow \mathbb{R}$ is a function with the Lipschitz condition. Suppose there exist a Lyapunov function $V(t, z(t))$ and a family of class-K functions[1] $\hat{g}_i$ $(i = 1, 2, 3)$ satisfying

$$ \hat{g}_1(\|z(t)\|) \leq V(t, z(t)) \leq \hat{g}_2(\|z(t)\|), \tag{11} $$

$$ {}_0^C\mathcal{D}_t^{\alpha} V(t, z(t)) \leq -\hat{g}_3(\|z(t)\|) \tag{12} $$

Then system (10) is asymptotical stable, i.e., $\lim_{t\to\infty} z(t) = 0$.

Next, let us introduce some basic notions and notations about the radial basis function NN (RBFNN) [43, 47]. The goal of the control procedure is to establish a adaptive NN control scheme, which enables the tracking signal $x_1(t)$ and the given reference signal $x_d(t)$ are synchronized.

A RBFNN can be formed as

$$ \hat{f}(z(t)) = \theta^T(t)\vartheta(z(t)). \tag{13} $$

where $z(t) = (z_1(t), z_2(t), \cdots, z_n(t))^T \in C^1(T, \Omega)$ and $\hat{f}$ are the input-variable and the output-variable, respectively, $\theta(t) = (\theta_1(t), \theta_2(t), \cdots, \theta_m(t))^T$ is an adjustable parameter vector, $\vartheta(z(t)) = (\vartheta_1(z(t)), \vartheta_2(z(t)), \cdots, \vartheta_m(z(t)))^T$ with $\vartheta_j(z(t)) = (\vartheta_j(z_1(t)), \vartheta_j(z_2(t)), \cdots, \vartheta_j(z_n(t)))^T$ $(j = 1, 2, \cdots, m)$ being a continuous function, called the regressor variable. To illustrate its structure, we refer to **Figure 1**.

Suppose that all of the continuous functions $\vartheta_1(z(t)), \vartheta_2(z(t)), \cdots, \vartheta_m(z(t))$ in the above RBFNN are chosen as Gaussian functions, that is, for $j = 1, 2, \cdots, m$,

$$ \vartheta_j(z(t)) = \exp\left(-\frac{\|z(t) - c_j\|^2}{\sigma_j^2}\right), $$

where $c_j = [c_{j1}, c_{j2}, ..., c_{jn}]^T$ is the center vector and $\sigma_j > 0$ is the width of the Gaussian function $\vartheta_j(z(t))$. Then the next lemma is obtained.

Lemma 5 ([35]). *Let $f: \Omega \longrightarrow \mathbb{R}$ be a Lipschitz function. For each $z \in C^1(T, \Omega)$ and for each $\varepsilon > 0$, there is a RBFNN fulfilling Equation (13) and the following property:*

$$ \sup_{t \in T} |f(z(t)) - \theta^T(t)\vartheta(z(t))| \leq \varepsilon. \tag{14} $$

[1] A function $\hat{g}:[0,\infty) \longrightarrow T$ is said to belong to class-K if it is strictly increasing, continuous and $\hat{g}(0) = 0$.

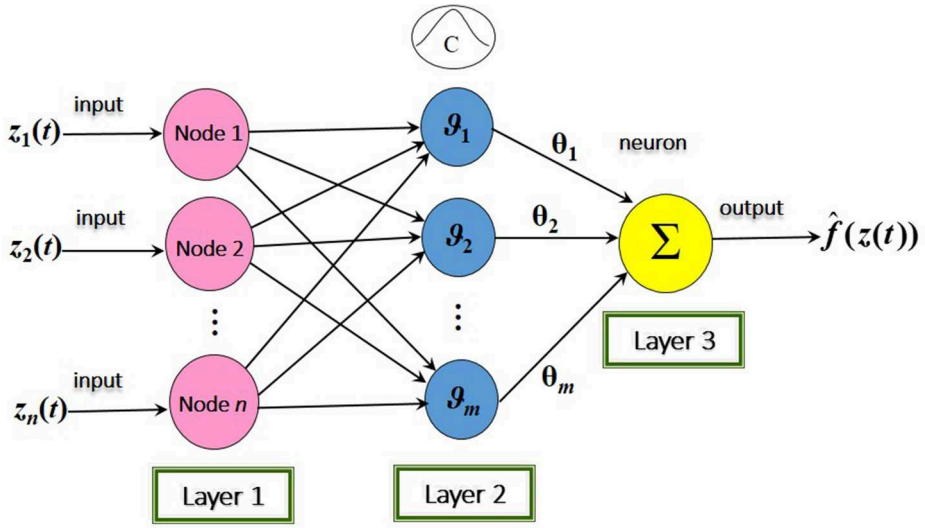

FIGURE 1 | The structure of RBFNN.

It is well-known that non-linear theory has yet been widely applied in the stability analysis of integer-order non-linear PMSMs. Yu et al. [48] investigated a type of classical PMSMs, which are described as follows:

$$\begin{cases} \dfrac{d\omega}{dt} = \sigma\left(i_q - \omega\right), \\ \dfrac{di_q}{dt} = -i_q - \omega i_d + \gamma\omega, \\ \dfrac{di_d}{dt} = -i_d + \omega i_q + u_d, \end{cases} \tag{15}$$

Yu et al. [48] also studied that when the parameters σ, γ of a PMSM decrease in a certain range, chaos will appear in the PMSM. To eliminate chaos in PMSM drive systems, they treated u_d as an adjustable variable, and proposed an adaptive NN control method based on backstepping control technique. It is well-known that backstepping technique usually makes great efforts to the effective control of integer-order triangular non-linear systems. Nevertheless, it is difficult to incorporate backstepping control technique into FONSs because of the complexities of fractional derivatives of composite functions. Moreover, the applications of FONSs broadly cover a great deal of fields, such as physics, chemistry, mathematics, etc., which suggests that the mathematical structures modeled by FONSs are more accurate and more practical.

Based on the aforementioned facts, this paper concerns a class of FOPMSMs. For simplicity, denote $\omega = x_1$, $i_q = x_2$, $i_d = x_3$ in system (15), and extend system (15) into the next fractional-order form:

$$\begin{cases} {}_0^C\mathcal{D}_t^\alpha x_1(t) = \sigma\left(x_2(t) - x_1(t)\right), \\ {}_0^C\mathcal{D}_t^\alpha x_2(t) = -x_2(t) - x_1(t)x_3(t) + \gamma x_1(t), \\ {}_0^C\mathcal{D}_t^\alpha x_3(t) = -x_3(t) + x_1(t)x_2(t) + u_d(t), \end{cases} \tag{16}$$

where $0 < \alpha < 1$, $x(t) = [x_1(t), x_2(t), x_3(t)]^T \in \mathbb{R}^3$ is a measurable state-variable, $x_1(t) \in \mathbb{R}$ is an output-variable, $u_d(t) \in \mathbb{R}$ is an input-variable, σ and γ are positive constants, both of them represent system operating parameters.

3. ADAPTIVE NEURAL NETWORK BACKSTEPPING CONTROL OF FOPMSMS

In this section, we will improve the conventional control method combined with backstepping technique, by which the chaos of FOPMSMs realizes to be eliminated or restrained in a high effective manner. The design process includes three steps. Each of them will construct a virtual control variable based on a proper Lyapunov function. At the end, a controller in real sense will be produced to manipulate FOPMSM. Assume that $x_d(t)$ is a given reference signal. Our goal is to establish an appropriate controller $u_d(t)$, ensuring that the tracking error $e(t) := x_1(t) - x_d(t)$ will ultimately converge to an arbitrarily small neighborhood of the origin. Next, we present a recursive backstepping procedure to reach our goal in three steps:

Step 1: From (16), we obtain

$$\begin{aligned} {}_0^C\mathcal{D}_t^\alpha e(t) &= {}_0^C\mathcal{D}_t^\alpha x_1(t) - {}_0^C\mathcal{D}_t^\alpha x_d(t) \\ &= \sigma\left(x_2(t) - x_1(t)\right) - {}_0^C\mathcal{D}_t^\alpha x_d(t) \end{aligned} \tag{17}$$

The virtual control input $\alpha_1(e(t), x_1(t), x_d(t))$ is adopted as

$$\begin{aligned}\alpha_1(e(t), x_1(t), x_d(t)) = x_1(t) - \frac{1}{\sigma}\big[k_{11}e(t) + k_{21}\text{sign}(e(t)) \\ - {}_0^C\mathcal{D}_t^\alpha x_d(t)\big]\end{aligned} \tag{18}$$

where $k_{11} > 0$, $k_{21} > 0$ are design parameters, sign$(\cdot)$ denotes a signum function.

Denote $\alpha_1(t) = \alpha_1(e(t), x_1(t), x_d(t))$. Let

$$e_1(t) = x_2(t) - \alpha_1(t). \tag{19}$$

Introduce Equations (18) and (19) into Equation (17) yields

$${}_0^C\mathcal{D}_t^\alpha e(t) = -k_{11}e(t) - k_{21}\text{sign}(e(t)) + \sigma e_1(t). \tag{20}$$

Multiplying $e(t)$ with Equation (20) generates

$$\begin{aligned}e(t){}_0^C\mathcal{D}_t^\alpha e(t) &= -k_{21}|e(t)| + \sigma e(t)e_1(t) - k_{11}e^2(t) \\ &\le \sigma e(t)e_1(t) - k_{11}e^2(t)\end{aligned} \tag{21}$$

Let the Lyapunov function candidate $V_1(t)$ be taken as

$$V_1(t) = \frac{1}{2}e^2(t) \tag{22}$$

By Lemma 3 and Equation (21), one obtains

$$\begin{aligned}{}_0^C\mathcal{D}_t^\alpha V_1(t) = \frac{1}{2}{}_0^C\mathcal{D}_t^\alpha e^2(t) &\le e(t){}_0^C\mathcal{D}_t^\alpha e(t) \\ &\le -k_{11}e^2(t) + \sigma e(t)e_1(t) \\ &= -\kappa_1 V_1(t) + \sigma e(t)e_1(t)\end{aligned} \tag{23}$$

where $\kappa_1 = 2k_{11}$ is a positive constant.

Step 2: From Equations (16) and (19), we have

$$\begin{aligned}{}_0^C\mathcal{D}_t^\alpha e_1(t) &= {}_0^C\mathcal{D}_t^\alpha x_2(t) - {}_0^C\mathcal{D}_t^\alpha \alpha_1(t)) \\ &= -x_2(t) - x_1(t)x_3(t) + \gamma x_1(t) - {}_0^C\mathcal{D}_t^\alpha \alpha_1(t) \\ &= -x_2(t) - x_1(t)x_3(t) + \gamma x_1(t) - F_1(x_1(t))\end{aligned} \tag{24}$$

where $F_1\big(x_1(t)\big) = {}_0^C D_t^\alpha \alpha_1(t)$ is an unknown function. To approximate $F_1\big(x_1(t)\big)$, we adopt a RBFNN formulated by

$$\hat{F}_1\big(x_1(t), \theta_1(t)\big) = \theta_1^T(t)\vartheta_1(x_1(t)). \tag{25}$$

Suppose θ_1^* is the optimal parameter, which is represented as

$$\theta_1^* = \arg\min_{\theta_1(t)}\left[\sup_{x_1(t)}\left|F_1\big(x_1(t)\big) - \hat{F}_1\big(x_1(t), \theta_1(t)\big)\right|\right]. \tag{26}$$

Here, θ_1^* is presented for the purpose of analysis, in other words, it is not required in the controller design procedure.

Define the parameter estimation error $\tilde{\theta}_1(t)$ as

$$\tilde{\theta}_1(t) = \theta_1(t) - \theta_1^*, \tag{27}$$

Also, formulate the optimal approximate error $\epsilon_1\big(x_1(t)\big)$ by

$$\epsilon_1\big(x_1(t)\big) = \hat{F}_1\big(x_1(t), \theta_1^*\big) - F_1\big(x_1(t)\big), \tag{28}$$

According to Tong and Li [49], we know that $\epsilon_1\big(x_1(t)\big)$ is bounded. Therefore,

$$|\epsilon_1\big(x_1(t)\big)| \le \bar{\epsilon}_1, \tag{29}$$

where $\bar{\epsilon}_1$ is a known constant. Consequently,

$$\begin{aligned}&\hat{F}_1\big(x_1(t), \theta_1(t)\big) - F_1\big(x_1(t)\big) \\ &= \hat{F}_1\big(x_1(t), \theta_1(t)\big) - \hat{F}_1\big(x_1(t), \theta_1^*\big) + \hat{F}_1\big(x_1(t), \theta_1^*\big) - F_1\big(x_1(t)\big) \\ &= \theta_1^T(t)\vartheta_1(x_1(t)) - \theta_1^*\vartheta_1(x_1(t)) + \epsilon_1(x_1(t)) \\ &= \tilde{\theta}_1^T(t)\vartheta_1(x_1(t)) + \epsilon_1(x_1(t)).\end{aligned} \tag{30}$$

Define the virtual control input by

$$\begin{aligned}\alpha_2(t) = -x_1^{-1}\big[\theta_1^T(t)\vartheta_1(x_1(t)) + x_2(t) - k_{12}e_1(t) \\ -k_{22}\text{sign}(e_1(t)) - \sigma e(t)\big] + \gamma\end{aligned} \tag{31}$$

where $k_{12} > 0$ and $k_{22} > \bar{\epsilon}_1$ are design parameters.

Implement the following fractional-order adaptation law:

$${}_0^C\mathcal{D}_t^\alpha \theta_1(t) = -e_1(t)\vartheta_1(x_1(t)) - \rho_1\theta_1(t), \tag{32}$$

where ρ_1 is a positive design parameters. Noting that the α-th order derivatives of constants are equal to 0, by Equation (27), we immediately get

$${}_0^C\mathcal{D}_t^\alpha \tilde{\theta}_1(t) = {}_0^C\mathcal{D}_t^\alpha \theta_1(t). \tag{33}$$

Put

$$e_2(t) = x_3(t) - \alpha_2(t). \tag{34}$$

Then Equations (24), (30), and (31) lead to

$$\begin{aligned}{}_0^C\mathcal{D}_t^\alpha e_1(t) &= -x_2(t) - x_1(t)x_3(t) + \gamma x_1(t) - F_1(x_1(t)) \\ &= -x_2(t) - x_1(t)x_3(t) + \gamma x_1(t) + \tilde{\theta}_1^T(t)\vartheta_1(x_1(t)) \\ &\quad + \epsilon_1(x_1(t)) - \theta_1^T(t)\vartheta_1(x_1(t)) \\ &= -x_1(t)e_2(t) - k_{12}e_1(t) - k_{22}\text{sign}(e_1(t)) - \sigma e(t) \\ &\quad + \tilde{\theta}_1^T(t)\vartheta_1(x_1(t)) + \epsilon_1(x_1(t)).\end{aligned} \tag{35}$$

By multiplying $e_1(t)$ with (35), we obtain

$$\begin{aligned} e_1(t){}_0^C\mathcal{D}_t^\alpha e_1(t) =& -x_1(t)e_1(t)e_2(t) - k_{12}e_1^2(t) \\ & - k_{22}|e_1(t)| - \sigma e_1(t)e(t) \\ & + e_1(t)\tilde{\theta}_1^T(t)\vartheta_1(x_1(t)) + e_1(t)\epsilon_1(x_1(t)) \\ \le & -x_1(t)e_1(t)e_2(t) - k_{12}e_1^2(t) - \sigma e_1(t)e(t) \\ & + e_1(t)\tilde{\theta}_1^T(t)\vartheta_1(x_1(t)) + |e_1(t)|\bar{\epsilon_1} \\ \le & -x_1(t)e_1(t)e_2(t) - k_{12}e_1^2(t) - \sigma e_1(t)e(t) \\ & + e_1(t)\tilde{\theta}_1^T(t)\vartheta_1(x_1(t)) \end{aligned} \tag{36}$$

Adopt the next Lyapunov function candidate $V_2(t)$:

$$V_2(t) = V_1(t) + \frac{1}{2}e_1^2(t) + \frac{1}{2}\tilde{\theta}_1^T(t)\tilde{\theta}_1(t) \tag{37}$$

Applying Lemma 3 and Equation (23), ont gets

$$\begin{aligned} {}_0^C\mathcal{D}_t^\alpha V_2(t) =& {}_0^C\mathcal{D}_t^\alpha V_1(t) + \frac{1}{2}{}_0^C\mathcal{D}_t^\alpha e_1^2(t) + \frac{1}{2}{}_0^C\mathcal{D}_t^\alpha \tilde{\theta}_1^T(t)\tilde{\theta}_1(t) \\ \le & -\kappa_1 V_1(t) + \sigma e_1(t)e(t) + e_1(t){}_0^C\mathcal{D}_t^\alpha e_1(t) \\ & + \tilde{\theta}_1^T(t){}_0^C\mathcal{D}_t^\alpha \tilde{\theta}_1(t) \\ =& -\kappa_1 V_1(t) + \sigma e_1(t)e(t) + e_1(t){}_0^C\mathcal{D}_t^\alpha e_1(t) \\ & + \tilde{\theta}_1^T(t){}_0^C\mathcal{D}_t^\alpha \theta_1(t) \end{aligned} \tag{38}$$

Substituting Equations (36) and (32) into Equation (38) derives

$$\begin{aligned} {}_0^C\mathcal{D}_t^\alpha V_2(t) \le & -\kappa_1 V_1(t) - x_1(t)e_1(t)e_2(t) - k_{12}e_1^2(t) \\ & + e_1(t)\tilde{\theta}_1^T(t)\vartheta_1(x_1(t)) + \tilde{\theta}_1^T(t){}_0^C\mathcal{D}_t^\alpha \theta_1(t) \\ =& -\kappa_1 V_1(t) - k_{12}e_1^2(t) - x_1(t)e_1(t)e_2(t) \\ & - \rho_1\tilde{\theta}_1^T(t)\theta_1(t) \\ =& -\kappa_1 V_1(t) - k_{12}e_1^2(t) - x_1(t)e_1(t)e_2(t) \\ & - \rho_1\tilde{\theta}_1^T(t)\tilde{\theta}_1(t) - \rho_1\tilde{\theta}_1^T(t)\theta_1^* \\ \le & -\kappa_1 V_1(t) - k_{12}e_1^2(t) - x_1(t)e_1(t)e_2(t) \\ & - \frac{\rho_1}{2}\tilde{\theta}_1^T(t)\tilde{\theta}_1(t) + \frac{\rho_1}{2}\theta_1^{*T}(t)\theta_1^* \\ \le & -\kappa_2 V_2(t) - x_1(t)e_1(t)e_2(t) + H_1 \end{aligned} \tag{39}$$

where $\kappa_2 = \min\{\kappa_1, 2k_{12}, \rho_1\}$ and $H_1 = \frac{\rho_1}{2}\theta_1^{*T}\theta_1^*$ are positive constants.

Step 3: Using Equation (34), one has

$$\begin{aligned} {}_0^C\mathcal{D}_t^\alpha e_2(t) =& {}_0^C\mathcal{D}_t^\alpha x_3(t) - {}_0^C\mathcal{D}_t^\alpha \alpha_2(t) \\ =& -x_3(t) + x_1(t)x_2(t) + u_d(t) - {}_0^C\mathcal{D}_t^\alpha \alpha_2(t) \\ =& -x_3(t) + x_1(t)x_2(t) + u_d(t) - F_2\big(x_1(t), x_2(t)\big) \end{aligned} \tag{40}$$

where $F_2\big(x_1(t), x_2(t)\big) = {}_0^C D_t^\alpha \alpha_2(t)$ is unknown. We approximate $F_2\big(x_1(t), x_2(t)\big)$ via RBFNN as follows:

$$\hat{F}_1\big(x_1(t), x_2(t), \theta_2(t)\big) = \theta_2^T(t)\vartheta_2(x_1(t), x_2(t)). \tag{41}$$

Furthermore, Equation (40) can be reformulated by

$$\begin{aligned} {}_0^C\mathcal{D}_t^\alpha e_2(t) =& -x_3(t) + x_1(t)x_2(t) + u_d(t) - F_2\big(x_1(t), x_2(t)\big) \\ =& -x_3(t) + x_1(t)x_2(t) + u_d(t) - F_2\big(x_1(t), x_2(t)\big) \\ & + \hat{F}_2(\underline{x_2}(t), \theta_2(t)) - \hat{F}_2(\underline{x_2}(t), \theta_2(t)) \\ =& -x_3(t) + x_1(t)x_2(t) + u_d(t) + \tilde{\theta}_2^T\vartheta_2(x_1(t), x_2(t)) \\ & + \epsilon_2(x_1(t), x_2(t)) - \theta_2^T\vartheta_2(x_1(t), x_2(t)). \end{aligned} \tag{42}$$

Let the virtual control input be expressed by

$$\begin{aligned} u_d(t) = & -k_{13}e_2(t) + x_1(t)e_1(t) - k_{23}\text{sign}(e_2(t)) + x_3(t) \\ & - x_1(t)x_2(t) + \theta_2^T\vartheta_2(x_1(t), x_2(t)) \end{aligned} \tag{43}$$

Design the fractional-order adaptation law as

$${}_0^C\mathcal{D}_t^\alpha \theta_2(t) = -e_2(t)\vartheta_2(x_1(t), x_2(t)) - \rho_2\theta_2(t), \tag{44}$$

where $k_{13} > 0$, $k_{23} > \bar{\epsilon}_2$ ($\bar{\epsilon}_2$ are design parameters with $\|\epsilon_2(x_1(t), x_2(t))\| \le \bar{\epsilon}_2$), $\rho_2 > 0$. Substitute it into Equation (43). By multiplying $e_2(t)$ with Equation (42), we get

$$\begin{aligned} e_2(t){}_0^C\mathcal{D}_t^\alpha e_2(t) =& -k_{13}e_2^2(t) + x_1(t)e_1(t)e_2(t) - k_{23}|e_2(t)| \\ & + e_2(t)\tilde{\theta}_2^T\vartheta_2(x_1(t), x_2(t)) + e_2(t)\epsilon_2(x_1(t), x_2(t)). \end{aligned} \tag{45}$$

Choose the Lyapunov function $V_3(t)$ as

$$V_3(t) = \frac{1}{2}e_2^2(t) + \frac{1}{2}\tilde{\theta}_2^T(t)\tilde{\theta}_2(t) + V_2(t) \tag{46}$$

Employing Lemma 3 with Equations (39), (44), and (45) together gives

$$\begin{aligned} {}_0^C\mathcal{D}_t^\alpha V_3(t) =& {}_0^C\mathcal{D}_t^\alpha V_2(t) + \frac{1}{2}{}_0^C\mathcal{D}_t^\alpha e_2^2(t) + \frac{1}{2}{}_0^C\mathcal{D}_t^\alpha \tilde{\theta}_2^T(t)\tilde{\theta}_2(t) \\ \le & -\kappa_2 V_2(t) - x_1(t)e_1(t)e_2(t) + H_1 + e_2(t){}_0^C\mathcal{D}_t^\alpha e_2(t) \\ & + \tilde{\theta}_2^T(t){}_0^C\mathcal{D}_t^\alpha \tilde{\theta}_2(t)) \\ \le & -\kappa_2 V_2(t) + H_1 - k_{13}e_2^2(t) - \rho_2\tilde{\theta}_2^T(t)\theta_2(t) \\ =& -\kappa_2 V_2(t) + H_1 - k_{13}e_2^2(t) - \rho_2\tilde{\theta}_1^T(t)\tilde{\theta}_1(t) \\ & - \rho_2\tilde{\theta}_1^T(t)\theta_1^* \\ \le & -\kappa_2 V_2(t) + H_1 - k_{13}e_2^2(t) - \frac{\rho_2}{2}\tilde{\theta}_2^T(t)\tilde{\theta}_2(t) \\ & + \frac{\rho_2}{2}\theta_2^{*T}\theta_2^* \\ \le & -\kappa_3 V_3(t) + H_2 \end{aligned} \tag{47}$$

where $\kappa_3 = \min\{\kappa_2, 2k_{13}, \rho_2\}$ and $H_2 = H_1 + \frac{1}{2}\rho_1\theta_2^{*T}\theta_2^*$ are positive constants.

Theorem 1. *In system (16), if the control outputs are formulated by Equations (18), (31), and (43), and the adaptation law is designed as Equations (32) and (44), then the tracking error $e(t)$ must tend to a sufficiently small neighborhood of the equilibrium point.*

Proof: Applying (47), one gets

$$ {}_0^C\mathcal{D}_t^\alpha V_3(t) + \bar{Q}(t) = -\kappa_3 V_3(t) + H_2 \tag{48}$$

where $\bar{Q}(t) \geq 0$. By the implementation of the Laplace transform on Equation (48), we obtain

$$\begin{aligned} V_3(s) &= \frac{s^{\alpha-1}}{s^\alpha + \kappa_3}V_3(0) + \frac{H_2}{s(s^\alpha + \kappa_3)} - \frac{M(s)}{s^\alpha + \kappa_3} \\ &= \frac{s^{\alpha-1}}{s^\alpha + \kappa_3}V_3(0) + \frac{s^{\alpha-(1+\alpha)}H_2}{s^\alpha + \kappa_3} - \frac{M(s)}{s^\alpha + \kappa_3} \end{aligned} \tag{49}$$

where $V_3(s)$ and $M(s)$ are given by the Laplace transform on $V_3(t)$ and $\bar{Q}(t)$, respectively.

By Equations (4), (49), $V_3(t)$ can be rearranged as

$$\begin{aligned} V_3(t) = {} & V_3(0)E_{\alpha,1}(-\kappa_3 t^\alpha) + H_2 t^\alpha E_{\alpha,1+\alpha}(-\kappa_3 t^\alpha) \\ & - \bar{Q}(t) * t^{-1}E_{\alpha,0}(-\kappa_3 t^\alpha) \end{aligned} \tag{50}$$

where $*$ denotes the convolution between functions. Since $\bar{Q}(t)$ and $t^{-1}E_{\alpha,0}(-\kappa_3 t^\alpha)$ are non-negative,

$$\bar{Q}(t) * t^{-1}E_{\alpha,0}(-\kappa_3 t^\alpha) \geq 0.$$

Additionally, we have

$$|V_3(t)| \leq |V_3(0)|E_{\alpha,1}(-\kappa_3 t^\alpha) + H_2 t^\alpha E_{\alpha,1+\alpha}(-\kappa_3 t^\alpha). \tag{51}$$

Note that $\arg(-\kappa_3 t^\alpha) = -\pi$, $|-\kappa_3 t^\alpha| \geq 0$ for any $t \geq 0$ and $\alpha \in (0, 2)$. Employing Lemma 2, we deduce that there is a positive constant C with

$$|E_{\alpha,1}(-\kappa_3 t^\alpha)| \leq \frac{C}{1 + \kappa_3 t^\alpha}. \tag{52}$$

It follows from Equation (52) that

$$\lim_{t\to\infty} |V_3(0)|E_{\alpha,1}(-\kappa_3 t^\alpha) = 0. \tag{53}$$

Therefore, for an arbitrary positive constant ε, there exists a positive constant t_1 fulfilling that

$$|V_3(0)|E_{\alpha,1}(-\kappa_3 t^\alpha) < \frac{\varepsilon}{3}, \quad \forall t > t_1. \tag{54}$$

On the other hand, by employing Lemma 1, we get

$$E_{\alpha,\alpha+1}(-\kappa_n t^\alpha) = \frac{1}{\Gamma(1)\kappa_n t^\alpha} + o\left(\frac{1}{|\kappa_n t^\alpha|^{1+1}}\right). \tag{55}$$

From Equation (55), for an arbitrary $\varepsilon > 0$, there is a positive constant t_2 with

$$H_2 t^\alpha E_{\alpha,\alpha+1}(-\kappa_3 t^\alpha) \leq \frac{H_2}{\kappa_3} + \frac{\varepsilon}{3}, \quad \forall t > t_2. \tag{56}$$

Note that the design parameter can be adjusted with $\frac{H_2}{\kappa_3} \leq \frac{\varepsilon}{3}$. Thus, coupling of Equations (51), (54), and (56) yields

$$|V_3(t)| < \varepsilon. \tag{57}$$

In view of Equation (57) and the definition of $V_3(t)$, we conclude that all signals and estimation errors are bounded in the closed-loop system. Further, the tracking signal $e(t)$ will ultimately tend toward a sufficiently small neighborhood of the equilibrium point with radius $\varepsilon \geq \frac{1}{2}e^2(t)$ for every $t > \min\{t_1, t_2\}$. □

Remark 1. *Theorem 1 can be extended to the stability analysis of many other FONSs. Employing fractional-order Lyapunov stability criterion. we know that if there are two positive constants ϕ_1, ϕ_2 such that ${}_0^C\mathcal{D}_t^\alpha V(t) \leq -\phi_1 V(t) + \phi_2$, where $V(t) = \frac{1}{2}y^T(t)y(t)$ is a Lyapunov function, then $y(t) \in \mathbb{R}^n$ is globally bounded and $y(t) \leq \frac{\phi_2}{\phi_1}$ holds whenever the time variable t is sufficiently large.*

Remark 2. *In practice, the system parameters σ and γ for the model of FOPMSM are uncertain in general. Thereby, we can take advantage of the RBFNNs and adopt the corresponding adaptation law to estimate the unknown system parameters, analogizing to our proposed estimation formula (25). For the sake of simplicity, we assume that the system parameters are constants.*

Remark 3. *In the proposed adaptive NN backstepping control scheme, the designed controller determined by Equations (20), (31), and (43) is apparently simpler than the ones without using NN backstepping technique. Meanwhile, it is able to avert superfluous terms aroused by repeated derivation on virtual control inputs. This is beneficial especially for FONSs, in which there are a larger amount of complicated terms of fractional derivatives. For the detail, the readers may refer to Appendix B of the literature [48].*

4. NUMERICAL SIMULATION EXAMPLE

Let us consider the next non-linear FOPMSM by setting $\sigma = 5.6$, $\gamma = 230$ and $x_i(t) = y_i(t)$ $(i = 1, 2, 3)$ in system (16):

$$\begin{cases} {}_0^C\mathcal{D}_t^\alpha y_1(t) = 5.6(y_2(t) - y_1(t)), \\ {}_0^C\mathcal{D}_t^\alpha y_2(t) = -y_2(t) - y_1(t)y_3(t) + 230y_1(t), \\ {}_0^C\mathcal{D}_t^\alpha y_3(t) = -y_3(t) + y_1(t)y_2(t) + u_d(t). \end{cases} \tag{58}$$

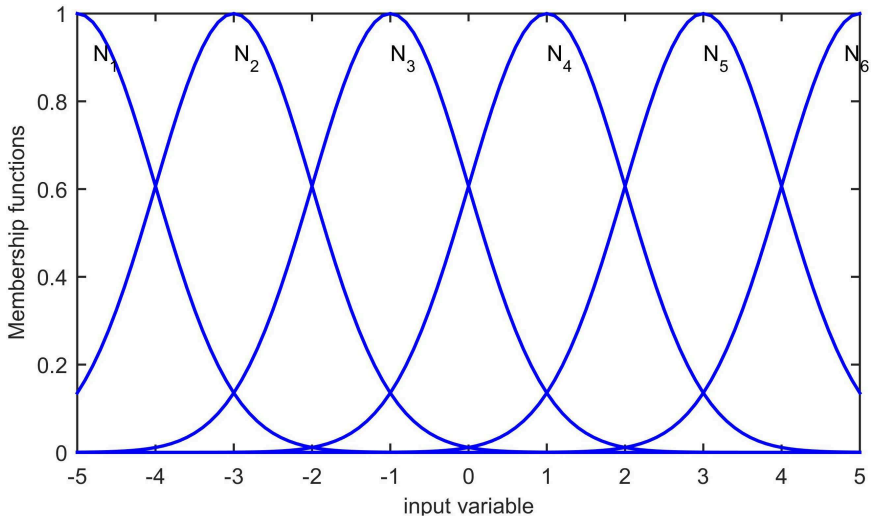

FIGURE 2 | The radial basis functions for RBFNN.

system is proceeded under the initial condition $y_0 = (-2, -0.8, 0.6)$. Given a reference signal $y_d(t) = \sin t$. The chosen parameters k_{1i} $(i = 1, 2, 3)$ should be >0. However, if k_{1i} are too large, the control gain will increase, which will consume more control energy. Therefore, in the simulation, the selected parameters k_{1i} are very small such that the synchronization control performs perfectly. This also shows the effectiveness of our control algorithm from another viewpoint. The adaptive parameters change much faster when the parameters are selected much larger. Based on the above considerations, The control parameters are selected as $k_{11} = k_{12} = 1$, $k_{13} = 3$, $\rho_1 = \rho_2 = 0.5$, then we have $\kappa_1 = \kappa_2 = \kappa_3 = 0.5$.

In the aforementioned settings, there are two RBFNNs:

The first one, endowed with the input $y_1(t)$, relies on the Gaussian radial basis functions expressed by

$$\vartheta_1(y_1(t)) = \exp\left[-\frac{1}{2}(y_1(t)+5)^2\right], \quad \vartheta_2(y_1(t)) = \exp\left[-\frac{1}{2}(y_1(t)+3)^2\right],$$
$$\vartheta_3(y_1(t)) = \exp\left[-\frac{1}{2}(y_1(t)+1)^2\right], \quad \vartheta_4(y_1(t)) = \exp\left[-\frac{1}{2}(y_1(t)-1)^2\right],$$
$$\vartheta_5(y_1(t)) = \exp\left[-\frac{1}{2}(y_1(t)-3)^2\right], \quad \vartheta_6(y_1(t)) = \exp\left[-\frac{1}{2}(y_1(t)-5)^2\right],$$

respectively. The radial basis functions are shown in **Figure 2**. The initial condition is taken as $\theta_1(0) = [1, 1, 1, 1, 1, 1]^T \in \mathbb{R}^6$, uniformly distributed on $[-5, 5]$.

Another RBFNN utilizes $y_1(t)$ and $y_2(t)$ as its inputs. Choose the Gaussian radial basis functions to be the same as that of the previous RBFNN for every input. The initial condition is fixed as $\theta_2(0) = [1, 1, \cdots, 1]^T \in \mathbb{R}^{36}$.

On the basis of the above settings, the drive system of FOPMSM is simulated as follows:

Firstly, when $\alpha = 0.98$ and $u_d(t) = 0$, the chaotic phenomenon of the FOPMSM drive system is tested, demonstrating that system (58) is not stable, as illustrated in **Figure 3**.

Secondarily, we apply the proposed adaptive RBFNN backstepping method in the control procedure of chaotic FOPMSM, which is depicted in **Figure 4**.

Finally, as a summary, it is evident that the proposed controller makes an effective effort to restrain the chaos of FOPMSM drive system, and it embodies desirable performance during the signal tracking.

5. CONCLUSION

This work provides a framework to study stabilization control of chaotic FOPMSMs on the basis of extended Lyapunov stability criterion. Our results as well as numerical simulations indicate that when the proposed adaptive NN backstepping-based control scheme is employed to control chaotic FOPMSMs, it indeed facilitates to overcome the inherent drawback "explosion of complexity." It is demonstrated that chaos and oscillation may appear apparently in the system when the system is uncontrolled. Through the control proceeding, the variables become regular, the chaos oscillation is suppressed, and the task of signal tracking is perfectly accomplished. The problem about how to further construct an adaptive NN backstepping control scheme for generalized FOPMSMs with more input uncertainties and non-linearities is open, which is one task of our future works.

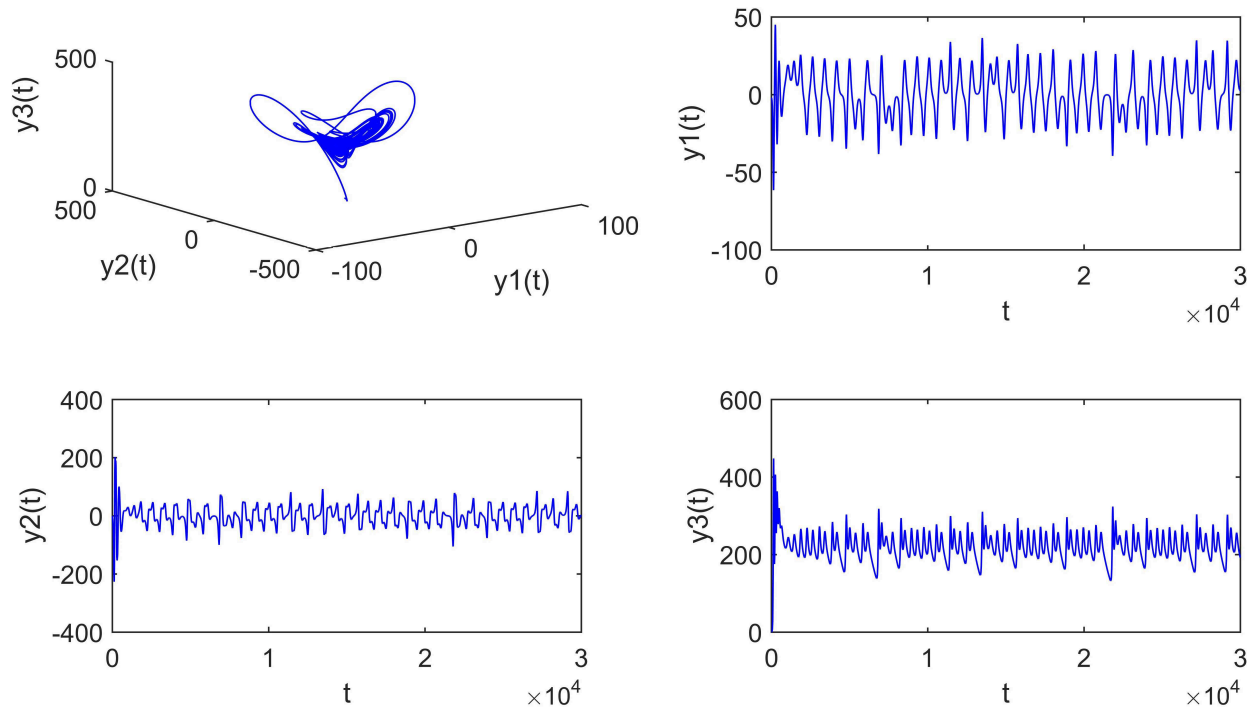

FIGURE 3 | Dynamic behavior of FOPMSM.

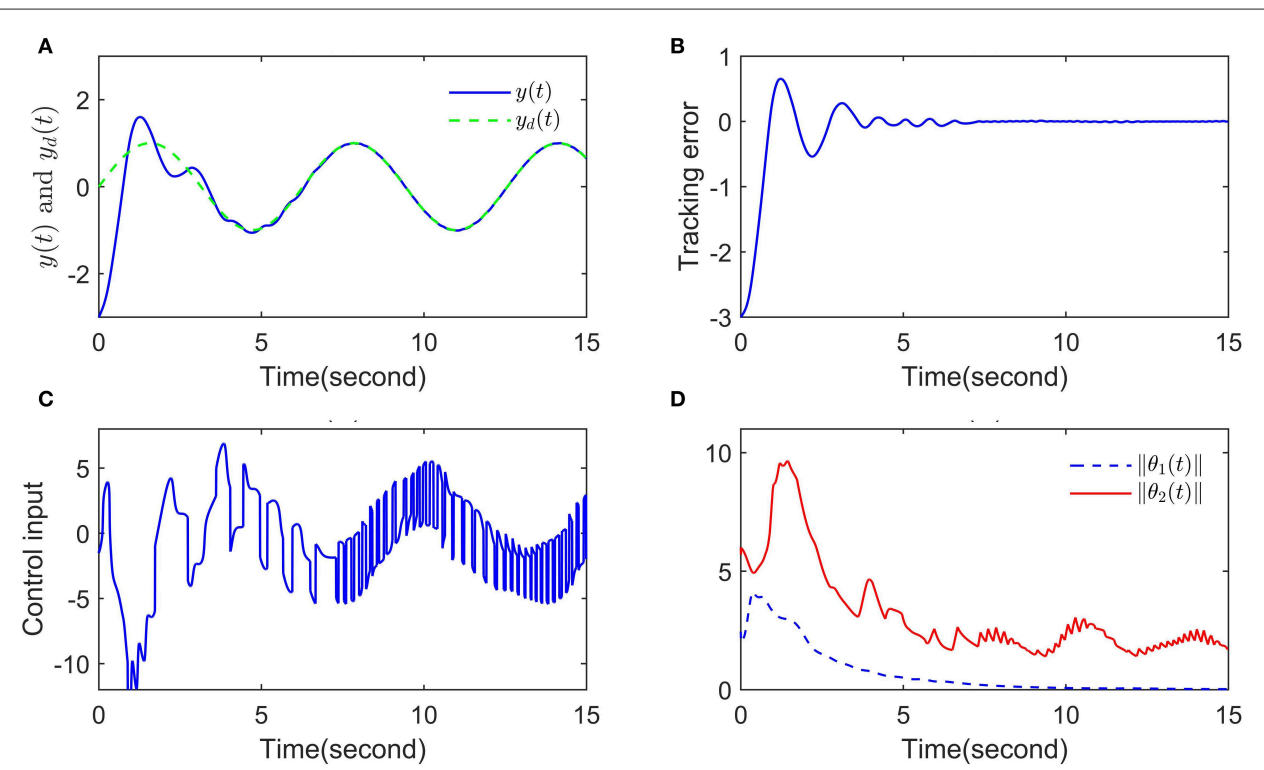

FIGURE 4 | The simulation diagrams, **(A)** The signals $y(t)$ and $y_d(t)$, **(B)** The tracking error, **(C)** The control input, **(D)** The parameter norms of RBFNN.

DATA AVAILABILITY STATEMENT

All datasets generated for this study are included in the article/supplementary material.

AUTHOR CONTRIBUTIONS

GX, FL, and BQ contributed the conception and design of the study. GX organized the literature. FL performed the design of figures. GX wrote the first draft of the manuscript. All authors contributed to the manuscript revision, read, and approved the submitted version.

FUNDING

This work was supported the Basic Ability Promotion Project for Young and Middle-aged Teachers of Guangxi Colleges and Universities (Grant No. 2019KY0669), the Scientific Research Development Fund of Young Researchers of Guangxi University of Finance and Economics (Grant No. 2019QNB18).

ACKNOWLEDGMENTS

The authors would like to express their sincere gratitude to the reviewers and the editors for their careful reviews and constructive recommendations.

REFERENCES

1. Podlubny I. *Fractional Differential Equations*. San Diego, CA: Academic Press (1999).
2. Bagley RL, Torvik PJ. Fractional calculus–a different approach to the analysis of viscoelastically damped structures. *AIAA J*. (1983) **21**:741–8. doi: 10.2514/3.8142
3. Chen W, Ye L, Sun H. Fractional diffusion equations by the Kansa method. *Comput Math Appl*. (2010) **59**:1614–20. doi: 10.1016/j.camwa.2009.08.004
4. Radwan AG, Elwakil AS, Soliman AM. Fractional-order sinusoidal oscillators: design procedure and practical examples. *IEEE Trans Circuits Syst I Reg Pap*. (2008) **55**:2051–63. doi: 10.1109/TCSI.2008.918196
5. Wang J, Ibrahim AG, Fečkan M. Nonlocal impulsive fractional differential inclusions with fractional sectorial operators on Banach spaces. *Appl Math Comput*. (2015) **257**:103–18. doi: 10.1016/j.amc.2014.04.093
6. Podlubny I. Geometric and physical interpretation of fractional integration and fractional differentiation. *Fract Calculus Appl Anal*. (2002) **5**:367–86. doi: 10.1016/j.sigpro.2014.05.026
7. Baleanu D, Golmankhaneh AK, Golmankhaneh AK. On electromagnetic field in fractional space. *Nonlin Anal Real World Appl*. (2010) **11**:288–92. doi: 10.1016/j.nonrwa.2008.10.058
8. Kilbas AAA, Srivastava HM, Trujillo JJ. *Theory and Applications of Fractional Differential Equations*. Vol. 204. Amsterdam: Elsevier Science Limited (2006).
9. Tsirimokou G, Psychalinos C, Elwakil AS. Fractional-order electronically controlled generalized filters. *Int J Circuit Theory Appl*. (2017) **45**:595–612. doi: 10.1002/cta.2250
10. Tsirimokou G, Psychalinos C, Elwakil A. *Design of CMOS Analog Integrated Fractional-Order Circuits: Applications in Medicine and Biology*. Cham: Springer (2017).
11. Zhou Y, Liu H, Cao J, Li S. Composite learning fuzzy synchronization for incommensurate fractional-order chaotic systems with time-varying delays. *Int J Adapt Control*. (2019) 33:1739–58. doi: 10.1002/acs.2967
12. Wang LX. *Adaptive Fuzzy Systems and Control: Design and Stability Analysis*. Englewood Cliffs, NJ: Prentice-Hall, Inc. (1994).
13. Radwan AG, Soliman A, Elwakil AS, Sedeek A. On the stability of linear systems with fractional-order elements. *Chaos Solit Fract*. (2009) **40**:2317–28. doi: 10.1016/j.chaos.2007.10.033
14. You X, Song Q, Zhao Z. Global Mittag-Leffler stability and synchronization of discrete-time fractional-order complex-valued neural networks with time delay. *Neural Netw*. (2020) **122**:382–94. doi: 10.1016/j.neunet.2019.11.004
15. You X, Song Q, Zhao Z. Existence and finite-time stability of discrete fractional-order complex-valued neural networks with time delays. *Neural Netw*. (2020) **123**:248–60. doi: 10.1016/j.neunet.2019.12.012
16. Liu H, Pan Y, Cao J, Zhou Y, Wang H. Positivity and stability analysis for fractional-order delayed systems: a T-S fuzzy model approach. *IEEE Trans Fuzzy Syst*. (2020). doi: 10.1109/TFUZZ.2020.2966420. [Epub ahead of print].
17. Kurths J, Boccaletti S, Grebogi C, Lai YC. Introduction: control and synchronization in chaotic dynamical systems. *Chaos*. (2003) **13**:126–7. doi: 10.1063/1.1554606
18. Radwan AG, Moaddy K, Salama KN, Momani S, Hashim I. Control and switching synchronization of fractional order chaotic systems using active control technique. *J Adv Res*. (2014) **5**:125–32. doi: 10.1016/j.jare.2013.01.003
19. Kuroe Y, Hayashi S. Analysis of bifurcation in power electronic induction motor drive systems. In: *20th Annual IEEE Power Electronics Specialists Conference*. Milwaukee, WI: IEEE (1989). p. 923–30.
20. Chen J, Chau K, Siu S, Chan C. Experimental stabilization of chaos in a voltage-mode DC drive system. *IEEE Trans Circuits Syst I Fundam Theory Appl*. (2000) **47**:1093–5. doi: 10.1109/81.855466
21. Robert B, Alin F, Goeldel C. Aperiodic and chaotic dynamics in hybrid step motor-new experimental results. In: *ISIE 2001. 2001 IEEE International Symposium on Industrial Electronics Proceedings (Cat. No. 01TH8570)*. Vol. 3. Pusan: IEEE (2001). p. 2136–41.
22. Gao Y, Chau K, Ye S. A novel chaotic-speed single-phase induction motor drive for cooling fans. In: *Fourtieth IAS Annual Meeting. Conference Record of the 2005 Industry Applications Conference, 2005*. Vol. 2. IEEE (2005). p. 1337–41.
23. Wei D, Luo X. Passive adaptive control of chaos in synchronous reluctance motor. *Chin Phys B*. (2008) **17**:92–7. doi: 10.1088/1674-1056/17/1/017
24. Chau K, Chen J. Modeling, analysis, and experimentation of chaos in a switched reluctance drive system. *IEEE Trans Circuits Syst I Fundam Theory Appl*. (2003) **50**:712–6. doi: 10.1109/TCSI.2003.811030
25. Ott E, Grebogi C, Yorke JA. Controlling chaos. *Phys Rev Lett*. (1990) **64**:1196. doi: 10.1103/PhysRevLett.64.1196
26. Ren H, Liu D. Nonlinear feedback control of chaos in permanent magnet synchronous motor. *IEEE Trans Circuits Syst II Express Briefs*. (2006) **53**:45–50. doi: 10.1109/TCSII.2005.854592
27. Pan Y, Sun T, Yu H. On parameter convergence in least squares identification and adaptive control. *Int J Robust Nonlin*. (2019) 29:2898–911. doi: 10.1002/rnc.4527
28. Liu H, Wang, H, Cao J, Alsaedi A, Hayat T. Composite learning adaptive sliding mode control of fractional-order nonlinear systems with actuator faults. *J Franklin Inst*. (2019) 356:9580–99. doi: 10.1016/j.jfranklin.2019.02.042
29. Luo XS, Wang BH, Fang JQ, Wei DQ. Robust adaptive dynamic surface control of chaos in permanent magnet synchronous motor. *Phys Lett A*. (2007) **363**:71–7. doi: 10.1016/j.physleta.2006.10.074
30. Balasubramaniam P, Muthukumar P, Ratnavelu K. Theoretical and practical applications of fuzzy fractional integral sliding mode control for fractional-order dynamical system. *Nonlin Dyn*. (2015) **80**:249–67. doi: 10.1007/s11071-014-1865-4
31. Li H, Wang J, Wu L, Lam HK, Gao Y. Optimal guaranteed cost sliding-mode control of interval type-2 fuzzy time-delay systems. *IEEE Trans Fuzzy Syst*. (2018) **26**:246–57. doi: 10.1109/TFUZZ.2017.2648855
32. Harb AM. Nonlinear chaos control in a permanent magnet reluctance machine. *Chaos Solit Fract*. (2004) **19**:1217–24. doi: 10.1016/S0960-0779(03)00311-4
33. Stotsky A, Hedrick J, Yip P. The use of sliding modes to simplify the backstepping control method. In: *Proceedings of the 1997 American Control Conference (Cat. No. 97CH36041)*. Vol. 3. Albuquerque, NM: IEEE (1997). p. 1703–8. doi: 10.1109/ACC.1997.610875

34. Liu H, Pan Y, Li S, Chen Y. Adaptive fuzzy backstepping control of fractional-order nonlinear systems. *IEEE Trans Syst Man Cybern Syst*. (2017) **47**:2209–17. doi: 10.1109/TSMC.2016.2640950
35. Liu H, Pan Y, Jinde C, Hongxing W, Yan Z. Adaptive neural network backstepping control of fractionial-order nonlinear systems with actuator faults. *IEEE Trans Neural Netw Learn Syst*. (2020). doi: 10.1109/TNNLS.2020.2964044. [Epub ahead of print].
36. Gao H, Song Y, Wen C. Event-triggered adaptive neural network controller for uncertain nonlinear system. *Inform Sci*. (2020) **506**:148–60. doi: 10.1016/j.ins.2019.08.015
37. Bai W, Li T, Tong S. NN reinforcement learning adaptive control for a class of nonstrict-feedback discrete-time systems. *IEEE Trans Cybern*. (2020). doi: 10.1109/TCYB.2020.2963849. [Epub ahead of print].
38. Boulkroune A, Tadjine M, M'Saad M, Farza M. Fuzzy adaptive controller for MIMO nonlinear systems with known and unknown control direction. *Fuzzy Sets Syst*. (2010) **161**:797–820. doi: 10.1016/j.fss.2009.04.011
39. Boulkroune A, Bouzeriba A, Bouden T. Fuzzy generalized projective synchronization of incommensurate fractional-order chaotic systems. *Neurocomputing*. (2016) **173**:606–14. doi: 10.1016/j.neucom.2015.08.003
40. Shukla MK, Sharma BB. Backstepping based stabilization and synchronization of a class of fractional order chaotic systems. *Chaos Solit Fract*. (2017) **102**:274–84. doi: 10.1016/j.chaos.2017.05.015
41. Zhou J, Wen C, Wang W, Yang F. Adaptive backstepping control of nonlinear uncertain systems with quantized states. *IEEE Trans Autom Control*. (2019) **64**:4756–63. doi: 10.1109/TAC.2019.2906931
42. Yip PP, Hedrick JK. Adaptive dynamic surface control: a simplified algorithm for adaptive backstepping control of nonlinear systems. *Int J Control*. (1998) **71**:959–79. doi: 10.1080/002071798221650
43. Kwan C, Lewis FL. Robust backstepping control of induction motors using neural networks. *IEEE Trans Neural Netw*. (2000) **11**:1178–87. doi: 10.1109/72.870049
44. Dawson DM, Carroll JJ, Schneider M. Integrator backstepping control of a brush DC motor turning a robotic load. *IEEE Trans Control Syst Technol*. (1994) **2**:233–44. doi: 10.1109/87.317980
45. Fateh S, Fateh MM. Adaptive fuzzy control of robot manipulators with asymptotic tracking performance. *J Control Autom Electric Syst*. (2020) **31**:52–61. doi: 10.1007/s40313-019-00496-5
46. Li Y, Chen Y, Podlubny I. Mittag-Leffler stability of fractional order nonlinear dynamic systems. *Automatica*. (2009) **45**:1965–9. doi: 10.1016/j.automatica.2009.04.003
47. Li Y, Tong S. Adaptive neural networks decentralized FTC design for nonstrict-feedback nonlinear interconnected large-scale systems against actuator faults. *IEEE Trans Neural Netw Learn Syst*. (2016) **28**:2541–54. doi: 10.1109/TNNLS.2016.2598580
48. Yu J, Chen B, Yu H, Gao J. Adaptive fuzzy tracking control for the chaotic permanent magnet synchronous motor drive system via backstepping. *Nonlin Anal Real World Appl*. (2011) **12**:671–81. doi: 10.1016/j.nonrwa.2010.07.009
49. Tong S, Li Y. Adaptive fuzzy output feedback control of MIMO nonlinear systems with unknown dead-zone inputs. *IEEE Trans Fuzzy Syst*. (2012) **21**:134–46. doi: 10.1109/TFUZZ.2012.2204065

Conflict of Interest: The authors declare that the research was conducted in the absence of any commercial or financial relationships that could be construed as a potential conflict of interest.

frontiers in Physics

BRIEF RESEARCH REPORT
published: 05 May 2020
doi: 10.3389/fphy.2020.00122

Finite-Time Neural Network Backstepping Control of an Uncertain Fractional-Order Duffing System With Input Saturation

Hui Lv[1] *and Xiulan Zhang*[2]*

[1] Department of Applied Mathematics, Huainan Normal University, Huaina, China, [2] School of Mathematics and Physics, Guangxi University for Nationalities, Nanning, China

In this paper, neural network (NN) control of the fractional-order Duffing system (FODS) by using a backstepping method within finite time in the presence of input saturation has been investigated. A fractional-order filter with an order lying on the interval (1,2) was used to estimate the virtual input together with its fractional derivative, and this showed that the estimation error tends to a small region in some finite time. Fractional-order law is designed for the parameter of the NN, and an adaptive NN controller was given. The proposed method drives the tracking error, tending to an arbitrary small region within a finite time. The simulation results verify the validity of the proposed method.

Keywords: finite time control, fractional-order system, fractional filter, adaptive neural network control, chaos control

OPEN ACCESS

Edited by:
Muhammad Javaid, University of Management and Technology, Lahore, Pakistan

Reviewed by:
Lin Zhao, Qingdao University, China
Peijun Wang, Anhui Normal University, China
Shumin Ha, Shaanxi Normal University, China

***Correspondence:**
Xiulan Zhang
xlzhang@gxun.edu.cn

Specialty section:
This article was submitted to Mathematical Physics, a section of the journal Frontiers in Physics

Received: *14 February 2020*
Accepted: *27 March 2020*
Published: *05 May 2020*

Citation:
Lv H and Zhang X (2020) Finite-Time Neural Network Backstepping Control of an Uncertain Fractional-Order Duffing System With Input Saturation. Front. Phys. 8:122. doi: 10.3389/fphy.2020.00122

1. INTRODUCTION

It is a well-known fact that classical differential operators are local operators and cannot describe some complex properties. For example, Brownian motion, viscoelastic materials, anomalous diffusion, and irregular fluctuations in the turbulent velocity field have memory problems. Fractional-order differential operators are non-local and can well-characterize memory, genetic, and global correlation in the real world. The physical process is an important tool for describing physical processes and complex mechanics [1, 2]. In fact, fractional derivatives exhibit several advantages over integer derivatives: (1) fractional derivatives have a global correlation and can reflect the historical dependence of function development in the system; (2) the fractional derivative model is more consistent with the experimental results when simulating some complex properties, and the effect is better; and (3) when simulating complex mechanics and physical process problems, the expression of fractional-order model is more concise and the meaning is clearer [3, 4]. In view of these three advantages of fractional derivative, scholars have gradually used fractional differential equations to describe some practical problems. In recent decades, fractional calculus and fractional differential equations have developed rapidly and have gradually matured, and they have also been applied in other disciplines, such as quantum mechanics, economics and finance, turbulence, viscoelasticity theory, and superconductivity. A large number of papers on fractional calculus and fractional differential equations and works and so on have appeared [5–10]. The research contents include the theory and application of fractional calculus, the existence and uniqueness of solutions to the Cauchy problem, stability, controllability, the existence and uniqueness of solutions to boundary value problems, analytical solutions, and numerical algorithms. However, some research methods in integer-order differential equations cannot be directly applied to the study of fractional-order differential equations, and new theories and methods need to be sought. There

are many research fields for integer-order differential equations, and research fields for fractional-order differential equations are limited, and the solution mapping of fractional-order differential equations does not have a semigroup property. Therefore, there are many difficulties in the study of fractional differential equations.

On the other hand, it is well-known that chaos control is a research hot topic and has some successful applications. With the in-depth study of chaotic systems, people began to try to migrate the synchronization method of integer-order chaotic systems to the synchronization of fractional-order chaotic systems (FOCSs). This natural idea is not easy to implement. For this reason, some people try to use the Laplace transform method and time-frequency domain transformation method. By solving the s^{α} by using the Laplace transform method, finite time control was investigated in Tavazoei and Haeri [5]. Up to now, many control methods have been used to control or synchronize FOCSs, for example, adaptive robust control, adaptive fuzzy control (AFC), adaptive neural network control (ANNC), sliding mode control (SMC), command filtered control (CFC), etc. [11–18]. In Pham et al. [19], a three-dimensional FOCS that had no equilibrium was introduced and investigated, and it was shown that the system shows chaotic phenomenon when the order <2.7. In Zhang et al. [20], the lag projective synchronization of FOCSs with time-varying delays was considered by using a comparison principle of linear fractional equation. In Liu et al. [16], the NN was used to control FOCSs in the presence of input faults. It should be mentioned that above works do not consider the finite time stability is. Up to now, the finite time control of the FOCS has rarely been investigated [21–23].

Inspired with above discussion, we will address the finite time NN control of the fractional-order Deffuing system (FODS) with input saturation. Take some related works, such as Liu et al. [16] and Ha et al. [24, 25], the our work has included several features: (1) a fractional-order filter whose order lies on (1,2), designed to evaluate the immediate controller and its fractional derivative within some finite time. However, a fractional filter was also used in Liu et al. [16] and Ha et al. [25] whose order lies on (0, 1), and, in addition, the finite-time stability cannot be guaranteed; (2) to cancel the estimation error of the filter, a fractional-order compensated signal was proposed. Compared with the compensated signals proposed in Ha et al. [24], our method can obtain a more rapid convergence; and (3) in the FOCS's mode, we have considered the case of input saturation.

2. PRELIMINARIES

2.1. Description of the NN

The NN with three layers is expressed as

$$y_j(s,\mu_j)=\sum_{\eta=1}^{h}\omega_{j\eta}\varphi_{j\eta}\left(\sum_{i=1}^{n}\nu_{\eta i}s_i+\gamma_\eta\right)=\mu_j^T\chi_j(\cdot), \tag{1}$$

where $n, h, and m \in \mathbb{N}_+$ denote the amount of neurons three layers (input, middle, and output), $\mu_j = \begin{bmatrix}\omega_{j1}\\ \vdots \\ \omega_{jh}\end{bmatrix}$, and $\chi_j = \begin{bmatrix}\varphi_{j1}\left(\sum_{i=1}^{n}\nu_{1i}s_i+\gamma_1\right)\\ \vdots \\ \varphi_{jh}\left(\sum_{i=1}^{n}\nu_{hi}s_i+\gamma_h\right)\end{bmatrix}$. ν_{ji} denotes a weight whose value is on the interval $[-1, 1]$. Usually, $\varphi(\cdot)$ can be defined by

$$\varphi(\hbar)=\frac{e^{\hbar}-e^{-\hbar}}{e^{\hbar}+e^{-\hbar}}. \tag{2}$$

Then, the NN is given as

$$y=\theta^T\chi(\hbar) \tag{3}$$

with $\theta = \begin{bmatrix}\mu_1^T\\ \mu_2^T\\ \vdots \\ \mu_m^T\end{bmatrix}$, and $\chi(\hbar) = \begin{bmatrix}\chi_1(\hbar) & 0 & \cdots & 0\\ 0 & \chi_2(\hbar) & \cdots & 0\\ \vdots & \vdots & \ddots & \vdots\\ 0 & 0 & \cdots & \chi_m(\hbar)\end{bmatrix}$. Suppose that $f(\hbar), \hbar \in \mathbb{R}^n$ is unknown, then it can be approximated by the NN as

$$f(x)=\theta^{*T}\chi(\hbar)+\varepsilon(\hbar), \tag{4}$$

with $\varepsilon(\hbar)$ denoting the optimal approximation error, where

$$\theta^*=\arg\min_{\theta}\left[\sup|\hat{f}(\hbar)-f(\hbar)|\right], \tag{5}$$

with $\hat{f}(\hbar)=\theta^T(t)\chi(\hbar)$.

2.2. Basic Lemmas

The q-th fractional integral for a function $g(t)$ is defined as

$$\mathcal{I}^q g(t)=\frac{1}{\Gamma(q)}\int_0^t\frac{g(\tau)}{(t-\tau)^{1-q}}d\tau, \tag{6}$$

with $\Gamma(\cdot)$ representing Euler's function, and the q-th fractional-order derivative for a function $g(t)$, which has a k-th continuous derivative, is

$$\mathcal{D}^q g(t)=\frac{1}{\Gamma(k-q)}\int_0^t\frac{g^{(k)}(\tau)}{(t-\tau)^{q+1-k}}d\tau, \tag{7}$$

where $k-1\le q<k\,(k\in\mathbb{N})$. The following always assumes that $0<q\le 1$ for convenience. The fractional-order calculus has the following properties.

Lemma 1. *[16] For a smooth function $x(t)$, it holds that*

$$\frac{1}{2}\mathcal{D}^{\alpha}x^2(t)\le x(t)\mathcal{D}^{\alpha}x(t). \tag{8}$$

Lemma 2. *[22] Let $V(\zeta)$ be a smooth function satisfying $\mathcal{D}_t^q V(\zeta)+\alpha_1 V^{\alpha_2}(\zeta)\le 0$, $\zeta\in\Omega_1\subset\mathbb{R}^n$, $\alpha_1\in\mathbb{R}^+$, and $0<\alpha_2<1$. Then, one can find $\Omega_2\subset\mathbb{R}^n$, which holds that $V(\zeta)$ begins within Ω_2 will reach a sufficient small region in some finite time T^*.*

Lemma 3. *[23] Assume $g_1, g_2>0$, $0<g_3<1$, and*

$$\mathcal{D}_t^q V(\zeta)+g_1V(\zeta)+g_2V^{g_3}(\zeta)\le 0$$

where $\zeta\in\mathbb{R}^n$. Then, the system is finite time stable.

Lemma 4. *[23] Consider*

$$\begin{cases} \mathcal{D}_t^q \pi_1(t) = F(t), \\ F(t) = -g_4 \text{sign}(\pi_1(t) - \zeta(t)) + \pi_2(t) \\ \mathcal{D}_t^q \pi_2(t) = -g_5 \text{sign}(\pi_2(t) - F(t)), \end{cases}$$

where $\zeta(t) \subset \mathbb{R}$, $g_4, g_5 \in \mathbb{R}^+$. *Let*

$$\hat{e}_1 = \pi_1 - \zeta, \quad \hat{e}_2(t) = F - \mathcal{D}_t^q \zeta.$$

Then, $\hat{e}_1$ *and* $\hat{e}_2$ *are finite time stable.*

3. MAIN RESULTS

The integer-order Duffing system is written as

$$\ddot{y}(t) - y(t) + a\dot{y}(t) + y^3(t) = b\cos(\omega t) \tag{9}$$

where a, b are parameters. Denote $x_1(t) = y(t)$, $x_2(t) = \dot{y}(t)$, $x(t) = [x_1(t), x_2(t)]^T$ and $f(x(t)) = x_1(t) - ax_2(t) - x_1^3(t) + b\cos(\omega t)$. By putting the fractional calculus into system (9) and considering the input saturation, the controlled FODS is written as

$$\begin{cases} \mathcal{D}_t^q x_1(t) = x_2(t), \\ \mathcal{D}_t^q x_2(t) = \text{sat}(u(t)) + d(t) + f(x(t)). \end{cases} \tag{10}$$

in which $\text{sat}: u(t) \rightarrow \text{sat}(u(t))$ is called a saturator. It can be expressed as:

$$\text{sat}(u(t)) = \begin{cases} u_r, & u \geq u_r \\ u(t), & u_l < u(t) < u_r \\ u_l, & u \leq u_l, \end{cases} \tag{11}$$

with $u_r > 0, u_l < 0$. Denoting the term that exceeds the saturation limiter as $\gamma(t)$:

$$\gamma(t) = \begin{cases} u_r - u(t), & u(t) \geq u_r, \\ 0, & u_l < u(t) < u_r, \\ u_l - u(t), & u(t) \leq u_l. \end{cases} \tag{12}$$

For the target, let $x_1(t)$ track a known smooth signal $x_d(t) \in \mathbb{R}$ in finite time. In this paper, we have used the backstepping method. Define $e_1(t) = x_1(t) - x_d(t)$, and let us construct a virtual input $\alpha(t)$, giving us

$$\begin{aligned} \mathcal{D}_t^q e_1(t) &= x_2(t) - \mathcal{D}_t^q x_d(t) \\ &= \alpha(t) + \hat{\alpha}(t) - \alpha(t) + x_2(t) - \hat{\alpha}(t) - \mathcal{D}_t^q x_d(t) \\ &= \alpha(t) + \hat{\alpha}(t) - \alpha(t) + e_2(t) - \mathcal{D}_t^q x_d(t) \end{aligned} \tag{13}$$

with $e_2(t) = x_2(t) - \hat{\alpha}(t)$, and $\hat{\alpha}(t)$ being $\alpha(t)$'s estimation. Noting the estimation error is hard to be canceled, we have designed a compensated signal to solve this problem. Let

$$\mathcal{D}_t^q \beta_1(t) = -k_1\beta_1(t) + \hat{\alpha}(t) - \alpha(t) + \beta_2(t) - c_1 \text{sign}(\beta_1(t)), \tag{14}$$

where $\beta_2(t)$ is given later, $k_1, c_1 > 0$, and $\beta(0) = 0$. Using Lemma 4, we can estimate $\alpha(t)$ and $\mathcal{D}_t^q \alpha(t)$ as

$$\begin{cases} \mathcal{D}_t^q \pi_1(t) = F(t), \\ F(t) = -b_1 \text{sign}(\pi_1(t) - \alpha(t)) + \pi_2(t) \\ \mathcal{D}_t^q \pi_2(t) = -b_2 \text{sign}(\pi_2(t) - F(t)). \end{cases} \tag{15}$$

Thus, (15) and Lemma 4 imply that $\hat{\alpha}(t) = \pi_1(t)$ and $\mathcal{D}_t^q \hat{\alpha}(t) = F(t)$ within finite time. Let

$$\begin{cases} \tilde{e}_1(t) = e_1(t) - \beta_1(t), \\ \tilde{e}_2(t) = e_2(t) - \beta_2(t), \end{cases} \tag{16}$$

where $e_2(t) = x_2(t) - \hat{\alpha}(t)$. Then the victual signal is designed as

$$\alpha(t) = -k_1 e_1(t) + \mathcal{D}_t^q x_d(t) - a_1 \tilde{e}_1^{\nu}(t), \tag{17}$$

with $k_1 \in \mathbb{R}^+$, $\nu \in (0, 1)$. Define $V_1 = \frac{1}{2}\tilde{e}_1^2(t)$, according to Lemma 1, and its fractional-order derivative is

$$\begin{aligned} \mathcal{D}_t^q V_1 &\leq \tilde{e}_1(t) \mathcal{D}_t^q \tilde{e}_1(t) \\ &= \tilde{e}_1(t) \Big[\alpha(t) + \hat{\alpha(t)} - \alpha(t) + e_2(t) \\ &- \mathcal{D}_t^q x_d(t) + k_1\beta_1(t) - \hat{\alpha}(t) + \alpha(t) - \beta_2(t) \\ &+ c_1 \text{sign}(\beta_1(t)) \Big] \\ &= \tilde{e}_1(t) \Big[-k_1\tilde{e}_1(t) - a_1\tilde{e}_1^{\nu}(t) + e_2(t) + k_1\beta_1(t) - \beta_2(t) \\ &+ c_1 \text{sign}(\beta_1(t)) \Big] \\ &= -k_1\tilde{e}_1^2(t) - a_1\tilde{e}_1(t)\tilde{e}_1^{\nu}(t) + \tilde{e}_1(t)e_2(t) - \tilde{e}_1(t)\tilde{e}_2(t) \\ &+ c_1\tilde{e}_1(t)\text{sign}(\beta_1(t)) \\ &= -k_1\tilde{e}_1^2(t) - a_1\tilde{e}_1(t)\tilde{e}_1^{\nu}(t) + \tilde{e}_1(t)\tilde{e}_2(t) \\ &+ c_1\tilde{e}_1(t)\text{sign}(\beta_1(t)). \end{aligned} \tag{18}$$

It follows from (10), (11), (12), and (16) that

$$\begin{aligned} \mathcal{D}_t^q \tilde{e}_2(t) &= \text{sat}(u(t)) + d(t) + f(x(t)) - \mathcal{D}_t^q \hat{\alpha}(t) - \mathcal{D}_t^q \beta_2 \\ &= u(t) + \gamma(t) + d(t) + f(x(t)) - \mathcal{D}_t^q \hat{\alpha}(t) - \mathcal{D}_t^q \beta_2 \\ &= u(t) + \Theta(t) - \mathcal{D}_t^q \hat{\alpha}(t) - \mathcal{D}_t^q \beta_2 \end{aligned} \tag{19}$$

with $\Theta(t) = \gamma(t) + d(t) + f(x(t))$, $\mathcal{D}_t^q \hat{\alpha}(t)$ being driven from (15). The unknown function $\Theta(x)$ in (19) can be approximated by the NN as

$$\hat{\Theta}(t) = \theta^T(t)\chi(x(t)). \tag{20}$$

Let the optimal parameter of NN be $\theta^* = \arg\min_{\theta(t)} \left[\sup_{x(t)} \left| \hat{\Theta}(t) - \Theta(t) \right| \right]$. Define $\tilde{\theta}(t) = \theta(t) - \theta^*$, and $\epsilon(t) = \hat{\Theta}(t) - \Theta(t)$. In fact, according to universal approximation theorem of the NN, we know that, for any continuous non-linear function defined on a compact set, there is a NN in order for the optimal to be as small as possible [16, 26, 27]. Thus, it is possible

for us to assume the optimal estimation error is bounded, i.e., $|\epsilon| \leq \bar{\epsilon}$, where $\bar{\epsilon} \in \mathbb{R}^+$ is a constant. We then have

$$\begin{aligned}\hat{\Theta}(t) - \Theta(t) &= \theta(t)^T\chi(x(t)) - \theta(t)^{*T}\chi(x(t)) + \theta^{*T}\chi(x(t)) \\ &\quad - \Theta(t) = \tilde{\theta}^T(t)\chi(x(t)) - \epsilon_i(t).\end{aligned} \tag{21}$$

To meet the control objective, we can design the compensated signal as

$$\mathcal{D}_t^q\beta_2(t) = -k_2\beta_2(t) - \beta_1(t) - c_2\text{sign}(\beta_2(t)) \tag{22}$$

with $k_2, c_2 > 0$. Then, let us construct the final input as

$$u(t) = -k_2e_2(t) + \mathcal{D}_t^q\hat{\alpha}(t) - \hat{\theta}^T(t)\chi(x(t)) - \sigma\,\text{sign}(\tilde{e}_2(t)) - a_2\tilde{e}_2^{\nu}(t) \tag{23}$$

where $\sigma, a_2 > 0$, and $\sigma \geq \bar{\epsilon}$ can be satisfied. It follows from (22) and (23) into (19) that

$$\begin{aligned}\mathcal{D}_t^q\tilde{e}_2(t) &= -k_2e_2(t) - \hat{\theta}^T(t)\chi(x(t)) - \sigma\,\text{sign}(\tilde{e}_2(t)) \\ &\quad - a_2\tilde{e}_2^{\nu}(t) + \Theta(t) - \mathcal{D}_t^q\beta_2(t) \\ &= -k_2e_2(t) - \tilde{\theta}^T(t)\chi(x(t)) + \epsilon(t) - \sigma\,\text{sign}(\tilde{e}_2(t)) \\ &\quad - a_2\tilde{e}_2^{\nu}(t) + k_2\beta_2(t) \\ &\quad - \tilde{\beta}_1(t) + c_2\text{sign}(\beta_2(t)) \\ &= -k_2\tilde{e}_2(t) - \tilde{\theta}^T(t)\chi(x(t)) + \epsilon(t) - \sigma\,\text{sign}(\tilde{e}_2(t)) \\ &\quad - a_2\tilde{e}_2^{\nu}(t) - \tilde{\beta}_1(t) + c_2\text{sign}(\beta_2(t)).\end{aligned} \tag{24}$$

Then, (24) implies

$$\begin{aligned}\tilde{e}_2(t)\mathcal{D}_t^q\tilde{e}_2(t) &= -k_2\tilde{e}_2^2(t) - \tilde{e}_2(t)\tilde{\theta}^T(t)\chi(x(t)) + \tilde{e}_2(t)\epsilon(t) \\ &\quad - \sigma\tilde{e}_2(t)\text{sign}(\tilde{e}_2(t)) - a_2\tilde{e}_2(t)\tilde{e}_2^{\nu}(t) \\ &\quad - \tilde{e}_2(t)\tilde{e}_1(t) + c_2\tilde{e}_2(t)\text{sign}(\beta_2(t)) \\ &\leq -k_2\tilde{e}_2^2(t) - \tilde{e}_2\tilde{\theta}^T(t)\chi(x)(t) + |\tilde{e}_2(t)|\bar{\epsilon} \\ &\quad - \sigma|\tilde{e}_2(t)| - a_2\tilde{e}_2(t)\tilde{e}_2^{\nu}(t) - \tilde{e}_2(t)\tilde{e}_1(t) \\ &\quad + c_2\tilde{e}_2(t)\text{sign}(\beta_2(t)) \\ &\leq -k_2\tilde{e}_2^2(t) - e_2(t)\tilde{\theta}^T(t)\chi(x(t)) - a_2\tilde{e}_2(t)\tilde{e}_2^{\nu}(t) \\ &\quad - \tilde{e}_2(t)\tilde{e}_1(t) + c_2\tilde{e}_2(t)\text{sign}(\beta_2(t)).\end{aligned} \tag{25}$$

Define

$$V_2(t) = V_1(t) + \frac{1}{2}\tilde{e}_2^2(t). \tag{26}$$

According to (18), (25), and (26), we have

$$\begin{aligned}\mathcal{D}_t^qV_2(t) &= -k_1\tilde{e}_1^2(t) - a_1\tilde{e}_1(t)\tilde{e}_1^{\nu}(t) + c_1\tilde{e}_1(t)\text{sign}(\beta_1(t)) \\ &\quad - k_2\tilde{e}_2^2(t) - \tilde{e}_2\tilde{\theta}^T\chi(x(t)) \\ &\quad - a_2\tilde{e}_2(t)\tilde{e}_2^{\nu}(t) + c_2\tilde{e}_2(t)\text{sign}(\beta_2(t)) = -\sum_{j=1}^{2}k_j\tilde{e}_j^2(t) \\ &\quad - \sum_{j=1}^{2}a_j\tilde{e}_j(t)\tilde{e}_j^{\nu}(t) + \sum_{j=1}^{2}c_j\tilde{e}_j(t)\text{sign}(\beta_j(t)) \\ &\quad - \tilde{e}_2\tilde{\theta}^T(t)\chi(x(t)) \\ &= \sum_{j=1}^{2}\Big[-k_j\tilde{e}_j^2(t) - a_j\tilde{e}_j^{\nu+1}(t) + c_j\tilde{e}_j(t)\text{sign}(\beta_j(t))\Big] \\ &\quad - \tilde{e}_2(t)\tilde{\theta}^T(t)\chi(x(t)).\end{aligned} \tag{27}$$

The fractional-order adaptation law is

$$\mathcal{D}_t^q\theta(t) = \kappa_1\tilde{e}_2(t)\chi(x(t)) - \kappa_1\kappa_2\theta(t) \tag{28}$$

with $\kappa_1, \kappa_2 > 0$.
The following theorem provides a conclusion for the discussion.

Theorem 1. *Let the immediate controller be (17) with the fractional filter (15). Let the compensated signal be (14) and (22). Then, the NN controller (23) with adaptation law (28) drive $e_1(t)$ to be arbitrary small in finite time.*

Proof. Let

$$V(t) = V_2(t) + \frac{1}{2\kappa_1}\tilde{\theta}^T(t)\tilde{\theta}(t). \tag{29}$$

Then, based on (27), (28), and (29), we obtain

$$\begin{aligned}\mathcal{D}_t^qV(t) &\leq \textstyle\sum_{j=1}^{2}\Big[-k_j\tilde{e}_j^2(t) - a_j\tilde{e}_j^{\nu+1}(t) + c_j\tilde{e}_j(t)\text{sign}(\beta_j(t))\Big] \\ &\quad -e_2\tilde{\theta}^T(t)\chi(x(t)) + \tfrac{1}{\kappa_1}\tilde{\theta}^T(t)\mathcal{D}_t^q\theta(t) \\ &= \textstyle\sum_{j=1}^{2}\Big[-k_j\tilde{e}_j^2(t) - a_j\tilde{e}_j^{\nu+1}(t) + c_j\tilde{e}_j(t)\text{sign}(\beta_j(t))\Big] \\ &\quad -\kappa_2\tilde{\theta}^T(t)\theta(t) \\ &\leq \textstyle\sum_{j=1}^{2}\Big[-\frac{2k_j-c_j}{2}\tilde{e}_j^2(t) - a_j\tilde{e}_j^{\nu+1}(t)\Big] - \kappa_2\tilde{\theta}^T(t)\theta(t) \\ &\quad + \textstyle\sum_{j=1}^{2}\frac{c_j}{2} \\ &= \textstyle\sum_{j=1}^{2}\Big[-\frac{2k_j-c_j}{2}\tilde{e}_j^2(t) - a_j\tilde{e}_j^{\nu+1}(t)\Big] - \kappa_2\tilde{\theta}^T(t)(\tilde{\theta}(t) \\ &\quad +\theta^*(t)) + \textstyle\sum_{j=1}^{2}\frac{c_j}{2} \\ &\leq \textstyle\sum_{j=1}^{2}\Big[-\frac{2k_j-c_j}{2}\tilde{e}_j^2(t) - a_j\tilde{e}_j^{\nu+1}(t)\Big] - \frac{3\kappa_2}{4}\tilde{\theta}^T(t)\tilde{\theta}(t) \\ &\quad + \textstyle\sum_{j=1}^{2}\frac{c_j}{2} + \kappa_2\theta^{*T}\theta^*(t).\end{aligned} \tag{30}$$

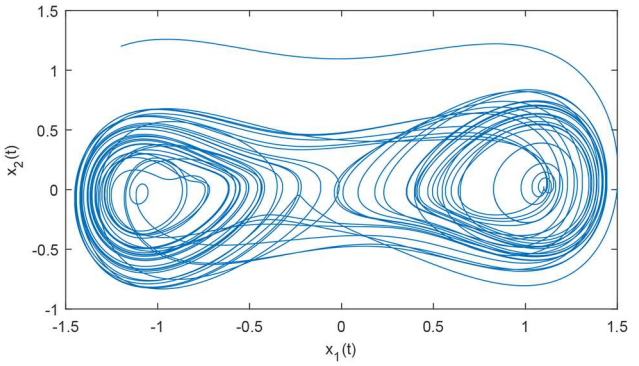

FIGURE 1 | Chaotic phenomenon of uncontrolled FODS (10).

Then, (30) implies

$$\begin{aligned}\mathcal{D}_t^q V(t) \le & \sum_{j=1}^{2}\left[-\frac{2k_j-c_j}{2}\tilde{e}_j^2(t)-a_j\tilde{e}_j^{\nu+1}(t)\right] \\ & -\left(\frac{\kappa_2}{2}\tilde{\theta}^T(t)\tilde{\theta}(t)\right)^{\frac{1}{2}(\nu+1)}-\frac{3\kappa_2}{4}\tilde{\theta}^T(t)\tilde{\theta}(t) \\ & +\kappa_2\theta^{*T}\theta_i^*+\sum_{j=1}^{2}\frac{c_j}{2}+\left(\frac{\kappa_2}{2}\tilde{\theta}^T(t)\tilde{\theta}(t)\right)^{\frac{1}{2}(\nu+1)}.\end{aligned} \tag{31}$$

If $\left(\frac{\kappa_{2i}}{2}\tilde{\theta}_i^T\tilde{\theta}_i\right)^{\frac{1}{2}(\nu+1)} \ge 1$, it is easy to know that

$$\begin{aligned}\left(\frac{\kappa_{2i}}{2}\tilde{\theta}^T(t)\tilde{\theta}(t)\right)^{\frac{1}{2}(\nu+1)} & -\frac{\kappa_2}{2}\tilde{\theta}^T(t)\tilde{\theta}(t)+\kappa_2\theta^{*T}\theta^* \\ & \le \frac{\kappa_2}{2}\tilde{\theta}^T(t)\tilde{\theta}(t)-\frac{\kappa_2}{2}\tilde{\theta}^T(t)\tilde{\theta}(t)+\kappa_2\theta^{*T}\theta^* \\ & = \kappa_2\theta^{*T}\theta^*.\end{aligned} \tag{32}$$

On the contrary, if $\left(\frac{\kappa_2}{2}\tilde{\theta}^T(t)\tilde{\theta}(t)\right)^{\frac{1}{2}(\nu+1)} < 1$, one has

$$\begin{aligned}\left(\frac{\kappa_2}{2}\tilde{\theta}^T\tilde{\theta}\right)^{\frac{1}{2}(\nu+1)} & -\frac{\kappa_2}{2}\tilde{\theta}^T\tilde{\theta}+\kappa_2\theta^{*T}\theta^* \\ & < 1-\frac{\kappa_2}{2}\tilde{\theta}^T(t)\tilde{\theta}(t)+\kappa_2\theta^{*T}\theta^* \le 1+\kappa_2\theta^{*T}\theta^*.\end{aligned} \tag{33}$$

Thus, it follows from (32) and (33) that

$$\left(\frac{\kappa_2}{2}\tilde{\theta}^T(t)\tilde{\theta}(t)\right)^{\frac{1}{2}(\nu+1)}-\frac{\kappa_2}{2}\tilde{\theta}^T(t)\tilde{\theta}(t)+\kappa_2\theta^{*T}\theta^* \le 1+\kappa_2\theta^{*T}\theta^*. \tag{34}$$

Substituting (34) into (31) yields

$$\begin{aligned}\mathcal{D}_t^q V(t) \le & \sum_{j=1}^{2}\left[-\frac{2k_j-c_j}{2}\tilde{e}_j^2(t)-a_j\tilde{e}_j^{\nu+1}(t)\right] \\ & -\left(\frac{\kappa_2}{2}\tilde{\theta}^T(t)\tilde{\theta}(t)\right)^{\frac{1}{2}(\nu+1)}-\frac{\kappa_2}{4}\tilde{\theta}^T(t)\tilde{\theta}(t) \\ & +\left[1+\kappa_2\theta^{*T}\theta^*\right]+\sum_{j=1}^{2}\frac{c_j}{2} \\ \le & -\varsigma_1 V-\varsigma_2 V^{\frac{\nu+1}{2}}+\varsigma_3\end{aligned} \tag{35}$$

with $\varsigma_1 = \min\left\{\frac{2k_1-c_1}{2}, \frac{2k_2-c_2}{2}, \frac{\kappa_{min}}{2}\right\}$, $\varsigma_2 = \min\left\{2^{\frac{\nu+1}{2}}a_1, 2^{\frac{\nu+1}{2}}a_2, \kappa_{min}^{\frac{\nu+1}{2}}\right\}$, and $\varsigma_3 = 1+\kappa_2\theta^{*T}\theta^*+\sum_{j=1}^{2}\frac{c_j}{2}$, and $\kappa_{min} = \min\{\kappa_1, \kappa_2\}$. As a result, (35) can be arranged as

$$\mathcal{D}_t^q V(t) \le -\left(\varsigma_1-\frac{\varsigma_3}{2V(t)}\right)V(t)-\left(\varsigma_2-\frac{\varsigma_3}{2V^{\frac{\nu+1}{2}}(t)}\right)V^{\frac{\nu+1}{2}}(t). \tag{36}$$

According to (36) and Lemma 3, when $k > \frac{1}{2}c$, $e_1(t)$ will tend to the region

$$|e_1(t)| \le \max\left\{\sqrt{\frac{\varsigma_3}{\varsigma_1}}, \sqrt{2\left(\frac{\varsigma_3}{2\varsigma_2}\right)^{\frac{\nu+1}{2}}}\right\}$$

in some finite time. Since $e_1(t) = \tilde{e}_1(t)+\beta_1(t), e_2(t) = \tilde{e}_2(t)+\beta_2(t)$, if $\beta_1(t)$ and $\beta_2(t)$ are bounded, then all signals are bounded. Let $V_3(t) = \frac{1}{2}\beta_1^2(t)+\frac{1}{2}\beta_2^2(t)$. Then, (14) and (22) imply

$$\begin{aligned}\mathcal{D}_t^q V_3 \le & \beta_1(t)\mathcal{D}_t^q\beta_1(t)+\beta_2(t)\mathcal{D}_t^q\beta_2(t) \\ = & -k_1\beta_1^2(t)+\beta_1(t)(\hat{\alpha(t)}-\alpha(t))+\beta_1(t)\beta_2(t) \\ & -c_1\beta_1(t)\text{sign}(\beta_1(t))-k_2\beta_2^2(t) \\ & -\beta_2(t)\beta_1(t)-c_2\beta_2(t)\text{sign}(\beta_2(t)) \\ \le & -\sum_{j=1}^{2}k_j\beta_j^2(t)-\sum_{j=1}^{2}c_j\beta_j\text{sign}(\beta_j(t))+\beta_1(t)(\hat{\alpha}(t) \\ & -\alpha(t)) \le -\sum_{j=1}^{2}k_j\beta_j^2(t)-\sum_{j=1}^{2}c_j|\beta_j(t)|+\sum_{j=1}^{2}\rho_j\beta_j\tilde{\alpha}(t),\end{aligned} \tag{37}$$

where $\tilde{\alpha}(t) = \hat{\alpha}(t)-\alpha(t)$. Then, it follows from (15) and Lemma 4 that $\tilde{\alpha}(t)$ is bounded in finite time. As a result, we have

$$\begin{aligned}\mathcal{D}_t^q V_3(t) \le & -\sum_{j=1}^{2}k_j\beta_j^2(t)-\sum_{j=1}^{2}c_j|\beta_j(t)|+\sum_{j=1}^{2}\rho_j\delta|\beta_j(t)| \\ & \le \underline{k}V_3(t)-\underline{c}\sqrt{V_3(t)}+\bar{\rho}\bar{\delta}\sqrt{V_3(t)} \\ & = \underline{k}V_3(t)-(\underline{c}-\bar{\rho}\bar{\delta})\sqrt{V_3(t)},\end{aligned} \tag{38}$$

where $\underline{k} = 2\min\{k_1, k_2\}$, $\underline{c} = \min\{c_1, c_2\}$, $\bar{\rho} = \max\{\rho_1, \rho_2\}$ and $\bar{\delta} = \max\{\delta_1, \delta_2\}$. Thus, (38) and Lemma 3 imply that $\beta_1(t)$ and $\beta_2(t)$ are finite time bounded. This concludes our proof. ■

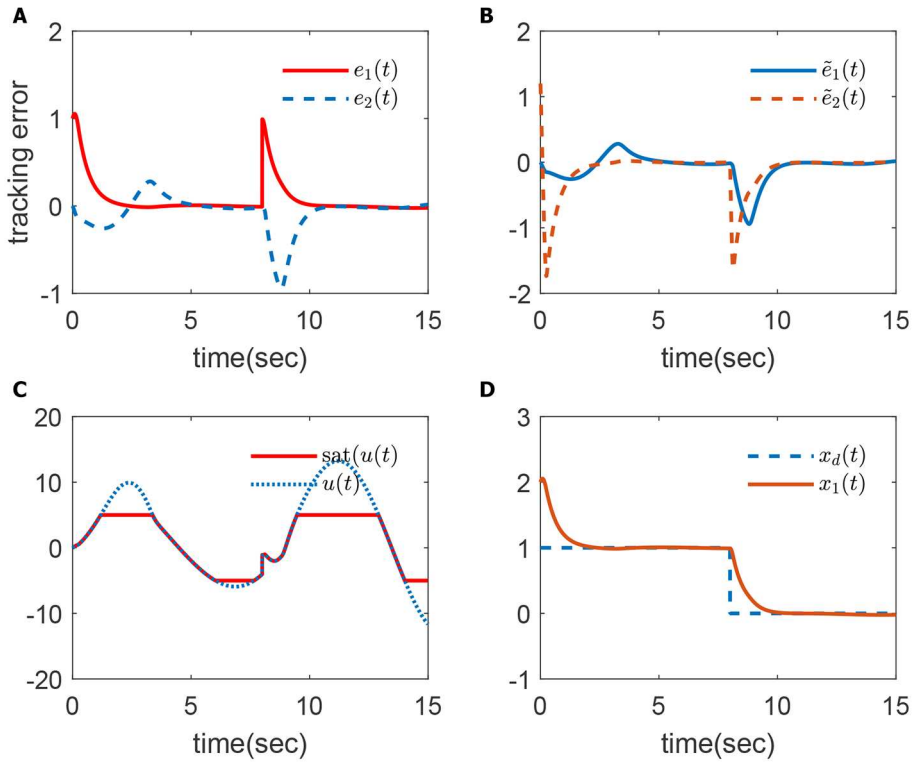

FIGURE 2 | Simulation1 results in **(A)** $e_1(t)$ and $e_2(t)$; **(B)** $\tilde{e}_1(t)$ and $\tilde{e}_2(t)$; **(C)** $u(t)$ and sat$(u(t))$; **(D)** $x_d(t)$ and $x_1(t)$.

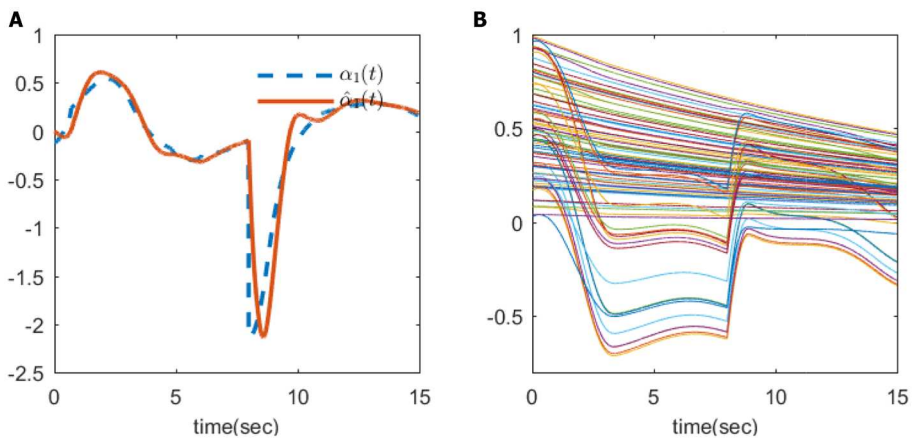

FIGURE 3 | Virtual input and NN parameters in **(A)** virtual inputs $\alpha_1(t)$ and $\alpha_2(t)$; **(B)** NN parameters.

Remark 1. *In this paper, the finite-control of fractional-order Duffing system was considered. It can be seen from the system model (10) that the non-linear function $f(x)$ is Lipschitz continuous. In addition, under the proposed controller (23), for any initial condition, the solution to the fractional-order Duffing system exists and is unique. In addition, from Theorem 1, it is obvious that all the signals in the closed loop system keep bounded. Thus, the solution of the controlled system (10) is stable.*

Remark 2. *In should be emphasized that the proposed fractional-order finite-time filter has very convergence ability compared with some related works, such as Liu et al. [16] and Ha et al. [25], where only the following class of lower filter (the order of the filter lying on (0,1)) is used:*

$$\mathcal{D}_t^q z(t) = \frac{1}{k}(z(t) - \alpha(t)), \tag{39}$$

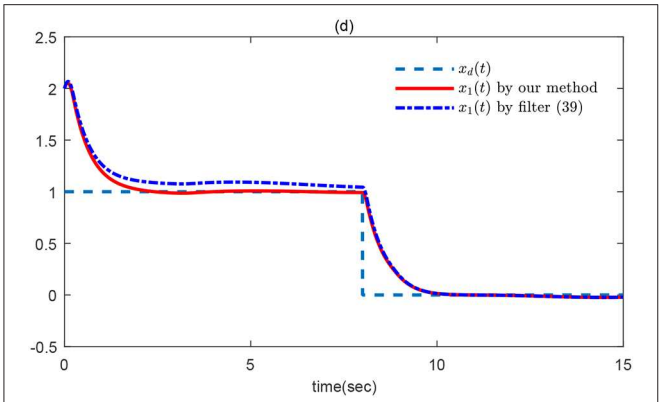

FIGURE 4 | Comparison results.

where $k > 0$. The fractional-order filter (39) can also guarantee that the approximation errors of the virtual input and its fractional converge to a small region of zero; however, the finite-time convergence cannot be guaranteed. In addition, to drive the approximation smaller, larger design parameter k should be used, which usually results in the signal $z(t)$ being too big. However, the proposed filter (15) has no such problems. To show the effectiveness of the proposed high order filter, some comparisons have been given in the following section.

4. SIMULATION RESULTS

In system (10), let parameters $a = 0.15, b = 0.23$, and the initial conditions be $x_1(0) = -1.2, x_2(0) = 1.2$. When $d(t) = u(t) = 0$, under above parameters and initial conditions, system (10) exhibits chaotic phenomenon, as shown in **Figure 1**.

In the simulation, let $x_1(0) = 2, x_2(0) = 0$, and let the reference signal be

$$x_d(t) = \begin{cases} 1, & t \leq 8, \\ 0, & t < 8. \end{cases} \tag{40}$$

The design parameters are $k_1 = k_2 = 0.9; a_1 = a_2 = 1, c_1 = c_2 = 1, \kappa_1 = \kappa_2 = 1, \nu = 0.70, b_1 = b_2 = 1$. The NN uses $x_1(t), x_2(t)$ as input variables with $\theta(0) = 0 \in \mathbb{R}^{81}$. The saturation parameters are $u_l = -5, u_r = 5$.

Then, the simulation results can be seen in **Figures 2–4**. The tracking errors $e_1(t)$ and $e_2(t)$ are given in **Figure 2A**, and we can see that the tracking error converges quickly. The compensated tracking errors are given in **Figure 2B**, where the proposed filter has very good approximation ability. The control input is given in **Figure 2C**. The tracking performance is in **Figure 2D**. The virtual input and its approximation is given in **Figure 3A**, and the NN parameters are shown in **Figure 3B**.

To show the rapid convergence speed of the proposed high-order filter, some comparative simulation results will be given here. Noting that in Liu et al. [16] and Ha et al. [25], the lower filter (39) was used. The simulation results under our filter (15) and (39) are given in **Figure 4**; in order to make a fair comparison, the design parameters in (39) are taken as 0.9 just the same as the value we took above. Obviously, compared with the lower filter (39), our method can guarantee a quicker convergence speed.

5. CONCLUSIONS

This paper addressed the finite time control of an unknown disturbed FODS in the presence of input saturation. By using the backstepping technique, a high order fractional filter with the order lying on (1,2) is proposed, and thus, the virtual input and its fractional derivative can be approximated. It is proven that the filter's approximation error can be enough small and can converge to the small region in some finite time. Then, an adaptive NN controller is given. The stability is proven strictly. In addition, the robustness of the proposed method is shown in simulation results. Our future research directions including how to design sliding mode surface for FODS and how to construct a high-order filter.

DATA AVAILABILITY STATEMENT

All datasets generated for this study are included in the article/supplementary material.

AUTHOR CONTRIBUTIONS

HL and XZ contributed the conception of the study. HL wrote the study and organized the literature. XZ wrote the simulation programs. All authors contributed to the manuscript revision, read, and approved the submitted version.

FUNDING

This work was supported by the Basic Ability Promotion Project for Young and Middle-aged Teachers of Guangxi Colleges and Universities (2020KY04022), the Key Natural Science Research Projects in Anhui Universities (KJ2019A0695), and the Xiangsihu Young Scholars Innovative Research Team of Guangxi University for Nationalities (2019RSCXSHQN02).

REFERENCES

1. Monje CA, Chen Y, Vinagre BM, Xue D, Feliu-Batlle V. *Fractional-Order Systems and Controls: Fundamentals and Applications*. London: Springer Science & Business Media Verlag (2010).
2. Luo Y, Chen YQ, Wang CY, Pi YG. Tuning fractional order proportional integral controllers for fractional order systems. *J Process Control.* (2010) **20**:823–31. doi: 10.1016/j.jprocont.2010.04.011
3. Munoz-Pacheco J, Zambrano-Serrano E, Volos C, Tacha O, Stouboulos I, Pham VT. A fractional order chaotic

system with a 3D grid of variable attractors. *Chaos Solit Fract.* (2018) **113**:69–78. doi: 10.1016/j.chaos.2018.05.015
4. Liu H, Pan Y, Cao J. Composite learning adaptive dynamic surface control of fractional-order nonlinear systems. *IEEE Trans Cybern.* (2019). doi: 10.1109/TCYB.2019.2938754. [Epub ahead of print].
5. Tavazoei MS, Haeri M. Chaotic attractors in incommensurate fractional order systems. *Phys D Nonlin Phenom.* (2008) **237**:2628–37. doi: 10.1016/j.physd.2008.03.037
6. Liu H, Pan Y, Cao J, Zhou Y, Wang H. Positivity and stability analysis for fractional-order delayed systems: a T-S fuzzy model approach. *IEEE Trans Fuzzy Syst.* (2020). doi: 10.1109/TFUZZ.2020.2966420. [Epub ahead of print].
7. Liu H, Pan Y, Li S, Chen Y. Adaptive fuzzy backstepping control of fractional-order nonlinear systems. *IEEE Trans Syst Man Cybern Syst.* (2017) **47**:2209–17. doi: 10.1109/TSMC.2016.2640950
8. Gallegos JA, Aguila-Camacho N, Duarte-Mermoud M. Vector Lyapunov-like functions for multi-order fractional systems with multiple time-varying delays. *Commun Nonlin Sci Numer Simul.* (2020) **83**:105089. doi: 10.1016/j.cnsns.2019.105089
9. Tlelo-Cuautle E, Pano-Azucena AD, Guillén-Fernández O, Silva-Juárez A. Synchronization and applications of fractional-order chaotic systems. In: Azar AT, Vaidyanathan S, editors. *Analog/Digital Implementation of Fractional Order Chaotic Circuits and Applications*. Cham: Springer (2020). p. 175–201. doi: 10.1007/978-3-030-31250-3_6
10. Yuan L, Yang Q. Parameter identification of fractional-order chaotic systems without or with noise: reply to comments. *Commun Nonlin Sci Numer Simul.* (2019) **67**:506–16. doi: 10.1016/j.cnsns.2018.07.032
11. Marir S, Chadli M. Robust admissibility and stabilization of uncertain singular fractional-order linear time-invariant systems. *IEEE/CAA J Autom Sinica.* (2019) **6**:685–92. doi: 10.1109/JAS.2019.1911480
12. Wei Y, Wang J, Liu T, Wang Y. Sufficient and necessary conditions for stabilizing singular fractional order systems with partially measurable state. *J Frank Inst.* (2019) **356**:1975–90. doi: 10.1016/j.jfranklin.2019.01.022
13. Boroujeni EA, Momeni HR. Non-fragile nonlinear fractional order observer design for a class of nonlinear fractional order systems. *Signal Process.* (2012) **92**:2365–70. doi: 10.1016/j.sigpro.2012.02.009
14. Efe MÖ. Fractional order systems in industrial automation-a survey. *IEEE Trans Ind Inform.* (2011) **7**:582–91. doi: 10.1109/TII.2011.2166775
15. Boulkroune A, Bouzeriba A, Bouden T, Azar AT. Fuzzy adaptive synchronization of uncertain fractional-order chaotic systems. In: Azar AT, Vaidyanathan S, editors. *Advances in Chaos Theory and Intelligent Control*. Cham: Springer (2016). p. 681–97. doi: 10.1007/978-3-319-30340-6_28
16. Liu H, Pan Y, Cao J, Wang H, Zhou Y. Adaptive neural network backstepping control of fractionial-order nonlinear systems with actuator faults. *IEEE Trans Neural Netw Learn Syst.* (2020). doi: 10.1109/TNNLS.2020.2964044. [Epub ahead of print].
17. Bouzeriba A, Boulkroune A, Bouden T. Projective synchronization of two different fractional-order chaotic systems via adaptive fuzzy control. *Neural Comput Appl.* (2016) **27**:1349–60. doi: 10.1007/s00521-015-1938-4
18. Mirzajani S, Aghababa MP, Heydari A. Adaptive control of nonlinear fractional-order systems using T-S fuzzy method. *Int J Mach Learn Cybern.* (2019) **10**:527–40. doi: 10.1007/s13042-017-0733-1
19. Pham VT, Ouannas A, Volos C, Kapitaniak T. A simple fractional-order chaotic system without equilibrium and its synchronization. *AEU Int J Electron Commun.* (2018) **86**:69–76. doi: 10.1016/j.aeue.2018.01.023
20. Zhang W, Cao J, Wu R, Alsaadi FE, Alsaedi A. Lag projective synchronization of fractional-order delayed chaotic systems. *J Frank Inst.* (2019) **356**:1522–34. doi: 10.1016/j.jfranklin.2018.10.024
21. Thanh NT, Phat VN. Improved approach for finite-time stability of nonlinear fractional-order systems with interval time-varying delay. *IEEE Trans Circuits Syst II Express Briefs.* (2018) **66**:1356–60. doi: 10.1109/TCSII.2018.2880777
22. Yang S, Yu J, Hu C, Jiang H. Finite-time synchronization of memristive neural networks with fractional-order. *IEEE Trans Syst Man Cybern Syst.* (2019). doi: 10.1109/TSMC.2019.2931046. [Epub ahead of print].
23. Liang J, Wu B, Liu L, Wang YE, Li C. Finite-time stability and finite-time boundedness of fractional order switched systems. *Trans Inst Meas Control.* (2019) **41**:3364–71. doi: 10.1177/0142331219826333
24. Ha S, Liu H, Li S. Adaptive fuzzy backstepping control of fractional-order chaotic systems with input saturation. *J Intell Fuzzy Syst.* (2019) **37**:6513–25. doi: 10.3233/JIFS-182623
25. Ha S, Liu H, Li S, Liu A. Backstepping-based adaptive fuzzy synchronization control for a class of fractional-order chaotic systems with input saturation. *Int J Fuzzy Syst.* (2019) **21**:1571–84. doi: 10.1007/s40815-019-00663-5
26. Xu W, Hu G, Ho DW, Feng Z. Distributed secure cooperative control under denial-of-service attacks from multiple adversaries. *IEEE Trans Cybern.* (2019). doi: 10.1109/TCYB.2019.2896160. [Epub ahead of print].
27. Wang P, Wen G, Yu X, Yu W, Wan Y. Synchronization of resilient complex networks under attacks. *IEEE Trans Syst Man Cybern Syst.* (2019). doi: 10.1109/TSMC.2019.2895027. [Epub ahead of print].

Conflict of Interest: The authors declare that the research was conducted in the absence of any commercial or financial relationships that could be construed as a potential conflict of interest.

frontiers in Physics

BRIEF RESEARCH REPORT
published: 21 May 2020
doi: 10.3389/fphy.2020.00155

Fuzzy Synchronization Control for Fractional-Order Chaotic Systems With Different Structures

Jin Xu[1], *Ning Li*[1], *Xiulan Zhang*[2*] *and Xiaoli Qin*[3]

[1] Department of Applied Mathematics, Huainan Normal University, Huainan, China, [2] School of Mathematics and Physics, Guangxi University for Nationalities, Nanning, China, [3] Department of Mathematics, Deyang High School, Chengdu Normal University, Deyang, China

This paper discusses the synchronization problem for a class of unknown fractional-order chaotic systems (FOCSs) with indeterminate external disturbances and non-symmetrical control gain. A paralleled adaptive fuzzy synchronization controller is constructed in which indeterminate non-linear functions are approximated by the fuzzy logic systems depending on fractional-order Lyapunov stability criteria and the fractional-order parameter adaptive law is designed to regulate corresponding parameters of the fuzzy systems. The proposed method guarantees the boundedness of all of the signals in the closed-loop system, and at the same time, it ensures the convergence of the synchronization error between the master and slave FOCSs. Finally, the feasibility is demonstrated by simulation studies.

Keywords: adaptive fuzzy control, fractional-order chaotic system, fractional-order adaptation, chaos synchronization, fuzzy logic system

OPEN ACCESS

Edited by:
Shaohui Wang,
Louisiana College, United States

Reviewed by:
Jia-Bao Liu,
Anhui Jianzhu University, China
Hongwei Liu,
Anhui University, China

***Correspondence:**
Xiulan Zhang
xlzhang@gxun.edu.cn

Specialty section:
This article was submitted to Mathematical Physics, a section of the journal Frontiers in Physics

Received: *31 March 2020*
Accepted: *15 April 2020*
Published: *21 May 2020*

Citation:
Xu J, Li N, Zhang X and Qin X (2020) Fuzzy Synchronization Control for Fractional-Order Chaotic Systems With Different Structures. Front. Phys. 8:155. doi: 10.3389/fphy.2020.00155

1. INTRODUCTION

The fractional calculus appeared in the same era as the classical integer-order calculus, but due to the facts that the fractional-order calculus lacks actual background and its theory is complex, the fractional calculus has rarely been investigated by scholars. Recently, it has been shown that fractional calculus not only provides new mathematical methods for practical systems but also is especially well-suited for describing some dynamical behaviors of physical systems [1–5]. Consequently, the fractional-order calculus has been employed to describe phonology and thermal systems, signal processing and system identification [6, 7], control and robotics [8–11], and many other real-world systems. Since the fractional-order calculus has memory ability, in the description of complex dynamic systems, a model built depending on fractional-order calculus is more accurate than an integer-order one. The study for the fractional-order chaotic system (FOCS) has thus slowly become a hot research topic.

It is well-known that chaotic systems (integer-order or fractional-order) are sensitive to initial state values, i.e., the stability of systems will change obviously with small changes in initial values; thus, the synchronization control of FOCSs is challenging work. Some methods, such as PD control [12], PID control [13–15], adaptive fuzzy backstepping control [16–20], sliding mode control [21–25], and Lyapunov direct [26–28] and adaptive neural network control [29–32] have been used to control or synchronize fractional chaotic systems. Chen et al. [21] investigated the adaptive synchronization of FOCSs, where different structures of the master and slave FOCSs and the existence of external disturbances are ignored. In Wang et al. [33], the synchronization of FOCSs accompanied by external disturbances was studied. To handle the unmatched disturbances, in

He et al. [30], a robust synchronization method with non-linear input was proposed, but its control cost was very high. It should be mentioned that, in the above literature, the stability analysis of the synchronization of FOCSs still uses the ideal of linear systems. Generally speaking, the synchronization of FOCS systems with some unknown factors and external disturbances needs to be further researched.

Motivated by the above discussion, this paper aims to design a synchronization controller for a master and slave fractional-order chaotic system (FOCS) subject to different structures and external disturbances. The control gain matrix is assumed to be unknown. Fuzzy logic systems are used to approximate the unknown non-linear functions. Fractional-order parameter adaptive laws are designed to update the fuzzy parameters. The main contributions of this work are summarized as follows. (1) The non-symmetrical control gain matrix and external disturbances in FOCSs are considered. Besides, unlike some prior works, such as Liu et al. [16] and Pan et al. [31], the sequence-leading minor in the control gain matrix is not assumed to be zero. (2) Based on the Lyapunov stability theorem, fractional-order fuzzy parameter adaptive laws are designed.

2. PRELIMINARIES

The ν-th fractional-order integral is defined as:

$$ {}_0^C D_k^{-\nu} f(k) = \frac{1}{\Gamma(\nu)} \int_0^k (k-\tau)^{\nu-1} f(\tau) d\tau, \tag{1} $$

where $\Gamma(\cdot)$ function can be defined as

$$ \Gamma(z) = \int_0^\infty k^{z-1} e^{-k} dk. \tag{2} $$

The ν-th Caputo's derivative can be defined as:

$$ {}_0^C D_k^{\nu} f(k) = \frac{1}{\Gamma(n-\nu)} \int_0^k (k-\tau)^{n-\nu-1} f^{(n)}(\tau) d\tau, \tag{3} $$

clearly, where n is an integer satisfying $n-1 \le \nu < n$.

The Laplace transform of Caputo's fractional-order derivative (3) can be expressed by Li et al. [2]

$$ \begin{aligned} \mathscr{L}({}_0^C D_k^{\nu} f(k)) &= \int_0^\infty e^{-sk} {}_0^C D_k^{\nu} f(k) dk \\ &= s^\nu F(s) - \sum_{t=0}^{n-1} s^{\nu-t-1} f^{(t)}(0). \end{aligned} \tag{4} $$

When $0 < \nu < 1$, $\mathscr{L}({}_0^C D_k^{\nu} f(k)) = s^\nu F(s) - s^{\nu-1} f(0)$.

For simplicity, we suppose that $\nu \in (0,1)$ in the rest of this paper. The following conclusions will be given in advance.

Definition 1. Pudlubny [3] The Mittag-Leffler function can be given by

$$ E_{\nu,\xi}(z) = \sum_{t=0}^{\infty} \frac{z^t}{\Gamma(\nu t + \xi)}, \tag{5} $$

where $\nu, \xi > 0$, and $z \in C$, the Laplace transform of which is

$$ \mathscr{L}\{k^{\xi-1} E_{\nu,\xi}(-bk^\nu)\} = \frac{s^{\nu-\xi}}{s^\nu + b}. \tag{6} $$

Lemma 1. Pudlubny [3] If $m(k) \in C^1[0,T] (T > 0)$ (the symbol C^1 means that a function has a continuous derivative), the following equation satisfies:

$$ {}_0^C D_k^{-\nu} {}_0^C D_k^{\nu} m(k) = m(k) - m(0), \tag{7} $$

$$ {}_0^C D_k^{\nu} {}_0^C D_k^{-\nu} m(k) = m(k). \tag{8} $$

Lemma 2. (Lyapunov's second fractional-order method [34]) Suppose that $\boldsymbol{e}(k) = 0$ is an equilibrium point of the following FOCS:

$$ {}_0^C D_k^{\nu} \boldsymbol{e}(k) = \boldsymbol{h}(k, \boldsymbol{e}(k)), \tag{9} $$

where $\boldsymbol{e}(k) \in R^n$ is a system variable, and $\boldsymbol{h}(\boldsymbol{e}(k)) \in R^n$ is a non-linear function that has a Lipschitz local condition. If there exists a Lyapunov function $V(k, \boldsymbol{e}(k))$ and positive parameters a_1, a_2, a_3 such that

$$ a_1 ||\boldsymbol{e}(k)|| \le V(k, \boldsymbol{e}(k)) \le a_2 ||\boldsymbol{e}(k)||, \tag{10} $$

$$ {}_0^C D_k^{\nu} V(k, \boldsymbol{e}(k)) \le -a_3 ||\boldsymbol{e}(k)||, \tag{11} $$

then system (9) is asymptotically stable.

Lemma 3. Aguila-Camacho et al. [35] Suppose that $\boldsymbol{e}(k) \in R^n$ is a continuous and derivable function, then

$$ \frac{1}{2} {}_0^C D_k^{\nu} \boldsymbol{e}^T(k) \boldsymbol{e}(k) \le \boldsymbol{e}^T(k) {}_0^C D_k^{\nu} \boldsymbol{e}(k). \tag{12} $$

Lemma 4. Costa et al. [36] and Liu et al. [37] Let matrix $\boldsymbol{G} \in R^{n\times n}$ be the non-zero sequence-leading minor, then $\boldsymbol{G}$ can be factorized as $\boldsymbol{G} = \boldsymbol{G}_1 \boldsymbol{A}_g \boldsymbol{T}_g$, where $\boldsymbol{G}_1 \in R^{n\times n}$ is a positive matrix, $\boldsymbol{A}_g \in R^{n\times n}$ is a diagonal matrix whose diagonal line is $+1$ or -1 (signal of each of its elements is determined by corresponding the sequence-leading minor signal of $\boldsymbol{G}$), and $\boldsymbol{T}_g \in R^{n\times n}$ is a upper triangular matrix.

3. PROBLEM DESCRIPTION

3.1. System Dynamics

Suppose that the slave and respond FOCSs are separately defined as

$$ {}_0^C D_k^{\nu} \boldsymbol{x}(k) = \boldsymbol{h}(\boldsymbol{x}(k)), \tag{13} $$

$$ {}_0^C D_k^{\nu} \boldsymbol{y}(k) = \boldsymbol{p}(\boldsymbol{y}(k)) + \boldsymbol{G}\boldsymbol{u}(k) + \boldsymbol{D}(k), \tag{14} $$

where $\boldsymbol{x}(k) = [x_1(k), x_2(k), \cdots, x_n(k)]^T \in R^n$ and $\boldsymbol{y}(k) = [y_1(k), y_2(k), \cdots, y_n(k)]^T \in R^n$ are separately system measurable state variables of the drive system and respond system, $\boldsymbol{h}, \boldsymbol{p} : R^n \to R^n$ are uncertain non-linear continuous functions, $\boldsymbol{G} \in R^{n\times n}$ is an unknown constant matrix, $\boldsymbol{D}(k) \in R^{n\times n}$ is an indeterminate external disturbance, and $\boldsymbol{u}(k) \in R^n$ is the control input.

3.2. Introduction of a Fuzzy System

A fuzzy logic system includes the knowledge base, fuzzier, fuzzy inference engine based on the fuzzy rules and defuzzier [38–41]. The form of the j-th fuzzy rule is

$\mathcal{R}^{(j)}$: If x_1 is E_1^j, x_2 is E_2^j, $\cdots$, x_n is E_n^j, then $\hat{h}(\boldsymbol{x}(k))$ is C^j $(j = 1, 2, \cdots, N)$,

where $\boldsymbol{x}(k) = [x_1(k), x_2(k), \cdots, x_n(k)]^T \in \mathbb{R}^n$ and $\hat{h}(\boldsymbol{x}(k)) \in \mathbb{R}$ are respectively the input and the output of fuzzy logic systems. The output is

$$\hat{h}(\boldsymbol{x}(k)) = \frac{\sum_{j=1}^{N} \theta_j(k) \left[\prod_{i=1}^{n} \mu_{E_i^j}(x_i(k)) \right]}{\sum_{j=1}^{N} \left[\prod_{i=1}^{n} \mu_{E_i^j}(x_i(k)) \right]}, \tag{15}$$

where $\theta_j(k)$ is a value where the fuzzy membership function μ_{C^j} is maximum. Generally, we can consider that $\mu_{C^j}(\theta_j(k)) = 1$, and the fuzzy basic function is $\varphi_j(\boldsymbol{x}(k)) = \frac{\prod_{i=1}^{n} \mu_{E_i^j}(x_i(k))}{\sum_{j=1}^{N} \left[\prod_{i=1}^{n} \mu_{E_i^j}(x_i(k)) \right]}$. Let $\boldsymbol{\varphi}(\boldsymbol{x}(k)) = [\varphi_1(\boldsymbol{x}(k)), \varphi_2(\boldsymbol{x}(k)), \cdots, \varphi_N(\boldsymbol{x}(k))]^T$, $\boldsymbol{\theta}(k) = [\theta_1(k), \theta_2(k), \cdots, \theta_N(k)]^T$, then the output of fuzzy logic systems is written as

$$\hat{h}(\boldsymbol{x}(k)) = \boldsymbol{\theta}^T(k)\boldsymbol{\varphi}(\boldsymbol{x}(k)). \tag{16}$$

Theorem 1. Suppose that $p(\boldsymbol{x})$ is a continuous function defined on compact set Ω. For any constants $\varepsilon > 0$, there exists a fuzzy logic system approximating function $\hat{h}(\boldsymbol{x})$ forming (16) such that

$$\sup_{\Omega} |p(\boldsymbol{x}) - \hat{\boldsymbol{\theta}}^T \boldsymbol{\varphi}(\boldsymbol{x})| \leq \varepsilon, \tag{17}$$

where $\hat{\boldsymbol{\theta}}$ is an estimator of optimal vector $\boldsymbol{\theta}^*$.

3.3. Control Objective

The synchronization error can be defined as $\boldsymbol{e}(k) = \boldsymbol{y}(k) - \boldsymbol{x}(k)$. Our control objective is to design an adaptive controller such that the synchronization error tends to zero asymptotically (i.e., $\lim_{k\to\infty} ||\boldsymbol{e}(k)|| = 0$).

4. CONTROLLER DESIGN AND STABILITY ANALYSIS

Assumption 1. The control gain matric $\boldsymbol{G}$ has a non-zero sequence-leading minor whose signal is known.

Remark 1. *Assumption* 1 is not strict. In fact, the gain matrix of some actual systems (such as a visual servo and vehicle thermal management system [42]) is non-symmetrical. According to Lemma 4, one can factorize $\boldsymbol{G}$ as $\boldsymbol{G} = \boldsymbol{G}_1\boldsymbol{A}\boldsymbol{T}$, where $\boldsymbol{G}_1$ is an unknown positive definite matrix, $\boldsymbol{A}$ is a known matrix whose diagonal line is +1 or -1, $\boldsymbol{A}\boldsymbol{A} = \boldsymbol{I}_{n\times n}$ ($\boldsymbol{I}_{n\times n}$ is a n-order unitary matrix), and $\boldsymbol{T}$ is an uncertain upper triangle matrix.

Assumption 2. *The product of the external disturbance $\boldsymbol{D}(k)$ and the positive definite matrix $\boldsymbol{G}_1^{-1}$ is a function that is bounded, i.e., there exists an uncertain constant $M_i > 0$ so that*

$$|(\boldsymbol{G}_1^{-1}\boldsymbol{D}(k))_i| \leq M_i \ (\forall k > 0). \tag{18}$$

Remark 2. *Assumption 2 is not restrictive, and it is used in some similar literature, for example, in* Liu et al. [9], Rahmani et al. [10], and Ferdaus et al. [11]. *In fact, most commonly used disturbances satisfy Assumption 2.*

The dynamic equation of synchronization error is expressed as

$$\begin{aligned} {}_0^C D_k^v \boldsymbol{e}(k) &= {}_0^C D_k^v \left(\boldsymbol{y}(k) - \boldsymbol{x}(k)\right) \\ &= {}_0^C D_k^v \boldsymbol{y}(k) - {}_0^C D_k^v \boldsymbol{x}(k) \\ &= \boldsymbol{p}(\boldsymbol{y}(k)) - \boldsymbol{h}(\boldsymbol{x}(k)) + \boldsymbol{G}\boldsymbol{u}(k) + \boldsymbol{D}(k) \\ &= \boldsymbol{p}(\boldsymbol{y}(k)) - \boldsymbol{h}(\boldsymbol{x}(k)) + \boldsymbol{G}_1\boldsymbol{A}\boldsymbol{T}\boldsymbol{u}(k) + \boldsymbol{D}(k). \end{aligned} \tag{19}$$

Let $\boldsymbol{Q} = \boldsymbol{G}_1^{-1}$, then

$$\begin{aligned} \boldsymbol{Q}\,{}_0^C D_k^v \boldsymbol{e}(k) = \boldsymbol{Q}\boldsymbol{p}(\boldsymbol{y}(k)) - \boldsymbol{Q}\boldsymbol{h}(\boldsymbol{x}(k)) + (\boldsymbol{A}\boldsymbol{T} - \boldsymbol{A})\boldsymbol{u}(k) \\ + \boldsymbol{A}\boldsymbol{u}(k) + \boldsymbol{Q}\boldsymbol{D}(k). \end{aligned} \tag{20}$$

Denote $\boldsymbol{\gamma}(\boldsymbol{z}(k)) = \boldsymbol{\gamma}(\boldsymbol{x}(k), \boldsymbol{y}(k), \boldsymbol{u}(k)) = \boldsymbol{Q}\boldsymbol{p}(\boldsymbol{y}(k)) - \boldsymbol{Q}\boldsymbol{h}(\boldsymbol{x}(k)) + (\boldsymbol{A}\boldsymbol{T} - \boldsymbol{A})\boldsymbol{u}(k) = [\gamma_1(\boldsymbol{z}(k)), \gamma_2(\boldsymbol{z}(k)), \cdots, \gamma_n(\boldsymbol{z}(k))]^T$ as an indeterminate non-linear function; then, Equation (20) is expressed as

$$\boldsymbol{Q}\,{}_0^C D_k^{\mu} \boldsymbol{e}(k) = \boldsymbol{\gamma}(\boldsymbol{z}(k)) + \boldsymbol{A}\boldsymbol{u}(k) + \boldsymbol{Q}\boldsymbol{D}(k). \tag{21}$$

The indeterminate function $\boldsymbol{\gamma}(\boldsymbol{z}(k))$ can be approximated by the fuzzy logic system (16) as

$$\hat{\gamma}_i(\theta_i(k), \boldsymbol{z}(k)) = \theta_i(k)^T \varphi_i(\boldsymbol{z}(k)), i = 1, 2, \cdots, n. \tag{22}$$

Assume that the errors of the optimal parameter and the optimal estimated errors be respectively

$$\tilde{\theta}_i(k) = \theta_i(k) - \theta_i^*, \tag{23}$$

$$\varepsilon_i(\boldsymbol{z}(k)) = \gamma_i(\boldsymbol{z}(k)) - \hat{\gamma}_i(\theta_i^*, \boldsymbol{z}(k)). \tag{24}$$

From Boulkroune et al. [42] and Tong et al. [43] and Theorem 1, we assume that $|\varepsilon_i(\boldsymbol{z}(k))| \leq \varepsilon_i^*$ ($\varepsilon_i^* > 0$ is an uncertain constant). If we denote $\boldsymbol{\varepsilon}(\boldsymbol{z}(k)) = [\varepsilon_1(\boldsymbol{z}(k)), \varepsilon_2(\boldsymbol{z}(k)), \cdots, \varepsilon_n(\boldsymbol{z}(k))]^T$ and $\boldsymbol{\varepsilon}^* = [\varepsilon_1^*, \varepsilon_2^*, \cdots, \varepsilon_n^*]^T$, the estimated error of the indeterminate non-linear function can be written as

$$\begin{aligned} \boldsymbol{\gamma}(\boldsymbol{z}(k)) - \hat{\boldsymbol{\gamma}}(\boldsymbol{\theta}(k), \boldsymbol{z}(k)) &= \boldsymbol{\gamma}(\boldsymbol{z}(k)) - \hat{\boldsymbol{\gamma}}(\boldsymbol{\theta}^*, \boldsymbol{z}(k)) + \hat{\boldsymbol{\gamma}}(\boldsymbol{\theta}^*, \boldsymbol{z}(k)) \\ &\quad - \hat{\boldsymbol{\gamma}}(\boldsymbol{\theta}(k), \boldsymbol{z}(k)) \\ &= \boldsymbol{\varepsilon}(\boldsymbol{z}(k)) + \hat{\boldsymbol{\gamma}}(\boldsymbol{\theta}^*, \boldsymbol{z}(k)) - \hat{\boldsymbol{\gamma}}(\boldsymbol{\theta}(k), \boldsymbol{z}(k)) \\ &= \boldsymbol{\varepsilon}(\boldsymbol{z}(k)) - (\boldsymbol{\theta}(k) - \boldsymbol{\theta}^*)^T \boldsymbol{\varphi}(\boldsymbol{z}(k)) \\ &= \boldsymbol{\varepsilon}(\boldsymbol{z}(k)) - \tilde{\boldsymbol{\theta}}(k)^T \boldsymbol{\varphi}(\boldsymbol{z}(k)). \end{aligned} \tag{25}$$

From the above discussion, the controller $\boldsymbol{u}(k)$ can be designed as

$$\boldsymbol{u}(k) = -\boldsymbol{A}\Big[\boldsymbol{L}\boldsymbol{e}(k) + \boldsymbol{\theta}(k)^T\boldsymbol{\varphi}(\boldsymbol{z}(k)) + \boldsymbol{H}\text{sign}(\boldsymbol{e}(\text{k})) + \hat{\boldsymbol{M}}\text{sign}(\boldsymbol{e}(\text{k}))\Big], \tag{26}$$

where $\boldsymbol{L} = \text{diag}[l_1, l_2, \cdots, l_n] \in R^{n\times n}, l_1, l_2, \cdots, l_n > 0$ are parameters that need to be designed, $\boldsymbol{H}$ =diag$[\hat{\varepsilon}_1^*(k), \hat{\varepsilon}_2^*(k), \cdots, \hat{\varepsilon}_n^*(k)]$, $\hat{\varepsilon}_i^*(k)(i = 1, 2, \cdots, n)$ are estimated values of uncertain constants ε_i^*, and $\hat{\boldsymbol{M}}$ =diag$[\hat{M}_1(k), \hat{M}_2(k), \cdots, \hat{M}_n(k)]$, $\hat{M}_i(k)(i = 1, 2, \cdots, n)$ are estimated values of unknown constants M_i. For the sake of achieving the synchronization objective, this paper designs the following fractional-order parameter adaptive laws:

$$_0^C D_k^\nu \theta_i(k) = \lambda_i e_i(k)\varphi_i(\boldsymbol{z}(k)), \tag{27}$$

$$_0^C D_k^\nu \hat{\varepsilon}_i^*(k) = \xi_i|e_i(k)|, \tag{28}$$

$$_0^C D_k^\nu \hat{M}_i(k) = \mu_i|e_i(k)|, \tag{29}$$

where $\lambda_i, \xi_i, \mu_i > 0, i = 1, 2, \cdots, n$ are designed parameters.

To facilitate the coming stability analysis, let us display some results in advance.

Lemma 5. Suppose that $_0^C D_k^\nu e(k) \le 0$, then we have $e(k) \le e(0)$ on $[0, +\infty)$. On the contrary, $_0^C D_k^\nu e(k) \ge 0$ implies that $e(k) \ge e(0)$ on $[0, +\infty)$.

Proof. We only verify the first condition (the second condition is the same). Because $_0^C D_k^\nu e(k) \le 0$, there exists a non-negative function $h(k) = -[_0^C D_k^\nu e](k)$ satisfying

$$_0^C D_k^\nu e(k) + h(k) = 0. \tag{31}$$

Taking the Laplace transform on both sides of equation (31), we get $s^\nu E(s) - s^{\nu-1}e(0) + F(s) = 0$, where $E(s)$ and $F(s)$ are separately the Laplace transform of $e(k)$ and $h(k)$. It is simplified to

$$E(s) = \frac{e(0)}{s} - \frac{F(s)}{s^\nu}. \tag{32}$$

Taking the inverse Laplace transform on both sides of equation (32), we obtain

$$e(k) = e(0) - [D^{-\nu}h](k). \tag{33}$$

By the fractional-order integral (1), we have $[D^{-\nu}h](k) \ge 0$. Further, we have $e(k) \le e(0)$ on $[0, +\infty)$.

Remark 3. Lemma 5 shows the difference between a fractional-order derivative and an integer-order derivative, but it cannot be described as: if $_0^C D_k^\nu e(k) \le 0$, then $e(k)$ is monotonically decreasing on the interval $[0, +\infty)$; if $_0^C D_k^\nu e(k) \ge 0$, then $e(k)$ is monotonically increasing on the interval $[0, +\infty)$. To explain this, a counterexample is given as follows.

Example 1. Consider that $x(0) \ge 0$ is an initial value of the differential equation: $_0^C D_k^\nu x(k) = h(k, x) = \mu k^{\mu-1}$, where $0 < \mu < 1, 0 < \nu < 1$, and $k > 0$. Obviously, $h(k, x) \ge 0$, and the solution of the differential equation is $x(k) = x(0) + \frac{\mu\Gamma(\mu)k^{\mu-1+\nu}}{\Gamma(\mu+\nu)}$. It is clear that $\lim_{k\to+\infty} x(k) = x(0)$ when $0 < \mu \le 1-\nu$. Therefore, $x(k)$ is not monotonically increasing, defined on $k \in [0, +\infty)$.

Lemma 6. Suppose that $\boldsymbol{e}(k) \in R^n$ be a continuous one-order derivative, then

$$\frac{1}{2}{}_0^C D_k^\nu \boldsymbol{e}^T(k)\boldsymbol{Q}\boldsymbol{e}(k) \le \boldsymbol{e}^T(k)\boldsymbol{Q}{}_0^C D_k^\nu \boldsymbol{e}(k), \tag{34}$$

where $\boldsymbol{Q}$ is an arbitrary n-order positive definite matrix.

Proof. Since $\boldsymbol{Q}$ is a positive definite matrix, there exists an n-order non-singular symmetric matrix $\boldsymbol{B} = \boldsymbol{B}^T$ so that $\boldsymbol{Q} = \boldsymbol{B}^T\boldsymbol{B}$. From Lemmas 1, 2, and 3, we obtain

$$\begin{aligned}
\frac{1}{2}{}_0^C D_k^\nu \boldsymbol{e}^T(k)\boldsymbol{Q}\boldsymbol{e}(k) &= \frac{1}{2}{}_0^C D_k^\nu \boldsymbol{e}^T(k)\boldsymbol{B}^T\boldsymbol{B}\boldsymbol{e}(k) \\
&= \frac{1}{2}{}_0^C D_k^\nu \left(\boldsymbol{B}\boldsymbol{e}(k)\right)^T \boldsymbol{B}\boldsymbol{e}(k) \\
&\le \left(\boldsymbol{B}\boldsymbol{e}(k)\right)^T {}_0^C D_k^\nu \boldsymbol{B}\boldsymbol{e}(k) \\
&= \left(\boldsymbol{B}\boldsymbol{e}(k)\right)^T \boldsymbol{B}{}_0^C D_k^\nu \boldsymbol{e}(k) \\
&= \boldsymbol{e}^T(k)\boldsymbol{Q}{}_0^C D_k^\nu \boldsymbol{e}(k).
\end{aligned} \tag{35}$$

Lemma 7. Suppose that $V(k) = \frac{1}{2}\boldsymbol{x}^T(k)\boldsymbol{x}(k) + \frac{1}{2}\boldsymbol{y}^T(k)\boldsymbol{y}(k)$, where $\boldsymbol{x}(k)$ and $\boldsymbol{y}(k) \in R^n$ are continuous one-order derivatives. If there exists a constant $q > 0$ satisfying the following inequality

$$_0^C D_k^\nu V(k) \le -q\boldsymbol{x}^T(k)\boldsymbol{x}(k), \tag{36}$$

then $||\boldsymbol{x}(k)||$ and $||\boldsymbol{y}(k)||$ are both bounded, and $\boldsymbol{x}(k)$ tends to zero asymptotically, where $||\cdot||$ represents the Euclidian norm.

Proof. According to inequality (36), the following inequality holds:

$$_0^C D_k^\nu V(k) \le -q\boldsymbol{x}^T(k)\boldsymbol{x}(k) \le 0. \tag{37}$$

From Lemma 5, we know that $V(k) \le V(0)(\forall t \ge 0)$ when $V(k)$ defines on $[0, \infty)$. So, $||\boldsymbol{x}(k)|| \le \sqrt{2V(k)} \le \sqrt{2V(0)}$ and $||\boldsymbol{y}(k)|| \le \sqrt{2V(k)} \le \sqrt{2V(0)}$. Thereby, $||\boldsymbol{x}(k)||$ and $||\boldsymbol{y}(k)||$ are bounded.

Taking the ν-th integral on both sides of inequality $_0^C D_k^\nu V(k) \le -q\boldsymbol{x}^T(k)\boldsymbol{x}(k)$, we have

$$V(k) - V(0) \le -q{}_0^C D_k^{-\nu}\boldsymbol{x}^T(k)\boldsymbol{x}(k). \tag{38}$$

From the structure of $V(k)$, we have $\boldsymbol{x}^T(k)\boldsymbol{x}(k) \le 2V(k)$, and furthermore,

$$\boldsymbol{x}^T(k)\boldsymbol{x}(k) \le 2V(0) - 2q{}_0^C D_k^{-\nu}\boldsymbol{x}^T(k)\boldsymbol{x}(k). \tag{39}$$

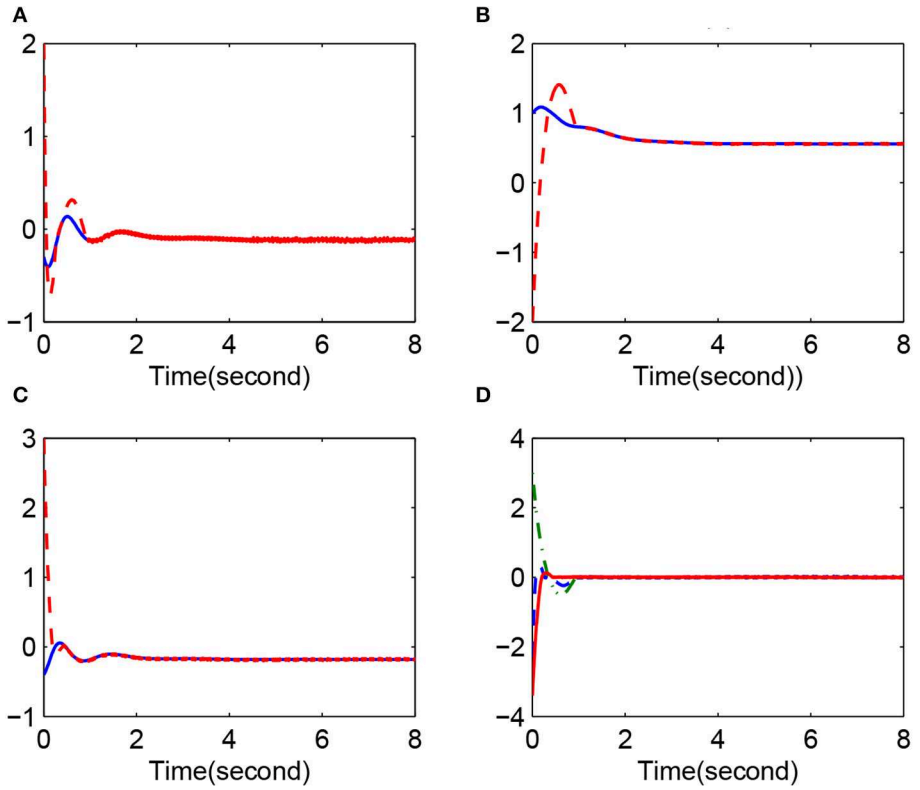

FIGURE 1 | Synchronization results of Case 1.

It follows from (39) that there exists a non-negative function $M(k)$ such that

$$\boldsymbol{x}^T(k)\boldsymbol{x}(k) + M(k) = 2V(0) - 2q_0^C D_k^{-\nu}\boldsymbol{x}^T(k)\boldsymbol{x}(k). \tag{40}$$

Taking the Laplace transform on (40), we obtain:

$$\boldsymbol{X}^T(s)\boldsymbol{X}(s) = 2V(0)\frac{s^{\nu-1}}{s^\nu + 2q} - \frac{s^\nu}{s^\nu + 2b}\boldsymbol{M}(s), \tag{41}$$

where $\boldsymbol{X}(s)$ and $\boldsymbol{M}(s)$ are respectively the Laplace transforms of $\boldsymbol{x}(k)$ and $M(k)$. Taking the inverse Laplace transform on both sides of equation (41), the solution is

$$\boldsymbol{x}^T(k)\boldsymbol{x}(k) = 2V(0)E_{\nu,1}(-2qk^\nu) - M(k) * \left[k^{-1}E_{\nu,0}(-2qk^\nu)\right], \tag{42}$$

where $*$ is the convolution. Since k^{-1} and $E_{\nu,0}(-2qk^\nu)$ are both non-negative functions, $\boldsymbol{x}^T(k)\boldsymbol{x}(k) \le 2V(0)E_{\nu,1}(-2qk^\nu)$. From Li et al. [2], we know that $\boldsymbol{x}(k)$ is M-L stable and $\boldsymbol{x}(k)$ tends to zero asymptotically, i.e., $\lim_{k\to\infty} ||\boldsymbol{x}(k)|| = 0$.

Lemma 8. Suppose that $V_0(k) = \frac{1}{2}\boldsymbol{z}^T(k)\boldsymbol{Q}_1\boldsymbol{z}(k) + \frac{1}{2}\boldsymbol{d}^T(k)\boldsymbol{Q}_2\boldsymbol{d}(k)$, where $\boldsymbol{z}(k), \boldsymbol{d}(k) \in R^n$ and $\boldsymbol{Q}_1, \boldsymbol{Q}_2 \in R^{n\times n}$ are both positive definite matrixes. If there exists a positive definite matrix $\boldsymbol{Q}_3$ and a constant $q_0 > 0$ satisfying

$${}_0^C D_k^\nu V_0(k) \le -q_0\boldsymbol{z}^T(k)\boldsymbol{Q}_3\boldsymbol{z}(k), \tag{43}$$

then $||\boldsymbol{z}(k)||$ and $||\boldsymbol{d}(k)||$ are bounded, and $\boldsymbol{z}(k)$ tends to zero asymptotically (i.e., $\lim_{k\to\infty} ||\boldsymbol{z}(k)|| = 0$).

The main results of the paper are given as follows.

Theorem 2. Under Assumption 1 and Assumption 2, the synchronization between the drive system (13) and the respond system (14) can be achieved on the work of the adaptive fuzzy controller (26) and fractional-order adaptive laws (27), (28), and (29). In addition, all the signals of the closed-loop system are bounded.

Proof. Since $\boldsymbol{A} = \boldsymbol{I}_{n\times n}$, substituting the controller (26) into the error dynamic equation (21) gives

$$\begin{aligned}\boldsymbol{Q}_0^C D_k^\nu \boldsymbol{e}(k) = &-\boldsymbol{L}\boldsymbol{e}(k) + \boldsymbol{\gamma}(\boldsymbol{z}(k)) - \boldsymbol{\theta}^T(k)\boldsymbol{\varphi}(\boldsymbol{z}(k)) \\ &- \boldsymbol{H}\text{sign}(\boldsymbol{e}(k)) - \hat{\boldsymbol{M}}\text{sign}(\boldsymbol{e}(k)) + \boldsymbol{Q}\boldsymbol{D}(k).\end{aligned} \tag{44}$$

It is simplified as

$$\begin{aligned}\boldsymbol{Q}_0^C D_k^\nu \boldsymbol{e}(k) = &-\boldsymbol{L}\boldsymbol{e}(k) + \boldsymbol{\varepsilon}(\boldsymbol{z}(k)) - \tilde{\boldsymbol{\theta}}(k)^T\boldsymbol{\varphi}(\boldsymbol{z}(k)) \\ &- \boldsymbol{H}\text{sign}(\boldsymbol{e}(k)) - \hat{\boldsymbol{M}}\text{sign}(\boldsymbol{e}(k)) + \boldsymbol{Q}\boldsymbol{D}(k).\end{aligned} \tag{45}$$

Let $\tilde{\varepsilon}_i^*(k) = \hat{\varepsilon}_i^*(k) - \varepsilon_i^*$ and $\tilde{M}_i(k) = \hat{M}_i(k) - M_i, i = 1, 2, \cdots, n$. Multiplying both sides of equation (45) by $\boldsymbol{e}^T(k)$ yields

$$\boldsymbol{e}^T(k)\boldsymbol{Q}_0^C D_k^\nu \boldsymbol{e}(k) = -\boldsymbol{e}^T(k)\boldsymbol{L}\boldsymbol{e}(k) + \boldsymbol{e}^T(k)\boldsymbol{\varepsilon}(\boldsymbol{z}(k)) + \boldsymbol{e}^T(k)\boldsymbol{Q}\boldsymbol{D}(k)$$

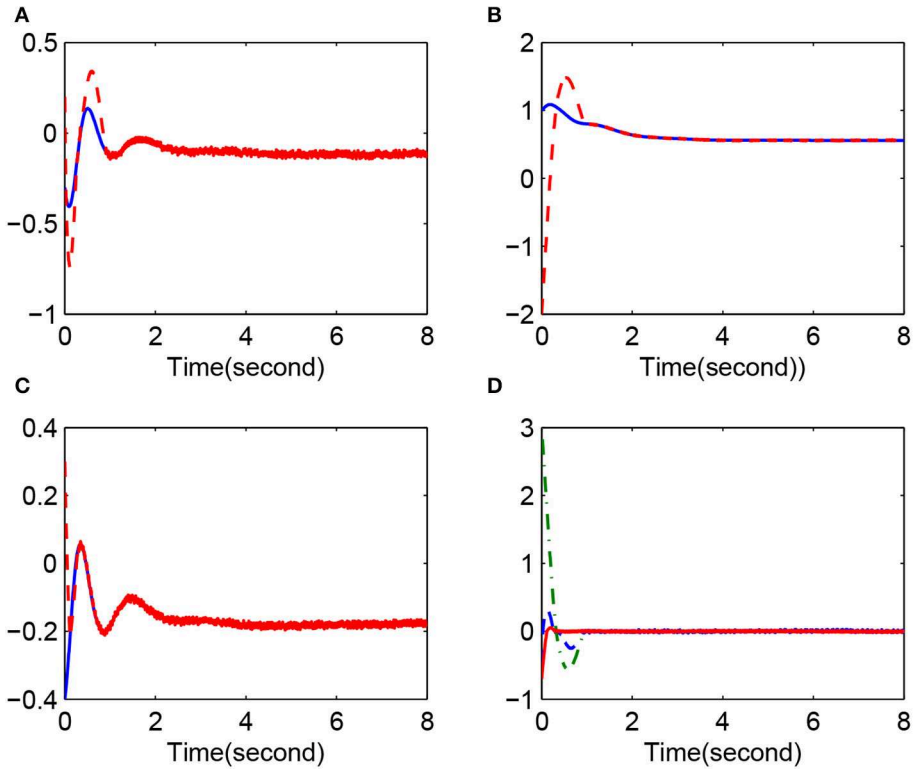

FIGURE 2 | Synchronization results of Case 2.

$$
\begin{aligned}
&-\boldsymbol{e}^T(k)\tilde{\boldsymbol{\theta}}(k)^T\boldsymbol{\varphi}(\boldsymbol{z}(k))-\boldsymbol{e}^T(k)\boldsymbol{H}\text{sign}(\boldsymbol{e}(\text{k}))-\boldsymbol{e}^{\text{T}}(\text{k})\hat{\boldsymbol{M}}\text{sign}(\boldsymbol{e}(\text{k}))\\
&\leq -\boldsymbol{e}^T(k)\boldsymbol{L}\boldsymbol{e}(k)+\sum_{i=1}^{n}|e_i(k)|\varepsilon_i^*-\sum_{i=1}^{n}e_i(k)\tilde{\theta}_i(k)^T\varphi_i(\boldsymbol{z}(k))-\\
&\sum_{i=1}^{n}|e_i(k)|\hat{\varepsilon}_i^*(k)-\sum_{i=1}^{n}|e_i(k)|\hat{M}_i(k)+\sum_{i=1}^{n}|e_i(k)|M_i\\
&=-\boldsymbol{e}^T(k)\boldsymbol{L}\boldsymbol{e}(k)-\sum_{i=1}^{n}e_i(k)\tilde{\theta}_i(k)^T\varphi_i(\boldsymbol{z}(k))-\sum_{i=1}^{n}|e_i(k)|\tilde{M}_i(k)\\
&-\sum_{i=1}^{n}|e_i(k)|\tilde{\varepsilon}_i^*(\boldsymbol{z}(k)). \qquad (46)
\end{aligned}
$$

Then, we have

$$
\begin{aligned}
V(k)=&\frac{1}{2}\boldsymbol{e}^T(k)\boldsymbol{Q}\boldsymbol{e}(k)+\frac{1}{2}\sum_{i=1}^{n}\frac{1}{\lambda_i}\tilde{\theta}_i(k)^T\tilde{\theta}_i(k)+\\
&\frac{1}{2}\sum_{i=1}^{n}\frac{1}{\xi_i}\left(\tilde{\varepsilon}_i^*(k)\right)^T\tilde{\varepsilon}_i^*(k)+\frac{1}{2}\sum_{i=1}^{n}\frac{1}{\mu_i}(\tilde{M}_i(k))^T\tilde{M}_i(k). \qquad (47)
\end{aligned}
$$

Because the ν-order Caputo derivative of a constant is zero, we have ${}_0^CD_k^\nu\theta_i(k)={}_0^CD_k^\nu\tilde{\theta}_i(k)$, ${}_0^CD_k^\nu\hat{\varepsilon}_i^*(k)={}_0^CD_k^\nu\tilde{\varepsilon}_i^*(k)$, and ${}_0^CD_k^\nu\hat{M}_i(k)={}_0^CD_k^\nu\tilde{M}_i(k)$, $i=1,2,\cdots,n$. By Lemma 3 and Lemma 6, taking the ν-order derivative of $V(k)$ in equality (47) yields

$$
\begin{aligned}
&{}_0^CD_k^\nu V(k)\leq e^T(k)\boldsymbol{Q}{}_0^CD_k^\nu e(k)+\sum_{i=1}^{n}\frac{1}{\lambda_i}\tilde{\theta}_i(k)^T{}_0^CD_k^\nu\tilde{\theta}_i(k)+\\
&\sum_{i=1}^{n}\frac{1}{\xi_i}\left(\tilde{\varepsilon}_i^*(k)\right)^T{}_0^CD_k^\nu\tilde{\varepsilon}_i^*(k)+\sum_{i=1}^{n}\frac{1}{\mu_i}(\tilde{M}_i(k))^T{}_0^CD_k^\nu\tilde{M}_i(k)\\
&\leq-\sum_{i=1}^{n}|e_i(k)|\tilde{\varepsilon}_i^*(k)-\sum_{i=1}^{n}e_i(k)\tilde{\theta}_i(k)^T\varphi_i(\boldsymbol{z}(k))-\\
&\boldsymbol{e}^T(k)\boldsymbol{L}\boldsymbol{e}(k)-\sum_{i=1}^{n}|e_i(k)|\tilde{M}_i(k)+\sum_{i=1}^{n}\frac{1}{\lambda_i}\tilde{\theta}_i(k)^T{}_0^CD_k^\nu\tilde{\theta}_i(k)\\
&+\sum_{i=1}^{n}\frac{1}{\xi_i}\left(\tilde{\varepsilon}_i^*(k)\right)^T{}_0^CD_k^\nu\tilde{\varepsilon}_i^*(k)+\sum_{i=1}^{n}\frac{1}{\mu_i}(\tilde{M}_i(k))^T{}_0^CD_k^\nu\tilde{M}_i(k). \qquad (48)
\end{aligned}
$$

Substituting (27), (28), and (29) into (48) gives

$$
{}_0^CD_k^\nu V(k)\leq-\boldsymbol{e}^T(k)\boldsymbol{L}\boldsymbol{e}(k)\leq-\frac{l_0}{\lambda_{\max}}\boldsymbol{e}^T(k)\boldsymbol{Q}\boldsymbol{e}(k), \qquad (49)
$$

where $l_0=\min\{l_1,l_2,\cdots,l_n\}$ and $\lambda_{\max}$ is a maximal eigenvalue in positive definite matrix $\boldsymbol{Q}$. From Lemma 8 and inequality (49), we know that the synchronization error satisfies $\lim_{k\to\infty}||\boldsymbol{e}(k)||=0$, and if ${}_0^CD_k^\nu\tilde{\theta}_i(k)$, ${}_0^CD_k^\nu\tilde{\varepsilon}_i^*(k)$, and ${}_0^CD_k^\nu\tilde{M}_i(k)$ are bounded, then ${}_0^CD_k^\nu\theta_i(k)$, ${}_0^CD_k^\nu\hat{\varepsilon}_i^*(k)$, and ${}_0^CD_k^\nu\hat{M}_i(k)$ are both bounded. Since

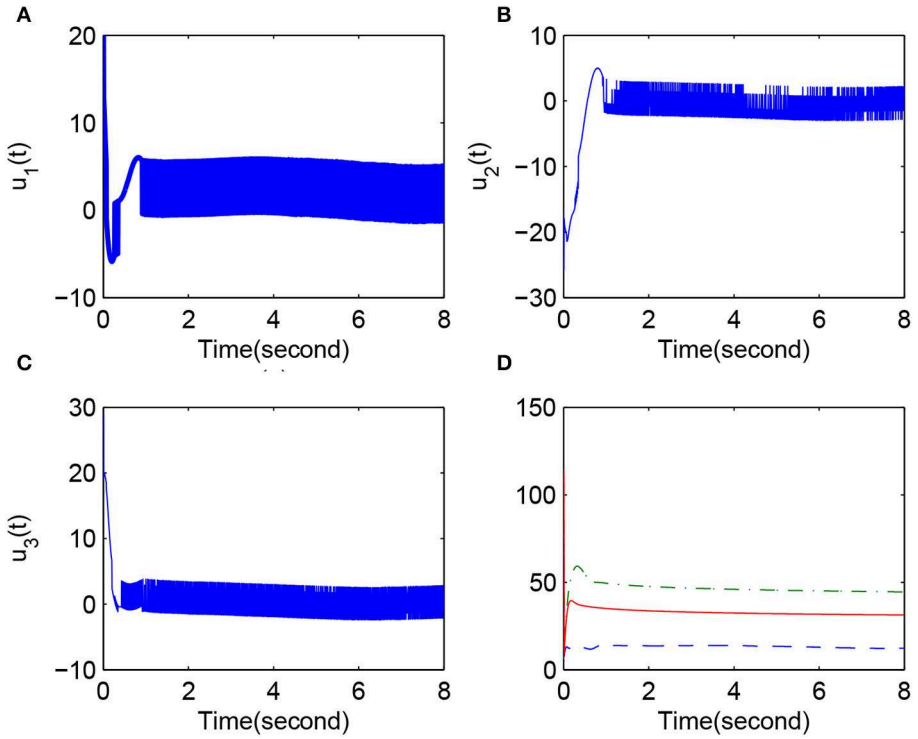

FIGURE 3 | Control variables and fuzzy logic system parameters of Case 3.

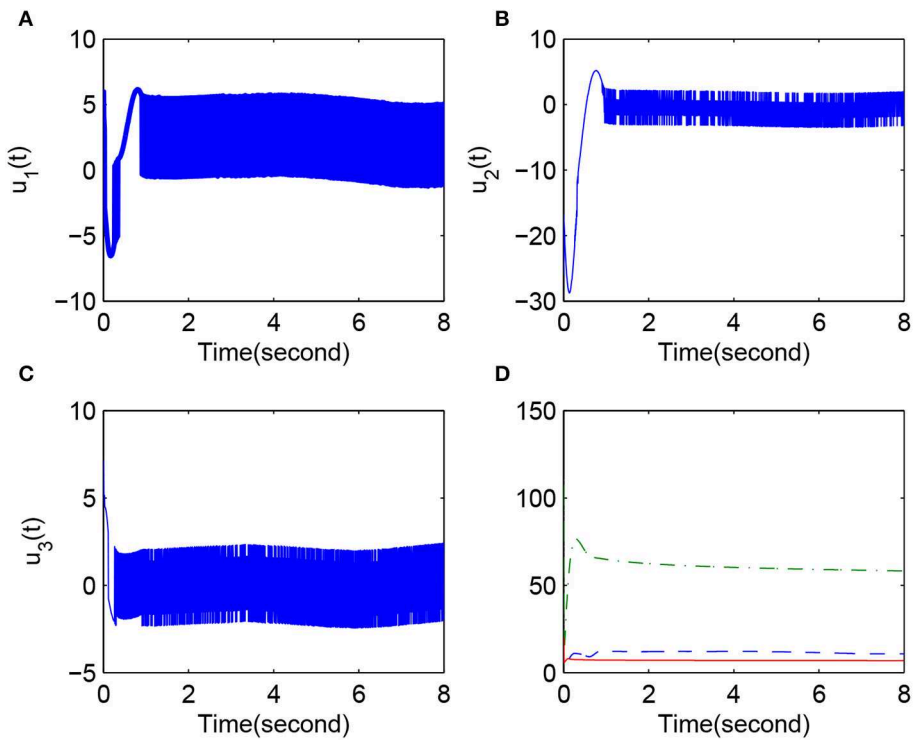

FIGURE 4 | Control variables and fuzzy logic system parameters of Case 4.

system (13) is a chaotic system, we know that $\boldsymbol{x}(k)$ is also bounded. Thus, $\boldsymbol{e}(k)$ is also bounded, which implies that $\boldsymbol{y}(k)$ is bounded, too. Consequently, by using (26), we get that $\boldsymbol{u}(k)$ is bounded. Thereby, all the signals in the closed-loop system are bounded.

Remark 4. For respond system (14), when $\boldsymbol{G} = \boldsymbol{E}$, the synchronization between the uncertain FOCSs was solved in Liu et al. [44]. However, this solution cannot solve the synchronization question for systems with uncertain non-symmetrical control gain; when $\boldsymbol{D}(k) = \boldsymbol{0}$, Ha et al. [45] researched the synchronization of FOCSs with indeterminate non-symmetrical control gain but also did not solve the synchronization question of systems with unknown disturbances. In contrast, by considering the above two conditions, this paper addresses the synchronization question for systems with uncertain non-symmetrical control gain and unknown disturbances.

5. NUMERICAL SIMULATION

In the simulation, the effectiveness of the controller is tested by researching the synchronization between the fractional-order Newton-Leipnik system [46, 47] and the fractional-order Lü system [48, 49].

The fractional-order Newton-Leipnik system is given as follows.

$$\boldsymbol{h}(\boldsymbol{x}(k)) = \begin{pmatrix} -0.4x_1(k) + x_2(k) + 10x_2(k)x_3(k) \\ -x_1(k) - 0.4x_2(k) + 5x_1(k)x_3(k) \\ 0.175x_3(k) - 5x_1(k)x_2(k) \end{pmatrix}. \tag{50}$$

The fractional-order Lü system can be written as:

$$\boldsymbol{p}(\boldsymbol{y}(k)) = \begin{pmatrix} -36y_1(k) + 36y_2(k) \\ 20y_2(k) - y_1(k)y_3(k) \\ -3y_3(k) + y_1(k)y_2(k) \end{pmatrix}. \tag{51}$$

The gain matrix $\boldsymbol{G}$ (which is non-symmetric) and its factorization (by Lemma 4) are as follows.

$$\begin{aligned} \boldsymbol{G} &= \begin{pmatrix} 1 & a & 0.3 \\ 0 & -0.4 & 0.2 \\ 0 & 0 & b \end{pmatrix} = \boldsymbol{G}_1\boldsymbol{A}\boldsymbol{T} \\ &= \begin{pmatrix} 1 & 0 & 0 \\ 0 & -0.2 & 0 \\ 0 & 0 & -0.3 \end{pmatrix} \begin{pmatrix} 1 & 0 & 0 \\ 0 & -1 & 0 \\ 0 & 0 & 1 \end{pmatrix} \begin{pmatrix} 1 & -0.2 & 0.3 \\ 0 & 2 & 1 \\ 0 & 0 & -3 \end{pmatrix}, \end{aligned} \tag{52}$$

where parameters a and b are separately $a = -0.2$ and $b = 0.9$. The external disturbance is

$$\boldsymbol{D}(t) = \begin{pmatrix} 0.15\sin(k) \\ 0.05\cos(k) \\ 0.1\cos(k) \end{pmatrix}. \tag{53}$$

It is easy to gather that the following inequality holds:

$$|\boldsymbol{G}_1^{-1}\boldsymbol{D}(k)| \leq \begin{pmatrix} 1 \\ 0.5 \\ 0.8 \end{pmatrix}. \tag{54}$$

The initial values of the drive system and respond system can be respectively $\boldsymbol{x}(0) = [-0.3, 1, -0.4]^T$ and $\boldsymbol{y}(0) = [2, -2, 3]^T$. When $\boldsymbol{u}(k) \equiv \boldsymbol{0}, \boldsymbol{D}(k) = \boldsymbol{0}$ and $\mu = 0.95$, the above two systems exhibit chaotic phenomena.

In the numerical simulation, the input variables of the fuzzy system are $\boldsymbol{x}(k), \boldsymbol{y}(k)$, and $\boldsymbol{u}(k)$. For inducing calculation of the fuzzy logic system, we will replace $\boldsymbol{x}(k)$ and $\boldsymbol{y}(k)$ by $\boldsymbol{e}(k)$. For $e_1(k), e_2(k)$, and $e_3(k)$, we can select five Gaussian membership functions whose mathematical expectations are respectively $-4, -2, 0, 2$, and 4 and whose parameters are ([1.2],[-4, -2, 0, 2, 4]), uniformly distributed in the interval $[-4, 4]$ for each input. Therefore, the number of the rules that are produced by the fuzzy logic system approximating function is $5^3 = 125$. In order to better test the effectiveness of the controller, we can chose adjustable parameters, which are represented by $\theta_1(0), \theta_2(0)$, and $\theta_3(0)$, as random vectors in 125 dimensions.

The other parameters of the controller are defined as $l_i = 5, \lambda_i = 500, \xi_i = 0.5$, and $\mu_i = 0.5$, and the estimated values of the fuzzy logic system approximating error are $\hat{\varepsilon}_1^*(0) = \hat{\varepsilon}_3^*(0) = 1.8$ and $\hat{\varepsilon}_2^*(0) = 1.5$. Estimators of the product between the uncertain external disturbance and unknown constant matrix are $\hat{M}_1(0) = 1, \hat{M}_2(0) = 0.4$, and $\hat{M}_3(0) = 0.3$. For the sake of better showing the simulation results, the initial value of the respond system is chosen as $\boldsymbol{y}(0) = [0.2, -2, 0.3]^T$, which is compared to $\boldsymbol{y}(0) = [2, -2, 3]^T$. The simulation results are shown separately in **Figures 1–4**, detailed explanations of which follow.

Case 1, in **Figure 1**, synchronization result: $x(0) = [-0.3, 1, -0.4]^T$ and $y(0) = [2, -2, 3]^T$. (**Figure 1A**) $x_1(k)$ (solid line) and $y_1(k)$ (dotted line); (**Figure 1B**) $x_2(k)$ (solid line) and $y_2(k)$ (dotted line); (**Figure 1C**) $x_3(k)$ (solid line) and $y_3(k)$ (dotted line); (**Figure 1D**) synchronization error $e_1(k)$ (dotted line), $e_2(k)$ (dashed line), and $e_3(k)$ (solid line).

Case 2, in **Figure 2**, synchronization result: $x(0) = [-0.3, 1, -0.4]^T$ and $y(0) = [0.2, -2, 0.3]^T$. (**Figure 2A**) $x_1(k)$ (solid line) and $y_1(k)$ (dotted line); (**Figure 2B**) $x_2(k)$ (solid line) and $y_2(k)$ (dotted line); (**Figure 2C**) $x_3(k)$ (solid line) and $y_3(k)$ (dotted line); (**Figure 2D**) synchronization error $e_1(k)$ (dotted line), $e_2(k)$ (dashed line), and $e_3(k)$ (solid line).

Case 3, in **Figure 3**, control variables and fuzzy logic system parameters: $x(0) = [-0.3, 1, -0.4]^T$ and $y(0) = [2, -2, 3]^T$. (**Figure 3A**) $u_1(t)$; (**Figure 3B**) $u_2(k)$; (**Figure 3C**) $u_3(k)$; (**Figure 3D**) $||\theta_1(k)||$ (dotted line), $||\theta_2(k)||$ (dashed line), and $||\theta_3(k)||$ (solid line).

Case 4, in **Figure 4**, control variables and fuzzy logic system parameters: $x(0) = [-0.3, 1, -0.4]^T$ and $y(0) = [0.2, -2, 0.3]^T$. (**Figure 4A**) $u_1(k)$; (**Figure 4B**) $u_2(k)$; (**Figure 4C**) $u_3(k)$; (**Figure 4D**) $||\theta_1(k)||$ (dotted line), $||\theta_2(k)||$ (dashed line), and $||\theta_3(k)||$ (solid line).

The simulation results clearly show that the convergence rate of synchronization error is fast when l_i is reasonable. **Figures 1**, **4** give the error change trend that the error is large at first and then gets smaller and smaller after a time, finally tending to zero asymptotically. Furthermore, from case 1 and case 2, we know that a minimal change in initial values can have obvious effects on the error but cannot affect the eventual convergence of

error. This implies that the fuzzy system proposed in this paper has good approximation performance. **Figures 3**, **4** display the changing situation of control variables and fuzzy logic system parameters, and it conforms to our expectations. In addition, from the above simulation results, we can see a chattering phenomenon because a discontinuous sign function is used in the synchronization controller.

6. CONCLUSION

In this paper, a robust adaptive fuzzy controller for indeterminate FOCSs with uncertain external disturbances and non-symmetrical control gain is proposed. The proposed method has good ability on the condition that each sequence-leading minor of the uncertain non-symmetrical gain matrix is non-zero, and the upper bound of the product of the positive definite matrix factorized by gain matrix and external disturbance is known. The stability of the closed-loop system is successfully discussed by using a fractional-order Lyapunov method and quadratic Lyapunov functions.

DATA AVAILABILITY STATEMENT

All datasets generated for this study are included in the article/supplementary material.

AUTHOR CONTRIBUTIONS

JX and XZ contributed the conception and design of the study. XQ and NL organized the literature. JX performed the design of figures and wrote the first draft of the manuscript. All authors contributed to manuscript revision and read and approved the submitted version.

FUNDING

This work was supported by the Basic Ability Promotion Project for Young and Middle-aged Teachers of Guangxi Colleges and Universities (2020KY04022), the Xiangsihu Young Scholars Innovative Research Teamof Guangxi University for Nationalities (2019RSCXSHQN02), and the Key Natural Science Research Projects in Anhui Universities (KJ2019A0696).

REFERENCES

1. Liu H, Pan Y, Cao J. Composite learning adaptive dynamic surface control of fractional-order nonlinear systems. *IEEE Trans Cybernet*. (2019). doi: 10.1109/TCYB20192938754. [Epub ahead of print].
2. Li Y, Chen Y, Podlubny I. Mittag–Leffler stability of fractional order nonlinear dynamic systems. *Automatica*. (2009) **45**:1965–9. doi: 10.1016/j.automatica.2009.04.003
3. Pudlubny I. *Fractional Differential Equations.* London: Academic Press (1999).
4. Liu H, Wang H, Cao J, Alsaedi A, Hayat T. Composite learning adaptive sliding mode control of fractional-order nonlinear systems with actuator faults. *J Franklin Inst*. (2019) **356**: 9580–99. doi: 10.1016/jjfranklin201902042
5. Qin X, Li S, Liu H. Adaptive fuzzy synchronization of uncertain fractional-order chaotic systems with different structures and time-delays. *Adv Diff Equat*. (2019) **2019**:174. doi: 10.1186/s13662-019-2117-1
6. Shah SM, Samar R, Khan NM, Raja MAZ. Fractional-order adaptive signal processing strategies for active noise control systems. *Nonlinear Dyn*. (2016) **85**:1363–76. doi: 10.1007/s11071-016-2765-6
7. Dabiri A, Nazari M, Butcher EA. The spectral parameter estimation method for parameter identification of linear fractional order systems. In: *American Control Conference (ACC)*. Boston, MA: IEEE (2016). p. 2772–7.
8. Wang Y, Gu L, Xu Y, Cao X. Practical tracking control of robot manipulators with continuous fractional-order nonsingular terminal sliding mode. *IEEE Trans Indus Electron*. (2016) **63**:6194–204. doi: 10.1109/TIE.2016.2569454
9. Liu H, Pan Y, Cao J, Zhou Y, Wang H. Positivity and stability analysis for fractional-order delayed systems: A T-S fuzzy model approach. *IEEE Trans Fuzzy Syst*. (2020). doi: 10.1109/TFUZZ20202966420. [Epub ahead of print].
10. Rahmani M, Ghanbari A, Ettefagh MM. Robust adaptive control of a bio-inspired robot manipulator using bat algorithm. *Expert Syst. Appl*. (2016) **56**:164–76. doi: 10.1016/j.eswa.2016.03.006
11. Ferdaus M, Pratama M, Anavatti SG, Garratt MA, Pan Y. Generic evolving self-organizing neuro-fuzzy control of bio-inspired unmanned aerial vehicles. *arXiv [Preprint]*. arXiv:180200635 (2018). doi: 10.1109/TFUZZ.2019.2917808
12. Pan Y, Er MJ, Sun T, Xu B, Yu H. Adaptive fuzzy PD control with stable H∞ tracking guarantee. *Neurocomputing*. (2017) **237**:71–8. doi: 10.1016/j.neucom.2016.08.091
13. Xu Y, Zhou J, Xue X, Fu W, Zhu W, Li C. An adaptively fast fuzzy fractional order PID control for pumped storage hydro unit using improved gravitational search algorithm. *Energy Convers Manage*. (2016) **111**:67–78. doi: 10.1016/j.enconman.2015.12.049
14. Pinsker JE, Lee JB, Dassau E, Seborg DE, Bradley PK, Gondhalekar R, et al. Randomized crossover comparison of personalized MPC and PID control algorithms for the artificial pancreas. *Diabetes Care*. (2016) **39**:1135–42. doi: 10.2337/dc15-2344
15. Ma D, Chen J, Liu A, Chen J, Niculescu SI. Explicit bounds for guaranteed stabilization by PID control of second-order unstable delay systems. *Automatica*. (2019) **100**:407–11. doi: 10.1016/j.automatica.2018.11.053
16. Liu H, Pan Y, Li S, Chen Y. Adaptive fuzzy backstepping control of fractional-order nonlinear systems. *IEEE Trans Syst Man Cybernet Syst*. (2017) **47**:2209–17. doi: 10.1109/TSMC.2016.2640950
17. Chang W, Li Y, Tong S. Adaptive fuzzy backstepping tracking control for flexible robotic manipulator. *IEEE CAA J Autom Sin*. (2018). doi: 10.1109/JAS.2017.7510886. [Epub ahead of print].
18. Liu YJ, Gao Y, Tong S, Li Y. Fuzzy approximation-based adaptive backstepping optimal control for a class of nonlinear discrete-time systems with dead-zone. *IEEE Trans Fuzzy Syst*. (2016) **24**:16–28. doi: 10.1109/TFUZZ.2015.2418000
19. Li H, Wang L, Du H, Boulkroune A. Adaptive fuzzy backstepping tracking control for strict-feedback systems with input delay. *IEEE Trans Fuzzy Syst*. (2017) **25**:642–52. doi: 10.1109/TFUZZ.2016.2567457
20. Xu D, Huang J, Su X, Shi P. Adaptive command-filtered fuzzy backstepping control for linear induction motor with unknown end effect. *Inform Sci*. (2019) **477**:118–31. doi: 10.1016/j.ins.2018.10.032
21. Chen DY, Zhao WL, Ma XY, Zhang RF. No-chattering sliding mode control chaos in Hindmarsh–Rose neurons with uncertain parameters. *Comput Math Appl*. (2011) **61**:3161–71. doi: 10.1016/j.camwa.2011.04.010
22. Farhat M, Barambones O, Sbita L. A new maximum power point method based on a sliding mode approach for solar energy harvesting. *Appl Energy*. (2017) **185**:1185–98. doi: 10.1016/j.apenergy.2016.03.055
23. Zhou Q, Yao D, Wang J, Wu C. Robust control of uncertain semi-Markovian jump systems using sliding mode control method. *Appl Math Comput*. (2016) **286**:72–87. doi: 10.1016/j.amc.2016.03.013
24. Li H, Wang J, Shi P. Output-feedback based sliding mode control for fuzzy systems with actuator saturation. *IEEE Trans Fuzzy Syst*. (2016) **24**:1282–93. doi: 10.1109/TFUZZ.2015.2513085

25. Jiang B, Karimi HR, Kao Y, Gao C. Reduced-order adaptive sliding mode control for nonlinear switching semi-Markovian jump delayed systems. *Inform Sci*. (2019) **477**:334–48. doi: 10.1016/j.ins.2018.10.054
26. Guo Y, Ma B. Extension of Lyapunov direct method about the fractional nonautonomous systems with order lying in (**1**, **2**). *Nonlinear Dyn*. (2016) **84**:1353–61. doi: 10.1007/s11071-015-2573-4
27. Dang QA, Hoang MT. Lyapunov direct method for investigating stability of nonstandard finite difference schemes for metapopulation models. *J Diff Equat Appl*. (2018) **24**:15–47. doi: 10.1080/10236198.2017.1391235
28. Tuan HT, Trinh H. Stability of fractional-order nonlinear systems by Lyapunov direct method. *IET Control Theory Appl*. (2017) 12:2417–22. doi: 10.1049/iet-cta.2018.5233
29. Wang H, Shi P, Li H, Zhou Q. Adaptive neural tracking control for a class of nonlinear systems with dynamic uncertainties. *IEEE Trans Cybernet*. (2017) **47**:3075–87. doi: 10.1109/TCYB.2016.2607166
30. He W, Chen Y, Yin Z. Adaptive neural network control of an uncertain robot with full-state constraints. *IEEE Trans Cybernet*. (2016) **46**:620–9. doi: 10.1109/TCYB.2015.2411285
31. Pan Y, Liu Y, Xu B, Yu H. Hybrid feedback feedforward: an efficient design of adaptive neural network control. *Neural Netw*. (2016) **76**:122–34. doi: 10.1016/j.neunet.2015.12.009
32. Li G, Sun C. Adaptive neural network backstepping control of fractional-order Chua–Hartley chaotic system. *Adv Diff Equat*. (2019) **2019**:148. doi: 10.1186/s13662-019-2099-z
33. Wang H, Liu YJ, Tong S. Adaptive control of a class of switched nonlinear discrete-time systems with unknown parameter. *Neurocomputing*. (2016) **21**4:1–6. doi: 10.1016/j.neucom.2016.03.072
34. Zhou P, Ding R, Cao YX. Multi drive-one response synchronization for fractional-order chaotic systems. *Nonlinear Dyn*. (2012) **70**:1263–71. doi: 10.1007/s11071-012-0531-y
35. Aguila-Camacho N, Duarte-Mermoud MA, Gallegos JA. Lyapunov functions for fractional order systems. *Commun Nonlinear Sci Numer Simul*. (2014) **19**:2951–7. doi: 10.1016/j.cnsns.2014.01.022
36. Costa RR, Hsu L, Imai AK, Kokotović P. Lyapunov-based adaptive control of MIMO systems. *Automatica*. (2003) **39**:1251–7. doi: 10.1016/S0005-1098(03)00085-2
37. Liu H, Pan Y, Cao J, Wang H, Zhou Y. Adaptive neural network backstepping control of fractionial-order nonlinear systems with actuator faults. *IEEE Trans Neural Netw Learn Syst*. (2020). doi: 10.1109/TNNLS20202964044. [Epub ahead of print].
38. Li Y, Sui S, Tong S. Adaptive fuzzy control design for stochastic nonlinear switched systems with arbitrary switchings and unmodeled dynamics. *IEEE Trans Cybernet*. (2017) **47**:403–14. doi: 10.1109/TCYB.2016.2518300
39. Li Y, Tong S. Adaptive fuzzy output-feedback stabilization control for a class of switched nonstrict-feedback nonlinear systems. *IEEE Trans Cybernet*. (2017) **47**:1007–16. doi: 10.1109/TCYB.2016.2536628
40. Liu Y, Park JH, Guo BZ, Shu Y. Further results on stabilization of chaotic systems based on fuzzy memory sampled-data control. *IEEE Trans Fuzzy Syst*. (2018) **26**:1040–5. doi: 10.1109/TFUZZ.2017.2686364
41. Liu YJ, Gong M, Tong S, Chen CP, Li DJ. Adaptive fuzzy output feedback control for a class of nonlinear systems with full state constraints. *IEEE Trans Fuzzy Syst*. (2018) **26**:2607–17. doi: 10.1109/TFUZZ.2018.2798577
42. Boulkroune A, Tadjine M, M'Saad M, Farza M. Fuzzy adaptive controller for MIMO nonlinear systems with known and unknown control direction. *Fuzzy Sets Syst*. (2010) **161**:797–820. doi: 10.1016/j.fss.2009.04.011
43. Tong S, Tang J, Wang T. Fuzzy adaptive control of multivariable nonlinear systems1. *Fuzzy Sets Systems*. (2000) **111**:153–67. doi: 10.1016/S0165-0114(98)00052-9
44. Liu H, Li S, Li G, Wang H. Adaptive controller design for a class of uncertain fractional-order nonlinear systems: an adaptive fuzzy approach. *Int J Fuzzy Syst*. (2018) **20**:366–79. doi: 10.1007/s40815-017-0371-5
45. Ha S, Liu H, Li S, Liu A. Backstepping-based adaptive fuzzy synchronization control for a class of fractional-order chaotic systems with input saturation. *Int J Fuzzy Syst*. (2019) **21**:1571–84. doi: 10.1007/s40815-019-00663-5
46. Sheu LJ, Chen HK, Chen JH, Tam LM, Chen WC, Lin KT, et al. Chaos in the Newton–Leipnik system with fractional order. *Chaos Solitons Fract*. (2008) **36**:98–103. doi: 10.1016/j.chaos.2006.06.013
47. Dar MR, Kant NA, Khanday FA. Electronic implementation of fractional-order newton–leipnik chaotic system with application to communication. *J Comput Nonlinear Dyn*. (2017) **12**:054502. doi: 10.1115/1.4036547
48. Lu J, Chen G, Yu X, Leung H. Design and analysis of multiscroll chaotic attractors from saturated function series. *IEEE Trans Circuits Syst I Regul Pap*. (2004) **51**:2476–90. doi: 10.1109/TCSI.2004.838151
49. Lu J, Yu S, Leung H, Chen G. Experimental verification of multidirectional multiscroll chaotic attractors. *IEEE Trans Circuits Syst I Regul Pap*. (2006) **53**:149–65. doi: 10.1109/TCSI.2005.854412

Conflict of Interest: The authors declare that the research was conducted in the absence of any commercial or financial relationships that could be construed as a potential conflict of interest.

frontiers in Physics

ORIGINAL RESEARCH
published: 04 June 2020
doi: 10.3389/fphy.2020.00146

I_1-Embeddability Under Gate-Sum Operation of Two I_1-Graphs

Guangfu Wang, Chenyang Li and Fengling Wang*

School of Science, East China Jiaotong University, Nanchang, China

An I_1-graph is one in which the vertices can be labeled by binary vectors such that the Hamming distance between two binary addresses is, to scale, the distance in the graph between the corresponding vertices. This study was designed to determine whether the gate-sum operation can inherit the I_1-embeddability. The subgraph H of a graph G is called a gate subgraph if, for every vertex $v \in V(G)$, there exists a vertex $x \in V(H)$ such that for every vertex u of H, x lies on a shortest path from v to u. The graph G is defined as the *gate-sum* of two graphs G_1 and G_2 with respect to H if H is a gate subgraph of at least one of G_1 and G_2, such that $G_1 \cup G_2 = G$, $G_1 \cap G_2 = H$, and both G_1 and G_2 are isometric subgraphs of G. In this article, we have shown that the gate-sum graph of two I_1-graphs is also an I_1-graph.

Keywords: hypercube, I_1-embeddability, gate subgraph, gate-sum, convex cuts

OPEN ACCESS

Edited by:
Jia-Bao Liu,
Anhui Jianzhu University, China

Reviewed by:
Xiaogang Liu,
Northwestern Polytechnical University, China
Huiqiu Lin,
East China University of Science and Technology, China

****Correspondence:***
Guangfu Wang
wgfmath@126.com

Specialty section:
This article was submitted to Mathematical Physics, a section of the journal Frontiers in Physics

Received: *22 March 2020*
Accepted: *14 April 2020*
Published: *04 June 2020*

Citation:
Wang G, Li C and Wang F (2020) I_1-Embeddability Under Gate-Sum Operation of Two I_1-Graphs. Front. Phys. 8:146. doi: 10.3389/fphy.2020.00146

1. INTRODUCTION

A computer network is a group of computer systems and other computing hardware devices that are linked together through communication channels to facilitate communication and resource-sharing among a wide range of users. Networks are usually visualized as a graph, with the computers or devices being represented by vertices and the connections between vertices shown as edges. Graham and Pollak [1] were concerned with message switching in interconnected loops of computers, and they studied the problem of addressing graphs with a ternary alphabet $\{0, 1, \delta\}$ such that any graph may be addressed with an edge distance of unity for some address length n. Blake and Gilchrist [2] restricted attention to the binary alphabet. They formulated a routing algorithm for message switching in computer networks that simplifies the computation of the minimum-length path between any two vertices. An *l_1-graph* is one in which the vertices can be labeled by binary vectors such that the Hamming distance between two binary addresses is, to scale, the distance in the graph of corresponding vertices [3]. The graph operation can construct a new graph from a given graph, and some properties can be inherited under these operations. Our motivation for this study was to determine which operations can inherit the l_1-embeddability. Thus, the purpose of this work is to determine the l_1-embeddability of the gate-sum graph of two l_1-graphs.

Let $G = (V, E)$ be a connected simple graph. The *distance* between two vertices u and v of G, denoted by $d_G(u, v)$, is the length of a shortest u–v path in G. Then $[V(G), d_G]$ is a graphic metric space associated with G [3]. A subgraph H of G is an *isometric subgraph* if $d_H(u, v) = d_G(u, v)$ for any $u, v \in H$. A subgraph of G is *convex* if, for any two vertices, it includes all of the shortest paths between them. Obviously, a convex subgraph of G is an isometric subgraph. Let $S \subset V(G)$ be any subset of vertices of G. The *induced subgraph* $G[S]$ is the graph that has the vertex set S and the edge set consisting of all edges in E for which both ends are in S [4].

Bandelt and Chepoi [5] introduced the definition of a gate subgraph. A subgraph H of a graph G is a *gate subgraph* if, for every vertex $v \in V(G)$, there exists a unique vertex $x \in V(H)$ such that x lies

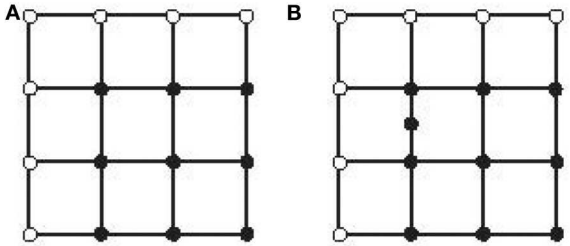

FIGURE 1 | Examples of a convex subgraph **(A)** and a gate subgraph **(B)**.

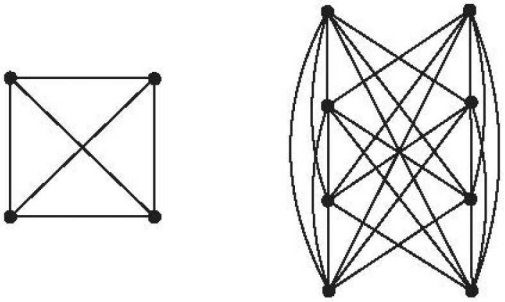

FIGURE 2 | The complete graph K_4 and the cocktail graph $K_{4\times2}$.

on the shortest path between v and any vertex $u \in V(H)$; x is called the *gate* of v. Hammack et al. [6] showed that a gate subgraph is convex, but that a convex subgraph may not be a gate subgraph. For example, each subgraph induced by the black vertices in **Figures 1A,B** is a convex subgraph in each graph. The subgraph shown in **Figure 1A** is a gate subgraph, whereas that in **Figure 1B** is not.

If u and v are two vertices of a path, the subsequence of this path starting with u and ending with v is the *segment* of this path from u to v. The *shortest path* P_{xy} is the path connecting x to y that has the fewest edges. Clearly, the segment of a shortest path is still a shortest path [7].

The l_1-*space* is the metric space of sequences whose series is absolutely convergent, denoted by (X, d_1). Thus, X is the set of all real sequences $x = (x_1, x_2, \ldots)$ such that $\sum_{k=1}^{\infty} |x_k| < \infty$, and the distance function is defined as $d_1(x, y) = \sum_{k=1}^{\infty} |x_k - y_k|$ for any $x, y \in X$. A graph G is an l_1-*graph* if $(V(G), d_G)$ is isometrically embeddable into some l_1-space. That is, there is a distance-preserving mapping φ from $V(G)$ into X such that $d_G(x, y) = d_1(\varphi(x), \varphi(y))$.

The *n-dimensional hypercube* Q_n is the graph whose vertices are ordered n-tuples of 0s and 1s, two vertices being joined if and only if they differ in exactly one coordinate.

Assouad and Deza [8] showed that a graph G is an l_1-graph if and only if G is *scale-*λ*-embeddable* into a hypercube Q_n for some positive integers λ and n, meaning that there exists a mapping $\phi : V(G) \to V(Q_n)$ such that

$$\lambda \cdot d_G(x, y) = d_{Q_n}(\phi(x), \phi(y))$$

for any $x, y \in V(G)$. The integer λ is the *scale* of G. The smallest such integer λ is called the *minimum scale* of G. According to Shpectorov [9], the minimum scale λ of G is equal to 1 or is even. In particular, if $\lambda = 1$, G is an isometric subgraph of Q_n, also called a *partial cube*.

Shpectorov [9] and Deza and Grishukhin [10] showed that a graph G is an l_1-*graph* if and only if it is an isometric subgraph of the Cartesian product of cocktail party graphs and half-cubes. The *cocktail party graph* $K_{n\times2}$ is a complete multipartite graph with n parts, each of cardinality 2, which is equivalent to a complete graph K_{2n} deleting a perfect matching, as shown in **Figure 2**. The hypercube Q_n is a bipartite graph, and the *half-cube* $\frac{1}{2}Q_n$ is the graph defined on one of two parts of this hypercube, with two vertices being joined if the distance between them in Q_n is 2.

An l_1-*rigid* graph is an l_1-graph that essentially admits a unique l_1-embedding. Shpectorov [9] showed that every l_1-rigid graph G is an isometric subgraph of a half-cube. He also proved that every l_1-*rigid* graph has scale 1 or 2. Deza and Laurent [11] proved that the complete graph K_n ($n \geq 4$) and the cocktail graph $K_{n\times2}$ ($n \geq 4$) are not l_1-rigid, where the variety of l_1-embeddings of $K_{n\times2}$ all come from that of the complete graph K_n. The half-cube graph $\frac{1}{2}Q_n$ ($n = 3, 4$) is l_1-rigid. Hence, they claim that, if G is not l_1-rigid, the variety of its l_1-embeddings arises from that of the complete graph. Deza and Tuma [12] and Chepoi et al. [13] studied the forbidden subgraphs of an l_1-rigid graph. They determined that an l_1-graph is l_1-rigid if and only if it is K_4-free.

Deza and Laurent [11] proved that the graph obtained by identifying single vertices from two l_1-graphs is also an l_1-graph. Wang and Zhang [14] proved that the graph obtained by gluing two l_1-graphs along an edge is also an l_1-graph if at least one of the original graphs is bipartite. However, for two non-bipartite graphs, this is not always the case. They also determined that even for two bipartite l_1-graphs, gluing a convex subgraph cannot guarantee the l_1-embeddability of the obtained graph. Naturally, we wondered if this result could be generalized.

Suppose that H_i is a subgraph of G_i, $i = 1, 2$. If H_1 is isomorphic to H_2, their vertices can be identified under some isomorphism as a new graph H such that the incidence relationship between vertices and edges remains. The resulting graph is called the H-*sum* of G_1 and G_2, denoted by $G_1 \cup_H G_2$. In particular, if H is a single vertex v or an edge $e = uv$, the H-sum is called the 1-*sum* or the 2-*sum*, denoted by $G_1 \cup_v G_2$ and $G_1 \cup_{uv} G_2$, respectively. Additionally, if G_1 and G_2 are isometric in $G_1 \cup_H G_2$, and H is a gate subgraph of at least one of G_1 and G_2, then $G_1 \cup_H G_2$ is called a *gate-sum* of G_1 and G_2, denoted by $G_1 \cup_H^g G_2$. Both G_1 and G_2 are isometric subgraphs of $G_1 \cup_H G_2$ if and only if $d_{G_1}(x, y) = d_{G_2}(x, y)$ for any $x, y \in H$.

For example, see the graph in **Figure 3**, where the marked K_4 is an isomorphic subgraph of G_1 and G_2. The K_4-sum graph $G_1 \cup_{K_4} G_2$, shown in **Figure 3C**, is obtained by identifying these two marked K_4 as the same subgraph. In particular, in **Figure 3B**, the marked K_4 is a gate subgraph of G_2. Obviously, both G_1 and G_2 are isometric subgraphs of $G_1 \cup_{K_4} G_2$. Therefore, it can be seen as a gate-sum graph $G_1 \cup_{K_4}^g G_2$ of G_1 and G_2 with respect to K_4.

In this paper, we have shown that the gate-sum graph of two l_1-graphs G_1 and G_2 is also an l_1-graph. The remainder of this article is organized as follows. In section 2, we have introduced the

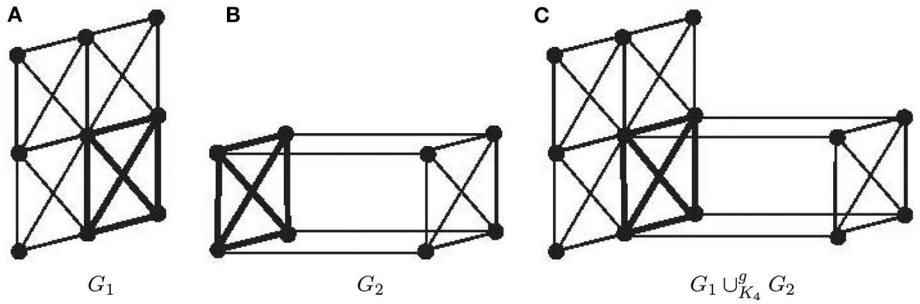

FIGURE 3 | The gate-sum graph $G_1 \cup^g_{K_4} G_2$ of G_1 and G_2 with respect to K_4.

concept of convex cuts of graphs, which are used to characterize the l_1-graphs. We have proven that the collection of convex cuts of the gate-sum graph $G_1 \cup^g_H G_2$ can be expanded by those of G_1 and G_2. We have then proven the main theorem. For the sake of brevity, we obtained the main result by omitting the proofs of certain lemmas. In section 3, we have presented detailed proofs of those lemmas that were not proved in section 2. Finally, we have presented our conclusions to this study in section 4.

2. CONVEX CUTS AND MAIN RESULTS

Deza and Tuma [12] introduced the concept of convex cuts, which can be used to characterize l_1-graphs. A *cut* $\{A, B\}$ of G is a partition of $V(G)$ into two nonempty parts. If both A and B are convex sets, then the cut $\{A, B\}$ is a *convex cut*. A cut $\{A, B\}$ of G *cuts* an edge uv if $u \in A$ and $v \in B$. An *edge cut* of G is a subset of $E(G)$ of the form $[S, \overline{S}]$, where S is a nonempty proper subset of $V(G)$, $\overline{S} = V \backslash S$, and $[S, \overline{S}]$ is the set of edges with one end in S and the other in $\overline{S}$. Similarly, we say that a cut $\{A, B\}$ of G *cuts* a subgraph H if $[A \cap V(H), B \cap V(H)]$ is an edge cut of H.

Deza and Tuma [12] and Deza et al. [15] proved the following theorem.

Theorem 2.1. ([12, 15]) *A graph G is scale-λ-embeddable into a hypercube if and only if there exists a collection $\mathcal{C}(G)$ of (not necessarily distinct) convex cuts of G such that every edge of G is cut by exactly λ cuts from $\mathcal{C}(G)$.*

For example, in the graph K_4 in **Figure 4**, the cuts $\{\{a\}, \{b, c, d\}\}$, $\{\{b\}, \{a, c, d\}\}$, $\{\{c\}, \{a, b, d\}\}$, $\{\{d\}, \{a, b, c\}\}$ are convex cuts. Every edge of K_4 is cut by exactly 2 cuts of $\{\{a\}, \{b, c, d\}\}$, $\{\{b\}, \{a, c, d\}\}$, $\{\{c\}, \{a, b, d\}\}$, and $\{\{d\}, \{a, b, c\}\}$. By Theorem 2.1, the graph K_4 is scale-2-embeddable into the hypercube Q_4.

Furthermore, Wang and Zhang [14] showed that the scale of an l_1-graph can be proportionally amplified.

Lemma 2.2. ([14]) *If a graph G is scale-λ-embeddable into a hypercube, then, for any positive integer r, G is scale-$r\lambda$-embeddable into a hypercube.*

Let G_1 and G_2 be two l_1-graphs and $G_1 \cup^g_H G_2$ be a gate-sum graph of G_1 and G_2. Without loss of generality, suppose that G_1 is scale-λ-embeddable into some hypercube and G_2 is scale-η-embeddable into some hypercube. By Theorem 2.1, there are two collections $\mathcal{C}(G_1)$ and $\mathcal{C}(G_2)$ such that every edge of G_1 and G_2 is cut by exactly λ and η cuts, respectively. According to Theorem 2.1 and Lemma 2.2, to prove $G_1 \cup^g_H G_2$ is an l_1-graph, it is sufficient to construct a collection $\mathcal{C}(G_1 \cup^g_H G_2)$ of convex cuts of $G_1 \cup^g_H G_2$ such that every edge of $G_1 \cup^g_H G_2$ is cut by exactly the same number of cuts. Now, we construct a collection of convex cuts of $G_1 \cup^g_H G_2$ from the convex cuts of $\mathcal{C}(G_1)$ and $\mathcal{C}(G_2)$.

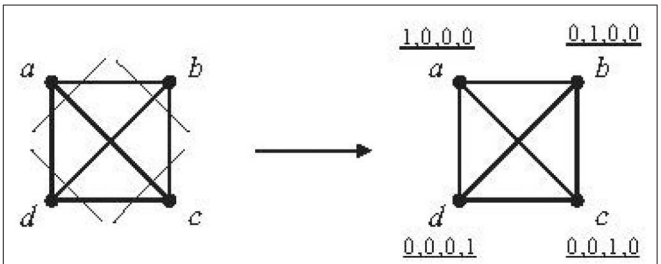

FIGURE 4 | Convex cuts and binary address of K_4.

We now define the *expansion* of convex cuts. Suppose that H is a subgraph of G and $\{A, B\}$ is a convex cut of H. If G has a convex cut $\{A', B'\}$ such that $A \subseteq A'$ and $B \subseteq B'$, then we say that the convex cut $\{A, B\}$ of H *expands* the convex cut $\{A', B'\}$ of G. We say that the collection $\mathcal{C}(H)$ *expands* a collection $\mathcal{C}(G)$ if every convex cut of $\mathcal{C}(H)$ can expand a convex cut of G. We also say that the collection $\mathcal{C}(H)$ is the *restriction* of $\mathcal{C}(G)$ on the subgraph H.

To enhance the readability of this paper, we list the following three lemmas without proofs. Their proofs have been given in section 3.

Lemma 2.3. *Suppose that $G_1 \cup^g_H G_2$ is a gate-sum graph of two l_1-graphs G_1 and G_2. Then, a convex cut of G_1 (or G_2) not cutting H can expand a convex cut of $G_1 \cup^g_H G_2$.*

Next, we will prove that two convex cuts of G_1 and G_2 can expand a convex cut of $G_1 \cup^g_H G_2$ if they cut the same edges of H. Suppose that the convex cut $\{A_1, B_1\}$ of G_1 is cutting H and that the cut $\{A_2, B_2\}$ is that of G_2. Then, $\{A_1, B_1\}$ and $\{A_2, B_2\}$ cut the same edges of H. If $A_1 \cap A_2 \neq \emptyset$, then $A_1 \cap B_2 = \emptyset$. If not, $A_1 \cap A_2 \neq \emptyset$ and $A_1 \cap B_2 \neq \emptyset$, which contradicts the assertion

that $\{A_1, B_1\}$ and $\{A_2, B_2\}$ cut the same edges of H. Similarly, we have $B_1 \cap B_2 \neq \emptyset$ and $B_1 \cap A_2 = \emptyset$. Because $A_i \cup B_i = V(G_i)$ $(i = 1, 2)$ and $V(G_1) \cap V(G_2) = V(H)$, we know that $A_1 \cap V(H) = A_1 \cap (A_1 \cup B_1) \cap (A_2 \cup B_2) = A_1 \cap A_2$ and $A_2 \cap V(H) = A_1 \cap A_2$. Similarly, $B_1 \cap V(H) = B_1 \cap B_2 = B_2 \cap V(H)$. Furthermore, we have that $V(H) = V(G_1) \cap V(G_2) = (A_1 \cup B_1) \cap (A_2 \cup B_2) = [A_1 \cap (A_2 \cup B_2)] \cup [B_1 \cap (A_2 \cup B_2)] = [A_1 \cap A_2] \cup [B_1 \cap B_2]$. We denote $V(H_A) = A_1 \cap A_2$ and $V(H_B) = B_1 \cap B_2$. Then, $V(H_A) \cup V(H_B) = V(H)$, and we have the following lemma.

Lemma 2.4. *Suppose that $G_1 \cup_H^g G_2$ is a gate-sum graph of two l_1-graphs G_1 and G_2. Assume that $\{A_1, B_1\}$ is a convex cut of G_1 and $\{A_2, B_2\}$ is that of G_2. If H is l_1-rigid, $\{A_1, B_1\}$ and $\{A_2, B_2\}$ cut the same edges of H. Then, $\{A_1, B_1\}$ and $\{A_2, B_2\}$ can together expand a convex cut $\{A_1 \cup_{V(H_A)} A_2, B_1 \cup_{V(H_B)} B_2\}$ of $G_1 \cup_H^g G_2$.*

If H is not l_1-rigid, then it has more than one kind of collection of convex cuts. Any two collections $\mathcal{C}(G_1)$ and $\mathcal{C}(G_2)$ may not be equal on H. Therefore, the convex cuts of $\mathcal{C}(G_1)$ and $\mathcal{C}(G_2)$ may not cut the same edges of H.

To solve this problem, we have proven that any kind of collection of convex cuts of H can expand two new collections of convex cuts of G_1 and G_2, respectively, such that they are equal on H.

Lemma 2.5. *Let H be an isometric subgraph of an l_1-graph G. If H is not l_1-rigid, each collection $\mathcal{C}(H)$ of H can expand a collection $\mathcal{C}(G)$ of G.*

We will now prove the main theorem of this work.

Theorem 2.6. *Suppose that $G_1 \cup_H^g G_2$ is a gate-sum graph of G_1 and G_2. If G_1 and G_2 are l_1-embeddable, then $G_1 \cup_H^g G_2$ is also l_1-embeddable.*

Proof: Without loss of generality, suppose that H is a gate subgraph of G_1. Because a gate subgraph is a convex subgraph, H is a convex subgraph of G_1. Then, H is an l_1-graph. Suppose that G_1 is scale-λ-embeddable into some hypercube and G_2 is scale-η-embeddable into some hypercube. By Theorem 2.1, there are two collections $\mathcal{C}(G_1)$ and $\mathcal{C}(G_2)$ such that every edge of G_1 and G_2 is cut by exactly λ and η cuts, respectively.

If H is l_1-rigid, H has only one kind of collection of convex cuts. Then, $\mathcal{C}(G_1)$ and $\mathcal{C}(G_2)$ have the same restriction on H (which means that $\lambda = \eta$).

If H is not l_1-rigid, the restriction on H of $\mathcal{C}(G_1)$ is not equal to that of $\mathcal{C}(G_2)$. Suppose that $\lambda \neq \eta$. By Lemma 2.2, G_2 is scale-$\lambda\eta$-embeddable into some hypercube. Then, G_2 has a collection $\mathcal{C}'(G_2)$ such that every edge of G_2 is cut by exactly $\lambda\eta$ cuts. By Lemma 2.5, every $\mathcal{C}(H)$ can expand a collection $\mathcal{C}(G_1)$. Obviously, the restriction on H of $\mathcal{C}'(G_2)$ is a kind of $\mathcal{C}(H)$. Thus, it can expand a new collection $\mathcal{C}'(G_1)$ of G_1 such that every edge of G_1 is cut by exactly $\lambda\eta$ cuts.

Hence, there always are two collections $\mathcal{C}'(G_1)$ and $\mathcal{C}'(G_2)$ for which the restrictions of them on H are equal, and every edge of G_1 and G_2 is cut by exactly $\lambda\eta$ cuts.

As $\mathcal{C}'(G_1)$ and $\mathcal{C}'(G_2)$ are equal on H, there are the same number of convex cuts of $\mathcal{C}'(G_1)$ and $\mathcal{C}'(G_2)$ cutting H. Denote the convex cuts of $\mathcal{C}'(G_1)$ that are cutting H as $\{A_1, B_1\}, ..., \{A_h, B_h\}$ and those of $\mathcal{C}'(G_2)$ as $\{A'_1, B'_1\}, ..., \{A'_h, B'_h\}$. Because the restrictions on H of $\mathcal{C}'(G_1)$ and $\mathcal{C}'(G_2)$ are equal, each convex cut of $\{A_1, B_1\}, ..., \{A_h, B_h\}$ must equal one of $\{A'_1, B'_1\}, ..., \{A'_h, B'_h\}$ on H. Without loss of generality, we assume that each pair of $\{A_i, B_i\}$ and $\{A'_i, B'_i\}$ cut the same edges of H $(1 \leq i \leq h)$. By Lemma 2.4, each pair of convex cuts $\{A_i, B_i\}$ and $\{A'_i, B'_i\}$ can together expand a convex cut $\{A_i \cup A'_i, B_i \cup B'_i\}$ of $G_1 \cup_H^g G_2$ $(1 \leq i \leq h)$. Then, every edge of H is cut by $\{A_i \cup A'_i, B_i \cup B'_i\}$ to give exactly $\lambda\eta$ cuts $(1 \leq i \leq h)$.

By Lemma 2.3, the convex cuts of $\mathcal{C}'(G_1)$ and $\mathcal{C}'(G_2)$ that do not cut H can expand the convex cuts of $G_1 \cup_H^g G_2$ that do not cut H.

Now, the convex cuts $\{A_i \cup A'_i, B_i \cup B'_i\}$ for $1 \leq i \leq h$, together with the convex cuts of $\mathcal{C}'(G_1)$ and $\mathcal{C}'(G_2)$ that do not cut H, form a collection of convex cuts of $G_1 \cup_H^g G_2$, such that every edge of $G_1 \cup_H^g G_2$ is cut by $\lambda\eta$ convex cuts. Therefore, by Theorem 2.1, the graph $G_1 \cup_H^g G_2$ is scale-$\lambda\eta$-embedded into some hypercube. This completes the proof. □

Note that, for any graph, a single vertex is a gate subgraph. A *cycle* is a closed path that originates and terminates at the same vertex. A graph is bipartite if and only if it contains no odd cycles [4]. Therefore, for any edge $e = uv$ of a bipartite graph, there is no vertex a such that $d(u, a) = d(v, a)$. The subgraph induced by an edge is then a gate subgraph in a bipartite graph. Obviously, both G_1 and G_2 are isometric subgraphs of the graphs $G_1 \cup_v G_2$ and $G_1 \cup_{uv} G_2$. The following corollaries can be immediately obtained from Theorem 2.6.

Corollary 2.7. ([11]). *Let G_1 and G_2 be two l_1-graphs. $G_1 \cup_v G_2$ is an l_1-graph.*

Corollary 2.8. ([14]). *Let G_1 and G_2 be two l_1-graphs. If at least one of them is bipartite, $G_1 \cup_{uv} G_2$ is an l_1-graph.*

3. PROOFS OF LEMMAS 2.3–2.5

3.1. Proof of Lemma 2.3

First, we need the following lemma.

Lemma 3.1. *Suppose that $G_1 \cup_H^g G_2$ is a gate-sum graph of G_1 and G_2. If H is a gate subgraph of G_1, then G_2 is a convex subgraph of $G_1 \cup_H^g G_2$.*

Proof: If G_2 is not a convex subgraph of $G_1 \cup_H^g G_2$, there are two vertices x_1 and x_2 lying in G_2 such that the shortest path $P_{x_1x_2}$ passes through a vertex v_3 of G_1. As this shortest path must pass through the vertices of the gate subgraph H of G_1, there are two vertices x'_1 and x'_2 of H on the x_1, v_3-path and x_2, v_3-path of $P_{x_1x_2}$, respectively. Note that both G_1 and G_2 are isometric subgraphs of $G_1 \cup_H^g G_2$. It is clear that the segment from x'_1 to x'_2 of $P_{x_1x_2}$ is a shortest path $P_{x'_1x'_2}$. Then, we have $P_{x'_1x'_2} = P_{x'_1v_3} + P_{v_3x'_2}$.

As H is a gate subgraph of G_1, there exists a unique gate a_3 of v_3 in H such that $P_{x'_1v_3} = P_{x'_1a_3} + P_{a_3v_3}$ and $P_{x'_2v_3} = P_{x'_2a_3} + P_{a_3v_3}$. Then, we have that $P_{x'_1x'_2} = P_{x'_1v_3} + P_{v_3x'_2} = P_{x'_1a_3} + P_{a_3v_3} + P_{x'_2a_3} + P_{a_3v_3} > P_{x'_1a_3} + P_{a_3x'_2}$, which contradicts the assertion that $P_{x'_1x'_2}$ is a shortest path. Thus, G_2 is a convex subgraph of $G_1 \cup_H^g G_2$. □

Proof of Lemma 2.3. Without loss of generality, suppose that H is a gate subgraph of G_1. We need only prove that a convex cut of G_1 or G_2 that does not cut H can expand a convex cut of $G_1 \cup_H^g G_2$.

Case 1. A convex cut of G_1 that does not cut H can expand that of $G_1 \cup_H^g G_2$.

Suppose $\{A, B\}$ is a convex cut of G_1 that does not cut H. Without loss of generality, we assume that $V(H) \subseteq B$. We now prove that $\{A, B \cup_{V(H)} V(G_2)\}$ is a convex cut of $G_1 \cup_H^g G_2$ that does not cut H and is expanded by $\{A, B\}$.

If A is not a convex set of $G_1 \cup_H^g G_2$, there are two vertices v_1 and v_2 belonging to A such that $P_{v_1v_2}$ of $G_1 \cup_H^g G_2$ passes through a vertex v_3 of $G[B] \cup_H G_2$. Therefore, $P_{v_1v_2} = P_{v_1v_3} + P_{v_3v_2}$. If all vertices of $P_{v_1v_2}$ lie entirely in G_1, A cannot be a convex set of G_1. Without loss of generality, suppose that v_3 lies in G_2. Note that H is a gate subgraph of G_1. There are two gates x_1 of v_1 and x_2 of v_2 in H, and these two gates lie in $P_{v_1v_3}$ and $P_{v_3v_2}$, respectively. Then, we have that $P_{v_1v_2} = P_{v_1x_1} + P_{x_1v_3} + P_{v_3x_2} + P_{x_2v_2}$. As G_1 is an isometric subgraph of $G_1 \cup_H^g G_2$, there is some $P_{x_1x_2}$ that lies entirely in G_1, and its length equals that of $P_{x_1x_2}$ of G_2. Then, $P_{v_1v_2} = P_{v_1x_1} + P_{x_1x_2} + P_{x_2v_2}$, and $P_{v_1v_2}$ lies entirely in G_1. As $P_{v_1v_2}$ passes through the vertices of H, and H belongs to B, A cannot be a convex set of G_1. Therefore, A is a convex set of $G_1 \cup_H^g G_2$.

If $B \cup_{V(H)} V(G_2)$ is not a convex set of $G_1 \cup_H^g G_2$, there are two vertices v_4 and v_5 belonging to $B \cup_{V(H)} V(G_2)$ such that $P_{v_4v_5}$ passes through a vertex v_6 in A and $P_{v_4v_5} = P_{v_4v_6} + P_{v_6v_5}$. Obviously, the path $P_{v_4v_6}$ does not intersect with $P_{v_6v_5}$ at any internal vertices. The segment of a shortest path is still a shortest path. This means that v_6 has two internally disjoint paths $P_{v_6v_4}$ and $P_{v_6v_5}$ that connect with the vertices in H. Thus, v_6 has at least two gates, which contradicts the statement that the gate is unique.

Both A and $B \cup_{V(H)} V(G_2)$ are convex sets of $G_1 \cup_H^g G_2$, and they contain all vertices of $G_1 \cup_H^g G_2$. Thus, $\{A, B \cup_{V(H)} V(G_2)\}$ is a convex cut of $G_1 \cup_H^g G_2$. Furthermore, note that $A = A$ and $B \subseteq B \cup_{V(H)} V(G_2)$, and so the convex cut $\{A, B \cup_{V(H)} V(G_2)\}$ is expanded by the convex cut $\{A, B\}$ of G_1.

Case 2. A convex cut of G_2 that does not cut H can expand that of $G_1 \cup_H^g G_2$.

Suppose that $\{C, D\}$ is a convex cut of G_2 that does not cut H. Without loss of generality, we assume that $H \subseteq D$. We now prove that the cut $\{C, D \cup_{V(H)} V(G_1)\}$ is a convex cut of $G_1 \cup_H^g G_2$ and is expanded by $\{C, D\}$.

By Lemma 3.1, it is obvious that C is a convex set of $G_1 \cup_H^g G_2$ because C is a convex set of G_2 and G_2 a convex subgraph of $G_1 \cup_H^g G_2$.

Suppose that the vertex set $D \cup_{V(H)} V(G_1)$ is not a convex set of $G_1 \cup_H^g G_2$. There will be two vertices v_1, v_2 of $D \cup_{V(H)} V(G_1)$ such that the shortest path $P_{v_1v_2}$ passes through a vertex v_3 of C. Let $P_{v_1v_3}$ and $P_{v_3v_2}$ denote the two segments of $P_{v_1v_2}$ divided by v_3. Because the vertices v_1, v_2 belong to $D \cup_{V(H)} V(G_1)$, we can find two vertices v_1', v_2' of D such that $v_1' \in P_{v_1v_3}$ and $v_2' \in P_{v_3v_2}$. Note that both G_1 and G_2 are isometric subgraphs of $G_1 \cup_H^g G_2$. It is clear that the segment from v_1' to v_2' of the path $P_{v_1v_2}$ is a shortest path, and it passes through the vertex v_3 of C, which contradicts the assertion that D is a convex set of G_2. Therefore, $D \cup_{V(H)} V(G_1)$ is a convex set of G.

As C and $D \cup_{V(H)} V(G_1)$ are convex sets of $G_1 \cup_H^g G_2$, $\{C, D \cup_{V(H)} V(G_1)\}$ is a convex cut of G and its two convex sets contain C and D, respectively. It follows that the convex cut $\{C, D\}$ of G_2 that does not cut H expands the convex cut $\{C, D \cup_{V(H)} V(G_1)\}$ of $G_1 \cup_H^g G_2$. This completes the proof. □

3.2. Proof of Lemma 2.4

Proof: Let G_1 and G_2 be two l_1-graphs and $G_1 \cup_H^g G_2$ be the gate-sum graph of G_1 and G_2. By Theorem 2.1, there are two collections $\mathcal{C}(G_1)$ and $\mathcal{C}(G_2)$ such that every edge of G_1 and G_2 is cut by exactly λ and η cuts, respectively, as H is l_1-rigid, $\mathcal{C}(G_1)$ and $\mathcal{C}(G_2)$ must be equal on H. For any convex cut $\{A_1, B_1\}$ of $\mathcal{C}(G_1)$, we can find a convex cut $\{A_2, B_2\}$ of $\mathcal{C}(G_2)$ that cuts the same edge of H.

Without loss of generality, suppose that H is a gate subgraph of an l_1-graph G_1. Suppose that x_1 of $V(H)$ is the gate of v_1 in G_1. If v_1 and x_1 belong to different convex sets, assume that v_1 lies in A_1 and x_1 belongs to $B_1 \cap V(H)$. There will be a vertex u in $A_1 \cap V(H)$ such that the shortest path P_{v_1u} must pass through the vertices of B_1, which contradicts the assertion that A_1 is a convex set. Then, both v_1 and x_1 belong to the same convex set A_1 or B_1.

Without loss of generality, suppose that v_1 and x_1 belong to A_1. We now show that $\{A_1 \cup_{V(H_A)} A_2, B_1 \cup_{V(H_B)} B_2\}$ is a convex cut of $G_1 \cup_H^g G_2$. First, we prove that $A_1 \cup_{V(H_A)} A_2$ is a convex set of $G_1 \cup_H^g G_2$. Consider two vertices v_1 and v_2 that belong to $A_1 \cup_{V(H_A)} A_2$.

Case 1. Both v_1 and v_2 lie in A_2.

As A_2 is a convex subset of G_2 and G_2 is a convex subgraph of $G_1 \cup_H^g G_2$, A_2 is a convex subset of $G_1 \cup_H^g G_2$. Obviously, $P_{v_1v_2}$ lies entirely in A_2.

Case 2. The vertex v_1 lies in A_1 and v_2 lies in A_2.

Because v_1 lies in A_1 and v_2 lies in A_2, the gate x_1 of v_1 belongs to $A_1 \cap V(H)$. As $\{A_1, B_1\}$ and $\{A_2, B_2\}$ cut the same edges of H, we have that $A_1 \cap V(H) = A_2 \cap V(H)$ and x_1 also belongs to A_2. Therefore, the shortest path $P_{v_1v_2}$ must pass through the vertices of H.

If $P_{v_1v_2}$ passes through the gate x_1 of v_1, we have that $P_{v_1v_2} = P_{v_1x_1} + P_{x_1v_2}$. Note that both G_1 and G_2 are isometric subgraphs of $G_1 \cup_H^g G_2$. As both v_1 and x_1 belong to A_1 and A_1 is a convex set, the path $P_{v_1x_1}$ lies entirely in A_1. Similarly, v_2 and x_1 belong to A_2, which is a convex set. Hence, $P_{v_2x_1}$ lies entirely in A_2. Thus, the shortest path $P_{v_1v_2}$ lies entirely in $A_1 \cup_{V(H_A)} A_2$.

If there is a shortest path $P_{v_1v_2}$ that does not pass through the gate x_1 of v_1, $P_{v_1v_2}$ will pass through a vertex x_3 of $V(H)$, which is not the gate of v_1, and $P_{v_1v_2} = P_{v_1x_3} + P_{x_3v_2}$.

We now prove that x_3 belongs to $A_1 \cap V(H)$. If this is not the case, then x_3 lies in $B_1 \cap V(H)$, and so $P_{v_1x_3} = P_{v_1x_1} + P_{x_1x_3}$ and $P_{x_1v_2} < P_{x_1x_3} + P_{x_3v_2}$. Furthermore, $P_{v_1x_3} + P_{x_3v_2} = P_{v_1x_1} + P_{x_1x_3} + P_{x_3v_2} > P_{v_1x_1} + P_{x_1v_2}$, which contradicts the assertion that $P_{v_1v_2}$ passes through x_3, but does not pass through the gate x_1.

As v_1 and x_3 belong to A_1, and x_3 and v_2 belong to A_2, we have that $P_{v_1x_3}$ lies entirely in A_1 and $P_{x_3v_2}$ lies entirely in A_2. Therefore, $P_{v_1v_2} = P_{v_1x_3} + P_{x_3v_2}$ lies entirely in $A_1 \cup_{V(H_A)} A_2$.

Hence, for any vertex v_1 of A_1 and any vertex v_2 of A_2, $P_{v_1v_2}$ lies entirely in $A_1 \cup_{V(H_A)} A_2$. This proves case 2.

Case 3. Both v_1 and v_2 lie in A_1.

If $P_{v_1v_2}$ does not pass through the vertices of G_2, then $P_{v_1v_2}$ lies in G_1. Note that A_1 is a convex subgraph of G_1, and $P_{v_1v_2}$ lies in A_1. If $P_{v_1v_2}$ passes through the vertices of G_2, it must pass through a vertex v_3 of A_2. From case 2, we know that both $P_{v_1v_3}$ and $P_{v_3v_2}$ lie in $A_1 \cup_{V(H_A)} A_2$ and that $P_{v_1v_2}$ lies entirely in $A_1 \cup_{V(H_A)} A_2$.

Summarizing the above three cases, for any two vertices v_1 and v_2 of $A_1 \cup_{V(H_A)} A_2$, we have that the shortest path $P_{v_1v_2}$ lies entirely in $A_1 \cup_{V(H_A)} A_2$. It follows that $A_1 \cup_{V(H_A)} A_2$ is a convex set of $G_1 \cup_H^g G_2$.

A similar proof shows that the set $B_1 \cup_{V(H_B)} B_2$ is also a convex set of $G_1 \cup_H^g G_2$. Then, $\{A_1 \cup_{V(H_A)} A_2, B_1 \cup_{V(H_B)} B_2\}$ is a convex cut of $G_1 \cup_H^g G_2$, and its two convex sets contain vertex sets A_1, A_2 and B_1, B_2, respectively. Thus, $\{A_1, B_1\}$ of G_1 and $\{A_2, B_2\}$ of G_2 together expand the convex cut $\{A_1 \cup_{V(H_A)} A_2, B_1 \cup_{V(H_B)} B_2\}$ of $G_1 \cup_H^g G_2$.

□

3.3. Proof of Lemma 2.5

To study the expansion of the collection of convex cuts, we have introduced a new characteristic of l_1-graphs. Shpectorov [9] and Deza and Grishukhin [10] characterized l_1-graphs as follows:

Theorem 3.2. ([9, 10]) *A graph G is an l_1-graph if and only if it is an isometric subgraph of the Cartesian product of cocktail party graphs and half-cubes.*

Suppose that H is an isometric subgraph of an l_1-graph G; H is also an l_1-graph. By Theorem 3.2, H is an isometric subgraph of the Cartesian product of some cocktail party graphs and half-cubes, and G is that of larger cocktail party graphs and larger half-cubes. To expand the collection of convex cuts of H to G, we need only expand the collection of convex cuts of the cocktail party graph and half-cube to a larger cocktail party graph and a larger half-cube, respectively. As the half-cube is l_1-rigid, it has a unique collection of convex cuts. Note that $\frac{1}{2}Q_m$ is a subgraph of $\frac{1}{2}Q_n$. Thus, we have that any collection $\mathcal{C}(\frac{1}{2}Q_m)$ of $\frac{1}{2}Q_m$ can expand a collection $\mathcal{C}(\frac{1}{2}Q_n)$ of $\frac{1}{2}Q_n$ ($m \leq n$). We need only examine whether any collection $\mathcal{C}(K_{m\times 2})$ can expand a collection $\mathcal{C}(K_{n\times 2})$ ($m \leq n$).

We require the definition of a vertex-transitive graph. An *automorphism* of a (simple) graph G is a permutation π of $V(G)$ that has the property that (u, v) is an edge of G if and only if $(\pi(u), \pi(v))$ is an edge of G. The set of all automorphisms of G, with the composition operation, is a group. This group is called the *automorphism group of G*. A graph G is *vertex-transitive* if the automorphism group of G acts transitively on $V(G)$ [16, 17].

In other words, a *vertex-transitive graph* is a graph G such that, given any two vertices v_1 and v_2 of G, there is some automorphism $f : V(G) \to V(G)$ such that $f(v_1) = v_2$.

For a complete graph K_n, we constructed its collection of convex cuts. Without loss of generality, assume that $V(K_n) = \{v_1, ..., v_n\}$. From Theorem 3.2, K_n is an l_1-graph. Suppose that K_n is scale-λ-embeddable into a hypercube. Theorem 2.1 implies that there is a collection $\mathcal{C}(K_n)$ such that every edge uv is cut by λ cuts (u, v belong to K_n and λ is even). We assume that $\{S_1, V(K_n) - S_1\}$ is a convex cut of $\mathcal{C}(K_n)$, and that both S_1 and $V(K_n) - S_1$ are convex sets of $V(K_n)$ ($|S_1| = q$). As the complete graph is vertex-transitive, each S_i constructs a convex cut of K_n of the form $S_i \subseteq V(K_n), |S_i| = q$ ($1 \leq i \leq \binom{n}{q}$). Then, we have that all convex cuts $\{S_i, V(K_n) - S_i\}, |S_i| = q$ ($1 \leq i \leq \binom{n}{q}$), form a collection of convex cuts of K_n such that every edge of K_n is cut by the same cuts.

Obviously, there are $\binom{n}{q}$ different convex cuts, and each convex cut acts on $q(n-q)$ edges. Note that the complete graph K_n has $\frac{n(n-1)}{2}$ edges and is vertex-transitive. Thus, we have that $\lambda = \frac{\binom{n}{q}q(n-q)}{\frac{n(n-1)}{2}} = 2\binom{n-2}{q-1}$.

For $m \leq n$, we can now prove that the collection $\mathcal{C}(K_{m\times 2})$ of $K_{m\times 2}$ can expand a collection $\mathcal{C}(K_{n\times 2})$ of $K_{n\times 2}$.

Theorem 3.3. *Let $K_{n\times 2}$ be a cocktail party graph and $K_{m\times 2}$ be a cocktail party subgraph of $K_{n\times 2}$. Every collection $\mathcal{C}(K_{m\times 2})$ of $K_{m\times 2}$ can expand a collection $\mathcal{C}(K_{n\times 2})$ of $K_{n\times 2}$.*

Proof: Obviously, the cocktail party graph $K_{n\times 2}$ has a complete subgraph K_n. Without loss of generality, assume that $V(K_n) = \{v_1, ..., v_n\}$, $V(K'_n) = \{v'_1, ..., v'_n\}$, and $V(K_{n\times 2}) = \{v_1, ..., v_n, v'_1, ..., v'_n\}$ such that $d_{K_{n\times 2}}(v_j, v'_j) = 2$ ($1 \leq j \leq n$), $d_{K_{n\times 2}}(v_i, v_j) = d_{K_{n\times 2}}(v_i, v'_j) = 1$ ($i \neq j$). If the vertex set S is a subset of $V(K_{n\times 2})$, then the vertex set $S' = \{x' | x \in S\}$ is a subset of $V(K'_{n\times 2})$.

First, we prove that every convex cut of $K_{n\times 2}$ has only two forms: $\{S \cup (V(K'_n) - S'), S' \cup (V(K_n) - S)\}$ and $\{V(K_n), V(K'_n)\}$.

Suppose that $\{A, B\}$ is a convex cut of $K_{n\times 2}$. If x belongs to A, x' will belong to B. If not, both x and x' belong to A, and A is a convex subset of $V(K_{n\times 2})$; all vertices of $V(K_{n\times 2})$ will then belong to A. Furthermore, B is an empty set, which contradicts both A and B being nonempty. We now have that the vertex sets S and S' belong to different convex sets of $\{A, B\}$. Without loss of generality, suppose that $S \subseteq A$ and $S' \subseteq B$. If $V(K_n) - S \subseteq A$, then $V(K'_n) - S' \subseteq B$ and $\{A, B\} = \{V(K_n), V(K'_n)\}$. If $V(K_n) - S \subseteq B$, then $V(K'_n) - S' \subseteq A$ and $\{A, B\} = \{S \cup (V(K'_n) - S'), S' \cup (V(K_n) - S)\}$.

Thus, the convex cut of $K_{n\times 2}$ has only two forms, $\{S \cup (V(K'_n) - S'), S' \cup (V(K_n) - S)\}$ and $\{V(K_n), V(K'_n)\}$.

Second, we prove that the collection of convex cuts $\{S_i \cup (V(K'_n) - S'_i), S'_i \cup (V(K_n) - S_i)\}, |S_i| = q$ ($1 \leq i \leq \binom{n}{q}$), together with some $\{V(K_n), V(K'_n)\}$ make the cocktail graph $K_{n\times 2}$ embeddable into some cubes.

For every edge uv in K_n, uv is cut by the convex cut $\{S_i \cup (V(K'_n) - S'_i), S'_i \cup (V(K_n) - S_i)\}$. We have that $u \in (S_i \cup (V(K'_n) - S'_i)) \cap V(K_n) = S_i$ and $v \in (S'_i \cup (V(K_n) - S_i)) \cap V(K_n) = V(K_n) - S_i$, or $u \in V(K_n) - S_i$ and $v \in S_i$. Note that $|S_i| = q$ and $V(K_n)$ has n vertices, so the number of convex cuts that cut edge uv is $2\binom{n-2}{q-1}$. This is similar to each edge $u'v'$ of K'_n.

If $u \in K_n$ and $v' \in K'_n$, uv' is cut by the convex cut $\{S_i \cup (V(K'_n) - S'_i), S'_i \cup (V(K_n) - S_i)\}$. We have that $u \in (S_i \cup (V(K'_n) - S'_i)) \cap V(K_n) = S_i$, $v' \in (S'_i \cup \{V(K_n) - S_i\}) \cap V(K'_n) = S'_i$, $u' \in S'_i$, and $v \in S_i$, or $u \in (S'_i \cup \{V(K_n) - S_i\}) \cap V(K_n) = V(K_n) - S_i$, $v' \in (S_i \cup (V(K'_n) - S'_i)) \cap V(K'_n) = V(K'_n) - S'_i$, $u' \in V(K'_n) - S'_i$, and $v \in V(K_n) - S_i$. Note that $|S_i| = |S'_i| = q$ and $|V(K_n) - S_i| =$

$|V(K'_n) - S'_i| = n - q$, so the number of convex cuts that cut edge uv' is $\binom{n-2}{q-2} + \binom{n-2}{n-q-2} = \binom{n-2}{q-2} + \binom{n-2}{q}$.

As $\frac{n-\sqrt{n}}{2} \leq q \leq \frac{n+\sqrt{n}}{2}$, $2\binom{n-2}{q-1} \geq \binom{n-2}{q-2} + \binom{n-2}{q}$. If $2\binom{n-2}{q-1} = \binom{n-2}{q-2} + \binom{n-2}{q}$, every edge of $K_{n\times 2}$ is cut by $2\binom{n-2}{q-1}$ cuts.

If $2\binom{n-2}{q-1} > \binom{n-2}{q-2} + \binom{n-2}{q}$, then $\frac{n-\sqrt{n}}{2} < q < \frac{n+\sqrt{n}}{2}$. Obviously, $\{V(K_n), V(K'_n)\}$ is a convex cut of $K_{n\times 2}$, which only cuts the edges with one end vertex in K_n and the other one in K'_n. Then, the collection $\{S_i \cup (V(K'_n) - S'_i), S'_i \cup (V(K_n) - S_i)\}$ $(1 \leq i \leq \binom{n}{q})$ together with $\{V(K_n), V(K'_n)\}$ form a new collection $\mathcal{C}'(K_{n\times 2})$ such that every edge of $K_{n\times 2}$ is cut by $2\binom{n-2}{q-1}$ cuts.

Let $2\binom{n-2}{q-1} < \binom{n-2}{q-2} + \binom{n-2}{q}$. If n is even, choose $T_i \subseteq V(K_n)$ such that $|T_i| = \frac{n}{2}$ $(1 \leq i \leq \binom{n}{\frac{n}{2}})$. If n is odd, choose $T_i \subseteq V(K_n)$ such that $|T_i| = \frac{n+1}{2}$ $(1 \leq i \leq \binom{n}{\frac{n+1}{2}})$. Then, $\{T_i \cup (V(K'_n) - T'_i), T'_i \cup (V(K_n) - T_i)\}$ is a convex cut of $K_{n\times 2}$. Obviously, the number of edges with both vertices in $V(K_n)$ (or $V(K'_n)$) that are cut by $\{T_i \cup (V(K'_n) - T'_i), T'_i \cup (V(K_n) - T_i)\}$ is greater than the number of edges that are cut by the same cut with one end vertex in K_n and the other vertex in K'_n. Thus, the collection $\{S_i \cup (V(K'_n) - S'_i), S'_i \cup (V(K_n) - S_i)\}$ $(1 \leq i \leq \binom{n}{q})$ together with $\{T_i \cup (V(K'_n) - T'_i), T'_i \cup (V(K_n) - T_i)\}$ $(1 \leq i \leq \binom{n}{\frac{n}{2}}$ $(\text{or}\binom{n}{\frac{n+1}{2}}))$ and $\{V(K_n), V(K'_n)\}$ form a new collection $\mathcal{C}'(K_{n\times 2})$ such that every edge of $K_{n\times 2}$ is cut by $2\binom{n-2}{q-1} + 2a\binom{n-2}{\frac{n}{2}-1}$ cuts. The constant a is the minimal number such that $2\binom{n-2}{q-1} + 2a\binom{n-2}{\frac{n}{2}-1} \geq \binom{n-2}{q-2} + \binom{n-2}{q} + a(\binom{n-2}{\frac{n}{2}-2} + \binom{n-2}{\frac{n}{2}})$.

Third, we prove that every collection of convex cuts of $K_{m\times 2}$ can expand that of $K_{n\times 2}$ $(m \leq n)$.

Similarly, each convex cut of $K_{m\times 2}$ has only two forms: $\{A \cup (V(K'_m) - A'), A' \cup (V(K_m) - A)\}$, and $\{V(K_m), V(K'_m)\}$.

Obviously, $(V(K_m) - A) \subseteq (V(K_n) - A)$ and $(V(K'_m) - A') \subseteq (V(K'_n) - A')$. Then, each convex cut $\{A \cup (V(K'_m) - A'), A' \cup (V(K_m) - A)\}$ of $\mathcal{C}(K_{m\times 2})$ can expand a convex cut $\{A \cup (V(K'_n) - A'), A' \cup (V(K_n) - A)\}$ of $\mathcal{C}(K_{n\times 2})$. Similarly, the convex cut $\{V(K_m), V(K'_m)\}$ expands the cut $\{V(K_n), V(K'_n)\}$.

Assume that $|A_i| = |A_j|$ is true for all convex cuts of $\mathcal{C}(K_{m\times 2})$ except the convex cut $\{V(K_m), V(K'_m)\}$. This means that $\{A_i \cup (V(K'_m) - A'_i), A'_i \cup (V(K_m) - A_i)\}$, $|A_i| = q$ $(1 \leq i \leq \binom{m}{q})$. Then, all of the cuts together with $\{V(K_m), V(K'_m)\}$ expand a collection of convex cuts of $K_{n\times 2}$, in the form $\{A_i \cup (V(K'_n) - A'_i), A'_i \cup (V(K_n) - A_i)\}$, $|A_i| = q$ $(1 \leq i \leq \binom{n}{q})$, together with $\{V(K_n), V(K'_n)\}$. By the second part, $\{A_i \cup (V(K'_n) - A'_i), A'_i \cup (V(K_n) - A_i)\}$, $|A_i| = q$ $(1 \leq i \leq \binom{n}{q})$, together with $\{V(K_n), V(K'_n)\}$ ensure that every edge of the graph $K_{n\times 2}$ is cut by the same cuts.

Let $|A_i| \neq |A_j|$ for some i and j of the convex cuts of $\mathcal{C}(K_{m\times 2})$. Without loss of generality, suppose that $\mathcal{C}(K_{m\times 2})$ has three kinds of convex cuts, formed as $\{A_i \cup (V(K'_n) - A'_i), A'_i \cup (V(K_n) - A_i)\}$, $|A_i| = q$ $(1 \leq i \leq \binom{n}{q})$, and $\{B_i \cup (V(K'_n) - B'_i), B'_i \cup (V(K_n) - B_i)\}$, $|B_i| = p$ $(1 \leq i \leq \binom{n}{p})$, together with $\{V(K_n), V(K'_n)\}$. By the above discussion, all of the convex cuts $\{A_i \cup (V(K'_n) - A'_i), A'_i \cup (V(K_n) - A_i)\}$, $|A_i| = q$ $(1 \leq i \leq \binom{n}{q})$, together with $\{V(K_n), V(K'_n)\}$ expand a collection $\mathcal{C}_1(K_{n\times 2})$ of convex cuts of $K_{n\times 2}$ such that every edge of $K_{n\times 2}$ is cut by the same cuts. Similarly, all of the convex cuts $\{B_i \cup (V(K'_n) - B'_i), B'_i \cup (V(K_n) - B_i)\}$, $|B_i| = p$ $(1 \leq i \leq \binom{n}{p})$, together with $\{V(K_n), V(K'_n)\}$ expand a collection $\mathcal{C}_2(K_{n\times 2})$ of convex cuts of $K_{n\times 2}$ such that every edge of $K_{n\times 2}$ is cut by the same cuts.

Obviously, the collection $\mathcal{C}_1(K_{n\times 2})$ together with the collection $\mathcal{C}_2(K_{n\times 2})$ is still a collection of convex cuts of $K_{n\times 2}$ such that every edge of $K_{n\times 2}$ is cut by the same cuts.

Therefore, every collection $\mathcal{C}(K_{m\times 2})$ of $K_{m\times 2}$ can expand a collection $\mathcal{C}(K_{n\times 2})$ such that every edge of $K_{n\times 2}$ is cut by the same number of cuts. □

We have that, for each cocktail party graph and half-cube, the collection $\mathcal{C}(\frac{1}{2}Q_m)$ can expand a collection $\mathcal{C}(\frac{1}{2}Q_n)$, and the collection $\mathcal{C}(K_{m\times 2})$ can expand a collection $\mathcal{C}(K_{n\times 2})$ $(m \leq n)$. By Theorem 3.2, we can prove that the collection of convex cuts of an l_1-graph can expand that of a larger l_1-graph.

Hammack et al. [6] introduced the *Cartesian product* $G\Box H$ of two graphs G and H as the graph whose vertex set is the Cartesian product $V(G) \times V(H)$. Two vertices (u, v) and (u', v') are adjacent in $G\Box H$ if and only if $u = u'$ and v is adjacent to v' in H, or $v = v'$ and u is adjacent to u' in G. Thus,

$$V(G\Box H) = \{(u, v) | u \in V(G) \text{ and } v \in V(H)\}$$
$$E(G\Box H) = \{(u, v)(u', v') | u = u', vv' \in E(H), \text{ or } uu' \in E(G), u = u'\}$$

The graphs G and H are called *factors* of the product $G\Box H$. Hammack et al. proved the following lemmas.

Lemma 3.4. ([6]) *A subgraph W of $G = G_1\Box \cdots \Box G_n$ is convex if and only if $W = W_1\Box \cdots \Box W_n$, where each W_i is convex in G_i.*

Lemma 3.5. ([6]) *If $G = G_1\Box \cdots \Box G_n$ and $x, y \in V(G)$, then*

$$d_G(x, y) = \sum_{i=1}^{n} d_{G_i}(p_i(x), p_i(y))$$

For any index $1 \leq i \leq n$, p_i is a projection map $p_i : G_1\Box \cdots \Box G_n \to G_i$, defined as $p_i(x_1, x_2, ..., x_n) = x_i$.

We can now prove that the convex cut of a Cartesian product can be represented by the convex cuts of all factors.

Theorem 3.6. *The cut $\{A, B\}$ is a convex cut of a graph $G = G_1\Box \cdots \Box G_n$ if and only if $\{A, B\}$ has the form $\{V(G_1) \times \cdots \times V(G_{i-1}) \times A_i \times V(G_{i+1}) \times \cdots \times V(G_n), V(G_1) \times \cdots \times V(G_{i-1}) \times B_i \times V(G_{i+1}) \times \cdots \times V(G_n)\}$ in which $\{A_i, B_i\}$ is a convex cut of G_i for $1 \leq i \leq n$.*

Proof: $\Longleftarrow$ Suppose that $G = G_1\Box \cdots \Box G_n$. If $\{A_i, B_i\}$ is a convex cut of G_i, then $G_i[A_i]$ and $G_i[B_i]$ are convex subgraphs of G_i $(1 \leq i \leq n)$. By Lemma 3.4, $G[A_i] = G_1\Box \cdots \Box G_{i-1}\Box G_i[A_i]\Box G_{i+1}\Box \cdots \Box G_n$ is a convex subgraph of G. Similarly, $G[B_i] = G_1\Box \cdots \Box G_{i-1}\Box G_i[B_i]\Box G_{i+1}\Box \cdots \Box G_n$ is also a convex subgraph of G.

Without loss of generality, suppose that

$$V(G) = \{(x_1, ..., x_i, ..., x_n) | x_i \in V(G_i)\}$$
$$V(G[A_i]) = \{(x_1, ..., x_{i-1}, y_i, x_{i+1}, ..., x_n) | x_j$$

$$\begin{aligned} &\in V(G_j), j \neq i, y_i \in A_i\} \\ &= \{V(G_1) \times \cdots \times V(G_{i-1}) \times A_i \times V(G_{i+1}) \\ &\quad \times \cdots \times V(G_n)\} \\ V(G[B_i]) \quad &= \{(x_1, ..., x_{i-1}, y_i, x_{i+1}, ..., x_n) | x_j \\ &\in V(G_j), j \neq i, y_i \in B_i\} \\ &= \{V(G_1) \times \cdots \times V(G_{i-1}) \times B_i \\ &\quad \times V(G_{i+1}) \times \cdots \times V(G_n)\}. \end{aligned}$$

As $\{A_i, B_i\}$ is a convex cut of G_i and the vertex y_i belongs to either A_i or B_i, we have that the cut $\{V(G[A_i]), V(G[B_i])\} = \{A, B\}$ is a partition of $V(G)$, and $\{A, B\}$ is a convex cut of G.

$\Longrightarrow$ Suppose that $\{A, B\}$ is a convex cut of G. Then, both $G[A]$ and $G[B]$ are convex subgraphs of G, and $B = \bar{A} = V(G) - A$. By Lemma 3.4, $G[A] = G_1[A_1] \square \cdots \square G_n[A_n]$ and each $G_i[A_i]$ is a convex subgraph of G_i $(1 \leq i \leq n)$.

We now prove that only one A_i is a proper subset of $V(G_i)$. If there are two proper subsets, without loss of generality, suppose that A_1 is a proper subset of $V(G_1)$, A_2 is that of $V(G_2)$, and $A_i = G_i$ $(3 \leq i \leq n)$, $V(G_j) - A_j = B_j$ $(1 \leq j \leq n)$. Then, we have that

$$\begin{aligned} A &= \{(x_1, x_2, ..., x_n) | x_i \in V(G_i), i \neq 1, 2, x_1 \in A_1, x_2 \in A_2\} \\ &= \{A_1 \times A_2 \times V(G_3) \times \cdots \times V(G_n)\} \end{aligned}$$

and

$$\begin{aligned} \bar{A} = B = &\{(x_1, x_2, ..., x_n) | x_i \in V(G_i), i \neq 1, 2, x_1 \notin A_1, x_2 \in A_2, \\ &\text{or } x_1 \in A_1, x_2 \notin A_2, \text{ or } x_1 \notin A_1, x_2 \notin A_2\} \\ = &\{[(B_1 \times A_2) \cup (A_1 \times B_2) \cup (B_1 \times B_2)] \times V(G_3) \\ &\times \cdots \times V(G_n)\}. \end{aligned}$$

Suppose that $x_1 \in A_1$, $x_2 \in A_2$, $y_1 \in B_1$, $y_2 \in B_2$, and $x_i \in G_i$ $(3 \leq i \leq n)$. We have two vertices $(y_1, x_2, x_3, x_4, ..., x_n) \in B_1 \times A_2 \times V(G_3) \times \cdots \times V(G_n)$ and $(x_1, y_2, x_3, x_4, ..., x_n) \in A_1 \times B_2 \times V(G_3) \times \cdots \times V(G_n)$. By Lemma 3.5, the distance between them is

$$\begin{aligned} &d_G((y_1, x_2, x_3, x_4, ..., x_n), (x_1, y_2, x_3, x_4, ..., x_n)) = d_{G_1}(y_1, x_1) \\ &\quad + d_{G_2}(x_2, y_2) \\ &\quad = d_G((y_1, x_2, x_3, x_4, ..., x_n), (x_1, x_2, x_3, x_4, ..., x_n)) \\ &\quad + d_G((x_1, x_2, x_3, x_4, ..., x_n), (x_1, y_2, x_3, x_4, ..., x_n)). \end{aligned}$$

However, vertex $(x_1, x_2, x_3, x_4, ..., x_n)$ belongs to $A_1 \times A_2 \times V(G_3) \times \cdots \times V(G_n)$, which means that there are two vertices in B and a shortest path between them through a vertex in A. Therefore, B is not a convex subset of $V(G)$, which contradicts the assertion that $\{A, B\}$ is a convex cut of G.

Thus, only one A_i is a proper subset of $V(G_i)$, and we have that

$$\begin{aligned} A &= \{(x_1, ..., x_{i-1}, y_i, x_{i+1}, ..., x_n) | x_j \in V(G_j), j \neq i, y_i \in A_i\} \\ &= \{V(G_1) \times \cdots \times V(G_{i-1}) \times A_i \times V(G_{i+1}) \times \cdots \times V(G_n)\}. \end{aligned}$$

Similarly, note that $V(G_j) - A_j = B_j$ $(1 \leq j \leq n)$, and so

$$\begin{aligned} B &= \{(x_1, ..., x_{i-1}, y_i, x_{i+1}, ..., x_n) | x_j \in V(G_j), j \neq i, y_i \notin A_i\} \\ &= \{V(G_1) \times \cdots \times V(G_{i-1}) \times B_i \times V(G_{i+1}) \times \cdots \times V(G_n)\}. \end{aligned}$$

As $G[A]$ and $G[B]$ are convex subgraphs of G, by Lemma 3.4, both $G_i[A_i]$ and $G_i[B_i]$ are convex subgraphs of G_i. Then, A_i and B_i are convex subsets of $V(G_i)$, and $\{A_i, B_i\}$ is a convex cut of G_i $(1 \leq i \leq n)$. □

Proof of Lemma 2.5. Let G be an l_1-graph and H be an isometric subgraph of G. By Theorem 2.1, there is a collection $\mathcal{C}(G)$ such that every edge of G is cut by exactly λ cuts.

As H is not l_1-rigid, H has another l_1-embedding. By Theorem 3.2, G is an isometric subgraph of the Cartesian product of cocktail party graphs and half-cubes. Let $\hat{G} = K_{m_1 \times 2} \square \cdots \square K_{m_p \times 2} \square \frac{1}{2}Q_{n_1} \square \cdots \square \frac{1}{2}Q_{n_q}$ be a Cartesian product that contains G as an isometric subgraph, such that each factor of $\hat{G}$ is minimal and the number of factors is minimal. Without loss of generality, we assume that $m_i \leq m_j$ and $n_i \leq n_j$ $(i < j)$.

Because H is an isometric subgraph of G and G is an l_1-graph, H is an l_1-graph. By Theorem 3.2, H has a minimal Cartesian product $\hat{H} = K_{m'_1 \times 2} \square \cdots \square K_{m'_s \times 2} \square \frac{1}{2}Q_{n'_1} \square \cdots \square \frac{1}{2}Q_{n'_t}$.

As H is an isometric subgraph of G and G is an isometric subgraph of $\hat{G}$, H is an isometric subgraph of $\hat{G}$. Because $\hat{H}$ may not be equal to $\hat{G}$, we have that $s \leq p$, $t \leq q$, and $m'_i \leq m_i$, $n'_j \leq n_j$ $(1 \leq i \leq s, 1 \leq j \leq t)$.

It is obvious that $\frac{1}{2}Q_{n'_i}$ is a convex subgraph of $\frac{1}{2}Q_{n_i}$ $(1 \leq i \leq t)$ and $K_{m'_i \times 2}$ is an isometric subgraph of $K_{m_i \times 2}$ $(1 \leq i \leq s)$.

As $\frac{1}{2}Q_n$ is l_1-rigid, the collection $\mathcal{C}(\frac{1}{2}Q_{n'_i})$ can expand a collection $\mathcal{C}(\frac{1}{2}Q_{n_i})$ for $1 \leq i \leq t$.

By Theorem 3.3, every collection $\mathcal{C}(K_{m'_i \times 2})$ can expand a collection $\mathcal{C}(K_{m_i \times 2})$ $(1 \leq i \leq s)$.

Without loss of generality, suppose that every collection of $\mathcal{C}(K_{m_j \times 2})$ $(1 \leq j \leq s)$ and $\mathcal{C}(\frac{1}{2}Q_{n_k})$ $(1 \leq k \leq t)$ cuts the edges of the corresponding factors $K_{m_j \times 2}$ and $\frac{1}{2}Q_{n_k}$ exactly $\lambda_1, \lambda_2, ..., \lambda_{s+t}$ times, respectively. Take the least common multiple $\lambda = [\lambda_1, \lambda_2, ..., \lambda_{s+t}]$. By Lemma 2.2, we have a list of collections $\mathcal{C}'(K_{m_j \times 2})$ $(1 \leq j \leq s)$ and $\mathcal{C}'(\frac{1}{2}Q_{n_k})$ $(1 \leq k \leq t)$ such that every edge of factors $K_{m_j \times 2}$ and $\frac{1}{2}Q_{n_k}$ is cut by exactly λ cuts.

By Theorem 3.6, each convex cut $\{A_{j_i}, B_{j_i}\}$ of $\mathcal{C}'(K_{m_j \times 2})$ $(1 \leq j \leq s)$ can expand a convex cut $\{A, B\}$ of G such that $\{p_j(A), p_j(B)\} = \{A_{j_i}, B_{j_i}\}$. This is similar to any convex cut $\{A_{k_i}, B_{k_i}\}$ of $\mathcal{C}'(\frac{1}{2}Q_{n_k})$ $(1 \leq k \leq t)$.

All such $\{A, B\}$ expanded by $\{A_{j_i}, B_{j_i}\}$ of $\mathcal{C}'(K_{m_j \times 2})$ $(1 \leq j \leq s)$ and $\{A_{k_i}, B_{k_i}\}$ of $\mathcal{C}'(\frac{1}{2}Q_{n_k})$ $(1 \leq k \leq t)$ form a collection $\mathcal{C}(G)$ and every edge of G is cut by exactly λ cuts of $\mathcal{C}(G)$. This completes the proof. □

4. CONCLUSION

In this study, we investigated the l_1-embeddability of the gate-sum graph of two l_1-graphs. We have shown that the gate-sum graph of two l_1-graphs G_1 and G_2 is still an l_1-graph.

DATA AVAILABILITY STATEMENT

The original contributions presented in the study are included in the article/supplementary materials, further inquiries can be directed to the corresponding author/s.

AUTHOR CONTRIBUTIONS

GW contributed the conception of gate-sum of the study. GW and CL contributed to the convex cuts of the gate-sum of two l_1-graphs. CL and FW organized the literature. FW performed the design of figures. All authors contributed to manuscript revision and read and approved the submitted version.

FUNDING

This work was supported by NSFC (Grant Nos. 11861032 and 11961026).

REFERENCES

1. Graham RL, Pollak HO. On the addressing problem for loop switching. *Bell Syst Tech J.* (1972) **50**:2495–519. doi: 10.1002/j.1538-7305.1971.tb02618.x
2. Blake I, Gilchrist J. Addresses for graphs. *IEEE Trans Inf Theory*. (1973) **19**:683–8. doi: 10.1109/TIT.1973.1055087
3. Deza M, Laurent M. *Geometry of Cuts and Metrics*. Berlin: Springer-Verlag (1997).
4. Diestel R. *Graph Theory*. Heidelberg: Springer-Verlag (2006).
5. Bandelt H, Chepoi V. Decomposition and l_1-embedding of weakly median graphs. *Eur J Combin.* (2000) **21**:701–14. doi: 10.1006/eujc.1999.0377
6. Hammack R, Imrich W, Klavžar S. *Handbook of Product Graphs*. Bosa Roca: CRC Press (2011).
7. Bondy J, Murty U. *Graph Theory*. New York, NY: Springer-Verlag (2008).
8. Assouad P, Deza M. Espaces metriques plongeables dans un hypercube: aspects combinatories. *Ann Discret Math.* (1980) **8**:197–210. doi: 10.1016/S0167-5060(08)70874-4
9. Shpectorov S. On scale embeddings of graphs into hypercubes. *Eur J Combin*. (1993) **14**:117–30.
10. Deza M, Grishukhin V. Hypermetric graphs. *Q J Math.* (1993) **44**:393–433. doi: 10.1093/qmath/44.4.399
11. Deza M, Laurent M. l_1-rigid graphs. *J Algebr Combin*. (1994) **3**:153–75.
12. Deza M, Tuma J. A note on l_1-rigid planar graphs. *Eur J Combin*. (1996) **17**:157–60. doi: 10.1006/eujc.1996.0014
13. Chepoi V, Deza M, Grishukhin V. Clin d'oeil on l_1-embeddable planar graphs. *Discret Appl Math*. (1997) **80**:3–19. doi: 10.1016/S0166-218X(97)00066-8
14. Wang G, Zhang H. l_1-embeddability under the edge-gluing operation on graphs. *Discret Math.* (2013) **313**:2115–8. doi: 10.1016/j.disc.2013.04.032
15. Deza M, Grishukhin V, Shtogrin M. *Scale-Isometric Polytopal Graphs in Hypercubes and Cubic Lattices*. London: Imperical College Press (2004).
16. Biggs N. *Algebraic Graph Theory*. Cambridge, UK: Cambridge University Press (1993).
17. Godsil C, Royle G. *Algebraic Graph Theory*. New York, NY: Springer-Verlag (2001).

Conflict of Interest: The authors declare that the research was conducted in the absence of any commercial or financial relationships that could be construed as a potential conflict of interest.

frontiers in Physics

BRIEF RESEARCH REPORT
published: 05 June 2020
doi: 10.3389/fphy.2020.00182

Neural Network Backstepping Controller Design for Uncertain Permanent Magnet Synchronous Motor Drive Chaotic Systems via Command Filter

Ricai Luo[1], *Yanping Deng*[2*] *and Yuling Xie*[3]

[1] School of Mathematics and Statistics, Hechi University, Yizhou, China, [2] School of Mathematics and Physics, Guangxi University for Nationalities, Nanning, China, [3] Department of Trial Production, North Institute of Automatic Control Technology, Taiyuan, China

In this study, an adaptive neural network (NN) command filtered control (CFC) method is proposed for a permanent magnet synchronous motor (PMSM) system with system uncertainties and external disturbance by means of a backstepping technique. At every backstepping step, a novel command filter is proposed, and the complicated virtual input and its derivative together can be approximated by this filter. The "explosion of complexity" problem in conventional backstepping design can be avoided because we do not need to calculate the derivative of the virtual input repeatedly. NNs are used to model system uncertainties and disturbances. Finally, an adaptive NN CFC is designed, and the convergence of the tracking error and the boundedness of all signals involved can be guaranteed. Finally, a simulation study is presented to verify the theoretical results.

Keywords: adaptive neural network control, command filtered control, backstepping, permanent magnet synchronous motor, chaos control

OPEN ACCESS

Edited by:
Jia-Bao Liu,
Anhui Jianzhu University, China

Reviewed by:
Guangming Xue,
Guangxi University of Finance and Economics, China
Shengda Zeng,
Jagiellonian University, Poland
Ahmed Zarzour,
British University in Egypt, Egypt

***Correspondence:**
Yanping Deng
ypdenggxun@163.com

Specialty section:
This article was submitted to Mathematical Physics, a section of the journal Frontiers in Physics

Received: *11 April 2020*
Accepted: *27 April 2020*
Published: *05 June 2020*

Citation:
Luo R, Deng Y and Xie Y (2020) Neural Network Backstepping Controller Design for Uncertain Permanent Magnet Synchronous Motor Drive Chaotic Systems via Command Filter. Front. Phys. 8:182. doi: 10.3389/fphy.2020.00182

1. INTRODUCTION

In the past several decades, adaptive backstepping control (ABC) has been used by more and more scholars due to its powerful ability in controlling non-linear systems. The ABC approach has some interesting properties. For example, it can achieve global ability and does not need a large amount of control energy. To increase the robustness of ABC, some other control methods, such as adaptive fuzzy control (AFC), adaptive neural network (NN) control, sliding mode control (SMC), etc., have been developed; the research results can be seen in references [1–10], and the references therein. However, the ABC approach has a drawback: the "explosion of complexity" problem, which is generated by differentiating the immediate virtual input repeatedly. Some efforts have been made to solve this problem, for example, in Liu et al. [6], virtual inputs were approximated by fuzzy systems, and in Ahn et al. [2], a sliding surface was used to avert the repeated calculation of the derivatives. Another approach, more powerful than these methods, is command filtered control (CFC), which was introduced by Farrell et al. [11] and Dong et al. [12], where several interesting results were presented to show that errors are of $o\left(\frac{1}{W}\right)$, with W being the frequency. To drive the tracking error toward a sufficiently small value, one can use large W. However, too large a W value usually means that too much control energy is used. Thus, some other control methods based on CFC have been developed, for example, in references [13–18], noting that the dimensions of the

virtual signal should be enlarged to involve the desired signal and its derivative. Yet, the above-mentioned literature only studied the estimation of some command derivatives, i.e., the results do not correspond to the ABC design. Thus, it is meaningful to develop more approaches to solve the above problem.

For more than 30 years, the control of chaotic systems has been paid increasing attention as an important field in non-linear scientific research and has gradually become widely used in engineering and other fields. The permanent magnet synchronous motor (PMSM) has attracted widespread attention due to its rapid dynamics, wide speed range, and simple structure. However, because the PMSM is a multivariate non-linear system and the system exhibits phenomena, such as Hope bifurcation, limit cycles, and chaotic attractors when the system parameters are in some ranges, the control of PMSM systems is still a challenging problem. Chaos in the PMSM system can destroy the stability of the system and even crash it, so it is very important to control this chaos. At present, there are many methods to control chaos in PMSM, such as the OGY method, delayed feedback control method, sliding mode control method, ABC, AFC, and so on [19–23]. In the actual application process, the OGY method requires certain system parameters, some of which cannot be achieved in actual control, whereas the delayed feedback control method has achieved good results in the PMSM chaos control, but the delay is very difficult. In Yu et al. [23], the AFC method was used, and in each step, fuzzy systems were used to model system uncertainties to avoid the repeated calculation of the virtual signal and its derivative. In Sun et al. [24], an internal motion model was used to control PMSM systems with uncertainties. In Yang et al. [25], an AFC CFC method was used where the system uncertainties are not considered. In Niu et al. [26], an output feedback CFC method was proposed for PMSM. In Zou et al. [27], command filtering-based AFC was introduced for PMSM where input saturation is considered. Some related work can be seen in references [28–32]. However, in these studies, fully unknown system models are not considered.

Based on the above discussion, we will introduce an NN CFC method for PMSM systems with fully unknown system models. We combine ABC with CFC and propose a one-order filter to approximate the virtual signal and its derivative at each backstepping step. As the last step, a robust controller is designed, and adaptation laws are also presented. Compared with related works, our contributions are as follows. (1) A one-order filter is introduced. In each step, it can be used to approximate the virtual signal together with its derivative. In addition, the proposed filter has very good approximation ability, and the error can be made as small as possible. By doing this, the "explosion of complexity" problem is avoided. Compared with some related methods, for example, in references [23, 28, 31], our methods are simpler and can be implemented earlier. (2) The proposed control signals with adaptation laws have a very concise form relative to some related methods, for example, dynamic surface control.

This paper is arranged as follows. The description of the PMSM, the controller design, and the stability analysis are presented in section 2. Section 3 gives the simulation results of the proposed method. Finally, section 4 gives the conclusions of this paper.

2. MAIN RESULTS

2.1. Problem Description

The mathematical model of a PMSM with a smooth air gap can be expressed as [23]

$$\begin{cases} \frac{d\omega}{dt} = \sigma(i_q - \omega) - \tilde{T}_L, \\ \frac{di_q}{dt} = -i_q - i_d\omega + \delta\omega + \tilde{u}_q, \\ \frac{di_d}{dt} = -i_d + i_q\omega + \tilde{u}_d, \end{cases} \tag{1}$$

where ω, i_d, i_q are system variables representing the angular velocity and shaft current of the motor, respectively, and $\tilde{T}_L$, $\tilde{u}_q$, and $\tilde{u}_d$ represent load torque and shaft voltage. When there are no external inputs, denoting $x = \omega, y = i_q, z = i_d$, and putting an input $u(t)$ to the third equation, the PMSM system (1) can be written as

$$\begin{cases} \dot{x} = \sigma(y - x), \\ \dot{y} = -y - xz + \delta x, \\ \dot{z} = -z + xy + u. \end{cases} \tag{2}$$

Let the tracking error be $\epsilon_1 = x - x^c$, with $x^c \in \mathcal{R}$ being a referenced signal. Our purpose is to implement a suitable control signal u such that $\epsilon_1(t)$ becomes as small as possible.

2.2. Backstepping Control Signal Design

The backstepping control procedures can be divided into the following three steps.

Step 1. It follows from (2) that:

$$\dot{x} = \sigma y + \Delta g_1(x), \tag{3}$$

where $\Delta g_1(x) = -\sigma x$ is assumed to be unknown. Then, $\Delta g_1(x)$ is estimated by using NN as

$$\Delta g_1 = \boldsymbol{W}_1^T \boldsymbol{\vartheta}_1 = \boldsymbol{W}_1^{*T} \boldsymbol{\vartheta}_1 + \varepsilon_1 \tag{4}$$

with $\boldsymbol{W}_1^T$ being the adjustable parameter of the NN, $\boldsymbol{W}_1^{*T}$ being the optimal parameter, and ε_1 being the optimal estimation error [33, 34]. Then, we can use the following virtual input

$$\rho_1 = -\frac{1}{\sigma}\left[k_1\epsilon_1 + \boldsymbol{W}_1^T\boldsymbol{\vartheta}_1(x) + \hat{\varepsilon}_1 \arctan\left(\frac{\tilde{\epsilon}_1}{\alpha_1}\right) - \dot{x}^c\right] \tag{5}$$

with $\hat{\varepsilon}_1$ being the estimation of ε_1, $k_1, \alpha_1 > 0$, and $\tilde{\epsilon}_1$ being a compensated tracking error. Thus, (3), (4), and (5) imply

$$\begin{aligned} \dot{\epsilon}_1 &= \sigma y + \Delta g_1 - \dot{x}^c \\ &= -k_1\epsilon_1 + \sigma\left(y - \rho_1\right) + \boldsymbol{W}_1^{*T}\boldsymbol{\vartheta}_1(x) + \varepsilon_1 - \boldsymbol{W}_1^T\boldsymbol{\vartheta}_1(x) \\ &\quad - \hat{\varepsilon}_1 \arctan\left(\frac{\tilde{\epsilon}_1}{\alpha_1}\right) \\ &= -k_1\epsilon_1 + \sigma\left(y^c - \rho_1\right) - \tilde{\boldsymbol{W}}_1^T\boldsymbol{\vartheta}_1(x) + \varepsilon_1 \\ &\quad - \hat{\varepsilon}_1 \arctan\left(\frac{\tilde{\epsilon}_1}{\alpha_1}\right) + \sigma\epsilon_2, \end{aligned} \tag{6}$$

with $\tilde{\boldsymbol{W}}_1^T = \boldsymbol{W}_1^T - \boldsymbol{W}_1^{*T}$ being the NN approximation error and $\epsilon_2 = y - y^c$ being filtered error. We can define the following signal:

$$\tilde{\epsilon}_1 = \epsilon_1 - \zeta_1 \tag{7}$$

where ζ_1 can be obtained by solving:

$$\dot{\zeta}_1 = -k_1\zeta_1 + \sigma\left(y^c - \rho_1\right) + \sigma\zeta_2 \tag{8}$$

with ζ_2 being defined in the next step and y^c being the solution of the following equation:

$$\dot{y}^c = -\varpi_2(y^c - \rho_1) \tag{9}$$

with $\varpi_2 > 0$. To solve (9), we can set $y^c(0) = 0$. We can use the following adaptation law:

$$\dot{\boldsymbol{W}}_1 = a_{11}\tilde{\epsilon}_1\boldsymbol{\vartheta}_1(x) - a_{11}a_{12}\boldsymbol{W}_1 \tag{10}$$

and

$$\dot{\hat{\varepsilon}}_1 = a_{41}\tilde{\epsilon}_1 \tanh\left(\frac{\tilde{\epsilon}_1}{\alpha_1}\right) - a_{41}a_{42}\hat{\varepsilon}_1 \tag{11}$$

respectively, with $a_{11}, a_{12}, a_{41}, a_{42} > 0$.

Step 2. According to the second equation of (2), we have

$$\dot{y} = -xz + \Delta g_2 \tag{12}$$

where $\Delta g_2 = -y + \delta x$ is unknown. We can use the NN to approximate it as

$$\Delta g_2 = \boldsymbol{W}_2^T\boldsymbol{\vartheta}_2 = \boldsymbol{W}_2^{*T}\boldsymbol{\vartheta}_2 + \varepsilon_2. \tag{13}$$

Define

$$\begin{cases} \epsilon_2 = y - y^c, \\ \tilde{\epsilon}_2 = \epsilon_2 - \zeta_2, \end{cases} \tag{14}$$

with

$$\dot{\zeta}_2 = -k_2\zeta_2 + z^c - \rho_2 + \zeta_3 \tag{15}$$

with $\zeta_2(0) = 0$,

$$\dot{z}^c = -\varpi_3(z^c - \rho_2), \tag{16}$$

$$\rho_2 = -k_2\epsilon_2 - \boldsymbol{W}_2^T\boldsymbol{\vartheta}_2 - \hat{\varepsilon}_2 \arctan\left(\frac{\tilde{\epsilon}_2}{\alpha_2}\right) + \dot{y}^c - \sigma\tilde{\epsilon}_1, \tag{17}$$

where $k_2, \alpha_2 > 0$. $\boldsymbol{W}_2$ and $\hat{\varepsilon}_2$ are updated by

$$\dot{\boldsymbol{W}}_2 = a_{21}\tilde{\epsilon}_2\boldsymbol{\vartheta}_2(\bar{\boldsymbol{x}}_2) - a_{21}a_{22}\boldsymbol{W}_2 \tag{18}$$

and

$$\dot{\hat{\varepsilon}}_2 = a_{51}\tilde{\epsilon}_2 \tanh\left(\frac{\tilde{\epsilon}_2}{\alpha_1}\right) - a_{51}a_{52}\hat{\varepsilon}_2 \tag{19}$$

with $a_{21}, a_{22}, a_{51}, a_{52} > 0$. Then we know

$$\begin{aligned} \dot{\epsilon}_2 &= z + \Delta g_2 - \dot{y}^c \\ &= -k_2\epsilon_2 + z - \rho_2 + \boldsymbol{W}_2^{*T}\boldsymbol{\vartheta}_2 + \varepsilon_2 - \boldsymbol{W}_2^T\boldsymbol{\vartheta}_2 \\ &\quad - \hat{\varepsilon}_2 \arctan\left(\frac{\tilde{\epsilon}_2}{\alpha_2}\right) - \sigma\tilde{\epsilon}_1 \\ &= -k_2\epsilon_2 + z^c - \rho_2 - \tilde{\boldsymbol{W}}_2^T\boldsymbol{\vartheta}_2 + \varepsilon_2 - \hat{\varepsilon}_2 \arctan\left(\frac{\tilde{\epsilon}_2}{\alpha_2}\right) \\ &\quad - \sigma\tilde{\epsilon}_1 + \epsilon_3. \end{aligned} \tag{20}$$

Step 3. According to the last equation of (2), we have

$$\dot{z} = \Delta g_3 + u \tag{21}$$

with $\Delta g_3(\boldsymbol{x}) = -z + xy$ being unknown. It can be approximated by

$$\Delta g_3 = \boldsymbol{W}_3^T\boldsymbol{\vartheta}_3 = \boldsymbol{W}_3^{*T}\boldsymbol{\vartheta}_3 + \varepsilon_3. \tag{22}$$

We can implement the controller as

$$u = -k_3\epsilon_3 - \boldsymbol{W}_3^T\boldsymbol{\vartheta}_3 - \hat{\varepsilon}_2 \arctan\left(\frac{\tilde{\epsilon}_3}{\alpha_3}\right) + \dot{z}^c - \epsilon_2 \tag{23}$$

with $k_3, \alpha_3 > 0$. Define

$$\begin{cases} \epsilon_3 = z - z^c, \\ \tilde{\epsilon}_3 = \epsilon_3 - \zeta_3, \end{cases} \tag{24}$$

with

$$\dot{\zeta}_3 = -k_3\zeta_3 - \zeta_2. \tag{25}$$

The parameters are updated by

$$\dot{\boldsymbol{W}}_3 = a_{31}\tilde{\epsilon}_3\boldsymbol{\vartheta}_2 - a_{31}a_{32}\boldsymbol{W}_3, \tag{26}$$

$$\dot{\hat{\varepsilon}}_3 = a_{61}\tilde{\epsilon}_3 \tanh\left(\frac{\tilde{\epsilon}_3}{\alpha_3}\right) - a_{61}a_{62}\hat{\varepsilon}_3 \tag{27}$$

with $c_{31}, c_{32}, c_{61}, c_{62} > 0$. As a result,

$$\begin{aligned} \dot{\epsilon}_3 &= \Delta g_3 - \dot{z}^c + u \\ &= -k_3\epsilon_3 + \boldsymbol{W}_3^{*T}\boldsymbol{\vartheta}_3(\tilde{\boldsymbol{x}}) + \varepsilon_3 - \boldsymbol{W}_3^T\boldsymbol{\vartheta}_3(\tilde{\boldsymbol{x}}) - \hat{\varepsilon}_3 \arctan \\ &\quad \left(\frac{\tilde{\epsilon}_3}{\alpha_3}\right) - \epsilon_2 \\ &= -k_3\epsilon_3 - \tilde{\boldsymbol{W}}_3^T\boldsymbol{\vartheta}_3(\tilde{\boldsymbol{x}}) + \varepsilon_3 - \hat{\varepsilon}_3 \arctan\left(\frac{\tilde{\epsilon}_3}{\alpha_3}\right) - \epsilon_2. \end{aligned} \tag{28}$$

Let us give the following reasonable assumption and lemma.

Assumption 1. *The NN approximate error is bounded, i.e., there exists ε_i^* such that $\varepsilon_i \le \varepsilon_i^*$.*

Lemma 1. *[15] If $\alpha > 0$ and $\kappa = 0.27846$, then we have*

$$|y| - y\tanh\left(\frac{y}{\alpha}\right) \le \kappa\alpha.$$

Then, we have

$$\begin{aligned}\dot{\tilde{\epsilon}}_1 &= -k_1\epsilon_1 + \sigma\left(y^c - \rho_1\right) - \tilde{\boldsymbol{W}}_1^T\boldsymbol{\vartheta}_1 + \varepsilon_1 - \hat{\varepsilon}_1\arctan\left(\frac{\tilde{\epsilon}_1}{\alpha_1}\right)\\ &\quad + \sigma\epsilon_2 - \dot{\zeta}_1\\ &= -k_1\epsilon_1 - \tilde{\boldsymbol{W}}_1^T\boldsymbol{\vartheta}_1 + \varepsilon_1 - k_1\zeta_1 - \hat{\varepsilon}_1\arctan\left(\frac{\tilde{\epsilon}_1}{\alpha_1}\right)\\ &\quad + \sigma\epsilon_2 - \sigma\zeta_2\\ &= -k_1\tilde{\epsilon}_1 + \sigma\tilde{\epsilon}_2 - \tilde{\boldsymbol{W}}_1^T\boldsymbol{\vartheta}_1 + \varepsilon_1 - \hat{\varepsilon}_1\arctan\left(\frac{\tilde{\epsilon}_1}{\alpha_1}\right),\end{aligned} \tag{29}$$

$$\begin{aligned}\dot{\tilde{\epsilon}}_2 &= -k_2\epsilon_2 + z^c - \rho_2 - \tilde{\boldsymbol{W}}_2^T\boldsymbol{\vartheta}_2 + \varepsilon_2 - \hat{\varepsilon}_2\arctan\left(\frac{\tilde{\epsilon}_2}{\alpha_2}\right)\\ &\quad - \sigma\tilde{\epsilon}_1 + \epsilon_3 - \dot{\zeta}_2\\ &= -k_2\epsilon_2 - \tilde{\boldsymbol{W}}_2^T\boldsymbol{\vartheta}_2 + \varepsilon_2 - \zeta_3 - \hat{\varepsilon}_2\arctan\left(\frac{\tilde{\epsilon}_2}{\alpha_2}\right)\\ &\quad - \sigma\tilde{\epsilon}_1 + \epsilon_3 - k_2\zeta_2\\ &= -k_2\tilde{\epsilon}_2 - \tilde{\boldsymbol{W}}_2^T\boldsymbol{\vartheta}_2 + \varepsilon_2 + \tilde{\epsilon}_3 - \hat{\varepsilon}_2\arctan\left(\frac{\tilde{\epsilon}_2}{\alpha_2}\right) - \sigma\tilde{\epsilon}_1,\end{aligned} \tag{30}$$

$$\begin{aligned}\dot{\tilde{\epsilon}}_3 &= -k_3\epsilon_3 - \tilde{\boldsymbol{W}}_3^T\boldsymbol{\vartheta}_3 + \varepsilon_3 - \dot{\zeta}_3 - \epsilon_2 - \hat{\varepsilon}_3\arctan\left(\frac{\tilde{\epsilon}_3}{\alpha_3}\right)\\ &= -k_3\tilde{\epsilon}_3 - \tilde{\boldsymbol{W}}_3^T\boldsymbol{\vartheta}_3(\bar{\boldsymbol{x}}) + \varepsilon_3 - \tilde{\epsilon}_2 - \hat{\varepsilon}_3\arctan\left(\frac{\tilde{\epsilon}_3}{\alpha_3}\right).\end{aligned} \tag{31}$$

Theorem 1. *When $|x_i^c - z_i| \le b$ with $b > 0$, then (8), (15), and (25) imply*

$$\|\boldsymbol{\zeta}\| \le \frac{c}{2\hat{k}}\left(1 - e^{-2\hat{k}t}\right) \tag{32}$$

with $\boldsymbol{\zeta} = [\zeta_1, \zeta_2, \zeta_3]^T \in \mathcal{R}^3$, $\hat{k} = \frac{1}{2}\min\{k_1, k_2, k_3\}$, and $c = b + \sigma$.

Proof. Let $V_1 = \frac{1}{2}\|\boldsymbol{\zeta}\|^2$. It follows from (8), (15), and (25) that

$$\begin{aligned}\dot{V}_1 &= -\sum_{i=1}^{3} k_i\zeta_i^2 + \sigma\zeta_1\left(y^c - \rho_1\right) + \zeta_2\left(z^c - \rho_2\right)\\ &\le -2\hat{k}\|\boldsymbol{\zeta}\|^2 + A\|\boldsymbol{\zeta}\|\\ &\le -4\hat{k}V_1 + \sqrt{2}a\sqrt{V_1}.\end{aligned} \tag{33}$$

As a result, it follows from (33) that (32) satisfies. ■

Theorem 2. *Consider (2) satisfying Assumption 1. Virtual inputs are given by (5) and (17) under the filters (8), (9), (15), (16), and (25). The adaptation laws are (10), (18), (26), (11), (19), and (27). Then, the controller (23) ensures the convergences of $\tilde{\epsilon}_1$, $\tilde{\epsilon}_2$ and $\tilde{\epsilon}_3$ to a small region.*

Proof. Define

$$V = \frac{1}{2}\sum_{i=1}^{3}\tilde{\epsilon}_i^2 + \sum_{i=1}^{3}\frac{1}{2c_{i1}}\tilde{\boldsymbol{W}}_i^T\tilde{\boldsymbol{W}}_i + \sum_{i=1}^{3}\frac{1}{2c_{i+3,1}}\tilde{\varepsilon}_i^2 \tag{34}$$

with $\tilde{\varepsilon}_i = \hat{\varepsilon}_i - \varepsilon_i^*$. Then, (29), (30), (31), Assumption 1, and Lemma 1 imply

$$\begin{aligned}\sum_{i=1}^{3}\tilde{\epsilon}_i\dot{\tilde{\epsilon}}_i &= \sum_{i=1}^{3}\tilde{e}_i\left[\varepsilon_i - \hat{\varepsilon}_i\arctan\left(\frac{\tilde{e}_i}{\alpha_i}\right)\right] - \tilde{\epsilon}_1\tilde{\boldsymbol{W}}_1^T\boldsymbol{\vartheta}_1 - \tilde{\epsilon}_2\tilde{\boldsymbol{W}}_2^T\boldsymbol{\vartheta}_2\\ &\quad - \tilde{\epsilon}_3\tilde{\boldsymbol{W}}_3^T\boldsymbol{\vartheta}_3 - \sum_{i=1}^{3}k_i\tilde{e}_i^2\\ &\le \sum_{i=1}^{3}\left[|\tilde{e}_i|\varepsilon_i^* - \tilde{e}_i\hat{\varepsilon}_i\arctan\left(\frac{\tilde{e}_i}{\alpha_i}\right)\right] - \tilde{\epsilon}_1\tilde{\boldsymbol{W}}_1^T\boldsymbol{\vartheta}_1\\ &\quad - \tilde{\epsilon}_2\tilde{\boldsymbol{W}}_2^T\boldsymbol{\vartheta}_2 - \tilde{\epsilon}_3\tilde{\boldsymbol{W}}_3^T\boldsymbol{\vartheta}_3 - \sum_{i=1}^{3}k_i\tilde{e}_i^2\\ &= \sum_{i=1}^{3}\left[|\tilde{e}_i|\varepsilon_i^* - \tilde{e}_i\hat{\varepsilon}_i\arctan\left(\frac{\tilde{e}_i}{\alpha_i}\right) - \tilde{e}_i\varepsilon_i^*\arctan\left(\frac{\tilde{e}_i}{\alpha_i}\right)\right]\\ &\quad - \tilde{\epsilon}_2\tilde{\boldsymbol{W}}_2^T\boldsymbol{\vartheta}_2 - \tilde{\epsilon}_1\tilde{\boldsymbol{W}}_1^T\boldsymbol{\vartheta}_1\\ &\quad + \sum_{i=1}^{3}\tilde{e}_i\varepsilon_i^*\arctan\left(\frac{\tilde{e}_i}{\alpha_i}\right) - \sum_{i=1}^{3}k_i\tilde{e}_i^2 - \tilde{\epsilon}_3 d^*\arctan\left(\frac{\tilde{\epsilon}_3}{\alpha_3}\right)\\ &\quad - \tilde{\epsilon}_3\tilde{\boldsymbol{W}}_3^T\boldsymbol{\vartheta}_3\\ &\le \sum_{i=1}^{3}\left[-\tilde{e}_i\hat{\varepsilon}_i\arctan\left(\frac{\tilde{e}_i}{\alpha_i}\right) + \tilde{e}_i\varepsilon_i^*\arctan\left(\frac{\tilde{e}_i}{\alpha_i}\right)\right]\\ &\quad - \sum_{i=1}^{3}k_i\tilde{e}_i^2 - \tilde{\epsilon}_2\tilde{\boldsymbol{W}}_2^T\boldsymbol{\vartheta}_2\\ &\quad - \tilde{\epsilon}_3\tilde{\boldsymbol{W}}_3^T\boldsymbol{\vartheta}_3 - \tilde{\epsilon}_1\tilde{\boldsymbol{W}}_1^T\boldsymbol{\vartheta}_1 + \kappa\sum_{i=1}^{3}\alpha_i\varepsilon_i^*\\ &= -\sum_{i=1}^{3}\tilde{e}_i\tilde{\varepsilon}_i\arctan\left(\frac{\tilde{e}_i}{\alpha_i}\right) - \sum_{i=1}^{3}k_i\tilde{e}_i^2 - \tilde{\epsilon}_2\tilde{\boldsymbol{W}}_2^T\boldsymbol{\vartheta}_2\\ &\quad - \tilde{\epsilon}_3\tilde{\boldsymbol{W}}_3^T\boldsymbol{\vartheta}_3 - \tilde{\epsilon}_1\tilde{\boldsymbol{W}}_1^T\boldsymbol{\vartheta}_1 + \kappa\sum_{i=1}^{3}\alpha_i\varepsilon_i^*.\end{aligned} \tag{35}$$

It follows from (10), (11), (18), (19), (26), and (27) that

$$\begin{aligned}\sum_{i=1}^{3}\frac{1}{a_{i1}}\tilde{\boldsymbol{W}}_i^T\dot{\tilde{\boldsymbol{W}}}_i &= \tilde{\epsilon}_2\tilde{\boldsymbol{W}}_2^T\boldsymbol{\vartheta}_2 + \tilde{\epsilon}_3\tilde{\boldsymbol{W}}_3^T\boldsymbol{\vartheta}_3 + \tilde{\epsilon}_1\tilde{\boldsymbol{W}}_1^T\boldsymbol{\vartheta}_1\\ &\quad - \sum_{i=1}^{3}a_{i2}\tilde{\boldsymbol{W}}_i^T\boldsymbol{W}_i\\ &= \tilde{\epsilon}_2\tilde{\boldsymbol{W}}_2^T\boldsymbol{\vartheta}_2 + \tilde{\epsilon}_3\tilde{\boldsymbol{W}}_3^T\boldsymbol{\vartheta}_3 + \tilde{\epsilon}_1\tilde{\boldsymbol{W}}_1^T\boldsymbol{\vartheta}_1\\ &\quad - \sum_{i=1}^{3}a_{i2}\tilde{\boldsymbol{W}}_i^T\left(\tilde{\boldsymbol{W}}_i + \boldsymbol{W}_i^*\right)\\ &\le \tilde{\epsilon}_2\tilde{\boldsymbol{W}}_2^T\boldsymbol{\vartheta}_2 + \tilde{\epsilon}_3\tilde{\boldsymbol{W}}_3^T\boldsymbol{\vartheta}_3 + \tilde{\epsilon}_1\tilde{\boldsymbol{W}}_1^T\boldsymbol{\vartheta}_1\\ &\quad - \sum_{i=1}^{3}\frac{a_{i2}}{2}\tilde{\boldsymbol{W}}_i^T\tilde{\boldsymbol{W}}_i + \sum_{i=1}^{3}\frac{a_{i2}}{2}\boldsymbol{W}_i^{*T}\boldsymbol{W}_i^*,\end{aligned} \tag{36}$$

$$\sum_{i=1}^{3}\frac{1}{2a_{i+3,1}}\tilde{\varepsilon}_i\dot{\tilde{\varepsilon}}_i=\sum_{i=1}^{3}\tilde{\varepsilon}_i\left[\tilde{e}_i\tanh\left(\frac{\tilde{e}_i}{\alpha_i}\right)-a_{i+3,2}\hat{\varepsilon}_i\right]$$
$$=\sum_{i=1}^{3}\tilde{\varepsilon}_i\tilde{e}_i\tanh\left(\frac{\tilde{e}_i}{\alpha_i}\right)-\sum_{i=1}^{3}a_{i+3,2}\tilde{\varepsilon}_i\left(\tilde{\varepsilon}_i+\varepsilon_i^*\right)$$
$$\leq\sum_{i=1}^{3}\tilde{\varepsilon}_i\tilde{e}_i\tanh\left(\frac{\tilde{e}_i}{\alpha_i}\right)-\sum_{i=1}^{3}\frac{a_{i+3,2}}{2}\tilde{\varepsilon}_i^2$$
$$+\sum_{i=1}^{3}\frac{a_{i+3,2}}{2}\varepsilon_i^{*2}. \tag{37}$$

As a result, (35), (36), and (37) imply

$$\dot{V}\leq-\sum_{i=1}^{3}k_i\tilde{\epsilon}_i^2+\kappa\sum_{i=1}^{3}\alpha_i\varepsilon_i^*-\sum_{i=1}^{3}\frac{a_{i+3,2}}{2}\tilde{\varepsilon}_i^2+\sum_{i=1}^{3}\frac{a_{i+3,2}}{2}\varepsilon_i^{*2}$$
$$-\sum_{i=1}^{3}\frac{a_{i2}}{2}\tilde{\boldsymbol{W}}_i^T\tilde{\boldsymbol{W}}_i+\sum_{i=1}^{3}\frac{a_{i2}}{2}\boldsymbol{W}_i^{*T}\boldsymbol{W}_i^*$$
$$=-\sum_{i=1}^{3}k_i\tilde{e}_i^2-\sum_{i=1}^{3}\frac{a_{i+3,2}}{2}\tilde{\varepsilon}_i^2-\sum_{i=1}^{3}\frac{a_{i2}}{2}\tilde{\boldsymbol{W}}_i^T\tilde{\boldsymbol{W}}_i+\kappa\sum_{i=1}^{3}\alpha_i\varepsilon_i^*$$
$$+\sum_{i=1}^{3}\frac{a_{i+3,2}}{2}\varepsilon_i^{*2}+\sum_{i=1}^{3}\frac{a_{i2}}{2}\boldsymbol{W}_i^{*T}\boldsymbol{W}_i^*$$
$$\leq-\frac{d_1}{2}\sum_{i=1}^{3}\tilde{e}_i^2-d_2\sum_{i=1}^{3}\frac{1}{2a_{i1}}\tilde{\boldsymbol{W}}_i^T\tilde{\boldsymbol{W}}_i-d_3\sum_{i=1}^{3}\frac{1}{2a_{i+3,1}}\tilde{\varepsilon}_i^2+d_4 \tag{38}$$

with $d_1=2\min\{k_1,k_2,k_3\}$, $d_2=\min\{a_{11}a_{12},a_{21}a_{22},a_{31}a_{32}\}$, $d_3=\min\{a_{41}a_{42},a_{51}a_{52},a_{61}a_{62}\}$, $d_4=\kappa\sum_{i=1}^{3}\alpha_i\varepsilon_i^*+\sum_{i=1}^{3}\frac{a_{i+3,2}}{2}\varepsilon_i^{*2}+\sum_{i=1}^{3}\frac{a_{i2}}{2}\boldsymbol{W}_i^{*T}\boldsymbol{W}_i^*$ being non-negative constants. Apparently, the constants d_1,d_2,d_3,d_4 are determined by design parameters and some unknown constant variable (see, the optimal NN parameter). Thus, (38) implies $\frac{1}{2}\sum_{i=1}^{3}\tilde{e}_i^2\leq\frac{d_4}{d_1}$, $\sum_{i=1}^{3}\frac{1}{2a_{i1}}\tilde{\boldsymbol{W}}_i^T\tilde{\boldsymbol{W}}_i\leq\frac{d_4}{d_2}$, $\sum_{i=1}^{3}\frac{1}{2a_{i+3,1}}\tilde{\varepsilon}_i^2\leq\frac{d_4}{d_3}$. As a result, all variables are indeed bounded, and $\tilde{e}_1$, $\tilde{e}_2$ and $\tilde{e}_3$ tend to a small region determined by design parameters. ■

Remark 1. *It should be emphasized that the conclusion of Theorem 1 is very representative, and it can be widely used in the field of automatic control, finite-time control, and backstepping control. However, the proposed method can only guarantee the that tracking error tends to a very small region.*

Remark 2. *In the controller design, the proposed method is different from some related methods, for example, those detailed in references [4, 33, 34]. We introduce an auxiliary signal to approximate the virtual input, and the approximation error can be made as small as possible.*

3. SIMULATION STUDY

In system (2), let $\sigma=5.45,\delta=20.0$, $x(0)=0.5,y(0)=-1,z(0)=0$. When $u(t)\equiv0$, the chaotic behavior of (2) can be seen in **Figure 1**.

Let the desired signal be x^c, defined by

$$x^c=\begin{cases}0 & t\in[0,8],\\ 2 & t>8.\end{cases}$$

With respect to the NNs, the basic functions are chosen on interval [-8 8], and five functions are used for each state. Their initial conditions are $\boldsymbol{W}_1(0)=\boldsymbol{0}_{1\times2}$, $\boldsymbol{W}_2(0)=\boldsymbol{0}_{1\times25}$, and $\boldsymbol{W}_3(0)=\boldsymbol{0}_{1\times125}$. The design parameters are $k_1=k_2=k_3=1.5,a_{i1}=6,a_{i2}=0.05,i=1,2,3,4,5,6,\alpha_1=\alpha_2=\alpha_3=1$.

The simulation results are presented in **Figure 2**. It can be seen in **Figure 2** that the tracking error has rapid convergence and the

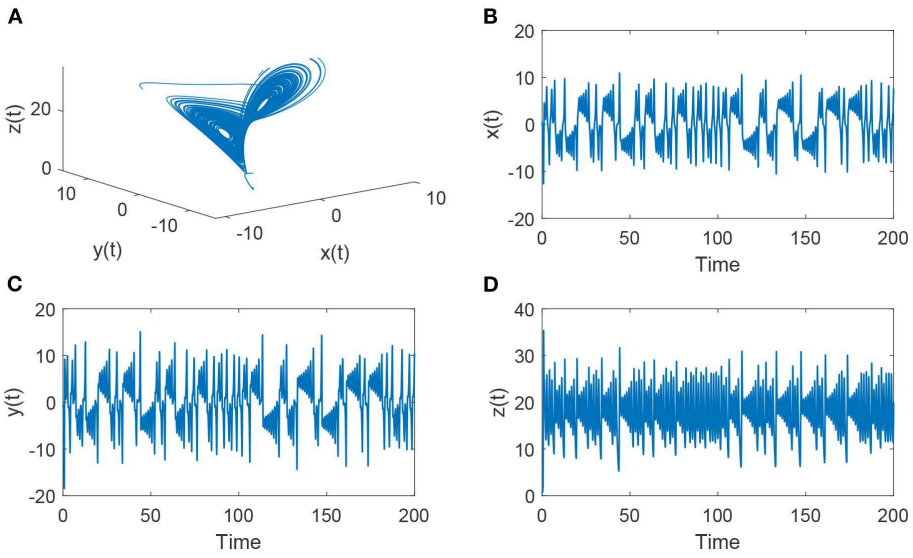

FIGURE 1 | Chaotic phenomenon of (2) in **(A)** $x-y-z$ space, **(B)** $x(t)$, **(C)** $y(t)$, and **(D)** $z(t)$.

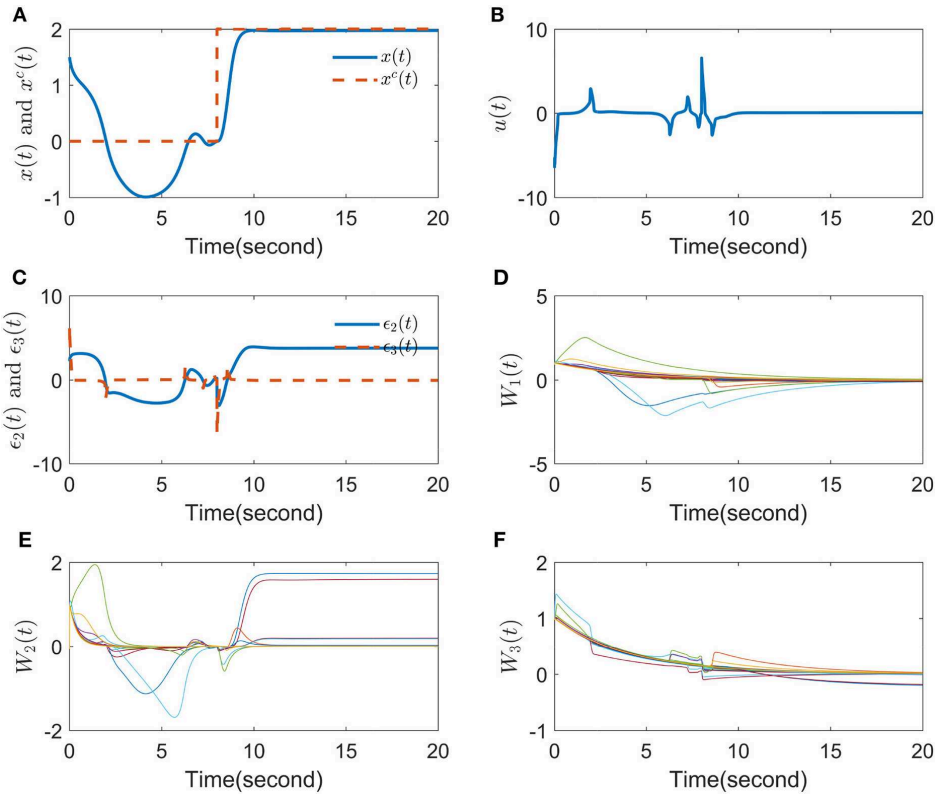

FIGURE 2 | Simulation results in **(A)** tracking performance, **(B)** control input, **(C)** compensated errors, **(D)** $W_1(t)$, **(E)** $W_2(t)$, and **(F)** $W_3(t)$.

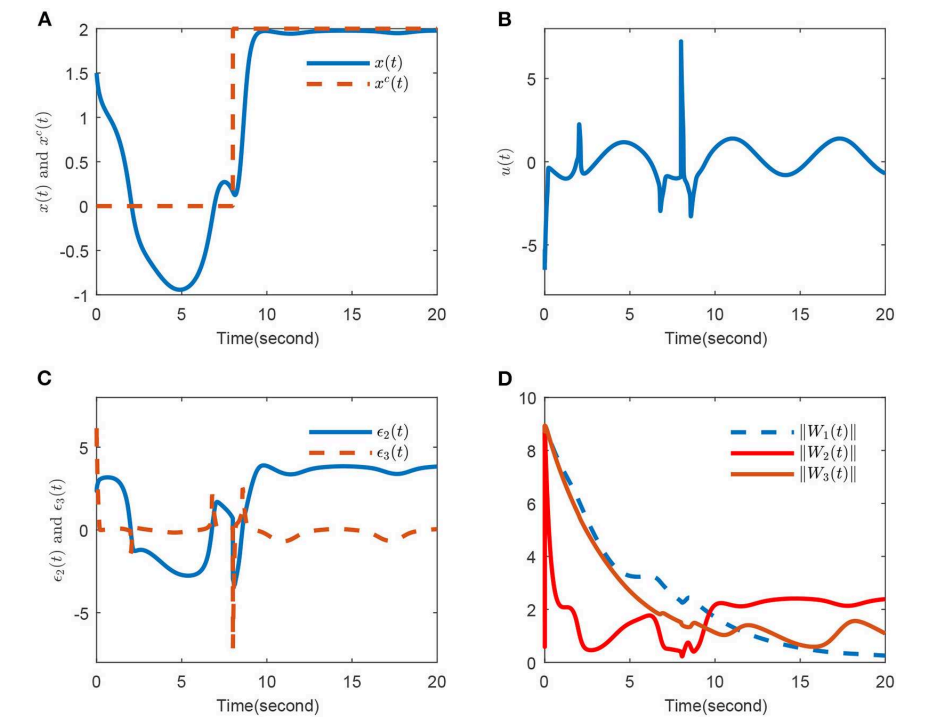

FIGURE 3 | Simulation results with external disturbance in **(A)** tracking performance, **(B)** control input, **(C)** compensated errors, **(D)** $\|W_1(t)\|$, $\|W_2(t)\|$ and $\|W_3(t)\|$.

signal $x(t)$ tracks $x^c(t)$ tightly; the control input $u(t)$ has a small amplitude, and it fluctuates very gently; the compensated error ϵ_3 converges to zero very quickly, but ϵ_2 does not converge to zero (in fact, in our method, it is not necessary for the compensated error to converge to zero); the parameters of the NNs also fluctuate gently.

To show the robustness of the proposed method, let us add an external term $0.95 \sin t$ into the third equation of the system (2). The simulation results are presented in **Figure 3**. Comparing **Figures 2**, **3**, we can see that under the external disturbance, the proposed method has very good robustness.

4. CONCLUSIONS

This paper presents an NN CFC method for PMSMs with fully unknown system models. To avoid the "explosion of complexity" problem, we propose a one-order command filter. It has been proven that the virtual input and its derivative can together be approximated by the proposed filter, and the approximation error can be made as small as possible. The proposed method is performed by using a backstepping technique. It is also shown that the proposed NN CFC can guarantee the boundedness of all signals. Investigating CFC for PMSMs with input constraints will be our future research direction.

DATA AVAILABILITY STATEMENT

All datasets generated for this study are included in the article/supplementary material.

AUTHOR CONTRIBUTIONS

RL contributed the conception of the study. YD wrote the study and organized the literature analysis. YX wrote the simulation programs. RL and YX revised the manuscript. All authors contributed to manuscript revision and read and approved the submitted version.

FUNDING

This work was supported by the Natural Science Foundation of Guangxi University for Nationalities (2019KJYB001), and the Guangxi Natural Science Foundation (2019GXNSFAA185007).

REFERENCES

1. Lin FJ, Shen PH, Hsu SP. Adaptive backstepping sliding mode control for linear induction motor drive. *IEEE Proc Electric Power Appl*. (2002) **149**:184–94. doi: 10.1049/ip-epa:20020138
2. Ahn KK, Nam DNC, Jin M. Adaptive backstepping control of an electrohydraulic actuator. *IEEE/ASME Trans Mechatron*. (2013) **19**:987–995. doi: 10.1109/TMECH.2013.2265312
3. Liu JB, Shi ZY, Pan YH, Cao J, Abdel-Aty M, Al-Juboori U. Computing the Laplacian spectrum of linear octagonal-quadrilateral networks and its applications. *Polycycl Aromat Comp*. (2020). doi: 10.1080/10406638.2020.1748666. [Epub ahead of print].
4. Liu JB, Zhao J, He H, Shao Z. Valency-based topological descriptors and structural property of the generalized sierpiński networks. *J Stat Phys*. (2019) **177**:1131–47. doi: 10.1007/s10955-019-02412-2
5. Zhou J, Wen C, Zhang Y. Adaptive backstepping control of a class of uncertain nonlinear systems with unknown backlash-like hysteresis. *IEEE Trans Autom Control*. (2004) **49**:1751–9. doi: 10.1109/TAC.2004.835398
6. Liu H, Pan Y, Li S, Chen Y. Adaptive fuzzy backstepping control of fractional-order nonlinear systems. *IEEE Trans Syst Man Cybern Syst*. (2017) **47**:2209–17. doi: 10.1109/TSMC.2016.2640950
7. Liu H, Pan Y, Jinde C, Hongxing W, Yan Z. Adaptive neural network backstepping control of fractionial-order nonlinear systems with actuator faults. *IEEE Trans Neural Netw Learn Syst*. (2020). doi: 10.1109/TNNLS.2020.2964044. [Epub ahead of print].
8. Salimi M, Soltani J, Zakipour A. Experimental design of the adaptive backstepping control technique for single-phase shunt active power filters. *IET Power Electron*. (2017) **10**:911–8. doi: 10.1049/iet-pel.2016.0366
9. Coban R. Adaptive backstepping sliding mode control with tuning functions for nonlinear uncertain systems. *Int J Syst Sci*. (2019) **50**:1517–29. doi: 10.1080/00207721.2019.1615571
10. Thien TD, Ba DX, Ahn KK. Adaptive backstepping sliding mode control for equilibrium position tracking of an electrohydraulic elastic manipulator. *IEEE Trans Ind Electron*. (2019) **67**:3860–9. doi: 10.1109/TIE.2019.2918475
11. Farrell JA, Polycarpou M, Sharma M, Dong W. Command filtered backstepping. *IEEE Trans Autom Control*. (2009) **54**:1391–5. doi: 10.1109/TAC.2009.2015562
12. Dong W, Farrell JA, Polycarpou MM, Djapic V, Sharma M. Command filtered adaptive backstepping. *IEEE Trans Control Syst Technol*. (2011) **20**:566–80. doi: 10.1109/TCST.2011.2121907
13. Liu H, Pan Y, Cao J. Composite learning adaptive dynamic surface control of fractional-order nonlinear systems. *IEEE Trans Cybern*. (2020) **50**:2557–67. doi: 10.1109/TCYB.2019.2938754
14. Fu C, Zhao L, Yu J, Yu H, Lin C. Neural network-based command filtered control for induction motors with input saturation. *IET Control Theory Appl*. (2017) **11**:2636–42. doi: 10.1049/iet-cta.2017.0059
15. Yu J, Shi P, Zhao L. Finite-time command filtered backstepping control for a class of nonlinear systems. *Automatica*. (2018) **92**:173–80. doi: 10.1016/j.automatica.2018.03.033
16. Ahanda JJBM, Mbede JB, Melingui A, Zobo BE. Robust adaptive command filtered control of a robotic manipulator with uncertain dynamic and joint space constraints. *Robotica*. (2018) **36**:767–86. doi: 10.1017/S0263574718000036
17. Pan Y, Wang H, Li X, Yu H. Adaptive command-filtered backstepping control of robot arms with compliant actuators. *IEEE Trans Control Syst Technol*. (2017) **26**:1149–56. doi: 10.1109/TCST.2017.2695600
18. Pan Y, Sun T, Liu Y, Yu H. Composite learning from adaptive backstepping neural network control. *Neural Netw*. (2017) **95**:134–42. doi: 10.1016/j.neunet.2017.08.005
19. Pillay P, Krishnan R. Modeling, simulation, and analysis of permanent-magnet motor drives. I. The permanent-magnet synchronous motor drive. *IEEE Trans Ind Appl*. (1989) **25**:265–73. doi: 10.1109/28.25541
20. Kommuri SK, Defoort M, Karimi HR, Veluvolu KC. A robust observer-based sensor fault-tolerant control for PMSM in electric vehicles. *IEEE Trans Ind Electron*. (2016) **63**:7671–81. doi: 10.1109/TIE.2016.2590993
21. Wang Y, Wang X, Xie W, Wang F, Dou M, Kennel RM, et al. Deadbeat model-predictive torque control with discrete space-vector modulation for PMSM drives. *IEEE Trans Ind Electron*. (2017) **64**:3537–47. doi: 10.1109/TIE.2017.2652338
22. Cai B, Zhao Y, Liu H, Xie M. A data-driven fault diagnosis methodology in three-phase inverters for PMSM drive systems. *IEEE Trans Power Electron*. (2016) **32**:5590–600. doi: 10.1109/TPEL.2016.2608842
23. Yu J, Chen B, Yu H, Gao J. Adaptive fuzzy tracking control for the chaotic permanent magnet synchronous motor drive system via

backstepping. *Nonlinear Anal Real World Appl*. (2011) **12**:671–81. doi: 10.1016/j.nonrwa.2010.07.009
24. Sun X, Shi Z, Chen L, Yang Z. Internal model control for a bearingless permanent magnet synchronous motor based on inverse system method. *IEEE Trans Energy Convers*. (2016) **31**:1539–48. doi: 10.1109/TEC.2016.2591925
25. Yang X, Yu J, Wang QG, Zhao L, Yu H, Lin C. Adaptive fuzzy finite-time command filtered tracking control for permanent magnet synchronous motors. *Neurocomputing*. (2019) **337**:110–9. doi: 10.1016/j.neucom.2019.01.057
26. Niu H, Yu J, Yu H, Lin C, Zhao L. Adaptive fuzzy output feedback and command filtering error compensation control for permanent magnet synchronous motors in electric vehicle drive systems. *J Frankl Inst*. (2017) **354**:6610–29. doi: 10.1016/j.jfranklin.2017.08.021
27. Zou M, Yu J, Ma Y, Zhao L, Lin C. Command filtering-based adaptive fuzzy control for permanent magnet synchronous motors with full-state constraints. *Inform Sci*. (2020) **518**:1–12. doi: 10.1016/j.ins.2020.01.004
28. Wang X, Chen Y, Lu Y, Li X, He W. Dynamic surface method-based adaptive backstepping control for the permanent magnet synchronous motor on parameter identification. *Proc Inst Mech Eng I J Syst Control Eng*. (2019) **233**:1172–81. doi: 10.1177/0959651818819237
29. Singh JP, Roy BK, Kuznetsov NV. Multistability and hidden attractors in the dynamics of permanent magnet synchronous motor. *Int J Bifurc Chaos*. (2019) **29**:1950056. doi: 10.1142/S0218127419500561
30. Wang M, Yu J, Ma Y, Yu H, Lin C. Discrete-time adaptive fuzzy speed regulation control for induction motors with input saturation via command filtering. *J Frankl Inst*. (2019) **356**:6145–59. doi: 10.1016/j.jfranklin.2019.05.023
31. Xu D, Wang G, Yan W, Yan X. A novel adaptive command-filtered backstepping sliding mode control for PV grid-connected system with energy storage. *Solar Energy*. (2019) **178**:222–30. doi: 10.1016/j.solener.2018.12.033
32. Errouissi R, Al-Durra A, Muyeen S, Leng S. Continuous-time model predictive control of a permanent magnet synchronous motor drive with disturbance decoupling. *IET Electric Power Appl*. (2017) **11**:697–706. doi: 10.1049/iet-epa.2016.0499
33. Liu H, Wang H, Cao J, Alsaedi A, Hayat T. Composite learning adaptive sliding mode control of fractional-order nonlinear systems with actuator faults. *J Frankl Inst*. (2019) **356**:9580–99. doi: 10.1016/j.jfranklin.2019.02.042
34. Liu H, Pan Y, Cao J, Zhou Y, Wang H. Positivity and stability analysis for fractional-order delayed systems: a T-S fuzzy model approach. *IEEE Trans Fuzzy Syst*. (2020). doi: 10.1109/TFUZZ.2020.2966420. [Epub ahead of print].

Conflict of Interest: The authors declare that the research was conducted in the absence of any commercial or financial relationships that could be construed as a potential conflict of interest.

frontiers in Physics

ORIGINAL RESEARCH
published: 09 June 2020
doi: 10.3389/fphy.2020.00175

Necessary and Sufficient Conditions for Expressing Quadratic Rational Bézier Curves

Chaoyu Yang[1*†], *Jie Yang*[2†], *Ying Liu*[1] *and Xianya Geng*[3]

[1] School of Economics and Management, Anhui University of Science and Technology, Huainan, China, [2] School of Computing and Information Technology, Faculty of Engineering and Information Sciences, University of Wollongong, Wollongong, NSW, Australia, [3] School of Mathematics and Physics, Anhui University of Science and Technology, Huainan, China

Quadratic rational Bézier curve transformation is widely used in the field of computational geometry. In this paper, we offer several important characteristics of the quadratic rational Bézier curve. More precisely, on the basis of proving its monotonicity, the necessary and sufficient conditions for transforming a quadratic rational Bézier curve into a point, line segment, parabola, elliptic arc, circular arc, and hyperbola are proved, respectively.

Keywords: Bézier curve, quadratic rational, necessary and sufficient conditions, geometry, computer aided geometric design

OPEN ACCESS

Edited by:
Jia-Bao Liu,
Anhui Jianzhu University, China

Reviewed by:
Qin Zhao,
Hubei University, China
Liangchen Li,
Luoyang Normal University, China
Jianbing Liu,
West Virginia University, United States

***Correspondence:**
Chaoyu Yang
yangchy@aust.edu.cn

†These authors have contributed equally to this work

Specialty section:
This article was submitted to Mathematical Physics, a section of the journal Frontiers in Physics

Received: *25 March 2020*
Accepted: *24 April 2020*
Published: *09 June 2020*

Citation:
Yang C, Yang J, Liu Y and Geng X (2020) Necessary and Sufficient Conditions for Expressing Quadratic Rational Bézier Curves. Front. Phys. 8:175. doi: 10.3389/fphy.2020.00175

1. INTRODUCTION

Bézier curves have wide application in computer-aided geometric design, being used to provide precisely described points along a given curve [1]. Compared to other methods, such as the French curve, Bézier-based approaches are more computationally affordable and reliable. Additionally, the advantages of the Bézier curve in geometric design include its simple but clear mathematical function [2]. For instance, it is capable of incorporating both conic sections and parametric cubic curves as special cases [3]. As such, one can deal with two different curves simultaneously using one unique computational procedure. Some preliminary studies and applications of Bézier curves can be found in Lu et al. [4], Lee [5], and Han [6].

In this paper, to better understand the basic characteristics of Bézier curves, we conduct some fundamental research. In particular, we discuss the necessary and sufficient conditions for representing six different basic shapes, including a point, line segment, parabola, elliptic arc, circular arc, and hyperbola, using Bézier curves [7, 8]. These results play a fundamental role in the shape formulation and can help in facilitating any subsequent computer-based geometric design.

To begin with, we introduce the mathematical model of the quadratic rational Bézier curve [1].

Definition 1. *The quadratic rational Bézier curve is defined as follows:*

$$p(t) = \frac{(1-t)^2\omega_0 P_0 + 2t(1-t)\omega_1 P_1 + t^2\omega_2 P_2}{(1-t)^2\omega_0 + 2t(1-t)\omega_1 + t^2\omega_2}, \quad t \in [0,1], \tag{1}$$

where

$$t = \frac{\sqrt{\omega_0}\mu}{\sqrt{\omega_0}\mu + \sqrt{\omega_2}(1-\mu)}, \quad \mu \in [0,1], \tag{2}$$

and ω_0 and ω_2 are not zero values at the same time.

The monotonicity of Formula (1.2) is discussed below. Let $\mu_1 \in [0,1], \mu_2 \in [0,1]$, and $\mu_1 \leq \mu_2$. Accordingly, in the case of $\mu_1 = 0$, we have:

$$t_1 = \frac{\sqrt{\omega_0}\mu_1}{\sqrt{\omega_0}\mu_1 + \sqrt{\omega_2}(1-\mu_1)} = 0. \tag{3}$$

Note that $1 \geq \mu_2 > \mu_1 \geq 0$, and $t_2 = \frac{\sqrt{\omega_0}\mu_2}{\sqrt{\omega_0}\mu_2 + \sqrt{\omega_2}(1-\mu_2)} \geq 0$; then it is easy to have $t_2 \geq t_1 = 0$.

In the case of $\mu_1 \neq 0$ and $\mu_2 \neq 0$, according to Formula (1.2), we have:

$$\begin{aligned}\frac{t_1}{t_2} &= \frac{\sqrt{\omega_0}\mu_1}{\sqrt{\omega_0}\mu_1 + \sqrt{\omega_2}(1-\mu_1)} \Big/ \frac{\sqrt{\omega_0}\mu_2}{\sqrt{\omega_0}\mu_2 + \sqrt{\omega_2}(1-\mu_2)} \\ &= (\sqrt{\omega_0} + \sqrt{\omega_2}(\frac{1}{\mu_2} - 1)) \,/\, (\sqrt{\omega_0} + \sqrt{\omega_2}(\frac{1}{\mu_1} - 1)) \leq 1.\end{aligned} \tag{4}$$

In other words, we have the conclusion that t is monotonically increasing [9–11]. Furthermore, if we apply linear transformation to Formula (1.1), it is easy to know

$$\begin{aligned}p(\mu) &= \frac{\omega_0\omega_2(1-\mu)^2P_0 + 2\sqrt{\omega_0}\sqrt{\omega_2}\omega_1\mu(1-\mu)P_1 + \omega_0\omega_2\mu^2P_2}{\omega_0\omega_2(1-\mu)^2 + 2\sqrt{\omega_0}\sqrt{\omega_2}\omega_1\mu(1-\mu) + \omega_0\omega_2\mu^2} \\ &= ((1-\mu)^2P_0 + 2\sqrt{\frac{\omega_1^2}{\omega_0\omega_2}}\mu(1-\mu)P_1 + \mu^2P_2)/((1-\mu)^2 \\ &\quad + 2\sqrt{\frac{\omega_1^2}{\omega_0\omega_2}}\mu(1-\mu) + \mu^2).\end{aligned} \tag{5}$$

Let $\omega = \sqrt{\frac{\omega_1^2}{\omega_0\omega_2}}$ and substitute μ with t in the standard form of the quadratic rational Bézier curve. To this end, we have the simplified version of the quadratic rational Bézier curve, which is expressed as follows:

$$p(t) = \frac{(1-t)^2P_0 + 2\omega t(1-t)P_1 + t^2P_2}{(1-t)^2 + 2\omega t(1-t) + t^2}. \tag{6}$$

2. SUFFICIENT AND NECESSARY CONDITIONS FOR A QUADRATIC RATIONAL BÉZIER CURVE TO DEGENERATE INTO A POINT

Theorem 1. *A quadratic rational Bézier curve degenerates into a point if and only if three control points P_0, P_1, P_2 coincide.*

Proof: Assume that the quadratic rational Bézier curve degenerates to a point P_A. That is,

$$\begin{aligned}p(t) = \frac{(1-t)^2P_0 + 2\omega t(1-t)P_1 + t^2P_2}{(1-t)^2 + 2\omega t(1-t) + t^2} = P_A \Leftrightarrow \\ (1-t)^2(P_0 - P_A) + 2t(1-t)\omega(P_1 - P_A) + t^2(P_2 - P_A) = 0.\end{aligned} \tag{7}$$

As can be seen from Formula (7), when $t \in (0,1)$, we have $(1-t)^2 \neq 0, t^2 \neq 0, 2t(1-t) \neq 0$, so $P_0 = P_A, P_1 = P_A, P_2 = P_A$. That is, when the quadratic rational Bézier curve degenerates into a point, P_0, P_1, P_2 are the same point of P_A.

On the other hand, when three control points coincide (say, the same point P_A), we know that:

$$p(t) = \frac{(1-t)^2P_A + 2t(1-t)\omega P_A + t^2P_A}{(1-t)^2 + 2t(1-t)\omega + t^2} = P_A. \tag{8}$$

As can be seen from Formula (8), when three control points P_0, P_1, P_2 coincide, the quadratic rational Bézier curve degenerates into a point [12, 13].

Algorithm 1: To degenerate a Quadratic Rational Bézier Curve into a Point

Input: Control Points of Bezier Curve
Output: Points degenerated by Bezier Curve

Input Bézier Curve control points
Set coordinates of control points $P_1 = P_0$ and $P_2 = P_0$
Output coordinates of control points P_0, P_1, P_2
if the number of control points < 3 **then**
    goto Step 1.
end if
Initializing the independent variable t in the standard formula of the quadratic rational Bezier curve to 0, *Set* $t = 0$
for $t = 0; t \leq 1; t+ = 0.00125$ **do**
    Calculate the standard formula of the quadratic rational Bezier Curve.
    $x = \frac{(1-t)^2x_0 + 2t(1-t)\omega x_1 + t^2x_2}{(1-t)^2 + 2t(1-t)\omega + t^2}, y = \frac{(1-t)^2y_0 + 2t(1-t)\omega y_1 + t^2y_2}{(1-t)^2 + 2t(1-t)\omega + t^2}$
end for
Output Bezier Curve.
Clear Bezier Curve, Bezier Curve control points. **goto** Step 1.
return

3. NECESSARY AND SUFFICIENT CONDITIONS FOR DEGRADATION OF A QUADRATIC RATIONAL BÉZIER CURVE INTO A LINEAR SECTION

Theorem 2. *The quadratic rational Bézier curve degenerates into a straight line segment if and only if the control points P_0, P_2 do not coincide, the weight factor $\omega = 0$, or the control point P_1 is on the line segment* [14–16].

Proof: First, we assume that one point is with two coordinates; alternatively, we have $P_0 = (x_0, y_0)$, $P_1 = (x_1, y_1)$, and $P_2 = (x_2, y_2)$. As such, for an arbitrary point $p(t) = (x, y)$, according to Formula (6) it is easy to have:

$$\begin{aligned}x &= \frac{(1-t)^2x_0 + 2t(1-t)\omega x_1 + t^2x_2}{(1-t)^2 + 2t(1-t)\omega + t^2}, \\ y &= \frac{(1-t)^2y_0 + 2t(1-t)\omega y_1 + t^2y_2}{(1-t)^2 + 2t(1-t)\omega + t^2},\end{aligned} \tag{9}$$

On the other hand, a general form for a line function can be expressed as: $y = ax + b$, where a, and b is a constant [17]. Then, substituting x and y using Formula (12), we can get:

$$\begin{aligned}&\frac{(1-t)^2y_0 + 2t(1-t)\omega y_1 + t^2y_2}{(1-t)^2 + 2t(1-t)\omega + t^2}\\ &= a\,\frac{(1-t)^2x_0 + 2t(1-t)\omega x_1 + t^2x_2}{(1-t)^2 + 2t(1-t)\omega + t^2} + b,\end{aligned} \tag{10}$$

If we simplify the above formula, it is easy to know:

$$\begin{aligned}&(y_0 - ax_0 - b + y_2 - ax_2 - b - 2y_1\omega + 2ax_1\omega + 2b\omega)t^2\\ &- 2(y_0 - ax_0 - b - y_1\omega + ax_1\omega + b\omega)t + y_0 - ax_0 - b = 0.\end{aligned} \tag{11}$$

First, we assume that one point is with two coordinates; alternatively, we have $P_0 = (x_0, y_0)$, $P_1 = (x_1, y_1)$, and $P_2 = (x_2, y_2)$. As such, for an arbitrary point $p(t) = (x, y)$, according to Formula (6) it is easy to have:

$$\begin{aligned}x &= \frac{(1-t)^2x_0 + 2t(1-t)\omega x_1 + t^2x_2}{(1-t)^2 + 2t(1-t)\omega + t^2},\\ y &= \frac{(1-t)^2y_0 + 2t(1-t)\omega y_1 + t^2y_2}{(1-t)^2 + 2t(1-t)\omega + t^2},\end{aligned} \tag{12}$$

Now, control points P_0 and P_2 are the first and last points of the Bézier curve. As they are all on the Bézier curve, they will also be on the straight line [18–20]. Alternatively, we have:

$$y_0 = ax_0 + b, y_2 = ax_2 + b. \tag{13}$$

Therefore, Formula (11) is further simplified:

$$(y_1 - ax_1 - b)(\omega t - \omega t^2) = 0. \tag{14}$$

Next, Formula (14) is analyzed in the following aspects:

1. If the control point P_1 is also on the Bézier curve (or on the straight line), then $y_1 - ax_1 - b = 0$, and Formula (14) clearly holds.
2. If the control point P_1 is not on the Bézier curve (or not on the straight line), then $y_1 - ax_1 - b \neq 0$, and Formula (14) can be simplified as
$$-\omega t^2 + \omega t = 0. \tag{15}$$

Therefore, when $t \in [0, 1]$, in order to make Formula (15) hold, we have $\omega = 0$.

As such, it is proved that when the quadratic rational Bézier curve degenerates into a straight line segment, two conditions are met: (1) the weight factor $\omega = 0$, or (2) the control point P_1 is on the line segment with the control point P_0, P_2 as the end point. In the following, we discuss these two conditions separately.

1. According to Formula (6), when the weight factor $\omega = 0$, we have:
$$p(t) = \frac{(1-t)^2P_0 + 2\omega t(1-t)P_1 + t^2P_2}{(1-t)^2 + 2\omega t(1-t) + t^2} = \frac{(1-t)^2P_0 + t^2P_2}{(1-t)^2 + t^2}, \tag{16}$$

and

$$x = \frac{(1-t)^2x_0 + t^2x_2}{(1-t)^2 + t^2} = \frac{(1-t)^2x_0}{(1-t)^2 + t^2} + \frac{t^2x_2}{(1-t)^2 + t^2}. \tag{17}$$

$$y = \frac{(1-t)^2y_0 + t^2y_2}{(1-t)^2 + t^2} = \frac{(1-t)^2y_0}{(1-t)^2 + t^2} + \frac{t^2y_2}{(1-t)^2 + t^2}. \tag{18}$$

To simplify the calculation process, let us assume that:

$$\alpha = \frac{(1-t)^2}{(1-t)^2 + t^2}. \tag{19}$$

and

$$1 - \alpha = \frac{t^2}{(1-t)^2 + t^2}. \tag{20}$$

Now the following formula holds:

$$x = \alpha x_0 + (1-\alpha)x_2 \rightarrow x - x_2 = \alpha(x_0 - x_2). \tag{21}$$

$$y = \alpha y_0 + (1-\alpha)y_2 \rightarrow y - y_2 = \alpha(y_0 - y_2). \tag{22}$$

As the control points P_0, P_2 do not coincide, $x_0 \neq x_2, y_0 \neq y_2$,

$$\alpha = \frac{y - y_2}{y_0 - y_2} = \frac{x - x_2}{x_0 - x_2} \tag{23}$$

$$\frac{y}{y_0 - y_2} - \frac{x}{x_0 - x_2} = \frac{y_2}{y_0 - y_2} - \frac{x_2}{x_0 - x_2}, \tag{24}$$

where x_0, x_2, y_0, y_2 are constants. We assume that $\frac{1}{y_0 - y_2} = A$, $\frac{1}{x_0 - x_2} = B$, $\frac{y_2}{y_0 - y_2} - \frac{x_2}{x_0 - x_2} = C$ (that is, A,B,C are all constants). Accordingly, we know that $Ay - Bx = C$ is a line segment [21].

Algorithm 2: To Degenerate a Quadratic Rational Bézier Curve into a Linear section

Input: Control Points of Bezier Curve
Output: Linear section degenerated by Bezier Curve

Set $\omega = 0$
Input Bézier Curve control points P_0, P_1, P_2
if the number of control points < 3 **then**
    goto Step 2.
end if
Output coordinates of control points P_0, P_1, P_2
Output line segment between control points P_0, P_1 and P_1, P_2
Initializing the independent variable t in the standard formula of the quadratic rational Bezier curve to 0, *Set* $t = 0$
for $t = 0; t \leq 1; t+ = 0.00125$ **do**
    Calculate the standard formula of the quadratic rational Bezier Curve.
    $x = \frac{(1-t)^2x_0 + 2t(1-t)\omega x_1 + t^2x_2}{(1-t)^2 + 2t(1-t)\omega + t^2}, y = \frac{(1-t)^2y_0 + 2t(1-t)\omega y_1 + t^2y_2}{(1-t)^2 + 2t(1-t)\omega + t^2}$
end for
Output Bezier Curve.
Clear Bezier Curve, Bezier Curve control points. **goto** Step 1.
return

2. Let the conditional control point P_1 be the end point (on the line segment with the control points P_0 and P_2) [22]; thus, it can be seen that:

$$P_1 = (1-v)P_0 + vP_2, \quad v \in [0,1], \tag{25}$$

The Formula (25) can be substituted with Formula (6) to have:

$$p(t) = \frac{(1-t)^2 + 2t(1-t)\omega(1-v)}{(1-t)^2 + 2t(1-t)\omega + t^2}P_0 + \frac{(2t(1-t)\omega v + t^2}{(1-t)^2 + 2t(1-t)\omega + t^2}P_2. \tag{26}$$

Then we set:

$$u = \frac{(2t(1-t)\omega v + t^2}{(1-t)^2 + 2t(1-t)\omega + t^2}. \tag{27}$$

Comparing Formula (26) with Formula (27), it is easy to find that

$$p(t) = (1-u)P_0 + uP_2. \tag{28}$$

In conclusion, Formula (28) is the parametric formula of the line segment. When the control point P_1 is on the line segment with the control point (P_0, P_2) as the end point, Formula (26) can be written as the parametric formula of the line segment of Formula (28). As such, it is proved that it degenerates into a line segment [23, 24].

Algorithm 3: To degenerate a Quadratic Rational Bézier Curve into a Linear section

Input: Control Points of Bezier Curve
Output: Linear section degenerated by Bezier Curve
Set ω*isaarbitraryvalue*
Input Bézier Curve control points,P_0, P_1, P_2
if the number of control points < 3 **then**
  goto Step 2.
else
  if the number of control points $= 3$ **then**
    Set control point P_3 on line segment with the control points P_1 and P_2 as end points
  end if
end if
Output coordinates of control points P_0, P_1,P_2
Output line segment between control points P_0, P_1 and P_1, P_2
Initializing the independent variable t in the standard formula of the quadratic rational Bezier curve to 0, *Set* $t = 0$
for $t = 0; t \le 1; t+ = 0.00125$ **do**
  Calculate the standard formula of the quadratic rational Bezier Curve.
  $x = \frac{(1-t)^2x_0+2t(1-t)\omega x_1+t^2x_2}{(1-t)^2+2t(1-t)\omega+t^2}, y = \frac{(1-t)^2y_0+2t(1-t)\omega y_1+t^2y_2}{(1-t)^2+2t(1-t)\omega+t^2}$
end for
Output Bezier Curve.
Clear Bezier Curve, Bezier Curve control points. **goto** Step 1.
return

4. NECESSARY AND SUFFICIENT CONDITIONS FOR A QUADRATIC RATIONAL BÉZIER CURVE TO REPRESENT A SECTION OF ARC

Theorem 3. *Quadratic rational Bézier curves can be used to represent an arc if and only if* $|P_0P_1| = |P_2P_1|$ *and* $0 \le \omega \le 1$ [25].

Proof: The equation of a circle passing through three collinear points $Q_i(x_i, y_i)$, $(i = 1, 2, 3)$, on a rectangular coordinate plane is:

$$\begin{vmatrix} x^2+y^2 & x & y & 1 \\ x_0^2+y_0^2 & x_0 & y_0 & 1 \\ x_1^2+y_1^2 & x_1 & y_1 & 1 \\ x_2^2+y_2^2 & x_2 & y_2 & 1 \end{vmatrix} = 0. \tag{29}$$

Given three points that are not collinear, we have:

$$P_0(x_0, y_0, 0) = (-a, 0, 0), A(x_A, y_A, 0), P_2(x_2, y_2, 0) = (a, 0, 0). \tag{30}$$

The arc curve starts from point P_0 and passes through point A to point P_2. Now, let us find another control vertex P_1. To do so, P_0, A, P_2 are substituted into the three-point common-circle equation 29, and we get

$$\begin{vmatrix} x^2+y^2 & x & y & 1 \\ x_0^2+y_0^2 & x_0 & y_0 & 1 \\ x_A^2+y_A^2 & x_A & y_A & 1 \\ x_2^2+y_2^2 & x_2 & y_2 & 1 \end{vmatrix} = 0. \tag{31}$$

From Formula (30) to Formula (31), we can find that $x_0 = -a, y_0 = 0, x_2 = a, y_2 = 0$. Furthermore, by expanding the determinant 31 in the first row, we have

$$(x^2+y^2)\begin{vmatrix} -a & 0 & 1 \\ 0 & y_A & 1 \\ a & 0 & 1 \end{vmatrix} + (-1)x\begin{vmatrix} a^2 & 0 & 1 \\ y_A^2 & y_A & 1 \\ a^2 & 0 & 1 \end{vmatrix} + y\begin{vmatrix} a^2 & -a & 1 \\ y_A^2 & 0 & 1 \\ a^2 & a & 1 \end{vmatrix} + (-1)\begin{vmatrix} a^2 & -a & 0 \\ y_A^2 & 0 & y_A \\ a^2 & a & 0 \end{vmatrix} = 0. \tag{32}$$

Among them,

$$\begin{vmatrix} -a & 0 & 1 \\ 0 & y_A & 1 \\ a & 0 & 1 \end{vmatrix} = -2ay_A, \quad \begin{vmatrix} a^2 & 0 & 1 \\ y_A^2 & y_A & 1 \\ a^2 & 0 & 1 \end{vmatrix} = 0,$$
$$\begin{vmatrix} a^2 & -a & 1 \\ y_A^2 & 0 & 1 \\ a^2 & a & 1 \end{vmatrix} = -a^3 + ay_A^2 + ay_A^2 - a^3,$$
$$\begin{vmatrix} a^2 & -a & 0 \\ y_A^2 & 0 & y_A \\ a^2 & a & 0 \end{vmatrix} = -a^3y_A - a^3y_A. \tag{33}$$

Finally, the above formula can be simplified as follows:

$$(-2ay_A)(x^2+y^2)+y(-a^3+2ay_A^2-a^3)+2a^3y_A=0. \quad (34)$$

Because $y_A \neq 0$, it is easy to know

$$x^2+\left(y+\frac{a^2-y_A^2}{2y_A}\right)^2=a^2+\frac{(a^2-y_A^2)^2}{4y_A^2}. \quad (35)$$

On the other hand, as $x_A = 0$, we can add x_A to have

$$x^2+\left(y+\frac{a^2-(x_A^2+y_A^2)}{2y_A}\right)^2=a^2+\frac{(a^2-(x_A^2+y_A^2))^2}{4y_A^2}. \quad (36)$$

Summarizing the above formula, the coordinates of the center of the circle O are:

$$x_O=0, \quad y_O=\frac{a^2-(x_A^2+y_A^2)}{2y_A}. \quad (37)$$

The radius of the circle is:

$$r=\sqrt{a^2+\frac{(a^2-(x_A^2+y_A^2))^2}{4y_A^2}}. \quad (38)$$

The vertical lines of OP_0 and OP_2 are made from points P_0 and P_2, respectively. According to the symmetry, if two vertical lines intersect with the Y axis at point P_1, then point P_1 is the control vertex of the arc curve. That is,

$$y_1=\frac{2a^2y_A}{a^2-(x_A^2+y_A^2)}. \quad (39)$$

Accordingly, the coordinates of point P_1 are:

$$x_1=0, \quad y_1=\frac{2a^2y_A}{a^2-(x_A^2+y_A^2)}. \quad (40)$$

From the definition of the Bézier Curve in Formula (1), we have:

$$\begin{aligned} x(t)&=\frac{(1-t)^2\omega_0x_0+2t(1-t)\omega_1x_1+t^2\omega_2x_2}{(1-t)^2\omega_0+2t(1-t)\omega_1+t^2\omega_2},\\ y(t)&=\frac{(1-t)^2\omega_0y_0+2t(1-t)\omega_1y_1+t^2\omega_2y_2}{(1-t)^2\omega_0+2t(1-t)\omega_1+t^2\omega_2}. \end{aligned} \quad (41)$$

To simply Formula (41), we further introduce the Quadratic Bernstein Basis Function ($B_{i,2}(t)$), which can be expressed as follows:

$$B_{0,2}(t)=(1-t)^2, \quad B_{1,2}(t)=2t(1-t), \quad B_{2,2}(t)=t^2. \quad (42)$$

As such, Formula (41) can be rewritten by applying $B_{i,2}(t)$ in the following format:

$$\begin{aligned} x(t)&=\frac{-a\omega_0B_{0,2}(t)+a\omega_2B_{2,2}(t)}{\omega_0B_{0,2}(t)+\omega_1B_{1,2}(t)+\omega_2B_{2,2}(t)},\\ y(t)&=\frac{2t(1-t)\omega_1y_1}{\omega_0B_{0,2}(t)+\omega_1B_{1,2}(t)+\omega_2B_{2,2}(t)}. \end{aligned} \quad (43)$$

On the other hand, note that the standard equation of curve arc circle can be estimated as

$$x^2(t)+(y(t)+a\cot\theta)^2=a^2/\sin^2\theta. \quad (44)$$

Consequently, by substituting Formulas (43) into Equation (44), the following results are obtained:

$$\begin{aligned} &\left(\frac{-a\omega_0B_{0,2}(t)+a\omega_2B_{2,2}(t)}{\omega_0B_{0,2}(t)+\omega_1B_{1,2}(t)+\omega_2B_{2,2}(t)}\right)^2\\ &+\left(\frac{\omega_1y_1B_{1,2}(t)}{\omega_0B_{0,2}(t)+\omega_1B_{1,2}(t)+\omega_2B_{2,2}(t)}+a\cot\theta\right)^2=\frac{a^2}{\sin^2\theta}, \end{aligned} \quad (45)$$

Note that

$$\frac{a^2}{\sin^2\theta}-a^2\cot^2\theta=a^2. \quad (46)$$

As such, Formula (45) can be further simplified as

$$\begin{aligned} &a^2\omega_0^2B_{0,2}^2(t)+a^2\omega_2^2B_{2,2}^2(t)-2a^2\omega_0\omega_2B_{0,2}(t)B_{2,2}(t)+\omega_1^2y_1^2B_{1,2}^2(t)\\ &+(2\omega_1y_1B_{1,2}(t)a\cot\theta(\omega_0B_{0,2}(t)+\omega_1B_{1,2}(t)+\omega_2B_{2,2}(t))\\ &=a^2(\omega_0B_{0,2}(t)+\omega_1B_{1,2}(t)+\omega_2B_{2,2}(t))^2 \end{aligned} \quad (47)$$

Furthermore, according to Formula (38) and Formula (40), we can have

$$y_1\cot\theta=\frac{2a^2y_A}{a^2-(x_A^2+y_A^2)}\times\frac{(a^2-(x_A^2+y_A^2))}{2ay_A}=a, \quad (48)$$

and then,

$$(y_1^2+a^2)\omega_1^2B_{1,2}^2(t)-4a^2\omega_0\omega_2B_{0,2}(t)B_{2,2}(t)=0. \quad (49)$$

Again, we consider the Quadratic Bernstein Basis Function, and then the above formula (in Formula 49) can be simplified as follows:

$$((y_1^2+a^2)\omega_1^2-a^2\omega_0\omega_2)(1-t)^2t^2=0. \quad (50)$$

Next, according to Formula (40), we know

$$(\omega_1^2\sec^2\theta-\omega_0\omega_2)(1-t)^2t^2=0, \quad (51)$$

and $t\in(0,1)$, $t^2(1-t)^2\neq 0$. It is thus easy to know

$$\omega_1^2=\omega_0\omega_2\cos^2\theta. \quad (52)$$

According to the standard form of the quadratic rational Bézier curve (see Formula 6), we can further estimate $\omega_0=\omega_2=1, \omega_1=\cos\theta$, and the value range of θ of the center angle of the semicircle should be $0\leq\theta\leq\pi/2$ [26].

In summary, the rational quadratic Bézier expressions of arc curves passing through points P_0, A, P_2 are as follows,

$$C(t)=\frac{(1-t)^2P_0+2\cos(\theta)t(1-t)P_1+t^2P_2}{(1-t)^2+2\cos(\theta)t(1-t)+t^2}. \quad (53)$$

Compared with the standard formula of a rational quadratic Bézier, the following results are obtained,

$$\omega = \cos(\theta), \tag{54}$$

where $0 \leq \theta \leq \pi/2$, $0 \leq \omega \leq 1$. Consequently, the necessary and sufficient conditions for a rational quadratic Bézier curve to represent a circular arc are expressed as follows:

$$|P_0P_1| = |P_2P_1| \quad and \quad 0 \leq \omega \leq 1. \tag{55}$$

Algorithm 4: For a Quadratic Rational Bézier Curve to Represent a section of an Arc

Input: Control Points of Bezier Curve
Output: A section of Arc Represented by Bezier Curve

Set $-1 < \omega < 1$, *and* $\omega \neq 0$
Input Bézier Curve control points,P_0, P_1, P_2
if the number of control points < 3 **then**
  goto Step 2.
else
  if the number of control points $= 3$ **then**
    Set $|P_0P_1| = |P_1P_2|$:
      $P_2(y) = P_0(y)$
      $P_1(x) = \frac{P_0(x)+P_2(x)}{2}$
      $P_1(y) = P_0(y) - \frac{P_2(x)-P_0(x)}{2} \times \tan(\frac{\Pi}{3})$
  end if
end if
Output coordinates of control points P_0, P_1,P_2
Output line segment between control points P_0, P_1 and P_1, P_2
Initializing the independent variable t in the standard formula of the quadratic rational Bezier curve to 0, *Set* $t = 0$
for $t = 0; t \leq 1; t+ = 0.00125$ **do**
  Calculate the standard formula of the quadratic rational Bezier Curve.
  $x = \frac{(1-t)^2x_0+2t(1-t)\omega x_1+t^2x_2}{(1-t)^2+2t(1-t)\omega+t^2}, y = \frac{(1-t)^2y_0+2t(1-t)\omega y_1+t^2y_2}{(1-t)^2+2t(1-t)\omega+t^2}$
end for
Output Bezier Curve.
Clear Bezier Curve, Bezier Curve control points. **goto** Step 1.
return

5. NECESSARY AND SUFFICIENT CONDITIONS FOR QUADRATIC RATIONAL BÉZIER CURVES TO REPRESENT A PARABOLA, ELLIPTIC ARC AND HYPERBOLA

Theorem 4. *Quadratic rational Bézier curve represents a parabola, elliptic arc, and hyperbola if and only if* $\omega = \pm 1$, $-1 < \omega < 1$, *and* $\omega < -1$ *or* $\omega > 1$, *respectively* [27].

Proof: According to the second order Bernstein basis function of Formula (42), Bézier curve from Formula (1) is written as follows,

$$p(t) = \frac{\omega_0 B_{0,2}(t)P_0}{\sum_{j=0}^{2} B_{j,2}(t)\omega_j} + \frac{\omega_1 B_{1,2}(t)P_1}{\sum_{j=0}^{2} B_{j,2}(t)\omega_j} + \frac{\omega_2 B_{2,2}(t)P_2}{\sum_{j=0}^{2} B_{j,2}(t)\omega_j} = \sum_{i=0}^{2} R_{i,2}(t)P_i, \tag{56}$$

where

$$R_{i,2}(t) = \frac{\omega_i B_{i,2}(t)}{\sum_{j=0}^{2} B_{j,2}(t)\omega_j}. \tag{57}$$

Next, we introduce the Local Oblique Coordinate System P_1, S, T, so that $S = P_0 - P_1$, $T = P_2 - P_1$. Since point $P(t)$ is within $\delta P_0P_1P_2$ for arbitrary $t \in [0, 1]$, $P(t)$ can be rewritten as

$$\begin{aligned} P(t) &= P_1 + u(t)S + v(t)T \\ &= P_1 + u(t)(P_0 - P_1) + v(t)(P_2 - P_1) \\ &= u(t)P_0 + [1 - u(t) - v(t)]P_1 + v(t)P_2. \end{aligned} \tag{58}$$

Comparing the coefficients from both Formula (56) and Formula (58), we know that

$$\begin{aligned} R_{0,2}(t) &= u(t), \\ R_{1,2}(t) &= 1 - u(t) - v(t), \\ R_{2,2}(t) &= v(t). \end{aligned} \tag{59}$$

Let $k = \omega_0\omega_2/\omega_1^2$, where k is the shape-invariant factor of a conic, so

$$u(t)v(t) = R_{0,2}(t)\dot{R}_{2,2}(t) = \frac{1}{4}k[1 - u(t) - v(t)]^2. \tag{60}$$

Formula (60) is an implicit equation of a quadratic curve in the local oblique coordinate system P_1, S, T. The expansion of Formula (60) further indicates that:

$$ku^2(t) + (2k-4)u(t)v(t) + kv^2(t) - 2ku(t) - 2kv(t) + k = 0. \tag{61}$$

In the Cartesian coordinate system, the image of a binary quadratic equation can represent a conic curve, and all conic curves can be derived in the aforementioned way [1]. The equation has the following forms [28]:

$$Ax^2 + Bxy + Cy^2 + Dx + Ey + F = 0, \quad A, B, C \text{ are not all zero}, \tag{62}$$

where A, B, C, D, E, F are polynomial coefficients. If the following conditions are satisfied,

$$B^2 - 4AC < 0, \tag{63}$$

then Formula (62) represents an ellipse; furthermore, under the same condition, if the conic degenerates (that is, $A = C, B = 0$), the equation represents a circle. Additionally, if the following conditions are satisfied,

$$B^2 - 4AC = 0, \tag{64}$$

Algorithm 5: For Quadratic Rational Bézier Curves to Represent a Parabola, Elliptic Arc and Hyperbola

Input: Control Points of Bezier Curve

Output: A section of a Parabola, Elliptic Arc or Hyperbola Represented by a Bezier Curve

if Quadratic Rational Bézier Curves to Represent a Parabola **then**
  Set $\omega = 1$ *or* $\omega = -1$
end if
if Quadratic Rational Bézier Curves to Represent an Elliptic Arc **then**
  Set $-1 < \omega < 1, and\ \omega \neq 0$
end if
if Quadratic Rational Bézier Curves to Represent a Hyperbola **then**
  Set $\omega < -1$ *or* $\omega > 1$
end if
Input Bézier Curve control points P_0, P_1, P_2
if the number of control points < 3 **then**
  goto Step 2.
else
  if the number of control points $= 3$, and Quadratic Rational Bézier Curves to Represent an Elliptic Arc **then**
    Set $|P_0P_1| \neq |P_1P_2|$
  end if
end if
Output coordinates of control points P_0, P_1,P_2
Output line segment between control points P_0, P_1 and P_1, P_2
Initializing the independent variable t in the standard formula of the quadratic rational Bezier curve to 0, *Set* $t = 0$
for $t = 0; t \leq 1; t+ = 0.00125$ **do**
  Calculate the standard formula of the quadratic rational Bezier Curve.
  $x = \frac{(1-t)^2x_0+2t(1-t)\omega x_1+t^2x_2}{(1-t)^2+2t(1-t)\omega+t^2}, y = \frac{(1-t)^2y_0+2t(1-t)\omega y_1+t^2y_2}{(1-t)^2+2t(1-t)\omega+t^2}$
end for
Output Bezier Curve.
Clear Bezier Curve, Bezier Curve control points. **goto** Step 1.
return

then Formula (62) represents a parabola [29]. Finally, if the following conditions are satisfied,

$$B^2 - 4AC > 0 \tag{65}$$

then Formula (62) represents an hyperbola. The coefficients from Formula (61) and Formula (62) can be obtained as follows: $A = k, B = k - 2, C = k, D = -2k, E = -2k, F = k$. As such, we can get:

$$B^2 - 4AC = 1 - k. \tag{66}$$

We then provide the discussion and judgment of Formula (66). That is, from the condition of Formula (63), if the curve is an ellipse, then in Formula (66) we have $B^2 - 4AC = 1 - k < 0$. Therefore, when $k > 1$, the curve is an ellipse. From the condition of (64), if the curve is a parabola, then $B^2 - 4AC = 1 - k = 0$ (again see Formula 66). Therefore, when $k = 1$, the curve is a parabola. From the condition of 65, if the curve is a hyperbola, then $B^2 - 4AC = 1 - k > 0$, so when $k < 1$, the curve is a hyperbola.

Note that $k = \omega_0\omega_2/\omega_1^2$. In summary, under the standard form of the quadratic rational Bézier curve, we have $\omega_0 = \omega_2 = 1$, and $\omega = \omega_1$. Consequently, we prove that when $-1 < \omega < 1$, the quadratic rational Bézier curve is a ellipse; when $\omega = \pm 1$, the quadratic rational Bézier curve is a parabola; when $\omega < -1, or\ \omega > 1$, the quadratic rational Bézier curve is a hyperbola.

6. CONCLUSION

In this paper, we discuss the necessary and sufficient conditions for utilizing quadratic rational Bézier curves to represent different shapes, such as a point, line segment, parabola, elliptic arc, circular arc, and hyperbola. These results can be further used to facilitate other computer-aided geometric designs.

DATA AVAILABILITY STATEMENT

The raw data supporting the conclusions of this article will be made available by the authors, without undue reservation.

AUTHOR CONTRIBUTIONS

CY: conceptualization, methodology, software, validation, investigation, visualization, and writing original draft. JY: software, writing - review & editing, and supervision. YL: software, visualization, and writing - original draft. XG: writing - review & editing, validation, and visualization.

FUNDING

This work was supported by the National Natural Science Foundation of China (Grant No. 61873004, 51874003) and the Humanities and Social Sciences Foundation of Anhui Department of Education, China (Grant No. SK2017A0098). We would also like to thank JY from the University of Wollongong for his useful discussion.

REFERENCES

1. Walton DJ, Meek DS. G2 curve design with planar quadratic rational Bézier spiral segments. *Int J Comput Math*. (2013) **90**:325–40. doi: 10.1080/00207160.2012.716831
2. Zhang R. Improved derivative bounds of the rational quadratic Bézier curves. *Appl Math Comput*. (2015) **250**:492–6. doi: 10.1016/j.amc.2014.10.120
3. Shi M. Degree reduction of disk rational Bézier curves using multi-objective optimization techniques. *Int J Appl Math*. (2015) **45**:392–7.
4. Lu L, Jiang C, Xiang X. Some remarks on weighted Lupaş [formula omitted]-Bézier curves. *J Comput Appl Math*. (2017) **313**:393–6.
5. Lee E. The rational Bézier representation for conics. *Geometr Model*. (1987) **3**:5–19.
6. Han X. Quadratic trigonometric polynomial curves concerning local control. *Appl Numer Math*. (2006) **56**:105–15. doi: 10.1016/j.apnum.2005.02.013
7. Samreen S, Sarfraz M, Hussain MZ, Livesu M. Computer aided design using a rational quadratic trigonometric spline with interval shape control. In: *2017 International Conference on Computational Science and Computational Intelligence*. Las Vegas, NV: IEEE (2017). p. 246–51.
8. Bashir U, Abbas MA, Ali JA. The G2 and C2 rational quadratic trigonometric Bézier curve with two shape parameters with applications. *Appl Math Comput*. (2013) **219**:10183–97. doi: 10.1016/j.amc.2013.03.110
9. Xu C, Kim T, Farin GE. The eccentricity of conic sections formulated as rational Bézier quadratics. *Comput Aided Geometr Des*. (2010) **27**:458–60. doi: 10.1016/j.cagd.2010.04.001
10. Bastl B, Jttler B, Lvicka M, Schicho J, Šír Z. Spherical quadratic Bézier triangles with chord length parameterization and tripolar coordinates in space. *Comput Aided Geometr Des*. (2011) **28**:127–34. doi: 10.1016/j.cagd.2010.11.001
11. Hussain MZ, Irshad M, Sarfraz M, Zafar N. Interpolation of discrete time signals using cubic functions. In: *IEEE International Conference on Information Visualization*. Chicago, IL: IEEE (2015). p. 454–9.
12. Han L, Wu Y, Chu Y. Weighted Lupaş q-Bézier curves. *J Comput Appl Math*. (2016) **308**:318–29. doi: 10.1016/j.cam.2016.06.017
13. Han L-W, Chu Y, Qiu Z-Y. Generalized Bézier curves and surfaces based on Lupaş q-analogue of Bernstein operator. *J Comput Appl Math*. (2014) **261**:352–63. doi: 10.1016/j.cam.2013.11.016
14. Cattiaux-Huillard I, Albrecht G, Hernández-Mederos V. Optimal parameterization of rational quadratic curves. *Comput Aided Geometr Des*. (2009) **26**:725–32. doi: 10.1016/j.cagd.2009.03.008
15. Hussain M, Saleem S. C^1 rational quadratic trigonometric spline. *Egypt Inform J*. (2013) **14**:211–20. doi: 10.1016/j.eij.2013.09.002
16. Sarfraz M, Samreen S, Hussain MZ. Modeling of 2D objects with weighted Quadratic Trigonometric Spline. In: *13th International Conference on Computer Graphics, Imaging and Visualization*. Beni Mellal (2016). p. 29–34.
17. Lee T-K, Baek S-H, Choi Y-H, Oh S-Y. Smooth coverage path planning and control of mobile robots based on high resolution grid map representation. *Robot Auton Syst*. (2011) **59**:801–12. doi: 10.1016/j.robot.2011.06.002
18. Han X. Shape preserving piecewise rational interpolant with quartic numerator and quadratic denominator. *Appl Math Comput*. (2015) **251**:258–74. doi: 10.1016/j.amc.2014.11.067
19. Lamnii A, Oumellal F. A method for local interpolation with tension trigonometric spline curves and surfaces. *Appl Math Sci*. (2015) **9**:3019–35. doi: 10.12988/ams.2015.52154
20. Shi M. Degree reduction of classic disk rational Bézier curves in L_2 Norm. In: *2015 14th International Conference on Computer-Aided Design and Computer Graphics*. Xi'an: IEEE (2015). p. 202–3.
21. Xu A, Viriyasuthee C, Rekleitis I. Efficient complete coverage of a known arbitrary environment with applications to aerial operations. *Auton Robot*. (2014) **36**:365–81. doi: 10.1007/s10514-013-9364-x
22. Khan A, Noreen I, Habib Z. Coverage path planning of mobile robots using rational quadratic Bézier spline. In: *2016 International Conference on Frontiers of Information Technology*. Islamabad: IEEE (2016). p. 319–23.
23. Backman J, Piirainen P, Oksanen T. Smooth turning path generation for agricultural vehicles in headlands. *Biosyst Eng*. (2015) **139**:76–86. doi: 10.1016/j.biosystemseng.2015.08.005
24. Yu X, Roppel TA, Hung, JY. An optimization approach for planning robotic field coverage. In: *41st Annual Conference of the IEEE Inductrial Electronics Society*. Yokohama: IEEE (2015). p. 76–86.
25. Sara E, Pieter P. Exploiting lattice structures in shape grammar implementations. *AI EDAM*. (2018) **32**:147–61. doi: 10.1017/S0890060417000282
26. Li Y, Deng C, Jin W, Zhao N. On the bounds of the derivative of rational Bézier curves. *Appl Math Comput*. (2013) **219**:10425–33. doi: 10.1016/j.amc.2013.04.042
27. Deng C, Li Y, Mu X, Zhao Y. Characteristic conic of rational bilinear map. *J Comput Appl Math*. (2019) **346**:277–83. doi: 10.1016/j.cam.2018.07.012
28. LiZheng L, ChengKai J. Some remarks on weighted Lupaş[formula omitted]-Bézier curves. *J Comput. Appl. Math*. (2017) **313**:393–6. doi: 10.1016/j.cam.2016.09.044
29. Yan K, Cheng H-L, Ji Z, Zhang X, Lu H. Accelerating smooth molecular surface calculation. *J Math Biol*. (2018) **76**:779–93. doi: 10.1007/s00285-017-1156-z

Conflict of Interest: The authors declare that the research was conducted in the absence of any commercial or financial relationships that could be construed as a potential conflict of interest.

frontiers in Physics

BRIEF RESEARCH REPORT
published: 16 June 2020
doi: 10.3389/fphy.2020.00197

Generalization of the Cover Pebbling Number for Networks

Zheng-Jiang Xia and Zhen-Mu Hong*

School of Finance, Anhui University of Finance & Economics, Bengbu, China

Pebbling can be viewed as a model of resource transportation for networks. We use a graph to denote the network. A pebbling move on a graph consists of the removal of two pebbles from a vertex and the placement of one pebble on an adjacent vertex. The t-pebbling number of a graph G is the minimum number of pebbles so that we can move t pebbles on each vertex of G regardless of the original distribution of pebbles. Let ω be a positive function on $V(G)$; the ω-cover pebbling number of a graph G is the minimum number of pebbles so that we can reach a distribution with at least $\omega(v)$ pebbles on v for all $v \in V(G)$. In this paper, we give the ω-cover pebbling number of trees for nonnegative function ω, which generalized the t-pebbling number and the traditional weighted cover pebbling number of trees.

Keywords: network, tree, path partition, pebbling, cover pebbling

OPEN ACCESS

Edited by:
Jia-Bao Liu,
Anhui Jianzhu University, China

Reviewed by:
Fu-Tao Hu,
Anhui University, China
Zhi Qiao,
Sichuan Normal University, China
Xiang-jun Li,
Yangtze University, China

****Correspondence:***
Zheng-Jiang Xia
120150025@aufe.edu.cn

Specialty section:
This article was submitted to Mathematical Physics, a section of the journal Frontiers in Physics

Received: *12 April 2020*
Accepted: *04 May 2020*
Published: *16 June 2020*

Citation:
Xia Z-J and Hong Z-M (2020) Generalization of the Cover Pebbling Number for Networks. Front. Phys. 8:197. doi: 10.3389/fphy.2020.00197

Mathematics Subject Classification: 05C99, 05C72, 05C85.

1. INTRODUCTION

Pebbling in graphs was introduced by Chung [1]. It can also be viewed as a model of resource transportation for networks. Let G be a simple connected graph; we use $V(G)$ and $E(G)$ to denote the vertex set and edge set of G, respectively. $d(u, v)$ is the distance of u and v, and we write $u \sim v$ if they are adjacent. $N(v) = \{u|u \sim v\}$ is the neighbor of v, and $d(v) = |N(v)|$ is the degree of v. Let H be a subgraph of G; we use $d_H(v)$ to denote the degree of v in H.

A pebble distribution D on G is a function $D : V(G) \to N$ (N is the set of nonnegative integers), where $D(v)$ is the number of pebbles on v, $|D| = \sum_{v \in V(D)} D(v)$ is the *size* of D.

A *pebbling move* consists of the removal of two pebbles from a vertex and the placement of one pebble on an adjacent vertex. Let D and D' be two pebble distributions of G. If so, we say that D *contains* D' if $D(v) \geq D'(v)$ for all $v \in V(G)$, and D' is *reachable* from D if there is some sequence (probably empty) of pebbling moves (a pebbling sequence in short) starting from D and resulting in a distribution, which contains D'. For a graph G and a vertex v, we call v a *root* (or target vertex) if the goal is to place pebbles on v. If t pebbles can be moved to v from D by a sequence of pebbling moves, then we say that D is *t-fold v-solvable*, and v is *t-reachable* from D. If D is t-fold v-solvable for every vertex v, we say that D is *t-solvable*.

The t-pebbling number of a graph G, denoted by $f_t(G)$, is the smallest number m such that every distribution with size m is t-solvable. While $t = 1$, we use $f(G)$ instead of $f_1(G)$, which is called *the pebbling number* of G.

For any two graphs G and H, we define the *Cartesian product* $G \times H$ to be the graph with the vertex set $V(G \times H)$ and edge set the union of $\{((a, v), (b, v))|(a, b) \in E(G), v \in E(H)\}$ and $\{((u, x), (u, y))|u \in V(G), and (x, y) \in E(H)\}$.

To determine the pebbling number of a general graph G is difficult. The problem of whether a distribution is v-solvable for some $v \in V(G)$ was shown to be NP-complete [2, 3]. The problem of

deciding whether the pebbling number of a graph G is less than k was shown to be Π_2^p-complete [3]. The pebbling numbers of trees [4], cycles [5], hypercubes [1], and so on are determined. A conjecture called Graham's Conjecture is given by Chung [1].

Conjecture 1.1. (Graham's Conjecture) *Let G and H be two connected graphs; the pebbling number of the Cartesian product of G and H satisfies:*

$$f(G \times H) \leq f(G)f(H).$$

There are many results about Graham's Conjecture [6–10], while this conjecture is still open.

Definition 1.2. Let ω be a nonnegative function on $V(G)$ and D a distribution on $V(G)$. We say D is *ω-solvable* (or D solves ω) if we can reach a distribution D^* from D, by a sequence of pebbling moves, so that $D^*(v) \geq \omega(v)$ for all $v \in V(G)$. The *ω-cover pebbling number* of G, denoted by $\gamma_\omega(G)$, is the minimum number m so that every distribution D with size m is ω-solvable.

Definition 1.3. Let ω be a positive function on $V(G)$; define

$$s_\omega(v) = \sum_{u \in V(G)} \omega(u) 2^{d(u,v)},$$

and

$$s_\omega(G) = \max_{v \in V(G)} s_\omega(v).$$

The ω-cover pebbling number of a graph G has been determined for *positive* ω by [11].

Theorem 1.4. ([11]) *Let ω be a positive weight function on $V(G)$; the ω-cover pebbling number of G is*

$$\gamma_\omega(G) = s_\omega(G).$$

From Theorem 1.4, we can get

Theorem 1.5. *([11]) Let ω_1 be a positive function on G and ω_2 be a positive function on H. The function ω on $G \times H$ is given by $\omega((g,h)) = \omega_1(g)\omega_2(h)$, where $g \in V(G)$ and $h \in V(H)$, then $\gamma_\omega(G \times H) = \gamma_{\omega_1}(G)\gamma_{\omega_2}(H)$.*

We first generalize the definition of $s_\omega(T)$ while ω is a *nonnegative* function on a tree T. We will give the definition of path partition in the next section.

Definition 1.6. Given a tree T and a nonnegative function ω for each vertex $v \in V(T)$, and let $T_\omega(v)$ be the minimum subtree of T containing v and $W := \{u : \omega(u) > 0\}$. We give each edge in $T \backslash E(T_\omega(v))$ a direction toward $T_\omega(v)$ to get a directed graph, which is denoted by $\overrightarrow{T} \backslash E(T_\omega(v))$, and $(a_1, \ldots, a_n)$ is the size of the maximum path partition of $\overrightarrow{T} \backslash E(T_\omega(v))$. We define

$$s_\omega(v) = \sum_{u \in W} \omega(u) 2^{d(u,v)} + \sum_{i=1}^{n} 2^{a_i} - n.$$

and

$$s_\omega(T) = \max_{v \in V(T)} s_\omega(v).$$

Note that while ω is positive, then the two definitions of $s_\omega(T)$ are the same. Definition 1.6 is thus a generalization of Definition 1.3. In this paper, we generalize Theorem 1.4 while T is a tree and ω is nonnegative. Thus, our main result is as follows

Theorem 1.7. *Let T be a tree with a nonnegative weight function ω on $V(T)$. The ω-cover pebbling number of T is*

$$\gamma_\omega(T) = s_\omega(T).$$

Theorem 1.8. *Let T be a tree with a nonnegative weight function ω on $V(T)$. If $|W| = 1$, then Theorem 1.7 is equivalent to Theorem 2.2.*

Proof. If $|W| = 1$, assume that $\omega(v) = t$, and $\omega(u) = 0$ for $u \neq v$. We will show that $f_t(T, v) = s_\omega(T)$.

Assume the size of a maximum path partition of $\vec{T}_v$ is $(a_0, a_1, \ldots, a_n)$, and $d(v, v_0) = a_0$, P_0 is the longest directed path from v_0 to v. Then $(a_1, \ldots, a_n)$ must be the size of a maximum path partition in $\vec{T}_v \backslash P_0$. So $f_t(T, v) = s_\omega(v_0) \leq s_\omega(T)$.

Assume $s_\omega(T) = s_\omega(v_1)$, and $d(v_1, v) = a_0$. Let P_0 be the path connected v_1 and v, then $T_\omega(v_1) = P_0$; assume $(a_1, \ldots, a_n)$ is the size of the maximum path partition of $T \backslash E(T_\omega(v)) = T \backslash E(P_0)$, so $\alpha = (a_0, a_1, \ldots, a_n)$ is a path partition of $\vec{T}_v$, and $s_\alpha = s_\omega(v_1)$ by Corollary 2.3 and $f_t(T, v) \geq s_\omega(v_1) = s_\omega(T)$. ∎

Definition 1.9. ([12]) Given a sequence S of pebbling moves on G, *the transition digraph* obtained from S is a directed multigraph denoted $T(G, S)$ that has $V(G)$ as its vertex set. Each move $s \in S$ along edge uv (move off two pebbles from u and add one on v) is represented by a directed edge uv.

The following lemma is useful in the following sections.

Lemma 1.10. ([12], No-Cycle Lemma) *Let S be a sequence of pebbling moves on G, reaching a distribution D. Then there exists a sequence S^* of pebbling moves, thus reaching a distribution D^* where*

1. *On each vertex v, $D^*(v) \geq D(v)$;*
2. *$T(G, S^*)$ does not contain any directed cycles.*

2. PRELIMINARIES

We first introduce the path partition and the pebbling number of trees.

Definition 2.1. ([4]) Given a root v of a tree T, then we can view T as a directed graph $\overrightarrow{T_v}$ with edges directed toward v. *A path partition* is a set of nonoverlapping directed paths in which the union is $\overrightarrow{T_v}$. A path partition is said to *majorize* another if the non-increasing sequence of the path size majorizes that of the other (that is $(a_1, a_2, \ldots, a_r) > (b_1, b_2, \ldots, b_t)$ if and only if $a_i > b_i$, where $i = \min\{j : a_j \neq b_j\}$). A path partition of a tree $\overrightarrow{T_v}$ is said to be *maximum* if it majorizes all other path partitions. Note that, in this paper, the sequence of the size of a path partition is always non-increasing.

Note: By the definition of the maximum path partition, we can give a way to determine the size of the maximum path partition. First, we choose the longest directed path P_1 in $\overrightarrow{T_v}$, with length a_1. Then, we choose the longest directed path P_2 in $\overrightarrow{T_v}\backslash E(P_1)$, with length a_2, and so on. Moreover, it should be noted that the maximum path partition may not be unique, but the size of the maximum path partition must be unique.

Moews [4] found the t-pebbling number of trees by a path partition.

Theorem 2.2. ([4]) *Let T be a tree, $v \in V(T)$, and $(a_1, \ldots, a_n)$ be the size of the maximum path partition of $\overrightarrow{T_v}$. Then,*

$$f_t(T, v) = t2^{a_1} + \sum_{i=2}^{n} 2^{a_i} - n + 1,$$

$$f_t(T) = \max_{v \in V(T)} f_t(T, v).$$

Corollary 2.3. *Let T be a tree, $v \in V(T)$, and $\alpha = (a_1, \ldots, a_n)$ be the size of a path partition of $\overrightarrow{T_v}$, $s_\alpha := t2^{a_1} + \sum_{i=2}^{n} 2^{a_i} - n+1$. Then,*

$$f_t(T, v) = \max_{\alpha} s_\alpha.$$

Proof. Let α_0 be the size of the maximum path partition of $\overrightarrow{T_v}$. Then, $f_t(T, v) = s_{\alpha_0} \leq \max_\alpha s_\alpha$.

Assume $P_1, P_2, \ldots, P_n$ is a path partition of $\overrightarrow{T_v}$, and the length of P_i is a_i for $1 \leq i \leq n$. Note that for each P_i we should assume the two endpoints v_i and v_i' satisfy $d(v_i, v) > d(v_i', v)$. We put $t2^{a_1} - 1$ pebbles on v_1 and $2^{a_i} - 1$ pebbles on v_i for $2 \leq i \leq n$; it is clear that t pebbles cannot be moved to v from this distribution. Thus, for each α, $s_\alpha - 1 < f_t(T, v)$, so $s_\alpha \leq f_t(T, v)$ so $\max_\alpha s_\alpha \leq f_t(T, v)$. ∎

Definition 2.4. Let C be a *generalized distribution* on G, where $C(v)$ is an integer (may be negative) for all $v \in V(G)$. *A pebbling move* on G consists of the removal of two pebbles from a vertex v (with $C(v) \geq 2$) and the placement of one pebble on an adjacent vertex.

In the following, a *distribution* D means that $D(v) \geq 0$, and a *generalized distribution* C means $C(v)$ is an integer for all $v \in V(G)$.

Definition 2.5. A pebbling move from u to v under a distribution D is *executable* if $D(u) \geq 2$. A pebbling sequence S is a finite set of pebbling moves, assuming $S = (S_1, ..., S_k)$, where S_i is a pebbling move for $1 \leq i \leq k$, and the pebbling move S_i is in front of S_j if $1 \leq i < j \leq k$. We say the pebbling sequence S *executable*, if S_i is executable for $1 \leq i \leq k$.

Definition 2.6. Let ω be a nonnegative function on $V(G)$ and C be a generalized distribution on $V(G)$. We say C is *ω-solvable*, if we can reach a distribution C^* from C, by a sequence of pebbling moves so that $C^*(v) \geq \omega(v)$. In particular, if $\omega(v) = 0$ for all $v \in V(G)$, then we say that C is 0-*solvable*.

Lemma 2.7. *Let D be a distribution on a graph G and ω be a nonnegative function on $V(G)$, $C := D - \omega$. Then, D is ω-solvable if and only if C is 0-solvable.*

Proof. If C is 0-solvable, let δ be an executable pebbling sequence that reaches a distribution D^* so that $D^* > 0$ from C. It is then clear that δ is also an executable pebbling sequence that can reach a distribution D' so that $D' = D^* + \omega > \omega$ from D. Thus D is ω-solvable.

On the other hand, if D is ω-solvable, by Lemma 1.10, there exists a pebbling sequence S reaching a distribution D^* with $D^*(v) \geq \omega(v)$, and $T(G, S)$ does not contain any direct cycle. We can thus give a sequence of the vertices of G, as $(v_1, v_2, \ldots, v_n)$, so that each directed edge v_iv_j in $T(G, S)$ satisfies $i < j$. We can thus rearrange the sequence of pebbling moves S along the order $(v_1, v_2, \ldots, v_n)$. It means we first choose all pebbling moves in S that remove pebbles from v_1, choose all pebbling moves in S that remove pebbles from v_2, and so on, and we denote this sequence of pebbling moves by S'. We will show that S' is an executable pebbling sequence that reach $D^* - \omega$ from C.

In S', for each vertex $v \in V(G)$, the pebbling moves that move pebbles to v are in front of the pebbling moves that remove pebbles from v. We may thus assume that, for each vertex v_i, we first move α_i pebbles from other vertices to v_i and then remove β_i pebbles from v_i.

We only need to show that, for each $v_i \in V(G)$, the sequence of pebbling moves that removes β_i pebbles from v_i in S', denoted by σ_i, is executable. We use induction on i. If $i = 1$, and we can then get $D(v_1) - \beta_1 = D^*(v_1) \geq \omega(v_1) \Rightarrow D(v_1) - \omega(v_1) \geq \beta_1 \Rightarrow C(v_1) \geq \beta_1$, and so σ_1 is executable.

Assume σ_h is executable for $h < i$. By induction, the pebbling sequence that moves α_i pebbles to v_i is executable. Moreover, we can get $D(v_i) + \alpha_i - \beta_i = D^*(v_i) \Rightarrow D(v_i) + \alpha_i - \omega(v_i) - \beta_i = D^*(v_i) - \omega(v_i) \geq 0 \Rightarrow D(v_i) - \omega(v_i) + \alpha_i \geq \beta_i \Rightarrow C(v_i) + \alpha_i \geq \beta_i$. Thus σ_i is executable.

So S' is an executable pebbling sequence that reaching $D^* - \omega$ from C. Note that $D^* - \omega \geq 0$, and this completes the proof. ∎

Definition 2.8. Let D be a distribution on a tree T and ω be a nonnegative function on $V(T)$. $C := D - \omega$ is called the *induced generalized distribution* from D and ω of T. Let v be a leaf of T and u be its neighbor in T. The *induced generalized distribution* C' on $T \setminus v$ is given: if $C(v) \geq 0$, then $C'(u) = C(u) + \lfloor C(v)/2 \rfloor$, and if $C(v) < 0$, then $C'(u) = C(u) + 2C(v)$, keeping $C'(x) = C(x)$ unchanged for all $x \neq u$.

Lemma 2.9. *Let D be a distribution on a tree T and ω be a nonnegative function on $V(T)$. $C := D - \omega$, v is a leaf of T, and C' is the induced generalized distribution from D and ω of $T\backslash v$. Then, C is 0-solvable in T if and only if C' is 0-solvable in $T\backslash v$.*

Proof. Firstly, we assume C is 0-solvable in T, and there is a pebbling sequence σ reaching a distribution C^* from C with $C^*(x) \geq 0$ for each $x \in V(T)$.

Case 1.1. $C(v) \geq 0$. By Lemma 1.10, we may assume that no pebble has been moved from u to v; at most, therefore, $\lfloor C(v)/2 \rfloor$

pebbles can be moved from v to u. We may assume the first step of σ is to move $\lfloor C(v)/2 \rfloor$ pebbles from v to u, so the left steps makes C' solve 0 on $T\backslash v$.

Case 1.2. $C(v) < 0$. By Lemma 1.10, we may assume that no pebble has been moved from v to u. So we may assume the last step of σ is to move $-C(v)$ pebbles from u to v, and so the steps before it makes C' solve 0 on $T\backslash v$.

Secondly, we assume C' is 0-solvable in $T\backslash v$, and there is a pebbling sequence δ reaching a distribution C^* from C' with $C^*(x) \geq 0$ for each $x \in V(T\backslash v)$.

Case 2.1. $C(v) \geq 0$. First, we move $\lfloor C(v)/2 \rfloor$ pebbles from v to u, and the left steps are just δ; this sequence makes C solve 0.

Case 2.2. $C(v) < 0$. After the pebbling sequence δ, we move $-C(v)$ pebbles from u to v; this sequence makes C solve 0. ∎

Notations: Assume T^* is a subtree of T, then T^* can be obtained from T by deleting the leaves of the subtree of T (the vertex with degree one) one by one. For each subtree T^* of T, therefore, we can get an induced generalized distribution C^*. In particular, for each vertex $v \in V(T)$, let T_v be a subtree containing v and all of its neighbors. We use C_v to denote the induced generalized distribution from D and ω of T_v and $\widehat{C}(v)$ to denote the induced generalized distribution of $\{v\}$.

Corollary 2.10. *Let D be a distribution on a tree T, ω be a nonnegative function on $V(T)$, and $\widehat{C}(v)$ be the induced generalized distribution from D and ω of $\{v\}$. D is not ω-solvable is equivalent to $\widehat{C}(v) < 0$ for each $v \in V(T)$.*

Proof. From Lemma 2.7 and Lemma 2.9, the result follows by induction. ∎

Lemma 2.11. *Let D be a distribution on a tree T, which is not ω-solvable with $|D| = \gamma_\omega(T) - 1$. For each vertex $x \in V(T)$, which is not a leaf of T, there exists a vertex $y \in N(x)$, so that $C_x(y) \geq 0$.*

Proof. If $C_x(x') < 0$, for all $x' \in N(x)$, assume $y, z \in N(x)$ with $C_x(z) \leq C_x(y) < 0$. We delete all other vertices to the left $T_1 = yxz$ and its induced generalized distribution C_1. Then, $C_1(y) = C_x(y)$, $C_1(z) = C_x(z)$ and $\widehat{C}(x) = C_1(x) + 2C_1(y) + 2C_1(z) \leq -1$ by Corollary 2.10. Note that $C_1(x) = D(x) - w(x) + \sum_{x' \in N(x), x' \notin \{y,z\}} 2C_x(x')$. Thus, $C_1(x) - D(x) \leq 0$ and $C_1(x) + 2C_1(z) - D(x) \leq 0$. Now, we remove $D(x)$ pebbles from x and put $D(x) + 1$ pebbles on y to get a new distribution D' with $|D'| = |D| + 1$. The induced generalized distribution from D' and ω of $\{y\}$ is denoted by $\widehat{C}'(y)$. Then, $\widehat{C}'(y) = (C_1(y) + D(x) + 1) + 2(C_1(x) + 2C_1(z) - D(x)) = (C_1(x) + 2C_1(y) + 2C_1(z)) + (C_1(z) - C_1(y)) + C_1(z) + (C_1(x) - D(x)) + 1 \leq -1 + 0 - 1 + 0 + 1 = -1$, and so D' is not ω-solvable by Corollary 2.10, a contradiction to $|D'| = \gamma_\omega(T)$, and we are done. ∎

Theorem 2.12. *Let ω be a nonnegative function on $V(T)$ and D be a distribution that is not ω-solvable with $|D| = \gamma_\omega(T) - 1$. All pebbles are then distributed on the leaves of T.*

Proof. If $D(x) > 0$ for some vertex $x \in V(T)$, which is not a leaf, then $N(x)$ has at least two vertices. By Lemma 2.11, there exists a vertex $y \in N(x)$ with $C_x(y) \geq 0$. We first show that there exists a vertex $z \in N(x)$ with $C_x(z) < 0$.

If not, that means for all $v \in N(x)$, $C_x(v) \geq 0$. Note that $D(x) > 0$, and thus $\widehat{C}(x) = D(x) + \sum_{v \in N(x)} \lfloor C_x(v)/2 \rfloor > 0$. By Corollary 2.10, D is ω-solvable, a contradiction. Thus, there exists a vertex $z \in N(x)$ with $C_x(z) < 0$.

Let $T_1 = yxz$ be the subtree of T, with induced generalized distribution C_1. Then, $C_1(z) = C_x(z)$, $C_1(y) = C_x(y)$, and $\widehat{C}(x) = C_1(x) + \lfloor C_1(y)/2 \rfloor + 2C_1(z) < 0$.

Now, consider the new distribution D^*, with $D^*(y) = D(y) + D(x) + 1$, $D^*(x) = 0$, and $D^*(v) = D(v)$; $|D^*| = \gamma_\omega(T)$. The induced generalized distribution from D^* and ω of $\{x\}$ is given by $\widehat{C^*}(x) = (C_1(x) - D(x)) + \lfloor (C_1(y) + D(x) + 1)/2 \rfloor + 2C_1(z)$.

If $D(x) = 1$, then $\widehat{C^*}(x) = C_1(x) + \lfloor C_1(y)/2 \rfloor + 2C_1(z) = \widehat{C}(x) < 0$;

If $D(x) \geq 2$, then $\widehat{C^*}(x) \leq C_1(x) - D(x) + \lfloor C_1(y)/2 \rfloor + D(x)/2 + 1 + 2C_1(z) = \widehat{C}(x) + 1 - D(x)/2 \leq \widehat{C}(x) < 0$.

By Corollary 2.10, D^* is not ω-solvable, a contradiction to $|D^*| = \gamma_\omega(T)$. This completes the proof. ∎

From Theorem 2.12, for a given integer p with $p < \gamma_\omega(T)$, there must exist a distribution D, which is not ω-solvable with $|D| = p$, and all pebbles are distributed on the leaves of T.

3. THE GENERALIZATION OF THE COVER PEBBLING NUMBER ON TREES

Assume that $s_\omega(v_0) = s_\omega(T)$ for some $v_0 \in V(T)$; it should be noted that $\overrightarrow{T} \backslash E(T_\omega(v_0))$ is a directed graph. We define $d_\omega(u, l)$ to be the length of the maximal path containing u in all maximum path partitions of $\overrightarrow{T} \backslash E(T_\omega(v_0))$. If ω is clear, then we use $d(u, l)$ for short (note that $d(u, l)$ maybe 0). Let P_α be a maximal path partition of $\overrightarrow{T} \backslash E(T_\omega(v_0))$; then, $d_\omega(u, l) = \max_{P_\alpha}\{|P| : u \in P, P \in P_\alpha\}$.

Lemma 3.1. *Assume that $s_\omega(v_0) = s_\omega(T)$ for some $v_0 \in V(T)$; then for each vertex $u \in V(T)$ and $d(u, v_0) \geq d(u, l)$.*

Proof. Assume $u, v \in V(T)$. There is exactly one subpath of T with endpoints u and v, and we denote this path by P_{uv}. We thus have $P_{uv} = P_{vu}$.

If $|W| = 1$, we may assume that $\omega(v) = t$, and $\omega(u) = 0$ for $u \neq v$. By the proof of Theorem 1.8, we know that $f_t(T, v) = s_\omega(v_0)$. Let $(a_1, a_2, \ldots, a_n)$ be the size of the maximum path partition of $\overrightarrow{T_v}$. Then $d(v, v_0) = \max_{u \in V(T)} d(v, u) = a_1$. Assume P_1 is the maximal path containing u in $\overrightarrow{T_v} \backslash P_{v_0,v}$, and $P_1 \cap P_{v_0 v} = v_1$. The length of $P_{v_0 v}$ (P_1) is thus a_1 ($d(u, l)$) and $d(v_1, v_0) \leq d(u, v_0)$. If $d(u, v_0) < d(u, l)$, then $d(v_1, v_0) < d(u, l)$, and we get a path $P_1 \cup P_{v_1 v}$ with length $a_1 - d(v_1, v_0) + d(u, l) > a_1$, a contradiction to the maximum of a_1, and thus $d(u, v_0) \geq d(u, l)$.

If $|W| \geq 2$, we only need to show it while $u \in V(T_\omega(v_0))$.

If $d(u, v_0) < d(u, l)$ for some $u \in V(T_\omega(v_0))$, there exists a leaf v_1 in $\overrightarrow{T} \backslash E(T_\omega(v_0))$ so that $d(u, l) = d(u, v_1)$, and we will show that $s_\omega(v_1) > s_\omega(v_0)$.

Let $TC(v)$ be the component of $T\backslash u$ containing the vertex v. We thus have $TC(v_1) \cap W = \emptyset$.

Case 1. $TC(v_0) \cap W \neq \emptyset$.

Assume $w_1 \in TC(v_0) \cap W$, then $d(w_1, v_1) \geq d(u, v_1) + 1$ and

$$d(w_1, v_1) - d(w_1, v_0) \geq d(u, v_1) - d(u, v_0) + 2 \geq 3.$$

Note that $\overrightarrow{T}\backslash E(T_\omega(v_0) \cup P_{v_1u}) \subseteq \overrightarrow{T}\backslash E(T_\omega(v_1))$. So

$$\begin{aligned}
&s_\omega(v_1) - s_\omega(v_0)\\
&\geq \sum_{x\in W} \omega(x)(2^{d(x,v_1)} - 2^{d(x,v_0)}) - 2^{d(u,v_1)}\\
&\geq \omega(w_1)(2^{d(w_1,v_1)} - 2^{d(w_1,v_0)}) - 2^{d(u,v_1)}\\
&\geq 2^{d(w_1,v_1)} - 2^{d(w_1,v_0)} - 2^{d(u,v_1)}\\
&\geq 2^{d(w_1,v_1)} - \frac{2^{d(w_1,v_1)}}{8} - \frac{2^{d(w_1,v_1)}}{2}\\
&= \frac{3\cdot 2^{d(w_1,v_1)}}{8} > 0.
\end{aligned}$$

Hence, $s_\omega(v_1) > s_\omega(v_0)$, which is a contradiction to $s_\omega(v_0) = s_\omega(T)$.

Case 2. $TC(v_0) \cap W = \emptyset$.

Let $\tau_\omega(v) = \sum_{x\in W} \omega(x)2^{d(x,v)}$. If so, then $\tau_\omega(v_0) = 2^{d(u,v_0)}\tau_\omega(u)$, and $\tau_\omega(v_1) = 2^{d(u,v_1)}\tau_\omega(u)$. For $|W| \geq 2$, $\tau_\omega(u) \geq 2^0 + 2^1 = 3$.

Note that $\overrightarrow{T}\backslash E(T_\omega(v_0) \cup P_{v_1u}) \subseteq \overrightarrow{T}\backslash E(T_\omega(v_1))$. So

$$\begin{aligned}
&s_\omega(v_1) - s_\omega(v_0)\\
&\geq 2^{d(u,v_1)}\tau_\omega(u) - 2^{d(u,v_0)}\tau_\omega(u) - 2^{d(u,v_1)}\\
&= \tau_\omega(u)(2^{d(u,v_1)} - 2^{d(u,v_0)}) - 2^{d(u,v_1)}\\
&\geq 3(2^{d(u,v_1)} - 2^{d(u,v_0)}) - 2^{d(u,v_1)}\\
&\geq 3(2^{d(u,v_1)} - \frac{2^{d(u,v_1)}}{2}) - 2^{d(u,v_1)}\\
&= \frac{2^{d(u,v_1)}}{2} > 0.
\end{aligned}$$

Hence, $s_\omega(v_1) > s_\omega(v_0)$, which is a contradiction to $s_\omega(v_0) = s_\omega(T)$, and this completes the proof. ∎

Corollary 3.2. *Let ω be a nonnegative function in $V(T)$, for some $v \in W$, and ω' be a nonnegative function satisfying $\omega'(v) = \omega(v) - 1$, $\omega'(u) = \omega(u)$ for other vertices in T. If so, then*

$$s_\omega(T) \geq s_{\omega'}(T) + 2^{d_\omega(v,l)}.$$

Proof. Assume that there exist v_1 and v_2, so that $s_\omega(v_1) = s_\omega(T)$ and $s_{\omega'}(v_2) = s_{\omega'}(T)$.

By the definition of $s_\omega(v)$, if $\omega(v) \geq 2$, then $d_\omega(v, l) = d_{\omega'}(v, l)$, we have

$$\begin{aligned}
s_\omega(T) = s_\omega(v_1) &\geq s_\omega(v_2)\\
&= s_{\omega'}(v_2) + 2^{d(v,v_2)}\\
&\geq s_{\omega'}(v_2) + 2^{d_{\omega'}(v,l)} \text{ (by Lemma 3.1)}\\
&= s_{\omega'}(T) + 2^{d_{\omega'}(v,l)}.
\end{aligned}$$

If $\omega(v) = 1$, the difference between $\overrightarrow{T}\backslash T_\omega(v_1)$ and $\overrightarrow{T}\backslash T_{\omega'}(v_2)$ is just the length of the maximal path containing v, we have

$$\begin{aligned}
s_\omega(T) = s_\omega(v_1) &\geq s_\omega(v_2)\\
&= s_{\omega'}(v_2) + 2^{d(v,v_2)} + 2^{d_\omega(v,l)} - 2^{d_{\omega'}(v,l)}\\
&\geq s_{\omega'}(v_2) + 2^{d_\omega(v,l)} \text{ (by Lemma 3.1)}\\
&= s_{\omega'}(T) + 2^{d_\omega(v,l)}.
\end{aligned}$$

∎

The proof of Theorem 1.7:

The lower bound holds clearly, as we put $2^{a_i} - 1$ pebbles on the leaf of each path for $1 \leq i \leq n$ (no pebble can then be moved to $T_\omega(v)$), and $\sum_{u\in S} w(u)2^{d(u,v)} - 1$ pebbles on v, obviously it is not ω-solvable.

For the upper bound, it holds if $|\omega| = 1$ or $|W| = 1$ by the proof of Theorem 1.8. It also holds for $|T| \leq 2$ by Theorem 2.2 and Theorem 1.4. We may thus assume that $|\omega| \geq 2$, $|W| \geq 2$, and $|T| \geq 3$.

If the result is false for some T and ω, then we choose one counterexample T and its weight ω so that $|T|$ and $|\omega|$ are both minimal. It means the upper bound holds for T' and its weight ω' if $|T'| < |T|$ or $|\omega'| < |\omega|$.

Let D be a distribution on T, which is not ω-solvable with size $s_\omega(T)$. By Theorem 2.12, we may assume that all pebbles are distributed on the leaves of T.

Assume $s_\omega(v_0) = s_\omega(T)$. There exists $x \in W\backslash v_0$ satisfying $d_{T_\omega(v_0)}(x) = 1$. If $d_T(x) \neq 1$, we can get $d(x, l) > 0$, and there exists a nonempty component in $T\backslash E(T_\omega(v_0))$, which is connected with x. Say T_1 and $b_1 \geq b_2 \geq \ldots \geq b_m$ is the size of the maximum path partition of T_1.

Case 1. $D(T_1)$ cannot move a pebble to x. $|D(T_1)| \leq \sum_{i=1}^{m} 2^{b_i} - m$, and we consider D on $T\backslash T_1$, $|D(T\backslash T_1)| \geq s_\omega(T) - D(T_1) \geq s_\omega(T\backslash T_1)$, and $D(T\backslash T_1)$ is not ω-solvable, a contradiction to the minimum of $|T|$.

Case 2. $D(T_1)$ can move one pebble to x. It costs us at most $2^{b_1} = 2^{d_\omega(x,l)}$ pebbles on T_1. The left pebbles on T is not ω'-solvable (ω' satisfies $\omega'(x) = \omega(x) - 1$, and it is unchanged for other vertices in T). From the minimum of $|\omega|$ and Corollary 3.2, we thus have $|D| < s_{\omega'}(T) + 2^{d_\omega(x,l)} \leq s_\omega(T)$, a contradiction to $|D| = s_\omega(T)$.

We may therefore assume $d_T(x) = 1$.

We claim that $D(x) = 0$. Otherwise, let ω' satisfy $\omega'(x) = \omega(x) - 1$ and $\omega'(v) = \omega(v)$ for $v \neq x$. Regardless of one pebble being on x, we know that $|D| - 1$ other pebbles cannot solve ω'. From the minimum of $|\omega|$, we have $|D| - 1 \leq s_{\omega'}(T) - 1$. By Corollary 3.2, $s_{\omega'}(T) + 1 \leq s_\omega(T)$, so $|D| \leq s_\omega(T) - 1$, a contradiction to $|D| = s_\omega(T)$, so $D(x) = 0$.

Assuming that $x' \sim x$ in T, we then delete x. Let $C'(x') = C(x') + 2C(x)$ and $C'(v) = C(v)$ otherwise. Note that all pebbles are distributed on the leaves of T, so $C'(x) = D(x') - \omega(x') - 2(D(x) - \omega(x)) = -\omega(x') - 2\omega(x)$. By Lemma 2.9, D is not ω-solvable in T is equivalent to D is not ω'-solvable in $T\backslash x$, where $\omega'(x') = \omega(x') + 2\omega(x)$ and $\omega'(v) = \omega(v)$ for $v \neq x$. By the minimum of $|T|$, we have $|D| \leq s_{\omega'}(T\backslash x) - 1$, note that $x \neq v_0$, we have $s_{\omega'}(T\backslash x) = s_\omega(T)$, a contradiction to $|D| = s_\omega(T)$. This completes the proof. ∎

Moreover, by Theorem 1.7, we can immediately get

Corollary 3.3. *Let T be a tree, and let ω be a nonnegative function on $V(T)$, $W = \{v \in V(T) : \omega(v) > 0\}$, $L = \{v \in V(T) : d(v) = 1\}$, then if $L \subseteq W$,*

$$\gamma_\omega(T) = \max_{v \in V(T)} \sum_{u \in V(T)} \omega(u) 2^{d(u,v)}.$$

Theorem 1.4 gives a sufficient condition of a nonnegative weight function ω on $V(G)$ for a graph G so that the ω-cover pebbling number of G is

$$\gamma_\omega(G) = \max_{v \in V(G)} \sum_{u \in V(G)} \omega(u) 2^{d(u,v)}.$$

Corollary 3.3 gives a weaker sufficient condition of a nonnegative weight function ω on $V(T)$ for a tree T so that the ω-cover pebbling number of T is

$$\gamma_w(T) = \max_{v \in V(T)} \sum_{u \in V(T)} \omega(u) 2^{d(u,v)}.$$

Here, we explore some problems.

Problem 3.4. *Give a weaker sufficient condition of a nonnegative function ω on $V(G)$ for a graph G so that the ω-cover pebbling number of G is*

$$\gamma_\omega(G) = \max_{v \in V(G)} \sum_{u \in V(G)} \omega(u) 2^{d(u,v)}.$$

Problem 3.5. *For a nonnegative function ω, determine the ω-cover pebbling number of more graphs, such as cycles, hypercubes, and so on.*

We also give a conjecture which is similar to Graham's Conjecture.

Conjecture 3.6. *Let ω_1 be a nonnegative function on G and ω_2 be a nonnegative function on H. The function ω on $G \times H$ is given by $\omega((g,h)) = \omega_1(g)\omega_2(h)$, where $g \in V(G)$ and $h \in V(H)$, then $\gamma_\omega(G \times H) \leq \gamma_{\omega_1}(G)\gamma_{\omega_2}(H)$.*

DATA AVAILABILITY STATEMENT

The original contributions presented in the study are included in the article/supplementary materials, further inquiries can be directed to the corresponding authors.

AUTHOR CONTRIBUTIONS

Z-JX provided this topic and wrote the paper. Z-JX and Z-MH solved the problem. Z-MH reviewed and edited the manuscript. All authors contributed to the article and approved the submitted version.

FUNDING

This research was supported by Key Projects in Natural Science Research of Anhui Provincial Department of Education (No. KJ2018A0438) to (Z-JX) and by NSFC (No. 11601002) to (Z-MH).

ACKNOWLEDGMENTS

This manuscript has been released as a pre-print at http://export.arxiv.org/pdf/1903.04867 (Z-JX and Z-MH). The authors are grateful for the many useful comments provided by the referees.

REFERENCES

1. Chung FRK. Pebbling in hypercubes. *SIAM J Discrete Math.* (1989) **2**:467–72. doi: 10.1137/0402041
2. Lewis T, Cusack CA, Dion L. The complexity of pebbling reachability and solvability in planar and outerplanar graphs. *Discrete Appl Math.* (2014) **172**:62–74. doi: 10.1016/j.dam.2014.03.008
3. Milans K, Clark B. The complexity of graph pebbling. *SIAM J Discrete Math.* (2006) **20**:769–98. doi: 10.1137/050636218
4. Moews D. Pebbling graphs. *J Combin Theory Ser B.* (1992) **55**:244–52. doi: 10.1016/0095-8956(92)90043-W
5. Pachter L, Snevily HS, Voxman B. On pebbling graphs. *Congr Numer.* (1995) **107**:65–80. doi: 10.1016/S0166-218X(97)00073-5
6. Snevily HS, Foster JA. The 2-pebbling property and conjecture of Graham's. *Graphs Combin.* (2000) **16**:231–44. doi: 10.1007/PL00021179
7. Xia ZJ, Hong ZM. *Generalization of the Cover Pebbling Number on Trees* (2019). Available online at: http://export.arxiv.org/pdf/1903.04867.
8. Hurlbert GH. General graph pebbling. *Discrete Appl Math.* (2013) **16**:1221–31. doi: 10.1016/j.dam.2012.03.010
9. Liu J-B, Wang S, Wang C, Hayat S. Further results on computation of topological indices of certain networks. *IET Control Theory Appl.* (2017) 11:2065–71. doi: 10.1049/iet-cta.2016.1237
10. Liu J-B, Wang WR, Zhang YM, Pan XF. On degree resistance distance of cacti. *Discrete Appl Math.* (2016) 203:217–25. doi: 10.1016/j.dam.2015.09.006
11. Sjostrand J. The cover pebbling theorem. *Electron J Combin.* (2005) **12**:5. doi: 10.37236/1989
12. Crull B, Cundif T, Feltman P, Hurlbert G, Pudwell L, Szaniszlo Z, et al. The cover pebbling number of graphs. *Discrete Math.* (2005) **296**:15–23. doi: 10.1016/j.disc.2005.03.009

Conflict of Interest: The authors declare that the research was conducted in the absence of any commercial or financial relationships that could be construed as a potential conflict of interest.

frontiers in Physics

BRIEF RESEARCH REPORT
published: 19 June 2020
doi: 10.3389/fphy.2020.00208

On the Boundary of Incidence Energy and Its Extremum Structure of Tricycle Graphs

Hongyan Lu[1]* *and Zhongxun Zhu*[2]*

[1] College of Science, Xijing University, Xi'an, China, [2] Faculty of Mathematics and Statistics, South Central University for Nationalities, Wuhan, China

With the wide application of graph theory in circuit layout, signal flow chart and power system, more and more attention has been paid to the network topology analysis method of graph theory. In this paper, we construct a graph transformation which can reflect the monotonicity of coefficients and reduce the number of graphs. A sharp lower bound for incidence energy in the tricyclic graphs is given and all the extremal structures are characterized. The most interesting things that we find two different classes tricyclic graphs have the same signless Laplacian characteristic polynomials and one of the extremal graphs beyond all expectations.

Keywords: incidence energy, extremal graph, tricyclic graph, Laplacian matrix, signless Laplacian coefficients

OPEN ACCESS

Edited by:
Muhammad Javaid, University of Management and Technology, Pakistan

Reviewed by:
Sunil Kumar, National Institute of Technology, Jamshedpur, India
Boyi He, Sichuan Normal University, China
Zixuan Yang, Xi'an Jiaotong University, China

***Correspondence:**
Hongyan Lu
lhyy116@163.com
Zhongxun Zhu
zzxun73@163.com

Specialty section:
This article was submitted to Mathematical Physics, a section of the journal Frontiers in Physics

Received: *20 March 2020*
Accepted: *15 May 2020*
Published: *19 June 2020*

Citation:
Lu H and Zhu Z (2020) On the Boundary of Incidence Energy and Its Extremum Structure of Tricycle Graphs. Front. Phys. 8:208. doi: 10.3389/fphy.2020.00208

1. INTRODUCTION

Graph theory is a branch of discrete mathematics, Its research object is abstracted from the actual problem. For example, the geometric structure of an electrical network can be represented as a corresponding line graph. In the graph, the properties of circuit elements are ignored, the length and bending of edges are not important, but the connection between nodes and branches is highlighted. Each element in the network is replaced by a line segment, which is called a branch, and the endpoint of each element or the point connected by several elements is represented by an origin, which is called a node. The set of points and lines is called a network graph and is represented by G. Let $G = (V, E)$ be a simple connected graph with n vertices, m edges [1]. Let P_n, C_n and S_n be the path, the cycle and the star with n vertices, respectively [1]. Let $N_G(v) = \{u|uv \in E(G)\}$, denote by $d_G(v) = |N_G(v)|$ the degree of the vertex v of G. We know that $L(G) = D(G) - A(G)$ is the *Laplacian matrix* of G, and $A(G)$ is $(0, 1)$ adjacency matrix, $D(G)$ is degree diagonal matrix. Corresponding to the Laplacian matrix, $Q(G) = D(G) + A(G)$ is called the *signless Laplacian matrix* of a graph [2]. The Laplacian characteristic polynomials and signless Laplacian characteristic are defined as the following

$$L(G; \lambda) = det(\lambda I - L(G)) = \sum_{i=0}^{n} (-1)^i c_i(G) \lambda^{n-i},$$

$$Q(G; \lambda) = det(\lambda I - Q(G)) = \sum_{i=0}^{n} (-1)^i \varphi_i(G) \lambda^{n-i}.$$

For G, H, if $c_i(G) \leq c_i(H), i = 1, 2, \ldots, n$, we call that $G \preceq' H$. If $\varphi_i(G) \leq \varphi_i(H)$, $i = 1, 2, \ldots, n$, we call that $G \preceq H$ [3, 4].

Denote by $\mathscr{G}_{n,m}$ the set of simple connected graphs of order n and size m. If $m = n - 1 + c$, G denotes a *c-cyclic graph*. If $c = 0, 1, 2$, and 3, G represents a tree, unicyclic graph, bicyclic graph and tricyclic graph, respectively [1]. Recently, with further research on the power system network, the study of the structure and properties of the partial ordering sets $(\mathscr{G}_{n,m}, \preceq')$ and $(\mathscr{G}_{n,m}, \preceq)$ have attracted much attention. For $m = n - 1$, Mohar [5] proved that there is unique maximal element and unique minimal element in $(\mathscr{G}_{n,n-1}, \preceq')$. Since $L(G; \lambda) = Q(G; \lambda)$ for bipartite graph, then $(\mathscr{G}_{n,n-1}, \preceq)$ has the same structure and properties as $(\mathscr{G}_{n,n-1}, \preceq')$. For $m = n$, Stevanović and Ilić [6] showed that there is also unique maximal element and unique minimal element in $(\mathscr{G}_{n,n}, \preceq')$. But for $(\mathscr{G}_{n,n}, \preceq)$, Li et al. [7] given the extremal elements in $(\mathscr{G}_{n,n}, \preceq)$. He and Shan [8] obtained the unique minimal element in $(\mathscr{G}_{n,n+1}, \preceq')$, and in Zhang and Zhang [3], two minimal elements in $(\mathscr{G}_{n,n+1}, \preceq)$ were determined by Zhang and Zhang. For simplicity, denote the class of connected tricyclic graphs order n, i.e., $\mathscr{G}_{n,n+2}$ by $\mathscr{T}_n$ [9]. Pai et al. [10] characterized the unique minimal element in $(\mathscr{T}_n, \preceq')$. Based on these works, we focus on the structure and properties of the partial ordering sets $(\mathscr{T}_n, \preceq)$.

2. PRELIMINARIES

In this section, we introduce some graphic transformations and lemmas, which will be used to prove our main results.

If a connected graph has only one cycle whose length is odd, the graph is odd unicyclic. If the components of a spanning subgraph of G are trees or odd unicyclic graphs, the subgraph is called a *TU-subgraph* of G [3]. Let H be a TU-subgraph of G, which contains c odd unicyclic graphs and s trees $T_1, \ldots, T_s$ of orders $n_1, \ldots, n_s$, respectively. So the weight of H $\omega(H) = 4^c \prod_{i=1}^{s} n_i$. If there contains no tree in H, so $\omega(H) = 4^c$. If H is empty graph,there is no H, so $\omega(H) = 0$. We can express the signless Laplacian coefficients $\varphi_i(G)$ by the weight of TU-subgraphs of G [11].

Lemma 2.1. *[12] Let $Q(G; \lambda) = det(\lambda I - Q(G)) = \sum_{i=0}^{n}(-1)^i \varphi_i(G)\lambda^{n-i}$ be the characteristic polynomial of the signless Laplacian matrix of a graph G of order n. Then $\varphi_i(G) = \sum_{H_i} \omega(H_i)$, $i = 1, \ldots, n$, where the summation runs over all TU-subgraph H_i of G with i edges.*

Definition 1. *[8] Let G be a simple connected graph with n vertices and uv be a non-pendent edge, which is not contained in any cycles of G. Let $G_{uv} = G - \{vx | x \in N_G(v) \setminus \{u\}\} + \{ux | x \in N_G(v) \setminus \{u\}\}$. We say that G_{uv} is an α-transformation of G.*

Lemma 2.2. *[3] Let G be a connected graph of order $n \geq 4$, and G_{uv} be obtained from G by α-transformation. Then $G_{uv} \preceq G$, i.e., $\varphi_i(G_{uv}) \leq \varphi_i(G)$, $i = 0, 1, \ldots, n$, with equality if and only if either $i \in \{0, 1, n\}$ when G is non-bipartite, or $i \in \{0, 1, n-1, n\}$ for otherwise.*

The proof of the following lemma can be found in many places in the literature (see, such as [13]).

Lemma 2.3. *[14] $L(G; \lambda) = Q(G; \lambda)$ if and only if the graph G is bipartite.*

Lemma 2.4. *[15] Let $f(\lambda)$ and $g(\lambda)$ be two real polynomials arranged according to decreasing exponents. If their coefficients are alternate about positive and negative, then the coefficients of $f(\lambda)g(\lambda)$ also are alternate about positive and negative.*

Let G be a connected graph with at least one cycle, the base of G is represented by $\widehat{G}$, which is the minimal connected subgraph containing all the cycles of G [16]. So $\widehat{G}$ is the unique subgraph of G, which contains no pendant vertex. G can be obtained from $\widehat{G}$ by planting trees to some vertices of $\widehat{G}$ [17]. Hoffman and Smith [18] define an *internal path* of G as a walk $u_0u_1 \ldots u_s (s \geq 1)$,and the vertices $u_0, u_1, \ldots, u_{s-1}$ are distinct, $d(u_0) > 2, d(u_s) > 2$, and $d(u_i) = 2$, whenever $0 < i < s$. An internal path is closed, if $u_0 = u_s$.

Definition 2. *[19] Let $G = (V, E)$ be a connected graph and the base of G is $\widehat{G}$. Let u, v, w be three consecutive vertices in an internal path of length at least 4 of $\widehat{G}$, which satisfy $N_G(u) \cap N_G(v) = \emptyset$, $N_G(w) \cap N_G(v) = \emptyset$ and $N_G(u) \cap N_G(w) = \{v\}$. We can delete all edges vz for $z \in N_G(v)\setminus\{u, w\}$, wz for $z \in N_G(w)$ and add all edges uz for $z \in (N_G(v) \cup N_G(w))\setminus\{u, v\}$ from G and get the graph $G'(u, v, w)$. G to $G'(u, v, w)$ is called a β-transformation of G.*

Lemma 2.5. *Let $G = (V, E)$ be a connected graph and the base of G is $\widehat{G}$. Let u, v, w be three consecutive vertices in an internal path of length at least 4 of $\widehat{G}$, and $G'(u, v, w)$ be a graph obtained from G by β-transformation [19]. So $G'(u, v, w) \preceq G$, that is, $\varphi_i(G'(u, v, w)) \leq \varphi_i(G)$ for $i \in \{0, 1, 2, \ldots, n\}$, with equality if and only if $i \in \{0, 1\}$ when G is non-bipartite, and $i \in \{0, 1, n\}$ when G is bipartite.*

Proof: $\varphi_0(G'(u, v, w)) = \varphi_0(G) = 1$ and $\varphi_1(G'(u, v, w)) = \varphi_1(G) = 2|E|$. Moreover, $\varphi_n(G'(u, v, w)) = \varphi_n(G) = 0$ for bipartite graph. Now assume that $2 \leq i \leq n$. Let $\mathscr{H}$ and $\mathscr{H}$ be the set of all TU-subgraphs of $G'(u, v, w)$ and G with i edges, respectively. For an arbitrary TU-subgraph $H' \in \mathscr{H}$, denote by the R' connected component of H' containing u [3]. Let $f : \mathscr{H} \to \mathscr{H}$ with $H' \to H = f(H')$, where $V(H) = V(H')$ and

$$\begin{aligned} E(H) = {} & E(H') - \{ux | x \in N_{R'}(u) \cap N_G(v)\} - \{ux | x \in N_{R'}(u) \cap N_G(w) \setminus \{v\}\} \\ & + \{vx | x \in N_{R'}(u) \cap N_G(v)\} + \{wx | x \in N_{R'}(u) \cap N_G(w) \setminus \{v\}\}. \end{aligned}$$

Then f is injective from $\mathscr{H} \to \mathscr{H}$.

Case 1. u, v, w belongs the component S'. So $f(S')$ is a component of H, which in the same order as S'. Then $\omega(H) = \omega(H')$.

Case 2. u, v, w belong to at least two components of H'.

Case 2.1. u is not in an odd unicyclic component of H'. Then u is contained in a tree component of H'. Assume that there exist $x_1 + 1$ vertices in the connected component which contains u in $H - uv$ [3], $x_2 + 1$ vertices in the connected component which contains w in $H - wv$ and $x_3 + 1$ vertices in the connected component which contains v in $H - uv - vw$, where $x_1, x_2, x_3 \geq 0$. Let N indicate the weight of the components of H', which contain no u, v, w.

(i) If $uv \in E(H')and uw \notin E(H')$, then

$$\begin{aligned}\omega(H') &= (x_1+x_2+x_3+2)\cdot 1\cdot N,\\ \omega(H) &= (x_1+x_3+2)(x_2+1)\cdot 1\cdot N,\\ \omega(H)-\omega(H') &= x_2(x_1+x_3+1)N \geq 0.\end{aligned}$$

(ii) If $uv \notin E(H')and uw \in E(H')$, then

$$\begin{aligned}\omega(H') &= (x_1+x_2+x_3+2)\cdot 1\cdot N,\\ \omega(H) &= (x_2+x_3+2)(x_1+1)\cdot N,\\ \omega(H)-\omega(H') &= x_1(x_2+x_3+1)N \geq 0.\end{aligned}$$

(iii) If $uv \notin E(H')and uw \notin E(H')$, then

$$\begin{aligned}\omega(H') &= (x_1+x_2+x_3+1)\cdot 1\cdot 1\cdot N,\\ \omega(H) &= (x_1+1)(x_2+1)(x_3+1)\cdot N,\\ \omega(H)-\omega(H') &= (x_1x_2x_3+x_1x_2+x_1x_3+x_2x_3-1)N \geq 0.\end{aligned}$$

Case 2.2. u is in an odd unicyclic component S' of H'. Let C' be a subgraph of S', which corresponds to an odd cycle C in G.

(i) If $uv \notin E(H'), uw \notin E(H')$, and $C = C'$, let S be the component containing C in H. So there are the same components in H' and H, except for S', $\{v\}$, $\{w\}$ in H', which correspond to the component S containing u, two components S_1 containing v and S_2 containing w of order at least 1, respectively, in H. If $uv \notin E(H'), uw \notin E(H')$, and $C \neq C'$. So there are the same components in H' and H, except for S', $\{v\}$, $\{w\}$ in H', which correspond to two tree components S_1 containing u, w of order at least 4 since u, v, w are three consecutive vertices in an internal path of length at least 4 of $\widehat{G}$, and S_2 containing v of order at least 1, in H. So

$$\begin{aligned}\omega(H') &= 4\cdot 1\cdot 1\cdot N,\\ \omega(H) &\geq 4\cdot 1\cdot 1\cdot N,\\ \omega(H)-\omega(H') &\geq 0.\end{aligned}$$

(ii) If $uv \notin E(H'), uw \in E(H')$ or $uv \in E(H'), uw \notin E(H')$, and $C = C'$, So there are the same components in H' and H, except for S', $\{v\}$ or $\{w\}$ in H', which correspond to an odd unicyclic component S containing C and a tree component S_1 containing v, w of order at least 2. So

$$\begin{aligned}\omega(H') &= 4\cdot 1\cdot N,\\ \omega(H) &\geq 4\cdot 2\cdot N,\\ \omega(H)-\omega(H') &\geq 4N > 0.\end{aligned}$$

If $uv \notin E(H'), uw \in E(H')$ or $uv \in E(H'), uw \notin E(H')$, and $C \neq C'$, So there are the same components in H' and H, except for S', $\{v\}$ or $\{w\}$ in H', which correspond to a tree component S containing u, v, w of order at least 5. So

$$\begin{aligned}\omega(H') &= 4\cdot 1\cdot N,\\ \omega(H) &\geq 4\cdot N,\\ \omega(H)-\omega(H') &\geq 0.\end{aligned}$$

Then by Lemma 2.1, we have $\varphi_i(G'(u,v,w)) = \sum_{H_i' \in \mathscr{G}} \omega(H_i') \leq \sum_{H_i \in \mathscr{G}} \omega(H_i) = \varphi_i(G)$

Hence the results hold. □

Similarly, we can prove the following result.

Lemma 2.6. *[19] Let $G = (V, E)$ be a connected graph with base $\widehat{G}$. Let u, v, w be three consecutive vertices in an internal path $P = u_1u_2\ldots u_k$ with $k = 4$ of $\widehat{G}$ and $u_1u_k \notin E(\widehat{G})$. Let $G'(u, v, w)$ be a graph obtained from G by β-transformation, then $G'(u, v, w) \preceq G$, that is, $\varphi_i(G'(u, v, w)) \leq \varphi_i(G)$ for $i \in \{0, 1, 2, \ldots, n\}$, with equality if and only if $i \in \{0, 1\}$ when G is non-bipartite, and $i \in \{0, 1, n\}$ when G is bipartite.*

By Li et al. [20], There are the following four types of bases in tricyclic graphs(as shown in **Figures 1–4**): $G_j^3(j = 1, \ldots, 7)$, $G_j^4(j = 1, \ldots, 4)$, $G_j^6(j = 1, \ldots, 3)$ and G_1^7. Let

$$\mathscr{T}_n^3 = \{G|\widehat{G} \cong G_j^3, j \in \{1, \ldots, 7\}\}; \quad \mathscr{T}_n^4 = \{G|\widehat{G} \cong G_j^4, j \in \{1, \ldots, 4\}\};$$
$$\mathscr{T}_n^6 = \{G|\widehat{G} \cong G_j^6, j \in \{1, \ldots, 3\}\}; \quad \mathscr{T}_n^7 = \{G|\widehat{G} \cong G_1^7\}.$$

Then $\mathscr{T}_n = \mathscr{T}_n^3 \cup \mathscr{T}_n^4 \cup \mathscr{T}_n^6 \cup \mathscr{T}_n^7$.

Let $T_1^3(n-7, 0, 0, 0, 0, 0, 0)$, $T_1^4(n-6, 0, 0, 0, 0, 0)$, $T_1^6(n-5, 0, 0, 0, 0)$ and $T_1^7(n-4, 0, 0, 0)$ be the graphs as shown in **Figure 5**.

Lemma 2.7. *[10]*

(i) *If $G \in \mathscr{T}_n^3$, then for every $i = 0, 1, \ldots, n$, $c_i(G) \geq c_i(T_1^3(n-7, 0, 0, 0, 0, 0, 0))$, with equality if and only if $i \in \{0, 1, n\}$.*
(ii) *If $G \in \mathscr{T}_n^4$, then for every $i = 0, 1, \ldots, n$, $c_i(G) \geq c_i(T_1^4(n-6, 0, 0, 0, 0, 0))$, with equality if and only if $i \in \{0, 1, n\}$.*
(iii) *If $G \in \mathscr{T}_n^6$, then for every $i = 0, 1, \ldots, n$, $c_i(G) \geq c_i(T_1^6(n-5, 0, 0, 0, 0))$, with equality if and only if $i \in \{0, 1, n\}$.*
(iv) *If $G \in \mathscr{T}_n^7$, then for every $i = 0, 1, \ldots, n$, $c_i(G) \geq c_i(T_1^7(n-4, 0, 0, 0))$, with equality if and only if $i \in \{0, 1, n\}$.*

For $i = 3, 4, 6, 7$, let $\mathscr{T}_n^{i,e}$ (resp., $\mathscr{T}_n^{i,o}$) be the set of bipartite tricyclic graphs (resp., non-bipartite tricyclic graphs) in $\mathscr{T}_n^i$, then $\mathscr{T}_n^i = \mathscr{T}_n^{i,e} \cup \mathscr{T}_n^{i,o}$. From lemmas 2.3 and 2.7, we get

Corollary 2.8. *[10]*

(i) *If $G \in \mathscr{T}_n^{3,e}$, then for every $i = 0, 1, \ldots, n$, $\varphi_i(G) \geq \varphi_i(T_1^3(n-7, 0, 0, 0, 0, 0, 0))$, with equality if and only if $i \in \{0, 1, n\}$.*
(ii) *If $G \in \mathscr{T}_n^{4,e}$, then for every $i = 0, 1, \ldots, n$, $\varphi_i(G) \geq \varphi_i(T_1^4(n-6, 0, 0, 0, 0, 0))$, with equality if and only if $i \in \{0, 1, n\}$.*
(iii) *If $G \in \mathscr{T}_n^{6,e}$, then for every $i = 0, 1, \ldots, n$, $\varphi_i(G) \geq \varphi_i(T_1^6(n-5, 0, 0, 0, 0))$, with equality if and only if $i \in \{0, 1, n\}$.*
(iv) *If $G \in \mathscr{T}_n^{7,e}$, then for every $i = 0, 1, \ldots, n$, $\varphi_i(G) \geq \varphi_i(T_1^7(n-4, 0, 0, 0))$, with equality if and only if $i \in \{0, 1, n\}$.*

Theorem 2.9. *[10] Let G be a connected tricyclic graph on n vertices and i be an integer, $0 \leq i \leq n$. Then $c_i(G) \geq c_i(T_1^7(n-4, 0, 0, 0))$.*

Repeated by lemmas 2.2, 2.5, and 2.6, we get the following conclusion

Theorem 2.10. *Let G be a graph in $\mathscr{T}_n^{3,o} \cup \mathscr{T}_n^{4,o} \cup \mathscr{T}_n^{6,o} \cup \mathscr{T}_n^{7,o}$. So there is a tricyclic graph G' with order n, such that $G' \preceq G$,. The base of G' is one of graphs in $\{T_i^3|j = 1, 2, \ldots, 9\} \cup \{T_i^4|j = 1, 2, \ldots, 20\} \cup \{T_i^6|j = 1, 2, \ldots, 24\} \cup \{T_i^7|j = 1, 2, \ldots, 7\}$(these base graphs are as shown in **Figures 7–9**.*

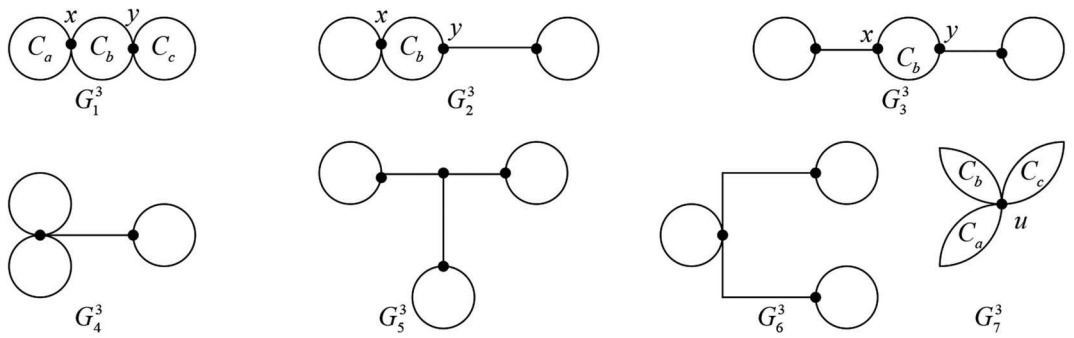

FIGURE 1 | The graphs $G_i^3 (i = 1, 2, \ldots, 7)$.

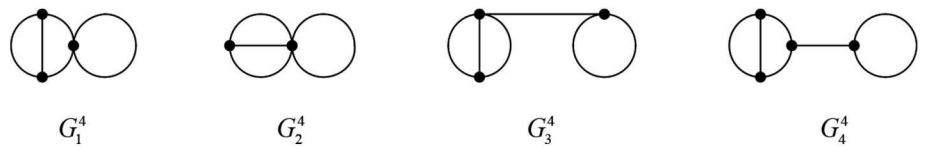

FIGURE 2 | The graphs $G_i^4 (i = 1, 2, \ldots, 4)$.

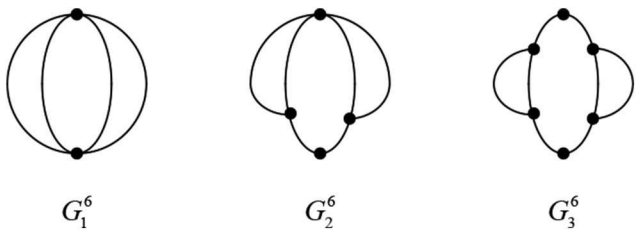

FIGURE 3 | The graphs $G_i^6 (i = 1, 2, 3)$.

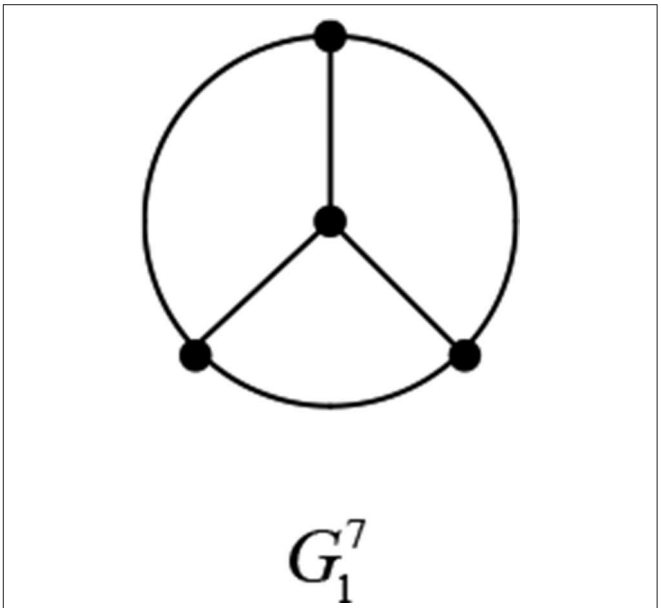

FIGURE 4 | The graph G_1^7.

3. THE SIGNLESS LAPLACIAN COEFFICIENTS OF GRAPHS IN T_N

Now we consider the minimal element in the partial ordering set $(\mathscr{T}_n, \preceq)$.

For $i = 1, 2, \ldots, 9$, let $T_i^3(s_1, s_2, \ldots, s_{|T_i^3|})$ be the graph obtained from T_i^3 (as shown in **Figure 6**) by attaching s_j pendent edges at $u_j (j = 1, 2, \ldots, |T_i^3|)$, where $n = s_1 + s_2 + \cdots + s_{|T_i^3|} + |T_i^3|$.

Lemma 3.1. *For $j = 1, 2, \ldots, 9$, $T_j^3(s_1 + s_2 + \cdots + s_{|T_j^3|}, 0, \ldots, 0) \preceq T_j^3(s_1, s_2, \ldots, s_{|T_j^3|})$, that is, $\phi_i(T_j^3(s_1 + s_2 + \cdots + s_{|T_j^3|}, 0, \ldots, 0)) \leq \phi_i(T_j^3(s_1, s_2, \ldots, s_{|T_j^3|}))$, $i = 0, 1, \ldots, n$. The equality holds if and only if $s_2 = \cdots = s_{|T_j^3|} = 0$.*

Proof: For convenience, let $G = T_j^3(s_1, s_2, \ldots, s_{|T_j^3|})$ and $G' = T_j^3(s_1 + s_2 + \cdots + s_{|T_j^3|}, 0, \ldots, 0)$ for $j = 1, 2, \ldots, 9$. Note that $\phi_0(G) = 1 = \phi_0(G'), \phi_1(G) = 2(n + 2) = \phi_1(G')$. For $2 \leq i \leq n$, let $\mathscr{H}$ and $\mathscr{H}'$ be the set of all TU-subgraphs of G' and G with exactly i edges, respectively [3]. Let

$$\mathscr{H}'^{(1)} = \{H' \in \mathscr{H} | H' \textit{ contains no odd cycle}\},$$
$$\mathscr{H}'^{(2)} = \{H' \in \mathscr{H} | H' \textit{ contains an odd cycle}\},$$
$$\mathscr{H}'^{(3)} = \{H' \in \mathscr{H} | H' \textit{ contains two odd cycles}\}.$$

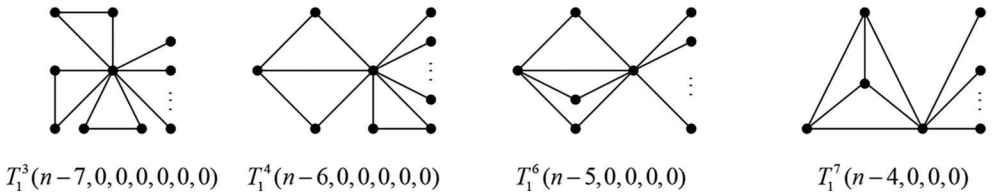

FIGURE 5 | The extremal graphs.

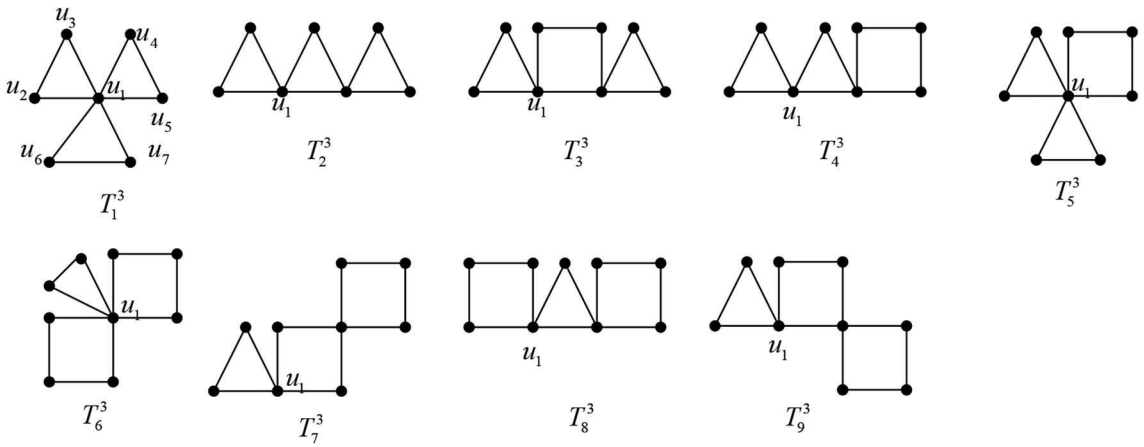

FIGURE 6 | The graphs $T_i^3 (i = 1, 2, \ldots, 9)$.

Similarly for $\mathscr{H}^{(1)}$, $\mathscr{H}^{(2)}$, and $\mathscr{H}^{(3)}$. We only prove the case for $j = 1$, the others can be proved similarly.

Let $f : \mathscr{H} \to \mathscr{H}$ with $H' \to H = f(H')$, where $V(H) = V(H')$ and

$$\begin{aligned} E(H') = E(H) &- \{u_1x | x \in N_{R'}(u_1) \cap N_G(u_2) \setminus \{u_3\}\} \\ &- \{u_1x | x \in N_{R'}(u_1) \cap N_G(u_3) \setminus \{u_2\}\} \\ &- \{u_1x | x \in N_{R'}(u_1) \cap N_G(u_4) \setminus \{u_5\}\} \\ &- \{u_1x | x \in N_{R'}(u_1) \cap N_G(u_5) \setminus \{u_4\}\} \\ &- \{u_1x | x \in N_{R'}(u_1) \cap N_G(u_6) \setminus \{u_7\}\} \\ &- \{u_1x | x \in N_{R'}(u_1) \cap N_G(u_7) \setminus \{u_6\}\} \\ &+ \{u_2x | x \in N_{R'}(u_1) \cap N_G(u_2) \setminus \{u_3\}\} \\ &+ \{u_3x | x \in N_{R'}(u_1) \cap N_G(u_3) \setminus \{u_2\}\} \\ &+ \{u_4x | x \in N_{R'}(u_1) \cap N_G(u_4) \setminus \{u_5\}\} \\ &+ \{u_5x | x \in N_{R'}(u_1) \cap N_G(u_5) \setminus \{u_4\}\} \\ &+ \{u_6x | x \in N_{R'}(u_1) \cap N_G(u_6) \setminus \{u_7\}\} \\ &+ \{u_7x | x \in N_{R'}(u_1) \cap N_G(u_7) \setminus \{u_6\}\} \end{aligned}$$

for R' being a component of H' containing u_1. Obviously, f is injective and $f(\mathscr{H}'^{(k)}) \subseteq \mathscr{H}^{(k)}$ for $j = 1, 2, 3$. From the procedure of proof in Theorem 3.1 [10], we have

$$\sum_{H' \in \mathscr{H}'^{(1)}} \omega(H') < \sum_{H \in \mathscr{H}^{(1)}} \omega(H).$$

Note that $\mathscr{H}'^{(3)} = \emptyset$ for $j = 1$. For $H' \in \mathscr{H}'^{(2)}$, without loss of generality, we assume that R' contains $C_3 = u_1u_2u_3u_1$ as a subgraph. Let R be the component of H corresponding to R', obviously, R also contains $C_3 = u_1u_2u_3u_1$. It is obvious that H', H have the same number of components and the product of the order of components which contain no $u_i (i = 1, 2, \ldots, 7)$ of H' is the same as H. The order of the tree components of H', which include at least one of $u_i (i = 4, \ldots, 7)$ are no more than the corresponding ones of H, then $\omega(f(H')) \geq \omega(H')$. Hence

$$\begin{aligned} \phi_i(G) &= \sum_{H \in \mathscr{H}^{(1)}} \omega(H) + \sum_{H \in \mathscr{H}^{(2)}} \omega(H) + \sum_{H \in \mathscr{H}^{(3)}} \omega(H) \\ &\geq \sum_{H' \in \mathscr{H}'^{(1)}} \omega(H') + \sum_{H' \in \mathscr{H}'^{(2)}} \omega(H') + \sum_{H' \in \mathscr{H}'^{(3)}} \omega(H') = \phi_i(G'). \end{aligned}$$

The equality holds if and only if $s_2 = \cdots = s_7 = 0$. □

For $i = 1, 2, \ldots, 20$, let $T_i^4(s_1, s_2, \ldots, s_{|T_i^4|})$ be the graph obtained from T_i^4 (as shown in **Figure 7**) by attaching s_j pendent edges at $u_j (j = 1, 2, \ldots, |T_i^4|)$, where $n = s_1 + s_2 + \cdots + s_{|T_i^4|} + |T_i^4|$. Similar to the proof of Lemma 3.1, we have

Lemma 3.2. *For* $j = 1, 2, \ldots, 20$, $T_j^4(s_1 + s_2 + \cdots + s_{|T_j^4|}, 0, \ldots, 0) \preceq T_j^4(s_1, s_2, \ldots, s_{|T_j^4|})$, *that is,* $\phi_i(T_j^4(s_1 + s_2 + \cdots + s_{|T_j^4|}, 0, \ldots, 0)) \leq \phi_i(T_j^4(s_1, s_2, \ldots, s_{|T_j^4|}))$, $i = 0, 1, \ldots, n$. *The equality holds if and only if* $s_2 = \cdots = s_{|T_j^4|} = 0$.

For $i = 1, 2, \ldots, 7$, let $T_i^7(s_1, s_2, \ldots, s_{|T_i^7|})$ be the graph obtained from T_i^7 (as shown in **Figure 8**) by attaching s_j pendent edges at $u_j (j = 1, 2, \ldots, |T_i^7|)$, where $n = s_1 + s_2 + \cdots + s_{|T_i^7|} + |T_i^7|$. Similar to the proof of Lemma 3.1, we have

Lemma 3.3. *For* $j = 1, 2, \ldots, 7$, $T_j^7(s_1+s_2+\cdots+s_{|T_j^7|}, 0, \ldots, 0) \preceq T_j^7(s_1, s_2, \ldots, s_{|T_j^7|})$, *that is,* $\phi_i(T_j^7(s_1+s_2+\cdots+s_{|T_j^7|}, 0, \ldots, 0)) \leq \phi_i(T_j^7(s_1, s_2, \ldots, s_{|T_j^7|}))$, $i = 0, 1, \ldots, n$. *The equality holds if and only if* $s_2 = \cdots = s_{|T_j^7|} = 0$.

For $i = 1, 2, \ldots, 24$, let $T_i^6(s_1, s_2, \ldots, s_{|T_i^6|})$ be the graph obtained from T_i^6 (as shown in **Figure 9**) by attaching s_j pendent edges at $u_j (j = 1, 2, \ldots, |T_i^6|)$, where $n = s_1+s_2+\cdots+s_{|T_i^6|}+|T_i^6|$. Similar to the proof of Lemma 3.1, we have

Lemma 3.4. *For* $j = 1, 2, \ldots, 24$, $T_j^6(s_1 + s_2 + \cdots + s_{|T_j^6|}, 0, \ldots, 0) \preceq T_j^6(s_1, s_2, \ldots, s_{|T_j^6|})$, *that is,* $\phi_i(T_j^6(s_1+s_2+\cdots+s_{|T_j^6|}, 0, \ldots, 0)) \leq \phi_i(T_j^6(s_1, s_2, \ldots, s_{|T_j^6|}))$, $i = 0, 1, \ldots, n$. *The equality holds if and only if* $s_2 = \cdots = s_{|T_j^6|} = 0$.

Lemma 3.5. *For* $n \geq |T_j^3| (j = 1, 2, \ldots, 9)$,

(i) $T_2^3(n-7, 0, 0, 0, 0, 0, 0) \succeq T_1^3(n-7, 0, 0, 0, 0, 0, 0)$.

(ii) $T_j^3(n-8, 0, 0, 0, 0, 0, 0, 0) \succeq T_5^3(n-8, 0, 0, 0, 0, 0, 0, 0)$ *for* $j = 3, 4$.

(iii) $T_j^3(n-9, 0, 0, 0, 0, 0, 0, 0, 0) \succeq T_6^3(n-9, 0, 0, 0, 0, 0, 0, 0, 0)$ *for* $j = 7, 8, 9$.

Proof: (i) We have

$$\begin{aligned}
&Q(T_2^3(n-7, 0, \ldots, 0)) - Q(T_1^3(n-7, 0, 0, 0, 0, 0, 0))\\
=\ &(x-1)^{n-8}[2(n-5)x^6 - (18n-90)x^5 + (62n-302)x^4\\
&-(102n-462)x^3\\
&+(80n-296)x^2 - (24n-24)x + 32].
\end{aligned}$$

Further by Lemma 2.3, $T_2^3(n-7, 0, 0, 0, 0, 0, 0) \succeq T_1^3(n-7, 0, 0, 0, 0, 0, 0)$.

$$\begin{aligned}
&Q(T_3^3(n-8, 0, 0, 0, 0, 0, 0, 0, 0)) - Q(T_5^3(n-8, 0, 0, 0, 0, 0, 0, 0, 0))\\
=\ &(x-1)^{n-9}[(2n-12)x^7 - (22n-132)x^6 + (96n-568)x^5\\
&-(212n-1208)x^4\\
&+(250n-1308)x^3 - (150n-628)x^2 + (36n-32)x - 48],\\
&Q(T_4^3(n-8, 0, 0, 0, 0, 0, 0, 0, 0)) - Q(T_5^3(n-8, 0, 0, 0, 0, 0, 0, 0, 0))\\
=\ &(x-1)^{n-9}[(2n-11)x^7 - (23n-125)x^6 + (104n-546)x^5\\
&-(233n-1128)x^4\\
&+(266n-1047)x^3 - (140n-219)x^2 + (24n+200)x - 68],\\
&Q(T_7^3(n-9, 0, 0, 0, 0, 0, 0, 0, 0)) - Q(T_6^3(n-9, 0, 0, 0, 0, 0, 0, 0, 0))\\
=\ &(x-1)^{n-10}[(2n-14)x^8 - (26n-182)x^7 + (138n-958)x^6\\
&-(382n-2594)x^5\\
&+(580n-3748)x^4 - (456n-5608)x^3 + (144n-464)x^2 - 192x],\\
&Q(T_8^3(n-9, 0, 0, 0, 0, 0, 0, 0, 0)) - Q(T_6^3(n-9, 0, 0, 0, 0, 0, 0, 0, 0))\\
=\ &(x-1)^{n-10}[(2n-14)x^8 - (26n-182)x^7 + (138n-948)x^6\\
&-(364n-2512)x^5\\
&+(520n-3520)x^4 - (368n-2400)x^3 + (96n-576)x^2],\\
&Q(T_9^3(n-9, 0, 0, 0, 0, 0, 0, 0, 0)) - Q(T_6^3(n-9, 0, 0, 0, 0, 0, 0, 0, 0))\\
=\ &(x-1)^{n-10}[(2n-14)x^8 - (26n-182)x^7 + (136n-944)x^6\\
&-(364n-2468)x^5\\
&+(522n-3350)x^4 - (378n-2102)x^3 + (108n-300)x^2 - 144x].
\end{aligned}$$

So (ii) and (iii) hold. □

Lemma 3.6. *For* $n \geq |T_j^4| (j = 1, \ldots, 20)$,

(i) $T_j^4(n - |T_j^4|, 0, \ldots, 0) \succeq T_1^4(n-6, 0, \ldots, 0)$ *for* $j = 2, 5, 6, 10, 15, 16, 17$

(ii) $T_j^4(n - |T_j^4|, 0, \ldots, 0) \succeq T_4^4(n-7, 0, \ldots, 0)$ *for* $j = 3, 7, 8, 9, 18, 19, 20$.

(iii) $T_j^4(n-|T_j^4|, 0, \ldots, 0) \succeq T_{14}^4(n-7, 0, \ldots, 0)$ *for* $j = 11, 12, 13$.

Proof:

$$\begin{aligned}
&Q(T_2^4(n-6, 0, \ldots, 0)) - Q(T_1^4(n-6, 0, \ldots, 0))\\
=\ &(x-1)^{n-7}[(n-4)x^5 - (8n-32)x^4 + (23n-88)x^3\\
&-(28n-92)x^2 + (12n-16)x - 16],\\
&Q(T_3^4(n-7, 0, \ldots, 0)) - Q(T_4^4(n-7, 0, \ldots, 0))\\
=\ &(x-1)^{n-8}[(n-5)x^6 - (10n-50)x^5 + (38n-188)x^4\\
&-(68n-382)x^3 +\\
&(56n-256)x^2 - (16n-64)x],\\
&Q(T_{11}^4(n-8, 0, \ldots, 0)) - Q(T_{14}^4(n-7, 0, \ldots, 0))\\
=\ &(x-1)^{n-9}[(2n-10)x^7 - (24n-120)x^6 + (110n-539)x^5\\
&-(241n-1107)x^4 +\\
&(255n-971)x^3 - (111n-161)x^2 + (9n+144)x - 12],
\end{aligned}$$

By the results of **Appendix**, the results hold. □

Lemma 3.7. *For* $n \geq |T_j^7| (j = 1, \ldots, 7)$, $T_j^7(n - |T_j^7|, 0, \ldots, 0) \succeq T_1^7(n-4, 0, 0, 0)$.

Proof: We have

$$\begin{aligned}
&Q(T_2^7(n-5, 0, \ldots, 0)) - Q(T_1^7(n-4, 0, \ldots, 0))\\
=\ &(x-1)^{n-6}[(n-3)x^4 - (8n-28)x^3 + (18n-68)x^2\\
&-(12n-48)x],\\
&Q(T_3^7(n-6, 0, \ldots, 0)) - Q(T_1^7(n-4, 0, \ldots, 0))\\
=\ &(x-1)^{n-7}[(2n-7)x^5 - (19n-73)x^4 + (55n-213)x^3\\
&-(57n-199)x^2 + (19n-40)x - 12],\\
&Q(T_4^7(n-7, 0, \ldots, 0)) - Q(T_1^7(n-4, 0, \ldots, 0))\\
=\ &(x-1)^{n-8}[(3n-12)x^6 - (33n-140)x^5 + (126n-536)x^4\\
&-(210n-828)x^3 + (151n-432)x^2 - (37n+48)x + 60],\\
&Q(T_5^7(n-7, 0, \ldots, 0)) - Q(T_1^7(n-4, 0, \ldots, 0))\\
=\ &(x-1)^{n-8}[(3n-12)x^6 - (33n-140)x^5 + (126n-540)x^4\\
&-(210n-858)x^3 + (152n-514)x^2 - (39n+36)x + 39],\\
&Q(T_6^7(n-8, 0, \ldots, 0)) - Q(T_1^7(n-4, 0, \ldots, 0))\\
=\ &(x-1)^{n-9}[(4n-18)x^7 - (50n-238)x^6 + (233n-1139)x^5\\
&-(521n-2541)x^4 + (584n-2713)x^3\\
&-(301n-1171)x^2 + (50n-40) - 32],\\
&Q(T_7^7(n-9, 0, \ldots, 0)) - Q(T_1^7(n-4, 0, \ldots, 0))\\
=\ &(x-1)^{n-10}[(5n-25)x^8 - (70n-368)x^7 + (385n-2086)x^6\\
&-(1085n-5938)x^5 + (2684n-9039)x^4 - (1415n-7004)x^3\\
&+(572n-21122)x^2 - (76n+128)x + 80].
\end{aligned}$$

So the results hold. □

Theorem 3.8. *For $G \in \mathscr{T}_n^3 \cup \mathscr{T}_n^4 \cup \mathscr{T}_n^7$, $G \succeq T_1^7(n-4,0,0,0)$. The equality holds if and only if $G \cong T_1^7(n-4,0,0,0)$.*

Proof: If $G \in \mathscr{T}_n^{3,e} \cup \mathscr{T}_n^{4,e} \cup \mathscr{T}_n^{7,e}$, by Theorem 2.9, the results hold.

If $G \in \mathscr{T}_n^{3,o} \cup \mathscr{T}_n^{4,o} \cup \mathscr{T}_n^{7,o}$, by direct calculation, we have

$$\begin{aligned}
&Q(T_1^3(n-7,0,\ldots,0)) - Q(T_1^7(n-4,0,\ldots,0))\\
=\ &(x-1)^{n-8}[3x^6-(3n+16)x^5+(16n+54)x^4\\
&-(30n+156)x^3+(24n+259)x^2-(7n+204)x+60]\\
&Q(T_5^3(n-8,0,\ldots,0)) - Q(T_1^7(n-4,0,\ldots,0))\\
=\ &(x-1)^{n-9}[nx^7-(14n-16)x^6+(66n-84)x^5\\
&-(144n-108)x^4+(157n+100)x^3-(82n+316)x^2\\
&+(16n+224)x-48],\\
&Q(T_6^3(n-9,0,\ldots,0)) - Q(T_1^7(n-4,0,\ldots,0))\\
=\ &(x-1)^{n-10}[(2n-4)x^8-(28n-70)x^7+(148n-391)x^6\\
&-(393n-994)x^5+(570n-1221)x^4\\
&-(451n-616)x^3+(180n+16)x^2-(28n+96)x+16],\\
&Q(T_1^4(n-6,0,\ldots,0)) - Q(T_1^7(n-4,0,\ldots,0))\\
=\ &(x-1)^{n-7}[2x^5-(2n+8)x^4+(8n+26)x^3\\
&-(10n+68)x^2+(4n+80)x-32]\\
&Q(T_4^4(n-7,0,\ldots,0)) - Q(T_1^7(n-4,0,\ldots,0))\\
=\ &(x-1)^{n-8}[(n-1)x^6-(12n-22)x^5+(46n-85)x^4\\
&-(75n-96)x^3+(52n+16)x^2-(12n+64)x+16]\\
&Q(T_{14}^4(n-7,0,\ldots,0)) - Q(T_1^7(n-4,0,\ldots,0))\\
=\ &(x-1)^{n-8}[(n-1)x^6-(12n-24)x^5+(47n-107)x^4\\
&-(80n-176)x^3+(60n-108)x^2-(16n-16)x].
\end{aligned}$$

Further by Theorem 2.10 and lemmas 3.2–3.4, 3.6–3.8, we have $G \succeq T_1^7(n-4,0,0,0)$. □

Lemma 3.9. *For $n \geq |T_j^6|(j=1,\ldots,9,11,\ldots,24)$, $T_j^6(n-|T_j^6|,0,\ldots,0) \succeq T_1^6(n-4,0,0,0)$.*

Proof: We have

$$\begin{aligned}
&Q(T_2^6(n-6,0,\ldots,0)) - Q(T_1^6(n-5,0,\ldots,0))\\
=\ &(x-1)^{n-7}[(n-3)x^5-(9n-29)x^4+(25n-76)x^3\\
-\ &(26n-56)x^2+(8n+16)x-16]
\end{aligned}$$

By the results of **Appendix**, the results hold. □

Theorem 3.10. *For $G \in \mathscr{T}_n^6$, $G \succeq T_{10}^6(n-5,0,0,0)$ or $G \succeq T_1^6(n-5,0,0,0)$. The equality holds if and only if $G \cong T_1^6(n-5,0,0,0,0)$ or $G \cong T_{10}^6(n-5,0,0,0)$.*

Proof: If $G \in \mathscr{T}_n^{6,e}$, by Theorem 2.9 and

$$Q(T_1^6(n-5,0,\ldots,0)) - Q(T_1^7(n-4,0,\ldots,0)) = 0 \quad (1)$$

we have $G \succeq T_1^6(n-5,0,0,0)$.

If $G \in \mathscr{T}_n^{6,o}$, by Theorem 2.10, lemmas 3.5 and 3.9, we have $G \succeq T_{10}^6(n-7,0,\ldots,0)$ or $G \succeq T_1^6(n-5,0,0,0)$. □

Remark: By (3.1), $T_1^6(n-5,0,\ldots,0)$ and $T_1^7(n-4,0,\ldots,0)$ have the same signless Laplacian characteristic polynomials.

Theorem 3.11. *$T_{10}^6(n-7,0,\ldots,0)$, $T_1^6(n-5,0,0,0)$, $T_1^7(n-4,0,0,0)$ are the only three minimal elements in the partial set $(\mathscr{T}_n, \succeq)$.*

Proof: By (3.1), theorems 3.8 and 3.10, it is obvious that $T_1^6(n-5,0,0,0)$, $T_1^7(n-4,0,0,0)$ are the minimal elements in the partial set $(\mathscr{T}_n, \succeq)$.

Note that if there is a graph G_0 in $\mathscr{T}_n^3 \cup \mathscr{T}_n^4 \cup \mathscr{T}_n^{6,e} \cup \mathscr{T}_n^7$ such that $T_{10}^6(n-7,0,\ldots,0) \succeq G_0$, then by Theorem 3.8 and (3.1), we have $T_{10}^6(n-7,0,\ldots,0) \succeq T_1^6(n-5,0,0,0)$. But

$$\begin{aligned}
&Q(T_{10}^6(n-7,0,\ldots,0)) - Q(T_1^6(n-5,0,\ldots,0))\\
=\ &(x-1)^{n-8}[(2n-6)x^6-(22n-76)x^5+(83n-308)x^4\\
&-(137n-542)x^3\\
&+(98n-448)x^2-(24n-192)x-48],
\end{aligned}$$

it is a contradiction.

Hence the results hold. □

4. THE INCIDENCE ENERGY OF TRICYCLIC GRAPHS

The incidence energy $IE(G)$ of a graph G is defined to be the sum of the square root of all eigenvalues of $Q(G)$[3].

Theorem 4.1. *[11] Let G and G' be two graphs of order n, if $\varphi_k(G) \preceq \varphi_k(G')$ for $1 \leq k \leq n$, then $IE(G) \leq IE(G')$. In particular, if at least one of inequalities is strict, then $IE(G) < IE(G')$.*

Theorem 4.2. *If $G \in \mathscr{T}_n$, then $IE(G) \geq IE(T_1^6(n-5,0,0,0,0)) = IE(T_1^7(n-4,0,0,0))$. The equality holds if and only if $G \cong T_1^6(n-5,0,0,0,0)$, or $G \cong T_1^7(n-4,0,0,0)$.*

Proof: By Theorem 3.11, we have

$IE(G) \geq min\{IE(T_{10}^6(n-7,0,\cdots,0)), IE(T_1^6(n-5,0,0,0,0)), IE(T_1^7(n-4,0,0,0))\}$.

Note that

$$\begin{aligned}
Q(T_1^7(n-4,0,\ldots,0)) &= (x-1)^{n-5}[(x^5-(n+9)x^4\\
&\quad +(9n+24)x^3-(24n+32)x^2\\
&\quad +(20n+48)x-48]\\
&= (x-1)^{n-5}(x-2)^2[x^3-(n+5)x^2\\
&\quad +5nx-12],\\
Q(T_{10}^6(n-7,0,\ldots,0)) &= x(x-1)^{n-8}[(x^7-(n+12)x^6\\
&\quad +(14n+48)x^5-(76n+56)x^4+\\
&\quad (203n-83)x^3-(278n-230)x^2\\
&\quad +(182n-128)x-44n]\\
&= x(x-1)^{n-7}(x-2)[x^5-(n+9)x^4\\
&\quad +(11n+19)x^3-(41n-19)x^2\\
&\quad +(58n-64)x-22n].
\end{aligned}$$

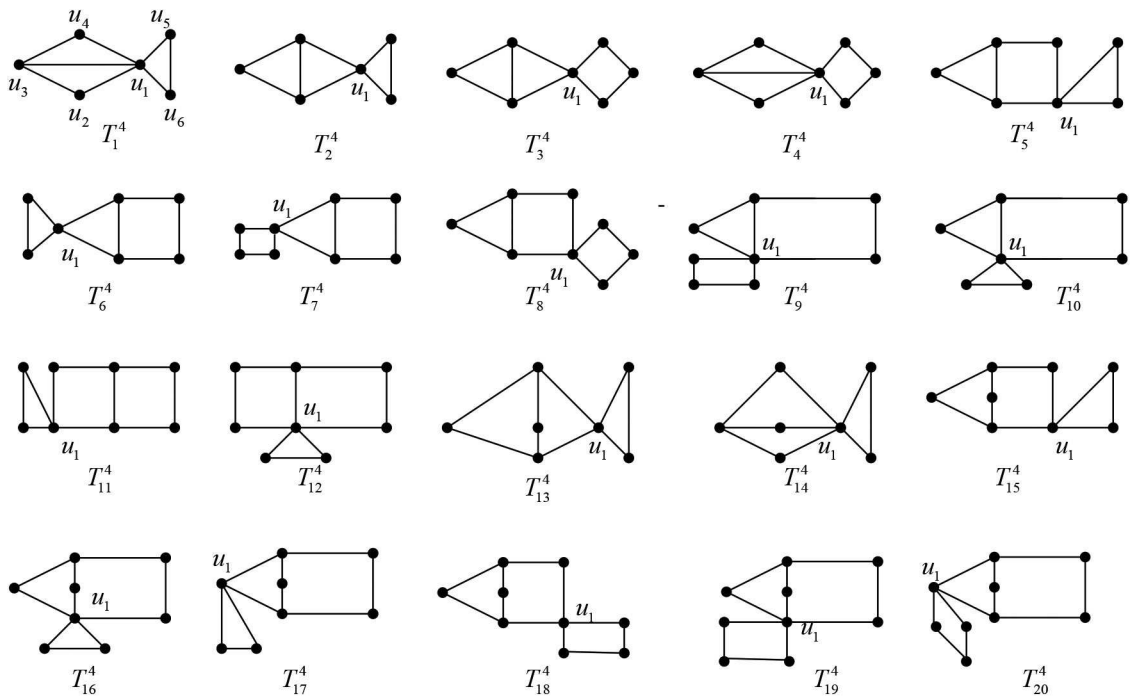

FIGURE 7 | The graphs $T_i^4 (i = 1, 2, \ldots, 20)$.

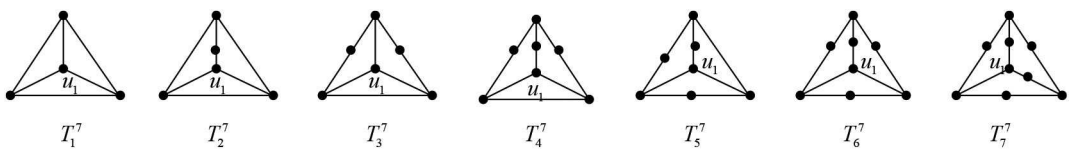

FIGURE 8 | The graphs $T_i^7 (i = 1, 2, \ldots, 7)$.

Let $\alpha_1 \geq \alpha_2 \geq \alpha_3$ be the roots of $x^3 - (n+5)x^2 + 5nx - 12 = 0$, and $\beta_1 \geq \beta_2 \geq \beta_3 \geq \beta_4 \geq \beta_5$ be the roots of $x^5 - (n+9)x^4 + (11n+19)x^3 - (41n-19)x^2 + (58n-64)x - 22n = 0$, then

$$\begin{aligned} IE(T_1^7) &= (n-5) + 2\sqrt{2} + \sqrt{\alpha_1} + \sqrt{\alpha_2} + \sqrt{\alpha_3} \\ IE(T_{10}^6) &= (n-7) + \sqrt{2} + \sqrt{\beta_1} + \sqrt{\beta_2} + \sqrt{\beta_3} + \sqrt{\beta_4} + \sqrt{\beta_5}. \end{aligned}$$

If $n \leq 40$, by Matlab7.0 it is easy to see $IE(T_{10}^6) > IE(T_1^7)$ holds.

If $n \geq 40$, it is easy to see that $n - 0.07 \leq \alpha_1 \leq n + 0.07$, $4.93 \leq \alpha_2 \leq 5$, $0 \leq \alpha_3 \leq 0.07$ and $n - 1.98 \leq \beta_1 \leq n - 1.9$, $4.58 \leq \beta_2 \leq 4.62, 3.41 \leq \beta_3 \leq 3.42, 2.37 \leq \beta_4 \leq 2.39, 0.54 \leq \beta_5 \leq 0.55$.

$$6.261 + \sqrt{n - 1.98} \leq \sum_{i=1}^{5} \sqrt{\beta_i} \leq 6.286 + \sqrt{n - 1.9},$$

$$2.22 + \sqrt{n - 0.07} \leq \sum_{i=1}^{3} \sqrt{\alpha_i} \leq 2.5 + \sqrt{n + 0.07},$$

$$3.597 \leq \sum_{i=1}^{5} \sqrt{\beta_i} - \sum_{i=1}^{3} \sqrt{\alpha_i} \leq 3.92.$$

It is easy to see that

$$\begin{aligned} IE(T_{10}^6) - IE(T_1^7) &= \sum_{i=1}^{5} \sqrt{\beta_i} - \sum_{i=1}^{3} \sqrt{\alpha_i} - 2 - \sqrt{2} \\ &\geq 3.597 - 2 - \sqrt{2} > 0. \end{aligned}$$

So the assertions hold. □

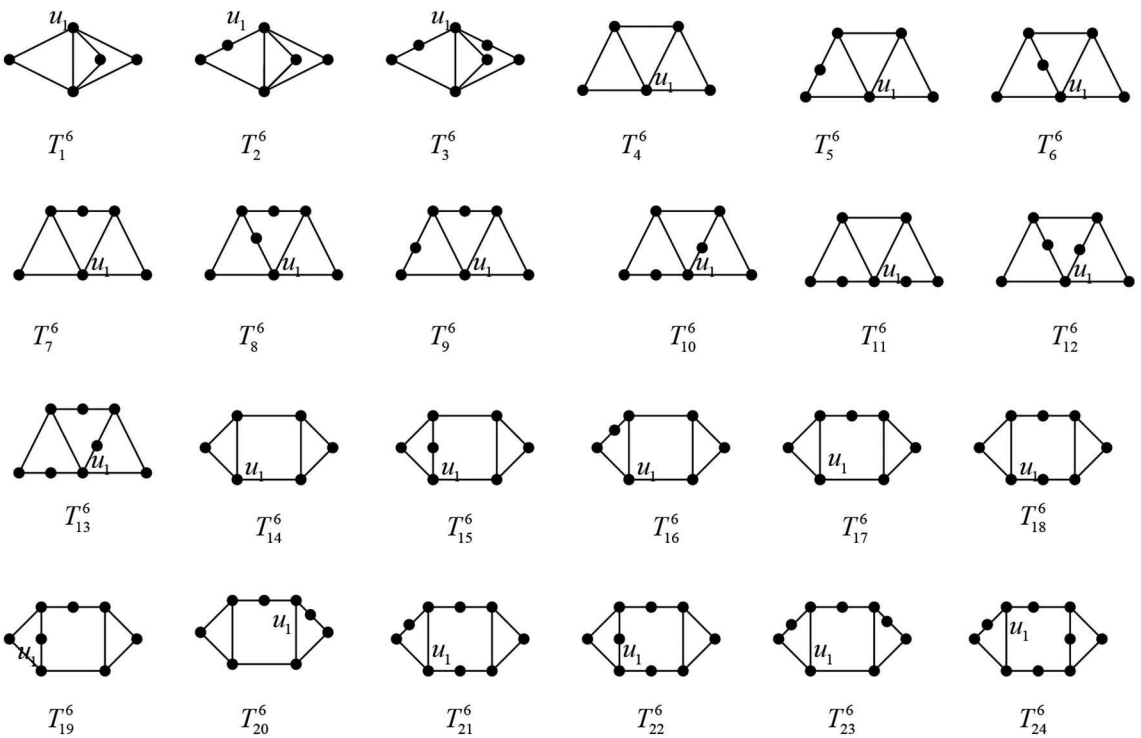

FIGURE 9 | The graphs $T_i^6 (i = 1, 2, \ldots, 24)$.

5. CONCLUSION AND EXTENSION

This paper propose an appropriate graph transformation to reflect the monotonicity of the coefficients, and give a sharp lower bound for incidence energy in the class of tricyclic graphs and characterize the extremal structures. The study on boundary of the incidence energy and its extremum structure of tricyclic graphs enriches and develops the study of the graph structure, but also connects the mathematical branch with other disciplines such as biology, physics and chemistry. It promotes the development of some theories of graph theory. It promotes the development of graph structure, the development of graph theory, and the study of graph theory and its application. For example, mathematical biology, application of graph theory in power system, molecular structure based on graph theory. Furthermore, similar to the graph energy, the incidence energy also reflects some physical and chemical properties of conjugated molecules, such as melting point and boiling point, this provides a theoretical reference for the researchers of the synthesis of new materials and new materials, and saves the cost for the development of new materials and new materials to a certain extent. Based on the extensive application of graph theory in many fields, the findings of this study have many important implications for future practice.

DATA AVAILABILITY STATEMENT

The original contributions presented in the study are included in the article/**Supplementary Materials**, further inquiries can be directed to the corresponding author/s.

AUTHOR CONTRIBUTIONS

ZZ contributed to the conception of the study, performed the data analyses, and wrote the manuscript. HL contributed significantly to analysis and manuscript preparation and helped to perform the analysis with constructive discussions.

FUNDING

This work was supported by the Scientific Research Project of Education Department of Shaanxi Province (19JK0906).

SUPPLEMENTARY MATERIAL

The Supplementary Material for this article can be found online at: https://www.frontiersin.org/articles/10.3389/fphy.2020.00208/full#supplementary-material

REFERENCES

1. Bollobás B. *Modern Graph Theory*. Berlin; New York, NY: Springer-Verlag (1998). doi: 10.1007/978-1-4612-0619-4
2. Cvetković D, Simić S. Towards a spectral theory of graphs based on the signless Laplacian. *Int Publ Inst Math.* (2009) **85**:19–33. doi: 10.1016/j.laa.2009.05.020
3. Zhang J, Zhang X. The signless Laplacian coefficients and incidence energy of bicyclic graphs. *Linear Algebra Appl.* (2013) **439**:385–6. doi: 10.1016/j.laa.2013.10.026
4. Lin HQ, Hong Y, Shu JL. Some relations between the eigenvalues of adjacency, Laplacian and signless Laplacian mattrix of a graph. *Graphs Combin*. (2015) **31**:669–71. doi: 10.1007/s00373-013-13980-5
5. Mohar B. On the Laplacian coefficients of acyclic graphs. *Linear Algebra Appl.* (2007) **722**:736–41. doi: 10.1016/j.laa.2006.12.005
6. Stevanović D,Ilić A. On the Laplacian coefficients of unicyclic graphs. *Linear Algebra Appl.* (2009) **430**:2290–300. doi: 10.1016/j.laa.2008.12.006
7. Li HH, Tam BS, Su L. On the signless Laplcaian coefficients of unicyclic graphs. *Linear Algebra Appl.* (2013) **439**:2008–28. doi: 10.1016/j.laa.2013.05.030
8. He C X, Shan H Y. On the Laplacian coefficients of bicyclic graphs. *Discrete Math.* (2010) **310**:3404–12. doi: 10.1016/j.disc.2010.08.012
9. Zhu ZX, Lu HY. On the general sun-connectivity index of tricyclic graphs. *J Appl Math Comput*. (2016) **51**:177–88. doi: 10.1007/s12190-015-0898-2
10. Pai X, Liu S, Guo J. On the Laplacian coefficients of tricyclic graphs. *J Math Anal Appl.* (2013) **405**:200–8. doi: 10.1016/j.jmaa.2013.03.059
11. Mirzakhah M, Kiani D. Some results on signless Laplacian coefficients of graphs. *Linear Algebra Appl.* (2012) **437**:2243–51. doi: 10.1016/j.laa.2012.05.022
12. Liu JB, Zhao J, Cai Z. On the generalized adjacency, Laplacian and signless Laplacian spectra of the weighted edge corona networks. *Phys A*. (2020) **540**:123073. doi: 10.1016/j.physa.2019.123073
13. Merris R. Laplacian matrices of graphs. *Linear Algebra Appl.* (1994) **197–8**:143–76. doi: 10.1016/0024-3795(94)90486-3
14. Cvetković D, Rowlinson P, Simić S. Singless Laplacians of finite graphs. *Linear Algebra Appl.* (2007) **432**:155–71. doi: 10.1109/ICACIA.2010.5709937
15. Tan SW. On the Laplacian coefficients of unicyclic graphs with prescribed matching number. *Discrete Math.* (2011) **311**:582–94. doi: 10.1016/j.disc.2010.12.022
16. Hoffman AJ, Smith JH. On the spectral radii of topologically equivalent graphs. In: Fiedler, Editor. *Recent Advances in Graph Theory*. New York, NY: Academia Praha (1975). p. 273–81.
17. Guo S. On the spectral radius of bicycle graphs with n vertics and diameter d. *Linear Algebra Appl.* (2007) **422**:119–32. doi: 10.1016/j.laa.2006.09.011
18. Tan SW. On the Laplacian coefficients and Laplacian-like energy of bicyclic graphs. *Linear Multilin AlgebRA*. (2012) **60**:1071–92. doi: 10.1080/03081087.2011.643473
19. Wang WH, Zhong L, Zheng LJ. The signless Laplacian coefficients and the incidence energy of the graphs without even cycles. *Linear Algebra Appl.* (2019) **563**:476–93. doi: 10.1016/j.laa.2018.10.025
20. Li SC, Li XC, Zhu ZX. On tricyclic graphs with minimal energy. *Match-Commun Math Comput Chem*. (2008) **59**:397–419. doi: 10.1111/j.1467-9892.2007.00552.x

Conflict of Interest: The authors declare that the research was conducted in the absence of any commercial or financial relationships that could be construed as a potential conflict of interest.

frontiers in Physics

BRIEF RESEARCH REPORT
published: 19 June 2020
doi: 10.3389/fphy.2020.00190

Set-Valued Weighted Value at Risk and Its Computation

Yichuan Dong[1,2], *Yijun Hu*[1,2] *and Yu Feng*[1,2]*

[1] School of Mathematics and Statistics, Wuhan University, Wuhan, China, [2] National Supercomputing Center in Shenzhen, Shenzhen, China

In this paper, we propose a new class of set-valued coherent risk measures called the set-valued weighted value at risk. Firstly, the "regulator" version is independent of other market scenarios. The second version, which is called the market extension, is related to different market scenarios. The proofs of the properties of both versions are given, and equivalent representations are provided that enable us to compute the values of both versions of set-valued weighted value at risk. Finally, we offer examples to illustrate various features of the theoretical constructions of the set-valued weighted value at risk.

Mathematics Subject Classification (2010): 91B30 91B32 91B70.

Keywords: set-valued coherent risk measure, set-valued average value at risk, set-valued weighted value at risk, representation, market extension

OPEN ACCESS

Edited by:
Muhammad Javaid, University of Management and Technology, Lahore, Pakistan

Reviewed by:
Su Guicong, Jagiellonian University, Poland
Chunyan Li, Chongqing University of Science and Technology, China
Liu Xi Xian, University of International Business and Economics, China

***Correspondence:**
Yu Feng
fengyuffyy@whu.edu.cn

Specialty section:
This article was submitted to Mathematical and Statistical Physics, a section of the journal Frontiers in Physics

Received: *29 March 2020*
Accepted: *30 April 2020*
Published: *19 June 2020*

Citation:
Dong Y, Hu Y and Feng Y (2020) Set-Valued Weighted Value at Risk and Its Computation. Front. Phys. 8:190. doi: 10.3389/fphy.2020.00190

1. INTRODUCTION

Weighted value at risk for one-dimension random variables may be one of the most popular coherent risk measures (see [1]). Artzner et al. [2] initially introduced the first coherent risk measure by proposing four axioms. Cherny [1] showed that weighted value at risk possesses some desirable properties that are not shared by Expected Shortfall. For further details on Expected Shortfall, we refer the reader to Föllmer and Schied [3]. Weighted value at risk first appeared in Kusuoka [4]. Acerbi [5, 6] called it the spectral risk measure.

Jouini et al. [7] demonstrated that a set of set-valued risk measures are suitable for evaluating multivariate risks in market models with transaction costs/bid-ask spreads. Additional set-valued risk measures have since been introduced and studied (see [8–13], and the references therein).

Hamel et al. [11] introduced set-valued average value at risk, and reasons for using set-valued functions as risk measures have been further addressed from both financial and mathematical perspectives (see [14–17]), and the reference there in).

In this paper, we will extend the traditional weighted value at risk to a set-valued version for multivariate random variables. Therefore, we demonstrate their core properties and provide an alternative representation for computing their values. The first version is called "regulator weighted value at risk" since it does not take trading opportunities into account. The second version is called "the market extension" since it relates to a specific market scenario. These two versions are set-valued coherent risk measures. Then, we derive a benchmark when introducing set-valued weighted value at risk that can reflect the risk tolerance of the trader/regulator; see Remark 2.2 below. Finally, we offer examples to illustrate various features of the theoretical constructions of the set-valued weighted value at risk.

The remainder of this article is organized as follows. Section 2 introduces a primal and an equivalent representation of set-valued weighted value at risk, including the "regulator" and "the market extension" cases. The essential properties of both cases are then proven. In section 3,

examples are given to illustrate the theoretical construction of the set-valued weighted value at risk.

2. SET-VALUED WEIGHTED VALUE AT RISK

2.1. The Regulator Case

Let $(\Omega, \mathscr{F}, P)$ be a probability space and $d \geq 1$ be a positive integer. A multivariate random variable is an $\mathscr{F}$-measurable function $\mathbf{X}: \Omega \to \mathbf{R}^d$ for $d \geq 2$. Here, $d = 1$ represents a one-dimension random variate. Denote by $L_d^0 := L_d^0(\Omega, \mathscr{F}, P)$ the linear space of the equivalence classes (with respect to the probability P) of $\mathbf{R}^d$-valued random variables. An element $\mathbf{X} \in L_d^0$ has components $X_1, \cdots, X_d$ in $L^0 := L_1^0$. Denote by $(L_d^0)_+$ the set of $\mathbf{R}^d$-valued random variables with P almost surely non-negative components and by $L_d^1 := L_d^1(\Omega, \mathscr{F}, P)$ the linear space of all $\mathbf{X} = (X_1, \cdots, X_d) \in L_d^0$ with $\int_\Omega X_i dP < +\infty$, $1 \leq i \leq d$. We also define $E[\mathbf{X}] = (EX_1, \cdots, EX_d)^T$ for $\mathbf{X} \in L_d^1$, the transpose of row vector $(EX_1, \cdots, EX_d)$. Define $(L_d^1)_+ = L_d^1 \cap (L_d^0)_+$. If $d = 1$, we write L^0, L_+^0 and L_+^1 for L_1^0, $(L_d^0)_+$ and $(L_d^1)_+$, respectively. For $\alpha \in \mathbf{R}^d$, the symbol $\mathrm{diag}(\alpha)$ denotes the $d \times d$ matrix with the components of the vector α as entries on its main diagonal and zero entries elsewhere. x^+ stands for $\max(x, 0)$ for $x \in \mathbf{R}$ [see [18–21]] and the reference therein).

The next definition offers an essential representation for set-valued weighted value at risk, which is an extension of the scalar case given by Cherny [1] to the set-valued case. It involves a linear subspace $\mathbf{M} \subseteq \mathbf{R}^d$, called the space of eligible assets, which we adopt from Hamel et al. [11]. We will also employ a benchmark level, which is one of the novelties of this article; see Remark 2.2 below. A natural choice for $\mathbf{M}$ is $\mathbf{M} = \mathbf{R}^m \times \{0\}^{d-m}$, $1 \leq m \leq d$, i.e., the first m of d assets are eligible as deposits (see [7, 11, 22]). We denote $\mathbf{M}_+ = \mathbf{M} \bigcap \mathbf{R}_+^d$, where $\mathbf{R}_+^d$ stands for the class of elements in $\mathbf{R}^d$ with non-negative components. We assume that $\mathbf{M}_+$ is non-trivial, i.e., $\mathbf{M}_+ \neq \{\mathbf{0}\}$.

Generally speaking, a scalar multivariate risk measure is any mapping from L_d^0 to $\mathbf{R}$. A set-valued risk measure is any mapping ρ from L_d^0 to a class of subsets of $\mathbf{R}^d$. $\rho(\mathbf{X})$ is interpreted as a set of acceptable margins of portfolio $\mathbf{X}$ (see [23–27]) and the reference therein).

Definition 2.1 Let $\theta \in (0,1)$ and $\mu := (\mu_1, \cdots, \mu_d)$ be a probability on $[\theta, 1]^d$. For $\mathbf{X} \in L_d^0$, the set-valued weighted value at risk at $\mathbf{X}$ with respect to μ is defined as

$$WVaR_\mu(\mathbf{X}) := \left\{ \int_{[\theta,1]^d} \mathrm{diag}(\alpha)^{-1} E[\mathbf{Z}] \mu(d\alpha) - z; \right. \\ \left. \mathbf{Z} \in (L_d^1)_+, \mathbf{X} + \mathbf{Z} - z \in (L_d^0)_+, z \in \mathbf{R}^d \right\} \cap \mathbf{M}, \tag{2.1}$$

where $\int_{[\theta,1]^d} \mathrm{diag}(\alpha)^{-1} E[\mathbf{Z}] \mu(d\alpha) - z := \left[\int_{[\theta,1]} \frac{1}{\alpha_i} E[Z_i] \mu_i(d\alpha_i) - z_i \right]_{i=1}^d := \left(\int_{[\theta,1]} \frac{1}{\alpha_1} E[Z_1] \mu_1(d\alpha_1) - z_1, \cdots, \int_{[\theta,1]} \frac{1}{\alpha_1} E[Z_d] \mu_d(d\alpha_d) - z_d \right)^T$ for $\mathbf{Z} = (Z_1, \cdots, Z_d) \in (L_d^1)_+$ and $z = (z_1, \cdots, z_d) \in \mathbf{R}^d$.

Remark 2.1 If μ is a Dirac measure at some $\alpha \in (0,1]^d$, that is, $\mu(\{\alpha\}) = 1$, then Definition 2.1 reverts to the definition of the set-valued regulator average value at risk of Hamel et al. [11] (Definition 2.1) because the benchmark level θ can be small enough. Moreover, in Example 3.2 below, we show that the $WVaR_\mu$ is better suited to the change in the market than the regulator average value at risk of Hamel et al. [11].

Remark 2.2 The financial interpretation of the benchmark level θ is as follows. Initially, it stems from the confidence level $1 - \alpha$ of value at risk. Given a confidence level $1 - \alpha \in (0,1)$, the value at risk at $X \in L^0$ is defined as $\mathrm{VaR}_{1-\alpha}(X) := \inf\{t \in \mathbf{R};\ P(X > t) \leq \alpha\}$. From a practical perspective, in reality, the parameter $1 - \alpha$ can be very close to but cannot be 1. Thus, α can be very close to but cannot be zero, which motivates the introduction of the benchmark level θ, which reflects the risk tolerance of the investor/regulator in terms of probability. See Basel Committee [28–31] for the reasonability of the benchmark level. Therefore, the benchmark level θ can be very close to zero but cannot be exactly zero. Examples 3.1 and 3.2 below take this perspective into account.

Remark 2.3 In definition 2.1, the intersection with $\mathbf{M}$ has the following interpretation. To cancel the risk of portfolio $\mathbf{X}$, we would like to obtain a set of all margins when measuring the risk of portfolio $\mathbf{X}$. Intersecting with the set $\mathbf{M}$, $WVaR_\mu(\mathbf{X})$ shows both the valid margins and the aggregated margins, which aggregates the valid margins from the d-dimension to the m-dimension. The other $(d-m)$-dimension of $WVaR_\mu(\mathbf{X})$ should be zero. Aggregating the margin has plenty of financial explanations. For example, each element of the vector represents the amounts in a specific currency. Suppose that m different currencies should be taken into consideration. For the regulator, there is no need to ask for a d-dimensional margin. They could aggregate d elements of the margin into m elements that represent m different currencies. When considering the margin needed by a company with different departments, this idea is also reasonable. The decision-maker of a company may simply want to figure out the sum of the margins of different departments. More details can be found in Jouini et al. [7].

The next proposition provides another equivalent representation of $WVaR_\mu$ under the condition $\mathbf{M} = \mathbf{R}^m \times \{0\}^{d-m}$, which is easier to compute than (2.1).

Proposition 2.1 Let $\mathbf{M} = \mathbf{R}^m \times \{0\}^{d-m}$ (hence $\mathbf{M}_+ = \mathbf{R}_+^m \times \{0\}^{d-m}$). The set-valued weighted value at risk takes the following equivalent representation:

$$WVaR_\mu(\mathbf{X}) = \left(\left[\inf_{z_i \in \mathbf{R}} \left\{ \int_{[\theta,1]} \frac{1}{\alpha_i} E[(-X_i + z_i)^+] \mu_i(d\alpha_i) - z_i \right\} \right]_{i=1}^m + \mathbf{R}_+^m \right) \times \{0\}^{d-m}$$

for $\mathbf{X} = (X_1, \cdots, X_d) \in L_d^0$.

Proof Considering a component of the portfolio, we know that the two conditions $Z_i \in L_+^1$ and $X_i + Z_i - z_i \in L_+^0$ are

equivalent to $Z_i \geq (-X_i + z_i)^+$ for $1 \leq i \leq d$. Therefore, $\{\int_{[\theta,1]} \frac{1}{\alpha_i} E[Z_i]\mu_i(d\alpha_i) - z_i;\ Z_i \in L^1_+, X_i + Z_i - z_i \in L^0_+, z_i \in \mathbf{R}\}$ is equal to $\inf_{z_i \in \mathbf{R}}\{\int_{[\theta,1]} \frac{1}{\alpha_i} E[(-X_i + z_i)^+]\mu_i(d\alpha_i) - z_i\} + \mathbf{R}_+$. After intersecting with the set $\mathbf{M}$, we have that

$$WVaR_\mu(\mathbf{X}) = \left(\left[\inf_{z_i \in \mathbf{R}} \left\{\int_{[\theta,1]} \frac{1}{\alpha_i} E[(-X_i + z_i)^+]\mu_i(d\alpha_i) - z_i\right\}\right]_{i=1}^m + \mathbf{R}_+^m\right) \times \{0\}^{d-m}. \quad (1)$$

Proposition 2.1 is proved.

The next proposition will show that when $\mathbf{M} = \mathbf{R}^m \times \{0\}^{d-m}$, the set-valued weighted value at risk is exactly a set-valued coherent risk measure in the sense of Jouini et al. [7].

Proposition 2.2 Let $\mathbf{M} = \mathbf{R}^m \times \{0\}^{d-m}$. Then, the function $\mathbf{X} \longrightarrow WVaR_\mu(\mathbf{X})$ meets the listed properties:

(a) Positive homogeneity: for any $\mathbf{X} \in L^0_d$ and any $s > 0$, $WVaR_\mu(s\mathbf{X}) = sWVaR_\mu(\mathbf{X})$.
(b) Subadditivity: for any $\mathbf{X}^1, \mathbf{X}^2 \in L^0_d$, $WVaR_\mu(\mathbf{X}^1 + \mathbf{X}^2) \supseteq WVaR_\mu(\mathbf{X}^1) + WVaR_\mu(\mathbf{X}^2)$.
(c) $\mathbf{M}$-translation invariance: for any $\mathbf{X} \in L^0_d$ and any $u \in \mathbf{R}^m$, $WVaR_\mu(\mathbf{X} + \bar{u}) = WVaR_\mu(\mathbf{X}) - \bar{u}$, where $\bar{u} = u \times \{0\}^{d-m}$.
(d) Monotonicity with respect to $(L^0_d)_+$: for any $\mathbf{X}^1, \mathbf{X}^2 \in (L^0_d)_+$ with $\mathbf{X}^2 \geq \mathbf{X}^1$, which means that $\mathbf{X}^2 - \mathbf{X}^1 \in (L^0_d)_+$, we have $WVaR_\mu(\mathbf{X}^2) \supseteq WVaR_\mu(\mathbf{X}^1)$.
(e) It satisfies that $WVaR_\mu(\mathbf{X}) + \mathbf{M}_+ = WVaR_\mu(\mathbf{X})$ for $\mathbf{X} \in L^0_d$. Particularly, $WVaR_\mu(\mathbf{0})$ is a convex cone.

Proof (a) For $\mathbf{X} = (X_1, \cdots, X_d) \in L^0_d$ and $s > 0$,

$$\begin{aligned}
WVaR_\mu(s\mathbf{X}) =& \left(\left[\inf_{z_i \in \mathbf{R}} \left(-z_i + \int_{[\theta,1]} \frac{1}{\alpha_i} E\left[(z_i - sX_i)^+\right]\mu_i(d\alpha_i)\right)\right]_{i=1}^m + \mathbf{R}_+^m\right) \times \{0\}^{d-m} \\
=& \left(\left[\inf_{z_i \in \mathbf{R}} \left(-z_i + s\int_{[\theta,1]} \frac{1}{\alpha_i} E\left[\left(\frac{z_i}{s} - X_i\right)^+\right]\mu_i(d\alpha_i)\right)\right]_{i=1}^m + \mathbf{R}_+^m\right) \times \{0\}^{d-m} \\
=& \left(\left[s\inf_{z_i \in \mathbf{R}} \left(-\frac{z_i}{s} + \int_{[\theta,1]} \frac{1}{\alpha_i} E\left[\left(\frac{z_i}{s} - X_i\right)^+\right]\mu_i(d\alpha_i)\right)\right]_{i=1}^m + \mathbf{R}_+^m\right) \times \{0\}^{d-m} \\
=& \left(\left[s\inf_{\frac{z_i}{s} \in \mathbf{R}} \left(-\frac{z_i}{s} + \int_{[\theta,1]} \frac{1}{\alpha_i} E\left[\left(\frac{z_i}{s} - X_i\right)^+\right]\mu_i(d\alpha_i)\right)\right]_{i=1}^m + \mathbf{R}_+^m\right) \times \{0\}^{d-m} \\
=& sWVaR_\mu(\mathbf{X}).
\end{aligned}$$

(b) For $\mathbf{X}^1 = (X^1_1, \cdots, X^1_d)$, $\mathbf{X}^2 = (X^2_1, \cdots, X^2_d) \in L^0_d$,

$$\begin{aligned}
WVaR_\mu(\mathbf{X}^1 + \mathbf{X}^2) =& \left(\left[\inf_{z_i \in \mathbf{R}} \left(-z_i + \int_{[\theta,1]} \frac{1}{\alpha_i} E\left[\left(z_i - X^1_i - X^2_i\right)^+\right]\mu_i(d\alpha_i)\right)\right]_{i=1}^m + \mathbf{R}_+^m\right) \times \{0\}^{d-m} \\
\supseteq& \left(\left[\inf_{z^1_i + z^2_i = z_i \in \mathbf{R}} \left(-z_i + \int_{[\theta,1]} \frac{1}{\alpha_i} E\left[\left(z^1_i - X^1_i\right)^+ + \left(z^2_i - X^2_i\right)^+\right]\mu_i(d\alpha_i)\right)\right]_{i=1}^m + \mathbf{R}_+^m\right) \times \{0\}^{d-m} \\
=& \left(\left[\inf_{z^1_i \in \mathbf{R}} \left(-z^1_i + \int_{[\theta,1]} \frac{1}{\alpha_i} E\left[\left(z^1_i - X^1_i\right)^+\right]\mu_i(d\alpha_i)\right)\right]_{i=1}^m + \mathbf{R}_+^m + \left[\inf_{z^2_i \in \mathbf{R}} \left(-z^2_i + \int_{[\theta,1]} \frac{1}{\alpha_i} E\left[\left(z^2_i - X^2_i\right)^+\right]\mu_i(d\alpha_i)\right)\right]_{i=1}^m + \mathbf{R}_+^m\right) \times \{0\}^{d-m} \\
=& WVaR_\mu(\mathbf{X}^1) + WVaR_\mu(\mathbf{X}^2).
\end{aligned}$$

(c) For $u = (u_1, \cdots, u_m) \in \mathbf{R}^m$,

$$\begin{aligned}
WVaR_\mu(\mathbf{X} + \bar{u}) =& \left(\left[\inf_{z_i \in \mathbf{R}} \left(-z_i + \int_{[\theta,1]} \frac{1}{\alpha_i} E\left[(z_i - \bar{u}_i - X_i)^+\right]\mu_i(d\alpha_i)\right)\right]_{i=1}^m + \mathbf{R}_+^m\right) \times \{0\}^{d-m} \\
=& \left(\left[\inf_{z_i \in \mathbf{R}} \left(-(z_i - \bar{u}_i) + \int_{[\theta,1]} \frac{1}{\alpha_i} E\left[(z_i - \bar{u}_i - X_i)^+\right]\mu_i(d\alpha_i) - \bar{u}_i\right)\right]_{i=1}^m + \mathbf{R}_+^m\right) \times \{0\}^{d-m} \\
=& WVaR_\mu(\mathbf{X}) - \bar{u}.
\end{aligned}$$

(d) Given $\mathbf{X}^1 = (X^1_1, \cdots, X^1_d)$, $\mathbf{X}^2 = (X^2_1, \cdots, X^2_d) \in L^0_d$ with $\mathbf{X}^2 - \mathbf{X}^1 \in (L^0_d)_+$, we have $(z_i - X^2_i)^+ \leq (z_i - X^1_i)^+$ for each $z_i \in \mathbf{R}$, $1 \leq i \leq d$. Hence,

$$\inf_{z_i \in \mathbf{R}} \left(-z_i + \int_{[\theta,1]} \frac{1}{\alpha_i} E\left[\left(z_i - X^2_i\right)^+\right]\mu_i(d\alpha_i)\right) \leq \inf_{z_i \in \mathbf{R}} \left(-z_i + \int_{[\theta,1]} \frac{1}{\alpha_i} E\left[\left(z_i - X^1_i\right)^+\right]\mu_i(d\alpha_i)\right).$$

Therefore,

$$\left[\inf_{z_i \in \mathbf{R}} \left(-z_i + \int_{[\theta,1]} \frac{1}{\alpha_i} E\left[\left(z_i - X^2_i\right)^+\right]\mu_i(d\alpha_i)\right)\right]_{i=1}^m \leq \left[\inf_{z_i \in \mathbf{R}} \left(-z_i + \int_{[\theta,1]} \frac{1}{\alpha_i} E\left[\left(z_i - X^1_i\right)^+\right]\mu_i(d\alpha_i)\right)\right]_{i=1}^m.$$

Consequently,

$$\left(\left[\inf_{z_i\in\mathbf{R}}(-z_i \quad + \int_{[\theta,1]}\frac{1}{\alpha_i}E\left[\left(z_i-X_i^2\right)^+\right]\mu_i(d\alpha_i)\right)\right]_{i=1}^m + \mathbf{R}_+^m\Bigg)\times\{0\}^{d-m}$$
$$\supseteq\left(\left[\inf_{z_i\in\mathbf{R}}\left(-z_i+\int_{[\theta,1]}\frac{1}{\alpha_i}E\left[\left(z_i-X_i^1\right)^+\right]\mu_i(d\alpha_i)\right)\right]_{i=1}^m + \mathbf{R}_+^m\right)\times\{0\}^{d-m},$$

which implies that $WVaR_\mu(\mathbf{X}^2)\supseteq WVaR_\mu(\mathbf{X}^1)$.

(e) It is not difficult to verify that $WVaR_\mu(\mathbf{X})+\mathbf{M}_+ = WVaR_\mu(\mathbf{X})$ and that $WVaR_\mu(0)$ is a convex cone.

2.2. The Market Extension

The weighted value at risk from Definition 2.1 does not take into account the investment preferences of investors. Therefore, we define its market extension by replacing $(L_d^0)_+$ with a general closed convex cone K containing $(L_d^0)_+$ (see [7] or [8] for further motivation).

Definition 2.2 Let $\widetilde{K}$ be a closed convex cone that contains $(L_d^1)_+$ and K be a closed convex cone that contains $(L_d^0)_+$. The extended version of the set-valued weighted value at risk is defined as

$$WVaR_\mu^{ext}(\mathbf{X}) := \left\{\int_{[\theta,1]^d}\mathrm{diag}(\alpha)^{-1}E[\mathbf{Z}]\mu(d\alpha)-z;\ \mathbf{Z}\in\widetilde{K},\mathbf{X}+\mathbf{Z}-z\in K,z\in\mathbf{R}^d\right\}\cap\mathbf{M}.$$

In the proof of Proposition 2.1, through the same argument, we present the following proposition, which provides another equivalent representation of $WVaR_\mu^{ext}(\cdot)$.

Proposition 2.3 Let $\mathbf{M}=\mathbf{R}^m\times\{0\}^{d-m}$. $WVaR_\mu^{ext}$ has the following equivalent representation:

$$WVaR_\mu^{ext}(\mathbf{X})=\left(\left[\inf_{z_i\in\mathbf{R}}\left(\int_{[\theta,1]}\frac{1}{\alpha_i}E\left[(-X_i+z_i)^+\right]\mu_i(d\alpha_i)-z_i\right)\right]_{i=1}^m + C\right)\times\{0\}^{d-m}$$

where C is a closed convex cone that contains $\mathbf{R}_+^d$.

The next proposition will show that when $\mathbf{M}=\mathbf{R}^m\times\{0\}^{d-m}$, $WVaR_\mu^{ext}$ is exactly a set-valued coherent risk measure in the sense of Jouini et al. [7].

Proposition 2.4 Let $\mathbf{M}=\mathbf{R}^m\times\{0\}^{d-m}$. Then, the function $\mathbf{X}\longrightarrow WVaR_\mu^{ext}(\mathbf{X})$ satisfies the following properties:

(a) Positive Homogeneity: for each $\mathbf{X}\in L_d^0$ and each $s>0$, $WVaR_\mu^{ext}(s\mathbf{X})=sWVaR_\mu^{ext}(\mathbf{X})$.

(b) Subadditivity: for each $\mathbf{X}^1,\mathbf{X}^2\in L_d^0$, $WVaR_\mu^{ext}(\mathbf{X}^1+\mathbf{X}^2)\supseteq WVaR_\mu^{ext}(\mathbf{X}^1)+WVaR_\mu^{ext}(\mathbf{X}^2)$.

(c) $\mathbf{M}$-translation invariance: for each $\mathbf{X}\in L_d^0$ and each $u\in\mathbf{R}^m$, $WVaR_\mu^{ext}(\mathbf{X}+\bar{u})=WVaR_\mu^{ext}(\mathbf{X})-\bar{u}$, where $\bar{u}=u\times\{0\}^{d-m}$.

(d) Monotonicity with respect to K: for any $\mathbf{X}^1,\mathbf{X}^2\in K$ and $\mathbf{X}^2\succeq_K\mathbf{X}^1$, which means that $\mathbf{X}^2-\mathbf{X}^1\in K$, we have $WVaR_\mu^{ext}(\mathbf{X}^2)\supseteq WVaR_\mu^{ext}(\mathbf{X}^1)$.

(e) For each $\mathbf{X}\in L_d^0$, the set $WVaR_\mu^{ext}(\mathbf{X})\subset\mathbf{M}$ is convex and satisfies that $WVaR_\mu^{ext}(\mathbf{X})+C_M=WVaR_\mu^{ext}(\mathbf{X})$, where $C_M:=C\bigcap M$ and C is as in Proposition 2.3. In particular, $WVaR_\mu^{ext}(\mathbf{0})$ is a convex cone that satisfies $C_M\subseteq WVaR_\mu^{ext}(\mathbf{0})$ and $WVaR_\mu^{ext}(\mathbf{0})\bigcap-\mathbf{C_M}=\{\mathbf{0}\}$.

Proof: (a) For $\mathbf{X}\in L_d^0$ and $s>0$, we have

$$\begin{aligned}WVaR_\mu^{ext}(s\mathbf{X})&=\left\{\int_{[\theta,1]^d}\mathrm{diag}(\alpha)^{-1}E[\mathbf{Z}]\mu(d\alpha)-z;\ \mathbf{Z}\in\widetilde{K},s\mathbf{X}+\mathbf{Z}-z\in K,z\in\mathbf{R}^d\right\}\cap\mathbf{M}\\&=\left\{\int_{[\theta,1]^d}\mathrm{diag}(\alpha)^{-1}E[\mathbf{Z}]\mu(d\alpha)-z;\ \frac{\mathbf{Z}}{s}\in\widetilde{K},s(\mathbf{X}+\frac{\mathbf{Z}}{s}-\frac{z}{s})\in K,\frac{z}{s}\in\mathbf{R}^d\right\}\cap\mathbf{M}\\&=\left\{s\left(\int_{[\theta,1]^d}\mathrm{diag}(\alpha)^{-1}E\left[\frac{\mathbf{Z}}{s}\right]\mu(d\alpha)-\frac{z}{s}\right);\ \frac{\mathbf{Z}}{s}\in\widetilde{K},\mathbf{X}+\frac{\mathbf{Z}}{s}-\frac{z}{s}\in K,\frac{z}{s}\in\mathbf{R}^d\right\}\cap\mathbf{M}\\&=sWVaR_\mu^{ext}(\mathbf{X}).\end{aligned}$$

(b) For $\mathbf{X}^1,\mathbf{X}^2\in L_d^0$,

$$\begin{aligned}&WVaR_\mu^{ext}(\mathbf{X}^1)+WVaR_\mu^{ext}(\mathbf{X}^2)\\&=\left\{\int_{[\theta,1]^d}\mathrm{diag}(\alpha)^{-1}E[\mathbf{Z}^1]\mu(d\alpha)-z^1+\int_{[\theta,1]}diag(\alpha)^{-1}E[\mathbf{Z}^2]\mu(d\alpha)-z^2;\ \mathbf{Z}^1,\mathbf{Z}^2\in\widetilde{K},\mathbf{X}^1+\mathbf{Z}^1-z^1\in K,\mathbf{X}^2+\mathbf{Z}^2-z^2\in K,z^1,z^2\in\mathbf{R}^d\right\}\cap\mathbf{M}\\&\subseteq\left\{\int_{[\theta,1]^d}\mathrm{diag}(\alpha)^{-1}E[\mathbf{Z}^1+\mathbf{Z}^2]\mu(d\alpha)-(z^1+z^2);\ \mathbf{Z}^1+\mathbf{Z}^2\in\widetilde{K},\mathbf{X}^1+\mathbf{X}^2+\mathbf{Z}^1+\mathbf{Z}^2-(z^1+z^2)\in K,z^1+z^2\in\mathbf{R}^d\right\}\cap\mathbf{M}\\&=\left\{\int_{[\theta,1]^d}\mathrm{diag}(\alpha)^{-1}E[\mathbf{Z}]\mu(d\alpha)-z;\ \mathbf{Z}\in\widetilde{K},\mathbf{X}^1+\mathbf{X}^2+\mathbf{Z}-z\in K,z\in\mathbf{R}^d\right\}\cap\mathbf{M}\\&=WVaR_\mu^{ext}(\mathbf{X}^1+\mathbf{X}^2).\end{aligned}$$

(c) It is straightforward.

(d) $WVaR_{\mu}^{ext}$ is K-monotone because for $\mathbf{Y} \in K$, we have $\mathbf{Y} + K \subseteq K$, and therefore, $WVaR_{\mu}^{ext}(\mathbf{X} - \mathbf{Y}) = \left\{\int_{[\theta,1]^d} \text{diag}(\alpha)^{-1} E[\mathbf{Z}]\mu(d\alpha) - z;\ \mathbf{Z} \in \widetilde{K}, \mathbf{X} + \mathbf{Z} - z \in \mathbf{Y} + K, z \in \mathbf{R}^d\right\} \cap \mathbf{M} \subseteq WVaR_{\mu}^{ext}(\mathbf{X})$.

(e) It is straightforward. Proposition 2.4 is proved.

3. EXAMPLES

In this part, we give two examples of computing $WVaR_{\mu}$. In the rest of the paper, we will consider a finite financial market, that is, we assume that $(\Omega, \mathscr{F}, P)$ is a finite probability space. Namely, let $|\Omega| = N$, $\mathscr{F} = 2^{\Omega}$, $P = (p_1, p_2, ..., p_N)$ with $\sum_{n=1}^{N} p_n = 1$ and $P(\{\omega_n\}) = p_n$, $n = 1, 2, ..., N$. Here, N is a strictly positive number, and the probability measure P is given by N.

The first example is motivated by Hamel et al. [11] (Example 3.1).

Example 3.1 Suppose that the elements of a portfolio are $d = 2$ and $\mathbf{M} = \mathbf{R}^2$ (hence all the initial portfolios are eligible). In a binary model with $N = 2$ and $P = (0.4, 0.6)$, the potential income is given by

$$\mathbf{X}(\omega_1) = (12, -20)^T, \quad \mathbf{X}(\omega_2) = (4, -6)^T.$$

We set the benchmark level $\theta = 0.01$ and let $\mu_1 = \mu_2 := \nu$. If ν is set to be uniformly distributed on $[\theta,\ 1]$, that is, for Borel measurable set $A \subset [\theta,\ 1]$,

$$\nu(A) := \int_A f(x)dx,$$

where $f(x) = \frac{1}{1-\theta}$ for $\theta \leq x \leq 1$. By a simple calculation, we have that

$$WVaR_{\mu}(\mathbf{X}) = (-4,\ 20)^T + \mathbf{R}_+^2.$$

If we let ν be a (discrete) probability law with $\nu(\{0.01\}) = \nu(\{0.02\}) = 0.5$, then calculation shows that

$$WVaR_{\mu}(\mathbf{X}) = (-4,\ 20)^T + \mathbf{R}_+^2$$

again. For the first and second assets, the margins that the manager/regulator needs for compensating the risk are at least 4 units and −20 units, respectively.

In the above example, the value of $WVaR_{\mu}(\mathbf{X})$ is equal to that of $AV@R_{\alpha}^{reg}(\mathbf{X})$, the set-valued regulator average value at risk (see [11], Definition 2.1 and Example 3.1), where $\alpha = (0.01,\ 0.02)^T$. The next example will show that the values of $WVaR_{\mu}(\mathbf{X})$ and $AV@R_{\alpha}^{reg}(\mathbf{X})$ are not necessarily the same and that $WVaR_{\mu}(\mathbf{X})$ is better suited to a market featuring extreme events than is $AV@R_{\alpha}^{reg}(\mathbf{X})$.

Example 3.2 Let all the input parameters and the potential incomes of $\mathbf{X}$ be as in Example 3.1 except for the probability law P and the probability measure μ. Here, we set $P = (0.99,\ 0.01)$. If ν is set to be uniformly distributed on $[\theta,\ 1]$, then

$$WVaR_{\mu}(\mathbf{X}) = (-11.628,\ 20)^T + \mathbf{R}_+^2.$$

If ν is again a (discrete) probability law with $\nu(\{0.01\}) = \nu(\{0.02\}) = 0.5$, then,

$$WVaR_{\mu}(\mathbf{X}) = (-6,\ 20)^T + \mathbf{R}_+^2.$$

In contrast to the above example, the probability measure μ concerning the confidence levels does affect the risk measure because the minimal margin to cancel the risk for a manager/regulator covers the worst case only for the second asset, which is −20 units.

On the other hand,

$$AV@R_{\alpha}^{reg}(\mathbf{X}) = (-4,\ 20)^T + \mathbf{R}_+^2,$$

where $\alpha = (0.01,\ 0.02)^T$, which is the same as in Example 3.1.

From the above two examples, we observe that when all the input parameters remain the same except for the change in the (binary) probability law P from (0.4, 0.6) to (0.99, 0.01), the minimal risk-compensating portfolio of $WVaR_{\mu}(\mathbf{X})$ changes from (−4, 20) to (−11.628, 20) and (−6, 20), respectively, whereas the minimal risk-compensating portfolio of $AV@R_{\alpha}^{reg}(\mathbf{X})$ remains unchanged, which is (−4, 20). Thus, we conclude that $WVaR_{\mu}(\mathbf{X})$ can reflect the change in the market, that is, the change in the (binary) probability P, whereas $AV@R_{\alpha}^{reg}(\mathbf{X})$ cannot. In the case of $P = (0.99,\ 0.01)$, the event with probability 0.01 could be regarded as an extreme event compared with the other event with probability 0.99. Therefore, we conclude that $WVaR_{\mu}$ is better suited to a market featuring extreme events than is $AV@R_{\alpha}^{reg}$.

4. CONCLUSIONS

In this paper, we proposed two new classes of set-valued coherent risk measures: the "regulator" version and "market" version. Their essential properties are discussed, and equivalent representations are given. Moreover, the coherency of the set-valued weighted value at risk is characterized. These newly introduced set-valued risk measures complement the study of set-valued risk measures. Examples are also presented that show that set-valued weighted value at risk is better suited to a market featuring extreme events than is $AV@R_{\alpha}^{reg}$.

DATA AVAILABILITY STATEMENT

The original contributions presented in the study are included in the article/supplementary materials, further inquiries can be directed to the corresponding author/s.

AUTHOR CONTRIBUTIONS

YD, YH, and YF: conceptualization, formal analysis, writing-original draft preparation, writing-review and editing, and funding acquisition. All authors contributed to the article and approved the submitted version.

FUNDING

This work was supported by the National Key Research and Development Program of China (Grant No. 2018YFB0204403) and Shenzhen Grade E Scientific and Engineering Calculation Key Laboratory under Grant No. ZDSYS201703031711426. It was also supported by the National Natural Science Foundation of China (No. 1137 1284).

REFERENCES

1. Cherny AS. Weighted *V@R* and its properties. *Finance Stochast.* (2006) 10:367–93. doi: 10.1007/s00780-006-0009-1
2. Artzner P, Delbaen F, Eber JM, Heath D. Coherent measures of risk. *Math Finance.* (1999) 9:203–28. doi: 10.1111/1467-9965.00068
3. Föllmer H, Schied A. *Stochastic Finance: An Introduction in Discrete Time*. 3rd Edn. Berlin: Walter de Gruyter & Co (2011).
4. Kusuoka S. On law invariant coherent risk measures. *Adv Math Econ.* (2001) 3:83–95. doi: 10.1007/978-4-431-67891-5_4
5. Acerbi C. Spectral meausure of risk: a coherent representation of subjective risk aversion. *J Bank Finance.* (2002) **26**:1505–18. doi: 10.1016/S0378-4266(02)00281-9
6. Acerbi C. Coherent representations of subjective risk aversion. In: Szegö G, editor. *Risk Measure for the 21st Century*. New York, NY: Wiley (2004) p. 147–207.
7. Jouini W, Meddeb M, Touzi N. Vector-valued coheret risk measures. *Finance Stochast.* (2004) 8:531–52. doi: 10.1007/s00780-004-0127-6
8. Hamel AH. A duality theory for set-valued functions I. *Set-Valued Anal.* (2009) 17:153–82. doi: 10.1007/s11228-009-0109-0
9. Hamel AH, Heyde F. Duality for set-valued measures of risk. *SIAM J Financ Math.* (2010) 1:66–95. doi: 10.1137/080743494
10. Hamel AH, Heyde F, Rudloff B. Set-valued risk measures for conical market models. *Math Financ Econ.* (2011) 5:1–28. doi: 10.1007/s11579-011-0047-0
11. Hamel AH, Rudloff B, Yankova M. Set-valued average value at risk and its computation. *Math Financ Econ.* (2013) 7:229–46. doi: 10.1007/s11579-013-0094-9
12. Ararat C, Hamel AH, Rudloff B. Set-valued shortfall and divergence risk measures[J]. *Int J Theor Appl Finance.* (2017) 20:1750026. doi: 10.1142/S0219024917500261
13. Feinstein Z, Rudloff B. Multi-portfolio time consistency for set-valued convex and coherent risk measure. *Finance Stoch.* (2015) 19:67–107. doi: 10.1007/s00780-014-0247-6
14. Delbaen F. *Coherent Risk Measures on General Probability Spaces (Advances in Finance and Stoshatics)*. Berlin; Heidelberg; New York, NY: Springer (2002).
15. Hamel AH. *Translative Sets and Functions and Their Applications to Risk Measure Theory and Nonlinear Separation* (2006). Available online at: https://fam.tuwien.ac.at/events/abstracts/20060606.pdf.
16. Ararat C. *On set-valued functionals: multivariate risk measures and Aumann integrals[J]* (Dissertations & Theses - Gradworks). Princeton University, Princeton, NJ, United States (2015).
17. Artzner P, Delbaen F, Eber JM, Heath D. Thinking coherently. *Risk.* (1997) 10:68–71.
18. Chen J, Wang C, Zhang X-A, Ha M. A further discussion of structural risk minimization principle on set-valued probability space[C]. In: *Proceedings of International Conference on Machine Learning and Cybernetics, ICMLC.* Qingdao: IEEE (2010).
19. Yu F, Yichuan D, Jia-Bao L. Set-valued haezendonck-goovaerts risk measure and its properties[J]. *Discrete Dyn Nat Soc*. (2017) 2017:1–7. doi: 10.1155/2017/5320908
20. Deprez O, Gerber HU. On convex principles of premium calculation. *Insurance.* (1985) 4:179–89. doi: 10.1016/0167-6687(85)90014-9
21. Frittelli M, Rosazza Gianin E. Putting order in risk measures. *J Bank Finance.* (2002) 26:1473–86. doi: 10.1016/S0378-4266(02)00270-4
22. Artzner P, Delbaen F, Koch-Medina P. Risk measures and efficient use of capital. *Astin Bull.* (2009) 39:101–16. doi: 10.2143/AST.39.1.2038058
23. Rüschendorf L. *Mathematical Risk Analysis[M].* Berlin; Heidelberg: Springer (2013).
24. Föllmer H, Schied A. Convex measures of risk and trading constraints. *Finance Stochast.* (2002) 6:429–47. doi: 10.1007/s007800200072
25. Cascos I, Molchanov I. Multivariate risks and depth-trimmed regions. *Finance Stochast.* (2007) 11:373–97. doi: 10.1007/s00780-007-0043-7
26. Burgert C, Rüschendorf L. Consistent risk measures for portfolio vectors. *Insurance.* (2006) 38:289–97. doi: 10.1016/j.insmatheco.2005.08.008
27. Embrechts P, Puccetti G. Bounds for functions of multivariate risks. *J Multi Var Anal.* (2006) 97:526–47. doi: 10.1016/j.jmva.2005.04.001
28. Basel Committee. *Amendment to the Capital Accord to Incorporate Market Risks*. Basle Committee on Banking Supervision (1996).
29. Basel Committee. *International Convergence of Capital Measurement and Capital Standards: A Revised Framework (Comprehensive Version)*. Basle Committee on Banking Supervision (2006).
30. Basel Committee. *Guidelines for Computing Capital for Incremental Risk in the Traing Book*. Basel Committee on Banking Supervision (2009).
31. Basel Committee. *Revision to the Basel II Market Risk Framework*. Basel Committee on Banking Supervisiom (2011).

Conflict of Interest: The authors declare that the research was conducted in the absence of any commercial or financial relationships that could be construed as a potential conflict of interest.

frontiers in Physics

BRIEF RESEARCH REPORT
published: 10 July 2020
doi: 10.3389/fphy.2020.00239

A Relation Between Moore-Penrose Inverses of Hermitian Matrices and Its Application in Electrical Networks

Yujun Yang[1]*, *Dayong Wang*[2] and *Douglas J. Klein*[3]

[1] School of Mathematics and Information Sciences, Yantai University, Yantai, China, [2] Business School, Hohai University, Nanjing, China, [3] Department of Marine Sciences, Texas A&M University at Galveston, Galveston, TX, United States

A novel relation between the Moore-Penrose inverses of two nullity-1 $n \times n$ Hermitian matrices which share a common null eigenvector is established, and its application in electrical networks is illustrated by applying the result to Laplacian matrices of graphs.

Keywords: resistance distance, electrical network, Hermitian matrix, Laplacian matrix, Moore-Penrose inverse

OPEN ACCESS

Edited by:
Jia-Bao Liu,
Anhui Jianzhu University, China

Reviewed by:
Weigen Yan,
Jimei University, China
Zhongxun Zhu,
South-Central University for Nationalities, China
Guihai Yu,
Guizhou University of Finance and Economics, China

***Correspondence:**
Yujun Yang
yangyj@yahoo.com

Specialty section:
This article was submitted to Mathematical and Statistical Physics, a section of the journal Frontiers in Physics

Received: *17 April 2020*
Accepted: *02 June 2020*
Published: *10 July 2020*

Citation:
Yang Y, Wang D and Klein DJ (2020) A Relation Between Moore-Penrose Inverses of Hermitian Matrices and Its Application in Electrical Networks. Front. Phys. 8:239. doi: 10.3389/fphy.2020.00239

1. INTRODUCTION

The Hermitian matrices are an important class of matrices arising in many contexts. A complex squared matrix is called a *Hermitian matrix* if it is equal to its conjugate transpose, in other words, for all i and j, its (i, j)-th element (i.e., the element in the i-th row and j-th column) is equal to the complex conjugate of its (j, i)-th element. It is widely known that all the eigenvalues of a Hermitian matrix are real. In addition, it is easily seen that Hermitian matrices contain real symmetric matrices as special cases.

Let M be an $n \times m$ matrix. An $m \times n$ matrix X is called the *Moore-Penrose (generalized) inverse* of M, if X satisfies the following equations:

$$MXM = M, XMX = X, (MX)^H = MX, (XM)^H = XM,$$

where X^H represents the conjugate transpose of the matrix M. It is well-known [1] that for any matrix M, the Moore-Penrose inverse of M does exist and is unique. For this reason, the unique Moore-Penrose inverse of M is denoted by M^+.

We proceed to introduce a special class of Hermitian matrices – the Laplacian matrices of graphs, which play a fundamental role in graph theory and electrical network theory. Let $G = (V, E)$ be a connected weighted graph of order n. For each edge e of G, we assign a positive real number w_e to e, and we call w_e the *weight* of e. Then the adjacency matrix of G, denoted by A, is a $n \times n$ matrix such that the (i, j)-th element of A is equal to the weight of the edge ij if i and j are connected by an edge and 0 otherwise. Suppose that D is the $n \times n$ diagonal matrix such that the i-th diagonal element is equal to the sum of the weights of the edges incident to i. Then the *Laplacian matrix* L of G is defined as $L = D - A$. It is easily seen that the Laplacian matrix is real and symmetric. Thus, the Laplacian matrix is a Hermitian matrix. According to the definition of the Laplacian matrix, we readily seen that the Laplacian matrix is singular and not invertible.

It is natural to consider a weighted graph G as a (resistive) electrical network $\mathcal{N}$ by viewing each edge e as a resistor such that the conductance of the resistor is w_e, where w_e is the weight on e. In this guise, the *resistance distance* [2] between any two vertices i and j of G, denoted by $\Omega(i, j)$, is defined as the net effective resistance between corresponding nodes i and j in $\mathcal{N}$. It should be mentioned that resistance distance, as an important component of circuit theory, has been studied for a long time, dating back to the classical work of Kirchhoff in 1847. It is amazing

that the resistance distance turns out to have many purely mathematical interpretations, although it comes from physics and engineering, among which a fundamental one is the classical result which is given via the Moore-Penrose inverse of the Laplacian matrix [2]:

$$\Omega(i,j) = L^+_{ii} - 2L^+_{ij} + L^+_{jj}, \tag{1.1}$$

where L^+_{ij} denote the (i,j)-th element of L^+. Since the identification of resistance distance as a novel distance function on graphs, the resistance distance has been extensively studied in the literature of mathematics, physics, and chemistry. For more information on resistance distances, we refer the readers to recent papers [3–13] and references therein.

In this paper, a relation between the Moore-Penrose inverses of two nullity-1 $n \times n$ Hermitian matrices which share a common null eigenvector is established. Then its application in electrical networks is illustrated by applying the result to Laplacian matrices of graphs.

2. A RELATION BETWEEN MOORE-PENROSE INVERSES OF TWO HERMITIAN MATRICES

All the matrices considered in this section are square matrices of order n. For an invertible matrix M, we use M^{-1} to denote the inverse of M. Let I and $\mathbf{O}$ denote the identity matrix and zero matrix, respectively. This section is devoted to establish a relation between Moore-Penrose inverses of two Hermitian matrices of nullity-1 which share a common null eigenvector. To this end, we first give some properties on nullity-1 Hermitian matrices, which will be used in the later.

Lemma 2.1. *Let M be a nullity-1 Hermitian $n \times n$ matrix. Suppose that $0 = \lambda_1, \lambda_2, \ldots, \lambda_n$ are eigenvalues of M with corresponding orthonormal eigenvectors $u_1, u_2, \ldots, u_n$. Then*

$$M^+ = (M + u_1u_1^H)^{-1} - u_1u_1^H. \tag{2.1}$$

$$MM^+ = M^+M = I - u_1u_1^H. \tag{2.2}$$

$$u_1u_1^HM^+ = \mathbf{O}. \tag{2.3}$$

Proof: Let $U = (u_1, u_2, \ldots, u_n)$ and $\Lambda = \mathrm{diag}\{0, \lambda_2, \ldots, \lambda_n\}$. Then

$$M = U\Lambda U^H.$$

As $u_1u_1^H = U\mathrm{diag}\{1, 0, \ldots, 0\}U^H$, it follows that

$$\begin{aligned} M + u_1u_1^H &= U\Lambda U^H + U\mathrm{diag}\{1, 0, \ldots, 0\}U^H \\ &= U\mathrm{diag}\{1, \lambda_2, \ldots, \lambda_n\}U^H. \end{aligned}$$

Thus $M + u_1u_1^H$ is invertible with

$$(M + u_1u_1^H)^{-1} = U\mathrm{diag}\left\{1, \frac{1}{\lambda_2}, \ldots, \frac{1}{\lambda_n}\right\}U^H.$$

Consequently,

$$(M + u_1u_1^H)^{-1} - u_1u_1^H = U\mathrm{diag}\left\{0, \frac{1}{\lambda_2}, \ldots, \frac{1}{\lambda_n}\right\}U^H.$$

Thus it is easily verified by the definition of the Moore-Penrose inverse that

$$M^+ = (M + u_1u_1^H)^{-1} - u_1u_1^H.$$

To prove Equation (2.2), note first that

$$\begin{aligned} MM^+ = U\Lambda U^HU\Lambda_0H^H = U\Lambda\Lambda_0H^H \quad \text{and} \\ M^+M = U\Lambda_0U^HU\Lambda U^H = U\Lambda_0\Lambda U^H, \end{aligned}$$

where $\Lambda_0 = U\mathrm{diag}\left\{1, \frac{1}{\lambda_2}, \ldots, \frac{1}{\lambda_n}\right\}U^H$. Then, note that

$$\Lambda\Lambda_0 = \Lambda_0\Lambda = \mathrm{diag}\{0, 1, \ldots, 1\}.$$

Thus we have

$$\begin{aligned} MM^+ = M^+M &= U(\mathrm{diag}\{0, 1, \ldots, 1\})U^H \\ &= U(I - \mathrm{diag}\{1, 0, \ldots, 0\})U^H \\ &= UU^H - U\mathrm{diag}\{1, 0, \ldots, 0\}U^H = I - u_1u_1^H. \end{aligned}$$

For Equation (2.3), by the above arguments we have

$$\begin{aligned} u_1u_1^HM^+ &= (U\mathrm{diag}\{1, 0, \ldots, 0\}U^H)\left(U\mathrm{diag}\{0, \frac{1}{\lambda_2}, \ldots, \frac{1}{\lambda_n}\}U^H\right) \\ &= U\mathrm{diag}\{1, 0, \ldots, 0\}\mathrm{diag}\{0, \frac{1}{\lambda_2}, \ldots, \frac{1}{\lambda_n}\}U^H = \mathbf{O}, \end{aligned}$$

as required. ■

According to the properties given in Lemma 2.1, a relation between Moore-Penrose inverses of two Hermitian matrices of nullity-1 which share a common null eigenvector could be established, as given in the following result.

Theorem 2.2. *Let M and M' be two nullity-1 Hermitian $n \times n$ matrices which share a common null eigenvector. Then*

$$(M')^+ = M^+[I + (M' - M)M^+]^{-1}. \tag{2.4}$$

Proof. For the sake of simplicity, set $\Delta := M' - M$ and $\nabla := (M')^+ - M^+$. Then

$$M'(M')^+ = (M + \Delta)(M^+ + \nabla) = MM^+ + M\nabla + \Delta M^+ + \Delta\nabla. \tag{2.5}$$

Let u_1 be the common null eigenvector shared by M and M'. Then by Lemma 2.1, we know that

$$M'(M')^+ = MM^+ = I - u_1u_1^H.$$

Thus, Equation (2.5) gives

$$M\nabla + \Delta M^+ + \Delta\nabla = \mathbf{O},$$

that is,

$$M'\nabla = -\Delta M^+.$$

Left-multiply both sides of the above equation by $(M')^+$, we get

$$(M')^+M'\nabla = -(M')^+\Delta M^+.$$

Bearing in mind that $(M')^+M' = I - u_1u_1^H$ and that $(M')^+ = M^+ + \nabla$, we arrive at

$$(I - u_1u_1^H)\nabla = -(M^+ + \nabla)\Delta M^+,$$

that is,

$$\nabla - u_1u_1^H\nabla = -(M^+ + \nabla)\Delta M^+. \tag{2.6}$$

Since it is shown in Lemma 2.1 that

$$u_1u_1^H(M')^+ = u_1u_1^HM^+ = \mathbf{O},$$

we have

$$u_1u_1^H\nabla = u_1u_1^H[(M')^+ - M^+] = \mathbf{O}.$$

Hence Equation (2.6) becomes

$$\nabla = -M^+\Delta M^+ - \nabla\Delta M^+,$$

or equivalently,

$$\nabla(I + \Delta M^+) = -M^+\Delta M^+.$$

So if $I + \Delta M^+$ is invertible, then by right-multiplying the above equation by $(I + \Delta M^+)^{-1}$, we could obtain

$$\nabla = -M^+\Delta M^+(I + \Delta M^+)^{-1},$$

which yields

$$\begin{aligned}(M')^+ &= M^+ + \nabla = M^+ - M^+\Delta M^+(I + \Delta M^+)^{-1}\\ &= M^+\left[I - \Delta M^+(I + \Delta M^+)^{-1}\right]\\ &= M^+\left[I - (I + \Delta M^+)(I + \Delta M^+)^{-1} + (I + \Delta M^+)^{-1}\right]\\ &= M^+\left[I - I + (I + \Delta M^+)^{-1}\right]\\ &= M^+(I + \Delta M^+)^{-1}\end{aligned}$$

It remains to verify that $I + \Delta M^+$ is invertible. As

$$M^+ = (M + u_1u_1^H)^{-1} - u_1u_1^H,$$

it follows that

$$\begin{aligned}I + \Delta M^+ &= I + \Delta[(M + u_1u_1^H)^{-1} - u_1u_1^H]\\ &= I + \Delta(M + u_1u_1^H)^{-1} - \Delta u_1u_1^H\\ &= I + \Delta(M + u_1u_1^H)^{-1} - (M' - M)u_1u_1^H\\ &= I + \Delta(M + u_1u_1^H)^{-1} - M'u_1u_1^H + Mu_1u_1^H.\end{aligned}$$

Noticing that u_1 is an 0-eigenvalue eigenvector of M and M', it gives that

$$\begin{aligned}I + \Delta M^+ &= (M + u_1u_1^H)(M + u_1u_1^H)^{-1} + \Delta(M + u_1u_1^H)^{-1}\\ &= (M + u_1u_1^H + \Delta)(M + u_1u_1^H)^{-1}\\ &= (M' + u_1u_1^H)(M + u_1u_1^H)^{-1}.\end{aligned}$$

As $M + u_1u_1^H$ is non-singular, by the same reason we know that $M' + u_1u_1^H$ is non-singular, so that $I + \Delta M^+$ is invertible. The proof is complete. ■

Obviously, the Laplacian matrix is a Hermitian matrix. In addition, all the Laplacian matrices of connected graphs of the same order are nullity-1 and share the same eigenvector. Hence, Theorem 2.2 can be directly applied to Laplacian matrices. Let G and G' be weighted connected graphs of order n. As a straightforward consequence of Theorem 2.2, we have

Corollary 2.3. *Let G and G' be connected weighted graphs of order n with Laplacian matrices L and L', respectively. Then*

$$(L')^+ = L^+[I + (L' - L)L^+]^{-1}. \tag{2.7}$$

3. AN APPLICATION TO ELECTRICAL NETWORKS

The Laplacian matrix, also known as the Kirchhoff matrix, or admittance matrix, has wide applications in electrical networks. As introduced in the first section, the resistance distance could be computed in terms of the Moore-Penrose inverse of the Laplacian matrix. Actually, the computation of resistance distances is a classical problem in circuit theory and electrical network theory. Besides, this problem is relevant to a number of problems ranging from Lattice Green's functions, harmonic functions to random walks on graphs. For this reason, many researchers devote themselves to the computation of the resistance distance. With the development of more than 170 years, various formulae and techniques have been established, such as the traditional techniques like series and parallel circuits, Kirchhoff's laws and star-triangle transformation, as well as newly developed techniques like (algebraic, probabilistic, and combinatorial) formulae, local and global sum rules, recursion relations. In [14], a novel recursion formula for computing resistance distance is obtained. It turns out that resistance distances in some networks could be computed very easily by the recursion formula. In addition, the recursion formula extends the famous Rayleigh's monotonicity law by giving quantitative characterization to the law.

In this section, we use Corollary 2.3 to give a new proof to the recursion formula on resistance distances proposed in [14].

Theorem 3.1. *[14] Let G and G' be two weighted graphs which are the same except for the weights on an edge $e = ij$ are w_e and w'_e. For any two vertices p and q, denote the resistance distance between them in G and G' by $\Omega(p, q)$ and $\Omega'(p, q)$, respectively. Then*

$$\Omega'(p,q) = \Omega(p,q) - \frac{\delta\cdot[\Omega(p,i) + \Omega(q,j) - \Omega(p,j) - \Omega(q,i)]^2}{4[1 + \delta\cdot\Omega(i,j)]}, \tag{3.1}$$

where $\delta \equiv w'_e - w_e$.

Proof. Denote the Laplacian matrices of G and G' respectively by L and L', and let $\mathbf{e}$ be the (column) vector of order n whose components are 0 except the i-th and j-th components are respectively 1 and -1. Then

$$L' = L + \delta \cdot \mathbf{e}\mathbf{e}^H.$$

By Corollary 2.3, we have

$$(L')^+ = L^+[I + (L' - L)L^+]^{-1} = L^+(I + \delta \cdot \mathbf{e}\mathbf{e}^H L^+)^{-1}.$$

To compute $(L')^+$, we first compute $(I + \delta \cdot \mathbf{e}\mathbf{e}^H L^+)^{-1}$. Note that the elements of $I + \delta \cdot \mathbf{e}\mathbf{e}^H L^+$ are given by

$$[I + \delta \cdot \mathbf{e}\mathbf{e}^H L^+]_{kl} = \begin{cases} 1, & \text{if } k = l \neq i, j, \\ \delta \cdot (L^+_{il} - L^+_{jl}), & \text{if } k = i \text{ and } l \neq i, \\ 1 + \delta \cdot (L^+_{ii} - L^+_{ji}), & \text{if } k = l = i, \\ -\delta \cdot (L^+_{il} - L^+_{jl}), & \text{if } k = j \text{ and } l \neq j, \\ 1 - \delta \cdot (L^+_{ij} - L^+_{jj}), & \text{if } k = l = j, \\ 0 & \text{otherwise.} \end{cases}$$

Simple algebraic calculation leads to

$$\det(I + \delta \cdot \mathbf{e}\mathbf{e}^H L^+) = 1 + \delta \cdot (L^+_{ii} + L^+_{jj} - 2L^+_{ij}).$$

Then by the adjoint method, we could obtain the inverse of $I + \delta \cdot \mathbf{e}\mathbf{e}^H L^+$, whose elements are given by

$$[(I + \delta \cdot \mathbf{e}\mathbf{e}^H L^+)^{-1}]_{kl} = \begin{cases} 1, & \text{if } k = l \neq i, j, \\ -\dfrac{\delta \cdot (L^+_{il} - L^+_{jl})}{1 + \delta \cdot (L^+_{ii} + L^+_{jj} - 2L^+_{ij})}, & \text{if } k = i \text{ and } l \neq i, \\ 1 - \dfrac{\delta \cdot (L^+_{ii} - L^+_{ji})}{1 + \delta \cdot (L^+_{ii} + L^+_{jj} - 2L^+_{ij})}, & \text{if } k = l = i, \\ \dfrac{\delta \cdot (L^+_{il} - L^+_{jl})}{1 + \delta \cdot (L^+_{ii} + L^+_{jj} - 2L^+_{ij})}, & \text{if } k = j \text{ and } l \neq j, \\ 1 + \dfrac{\delta \cdot (L^+_{ij} - L^+_{jj})}{1 + \delta \cdot (L^+_{ii} + L^+_{jj} - 2L^+_{ij})}, & \text{if } k = l = j \\ 0, & \text{otherwise.} \end{cases}$$

Then, by algebraic calculation, we could obtain the product of L^+ and $(I + \delta \cdot \mathbf{e}\mathbf{e}^t L^+)^{-1}$. Thus, $(L')^+$ is obtained, whose elements are given below. For $1 \leq k, l \leq n$,

$$(L')^+_{kl} = L^+_{kl} - \frac{\delta \cdot (L^+_{ki} - L^+_{kj})(L^+_{il} - L^+_{jl})}{1 + \delta \cdot (L^+_{ii} + L^+_{jj} - 2L^+_{ij})}.$$

Now we are ready to prove Equation (3.1) according to the formula given in Equation (1.1). By Equation (1.1), we have

$$\begin{aligned} \Omega'(p,q) =& (L')^+_{pp} + (L')^+_{qq} - 2(L')^+_{pq} = L^+_{pp} + L^+_{qq} - 2L^+_{pq} \\ & - \frac{\delta \cdot (L^+_{pi} - L^+_{pj})^2 + \delta \cdot (L^+_{qi} - L^+_{qj})^2}{1 + \delta \cdot (L^+_{ii} + L^+_{jj} - 2L^+_{ij})} \\ & - \frac{2\delta \cdot [(L^+_{pi} - L^+_{pj})(L^+_{qi} - L^+_{qj})]}{1 + \delta \cdot (L^+_{ii} + L^+_{jj} - 2L^+_{ij})} \\ =& L^+_{pp} + L^+_{qq} - 2L^+_{pq} - \frac{\delta \cdot [(L^+_{pi} - L^+_{pj})^2 + (L^+_{qi} - L^+_{qj})^2]}{1 + \delta \cdot (L^+_{ii} + L^+_{jj} - 2L^+_{ij})} \\ & - \frac{2\delta \cdot [(L^+_{pi} - L^+_{pj})(L^+_{qi} - L^+_{qj})]}{1 + \delta \cdot (L^+_{ii} + L^+_{jj} - 2L^+_{ij})} \\ =& L^+_{pp} + L^+_{qq} - 2L^+_{pq} - \frac{\delta \cdot (L^+_{pi} - L^+_{pj} - L^+_{qi} + L^+_{qj})^2}{1 + \delta \cdot (L^+_{ii} + L^+_{jj} - 2L^+_{ij})} \\ =& L^+_{pp} + L^+_{qq} - 2L^+_{pq} \\ & - \delta \cdot \frac{\left[\begin{array}{c} (L^+_{pi} - L^+_{pj} - L^+_{qi} + L^+_{qj}) + \frac{1}{2}(L^+_{pp} - L^+_{pp} + L^+_{ii}) \\ -L^+_{ii} + L^+_{qq} - L^+_{qq} + L^+_{jj} - L^+_{jj}) \end{array} \right]^2}{1 + \delta \cdot (L^+_{ii} + L^+_{jj} - 2L^+_{ij})} \\ =& L^+_{pp} + L^+_{qq} - 2L^+_{pq} \\ & - \delta \cdot \frac{\left[\begin{array}{c} (-\frac{1}{2}L^+_{pp} + L^+_{pi} - \frac{1}{2}L^+_{ii}) + (\frac{1}{2}L^+_{pp} - L^+_{pj} + \frac{1}{2}L^+_{jj}) \\ +(\frac{1}{2}L^+_{qq} - L^+_{qi} + \frac{1}{2}L^+_{ii}) + (-\frac{1}{2}L^+_{qq} + L^+_{qj} - \frac{1}{2}L^+_{jj}) \end{array} \right]^2}{1 + \delta \cdot (L^+_{ii} + L^+_{jj} - L^+_{ij} - L^+_{ji})} \\ =& \Omega(p,q) - \frac{\delta \cdot [-\frac{1}{2}\Omega(p,i) + \frac{1}{2}\Omega(p,j) + \frac{1}{2}\Omega(q,i) - \frac{1}{2}\Omega(q,j)]^2}{[1 + \delta \cdot \Omega(i,j)]} \\ =& \Omega(p,q) - \frac{\delta \cdot [\Omega(p,i) + \Omega(q,j) - \Omega(p,j) - \Omega(q,i)]^2}{4[1 + \delta \cdot \Omega(i,j)]}. \end{aligned}$$

The proof is completed. ■

4. CONCLUSION

The Moore-Penrose inverse of the Hermitian matrix has various applications. In this paper, a relation between generalized inverses of two nullity-1 $n \times n$ Hermitian matrices which share a common null eigenvector is established, and a simple application in electrical networks is illustrated. Further applications of the relation needs to be revealed in the future.

DATA AVAILABILITY STATEMENT

The original contributions presented in the study are included in the article/supplementary material, further inquiries can be directed to the corresponding author/s.

AUTHOR CONTRIBUTIONS

All authors listed have made a substantial, direct and intellectual contribution to the work, and approved it for publication.

FUNDING

This research was funded by National Natural Science Foundation of China through grant number 116711347, and Natural Science Foundation of Shandong Province through grant number ZR2019YQ02.

ACKNOWLEDGMENTS

The authors would like to thank the reviewers for their careful reading of the manuscript and valuable suggestions.

REFERENCES

1. Ben-Israel A, Greville TN. Generalized Inverses: Theory and Application. New York, NY: Springer-Verlag (2003).
2. Klein DJ, Randić M. Resistance distance. *J Math Chem*. (1993) **12**:81–95. doi: 10.1007/BF01164627
3. Jiang Z, Yan W. Some two-point resistances of the Sierpinski gasket network. *J Stat Phys*. (2018) **172**:824–31. doi: 10.1007/s10955-018-2067-0
4. Liu Q, Liu J, Wang S. Resistance distance and Kirchhoff index of the corona-vertex and the corona-edge of subdivision graph. *IEEE Access*. (2018) **6**:55673–9. doi: 10.1109/ACCESS.2018.2871840
5. Yang Y, Rosenfeld VR. Some spectral invariants of the neighborhood corona of graphs. *Discrete Appl Math*. (2018) **247**:300–8. doi: 10.1016/j.dam.2018.03.052
6. Barrett W, Evans EJ, Francis AE. Resistance distance in straight linear 2-trees. *Discrete Appl Math*. (2019) **258**:13–34. doi: 10.1016/j.dam.2018.10.043
7. Cao J, Liu J, Wang S. Resistance distances in corona and neighborhood corona networks based on Laplacian generalized inverse approach. *J Alg Appl*. (2019) **18**:1950053. doi: 10.1142/S0219498819500531
8. Carmona, A.; Encinas, A. M.; Mitjana M. Resistance distances in extended or contracted networks. *Linear Alg Appl*. (2019) **576**:5–34. doi: 10.1016/j.laa.2018.01.026
9. Fan J, Zhu J, Tian L, Wang Q. Resistance distance in potting networks. *Phys A*. (2019) **540**:123053. doi: 10.1016/j.physa.2019.123053
10. Hong Y, Zhu Z, Luo A. Extremal graphs with diameter 2 for two indices on resistance-distance. *Discrete Math*. (2019) **342**:487–97. doi: 10.1016/j.disc.2018.10.023
11. Ye L, Yan W. Resistance between two vertices of almost complete bipartite graphs. *Discrete Appl Math*. (2019) **257**:299–306. doi: 10.1016/j.dam.2018.08.030
12. Thulasiraman K, Yadav M, Naik K. Network science meets circuit theory: resistance distance, Kirchhoff index, and Foster's theorems with generalizations and unification. *IEEE Trans Circuits Syst*. (2019) **66**:1090–103. doi: 10.1109/TCSI.2018.2880601
13. Yang Y, Klein DJ. Two-point resistances and random walks on stellated regular graphs. *J Phys A Math Theor*. (2019) **52**:775201. doi: 10.1088/1751-8121/aaf8e7
14. Yang Y, Klein DJ. A recursion formula for resistance distances and its applications. *Discrete Appl Math*. (2013) **161**:2702–15. doi: 10.1016/j.dam.2012.07.015

Conflict of Interest: The authors declare that the research was conducted in the absence of any commercial or financial relationships that could be construed as a potential conflict of interest.

frontiers in Physics

BRIEF RESEARCH REPORT
published: 14 July 2020
doi: 10.3389/fphy.2020.00235

Cluster Synchronization in Delayed Networks With Adaptive Coupling Strength via Pinning Control

Jianbao Zhang[1,2]*, *Zhongjun Ma*[3], *Xiaomei Li*[3] and *Jianlong Qiu*[2]

[1] School of Automation, Southeast University, Nanjing, China, [2] School of Information Science and Engineering, Linyi University, Linyi, China, [3] School of Mathematics and Computing Science, Guilin University of Electronic Technology, Guilin, China

Many previous studies have indicated that pinning control and adaptive feedback control are two of most effective strategies for achieving synchronization. In this paper, we present a mixed method integrating the two control strategies to realize cluster synchronization in delayed networks with directed couplings. Based on Lyapunov stability theory and matrix theory, several criteria on cluster synchronization are obtained. Compared with the previous results on cluster synchronization, the obtained criteria can be applied to delayed network with non-identical nodes, directed couplings, and time-varying coupling strength. Finally, numerical simulations are performed to verify the theoretical results.

Keywords: cluster synchronization, delayed network, pinning control, adaptive control, Lyapunov stability theory

OPEN ACCESS

Edited by:
Muhammad Javaid,
University of Management and Technology, Pakistan

Reviewed by:
Jin Zhou,
Wuhan University, China
Zhaoyan Wu,
Jiangxi Normal University, China

***Correspondence:**
Jianbao Zhang
jianbaozhang@163.com

Specialty section:
This article was submitted to Mathematical and Statistical Physics, a section of the journal Frontiers in Physics

Received: *30 March 2020*
Accepted: *29 May 2020*
Published: *14 July 2020*

Citation:
Zhang J, Ma Z, Li X and Qiu J (2020) Cluster Synchronization in Delayed Networks With Adaptive Coupling Strength via Pinning Control. Front. Phys. 8:235. doi: 10.3389/fphy.2020.00235

1. INTRODUCTION

In the past decade, more and more attention has been attracted to the problem of complex networks, which could be regarded as lots of dynamical nodes coupled with each other. As the result of the complex coupling effect, many different types of collective dynamical behaviors can be realized, such as complete synchronization [1, 2], cluster synchronization [3–5], exponential synchronization [6, 7], intermittent synchronization [8, 9], etc. Cluster synchronization, which is discussed in this paper, implies that the oscillators split into several clusters, and the oscillators in the same cluster synchronize with one another. Many researches have shown that there is a close interplay between cluster synchronization and network topologies. There are also some networks which can not realize a particular type of synchronization only via the inherent coupling effect of oneself. In order to realize cluster synchronization in networks without cluster structures, many various control schemes have been proposed during the past decades, for instance, adaptive feedback control [10, 11], pinning control [12, 13], intermittent control [14], and so on. The control approaches concerned in this paper are the famous pinning control and adaptive feedback control, both have been intensively investigated recently. First, we make a brief introduction to the background and related work of pinning control. Generally speaking, the node number of each complex network in the real world may be the massive level, and it is hard to control all nodes to realize a particular type of synchronization. In order to reduce the control gain and the number of controllers, pinning control is proposed as a more effective control approach [13]. The advantage of the pinning control approach is that it is only necessary to control a significantly smaller number of local controllers as compared to the randomly pinning scheme. Since the idea of pinning control was first developed, researchers concentrate their efforts on the popularization and application of the control approach [15–20]. For instance, by using the Schur complement and Lyapunov stability

theory, several pinning schemes were designed to realize lag synchronization between two coupled networks in [15]. It is also shown that a directed network can realize pinning synchronization in [17]. Pinning control scheme was also applied to drive a directed dynamical network with non-identical nodes to cluster synchronization [18]. Similarly, the intermittent pinning-control problem of directed heterogeneous dynamical networks has also been discussed in [19]. Second, it is worth to point out that adaptive control scheme is a feasible approach to avoid larger feedback control gains. Notice that the coupling strength of many real network can not be arbitrarily large, adaptive feedback control should be a valid method for achieving synchronization. During the recent years, researchers have made some great achievements on adaptive feedback control. In [21], cluster synchronization of an adaptive dynamical network with non-identical nodes was discussed.

Motivated by the discussions above, this paper aims to provide several novel criteria on cluster synchronization of complex networks with adaptive coupling strength via pinning control. We carry out a new dynamical network model possessing four characteristics, i.e., delayed dynamics, non-identical nodes, directed topology and time-varying coupling strength. To the best of our knowledge, there is no previous research discussing the problem of cluster synchronization of such a network model. However, the problem mentioned above should be an important issue of complex networks because of its wide applications in practical problems. Then we design proper pinning controllers and adaptive coupling strength, and sufficient conditions are derived to realize cluster synchronization by using Lyapunov stability theory and matrix theory. In order to illustrate the feasibility and validity of the obtained theoretical results, several numerical simulations are presented.

The rest of this paper is designed as follows. The network model is described and some necessary lemmas and assumptions are stated in section 2. Via pinning and adaptive controls, cluster synchronization in a delayed network is discussed and then some sufficient conditions are given in section 3. Numerical examples are obtained in section 4. Finally, in section 5, conclusions are presented.

2. MODEL DESCRIPTION AND PRELIMINARIES

Consider a network consisting of N nodes, which are divided into m communities $C_1, C_2, \ldots, C_m$, where $2 \leq m \leq N$. It is easy to see that there holds $\cup_{i=1}^{m} C_i = \{1, 2, \cdots, N\}$. If the ith node belongs to the jth cluster, then we define $\phi_i = j$. The function $f_{\phi_i} : R^n \to R^n$ can be employed to describe the local dynamics of each node in the ith cluster.

Now, we consider a delayed dynamic network described by the following equations,

$$\dot{x}_i(t) = f_{\phi_i}(t, x_i(t), x_i(t-\tau)) + \delta_i(t) \sum_{j=1}^{N} a_{ij} \Gamma x_j(t), \quad i = 1, 2, \cdots, N, \tag{1}$$

where $x_i(t) = (x_{i1}(t), x_{i2}(t), \cdots, x_{in}(t))^{\mathrm{T}} \in R^n$ is the state variable of node i; f_{ϕ_i} is differentiable and capable of performing abundant dynamical behaviors. If $\phi_i \neq \phi_j$, i.e., the ith node and the jth node belong to different clusters, then $f_{\phi_i} \neq f_{\phi_j}$. $\delta_i(t) > 0$ is a time-varying coupling strength. $\tau > 0$ is a constant. $\delta_i(t)$ is the time-varying coupling strength. $\Gamma \in R^{n \times n}$ is an inner-coupling matrix. For simplicity, we suppose that Γ is a positive definite diagonal matrix, that is, $\Gamma = diag(\rho_1, \rho_2, \ldots, \rho_n)$ with $\rho_i > 0$. The asymmetric matrix $A = (a_{ij})_{N \times N}$ describes the topology of the directed network, where $a_{ij} \geq 0, i \neq j$, is the weight of the edge from j to i. Here, the coupling matrix A is supposed to be diffusive, that is, a_{ii} are defined as $a_{ii} = -\sum_{j=1, j \neq i}^{N} a_{ij}, i = 1, 2, \cdots, N$.

At first, we give an assumption about the function f_{ϕ_i}, which has been widely employed in the previous researches on the problem of synchronization in complex networks. Most of the previous researches pointed out that many well-known chaotic systems have been checked to satisfy the following assumption, such as cellular neural networks and Chua's circuit [22].

Assumption 1 ([23]). For the vector-valued function $f_{\phi_i}(t, z_1, \bar{z}_1)$, there exist a constant L such that

$$\begin{aligned} &(z_1 - z_2)^T (f_{\phi_i}(t, z_1, \bar{z}_1) - f_{\phi_i}(t, z_2, \bar{z}_2)) \\ &\leq L((z_1 - z_2)^T (z_1 - z_2) + (\bar{z}_1 - \bar{z}_2)^T (\bar{z}_1 - \bar{z}_2)) \end{aligned}$$

for any $z_1, z_2, \bar{z}_1, \bar{z}_2 \in R^n, i = 1, 2, \ldots, N$.

By introducing the control inputs $u_i(t) \in R^n (i = 1, 2, \ldots, N)$, the controlled dynamical network with respect to the network (1) can be rewritten as

$$\begin{aligned} \dot{x}_i(t) = f_{\phi_i}(t, x_i(t), x_i(t-\tau)) + \delta_i(t) \sum_{j=1}^{N} a_{ij} \Gamma x_j(t) + u_i(t), \\ i = 1, 2, \ldots, N. \end{aligned} \tag{2}$$

Definition 1. Let $s_{\phi_i}(t) = s_{\phi_i}(t, t_0, s_0)$ be the solution of the following system

$$\dot{s}_{\phi_i}(t) = f_{\phi_i}(t, s_{\phi_i}(t), s_{\phi_i}(t-\tau)), \quad i = 1, 2, ..., N. \tag{3}$$

Defining the error variables by $e_i(t) = x_i(t) - s_{\phi_i}(t)$, $i = 1, 2, \ldots, N$, the oscillator network (2) is said to realize cluster synchronization, if the synchronization errors satisfy

$$\lim_{t \to +\infty} e_i(t) = 0, \quad i = 1, 2, \cdots N.$$

The following error system can be concluded from the Equations (2) and (3),

$$\begin{aligned} \dot{e}_i(t) = &f_{\phi_i}(t, x_i(t), x_i(t-\tau)) - f_{\phi_i}(t, s_{\phi_i}(t), s_{\phi_i}(t-\tau)) \\ &+ \delta_i(t) \sum_{j=1}^{N} a_{ij} \Gamma e_j(t) + \delta_i(t) \sum_{j=1}^{N} a_{ij} \Gamma s_{\phi_j}(t) + u_i(t), \\ &i = 1, 2, \cdots N. \end{aligned} \tag{4}$$

According to the definition of the diffusive coupling matrix A, one obtains that $\sum_{j=1}^{N} a_{ij} \Gamma s_{\phi_j}(t) = 0$ for $i \in G_{\phi_i} - \bar{G}_{\phi_i}$, where G_{ϕ_i}

denotes the index set consisting of all nodes in the ϕ_ith cluster and $\bar{G}_{\phi_i}$ represents the index set consisting of all nodes in the ϕ_ith cluster which have direct connections with some nodes in other clusters. In view of this property, the pinning controller is designed as

$$u_i(t) = -\theta_i\delta_i(t)d_i\Gamma(e_i(t)+e_i(t-\tau))-\theta_i\delta_i(t)\sum_{j=1}^{N}a_{ij}\Gamma s_{\phi_j}(t), \quad (5)$$

where $\theta_i = 1$ for $i \in \bar{G}_{\phi_i,}$ or $\theta_i = 0$ for $i \in G_{\phi_i} - \bar{G}_{\phi_i}$, and $d_i > 0$. The coupling strengths $\delta_i(t)$ are constructed by the following adaptive laws

$$\dot{\delta}_i(t) = \gamma_t\sigma_i e_i^T(t)\Gamma e_i(t), i = 1, 2, \cdots, N, \quad (6)$$

where the constant $\sigma_i > 0$ is the control gain, $\delta_i(0) > 0$, the $0-1$ switching function γ_t is defined as follows,

$$\gamma_t = \begin{cases} 1, & 0 < t \leq \mathrm{T}, \\ 0, & t > \mathrm{T}, \end{cases}$$

T is a positive constant. Here, $u_i(t)$ and $\delta_i(t)$ are different from the corresponding functions of the previous papers, such as [3, 12, 14, 21]. It is easy to see that each node in the network has a different coupling strength. By intuition, the first term in the controller (5) is used to synchronize all nodes in the same cluster, while the second term in the controller (5) is to weaken the influences of the couplings among different clusters.

Remark: The controller (5) only works on the nodes which have direct connections with some nodes in other clusters since $u_i(t) = 0$ for $i \in G_{\phi_i} - \bar{G}_{\phi_i}$. That is to say, only the nodes which have direct connections with some nodes in other clusters need to be pinned. In addition, the coupling strengths $\delta_i(t)$ are constructed by the adaptive laws. Therefore, the controller (5) is an pinning controller with adaptive strength.

3. SUFFICIENT CONDITIONS ON REALIZING CLUSTER SYNCHRONIZATION

In this section, the problem of cluster synchronization in delayed networks will be investigated by designing proper pinning controllers and adaptive coupling strength. Based on Lyapunov functional method and matrix theory, the following theorem is established.

Theorem 1. Let $\delta_i \triangleq \delta_i(t)$. Under Assumption 1, if there exists a positive definite matrix Q, such that the matrix H_1 is negative definite for $t \leq \mathrm{T}$, and the matrix H_2 is negative definite for $t > \mathrm{T}$, where

$$H_1 = \begin{pmatrix} LI_N \otimes I_n + (U-F)\otimes\Gamma + I_N \otimes Q - W \otimes \Gamma & -\frac{1}{2}(F\otimes\Gamma) \\ -\frac{1}{2}(F\otimes\Gamma) & LI_N \otimes I_n - I_N \otimes Q \end{pmatrix},$$

$$H_2 = \begin{pmatrix} LI_N \otimes I_n + (U-F)\otimes\Gamma + I_N \otimes Q & -\frac{1}{2}(F\otimes\Gamma) \\ -\frac{1}{2}(F\otimes\Gamma) & LI_N \otimes I_n - I_N \otimes Q \end{pmatrix},$$

$I_N(I_n)$ is the $N(n)$-dimensional identity matrix, $U = \frac{1}{2}(B + B^T)$,

$$B = \begin{pmatrix} \delta_1 a_{11} & \cdots & \frac{1}{2}(\delta_1 a_{1N} + \delta_N a_{N1}) \\ \vdots & \ddots & \vdots \\ \frac{1}{2}(\delta_N a_{N1} + \delta_1 a_{1N}) & \cdots & \delta_N a_{NN} \end{pmatrix},$$

$$F = diag(\theta_1\delta_1 d_1, \theta_2\delta_2 d_2, \cdots, \theta_N\delta_N d_N),$$

$$W = diag(\delta_1(\mathrm{T}) - \delta_1, \delta_2(\mathrm{T}) - \delta_2, \cdots, \delta_N(\mathrm{T}) - \delta_N),$$

then, by the local control (5) and the corresponding adaptive laws (6), the solutions $e_1(t), e_2(t), \ldots, e_N(t)$ of the system (4) satisfy $\lim_{t\to+\infty} e_i(t) = 0, i = 1, 2, \ldots, N$. That is, cluster synchronization in the network system (2) is realized.

Proof. Let

$$V(t) = \frac{1}{2}\sum_{i=1}^{N} e_i^T(t)e_i(t) + \sum_{i=1}^{N}\int_{t-\tau}^{t} e_i^T(s)Qe_i(s)ds + \sum_{i=1}^{N}\frac{1}{2\sigma_i}(\delta_i(\mathrm{T}) - \delta_i(t))^2.$$

Apparently, $V(t) = 0$ if and only if $e_i(t) \equiv 0, t \in [t-\tau, t]$ and $\delta_i(\mathrm{T}) - \delta_i(t) = 0$. Then, the derivate of $V(t)$ along the solution of error system (4) under control (5) is

$$\begin{aligned}
\dot{V}(t) =& \frac{1}{2}\sum_{i=1}^{N}\dot{e}_i^T(t)e_i(t) + \frac{1}{2}\sum_{i=1}^{N} e_i^T(t)\dot{e}_i(t) + \sum_{i=1}^{N} e_i^T(t)Qe_i(t) \\
&- \sum_{i=1}^{N} e_i^T(t-\tau)Qe_i(t-\tau) - \sum_{i=1}^{N}\frac{1}{\sigma_i}(\delta_i(\mathrm{T}) - \delta_i(t))\dot{\delta}_i(t) \\
=& \sum_{i=1}^{N} e_i^T(t)(f_{\phi_i}(t, x_i(t), x_i(t-\tau)) - f_{\phi_i}(t, s_{\phi_i}(t), s_{\phi_i}(t-\tau))) \\
&+ \frac{1}{2}\sum_{i=1}^{N} e_i^T(t)\sum_{j=1}^{N}(\delta_i(t)a_{ij} + \delta_j(t)a_{ji})\Gamma e_j(t) \\
&- \sum_{i=1}^{N} e_i^T(t)\theta_i\delta_i(t)d_i\Gamma e_i(t) - \sum_{i=1}^{N} e_i^T(t)\theta_i\delta_i(t)d_i\Gamma e_i(t-\tau) \\
&+ \sum_{i=1}^{N} e_i^T(t)Qe_i(t) - \sum_{i=1}^{N} e_i^T(t-\tau)Qe_i(t-\tau) \\
&- \sum_{i=1}^{N}\gamma_t(\delta_i(\mathrm{T}) - \delta_i(t))e_i^T(t)\Gamma e_i(t).
\end{aligned}$$

Denoting $e(t) = (e_1^T(t), e_2^T(t), \ldots, e_N^T(t))^T$, we obtain

$$e^T(t)(B\otimes\Gamma)e(t) = e^T(t)(B^T\otimes\Gamma)e(t).$$

That is, for $U = \frac{1}{2}(B + B^T)$, we have

$$e^T(t)(B\otimes\Gamma)e(t) = e^T(t)(U\otimes\Gamma)e(t).$$

According to Assumption 1, we have

$$\begin{aligned}\dot{V}(t) \leq & \sum_{i=1}^{N} L({e_i}^T(t)e_i(t) + {e_i}^T(t-\tau)e_i(t-\tau)) \\ & +e^T(t)(B\otimes\Gamma)e(t) - e^T(t)(F\otimes\Gamma)e(t) \\ & -e^T(t)(F\otimes\Gamma)e(t-\tau) + e^T(t)(I_N\otimes Q)e(t) \\ & -e^T(t-\tau)(I_N\otimes Q)e(t-\tau) - e^T(t)(\gamma_t W\otimes\Gamma)e(t) \\ = & \, e^T(t)(LI_N\otimes I_n)e(t) + e^T(t-\tau)(LI_N\otimes I_n)e(t-\tau) \\ & +e^T(t)U\otimes\Gamma)e(t) - e^T(t)(F\otimes\Gamma)e(t) \\ & -e^T(t)(F\otimes\Gamma)e(t-\tau) + e^T(t)(I_N\otimes Q)e(t) \\ & -e^T(t-\tau)(I_N\otimes Q)e(t-\tau) - e^T(t)(\gamma_t W\otimes\Gamma)e(t) \\ = & \, e^T(t)(LI_N\otimes I_n + (U-F)\otimes\Gamma + I_N\otimes Q - \gamma_t W\otimes\Gamma)e(t) \\ & -e^T(t)(F\otimes\Gamma)e(t-\tau) + e^T(t-\tau)(LI_N\otimes I_n) \\ & (-I_N\otimes Q)e(t-\tau).\end{aligned}$$

Denote $\eta^T(t) = (e^T(t), e^T(t-\tau))$. For $t \leq \mathrm{T}$, $\gamma_t = 1$, that is $\dot{\delta}_i(t) = \sigma_i e_i^T(t)\Gamma e_i(t)$. Therefore, we have

$$\begin{aligned}\dot{V}(t) \leq & \, e^T(t)(LI_N\otimes I_n + (U-F)\otimes\Gamma + I_N\otimes Q - W\otimes\Gamma)e(t) \\ & -e^T(t)(F\otimes\Gamma)e(t-\tau) + e^T(t-\tau)(LI_N\otimes I_n - I_N\otimes Q) \\ & e(t-\tau) \\ = & \, \eta^T(t)H_1\,\eta(t).\end{aligned}$$

Because of $H_1 < 0$, we know that $\dot{V}(t) \leq 0$, and the equality holds if and only if $e_i(t) = 0$ and $e_i(t-\tau) = 0$ for $i = 1, 2, \ldots, N$. For $t > \mathrm{T}$, $\gamma_t = 0$, that is $\dot{\delta}_i(t) = 0$. Then we obtain

$$\begin{aligned}\dot{V}(t) \leq & \, e^T(t)(LI_N\otimes I_n + (U-F)\otimes\Gamma + I_N\otimes Q)e(t) \\ & -e^T(t)(F\otimes\Gamma)e(t-\tau) + e^T(t-\tau)(LI_N\otimes I_n - I_N\otimes Q) \\ & e(t-\tau). \\ = & \, \eta^T(t)H_2\,\eta(t).\end{aligned}$$

As $H_2 < 0$, we know that $\dot{V}(t) \leq 0$, and the equality holds if and only if $e(t) = 0$ and $e_i(t-\tau) = 0$ for $i = 1, 2, \ldots, N$.

Therefore, the solutions $e_1(t), e_2(t), \ldots, e_N(t)$ of the system (4) satisfy $\lim_{t\to+\infty} e_i(t) = 0$ for $i = 1, 2, \ldots, N$. Thus, cluster synchronization in the network system (2) is realized under the local control (5) and the corresponding adaptive laws (6).

Let $Q = \Gamma = I_n$, we obtain the following corollary.

Corollary 1. Let $\delta_i \triangleq \delta_i(t)$. Under Assumption 1, if $\Gamma = I$, H_3 is negative definite for $t \leq \mathrm{T}$, and H_4 is negative definite for $t > \mathrm{T}$, where

$$H_3 = \begin{pmatrix} (L+1)I_N + U - F - W & -\frac{1}{2}F \\ -\frac{1}{2}F & (L-1)I_N \end{pmatrix},$$

$$H_4 = \begin{pmatrix} (L+1)I_N + U - F & -\frac{1}{2}F \\ -\frac{1}{2}F & (L-1)I_N \end{pmatrix},$$

$I_N(I_n)$ is the $N(n)$-dimensional identity matrix, $U = \frac{1}{2}(B + B^T)$,

$$B = \begin{pmatrix} \delta_1 a_{11} & \cdots & \frac{1}{2}(\delta_1 a_{1N} + \delta_N a_{N1}) \\ \vdots & \ddots & \vdots \\ \frac{1}{2}(\delta_N a_{N1} + \delta_1 a_{1N}) & \cdots & \delta_N a_{NN} \end{pmatrix},$$

$F = diag(\theta_1\delta_1 d_1, \theta_2\delta_2 d_2, \cdots, \theta_N\delta_N d_N)$, $W = diag(\delta_1(\mathrm{T}) - \delta_1, \delta_2(\mathrm{T}) - \delta_2, \cdots, \delta_N(\mathrm{T}) - \delta_N)$, then, by the local control (5) and the corresponding adaptive laws (6), the solutions $e_1(t), e_2(t), \ldots, e_N(t)$ of the system (4) satisfy

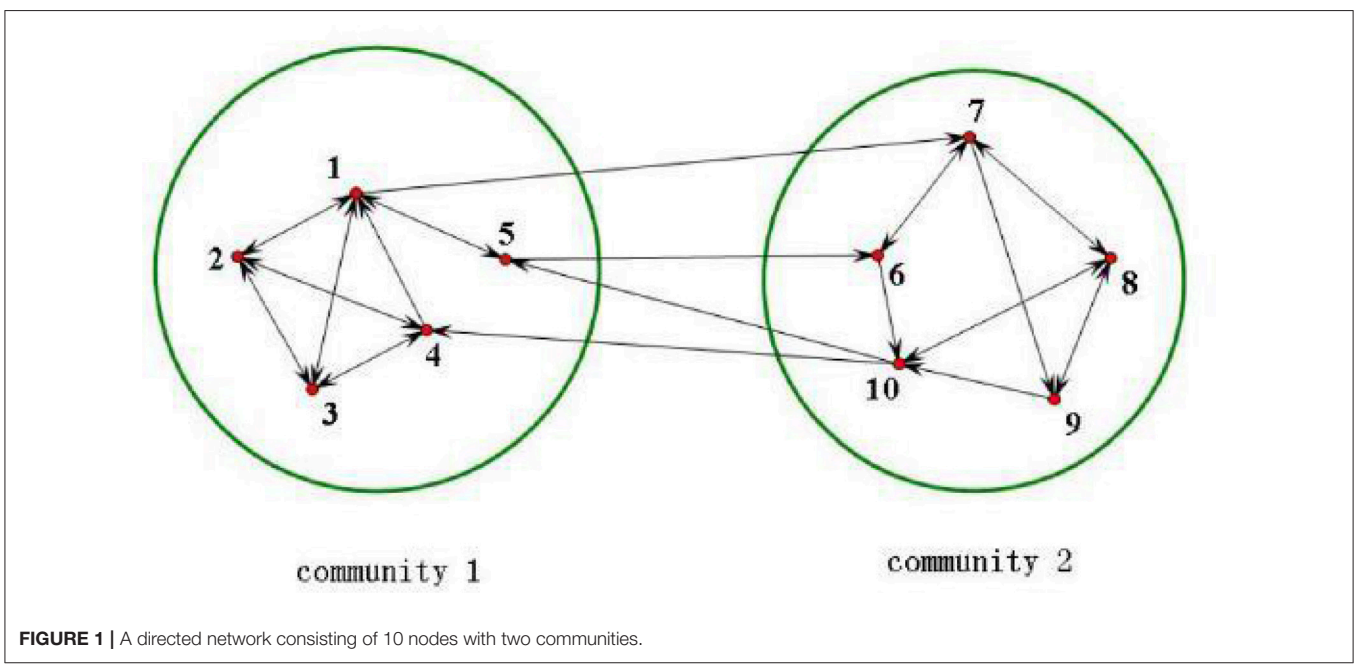

FIGURE 1 | A directed network consisting of 10 nodes with two communities.

$\lim_{t\to+\infty} e_i(t) = 0, i = 1, 2, \ldots, N$. That is, cluster synchronization in the network system (2) is realized.

4. NUMERICAL SIMULATIONS

In this section, we give a numerical example to verify the theorem given in the previous section.

Consider a directed network consisting of 10 nodes with two communities, the topological structure of which is shown in **Figure 1**. Choose the node dynamics of the five nodes in the first cluster as the time-delayed Chua's circuit, which is described by the following equations,

$$\dot{x}_i(t) = f_1(t, x_i(t), x_i(t-\tau)) = V_1 x_i(t) + w(x_i(t)) + v(x_i(t-\tau)), \tag{7}$$

where $x_i(t) = (x_{i1}(t), x_{i2}(t), x_{i3}(t))^T$, $w(x_i(t)) = (\frac{2}{7}x_{i1}(t) - \frac{3}{14}(|x_{i1}(t)+1| - |x_{i1}(t)-1|), 0, 0)^T$, and $v(x_i(t-\tau)) = 0.3(x_{i1}(t-\tau), 0, 0)^T$, $i = 1, 2, \ldots, 5$. Choose the node dynamics of the five nodes in the second cluster as the time-delayed 3-D neural network which is described by the following equations,

$$\dot{x}_i(t) = f_2(t, x_i(t), x_i(t-\tau)) = -I_3 x_i(t) + V_2 g(x_i(t)) + h(x_i(t-\tau)), \tag{8}$$

where $x_i(t) = (x_{i1}(t), x_{i2}(t), x_{i3}(t))^T$, $g(x_i(t)) = ((|x_{i1}(t)+1| - |x_{i1}(t)-1|)/2, (|x_{i2}(t)+1| - |x_{i2}(t)-1|)/2, (|x_{i3}(t)+1| - |x_{i3}(t)-1|)/2)^T$, $h(x_i(t-\tau)) = 0.3(x_{i1}(t-\tau), 0, 0)^T$, $i = 6, 7, \cdots, 10$.

Matrices V_1 and V_2 are, respectively, defined by

$$V_1 = \begin{pmatrix} 0 & 9 & 0 \\ 1 & -1 & 1 \\ 0 & -14.3 & 0 \end{pmatrix}, V_2 = \begin{pmatrix} 1.25 & -3.2 & -3.2 \\ -3.2 & 1.1 & -4.4 \\ -3.2 & -4.4 & 1 \end{pmatrix}.$$

Recalling that $\bar{G}_{\phi_i}$ denotes the set consisting of all nodes in the ϕ_ith cluster which have direct connections to the nodes in other clusters. It is easy to see that $\bar{G}_1 = \{1, 5\}$, $\bar{G}_2 = \{10\}$ and

$$A = \begin{pmatrix} -4 & 1 & 1 & 0 & 1 & 0 & 1 & 0 & 0 & 0 \\ 1 & -3 & 1 & 1 & 0 & 0 & 0 & 0 & 0 & 0 \\ 1 & 1 & -3 & 1 & 0 & 0 & 0 & 0 & 0 & 0 \\ 1 & 1 & 1 & -3 & 0 & 0 & 0 & 0 & 0 & 0 \\ 1 & 0 & 0 & 0 & -2 & 1 & 0 & 0 & 0 & 0 \\ 0 & 0 & 0 & 0 & 0 & -2 & 1 & 0 & 0 & 1 \\ 0 & 0 & 0 & 0 & 0 & 1 & -3 & 1 & 1 & 0 \\ 0 & 0 & 0 & 0 & 0 & 0 & 1 & -3 & 1 & 1 \\ 0 & 0 & 0 & 0 & 0 & 0 & 0 & 1 & -2 & 1 \\ 0 & 0 & 0 & 1 & 1 & 0 & 0 & 1 & 0 & -3 \end{pmatrix}.$$

According to the discussion in [18] and some simple calculations, Assumption 1 is satisfied for systems (7) and (8). And then we obtain $L = 21$. Let $\sigma_i = 2, \mathrm{T} = 2, \delta_i(0) = 15, \tau = 0.2, d_1 = d_5 = d_{10} = 20, d_2 = d_3 = d_4 = d_6 = d_7 = d_8 = d_9 = 0, \Gamma = 12I_3, Q = 22I_3$. It is easy to verify that $H_1 < 0$ for $0 \le t \le 2$ and $H_2 < 0$ for $t > 2$.

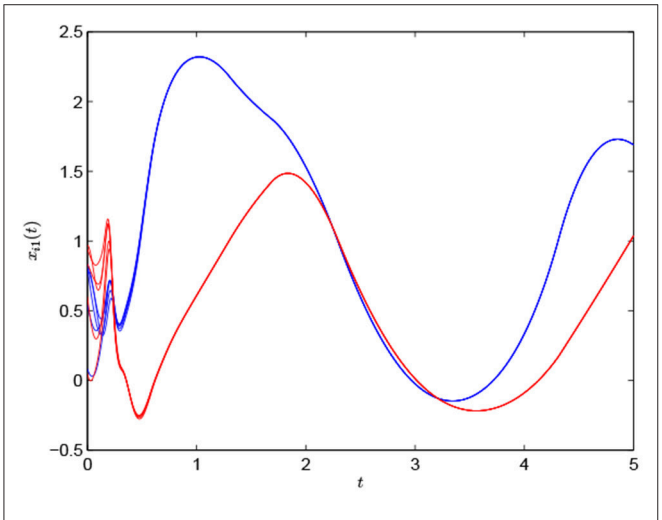

FIGURE 2 | The time evolution of the first component x_{i1} in the ith oscillator, $i = 1, \ldots, 10$.

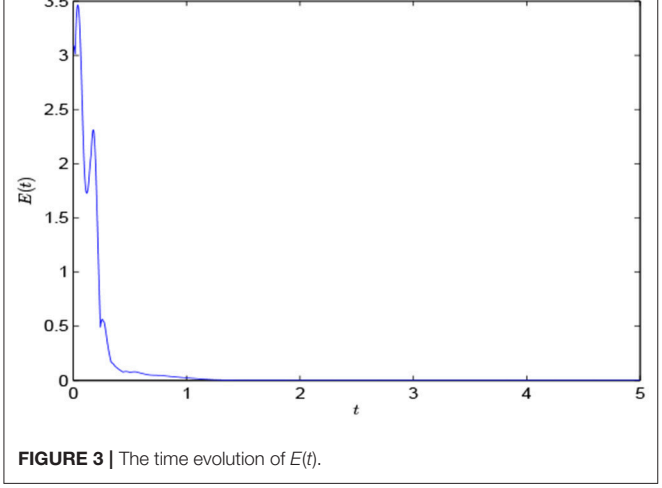

FIGURE 3 | The time evolution of $E(t)$.

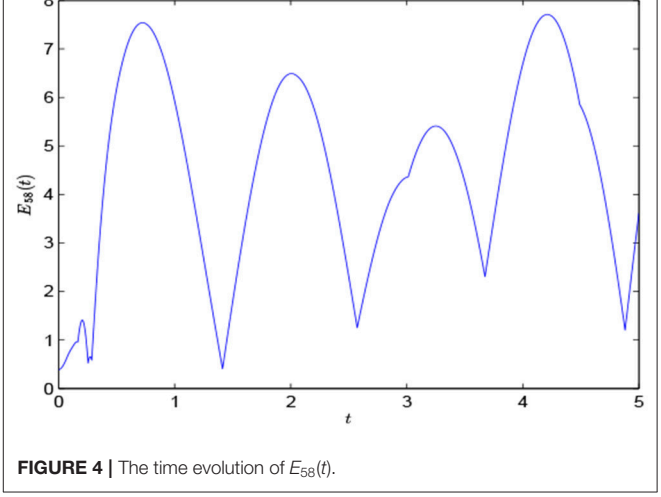

FIGURE 4 | The time evolution of $E_{58}(t)$.

Let the state of the Chua's circuit under initial condition be $s_1(t) = (-0.1, -0.2, -0.3)^T$, $t \in [-0.2, 0]$, and the state of the 3-D neural network under initial condition be $s_2(t) = (0.1, 0.2, 0.3)^T$, $t \in [-0.2, 0]$. Initial states of all nodes are constant functions on $[-0.2, 0]$. Here, the values of the initial constant functions are randomly chosen on $[-1, 1]$. Now we define $E(t) = \sum_{i=1}^{10} |x_i(t) - s_{\phi_i}(t)|$, $E_{ij}(t) = |x_i(t) - x_j(t)|, i = 1, 2, \ldots, 5, j = 6, \ldots, 10$, where the norm $|\cdot|$ of vector x is defined as $|x| = (x^T x)^{1/2}$. It is clear that the cluster synchronization is achieved if $E(t)$ converges to zero and $E_{ij}(t)$ do not converge to zero as $t \to +\infty$.

By the aid of Matlab, we obtain **Figure 2**, which shows the time evolutions of the component x_{i1}, $i = 1, \ldots, 10$. In **Figure 2**, the red lines represent the first five nodes, and the blue lines represent the latter five nodes. **Figures 3**, **4** show the time evolutions of $E(t)$ and $E_{58}(t)$, respectively. It is easy to see that the error $E(t)$ tends to zero, but E_{58} doesn't tend to zero when $t \to +\infty$. That is to say, 2-cluster synchronization is achieved, and the effectiveness of the theoretic results is verified.

5. CONCLUSIONS

In this paper, the problem of cluster synchronization in a complex network via pinning control has been investigated, and several novel criteria have been derived by utilizing the matrix theory and the stability analysis technique. The object of this research is a dynamical network possessing four characteristics, delayed dynamics, non-identical nodes, directed topology and time-varying coupling strength. And from the control schemes of this research, we present a novel mixed method, which integrated the pinning control and adaptive feedback control, to design proper pinning controllers and adaptive coupling strengths to realize cluster synchronization in such a dynamical network. For convenience, we also carried out a succinct and utilitarian corollary by simplifying the obtained conditions. Finally, numerical simulations are provided to illustrate the effectiveness of the proposed control methods.

DATA AVAILABILITY STATEMENT

The original contributions presented in the study are included in the article/supplementary material, further inquiries can be directed to the corresponding author/s.

AUTHOR CONTRIBUTIONS

JZ performed the theory derivation and wrote the first draft of the paper. ZM and XL provided the numerical experiments and contributed to the modification of this paper. JQ revised the first draft and made many helpful suggestions, which improve this paper greatly. All authors contributed to the article and approved the submitted version.

FUNDING

This work was supported by Natural Science Foundation of Guangxi Province (No. 2018GXNSFAA281068), Jiangsu Planned Projects for Postdoctoral Research Funds (No. 1701017A) and National Natural Science Foundation of China (Nos. 61877033, 11662001, and 11447005).

REFERENCES

1. Li CG, Chen GR. Synchronization in general complex dynamical networks with coupling delays. *Physica A.* (2004) **343**:263–78. doi: 10.1016/j.physa.2004.05.058
2. Daniel G, Birce O, Alyssa D, Hund TJ. Synchronization of pacemaking in the sinoatrial node: a mathematical modeling study. *Front Phys.* (2018) **6**:63. doi: 10.3389/fphy.2018.00063
3. Qin J, Fu W, Shi Y, Gao H, Kang Y. Leader-following practical cluster synchronization for networks of generic linear systems: an event-based approach. *IEEE T Neur Net Learn.* (2018) **30**:215–24. doi: 10.1109/TNNLS.2018.2817627
4. Blaha KA, Huang K, Rossa FD, Pecora L, Hossein-Zadeh M, Sorrentino F. Cluster synchronization in multilayer networks: a fully analog experiment with LC oscillators with physically dissimilar coupling. *Phys Rev Lett.* (2019) **122**:014101. doi: 10.1103/PhysRevLett.122.014101
5. Zhang JB, Ma ZJ, Chen GR. Robustness of cluster synchronous patterns in small-world networks with inter-cluster co-competition balance. *Chaos.* (2014) **24**:440–67. doi: 10.1063/1.4873524
6. Liu YJ, Guo BZ, Park JH, Lee SM. Nonfragile exponential synchronization of delayed complex dynamical networks with memory sampled-data control. *IEEE T Neur Net Learn.* (2018) **29**:118–28. doi: 10.1109/TNNLS.2016.2614709
7. Yang CD, Qiu JL, He HB. Exponential synchronization for a class of complex spatio-temporal networks with space-varying coefficients. *Neurocomputing.* (2015) **151**:401–7. doi: 10.1016/j.neucom.2014.09.025
8. Rubchinsky LL, Sungwoo A, Choongseok P. Dynamics of desynchronized episodes in intermittent synchronization. *Front Phys.* (2014) **2**:38. doi: 10.3389/fphy.2014.00038
9. Cai SM, Lei XQ, Liu ZR. Outer synchronization between two hybrid-coupled delayed dynamical networks via aperiodically adaptive intermittent pinning control. *Complexity.* (2016) **21**:593–605. doi: 10.1002/cplx.21837
10. Wu ZY, Xu XJ, Chen GR, Fu XC. Adaptive synchronization and pinning control of colored networks. *Chaos.* (2012) **22**:043137. doi: 10.1063/1.4769991
11. Pham VT, Vaidyanathan S, Volos C, Jafari S, Alsaadi FE, Alsaadi FE. Chaos in a simple snap system with only one nonlinearity, its adaptive control and real circuit design. *Arch Control Sci.* (2019) **29**:73–96. doi: 10.24425/acs.2019.127524
12. Liu ZX, Chen ZQ, Yuan ZZ. Pinning control of weighted general complex dynamical networks with delay. *Phsica A.* (2007) **375**:345–54. doi: 10.1016/j.physa.2006.09.009
13. Wang XF, Chen GR. Pinning control of scale-free dynamical networks. *Physica A.* (2002) **310**:521–31. doi: 10.1016/S0378-4371(02)00772-0
14. Xia WG, Cao JD. Pinning synchronization of delayed dynamical networks via periodically intermittent control. *Chaos.* (2009) **19**:013120. doi: 10.1063/1.3071933
15. Sun WG, Wang S, Wang GH, Wu YQ. Lag synchronization via pinning control between two coupled networks. *Nonlinear Dyn.* (2015) **79**:2659–66. doi: 10.1007/s11071-014-1838-7
16. DeLellis P, Garofalo F, Iudice FL. The partial pinning control strategy for large complex networks. *Automatica.* (2018) **89**:111–6. doi: 10.1016/j.automatica.2017.11.025
17. Nian FZ, Wang XY. Optimal pinning synchronization on directed complex network. *Chaos.* (2011) **21**:043131. doi: 10.1063/1.3665699
18. Wang G, Shen Y. Cluster synchronization of directed complex dynamical networks with nonidentical nodes via pinning control. *Int J Syst Sci.* (2012) **10**:1–10. doi: 10.1080/00207721.2012.659699

19. Cai SM, Jia Q, Liu ZR. Cluster synchronization for directed heterogeneous dynamical networks via decentralized adaptive intermittent pinning control. *Nonlinear Dynam.* (2015) **82**:689–702. doi: 10.1007/s11071-015-2187-x
20. Sun W, Sun M, Guan J, Jia Q. Robustness of coherence in noisy scale-free networks and applications to identification of influential spreaders. *IEEE Trans Circ II Express Briefs*. (2020) **67**:1274–8. doi: 10.1109/TCSII.2019.2929139
21. Wu XJ, Lu HT. Cluster synchronization in the adaptive complex dynamical networks via a novel approach. *Phys Lett A*. (2011) **375**:1559–65. doi: 10.1016/j.physleta.2011.02.052
22. Zhou J, Lu JA, Lv JH. Pinning adaptive synchronization of a general complex dynamical network. *Automatica.* (2008) **44**:996–1003. doi: 10.1016/j.automatica.2007.08.016
23. Hu C, Yu J, Jiang HJ, Teng ZD. Pinning synchronization of weighted complex networks with variable delays and adaptive coupling weights. *Nonlinear Dynam.* (2012) **67**:1373–85. doi: 10.1007/s11071-011-0074-7

Conflict of Interest: The authors declare that the research was conducted in the absence of any commercial or financial relationships that could be construed as a potential conflict of interest.

frontiers in Computational Neuroscience

ORIGINAL RESEARCH
published: 21 July 2020
doi: 10.3389/fncom.2020.00058

Cancer Risk Analysis Based on Improved Probabilistic Neural Network

Chaoyu Yang[1*†], *Jie Yang*[2†], *Ying Liu*[1] *and Xianya Geng*[3]

[1] School of Economics and Management, Anhui University of Science and Technology, Huainan, China, [2] Faculty of Engineering and Information Sciences, School of Computing and Information Technology, University of Wollongong, Wollongong, NSW, Australia, [3] School of Mathematics and Physics, Anhui University of Science and Technology, Huainan, China

The problem of cancer risk analysis is of great importance to health-service providers and medical researchers. In this study, we propose a novel Artificial Neural Network (ANN) algorithm based on the probabilistic framework, which aims to investigate patient patterns associated with their disease development. Compared to the traditional ANN where input features are directly extracted from raw data, the proposed probabilistic ANN manipulates original inputs according to their probability distribution. More precisely, the Naïve Bayes and Markov chain models are used to approximate the posterior distribution of the raw inputs, which provides a useful estimation of subsequent disease development. Later, this distribution information is further leveraged as additional input to train ANN. Additionally, to reduce the training cost and to boost the generalization capability, a sparse training strategy is also introduced. Experimentally, one of the largest cancer-related datasets is employed in this study. Compared to state-of-the-art methods, the proposed algorithm achieves a much better outcome, in terms of the prediction accuracy of subsequent disease development. The result also reveals the potential impact of patients' disease sequence on their future risk management.

Keywords: cancer risk analysis, artificial neural network, Naïve Bayes, Markov chain, sparse training

OPEN ACCESS

Edited by:
Jinde Cao,
Southeast University, China

Reviewed by:
Minjie Zhang,
Hubei University of Arts and Science, China
Jun Li,
Xi'an University of Science and Technology, China
Yongming Xia,
Aalborg University, Denmark

****Correspondence:***
Chaoyu Yang
yangchy@aust.edu.cn

†These authors have contributed equally to this work

Received: *17 April 2020*
Accepted: *22 May 2020*
Published: *21 July 2020*

Citation:
Yang C, Yang J, Liu Y and Geng X (2020) Cancer Risk Analysis Based on Improved Probabilistic Neural Network. Front. Comput. Neurosci. 14:58. doi: 10.3389/fncom.2020.00058

1. INTRODUCTION

Cancer is a complex health problem worldwide, which is closely monitored by scientists and authorities due to its high mortality rate. In the past decades, the pressure of cancer in public health sectors has gradually increased. A lot of effort has been put into cancer-related studies (Loud and Murphy, 2017), such as patient status monitoring, medical resource allocation, and survivability prediction, to name a few. According to the GLOBOCAN project (Sasikala et al., 2019), there will be more than 14.1 million new cancer-related cases (excluding skin cancer and melanoma) annually, accounting for ∼14.6% of global deaths. Even within developed countries, such as the United States, there are more than 1.68 million new patients and 600,000 deaths per year. In particular, **Table 1** shows the top eight cancer types from the United States in 2016, while the number of new cases and relevant deaths are also illustrated. For instance, there are about 150,000 new cases diagnosed with breast cancer and around 41,000 deaths, which contribute to a 16.4% ratio between new cases and death numbers. On the other hand, there are ∼24,000 new patients and 16,000 deaths related to brain and nervous system cancers, which leads to a significantly high ratio of 67.5%.

TABLE 1 | Number of new cancer-related patients and deaths from the United States in 2016.

Cancer types	New cases	New deaths
Digestive system	304,930	153,030
Respiratory system	243,820	162,510
Breast	149,260	40,890
Reproductive system	297,530	57,730
Urinary system	143,190	31,540
Lymphoma	81,080	21,270
Leukemia	60,140	24,400
Brain and other nervous systems	23,770	16,050

As such, the problem of how to monitor and predict cancer-disease development (to reduce its incidence rate) has attracted a lot of attention from different public and private sectors, and has become a major challenge and research focus. The last two decades have witnessed a huge development of computer science and information technologies, which have already taken on an important role in the cancer-related domain. In particular, data mining and machine learning approaches are more regularly employed due to their high performance in simulation and modeling. For example, the work in Heidari et al. (2018) proposed a machine learning based model to identify mammographic image features for short-term breast cancer prediction. Locally preserving projection (LPP) based features were considered, and the experiment was performed using a mammographic dataset collected from 500 women. The result further showed a huge improvement from their work compared to standard methods, such as the Liner Regression and Decision Tree methods. Additionally, a comparison between the Naïve Bayes and K-Nearest Neighbor (KNN) algorithms was provided in Amrane et al. (2018) for breast cancer classification. The experiment was performed using the Wisconsin dataset, while the result showed that KNN outperforms Naïve Bayes with the higher accuracy of 97.51% compared to that of 96.19%. Another breast cancer prediction work has been reported in Jamal et al. (2018), in which authors utilized the hybrid technique of Extreme Gradient Boosting technique and Support Vector Machine. Furthermore, they also applied the Principle Component Analysis (PCA) and K-Means Clustering method to reduce the problem dimensionality. Experimental results illustrated that the hybrid algorithm with a reduced-scale problem indeed improved the prediction performance of diagnosing breast cancer.

However, the majority of the existing research did not address the sequential nature of the disease's development. In other words, less work has been performed to explore the relationship between patients' previous disease and sequential ones. As a result, in this study our research aims to provide new insight into how disease development can be influenced or predicted based on patients' previous medical information. In particular, the Artificial Neural Network (ANN) algorithm is investigated as the optimization tool in our study. ANN is one of the most widely-used techniques for simulation and modeling, due to its ability to learn from complex inputs and to produce accurate outputs. Not surprisingly, we have observed a great number of ANN-based applications in the medical domain. For example, the work from Fakoor et al. (2013) developed a hybrid method by combining ANN with the Support Vector Machine and it was tested on several gene-expression datasets for cancer detection. The results revealed that the ANN-based work outperformed traditional methods via discovering intricate relationships behind risk factors. More recently, a convolutional neural network improvement for breast cancer classification was proposed in Ting et al. (2019). To classify incoming medical images into malignant, benign, and healthy patients, their work performed effectively to localize and identify breast cancer tissue. Other successful implementations of ANN-based models can be found in the survey of Siddiqui et al. (2020).

Despite the general interest in developing the ANN applications, several drawbacks still exist. Specifically, in the context of the disease development, we aim to explore the disease correlation and to identify related risk factors. The majority of traditional ANN applications, however, consider network inputs from the original data directly, while less work has been offered in terms of the input amendment or augment. On the other hand, the standard network training process is usually time consuming, in particular with a large number of inputs. Additionally, as for some real-world scenarios, the generalization performance of the standard ANN is far from being satisfactory.

To this end, in this study we propose a novel hybrid algorithm, based on the idea of Artificial Neural Network, Naïve Bayes, and Markov chain, to address the issue of predicting patients' disease development. In the proposed study, the methods of Naïve Bayes and Markov chain are first applied to estimate posterior possibilities of subsequent development, according to the patient's historical data. The estimation of subsequent possibility is able to establish a relationship model via capturing the underlying correlation of the disease development. Next, estimated possibilities are further leveraged as the input to the neural network, in addition to original inputs. Lastly, we also consider adopting a sparse training strategy for the network training, which is able to optimize the network structure and minimize the training error simultaneously. To the best of our knowledge, this is the first investigation combining the models of Bayesian Network and Markov chain to amend the input of the Artificial Neural Network. The proposed algorithm is further applied to one of the largest cancer-related datasets worldwide, and the comparison with state-of-the-art approaches is also considered.

The rest of this paper is organized as follows. Section 2 provides a review of literature in which several existing research topics are examined, including applications of data-mining techniques on the domain of cancer risk analysis, Artificial Neural Network, Naïve Bayes and Markov chain model. Section 3 provides the basic information about the research background, such as the description of the target dataset used in this study. Section 4 describes the proposed hybrid approach, including the input augment and sparse training. Then, section 5 discusses

experiments and comparison results, and finally section 6 concludes the study.

2. LITERATURE REVIEW

In this section, we will provide a brief review about existing cancer-related research. Then the fundamental work of Artificial Neural Network, Naïve Bayes and Markov chain model is also provided.

2.1. Cancer Risk Analysis

Cancer risk analysis is of great significance to healthcare providers and medical researchers. Several research works have attempted to provide a diverse range of the management and/or prediction strategies for cancer risk analysis. The ultimate goal is to provide precaution for people with a risk, as well as to monitor the disease development (or survivability prediction).

For the risk prediction, the work from Hart et al. (2018) employed a multi-parameterized neural network for lung cancer risk prediction, based on putative risk factors as well as clinical and demographic information. A comparison among Decision Tree, Support Vector Machine, Naïve Bayes, and K-Nearest Neighbors was conducted for a liver-cancer assessment. On the other hand, cancer survivability prediction is also an interesting topic that has been fervently researched throughout the years. The prediction task of cancer survivability is to monitor the possible survivability (the time span) based on the patient's status. For instance, Mayur et al. conducted a study on spinal cord cancer survivability by performing statistical analyses and fitting a Random Forest model (Mayur et al., 2019). The work from Wang et al. (2019) investigated the use of a tree ensemble-based two-stage regression model for advanced-stage lung cancer survival prediction. In addition, a comparison among multiple techniques, including Linear Regression, Decision Tree, Random Forest and Generalized Boosting Machines, and Support Vector Machine, was considered in Sharaf et al. (2015) to predict lung-cancer patient survival.

Despite the great interest in the work of cancer risk and survivability analysis, little research has been done in terms of the relationship between patients' past and current diagnoses. In other words, existing studies fail to address the possibility of subsequent diagnosis, given patients' previous medical conditions. Yet, this research question is of great importance, as it helps in providing prior knowledge of patients' future disease development. To gain an in-depth understanding of potential risk for subsequent diseases also works in increasing the healthcare quality and treatment services (Gupta et al., 2012; Aolin and Maxim, 2017). To bridge this gap, we propose a probabilistic model that takes into account the techniques of the Artificial Neural Network, Naïve Bayes, and Markov chain model.

2.2. Artificial Neural Network

The Artificial Neural Network (ANN) is one of the most popular data-mining algorithms, which is capable of responding to complex inputs and generating desired outputs. Due to its satisfactory performance and high accuracy, ANN has found its wide applications in numerous areas, such as pattern recognition, prediction, and statistical simulation, and so on. The most basic computing unit from ANN is the artificial neuron. Those neurons are designed in a similar way to biological neurons within the human brain. In general, input signals are transferred to biological neurons, and then inputs are further processed within their cell bodies. If a certain threshold is reached, neurons are activated to transfer output signals to other neurons. Accordingly, the artificial neuron follows the same procedure of biological neurons: input receiving, threshold activation, and output transferring. Mathematically, suppose the input signal to the i-th neuron is a vector of $\boldsymbol{x}_i$, the connection strength to the output is the weight $\boldsymbol{w}_i$, and its bias input is represented as b. Given the activation function $f(\cdot)$, the output for this i-th neuron can be expressed as follows:

$$y = f(\boldsymbol{x}_i^T \boldsymbol{w}_i + b). \tag{1}$$

In real-world applications, the selection of activation function and network structure (the number of hidden layers and/or neurons) is problematic. In general, there is no commonly-accepted formula giving clear insight into how to choose the activation function and/or to determine the network structure. This is usually decided by trial-and-error experiments or cross validation methods. Additionally, after deciding the activation function and network structure, a training process is required to update the internal network weights to minimize the error between the actual network and desired output. Some typical learning algorithms are Back Propagation, Resilient Propagation, and so on.

2.3. Naïve Bayes and Markov Chain

Bayesian theory offers a computational framework for estimating the conditional probability, which has proven to be effective for a wide range of applications. Text classification, spam detection, and sentiment analysis are just a few of their popular use cases. Assume that we have one training sample $\boldsymbol{x}$ and n possible class labels c_i ($\forall i \in n$). Then the posterior probability (for $\boldsymbol{x}$) of belonging to the i-th class [or $prob(c_i|\boldsymbol{x})$] can be expressed as:

$$prob(c_i|\boldsymbol{x}) = \frac{prob(\boldsymbol{x}|c_i)prob(c_i)}{prob(\boldsymbol{x})}, \forall i \in n, \tag{2}$$

where $prob(c_i)$ stands for the class prior probability, $prob(\boldsymbol{x})$ is the prior probability of $\boldsymbol{x}$, and $prob(\boldsymbol{x}|c_i)$ denotes the posterior probability of $\boldsymbol{x}$ given the condition of the c_i class.

Compared with other classification modes, Naïve Bayes (NB) consumes much less training time, and it can effectively solve small-scale learning problems. For instance, Kim et al. (2018) introduced a Naïve Bayes based text classification in a semantic tensor space model for document representation. URL classification is another classification application of Native Bayes, which is currently of research interest (Rajalakshmi and Aravindan, 2018). In addition, evaluation of a hot-engine test (Fan et al., 2018) and classification of impact damage on a rubber-textile conveyor belt (Andrejiova and Grincova, 2018) are just other use cases that have been investigated using the Naïve Bayes method, respectively.

On the other hand, the Markov chain model is usually utilized to calculate the transition probability from one state to another. In particular, the first order Markov chain operates under the assumption that future states for one particular object (or event) only depend on the current state, but not on other states that occurred before. In other words, let $\boldsymbol{x}_i$ $(i = 1, 2, \cdots, n)$ represent a sequence of random variables. Then the probability of moving to the next state (or $\boldsymbol{x}_{n+1}$) is estimated as:

$$prob(\boldsymbol{x}_{n+1}|(\boldsymbol{x}_n, \boldsymbol{x}_{n-1}, \cdots, \boldsymbol{x}_1)) = prob(\boldsymbol{x}_{n+1}|\boldsymbol{x}_n). \quad (3)$$

The Markov chain model proves to be effective in factoring the sequential characteristics of events. Existing applications of the Markov chain model are primarily in the domain of recommendation, speech recognition, and so on. For instance, Ye et al. (2015) and Lassoued et al. (2017) both discussed the use of Markov models in driving route and destination predictions, respectively. Krause and Zhang (2019) proposed a different approach by employing a hierarchical Markov model for short-term behavior prediction. Kurashima et al. (2013) had a slightly different approach when employing not only the Markov Chain model but also a topic model to represent the user interest.

2.4. Summary

In this section, we briefly review some existing research on applying the data-mining techniques in the medical domain. Additionally, we also offer a fundamental discussion on three popular methods, including the Artificial Neural Network, Naïve Bayes, and Markov chain model. Based on these three methods, we will then propose a novel prediction algorithm to monitor and predict patients' disease development, which is discussed in the coming sections.

3. STUDY BACKGROUND

The National Cancer Institute (NCI) established the Surveillance, Epidemiology and End Results (SEER) database in 1973[1]. This incidence database consists of de-identified patient data with different types of cancer diseases. Additionally, for each patient record, there are in total 124 features. These features cover both the demographical and clinical information. For example, demographics information include gender, ethnicity, year of birth, month, and year of diagnosis, age, and marital status of patients at diagnosis. Clinical information includes tumor primary site, tumor marker, tumor size, the types of treatment received, behavior codes, laterality, and histology. In addition, the cancer types involved in the database can be divided into nine categories: breast, colon and rectum, other digestive systems, female reproduction, lymphoid and leukemia, male reproduction, respiratory system, urinary system and other unspecified types. By November 2013, there were more than 1 million data records in the SEER database. Currently, it is the authoritative data source that provides reliable data support for clinical research. A huge number of research efforts have been conducted to utilize this database for different work, such as cancer survival prediction, correlation of medical factors, management of diseases recurrence, and etc.

[1] Available online at: https://seer.cancer.gov.

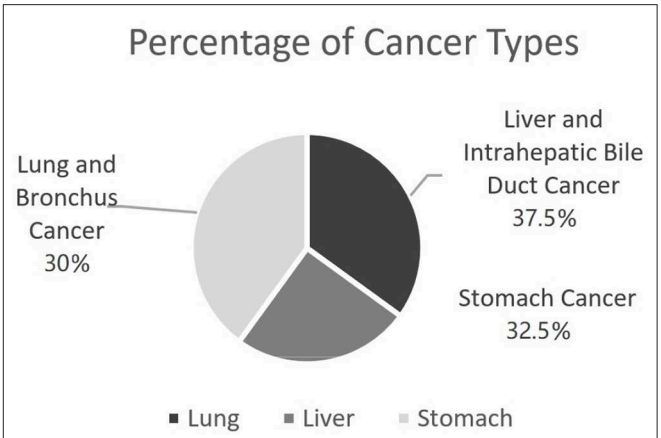

FIGURE 1 | Percentage of selected patients from three cancer types in SEER.

Again, the main purpose of this study is to investigate the possibility of being diagnosed with cancers given a previous medical condition. To model such a disease development, in this study we focus on three types of cancer data from SEER, including lung and bronchus cancer (C1), liver and intrahepatic bile duct cancer (C2), and stomach cancer (C3), respectively. **Figure 1** shows the percentage of selected patient samples from three types of cancers.

4. PROPOSED APPROACH

In this section, we propose a novel prediction algorithm by combining three different methods, including the Bayesian and Markov models, as well as the artificial neural network. Our approach is based on the assumption that the occurrence of a new type of cancer incidence is affiliated with the most recently (or previously) diagnosed cancer incidence, as well as patients' previous clinical details. Toward this end, Naïve Bayesian and Markov chain models are first used to establish the connection between the previous and current incidence, which offers a useful estimation of patient's future status. Then, the output from the two probabilistic models will be cast as the network input for the training process. Additionally, to improve the accuracy and learning efficiency, we further leverage a sparse training strategy for the target network. The pipeline of the proposed algorithm is then illustrated in **Figure 2**. Next, we will discuss different stages within our proposed algorithm.

4.1. Data Pre-processing

To begin with, the first stage is to preprocess the original SEER data to meet certain criteria, such as removal of missing values and data normalization. Among all 124 features, 19 independent features that may have an impact on the cancer prediction tasks were selected, including: gender, race, status, age, primary site, etc. The detail description and value distribution of selected attributes are provided in **Table 2**.

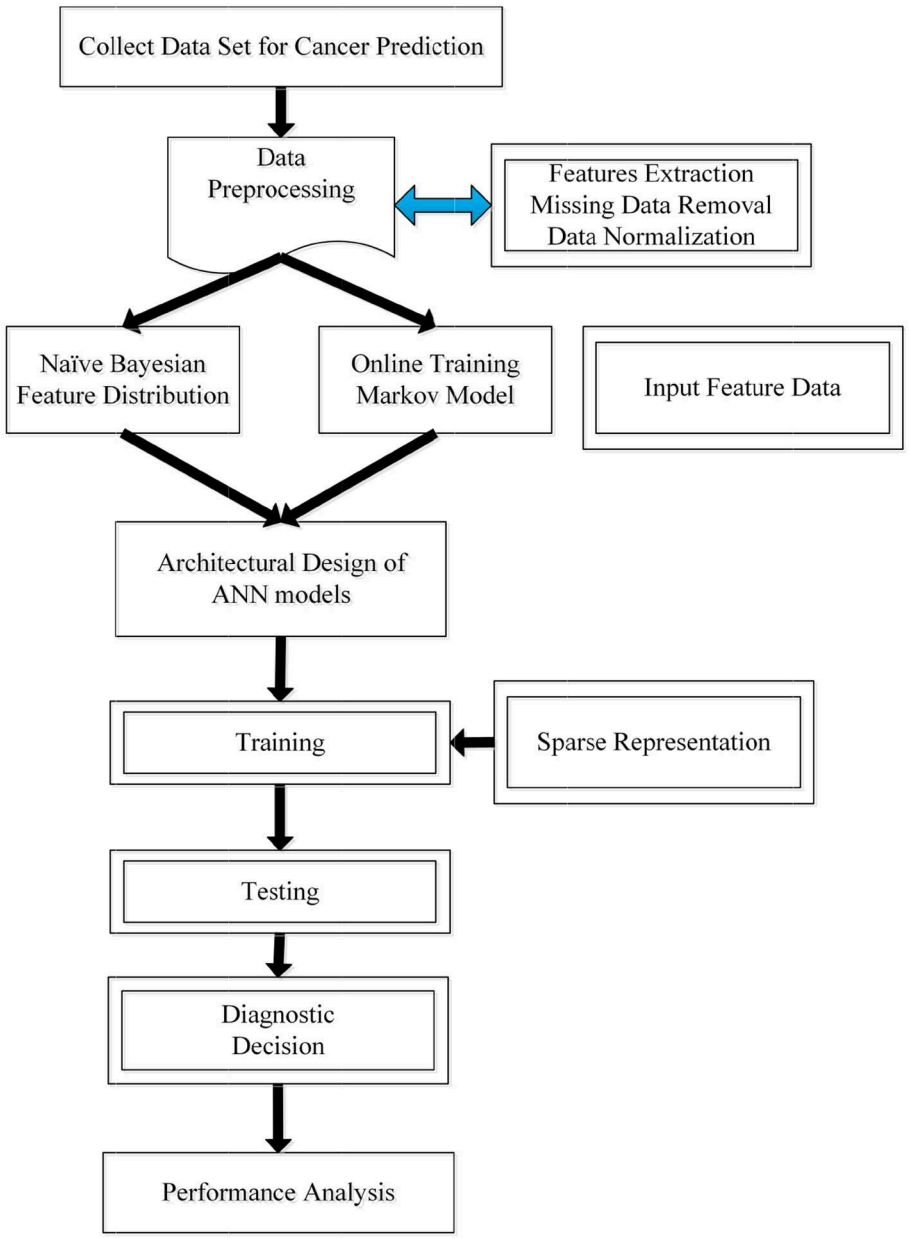

FIGURE 2 | The workflow of the proposed algorithm for predicting patients' disease development.

Among these features, four of them, namely SS_SURG, CSLYMPHN, EOD10_SZ, and CSEXTEN, contain massive amounts of missing values, ∼50% on average. One plausible reason could be the patients' refusal to provide adequate information. On the other hand, due to the evolution of SEER over time, some clinical features have only been collected in recent years. This makes it very impractical to backtrack those new features from previous records. For simplicity, patients' records with missing values will be removed in this study. That is, only completed data samples will be considered.

Next, we find that selected attributes can be divided into discrete and continuous attributes. For discrete attributes, it is easy to process compared to continuous ones. For example, the marital status attribute is divided into seven categories, while the gender one is cast into two categories. By contrast, for continuous data, the minimum-maximum normalization is employed in a way that the values from continuous features will be limited within the range of $[0, 1]$. Mathematically, let v_j^p be the value from the p-th sample and the j-th continuous feature, $min(\boldsymbol{v}_j)$ and $max(\boldsymbol{v}_j)$ is the minimal and maximal value of this j-th feature from all samples. Accordingly, the normalized value $\hat{v}_j^p$ will be

TABLE 2 | Variable descriptions and unique values.

Variable name	Description	Unique value count
PUBCSNUM	Patient's number	1,885,421
SEQ_NUM	Sequence number of all reported incidence	15
YEAR_DX	Year of diagnosis	Continuous
MDXRECMP	Month of diagnosis	12
SEX	Patient's gender	2
MAR_STAT	Marital status at diagnosis	7
RACE1V	Patient ethnicity	30
AGE_DX	Patient's age at diagnosis	Continuous
PRIMSITE	Primary site	51
LATERAL	Laterality	6
FIRSTPRM	First malignant primary indicator	2
HISTREC	Histology	37
GRADE	Histologic grading and differentiation	5
NO_SURG	Reason no cancer-directed surgery	8
EOD10_SZ	Tumor size	Continuous
SS_SURG	Site-specific surgery	30
CSLYMPHN	Involvement of lymph nodes	63
CSEXTEN	Extension of tumor	Continuous
ERSTATUS	Tumor marker 1–breast cancer	5
PRSTATUS	Tumor marker 2–breast cancer	5

estimated as follows:

$$\hat{v}_j^p = \frac{v_j^p - min(\boldsymbol{v}_j)}{max(\boldsymbol{v}_j) - min(\boldsymbol{v}_j)}. \tag{4}$$

4.2. Estimation of Subsequent Disease-Development

In this section, we will discuss the second stage of calculating the possibility of the subsequent disease-development, using the concept of Naïve Bayes and Markov chain model. Suppose we have a set of cancer diagnoses $\{D_i^p, \{v_{ij}^p\}_{j=1}^K\}_{i=1}^{\tau^p}$, where D_i^p is the i-th new type of cancer disease of patient p, and v_{ij}^p is the j^{th} feature of the i-th new cancer diagnosis of patient p, K is the number of attributes of the set $\{v_{ij}^p\}$, and τ^p is the total number of cancer types occurring for patient p. Then the research question can be reformulated as follows: given a patient's most-recent cancer diagnosis D_i^p and the set of patient health profile information at the time of diagnosis $\{v_{ij}^p\}_{j=1}^K$, the task is to predict the next most likely type of cancer to occur for that patient D_{i+1}^p. For example, patient P had been diagnosed with liver cancer before. In this case, we will investigate the following likelihood of patient P having other types of cancers (such as lung or stomach cancer). As a result, mathematically, our goal is to estimate the probability that patient P with the i-th disease D_i will also develop the $(i+1)$-th disease D_{i+1}, or the probability $P(D_{i+1}^p|D_i, v_i^p)$.

To address the aforementioned problem, we introduce a novel estimation method to calculate the posterior probability based on Naïve Bayes and Markov chain models. More precisely, with Naïve Bayes, we can investigate the dependence of the target variable on a patient's medical condition at the time they are diagnosed with D_i^p. Let $\{v_{ij}^p\}$ be the attribute list of the p-th patient. Accordingly, in the Bayes theory, we will have:

$$P(D_{i+1}^p|v_{i1}^p, v_{i2}^p, ...v_{iK}^p) \propto P(v_{i1}^p|D_{i+1}^p)P(v_{i2}^p|D_{i+1}^p)...P(v_{iK}^p|D_{i+1}^p)P(D_{i+1}^p), \tag{5}$$

where K is the number of attributes. Alternatively, we have

$$P(D_{i+1}^p|v_{i1}^p, v_{i2}^p, ...v_{iK}^p) \propto P(D_{i+1}^p)\prod_{j=1}^{K} P(v_{ij}^p|D_{i+1}^p). \tag{6}$$

The conditional probability $P(v_{ij}^p|D_{i+1}^p)$ can be calculated using the Laplace smoothing while avoiding the zero probability:

$$P(v_{ij}^p|D_{i+1}^p) = \frac{N(D_{i+1}^p, v_{ij}^p) + 1}{N(D_{i+1}^p) + K}. \tag{7}$$

On the other hand, we assume that the next disease relies primarily on the precedent disease, as well as the patient's current status. As such, the Markov chain model is accordingly employed to capture the probabilistic information conveyed by the sequence of diseases, that is identified from patients' medical history. In this study, we consider the first-order Markov model, and accordingly we can estimate the probability of the next disease as follows:

$$P(D_{i+1}^p|D_i^p, D_{i-1}^p, ..., D_2^p, D_1^p) = P(D_{i+1}^p|D_i^p). \tag{8}$$

Furthermore, the probability of $P(D_{i+1}^p|D_i^p)$ is calculated as follows:

$$P(D_{i+1}^p|D_i^p) = \frac{N(D_{i+1}^p, D_i^p)}{N(D_i^p)}, \tag{9}$$

where $N(D_{i+1}^p, D_i^p)$ is the number of patients with a disease D_{i+1} occurring right after the disease of D_i, and similarly $N(D_i^p)$ is the total number of patients with the disease D_i^p.

To incorporate both most-recent diagnosis and the patient's health condition into our proposed model, the above Markov and Naïve Bayes models are combined. Operating under the assumption that the patient's health condition set v_i^p and D_i^p are independently conditioned on D_{i+1}^p, the combination of the two models can be performed using the following approximation:

$$\begin{aligned} P(D_{i+1}^p|D_i^p, v_i^p) &= \frac{P(D_{i+1}^p|D_i^p)}{C(D_i^p, v_i^p)} \frac{P(D_{i+1}^p|v_{i1}^p, v_{i2}^p, ..., v_{iK}^p)}{P(D_{i+1}^p)}, \\ &= \frac{P(D_{i+1}^p|D_i^p)}{C(D_i^p, v_i^p)} \prod_{j=1}^{K} P(v_{ij}^p|D_{i+1}^p), \end{aligned} \tag{10}$$

where $P(D_{i+1}^p|D_i^p)$ and $P(v_{ij}^p|D_{i+1}^p)$ can be estimated by the Markov and Naïve Bayes models, respectively, and $C(D_i^p, v_i^p)$ is the normalization factor to ensure all probabilities summed to 1.

4.3. ANN Training

The previous section describes the details about the estimation of subsequent disease development. In the third stage of our proposed algorithm, the output from the previous stage will be cast as the input to feed into a neural network. **Figure 3** illustrates the structured input for ANN, while the probability estimation, together with the patient's profile, such as gender and age, are considered as a whole to train the network.

As for the network training process, internal weights will be optimized in a way that the actual network output fits the desired outputs well. Taken as an example, the backpropagation (BP)-based method is a typical way to train ANN via calculating gradients of the output error in relation to network weights. However, the BP-based training could suffer from some drawbacks, such as low convergence and poor generalization capability, in particular with a huge number of input features. In the context of our study, the network has 20 input features, which could be time-consuming for implementing the BP-based training.

To improve the training stability and the fast training speed, we adopt a sparse training strategy in this study, similar to our preliminary work in Yang and Ma (2016, 2019). The general idea is to generate a sparse network structure and to minimize the training error simultaneously. The concept of sparse representation, on the other hand, is under the assumption that a signal can be decomposed into a linear combination of few elementary signals. Consequently, given the target matrix $Y \in \mathbb{R}^{M\times L}$ and a known dictionary matrix $\mathcal{D} \in \mathbb{R}^{M\times N}$ that contains N columns, the sparse representation aims to minimize the solution sparsity and the reconstruction error:

$$X^* = \arg\min \mathcal{M}(X) \quad \text{subject to} \quad \|Y - \mathcal{D}X\|_2 \leqslant \epsilon, \tag{11}$$

where $\mathcal{M}(X)$ is a measure of the matrix sparsity, $\|Y - \mathcal{D}X\|_2$ denotes the reconstruction error, and ϵ is the bound on the error. One simple strategy for estimating $\mathcal{M}(X)$ is to consider the $l_{2,1}$-norm of X, or $\mathcal{M}(X) = \|X\|_{2,1} = \sum_q \|X_q\|_2$, where X_q denotes the q-th row of X.

Suppose there are L pairs $(\boldsymbol{x}_i, \boldsymbol{y}_i)$ of inputs $\boldsymbol{x}_i$ and desired outputs $\boldsymbol{y}_i$, while $X = [\boldsymbol{x}_1, \boldsymbol{x}_2, ..., \boldsymbol{x}_L]$ represents the entire input matrix and $Y = [\boldsymbol{y}_1, \boldsymbol{y}_2, ..., \boldsymbol{y}_L]$ is the desired output matrix. Additionally, assume that the target network is with a three-layer structure, which consists of Q-input, N-hidden and M-output neurons, respectively. Let $W_1 \in \mathbb{R}^{Q\times N}$ and $W_2 \in \mathbb{R}^{N\times M}$ denote the weight matrices from the hidden and output layer, respectively. As such, the output matrix from the hidden layer (Z) can be expressed as:

$$Z = f_1(XW_1), \tag{12}$$

where $f_1(\cdot)$ is the activation function of the hidden layer, and the i-th column from Z is in relation to the output of the i-th hidden neuron. Furthermore, the actual output from the entire network $\hat{Y}$ can be written as:

$$\hat{Y} = f_2(ZW_2), \tag{13}$$

where $f_2(\cdot)$ is the activation function for the output layers.

The proposed sparse training is then used to optimize the network structure, by selecting the most-important hidden neurons, while minimizing the output error simultaneously. Therefore, the neuron selection process is equivalent to finding a sparse representation for all hidden neurons. Consequently, the sparse training process is then cast as solving the following problem:

$$\min \|W_2\|_{2,1} \quad \text{subject to} \quad \left\|\tilde{Y} - ZW_2\right\|_2 \leq \epsilon, \tag{14}$$

where $\|W_2\|_{2,1}$ is the $l_{2,1}$-norm of the W_2 matrix, $\tilde{Y} = f_2^{-1}(Y)$, and ϵ is the bound on the network error. Note that in the proposed sparse training, we only consider optimizing or sparsifying the weight matrix W_2 between the hidden and output layer. As for the weight matrix W_1 in the previous input-and-hidden layer, we only randomly initialize once during the training and fix them in the subsequent process. The reason is 2-fold: (1) the training performance heavily depends on the output layer, so we focus on the W_2 optimization, instead of both layers; (2) W_2 is trained or adjusted based on the given W_1, as such a random W_1 matrix has a minimal impact on the final output.

4.4. Summary

In previous sections, we discuss three different stages from the proposed algorithm. Overall, we apply the Naïve Bayes and Markov chain model to estimate the probability of potential disease development. We then consider this probability result as the additional input, together with other original features, for training a network. At last, to minimize the impact from the huge number of input features, a sparse training strategy is further leveraged to optimize the network structure and minimize the training error simultaneously. Toward this end, Algorithm 1 summarizes the proposed method for investigating the cancer-risk analysis.

Algorithm 1: Proposed algorithm for cancer-risk prediction, based on an improved probabilistic neural network.

Stage 1: Data preprocessing, in terms of feature selection, removal of missing records, and perform data normalization.
Stage 2: Calculate the probability based on Equation (10).
Stage 3: Employ the probability result and original input features for network training:
Stage 3.1: Randomly assign weights to the input-hidden layer;
Stage 3.2: Solve the optimization problem in Equation (14) to obtain a spare weight matrix for the hidden-output layer;
Output the trained neural network.

5. EXPERIMENTAL RESULTS

This section describes experimental results by applying the proposed algorithm to explore a patient's disease development. The experimental setup and evaluation metrics are presented in section 5.1. In section 5.2, we discuss the probabilities based on their historical information and individual profiles, while

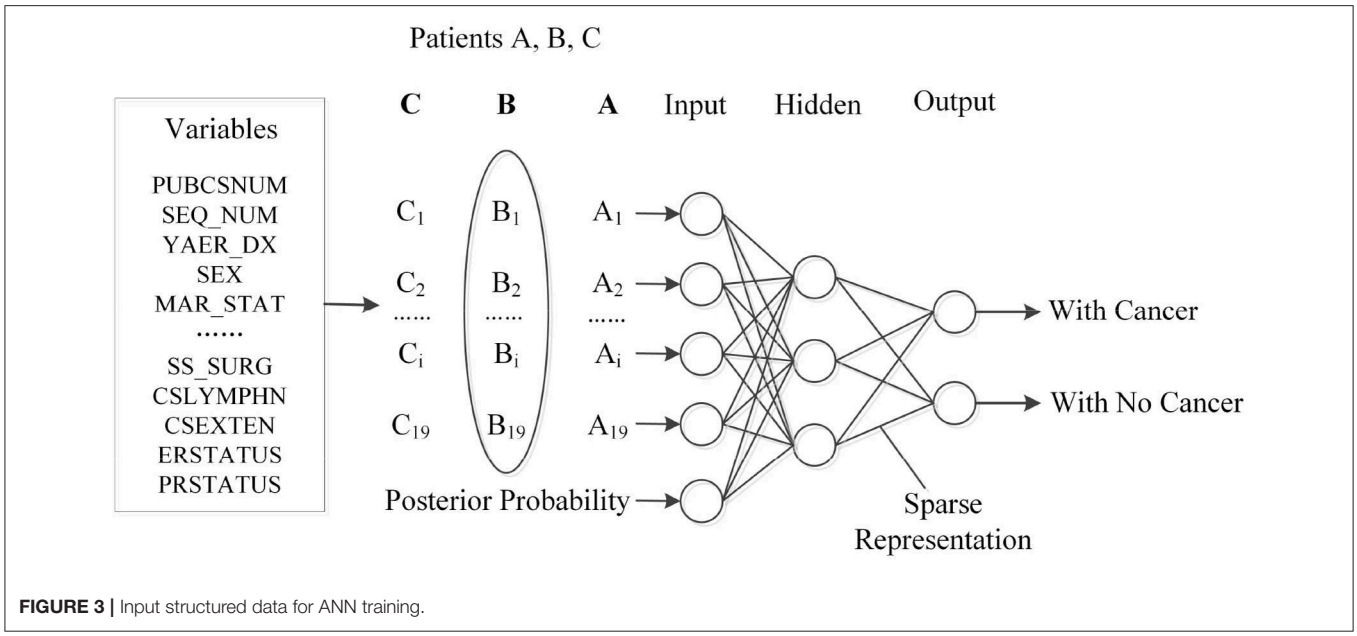

FIGURE 3 | Input structured data for ANN training.

the performance of the proposed method is then evaluated in section 5.3.

5.1. Experimental Setup

The target dataset includes 10,500 patients with lung cancer, 13,500 with liver cancer, and 12,000 with stomach cancer, respectively, which is a total of 36,000 samples. Each original sample has 19 features, while the majority of chosen features are categorical (or discrete), except for four attributes, such as the patient's age at diagnosis, year of diagnosis, tumor size, and extension of tumor. Again, continuous features will be normalized as described in section 4.1 during the pre-processing stage. We further applied the 3-fold cross validation method to randomly partition the entire dataset into two independent sets: a training and testing set. The size of the training and testing sets in all cases is 75 and 25%, respectively. The training set is used for training the network while the testing set is for evaluation purposes.

Additionally, for the employed neural network, we consider the activation function of the hidden and output layer as the Sigmoid function, which can be expressed as $f(z) = \frac{1}{[1+\exp(-z)]}$ (z is an arbitrary input). The layer between the input-and-hidden is initialized with random weights in the range [-1, +1]. The number of hidden neurons is set as 64. To solve the optimization problem in Equation (14), the orthogonal matching pursuit (OMP) algorithm is employed[2], which first measures the similarity between the residual error and the neuron outputs, and then selects the neuron that minimizes the residual error at each iteration. To halt the OMP solver, the termination criterion is set either when the maximal iteration (K) is reached or when the value of $\frac{\|\epsilon_k - \epsilon_{k-1}\|_2^2}{\|\epsilon_k\|_2^2}$ is less than a threshold α, where ϵ_k is the output error at the k-th iteration, and α is a user-defined value. Lastly, the following metrics are employed to evaluate the performance:

$$Recall = \frac{TP}{TP + FN}, \tag{15}$$

$$Precision = \frac{TP}{TP + FP}, \tag{16}$$

$$F1\ Score = 2 \times \frac{Precision \times Recall}{Precision + Recall}, \tag{17}$$

where TP denotes the true positive rate, FN is false negative rate, and FP represents the false positive, respectively.

5.2. Probabilities for Disease Prediction

In this section, we discuss the result of patients' disease probabilities using their previous medical information. As mentioned before, this temporary result, obtained from Naïve Bayes and Markov chain model, will be cast as the input to the subsequent network training. Therefore, an accurate estimation of posterior probabilities will certainly enhance the network performance. Before we discuss the result, the detail of forming the patients' historical information is provided first. Again, we are interested in three types of cancers in this study: lung, liver, and stomach cancer. As such, the entire dataset is grouped by the patient ID. These records are further sorted based on the date of disease diagnosis, while records are indexed from 0, and the maximum number of incidences from a patient is five. Note that some patients could have the problem of recurrence, thereby leading to more than three records. Next, the following procedure is considered:

1. If the patient only has one type of cancer, then her/his record is added directly to the final dataset;

[2]Available online at: https://scikit-learn.org.

TABLE 3 | Patient's conditional probabilities.

	$N(D_{i+1}^p, D_i^p)$	$N(D_i^p)$	$P(D_{i+1}^p \mid D_i^p, v_{ij}^p)$
$D_{i+1}^p = C1, D_i^p = C2$	10,864	24,085	0.4346
$D_{i+1}^p = C3, D_i^p = C2$	13,726	26,421	0.5756
$D_{i+1}^p = C2, D_i^p = C1$	6,821	16,548	0.3753
$D_{i+1}^p = C3, D_i^p = C1$	10,889	17,009	0.6588
$D_{i+1}^p = C2, D_i^p = C3$	2,112	6,981	0.3631
$D_{i+1}^p = C1, D_i^p = C3$	3,219	6,811	0.6312

Note that we label lung and bronchus cancer as C1, liver and intrahepatic bile duct cancer as C2, and stomach cancer as C3, respectively.

2. If the patient has a recurrence, then records with same type are merged by maintaining only one sample with the latest date of diagnosis.

Through the aforementioned process, redundant patients' records are removed, and the sequence of disease development is accordingly established for the following calculation. Lastly, the estimation result of posterior probabilities, given the patients' previous information, is presented in **Table 3**.

From the results presented in **Table 3**, there indeed exists some connection between patients' disease development. For instance, we observe that the probabilities from 50% of cases (three out of six) have exceed 57%, which indicates a potential correlation among different diseases. The highest value is found from patients with a type of lung cancer (C1), who have more than a 65% possibility to develop stomach cancer (C3). On the other hand, for patients who had stomach cancer (C3) previously, the chance is much lower (only about 36%) to develop liver cancer (C2). This preliminary result will then be cast as the input for the subsequent network training, while the comparison with other methods is discussed in the next section.

5.3. Comparison With Other Training Algorithms

Note that again in our proposed algorithm, the main contribution is 2-fold: (1) introducing the technique of Naïve Bayes and Markov chain models to estimate the posterior possibilities; (2) employing the sparse training strategy for the network training. As such, the following experiments are designed to evaluate the effectiveness of both the possibility result and the sparse training.

To begin, we consider comparing the performance of the standard ANN, combination model with Bayes and Markov (labeled as CBM), and the proposed models on the training and test set, respectively. Note that in the standard ANN, original features are directly fed into the network, while no additional input is considered. In the CBM method, the estimation for potential disease is considered but no additional neural network is attached. We run the experiments 10 times, and average results are summarized and presented in **Tables 4**, **5**, respectively.

When it comes to the training performance, we realize that the probability estimation for patients' status indeed helps in boosting the accuracy. For instance, both the CBM and proposed algorithms achieve better training outcome compared to that of the standard ANN method. Again, the major difference among the three methods lie in the input; the results suggest that the additional estimation of patients' status (based on their previous information) is capable of providing useful information that facilitates the subsequent ANN training.

TABLE 4 | Comparison of evaluation metrics from the training dataset.

	ANN (%)	CBM (%)	Proposed (%)
Overall accuracy	73.55	76.07	75.63
RECALL (C1)	98.64	98.84	98.05
RECALL (C2)	86.29	87.48	87.42
RECALL (C3)	46.14	49.61	50.92
Precision (C1)	69.28	72.49	71.73
Precision (C2)	59.72	63.02	63.07
Precision (C3)	89.42	91.76	90.84
F1 score (C1)	80.46	83.74	82.57
F1 score (C2)	73.81	76.49	75.38
F1 score (C3)	58.21	61.18	60.72

Again, the labels of C1, C2, and C3 represent the lung and bronchus, liver and intrahepatic bile duct cancer, and stomach cancer, respectively.

TABLE 5 | Comparison of evaluation metrics from the test dataset.

	ANN (%)	CBM (%)	Proposed (%)
Overall accuracy	68.78	70.63	72.47
RECALL (C1)	77.44	77.34	78.11
RECALL (C2)	81.82	82.03	83.79
RECALL (C3)	58.19	65.83	66.64
Precision (C1)	65.37	67.12	69.75
Precision (C2)	63.81	65.72	67.91
Precision (C3)	75.93	77.56	78.37
F1 score (C1)	78.34	75.39	78.95
F1 score (C2)	65.23	65.17	65.06
F1 score (C3)	52.89	59.52	63.63

Again, the labels of C1, C2, and C3 represent the lung and bronchus, liver and intrahepatic bile duct cancer, and stomach cancer, respectively.

On the other hand, we also observe the best generalization performance of the proposed algorithm from **Table 5**. The results from the test dataset indicate that the ANN performs the worst, while the CBM method comes second. However, we also notice that the training performance of the proposed algorithm (75.63%) is slightly lower than that of CBM (76.07%) from **Table 4**. The reason could be the overfitting of CBM to the training data, while the employed sparse neural network helps in improving the testing accuracy while avoiding the overfitting. As a result, the experimental results confirm the advantage of both the additional input from posterior probability and the sparse training in the proposed algorithm.

Next, the performance of our algorithm is compared with conventional methods, and the aim is to evaluate the effectiveness of the proposed method. More precisely, the Support Vector

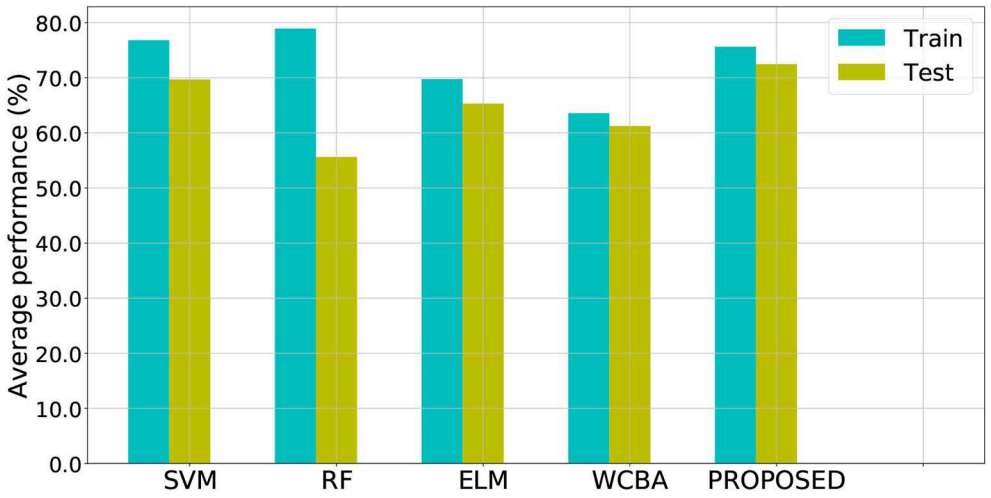

FIGURE 4 | Average training and testing accuracy obtained from different algorithms for prediction.

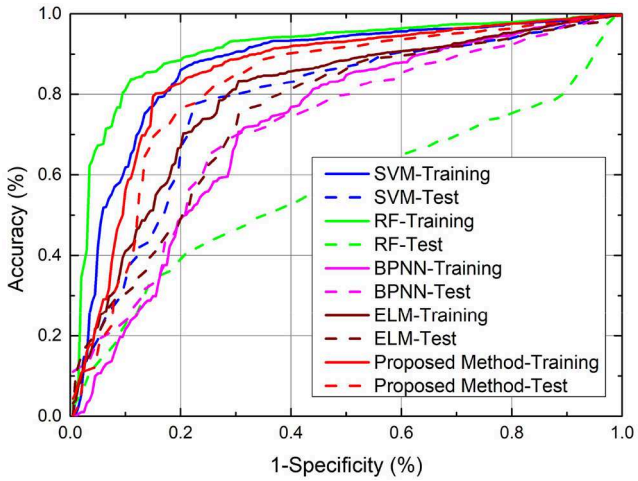

FIGURE 5 | Comparison of classification accuracy (ROC curves) from various methods.

Machine and Random Forest algorithms are included in this paper for comparison purposes:

1. Support Vector Machine (*SVM*) is one of the most popular kernel-based approaches, which has been demonstrated to perform well in various applications (Sharaf et al., 2015). Usually, the decision boundary formed by SVM is constructed by finding a hyperplane that achieves the maximum separation between classes. In this study, the implemented SVM is with the radial basis function (RBF) kernel, while the penalty parameter C of the error term is set as $C = 0.01$, and the Kernel coefficient γ is set as $\gamma = 0.1$;
2. Random Forest (*RF*) is one typical ensemble method, which establishes a forest by constructing a collection of element decision trees (Mayur et al., 2019). For each element tree, RF allows them to randomly choose a subset of features from the entire set, which enhances its flexibility and stability. Key hyperparameters within RF include the number of trees in the forest (*n_estimators*), the maximum depth of a tree (*max_depth*), and the number of features for splitting (*max_features*). In this study, we adopt the following: $max\_depth = 5$, $n\_estimators = 10$, and $max\_features = \sqrt{n\_features}$ (where *n_features* is the number of total features).
3. Extreme Learning Machine (*ELM*) is one typical network training algorithm, which initializes the network weights randomly and then update the weight matrix in the output layer based on a least-square model (Wang et al., 2020). Experiments have shown the advantage of ELM to have easy implementation and better generalization ability, compared to the traditional backpropagation training algorithm. As such, ELM is introduced to make a comparison with the proposed algorithm with a typical three-layer network, while the number of hidden neurons is set as 64.
4. The weighted association rules algorithm (*WCBA*) aims to generate association rules by combining a new attribute evaluation and prioritization techniques (Alwidian et al., 2018). More precisely, domain knowledge was employed to identify attributes with high significance. Then the statistical harmonic mean (HM) measurement was introduced to prioritize generated rules at the pruning and generation phases. Experimental results show its effectiveness by comparing existing rule-based classification methods.

Note that for SVM, RF, ELM, and WCBA, their inputs are from original data directly, without the additional posterior possibility information. We ran the experiments 10 times to obtain the average performance. As a result, both the training and test classification accuracy from different methods are shown in **Figure 4**, and the relevant ROC curves are also shown in **Figure 5**. Although the SVM and RF method have performed

better in the training cases, they seem to have problems with overfitting. In particular, the RF method leads to the highest accuracy of 78.93% from training, but with a poor testing accuracy of 55.62%. A similar problem was observed in the SVM method. By contrast, compared to those standard algorithms, the proposed approach achieves a notable improvement in terms of testing accuracy. For instance, our method leads to the best testing result of 72.47%, which is significantly better than the accuracy of SVM (69.70%), RF (55.62%), ELM (65.31%), and WCBA (61.25%), respectively. Overall, it is empirically confirmed that the proposed method outperforms existing training methods by improving the generalization capability.

6. CONCLUSIONS

Understanding patients' cancer risks, using their historical medical information, is of significant interest in healthcare management. There are still many challenges that remain, including high dimensionality and the heterogeneous structure of data. In this study, a novel algorithm based on the improved probabilistic neural network is proposed, with the ultimate aim of providing decision support for cancer-risk management. The main contribution of our work is 2-fold: (1) we factor the sequential state information with the first-order Markov chain and Naïve Bayes models; this sequential information is then represented as the posterior probability and cast as the additional input for training the neural network; (2) we consider adopting the sparse training strategy to boost the network performance, which is able to optimize the network structure and minimize the training error simultaneously. We test our method using one of the largest cancer-related datasets worldwide. Experimental results suggest that our proposed algorithm exhibits some potential for accurate predictions, compared to other conventional methods. Future work can then apply our method in a broader range of applications, or to develop more sophisticated probability-based neural networks.

DATA AVAILABILITY STATEMENT

The datasets analyzed for this study can be found in the link of https://seer.cancer.gov/.

AUTHOR CONTRIBUTIONS

CY: conceptualization, methodology, software, validation, investigation, visualization, and writing original draft. JY: software, writing—review and editing, and supervision. YL: software, visualization, and writing—original draft. XG: writing—review and editing, validation, and visualization. All authors contributed to the article and approved the submitted version.

FUNDING

This work was supported by the National Natural Science Foundation of China (Grant Nos. 61873004, 51874003), the Humanities and Social Sciences Foundation of Anhui Department of Education, China (Grant No. SK2017A0098).

REFERENCES

Alwidian, J., Hammo, B. H., and Obeid, N. (2018). WCBA: weighted classification based on association rules algorithm for breast cancer disease. *Appl. Soft Comput.* 62, 536–549. doi: 10.1016/j.asoc.2017.11.013

Amrane, M., Oukid, S., Gagaoua, I., and Ensarl, T. (2018). "Breast cancer classification using machine learning," in *2018 Electric Electronics, Computer Science, Biomedical Engineerings' Meeting (EBBT)* (Istanbul: IEEE), 1–4. doi: 10.1109/EBBT.2018.8391453

Andrejiova, M., and Grincova, A. (2018). Classification of impact damage on a rubber-textile conveyor belt using nave-bayes methodology. *Wear* 414–415, 59–67. doi: 10.1016/j.wear.2018.08.001

Aolin, X., and Maxim, R. (2017). Information-theoretic lower bounds on bayes risk in decentralized estimation. *IEEE Trans. Inform. Theory* 63, 1580–1600. doi: 10.1109/TIT.2016.2646342

Fakoor, R., Ladhak, F., Nazi, A., and Huber, M. (2013). "Using deep learning to enhance cancer diagnosis and classification," in *The 30th International Conference on Machine Learning (ICML 2013)* (Atlanta, GA), 1–7.

Fan, B., Feng, S., Che, Y., Mao, J., and Xie, Y. (2018). An oil monitoring method of wear evaluation for engine hot tests. *Int. J. Adv. Manuf. Technol.* 94, 3199–3207. doi: 10.1007/s00170-016-9473-8

Gupta, S., Kumar, D., and Sharma, A. (2012). Data mining classification techniques applied for breast cancer diagnosis and prognosis. *Indian J. Comput. Sci. Eng.* 2, 188–195.

Hart, G. R., Roffman, D. A., Decker, R., and Deng, J. (2018). A multi-parameterized artificial neural network for lung cancer risk prediction. *PLoS ONE* 13:e205264. doi: 10.1371/journal.pone.0205264

Heidari, M., Khuzani, A. Z., Hollingsworth, A. B., Danala, G., Mirniaharikandehei, S., Qiu, Y., et al. (2018). Prediction of breast cancer risk using a machine learning approach embedded with a locality preserving projection algorithm. *Phys. Med. Biol.* 63:035020. doi: 10.1088/1361-6560/aaa1ca

Jamal, A., Handayani, A., Septiandri, A. A., Ripmiatin, E., and Effendi, Y. (2018). Dimensionality reduction using pca and k-means clustering for breast cancer prediction. *Lontar Komput.* 09, 192–201. doi: 10.24843/LKJITI.2018.v09.i03.p08

Kim, H. J., Kim, J., and Lim, P. (2018). Towards perfect text classification with wikipedia-based semantic naïve bayes learning. *Neurocomputing* 315, 128–134. doi: 10.1016/j.neucom.2018.07.002

Krause, C. M., and Zhang, L. (2019). Short-term travel behavior prediction with gps, land use, and point of interest data. *Transport. Res. B Methodol.* 123, 349–361. doi: 10.1016/j.trb.2018.06.012

Kurashima, T., Iwata, T., Irie, G., and Fujimura, K. (2013). Travel route recommendation using geotagged photos. *Knowl. Inform. Syst.* 37, 37–60. doi: 10.1007/s10115-012-0580-z

Lassoued, Y., Monteil, J., Gu, Y., Russo, G., Shorten, R., and Mevissen, M. (2017). "A hidden markov model for route and destination prediction," in *IEEE 20th International Conference on Intelligent Transportation Systems (IEEE)* (Yokohama), 1–6. doi: 10.1109/ITSC.2017.8317888

Loud, J., and Murphy, J. (2017). Cancer screening and early detection in the 21st century. *Semin. Oncol. Nurs.* 33, 121–128. doi: 10.1016/j.soncn.2017.02.002

Mayur, S., Zaid, A., Jared, W. C., Richard, R., and Thomas, A. (2019). Sacroiliac joint fusion system for high-grade spondylolisthesis using 'reverse Bohlman technique': a technical report and overview of the literature. *World Neurosurg.* 124, 331–339. doi: 10.1016/j.wneu.2019.01.041

Rajalakshmi, R., and Aravindan, C. (2018). A naïve bayes approach for url classification with supervised feature selection and rejection framework. *Comput. Intell.* 34, 363–396. doi: 10.1111/coin.12158

Sasikala, S., Bharathi, M., Ezhilarasi, M., Senthil, S., and Reddy, M. (2019). Particle swarm optimization based fusion of ultrasound echographic and elastographic texture features for improved breast cancer detection. *Australas. Phys. Eng. Sci. Med.* 42, 677–688. doi: 10.1007/s13246-019-00765-2

Sharaf, H., Naveen, Z. Q., Samita, B., and Shakeel, K. (2015). "Reduction of variables for predicting breast cancer survivability using principal component analysis," in *2015 IEEE 28th International Symposium on Computer-Based Medical Systems* (Sao Carlos: IEEE Computer Society), 131–134.

Siddiqui, S., Athar, A., Khan, M., Abbas, S., Saeed, Y., Khan, M., et al. (2020). Modelling, simulation and optimization of diagnosis cardiovascular disease using computational intelligence approaches. *J. Med. Imaging Health Inform.* 10, 1005–1022. doi: 10.1166/jmihi.2020.2996

Ting, F. F., Tan, Y. J., and Sim, K. S. (2019). Convolutional neural network improvement for breast cancer classification. *Expert Syst. Appl.* 120, 103–115. doi: 10.1016/j.eswa.2018.11.008

Wang, P., Song, Q., Li, Y., Lv, S., Wang, J., Li, L., et al. (2020). Cross-task extreme learning machine for breast cancer image classification with deep convolutional features. *Biomed. Signal Process. Control* 57:101789. doi: 10.1016/j.bspc.2019.101789

Wang, Y., Wang, D., Ye, X., Wang, Y., Yin, Y., and Jin, Y. (2019). A tree ensemble-based two-stage model for advanced-stage colorectal cancer survival prediction. *Inform. Sci.* 474, 106–124. doi: 10.1016/j.ins.2018.09.046

Yang, J., and Ma, J. (2016). A structure optimization framework for feed-forward neural networks using sparse representation. *Knowl. Based Syst.* 109, 61–70. doi: 10.1016/j.knosys.2016.06.026

Yang, J., and Ma, J. (2019). Feed-forward neural network training using sparse representation. *Expert Syst. Appl.* 116, 255–264. doi: 10.1016/j.eswa.2018.08.038

Ye, N., Wang, Z. Q., Malekian, R., Lin, Q., and Wang, R. C. (2015). A method for driving route predictions based on hidden markov model. *Math. Probl. Eng.* 2015, 1–12. doi: 10.1155/2015/824532

Conflict of Interest: The authors declare that the research was conducted in the absence of any commercial or financial relationships that could be construed as a potential conflict of interest.

frontiers in Physics

BRIEF RESEARCH REPORT
published: 24 July 2020
doi: 10.3389/fphy.2020.00259

Research on Geographic Location Prediction Algorithm Based on Improved Teaching and Learning Optimization ELM

Zhen Yang[1] *and Zengwu Sun*[2]*

[1] *Chongqing Key Laboratory of Spatial Data Mining and Big Data Integration for Ecology and Environment, Rongzhi College of Chongqing Technology and Business University, Chongqing, China,* [2] *College of Medical Information Engineering, Shandong First Medical University & Shandong Academy of Medical Sciences, Tai'an, China*

With the rapid development of vehicle-mounted communication technology, GPS data is an effective method to predict the current road vehicle track based on vehicle-mounted data. GPS-oriented vehicle-mounted data position prediction method is currently a hot research work and an effective method to realize intelligent transportation. In this paper, an improvement scheme is proposed based on the problem of falling into local optimization existing in the basic algorithm of teaching and learning optimization algorithm. An interference operator is used to disturb teachers to enhance the kinetic energy of the population to jump out of local optimization. By comparing the performance of GA, PSO, TLBO, and ITLBO algorithms with four test functions, the results show that ITLBO has efficient optimization effect and generalization ability. Finally, the ITLBO-ELM algorithm has the best prediction effect by comparing the vehicle GPS data and comparing the experimental algorithms.

Keywords: GPS, learning optimization algorithm, ITLBO algorithms, ELM, prediction method

OPEN ACCESS

Edited by:
Jia-Bao Liu,
Anhui Jianzhu University, China

Reviewed by:
Hanliang Fu,
Illinois State University, United States
Li Shijin,
Yunnan University of Finance and Economics, China
Shaohui Wang,
Louisiana College, United States

***Correspondence:**
Zengwu Sun
sunzengwu@aliyun.com

Specialty section:
This article was submitted to Mathematical and Statistical Physics, a section of the journal Frontiers in Physics

Received: *15 April 2020*
Accepted: *10 June 2020*
Published: *24 July 2020*

Citation:
Yang Z and Sun Z (2020) Research on Geographic Location Prediction Algorithm Based on Improved Teaching and Learning Optimization ELM. Front. Phys. 8:259. doi: 10.3389/fphy.2020.00259

INTRODUCTION

As a new swarm intelligence algorithm, Teaching Learning Based Optimization (TLBO) simulates the process of teachers' teaching to students and students' learning and the process of students' learning from each other. Through teachers' teaching and students' learning from each other, students' learning performance can be improved. Because TLBO has the advantages of few parameters, simple thinking, easy understanding and strong robustness [1–4], it has attracted the attention of many scholars since it was put forward and has been applied in many fields. Such as reactive power optimization of power system [5], LQR controller optimization [6], IIR digital filter design [7], steelmaking and continuous casting scheduling problem [8], PID controller parameter optimization problem [9, 10], feature selection problem [11], HVDC optimization of voltage source converter [12], extension of global optimization technology to constrained optimization [13], analysis of financial time series data [14], neural network optimization [15], etc. Compared with the existing swarm intelligence algorithm, the algorithm obtains better results. Firstly, the basic TLBO algorithm is introduced, then the improved TBLO algorithm is studied, and then the performance of ITLBO algorithm is tested by using F1–F4 four test functions. Finally, GPS data is used to verify the advantages of ITLBO-ELM algorithm.

IMPROVED TEACHING AND LEARNING OPTIMIZATION ALGORITHM

Basic TLBO Algorithm

TLBO algorithm is an optimization algorithm proposed by teachers' teaching and students' learning social activities in the process of inspired teaching. Both teachers and students are candidate solutions in TLBO algorithm population. Assuming that there are a total of N individuals in the class, the individuals with the best academic performance, that is, the best fitness, are regarded as teachers, and the rest are students. The specific implementation process of TLBO is described as follows:

A. Population initialization

Teachers and students are individuals in the class. Assuming that the solution space of the optimization problem is S-dimensional, any individual Xi in the population is initialized in a random way:

$$X_i = L + r(U - L), \quad i = 1, 2, \ldots, n \tag{1}$$

In the formula, $U = (u_1, u_2, , \ldots, u_s)$ and $L = (l_1, l_2, , \ldots, l_s)$ are vectors formed by the upper and lower bounds of each variable, respectively; r is a random number between [0, 1].

B. Teaching stage

The best individual in the population is the teacher, and students improve their performance through the difference between the average value of teachers and classes. The i-th student X_i generates a new individual according to Equation (2):

$$X_i^{new} = X_i + D \tag{2}$$

Where X_i^{new} is an updated individual, only if $f(X_i^{new}) > f(X_i)$, X_i^{new} is accepted, i.e., $X_i = X_i^{new}$, otherwise X_i is kept unchanged; D is the difference between teacher X_t and student average X_m, which is described as follows:

$$D = r(X_t - T_f \times X_m) \tag{3}$$

Where X_i^{new} is the teacher; $X_m = \frac{1}{n}\sum_{i=1}^{n} X_i$ is the mean individual of the population; r is a random number between [0, 1]; the value of T_f teaching is only 0 or 1, which means that students may have learned all the knowledge of the teacher, or they may have learned nothing from the teacher. As a result, D may not be able to learn teachers' knowledge. T_f is a teaching factor and is generated by Equation (4):

$$T_f = R_{ound}[1 + rand\,(0, 1)] \tag{4}$$

Where R_{ound} represents the rounding function.

C. Learning Stage

In addition to learning from teachers, students also need to communicate with each other and learn from each other's strong points. Randomly select a student $X_k (i \neq k)$ from the class to carry out communication learning according to Equation (5):

$$X_i^{new} = \begin{cases} X_i + r(X_i - X_k), & if\ f(X_i) < f(X_k) \\ X_i + r(X_k - X_i), & \text{otherwise} \end{cases} \tag{5}$$

Where r is a random number between [0, 1]; $f(\cdot)$ is a fitness function; X_i^{new} is accepted only if $f(X_i^{new}) > f(X_i)$.

ITLBO Algorithm

Aiming at the shortcomings of the original TLBO, which is easy to fall into local optimization and low precision in the optimization process, an improved TLBO algorithm is proposed, which is recorded as ITLBO. In the process of TLBO optimization, a remedial period for the worst students is added. For the students with the worst academic performance in the class, the teacher will guide the students alone to quickly improve their knowledge. On this basis, an interference operator is used to disturb the teacher to enhance the kinetic energy for the population to jump out of the local optimal. The improvements are described below:

D. Remedial period

Assuming that the worst student in the class is X_w, the remedial process is as follows Equation (6):

$$X_w^{new} = r_1 X_w + r_2 (X_t - X_w) \tag{6}$$

Where r_1 and r_2 are random numbers between [0, 1]; X_w^{new} is an individual updated by X_w, only if $f(X_w^{new}) > f(X_w)$, X_w^{new} replaces X_w; Otherwise, a reverse solution is generated to replace the original X_w, and the reverse solution is generated according to the following Equation (7):

$$\overline{X_w} = U + L - X_w \tag{7}$$

Through tutoring or reverse learning for the worst students X_w, TLBO calculation points are used to speed up convergence and improve convergence accuracy. The strategy applied by X_w is to coach the worst students, which can directly improve the average value of the whole students. It is difficult to coach the best students to improve the average value of the whole students.

When TLBO algorithm solves complex multi-dimensional optimization problems, it is easy to fall into local optimization under finite iteration times. In order to further improve the global optimization capability of TLBO, interference operators are added in the search process $p_{ert}(t)$:

$$p_{ert}(t) = 0.1 \times r_3 \times (1 - t/t_{\max}) \tag{8}$$

The effect of interference operator $p_{ert}(t)$ on teacher X_t is as follow Equation (9):

$$X_t^{new} = X_t + p_{ert}(t) \times (U - L) \tag{9}$$

Where r_3 is a random number between [0, 1]; $p_{ert}(t)$ is the disturbance coefficient of the t-th iteration process. With the increase of t, $p_{ert}(t)$ gradually decreases, and the disturbance degree of interference operator to teachers gradually decreases. In the early stage of the search, $p_{ert}(t)$ is larger, which causes greater disturbance to the update of teachers' positions, increases population diversity, and effectively enhances X_t to jump out of the local optimization. In the later stage of search, $p_{ert}(t)$ gradually decreases to 0 to avoid affecting the local optimization and convergence of TLBO algorithm in the later stage.

The implementation process of ITLBO algorithm is shown in follow steps.

Step 1: Initialization parameters: class size n, dimension s, t_{max}, $t = 1$ and Initialize the population according to Equation (1).

Step 2: Calculate X_{max} and calculate D according to Equation (3) and calculate the new individual according to Equation (2) and update X_i.

Step 3: Individual X_j is randomly selected, new individuals are calculated according to Equation (5), and X_i is updated. Calculate X_w^{new}according to Equation (6); calculate the Directional Solution of X_w by Equation (7).

Step 4: Update X_w with New Individual or Reverse Solution, Choose the optimal individual X_w and calculate the interference operator according to Equation (8); according to Equation (9), update X_t.

Step 5: *If* $t > t_{max}$ $t = t+1$*; go to Step 2; or* Output optimal solution.

Extreme Learning Machine (ELM)

ELM has the advantages of simple structure, fast operation, and strong generalization ability and so on, and avoids the problem of local optimization. No matter in theoretical research or in practical application, ELM has attracted the attention of many machine learning researchers. However, ELM still has some difficult problems to solve. The input weight thresholds of ELM are given randomly. How to ensure that they are the optimal model parameters? Appropriate number of hidden layer nodes and hidden layer activation function can ensure the generalization ability and running speed of ELM, but the setting of hidden layer node number and selection of hidden layer activation function of ELM are difficult problems.

Extreme Learning Machine (ELM) is a novel learning algorithm for single-hidden layer feedforward neural networks (SLFNs). Compared neural network learning methods (such as BP neural network) have complicated parameter design in the training model and are easy to fall into local optimization. However, ELM only sets a reasonable number of hidden layer neurons, and the algorithm execution process does not need to iterate the hidden layer. Input weights and hidden layer thresholds are randomly generated and do not rely on training sample data. The weight matrix of the output layer is obtained through one-step analytical calculation, which avoids the complicated calculation process of repeated iteration of the traditional neural network and greatly improves the training speed of the network.

For any N random samples (x_i, t_i),$x_i = [x_{i1}, x_{i2}, ..., x_{in}]^T \in R^n$, n is the number of input layer nodes, $t_i = [t_{i1}, t_{i2}, ..., t_{im}]^T \in R^m$ the number of hidden layer nodes is m, and the hidden layer excitation function is g (x), then the mathematical model is as follows:

$$\sum_{i=1}^{L} \beta_i g(W_i \cdot X_j + b_i) = o_j \tag{10}$$

$$W = \begin{bmatrix} w_{11} & w_{12} & ... & w_{1n} \\ w_{21} & w_{22} & ... & w_{2n} \\ ... & ... & ... & ... \\ w_{L1} & w_{L2} & ... & w_{Ln} \end{bmatrix}_{L\times n} \tag{11}$$

$$\beta = \begin{bmatrix} \beta_{11} & \beta_{12} & ... & \beta_{1n} \\ \beta_{21} & \beta_{22} & ... & \beta_{2n} \\ ... & ... & ... & ... \\ \beta_{L1} & \beta_{L2} & ... & \beta_{Ln} \end{bmatrix}_{L\times n} \tag{12}$$

Where X_j and o_j are the input and output of the extreme learning machine, respectively, i.e., The input amount of location information of geographic information; W and β are both connection weight matrices; $g(x)$ is the excitation function; b is the bias matrix, $b = [b_1, b_2, \ldots, b_L]$, b_i is the i-th neuron bias.

In order to minimize the output error, define the learning objectives:

$$\lim \sum_{j=1}^{N} ||o_j - t_j|| = 0 \tag{13}$$

Through continuous learning and training, $W_{\tilde{i}}, b_{\tilde{i}}, \beta_{\tilde{i}}$ are obtained, see as Equation (14)

$$||H(\tilde{W_i}, \tilde{b_i})\tilde{\beta_i} - T'|| = \min_{W,b,\beta} ||H(\tilde{W_i}, \tilde{b_i})\tilde{\beta_i} - T'||, i = 1, 2, ..., L \tag{14}$$

Equation (14) is equal Equation (15).

$$E = \sum_{j=1}^{N} \left[\sum_{i=1}^{L} \beta_i g(W_i \cdot X_j + b_j) - t_j \right]^2 \tag{15}$$

The training process actually solves the linear process and is realized by outputting weights.

$$\tilde{\beta} = H^* T'' \tag{16}$$

Where $\boldsymbol{H}$ is the output matrix and $\boldsymbol{H^*}$ is the generalized inverse matrix of Moore-Penrose.

SIMULATION TEST AND ALGORITHM COMPARISON

Benchmark Test Function

In this paper, four benchmark functions are selected to test the algorithm.

The test functions are as follows:

A. Ackley's Function $f1$:

$$f(X) = -20\exp(-0.2\sqrt{\sum_{i=1}^{n} x_i^2/n}) - \exp(\sum_{i=1}^{n} \cos(2\pi x_i)/n) + 20 + e, |x_i| \le 32 \tag{17}$$

The optimal values are: $\min(f(X^*)) = f(0, 0, ..., 0) = 0$.

The function is a unimodal function with only one optimal value, but the surface is uneven.

B. Schweffel's Problem 1.2 function *f2*:

$$f(X) = \sum_{i=1}^{n} \left[\sum_{j=1}^{i} x_j \right]^2, |x_i| \leq 100 \tag{18}$$

The optimal values are: $\min(f(X^*)) = f(0, 0, ..., 0) = 0$

The function is a unimodal function, but the surface is smooth near the optimal value.

C. Generalized Schweffel's Problem 2.26 function *f3*:

$$f(X) = -\sum_{i=1}^{n} x_i \sin(\sqrt{|x_i|}), |x_i| \leq 500 \tag{19}$$

The optimal values are: .

The function is a multimodal function with multiple optimal values and uneven surface.

D. Generalized Rastrigin's function $f4$:

$$f(X) = \sum_{i=1}^{n} \left[x_i^2 - 10\cos(2\pi x_i) + 10 \right], |x_i| \leq 5.2 \tag{20}$$

The optimal values are: $\min(f(X^*)) = f(0, 0, ..., 0) = 0$.

The function is a multimodal function with multiple optimal values and uneven surface.

Test Results

Verify the experimental results of TLBO-ELM algorithm, The algorithm uses Python language to implement the server Dell T610 operating system uses Ubuntu 64 bits, 2 CPU: x5650 main frequency 2.6G with 12 cores and 24 threads, memory 64G, The algorithm is run independently on four commonly used Benchmark functions for 30 times, The maximum number of iterations is 1,000, 100 iteration times are recorded, respectively, 200,..., The average fitness value obtained 1,000 times describes the fitness value curve, The algorithms involved in the comparison include GA, PSO, TLBO and three commonly used swarm intelligence algorithms. The items to be compared include the average fitness value, the optimal result value, the worst result value and the standard deviation. The tested data are listed in detail in the test result comparison table. In order to compare the convergence performance of the four algorithms more vividly and clearly, the above three test functions are selected, and the convergence curves of the four algorithms on the selected functions are drawn, respectively. The test results are shown in **Table 1** for example:

Through the above test results and comparison tables, it can be seen that when testing functions $f4$ and $f1$, the optimal values found by ITLBO algorithm perform best and the curves are relatively smooth, TLBO is better and the curves fluctuate little, and PSO and GA perform poorly. The standard deviation of TLBO algorithm is similar to that of ITLBO algorithm, while the standard deviation of GA and PSO is larger, which shows that TLBO algorithm performs better in convergence stability. When testing $f3$ function, ITLBO algorithm finds the best optimal value, the curve is smoother, the standard deviation is lower, TLBO curve is smoother, the standard deviation is lower, but the convergence result value is not accurate enough. PSO and GA algorithms find the best value, the curve fluctuates greatly, and the standard deviation is higher. When function *f2* tests, ITLBO algorithm still shows better optimization accuracy and convergence stability than the other three algorithms.

On the four functions tested, ITLBO algorithm shows the advantages of good convergence stability, high optimization accuracy and so on, and shows good optimization ability. The accuracy of the optimal solution found by the artificial fish swarm algorithm is not high enough, but the stability is good. Genetic

TABLE 1 | Comparison of four function sequencing.

F	Algorithm	Optimal value	Worst value	Average value	Standard deviation
f1	GA	3.012	3129.46	263.871	167.787
	PSO	2.235	164.231	123.231	128.127
	TLBO	2.765	783.298	50.239	77.797
	ITLBO	0.732	813.956	23.321	72.712
f2	GA	$2.818e^{-15}$	35.286	7.271	6.332
	PSO	$3.412e^{-18}$	9.7339	4.689	3.967
	TLBO	$9.731e^{-18}$	6.2443	3.228	2.567
	ITLBO	$1.182e^{-21}$	8.150	1.298	2.487
f3	GA	−278.789	−90.877	−124.67	58.834
	PSO	−293.264	−151.18	−175.482	47.898
	TLBO	−302.179	−212.34	−217.178	34.238
	ITLBO	−398.038	−178.76	−234.156	29.727
f4	GA	3.988	1089.78	187.525	97.686
	PSO	2.373	287.787	54.633	18.787
	TLBO	2.722	276.676	41.842	14.778
	ITLBO	2.229	123.178	8.653	10.231

algorithm and particle swarm optimization algorithm have the worst performance in finding the optimal solution value of the four functions.

As we can see from that optimization graph, with the increase of iteration times, the optimization results of the algorithm also tend to be stable. The stable optimization values of genetic algorithm and particle swarm optimization algorithm are obviously higher than those of other algorithms. The curve of TLBO algorithm is relatively smooth, but the solution results are not very accurate. ITLBO algorithm has advantages in optimization speed, optimization accuracy and optimization stability compared with other three algorithms.

Random selection of iteration times is 100, 200, …, 1,000 times, respectively, to test the fitness value of the algorithm and the relationship between iteration times. See as **Figure 1**.

Comparative Study on GPS Vehicle Data Position Prediction

The data studied in this paper come from on-board GPS data. The data include: road number, vehicle ID, time, longitude, dimension, speed and position number. The data time is 15,000 on-board GPS data information from August 1, 2014 to August 31, 2014. Its data format is shown in **Table 2** below:

Location numbering is based on the location range represented by dimensions. Different numbers differ in geographical locations. When the longitude and latitude of different geographical positions are numbered at the same number, it means that the two positions are identified as similar or the same position, i.e., the correct position is predicted. Based on the map division of this grid, different geographic location information is divided into the same or similar geographic

TABLE 2 | Vehicle GPS data sheet.

ID	Date	Time	Longitude	Latitude	Position
4231	2014/2/3	06:01:18	30.583802	104.034407	86
464	2014/8/4	14:21:00	30.624811	104.136587	68
1	2014/3/3	21:19:15	30.624809	104.136612	67
123	2014/7/12	11:23:06	30.615417	104.040228	79
234	2014/8/13	14:47:59	30.651394	103.984025	20

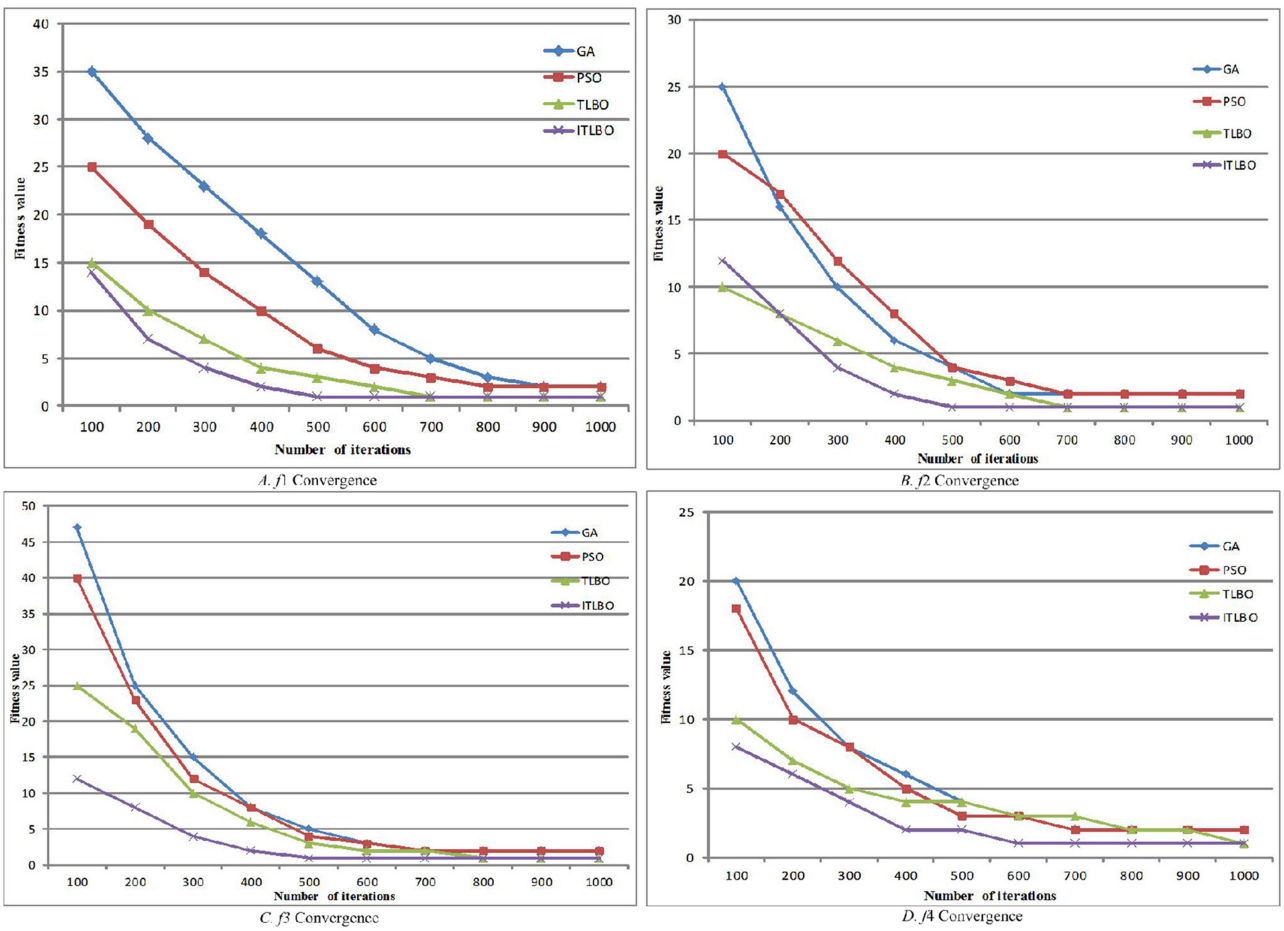

FIGURE 1 | Convergence comparison of four functions. **(A)** *f*1 Convergence. **(B)** *f*2 Convergence. **(C)** *f*3 Convergence. **(D)** *f*4 Convergence.

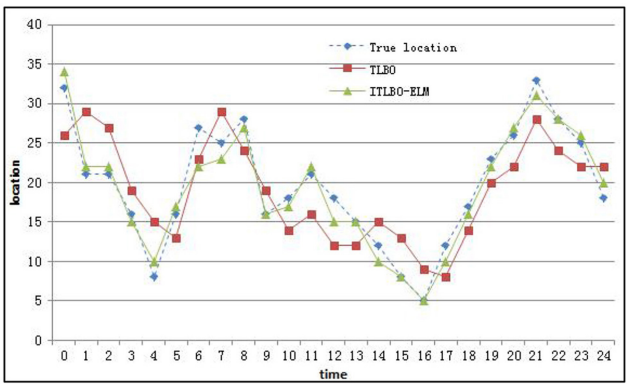

FIGURE 2 | Comparison of prediction effect of 1-day location.

spaces. The size of the grid also determines the accuracy of the prediction. When the grid is relatively large, the prediction effect is ideal. When there are many grids, the prediction effect may not be ideal. Under different grids, there may be two similar positions to deal with different grids. As a result, the grid size can also affect the accuracy of the experiment.

Through the processing and analysis of GPS data, this paper uses TLBO, ITLBO-ELM algorithms to compare the prediction results, and predicts different vehicle information from different road sections within the numbered range of the next position or related area. As shown in **Figure 2**.

Geographical locations are described by numerical numbers and different area numbers express different locations. The closer the data are, the shorter the distance between locations. As can be seen from **Figure 2**, ITLBO-ELM is closer to the real position than TLBO prediction method and ITLBO-ELM prediction method for prediction comparison of different positions at different time points. ITBLO combined with ELM algorithm is mainly to improve the convergence speed and accuracy of the algorithm. As can be seen from **Figure 2**, ITBLO-ELM algorithm has obvious advantages corresponding to other algorithms.

Geographic location information is encoded with specific area numbers and different area numbers express different geographic location information. There may be the same area numbers at different longitude and latitude. At this time, the location representation is similar. When judging from the effect of the actual position and the predicted position in **Figure 2**, there are obvious differences between the actual position and the TLBO prediction results, while in the whole prediction track process, the actual position area number is consistent with the ITLBO-ELM prediction results, and the two are relatively close. The experimental results show that ITLBO-ELM has good experimental results in overall performance.

CONCLUSION

In view of the poor prediction accuracy and effect in the geographic location information prediction algorithm, a prediction method based on improved teaching and learning optimization algorithm and ELM algorithm is proposed. The results show that ITLBO-ELM algorithm has high accuracy in predicting positions. The method proposed in this paper has good effect in predicting the position, considering the representation of position information under different coordinates. Further research work is carried out to predict the position information from different coordinates so as to reduce the prediction errors caused by coordinate differences. In the conclusion, in the future research work, whether more tests are considered in the algorithm to test the test effect of this paper. In the future research work, the convergence speed and position accuracy of the algorithm will be mainly considered.

DATA AVAILABILITY STATEMENT

The raw data supporting the conclusions of this article will be made available by the authors, without undue reservation.

AUTHOR CONTRIBUTIONS

All authors participated in the preparation and presentation of the manuscript.

FUNDING

This work was supported by the Science and Technology Research Program of Chongqing Municipal Education Commission (Grant No. KJZD-K201902101).

REFERENCES

1. Jiang W, Carter DR, Fu HL, Jacobson MG, Zipp KY, Jin J, et al. The impact of the biomass crop assistance program on the United States forest products market: an application of the global forest products model. *Forests.* (2019) **10**:1–12. doi: 10.3390/f10030215
2. Liu JB, Zhao J, Zhu ZX. On the number of spanning trees and normalized Laplacian of linear octagonal-quadrilateral networks. *Int J Quantum Chem.* (2019) **119**:1–21. doi: 10.1002/qua.25971
3. Liu JB, Zhao J, Cai Z. On the generalized adjacency, Laplacian and signless Laplacian spectra of the weighted edge corona networks. *Physica A.* (2020) **540**:1–11. doi: 10.1016/j.physa.2019.123073
4. Wei L, Li J, Ren L, Xu J. Exploring livelihood resilience and its impact on livelihood strategy in rural China. *Social Indicat Res.* (2020). doi: 10.1007/s11205-020-02347-2
5. Ghasemi M, Taghizadeh M, Ghavidel S, Aghaei J, Abbasian A. Solving optimal reactive power dispatch problem using a novel teaching-learning-based optimization algorithm. *Eng Appl Artif Intell.* (2015) **39**:100–8. doi: 10.1016/j.engappai.2014.12.001
6. Lee J, Chang H-J. Analysis of explicit model predictive control for path-following control. *PLoS ONE.* (2018) **13**:e0194110. doi: 10.1371/journal.pone.0194110
7. Singh R, Verma HK. Teaching–learning-based Optimization Algorithm for Parameter Identification in the Design of IIR Filters. *J Inst Eng.* (2013) **94**:285–94. doi: 10.1007/s40031-013-0063-y

8. Pan Q-K. An effective co-evolutionary artificial bee colony algorithm for steelmaking-continuous casting scheduling. *Eur J Operat Res.* (2016) **250**:702–14. doi: 10.1016/j.ejor.2015.10.007
9. Dib F, Boumhidi I. Hybrid algorithm DE-TLBO for optimal and PID control for multi-machine power system. *Int J Syst Assur Eng Manage.* (2017) **8**:S925–36. doi: 10.1007/s13198-016-0550-z
10. Luo Z, Guo Q, Zhao J, Xu S. Tuning of a PID controller using modified dynamic group based TLBO algorithm. *Int J Comput Appl.* (2017) **157**:17–23. doi: 10.5120/ijca2017912593
11. Satapathy SC, Naik A, Parvathi K. Unsupervised feature selection using rough set and teaching learning-based optimisation. *Int J Artif Intell Soft Comput.* (2013) **3**:244. doi: 10.1504/IJAISC.2013.053401
12. Yang B, Shu HC, Zhang RY, Huang LN, Zhang XS, Yu T. Interactive teaching-learning optimization for VSC-HVDC systems. *Kongzhi yu Juece/Control Decis.* (2019) **34**:325–34. doi: 10.13195/j.kzyjc.2017.1080
13. Wang BC, Li HX, Feng Y. An improved teaching-learning-based optimization for constrained evolutionary optimization. *Information Sci.* (2018) **456**:131–44 doi: 10.1016/j.ins.2018.04.083
14. Das SP, Padhy S. A novel hybrid model using teaching-learning-based optimization and a support vector machine for commodity futures index forecasting. *Int J Mach Learn Cybernet.* (2018) **9**:97–111. doi: 10.1007/s13042-015-0359-0
15. Han B, Zhou L, Zhang Z. LIDAR:assisted radial basis function neural network optimization for wind turbines. *IEEJ Trans Electr Electron Eng.* (2018) **13**:195–200. doi: 10.1002/tee.22514

Conflict of Interest: The authors declare that the research was conducted in the absence of any commercial or financial relationships that could be construed as a potential conflict of interest.

frontiers in Physics

BRIEF RESEARCH REPORT
published: 28 July 2020
doi: 10.3389/fphy.2020.00211

Computing the Mixed Metric Dimension of a Generalized Petersen Graph $P(n, 2)$

*Hassan Raza and Ying Ji**

Business School, University of Shanghai for Science and Technology, Shanghai, China

Let $\Gamma = (V, E)$ be a connected graph. A vertex $i \in V$ recognizes two elements (vertices or edges) $j, k \in E \cap V$, if $d_\Gamma(i, j) \neq d_\Gamma(i, k)$. A set S of vertices in a connected graph Γ is a mixed metric generator for Γ if every two distinct elements (vertices or edges) of Γ are recognized by some vertex of S. The smallest cardinality of a mixed metric generator for Γ is called the mixed metric dimension and is denoted by β_m. In this paper, the mixed metric dimension of a generalized Petersen graph $P(n, 2)$ is calculated. We established that a generalized Petersen graph $P(n, 2)$ has a mixed metric dimension equivalent to 4 for $n \equiv 0, 2(mod 4)$, and, for $n \equiv 1, 3(mod 4)$, the mixed metric dimension is 5. We thus determine that each graph of the family of a generalized Petersen graph $P(n, 2)$ has a constant mixed metric dimension.

2010 Mathematics Subject Classification: 05C12, 05C90

Keywords: mixed metric dimension, metric dimension, edge metric dimension, generalized Petersen graph, exact values

OPEN ACCESS

Edited by:
Shaohui Wang,
Louisiana College, United States

Reviewed by:
Muhammad Kamran Siddiqui,
COMSATS University Islamabad, Lahore Campus, Pakistan
Azmat Ullah Khan Niazi,
University of Lahore, Pakistan
Lidan Pei,
Hefei Normal University, China

****Correspondence:***
Ying Ji
jiying@usst.edu.cn

Specialty section:
This article was submitted to Mathematical and Statistical Physics, a section of the journal Frontiers in Physics

Received: *09 April 2020*
Accepted: *18 May 2020*
Published: *28 July 2020*

Citation:
Raza H and Ji Y (2020) Computing the Mixed Metric Dimension of a Generalized Petersen Graph P(n, 2). Front. Phys. 8:211. doi: 10.3389/fphy.2020.00211

1. INTRODUCTION

The aim of robot navigation functionality is to attain the coveted position promptly whenever it is desired. Let us imagine that robot navigation in a sensor network that can obtain the distances to a collection of landmarks. A robot's position is solely resolved by determining the subset of nodes in the sensor network. It can be achieved by the concept of landmarks in the graphs introduced in Khuller et al. [1]; this idea was later named the metric dimension. All the graphs considered here have no loops and are simple, measurable, and undirected.

Let $\Gamma = (V, E)$ be the graph of the distance $d_\Gamma(a, b)$ (or $d(a, b)$) among the vertices $a, b \in V(\Gamma)$ the minimum length of paths between them. For a vertex $a \in V$, distinguish two vertices in a graph, say b and c, if the condition $d_\Gamma(a, b) \neq d_\Gamma(a, c)$ holds. A set $R \subset V(\Gamma)$ is the metric generator if some chosen vertices of the set R recognizes a pair of distinguished vertices. The metric basis with the least number of elements is called the metric generator, and the cardinality of its metric basis is termed the metric dimension. The notation employed here is $\beta(\Gamma)$. The fundamental concept of the metric dimension was instated by Slater [2], and the notation of the metric dimension was initiated by Haray and Melter [3]. This concept was later studied by many researchers with unique modifications; for reference, see [4–8]. Some of the recent results on metric dimension and its further variations are studied in Shao et al. [9] and Raza et al. [10–13].

Lemma 1. *Suppose R is the distinguishing set of Γ and the vertices $a, b \in V(\Gamma)$. If $d_\Gamma(a, c) \neq d_\Gamma(a, c)$, for all vertices $c \in V(\Gamma)\backslash\{a, b\}$, then $\{a, b\} \bigcap R \neq \emptyset$.*

Analogous to this definition, Kelenc et al. [14] introduced the concept of edge metric dimension, and this was further studied in Zubrilina [15], Peterin and Yero [16], and Zhu et al. [17]. This distance between an edge $e = ab$ and a vertex c is given as follows

$$d(e, c) = min\{d(a, c), d(b, c)\}$$

A vertex $c \in V(\Gamma)$ distinguishes two edges of a graph $e_1, e_2 \in E(\Gamma)$ if $d_\Gamma(e_1, u) \neq d_\Gamma(e_2, u)$. The set $R_e \subset V$ is termed as the edge metric generator if some distinct edges of Γ are distinguished by the vertex set R_e. The cardinality of an edge metric generator is called an edge metric dimension, and it is depicted as $\beta_e(\Gamma)$. Having defined the notion of an edge metric generator, which distinctly recognizes every edge in a graph, a common assumption would be that any edge metric generator R_e would be a metric dimension as well. This assumption is far from reality, as indicated in Kelenc et al. [14], but there are several families of graphs where this occurs, that is, $\beta(\Gamma) = \beta_e(\Gamma)$. Some other distance related parameters are studied in Liu et al. [18–22].

In this paper, our focus is on mixed metric dimension, which is a mixed version of metric and edge metric dimension. A set R_m of vertices of a graph Γ is known as a mixed metric generator if any two distinct elements (vertices or edges) of a graph are recognized by some the vertex set of R_m. The least cardinality of a mixed metric generator for a graph is termed as a mixed metric dimension, denoted as $\beta_m(\Gamma)$. The idea is recently brought forward by Kelenc et al. [23].

Lemma 2. *Let for some vertex $a \in V(\Gamma)$, and let $R_m = V(\Gamma)\backslash a$, and if there is an element $b \in N(a)$, also for some $c \in R_m$, $d_\Gamma(ab, c) \neq d_\Gamma(b, c)$, then R_m is the mixed metric generator for the graph Γ.*

The notion of a mixed metric dimension clearly indicates that a mixed metric generator is also a standard metric generator and an edge metric generator, The following relationship is given in [23],

$$\beta_m(\Gamma) \max \geq \{\beta(\Gamma), \beta_e(\Gamma)\}$$

The following remark shows the structure of mixed metric dimension:

Remark 1: [23] Suppose for some graph Γ we have $2 \leq \beta_m \leq n$.

Recently, this concept has attracted some attention, and it has been studied by Raza et al. [24]. The authors discussed the mixed metric dimension among the prism graphs, which are commonly known as generalizes Petersen graphs $P(n, 1)$, and two families of convex polytopes A_n, R_n, further presenting the problem of finding $\beta_m(P(n, 2))$.

Some of the results regarding metric and edge metric dimension are given:

Remark 2: [14] For $n \geq 2$, the metric and edge metric dimension are, $\beta(\mathcal{P}_n) = \beta_e(\mathcal{P}_n) = 1$; for cycle graph, $\beta(\mathcal{C}_n) = \beta_e(\mathcal{C}_n) = 2$; for complete graph, $\beta(\mathcal{K}_n) = \beta_e(\mathcal{K}_n) = n - 1$; and for any complete bipartite graph $(\mathcal{K}_{r,t})$ different from $(\mathcal{K}_{1,1})$, $\beta(\mathcal{K}_{r,t}) = \beta_e(\mathcal{K}_{r,t}) = r + t - 2$.

1.1. Known Results

Next, we present some already known results for β_m,

Proposition 1: [23] For a path graph $(\mathcal{P}_n)$ order $n \geq 4$, we have $\beta_m(\mathcal{P}_n) = 2$.

Proposition 2: [23] Let us consider any two positive integers: e, f

$$\beta_m(K_{e,f}) = \begin{cases} e + f - 1, & \text{if } e = 2 \text{ or } f = 2; \\ e + f - 2, & \text{otherwise.} \end{cases}$$

Proposition 3: [23] For a grid graphs, $P_m \square P_n$, with $m \geq n \geq 2$, $\beta_m = 3$.

Proposition 4: [23] Let us assume cycle graph $(\mathcal{C}_n)$ of order $n \geq 4$, then $\beta_m(C_n) = 3$.

Lemma 3. [24]*The mixed metric generator R_m must contain vertices from both the outer and inner cycle for the prism graph D_n.*

Proof: For $P(n, 1)$, this holds, and, by the same intuition, this must be true for $P(n, 2)$. The mixed metric resolving set comprises of vertices from both the cycles, which contain vertices of outer and inner cycle, respectively. □

2. MAIN RESULT

The generalized Petersen graphs is introduced by Watkins [25]. The $P(n, \ell)$, where $n \geq 3$ and $1 \leq \ell \leq \lfloor \frac{n-1}{2} \rfloor$ (see **Figure 2**), which is the cubic graph consists of vertices and edges, is shown below.

$$\mathcal{V}(P(n, \ell)) = \{q_0, q_1, \ldots, q_{n-1}, p_0, p_1, \ldots, p_{n-1}\}$$

$$\mathcal{E}(P(n, \ell)) = \{q_i q_{i+1}, p_i p_{i+\ell}, q_i q_i | i = 0, 1, \ldots, n - 1\}$$

Example: We used the graph of $P(n, 8)$, as can be seen in **Figure 1**. The mixed metric generator for $P(n, 8)$ is $\beta_m = \{q_0, q_1, p_4, p_5\}$, and it can been seen from **Table 1** that all the representation of vertices and edges are distinct.

The graph of the generalized Petersen graph comprises of three types of edges, external edges, internal edges, and spokes between q_i and q_{i+1}, p_i and p_{i+m}, and q_i and p_i, respectively. The vertices q_i and p_i $(0 \leq i \leq n - 1)$ are termed as external and internal vertices, respectively.

The prism graph D_n is known as $P(n, 1)$ for $m = 1$. Some of the already known results are given as

Theorem 1. [26] *The metric dimension of $\mathcal{D}_n$, for $n \geq 4$:*

$$\beta(\mathcal{D}_n) = \begin{cases} 2, & n \text{ is odd;} \\ 3, & n \text{ is even.} \end{cases}$$

Theorem 2. [27] *When, $n \geq 4$, $\beta_e(\mathcal{D}_n) = 3$.*

Theorem 3. [24] *For $n \geq 5$,*

$$\beta_m(P(n, 1)) = \begin{cases} 3, & n \text{ is even;} \\ 4, & n \text{ is odd.} \end{cases}$$

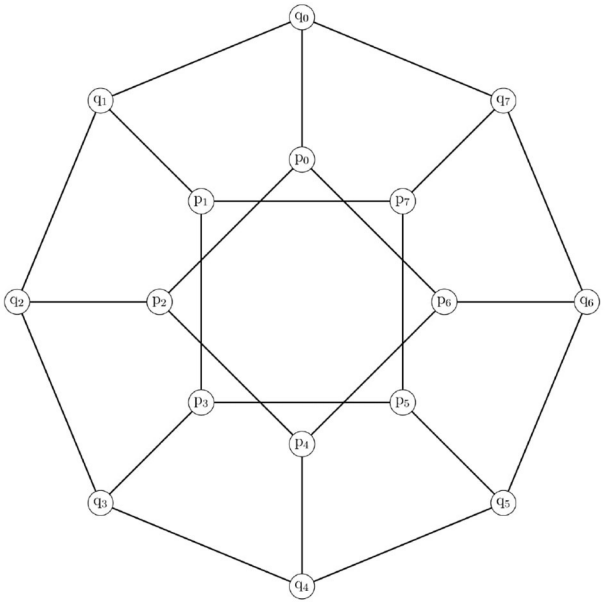

FIGURE 1 | The generalized Petersen graph $P(8, 2)$.

TABLE 1 | Codes for $P(n, 8)$.

v	$r_m(v)$	v	$r_m(v)$	e	$r_m(e)$	e	$r_m(e)$	e	$r_m(e)$
q_0	(0, 1, 3, 3)	p_0	(1, 2, 2, 4)	q_0q_1	(0, 0, 3, 3)	q_0p_0	(0, 1, 2, 3)	p_0p_2	(1, 2, 1, 4)
q_1	(1, 0, 3, 3)	p_1	(2, 1, 4, 2)	q_1q_2	(1, 0, 2, 3)	q_1p_1	(1, 0, 3, 2)	p_1p_3	(2, 1, 3, 1)
q_2	(2, 1, 2, 3)	p_2	(2, 2, 1, 4)	q_2q_3	(2, 1, 2, 2)	q_2p_2	(2, 1, 1, 3)	p_2p_4	(2, 2, 0, 3)
q_3	(3, 2, 2, 2)	p_3	(3, 2, 3, 1)	q_3q_4	(3, 2, 1, 2)	q_3p_3	(3, 2, 2, 1)	p_3p_5	(3, 2, 3, 0)
q_4	(4, 3, 1, 2)	p_4	(3, 3, 0, 3)	q_4q_5	(3, 3, 1, 1)	q_4p_4	(3, 3, 0, 2)	p_4p_6	(2, 3, 0, 3)
q_5	(3, 4, 2, 1)	p_5	(3, 3, 3, 0)	q_5q_6	(2, 3, 2, 1)	q_5p_5	(3, 3, 2, 0)	p_5p_7	(2, 2, 3, 0)
q_6	(2, 3, 2, 2)	p_6	(2, 3, 1, 3)	q_6q_7	(1, 2, 2, 2)	q_6p_6	(2, 3, 1, 2)	p_6p_0	(1, 2, 1, 3)
q_7	(1, 2, 3, 2)	p_7	(2, 2, 4, 1)	q_7q_0	(0, 1, 3, 2)	q_7p_7	(1, 2, 3, 1)	p_7p_1	(1, 2, 2, 1)

The known results for $P(n, 2)$ concerning metric and an edge metric dimension are

Theorem 4. [28] *For* $n \geq 5$, *the metric dimension is* $\beta(P(n, 2)) = 3$.

Theorem 5. [27] *For* $n \geq 5$, $\beta_e(P(n, 2)) = 3$.

It is quite natural to investigate the mixed metric dimension of $P(n, 2)$. Now, we will find mixed the metric dimension of $(P(n, 2))$, and for this the following lemmas are presented.

Lemma 4. ***Case 1:*** *If* $n \equiv 0(mod)4$, *then* $\beta_m(P(n, 2)) \leq 4$.

Proof: The proof is $n = 4r$, $r \geq 4$, where $r \in \mathbb{Z}^+$. The distinguishing vertices that will distinguish the whole vertices and edges of the graph are $R_m = \{q_0, q_1, p_{2r}, p_{2r+1}\}$. The following representations are presented with respect to R_m.

Representation of external vertices:

$$C_{R_m}(q_{2s}) = \begin{cases} (2s, 1, r-s+1, r+1), & 0 \leq s \leq 1; \\ (2s, s+1, r-s+1, r), & s = 2; \\ (s+2, s+2, r-s+1, r-s+2), & 3 \leq s \leq r; \\ (2r-s+2, 2r-s+3, s-r+1, & r+1 \leq s \leq 2r-2; \\ \quad s-r+1), & \\ (2, 3, s-r+1, s-r+1), & s = 2r-1. \end{cases}$$

and,

$$C_{R_m}(q_{2s+1}) = \begin{cases} (2s+1, 2s, s-r+1, r-s+1), & 0 \leq s \leq 2; \\ (s+3, s+2, 2, r-s+1), & 3 \leq s \leq r-1; \\ (r+2, r+2, 2, 1), & s = r; \\ (2r-s+2, 2r-s+2, & r+1 \leq s \leq 2r-3; \\ \quad s-r+2, s-r+1), & \\ (3, 4, s-r+2, r-s+1), & s = 2r-2; \\ (1, 2, s-r+2, s-r+1), & s = 2r-1. \end{cases}$$

Representation of internal vertices:

$$C_{R_m}(p_{2s}) = \begin{cases} (s+1, 2, r-s, r+2), & 0 \leq s \leq 1; \\ (s+1, s+1, r-s, r-s+3), & 2 \leq s \leq r; \\ (2r-s+1, 2r-s+2, & r+1 \leq s \leq 2r-1. \\ s-r, s-r+2), & \end{cases}$$

and,

$$C_{R_m}(p_{2s+1}) = \begin{cases} (s+2, s+1, r-s+2, r-s), & 0 \leq s \leq r-1; \\ (2r-s+1, r, s-r+3, s-r), & r \leq s \leq r+1; \\ (2r-s+1, 2r-s+1, & r+2 \leq s \leq 2r-1. \\ \quad s-r+3, s-r), & \end{cases}$$

Representation of external edges:

$$C_{R_m}(q_{2s}q_{2s+1}) = \begin{cases} (2s, s, r-s+1, r-s+1), & 0 \leq s \leq 1; \\ (2s, s+1, r-s+1, & s = 2; \\ \quad r-s+1), & \\ (s+2, s+2, r-s+1, & 3 \leq s \leq r; \\ \quad r-s+1), & \\ (2r-s+2, 2r-s+2, & r+1 \leq s \leq 2r-3; \\ \quad s-r+1, s-r+1), & \\ (3, 4, s-r+1, s-r+1), & s = 2r-2; \\ (1, 2, s-r+1, s-r+1), & s = 2r-1. \end{cases}$$

and,

$$C_{R_m}(q_{2s+1}q_{2s+2}) = \begin{cases} (2s+1, 2s, r-s, r-s+1), & 0 \leq s \leq 2; \\ (s+3, s+2, r-s, r-s+1), & 3 \leq s \leq r-1; \\ (2r-s+1, 2r-s+2, & r \leq s \leq 2r-3; \\ \quad s-r+2, s-r+1), & \\ (2, 3, s-r+2, s-r+1), & s = 2r-2; \\ (0, 1, s-r+2, s-r+1), & s = 2r-1. \end{cases}$$

Representation of external and internal edges:

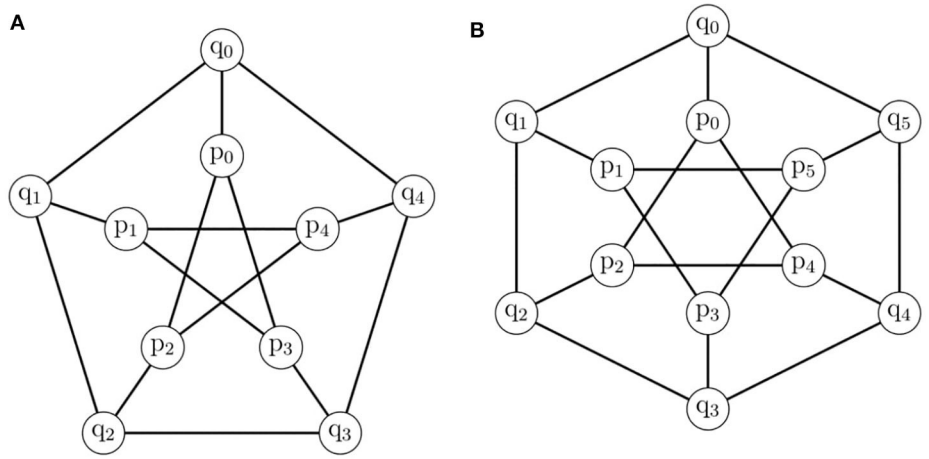

FIGURE 2 | (A) The generalized Petersen graph $P(5, 2)$, **(B)** The generalized Petersen graph $P(6, 2)$.

$$C_{R_m}(q_{2s}p_{2s}) = \begin{cases} (2s, 1, r-s, r+1), & 0 \le s \le 1; \\ (s+1, s+1, r-s, r-s+2), & 2 \le s \le r; \\ (2r-s+1, 2r-s+2, s-r, & r+1 \le s \le 2r-1. \\ \quad s-r+1), & \end{cases}$$

and,

$$C_{R_m}(q_{2s+1}q_{2s+1}) = \begin{cases} (2s+1, 2s, r-s+1, r-s), & 0 \le s \le 1; \\ (s+2, s+1, r-s+1, r-s), & 2 \le s \le r-1; \\ (r+1, r+1, 2, 0), & s = r; \\ (2r-s+1, 2r-s+1, & r+1 \le s \le 2r-2; \\ \quad s-r+2, s-r), & \\ (1, 2, s-r+2, s-r), & s = 2r-1. \end{cases}$$

Representation of internal edges:

$$C_{R_m}(p_{2s}p_{2s+2}) = \begin{cases} (1, 2, r-s-1, r-s+2), & s = 0; \\ (s+1, s+1, r-s-1, & 1 \le s \le r-1; \\ \quad r-s+2), & \\ (2r-s, r, s-r, 3), & r \le s \le r+1; \\ (2r-s, 2r-s+1, s-r, & r+2 \le s \le 2r-1. \\ \quad s-r+2), & \end{cases}$$

and,

$$C_{R_m}(p_{2s+1}p_{2s+3}) = \begin{cases} (2, 1, r-s+1, r-s-1), & s = 0; \\ (s+2, s+1, r-s+1, & 1 \le s \le r-3; \\ \quad r-s-1), & \\ (s+2, s+1, 3, r-s-1), & r-2 \le s \le r-1; \\ (2r-s, 2r-s, s-r+3, & r \le s \le 2r-2; \\ \quad s-r), & \\ (2, 1, s-r+3, s-r), & s = 2r-1. \end{cases}$$

□

Case 2: For $n \equiv 2(mod)4$, we have $\beta_m(P(n, 2) \le 4$

Proof: Now we can see $n = 4r + 2$, $r \ge 4$, where $r \in \mathbb{Z}^+$. The set of vertices that will distinguish the whole vertices and edges of the graph are $R_m = \{q_0, q_1, p_{2r+1}, p_{2r+2}\}$. The following representations are presented with respect to R_m.

Representation of external vertices:

$$C_{R_m}(q_{2s}) = \begin{cases} (2s, 2-s, r-s+2, r+1), & 0 \le s \le 1; \\ (2s, 3, r-s+2, r-s+2), & s = 2; \\ (s+2, s+2, r-s+2, r-s+2), & 3 \le s \le r; \\ (2r-s+3, 2r-s+4, & r+1 \le s \le 2r-1; \\ \quad s-r+1, s-r), & \\ (2, 3, s-r+1, s-r), & s = 2r. \end{cases}$$

and,

$$C_{R_m}(q_{2s+1}) = \begin{cases} (2s+1, 2s, s-r+1, r-s+2), & 0 \le s \le 2; \\ (s+3, s+2, r-s+1, r-s+1), & 3 \le s \le r; \\ (2r-s+3, 2r-s+4, & r+1 \le s \le 2r-2; \\ \quad s-r+1, s-r+1), & \\ (3, 5, s-r+1, s-r+1), & s = 2r-1; \\ (1, 3, s-r+1, s-r+1), & s = 2r. \end{cases}$$

Representation of internal vertices:

$$C_{R_m}(p_{2s}) = \begin{cases} (s+1, 2, r-s+3, r), & 0 \le s \le 1; \\ (s+1, r+1, r-s+3, r-s+1), & 2 \le s \le r; \\ (2r-s+2, 2r-s+3, & r+1 \le s \le 2r. \\ \quad s-r+2, s-r-1), & \end{cases}$$

and,

$$C_{R_m}(p_{2s+1}) = \begin{cases} (s+2, s+1, r-s, r-s+3), & 0 \le s \le r; \\ (2r-s+2, 2r-s+3, & r+1 \le s \le 2r. \\ \quad s-r, s-r+2), & \end{cases}$$

Representation of external edges:

$$C_{R_m}(q_{2s}q_{2s+1}) = \begin{cases} (2s, s, r-s+1, r+1), & 0 \le s \le 1; \\ (2s, s+1, r-s+1, r-s+2), & s = 2; \\ (s+2, s+2, r-s+1, & 3 \le s \le r; \\ \quad r-s+2), & \\ (2r-s+3, 2r-s+3, & r+1 \le s \le 2r-2; \\ \quad s-r+1, s-r), & \\ (3, 4, s-r+1, s-r), & s = 2r-1; \\ (1, 2, s-r+1, s-r), & s = 2r. \end{cases}$$

and,

$$C_{R_m}(q_{2s+1}q_{2s+2}) = \begin{cases} (2s+1, 2s, r-s+1, r-s+1), & 0 \le s \le 2; \\ (s+3, s+2, r-s+1, r-s+1), & 3 \le s \le r-1; \\ (2r-s+2, r+2, s-r+1, & r \le s \le r+1; \\ \quad s-r+1), & \\ (2r-s+2, 2r-s+3, s-r+1, & r+2 \le s \le 2r-2; \\ \quad s-r+1), & \\ (2, 3, s-r+1, s-r+1), & s = 2r-1; \\ (0, 1, s-r+1, s-r+1), & s = 2r. \end{cases}$$

Representation of external and internal edges:

$$C_{R_m}(q_{2s}p_{2s}) = \begin{cases} (2s, 1, r-s+2, r), & 0 \le s \le 1; \\ (s+1, s+1, r-s+2, r-s+1), & 2 \le s \le r; \\ (2r-s+2, 2r-s+3, & r+1 \le s \le 2r. \\ \quad s-r+1, s-r-1), & \end{cases}$$

and,

$$C_{R_m}(q_{2s+1}q_{2s+1}) = \begin{cases} (2s+1, 2s, r-s, r-s+2), & 0 \le s \le 1; \\ (s+2, s+1, r-s, r-s+2), & 2 \le s \le r; \\ (2r-s+2, 2r-s+2, & r+1 \le s \le 2r-1; \\ \quad s-r, s-r+1), & \\ (1, 2, s-r, s-r+1), & s = 2r. \end{cases}$$

Representation of internal edges:

$$C_{R_m}(p_{2s}p_{2s+2}) = \begin{cases} (s+1, 2, r-s+2, r-s), & 0 \le s \le 1; \\ (s+1, s+1, r-s+2, r-s), & 2 \le s \le r-1; \\ (2r-s+1, r+1, 3, 0), & r \le s \le r+1; \\ (2r-s+1, 2r-s+2, & r+2 \le s \le 2r. \\ \quad s-r+2, s-r-1), & \end{cases}$$

and,

$$C_{R_m}(p_{2s+1}p_{2s+3}) = \begin{cases} (s+2, s+1, r-s-1, & 0 \le s \le r-1; \\ \quad r-s+2), & \\ (2r-s+1, 2r-s+1, & r \le s \le r+1; \\ \quad s-r, 3), & \\ (2r-s+1, 2r-s+1, & r+2 \le s \le 2r-1; \\ \quad s-r, s-r+2), & \\ (2, 1, s-r, s-r+2), & s = 2r. \end{cases}$$

□

Now from lemma3, the resolving set R_m contains vertices from external and internal cycles; that is, the resolving set cannot comprise either external or internal vertices.

Lemma 5. *When $n \equiv 0, 2(mod4)$,then $\beta_m(P(n, 2)) \ge 4$.*

Proof: Suppose that $\beta_m(P(n, 2)) = 3$, the following contradictions arises:

Case 1: This is when the two fixed vertices are in the external cycle, $\{q_0, q_1\}$, and the other vertex lie in internal cycle p_ℓ, that is, $R_m = \{q_0, q_1, p_\ell\}$.
(i) If $0 \le \ell \le 1$ then, $r_m\{q_0|q_0, q_1, p_\ell\} = r_m\{q_0q_{n-1}|q_0, q_1, p_\ell\} = (0, 1, \ell+1)$.
(ii) If $\ell = 2, 4, \ldots, 2r$, then $r_m\{q_0|q_0, q_1, p_\ell\} = r_m\{q_0q_{n-1}|q_0, q_1, p_\ell\}$.
(iii) If $\ell = 3, 5, \ldots, 2r-1$, then $r_m\{q_0|q_0, q_1, p_\ell\} = r_m\{q_0q_{n-1}|q_0, q_1, p_\ell\}$.

Case 2: When internal cycle contains two fixed vertices that is $\{p_0, p_1\}$, and the other vertex lie in external cycle q_ℓ. That is $R_m = \{p_0, p_1, q_\ell\}$.
(i) If $0 \le \ell \le 3$, then $r_m\{q_0|p_0, p_1, q_\ell\} = r_m\{q_0q_{n-1}|p_0, p_1, q_\ell\} = (1, 2, \ell)$.
(ii) If $\ell = 4, 6, \ldots, 2r$, then $r_m\{q_0|p_0, p_1, q_\ell\} = r_m\{q_0q_{n-1}|p_0, p_1, q_\ell\}$.
(iii)If $\ell = 5$, then $r_m\{q_0|p_0, p_1, q_\ell\} = r_m\{q_0q_{n-1}|p_0, p_1, q_\ell\} = (1, 2, \ell)$.
(iv) If $\ell = 7, 9, \ldots, 4r-1$, then $r_m\{q_1|p_0, p_1, q_\ell\} = r_m\{q_1q_2|p_0, p_1, q_\ell\}$.

Similarly, other contradictions can be assumed; all the cases mentioned above suggest that $\beta_m(P(n, 2)) \ge 4$, which clearly indicates that $\beta_m(P(n, 2)) = 4$ for $n \equiv 0(mod4)$. Similar kind of contradictions can be proved for $n \equiv 2(mod4)$. □

Remark 3: From the above cases, it can be deduced that if the mixed metric generator R_m for $P(n, 2)$ contains two vertices of one cycle, then R_m contain at least two vertices of another cycle.

Lemma 6. *$\beta_m(P(n, 2) \le 5$, for $n \equiv 1(mod)4$*

Proof: **Case 1:** Now we can write, if $n = 4r+1$, $r \ge 4$, where $r \in \mathbb{Z}^+$. The set of vertices that will distinguish the whole vertices and the edges of the graph are $R_m = \{q_0, q_1, p_1, p_{2r+1}, p_{2r+2}\}$. The following representations are presented with respect to R_m.

Representation of external vertices:

$$C_{R_m}(q_{2s}) = \begin{cases} (2s, 2-2s, 2, r+1, r+1), & 0 \le s \le 1; \\ (2s, s, s+1, r-s+2, r-s+2), & s = 2; \\ (r+2, r+2, r+1, 2, 1), & s = r+1; \\ (2r-s+3, 2r-s+4, & r+2 \le s \le 2r-2; \\ \quad 2r-s+2, s-r+1, s-r), & \\ (3, 5, 3, s-r+1, s-r), & s = 2r-1; \\ (1, 3, 2, s-r+1, s-r), & s = 2r. \end{cases}$$

and,

$$C_{R_m}(q_{2s+1}) = \begin{cases} (2s+1, 1, s+1, r-s+1, r+1), & 0 \le s \le 1; \\ (2s+1, s+1, s+1, r-s+1, & s = 2; \\ \quad r-s+2), & \\ (s+3, s+2, s+1, r-s+1, & 3 \le s \le r-1; \\ \quad r-s+2), & \\ (2r-s+2, r+2, r+1, s-r+1, 2), & r \le s \le r+1; \\ (2r-s+2, 2r-s+3, 2r-s+2, & r+2 \le s \le 2r-2; \\ \quad s-r+1, s-r+1), & \\ (2, 4, 3, s-r+1, s-r+1), & s = 2r-1. \end{cases}$$

Representation of internal vertices:

$$C_{R_m}(p_{2s}) = \begin{cases} (s+1, 2-s, 3, r+s, r-s+1), & 0 \le s \le 1; \\ (s+1, s+1, s+2, r-s+3, & 2 \le s \le r-1; \\ \quad r-s+1), & \\ (r+1, s, 2r-s+1, 3, r-s+1), & r \le s \le r+1; \\ (2r-s+2, 2r-s+3, 2r-s+1, & r+2 \le s \le 2r-1; \\ \quad s-r+2, s-r-1), & \\ (2, 3, 1, s-r+1, s-r-1), & s = 2r. \end{cases}$$

and,

$$C_{R_m}(p_{2s+1}) = \begin{cases} (s+2, 2-s, s, r-s, r+s), & 0 \le s \le 1; \\ (s+2, s+1, s, r-s, r-s+3), & 2 \le s \le r-1; \\ (2r-s+1, r+2, s, s-r, 3), & r \le s \le r+1; \\ (2r-s+1, 2r-s+2, & r+2 \le s \le 2r-1. \\ \quad 2r-s+3, s-r, s-r+2), & \end{cases}$$

Representation of external edges:

$$C_{R_m}(q_{2s}q_{2s+1}) = \begin{cases} (2s, 1-s, s+1, r-s+1, r+1), & 0 \le s \le 1; \\ (2s, s, s+1, r-s+1, r-s+2), & s = 2; \\ (s+2, s+1, s+1, r-s+1, & 3 \le s \le r; \\ \quad r-s+2), & \\ (2r-s+2, 2r-s+3, & r+1 \le s \le 2r-2; \\ \quad 2r-s+2, s-r+1, s-r), & \\ (2, 4, 3, s-r+1, s-r), & s = 2r-1; \\ (0, 2, 2, s-r+1, s-r), & s = 2r. \end{cases}$$

and,

$$C_{R_m}(q_{2s+1}q_{2s+2}) = \begin{cases} (2s+1, s, s+1, r-s+1, & 0 \le s \le 1; \\ \quad ar-s+1), & \\ (2s+1, s+1, s+1, r-s+1, & s = 2; \\ \quad r-s+1), & \\ (2r-s+1, s+2, s+1, & 3 \le s \le r-1; \\ \quad r-s+1, r-s+1), & \\ (2r-s+2, r+1, 2r-s+1, & r \le s \le 2r-4; \\ \quad s-r+1, s-r+1), & \\ (5, 6, 4, s-r+1, s-r+1), & s = 2r-3; \\ (3, 5, 3, s-r+1, s-r+1), & s = 2r-2; \\ (1, 2, 3, s-r+1, s-r+1), & s = 2r-1. \end{cases}$$

Representation of external and internal edges:

$$C_{R_m}(q_{2s}p_{2s}) = \begin{cases} (2s, 2-s, 2, r+s, r-s+1), & 0 \le s \le 1; \\ (s+1, s, s+1, r-s+2, & 2 \le s \le r; \\ \quad r-s+1), & \\ (2r-s+2, r+1, 2r-s+1, & r+3 \le s \le 2r-1; \\ \quad s-r+1, s-r-1), & \\ (1, 3, 1, s-r+1, s-r-1), & s = 2r. \end{cases}$$

and,

$$C_{R_m}(q_{2s+1}p_{2s+1}) = \begin{cases} (2s+1, 1, s, r-s, r+s), & 0 \le s \le 1; \\ (s+2, s+1, s, r-s, r-s+2), & 2 \le s \le r-1; \\ (r+1, r+1, 2r-s, 0, 2), & s = r; \\ (2r-s+1, 2r-s+2, & r+1 \le s \le 2r-1. \\ \quad 2r-s+2, s-r, s-r+1), & \end{cases}$$

Representation of internal edges:

$$C_{R_m}(p_{2s}p_{2s+2}) = \begin{cases} (s+1, 1, 3, r+s, r-s), & 0 \le s \le 1; \\ (s+1, s, s+2, r-s+2, r-s), & 2 \le s \le r-1; \\ (2r-s+1, s, 2r-s, 3, 0), & r \le s \le r+1; \\ (2r-s+1, 2r-s+2, 2r-s, & r+2 \le s \le 2r-1; \\ \quad s-r+2, s-r-1), & \\ (2, 2, 0, s-r, s-r-1), & s = 2r. \end{cases}$$

and,

$$C_{R_m}(p_{2s+1}p_{2s+3}) = \begin{cases} (s+2, 2, s, r-s-1, r+s), & 0 \le s \le 1; \\ (s+2, s+1, s, r-s-1, & 2 \le s \le r-1; \\ \quad r-s+2), & \\ (2r-s, 2r-s+1, s, r-s, 3), & r \le s \le r+1; \\ (2r-s, 2r-s+1, 2r-s+2, & r+2 \le s \le 2r-1. \\ \quad s-r, s-r+2), & \end{cases}$$

□

Proof: **Case 2:** Now we can write, if $n = 4r+3$, $r \ge 4$, where $r \in \mathbb{Z}^+$. The set of vertices which will distinguish the whole vertices, and edges of graph are $R_m = \{q_0, q_1, p_1, p_{2r+3}, p_{2r+4}\}$. The following representations are presented with respect to R_m.
Representation of external vertices:

$$C_{R_m}(q_{2s}) = \begin{cases} (2s, 2-2s, 2, r+s+1, r+s+1), & 0 \le s \le 1; \\ (s+2, 2s-2, s+1, r-s+3, & 2 \le s \le 3; \\ \quad r-s+3), & \\ (s+2, s+1, s+1, r-s+3, r-s+3), & 4 \le s \le r+1; \\ (2r-s+4, 2r-s+5, 2r-s+3, & r+2 \le s \le 2r-1; \\ \quad s-r, s-r-1), & \\ (3, 5, 3, s-r, s-r-1), & s = 2r; \\ (1, 3, 2, s-r, s-r-1), & s = 2r+1. \end{cases}$$

and,

$$C_{R_m}(q_{2s+1}) = \begin{cases} (2s+1, 1, s+1, r-s+2, & 0 \le s \le 1; \\ \quad r+s+1), & \\ (s+3, 2s-1, s+1, r-s+2, & 2 \le s \le 3; \\ \quad r-s+3), & \\ (s+3, s+2, s+1, r-s+2, & 4 \le s \le r; \\ \quad r-s+3), & \\ (2r-s+3, 2r-s+4, & r+1 \le s \le r+2; \\ \quad 2r-s+3, s-r, 2), & \\ (2r-s+3, 2r-s+4, & r+3 \le s \le 2r-1; \\ \quad 2r-s+3, s-r, s-r), & \\ (2, 4, 3, s-r, s-r), & s = 2r. \end{cases}$$

Representation of internal vertices:

$$C_{R_m}(p_{2s}) = \begin{cases} (s+1, 2-s, 3, r+s, r-s+2), & 0 \le s \le 1; \\ (s+1, s, s+2, r-s+4, r-s+2), & 2 \le s \le r; \\ (2r-s+3, s, 2r-s+1, 3, r-s+1), & r+1 \le s \le r+2; \\ (2r-s+3, 2r-s+4, 2r-s+2, & r+3 \le s \le 2r+1. \\ \quad s-r+1, s-r-2), & \end{cases}$$

and,

$$C_{R_m}(p_{2s+1}) = \begin{cases} (s+2, 2, s, r-s+1, r+s), & 0 \le s \le 1; \\ (s+2, s+1, s, r-s+1, r-s+4), & 2 \le s \le r; \\ (2r-s+1, 2r-s+3, 2r-s+5, & r+1 \le s \le r+2; \\ \quad s-r-1, 3), & \\ (2r-s+2, 2r-s+3, 2r-s+4, & r+3 \le s \le 2r. \\ \quad s-r-1, s-r+1), & \end{cases}$$

Representation of external edges:

$$C_{R_m}(q_{2s}q_{2s+1}) = \begin{cases} (2s, 1-s, s+1, r+1, r+s+1), & 0 \le s \le 1; \\ (2s, s, s+1, r-s+2, r-s+3), & s = 2; \\ (s+2, s+1, s+1, r-s+2, & 3 \le s \le r; \\ \quad r-s+3), & \\ (2r-s+3, r+2, 2r-s+3, & r+1 \le s \le r+2; \\ \quad s-r, s-r+3), & \\ (2r-s+3, 2r-s+4, 2r-s+3, & r+3 \le s \le 2r-1; \\ \quad s-r, s-r-1), & \\ (2, 4, 3, s-r, s-r-1), & s = 2r; \\ (0, 2, 2, s-r, s-r-1), & s = 2r+1. \end{cases}$$

and,

$$C_{R_m}(q_{2s+1}q_{2s+2}) = \begin{cases} (2s+1, s, s+1, r-s+2, r+1), & 0 \le s \le 1; \\ (s+3, 2s-1, s+1, r-s+2, & 2 \le s \le 3; \\ \quad r-s+2), & \\ (s+3, s+2, s+1, r-s+2, & 4 \le s \le r; \\ \quad r-s+2), & \\ (2r-s+3, 2r-s+4, & r+1 \le s \le 2r-2; \\ \quad 2r-s+2, s-r, s-r), & \\ (3, 5, 3, s-r, s-r), & s = 2r-1; \\ (1, 3, 2, s-r, s-r), & s = 2r. \end{cases}$$

Representation of external and internal edges:

$$C_{R_m}(q_{2s}p_{2s}) = \begin{cases} (2s, 2-s, 2, r+s, r+1), & 0 \le s \le 1; \\ (s+1, s, s+1, r-s+3, & 2 \le s \le r; \\ \quad r-s+2), & \\ (2r-s+3, s, 2r-s+2, 2, & r+1 \le s \le r+2; \\ \quad r-s+2), & \\ (2r-s+3, 2r-s+4, 2r-s+2, & r+3 \le s \le 2r; \\ \quad s-r, s-r-2), & \\ (1, 3, 1, s-r, s-r-2), & s = 2r+1. \end{cases}$$

and,

$$C_{R_m}(q_{2s+1}p_{2s+1}) = \begin{cases} (2s+1, 1, s, r-s+1, r+s), & 0 \le s \le 1; \\ (s+2, s+1, s, r-s+1, & 2 \le s \le r; \\ \quad r-s+3), & \\ (2r-s+2, 2r-s+3, r+1, & s = r+1; \\ \quad s-r-1, 2), & \\ (2r-s+2, 2r-s+3, 2r & r+2 \le s \le 2r+1. \\ \quad -s+3, & \\ \quad s-r-2, s-r-1), & \end{cases}$$

Representation of internal edges:

$$C_{R_m}(p_{2s}p_{2s+2}) = \begin{cases} (s+1, 1, 3, r+s, r-s+1), & 0 \le s \le 1; \\ (s+1, s, s+2, r-s+3, r-s+1), & 2 \le s \le r-1; \\ (r+1, s, 2r-s+1, 3, 1), & r \le s \le r+1; \\ (2r-s+1, 2r-s+3, 2r-s+1, & r+2 \le s \le 2r; \\ \quad s-r+1, s-r-2), & \\ (2, 2, 0, s-r, s-r-2), & s = 2r+1. \end{cases}$$

and,

$$C_{R_m}(p_{2s+1}p_{2s+3}) = \begin{cases} (s+2, 2, s, r-s, r+s), & 0 \le s \le 1; \\ (s+2, s+1, s, r-s, r-s+4), & 2 \le s \le r-1; \\ (2r-s+1, r+1, s, 0, 3), & r \le s \le r+1; \\ (2r-s+1, 2r-s+2, 2r-s+3, & r+2 \le s \le 2r. \\ \quad s-r-1, s-r+1), & \end{cases}$$

□

Now, from lemma3, the resolving set R_m must contain vertices from both the external and internal cycles of graph.

Lemma 7. *Suppose* $n \equiv 1, 3(mod4)$,*then* $\beta_m \ge 5$.

Proof: Suppose that $\beta_m = 4$. If so, the following contradictions are assumed.

Case 1: When the external cycle contain three fixed vertices, $\{q_0, q_1, q_2\}$, and other vertex lie in the internal cycle p_ℓ.
(i) If $\ell = 0, 2, 4, \ldots, 2r$, then $r_m\{q_0|q_0, q_1, q_2, p_\ell\} = r_m\{q_0q_{n-1}|q_0, q_1, q_2, p_\ell\} = (0, 1, 2, \ell+1)$.
(ii) If $\ell = 1, 3, 5, \ldots, 4r-1$, then $r_m\{q_0|q_0, q_1, q_2, p_\ell\} = r_m\{q_0q_{n-1}|q_0, q_1, q_2, p_\ell\}$.

Case 2: When $\{p_0, p_1, p_2\}$ lie in the internal cycle and the other vertex lie in the external cycle q_ℓ.
(i) If $\ell = 0, 2, 4, \ldots, 2r$, then $r_m\{q_0|p_0, p_1, p_2, q_\ell\} = r_m\{q_0q_{n-1}|p_0, p_1, p_2, q_\ell\}$.
(ii) If $\ell = 1, 3, 5, \ldots, 2r+3$, then $r_m\{q_0|p_0, p_1, p_2, q_\ell\} = r_m\{q_0q_{n-1}|p_0, p_1, p_2, q_\ell\}$.

We already proved that for $n \equiv 1, 3(mod4)$, and the mixed metric dimension is $\beta_m \le 5$. From Remark2, we consider the following cases where the external and internal cycles comprise two vertices each.

Case 3: When two external vertices are fixed $\{q_0, q_1\}$, and the internal vertices are $\{p_0, p_\ell\}$.
(i) If $\ell = 0, 2, 4, \ldots, 2r$, then $r_m\{q_0|q_0, q_1, p_0, p_\ell\} = r_m\{q_0q_{n-1}|q_0, q_1, p_0, p_\ell\}$.
(ii) If $\ell = 1, 3, 5, \ldots, 4r-1$, then $r_m\{q_0|q_0, q_1, p_0, p_\ell\} = r_m\{q_0q_{n-1}|q_0, q_1, p_0, p_\ell\}$.

Because of the symmetry, other possible cases can also be derived. From all the above cases, therefore, it is proven that, for $n \equiv 1, 3(mod4)$, the mixed metric dimension is $\beta_m \ge 5$. We can therefore say $\beta_m = 5$ when $n \equiv 1, 3(mod4)$. □

Theorem 6. *For* $n \ge 7$, *we have a mixed metric dimension*

$$\beta_m(P(n, 2)) = \begin{cases} 4, & n \equiv 0, 2(mod4); \\ 5, & n \equiv 1, 3(mod4). \end{cases}$$

TABLE 2 | Mixed Metric generator β_m for $P(n, 2)$.

n	Basis	β_m
5	$\{q_0, q_3, p_1, p_2, p_4\}$	5
6	$\{q_0, q_3, p_1, p_2, p_4\}$	5
7	$\{q_0, q_3, p_1, p_2, p_4\}$	5
8	$\{q_0, q_1, p_4, p_5\}$	4
9	$\{q_0, q_3, p_5, p_6\}$	4
10	$\{q_0, q_1, p_5, p_6\}$	4
11	$\{q_0, q_2, p_6, p_7\}$	4
12	$\{q_0, q_1, p_6, p_7\}$	4
13	$\{q_0, q_2, p_7, p_8\}$	4
14	$\{q_0, q_2, p_7, p_8\}$	4
15	$\{q_0, q_2, p_{10}, p_{11}\}$	4

Proof: **Case 1:** When $n \equiv 0, 2(mod4)$.
From lemma 4,5, we have $\beta_m P(n, 2) = 4$.
Case 1: When $n \equiv 1, 3(mod4)$.
From lemma 6,7, we have $\beta_m P(n, 2) = 5$. □

For the remainder of the cases, when $n \leq 15$, the mixed metric dimension $\beta_m(P(n, 2))$ is calculated through the total enumeration method, shown in **Table 2**, along with the mixed metric basis.

3. CONCLUSION AND FURTHER RESEARCH

The recently introduced mixed metric dimension is calculated for $P(n, 2)$. It has been shown that $P(n, 2)$ has mixed metric dimension equal to 4 for $n \equiv 0, 2(mod4)$, and, for $n \equiv 1, 3(mod4)$, the mixed metric dimension is 5. This shows that each graph of the family of generalized Petersen $P(n, 2)$ has constant mixed metric dimension.

Theorem 7. [29] *For the graph of* $P(n, 3)$,

$$\beta(P(n, 3)) = \begin{cases} 4, & when\ n \equiv 0(mod6); \\ 3, & when\ n \equiv 1, (mod6). \end{cases}$$

and,

$$\beta(P(n, 3)) \leq \begin{cases} 5, & when\ n \equiv 2(mod6); \\ 4, & when\ n \equiv 3, 4, 5(mod6). \end{cases}$$

Theorem 8. [30] *For* $n \geq 17$, *we have,*

$$\beta(P(n, 4)) \leq \begin{cases} 3, & when\ n \equiv 0(mod4); \\ 4, & when\ n \equiv 1, 2, 3(mod4). \end{cases}$$

Theorem 9. [31] *The metric dimension of graph of* $P(2n, n)$ *is*

$$\beta(P(2n, n)) = \begin{cases} 3, & when\ n\ is\ even; \\ 4, & otherwise. \end{cases}$$

The standard metric dimension is examined for these as well as other known classes of generalized Petersen graphs; the mixed metric dimension for these as well as other graphs would therefore be intriguing to investigate. If the other variants of dimension are identified, a comparative study can be carried out; this could evaluate the relationship between $\beta(\Gamma)$, $\beta_e(\Gamma)$, and $\beta_m(\Gamma)$ in the different families of graphs.

DATA AVAILABILITY STATEMENT

The original contributions presented in the study are included in the article/supplementary materials, further inquiries can be directed to the corresponding author/s.

AUTHOR CONTRIBUTIONS

The main idea was presented by HR. YJ read and approved the final manuscript.

FUNDING

The work of HR was supported by Post-Doctoral fund of University of Shanghai for Science and Technology under the grant no. 5B19303001. The work of YJ was supported by the National Science Foundation of China under grant no. 71571055.

ACKNOWLEDGMENTS

We would like to express our sincere gratitude to the referees for a very careful reading of this paper and for all their insightful comments/criticism, which have led to a number of significant improvements to this paper.

REFERENCES

1. Khuller S, Raghavachari B, Rosenfeld A. Landmarks in graphs. *Discrete Appl Math*. (1996) **70**:217–29. doi: 10.1016/0166-218X(95)00106-2
2. Slater PJ, Leaves of trees. *Congr Numer*. (1975) **14**: 549–59.
3. Harary F, Melter RA. On the metric dimension of a graph. Ars Comb. (1976) **2**:191–5.
4. Chartrand G, Saenpholphat V, Zhang P. The independent resolving number of a graph. *Math Bohem*. (2003) **128**:379–93. Available online at: http://dml.cz/dmlcz/134003
5. Okamoto F, Phinezy B, Zhang P. The local metric dimension of a graph. *Math Bohem*. (2010) **135**:239–55. Available online at: http://dml.cz/dmlcz/140702

6. Sebő A, Tannier E. On metric generators of graph. *Math Oper Res*. (2004) **29**:383–93. doi: 10.1287/moor.1030.0070
7. Oellermann OR, Peters-Fransen J. The strong metric dimension of graphs and digraphs. *Discrete Appl Math*. (2007) **155**:356–64. doi: 10.1016/j.dam.2006.06.009
8. Trujillo-Rasua R, Yero IG. k-Metric antidimension: a privacy measure for social graphs. *Inform Sci*. (2016) **328**:403–17. doi: 10.1016/j.ins.2015.08.048
9. Shao Z, Wu P, Zhu E, Chen L. On metric dimension in some hex derived networks. *Sensors*. (2019) **19**:94. doi: 10.3390/s19010094
10. Raza H, Hayat S, Imran M, Pan XF. Fault-tolerant resolvability and extremal structures of graphs. *Mathematics*. (2019) **7**:78. doi: 10.3390/math7010078
11. Raza H, Hayat S, Pan XF. Binary locating-dominating sets in rotationally-symmetric convex polytopes. *Symmetry*. (2018) **10**:727. doi: 10.3390/sym10120727
12. Raza H, Hayat S, Pan XF. On the fault-tolerant metric dimension of certain interconnection networks. *J Appl Math Comput*. (2019) **60**:517–35. doi: 10.1007/s12190-018-01225-y
13. Raza H, Hayat S, Pan XF. On the fault-tolerant metric dimension of convex polytopes. *Appl Math Comput*. (2018) **339**:172–85. doi: 10.1016/j.amc.2018.07.010
14. Kelenc A, Tratnik N, Yero IG. Uniquely identifying the edges of a graph: the edge metric dimension. *Discrete Appl Math*. (2018) **251**:204–20. doi: 10.1016/j.dam.2018.05.052
15. Zubrilina N. On the edge dimension of a graph. *Discrete Math*. (2018) **341**:2083–8. doi: 10.1016/j.disc.2018.04.010
16. Peterin I, Yero IG. Edge metric dimension of some graph operations. *Bull Malay Math Sci Soc*. (2019) **43**:2465–77. doi: 10.1007/s40840-019-00816-7
17. Zhu E, Taranenko A, Shao Z, Xu J. On graphs with the maximum edge metric dimension. *Discrete Appl Math*. (2019) **257**:317–24. doi: 10.1016/j.dam.2018.08.031
18. Liu JB, Wang C, Wang S, Wei B. Zagreb indices and multiplicative Zagreb indices of Eulerian graphs. *Bull Malay Math Sci Soc*. (2019) **42**:67–78. doi: 10.1007/s40840-017-0463-2
19. Liu JB, Zhao J, Zhu Z. On the number of spanning trees and normalized Laplacian of linear octagonal quadrilateral networks. *Int J Quantum Chem*. (2019) **119**:e25971. doi: 10.1002/qua.25971
20. Liu JB, Zhao J, Min J, Cao J. The hosoya index of graphs formed by a fractal graph. *Fractals*. (2019) **27**:1950135–875. doi: 10.1142/S0218348X19501354
21. Liu JB, Zhao J, Cai ZQ. On the generalized adjacency, Laplacian and signless Laplacian spectra of the weighted edge corona networks. *Phys A Stat Mech Appl*. (2020) **540**:123073. doi: 10.1016/j.physa.2019.123073
22. Liu JB, Shi ZY, Pan YH, Cao J, Abdel-Aty M, Al-Juboori U. Computing the Laplacian spectrum of linear octagonal-quadrilateral networks and its applications. *Polycycl Aromat Compd*. (2020). doi: 10.1080/10406638.2020.1748666. [Epub ahead of print].
23. Kelenc A, Kuziak D, Taranenko A, Yero IG. Mixed metric dimension of graphs. *Appl Math Comput*. (2017) **314**:429–38. doi: 10.1016/j.amc.2017.07.027
24. Raza H, Liu JB, Qu S. On mixed metric dimension of rotationally symmetric graphs. *IEEE Access*. (2019) **8**:11560–9. doi: 10.1109/ACCESS.2019.2961191
25. Watkins ME. A theorem on Tait colorings with an application to the generalized Petersen graphs. *J Combinat Theory*. (1969) **6**:152–64. doi: 10.1016/S0021-9800(69)80116-X
26. Cáceres J, Hernando C, Mora M, Pelayo IM, Puertas ML, Seara C, Wood DR. On the metric dimension of cartesian products of graphs. *SIAM J Discrete Math*. (2007) **21**:423–41. doi: 10.1137/050641867
27. Filipović V, Kartelj A, Kratica J. Edge metric dimension of some generalized petersen graphs. *Results Math*. (2019) **74**:182. doi: 10.1007/s00025-019-1105-9
28. Javaid I, Rahim MT, Ali K. Families of regular graphs with constant metric dimension. *Utilitas Math*. (2008) **75**:21–34.
29. Imran M, Baig AQ, Shafiq MK, Tomescu I. On metric dimension of generalized petersen graphs $P(n, 3)$. *Ars Comb*. (2014) **117**:113–30.
30. Naz S, Salman M, Ali U, Javaid I, Bokhary SA. On the constant metric dimension of generalized Petersen graphs $P(n, 4)$. *Acta Math Sin*. (2014) **30**:1145–60. doi: 10.1007/s10114-014-2372-8
31. Imran M, Siddiqui MK, Naeem R. On the metric dimension of generalized petersen multigraphs. *IEEE Access*. (2018) **6**:74328–38. doi: 10.1109/ACCESS.2018.2883556

Conflict of Interest: The authors declare that the research was conducted in the absence of any commercial or financial relationships that could be construed as a potential conflict of interest.

frontiers in Physics

ORIGINAL RESEARCH
published: 07 August 2020
doi: 10.3389/fphy.2020.00224

A Neuro-Swarming Intelligence-Based Computing for Second Order Singular Periodic Non-linear Boundary Value Problems

Zulqurnain Sabir[1], *Muhammad Asif Zahoor Raja*[2,3], *Juan L. G. Guirao*[4]* *and Muhammad Shoaib*[5]

[1] Department of Mathematics and Statistics, Hazara University, Mansehra, Pakistan, [2] Future Technology Research Center, National Yunlin University of Science and Technology, Douliu, Taiwan, [3] Department of Electrical and Computer Engineering, COMSATS University Islamabad, Attock, Pakistan, [4] Department of Applied Mathematics and Statistics, Hospital de Marina, Technical University of Cartagena, Cartagena, Spain, [5] Department of Mathematics, COMSATS University Islamabad, Attock, Pakistan

In the present investigation, a novel neuro-swarming intelligence-based numerical computing solver is developed for solving second order non-linear singular periodic (NSP) boundary value problems (BVPs), i.e., NSP-BVPs, using the modeling strength of artificial neural networks (ANN) optimized with global search efficacy of particle swarm optimization (PSO) supported with the methodology of rapid local search by interior-point scheme (IPS), i.e., ANN-PSO-IPS. In order to check the proficiency, robustness, and stability of the designed ANN-PSO-IPS, two numerical problems of the NSP-BVPs have been presented for different numbers of neurons. The outcomes of the proposed ANN-PSO-IPS are compared with the available exact solutions to establish the worth of the solver in terms of accuracy and convergence, which is further endorsed through results of statistical performance metrics based on multiple implementations.

Keywords: singular periodic systems, particle swarm optimization, hybrid approach, interior-point scheme, artificial neural networks, statistical analysis

OPEN ACCESS

Edited by:
Shaohui Wang,
Louisiana College, United States

Reviewed by:
Yolanda Guerrero-Sánchez,
University of Murcia, Spain
Chaudry Masood Khalique,
North-West University, South Africa

***Correspondence:**
Juan L. G. Guirao
juan.garcia@upct.es

Specialty section:
This article was submitted to Mathematical and Statistical Physics, a section of the journal Frontiers in Physics

Received: *21 April 2020*
Accepted: *25 May 2020*
Published: *07 August 2020*

Citation:
Sabir Z, Raja MAZ, Guirao JLG and Shoaib M (2020) A Neuro-Swarming Intelligence-Based Computing for Second Order Singular Periodic Non-linear Boundary Value Problems. Front. Phys. 8:224. doi: 10.3389/fphy.2020.00224

INTRODUCTION

The singular differential equations have immense applications in a variety of areas of mathematics and physics, such as dynamics, nuclear physics, chemical reactions and atomic designs etc. The research investigations of non-linear singular periodic boundary value problems (NSP-BVPs) are mainly based on differential equation models. Due to non-linearity, singular points and the periodic nature of the mathematical models, only a few existing analytical and numerical approaches are available in literature to present the solutions of the NSP-BVPs [1–5]. A few problems are provided as Agarwal [6, 7] implemented a well-known numerical shooting approach to solve NSP-BVPs. Geng and Cui [8] presented the individuality and existence for solving the NSP-BVPs. Some other numerical techniques are employed to analyze the significance of the proposed problem NSP-BVPs [9–11].

Assadi et al. [12] exploited a fixed point iterative scheme, Xin et al. [13] a non-trivial solution of NSP-BVPs, El-Syed and Gaagar [14] provided the existence of a solution for non-linear singular differential equations, Wang et al. [15] and Wang and Ru [16] a positive solution of periodic equations. The general form of the second order non-linear NSP-BVPs is written as [8]:

$$\begin{cases} \dfrac{d^2\Psi(x)}{dx^2} + \dfrac{p(x)}{x^{\beta_1}(1-x)^{\delta_1}}\dfrac{d\Psi(x)}{dx} + \dfrac{q(x)}{x^{\beta_2}(1-x)^{\delta_2}}\Psi(x) \\ \quad + N(\Psi) = h(x), 0 < x < 1, \\ \Psi(0) = \Psi(1), \ \dfrac{d\Psi(0)}{dx} = \dfrac{d\Psi(1)}{dx}, \end{cases} \tag{1}$$

where $p(x)$ and $q(x)$ are continuous, $N(\Psi)$ is a function of Ψ. Moreover, β_1, δ_1, β_2, and δ_2 are the positive constant values. All of the above cited analytical/numerical schemes have their precise advantages, disadvantages, merits and demerits, while a stochastic numerical solver based on the intelligent computing approach by manipulating the strength of artificial neural networks (ANNs), particle swarm optimization (PSO), and interior-point scheme, i.e., ANN-PSO-IPS, has not been implemented to solve second order NSP-BVPs.

Researchers have widely studied the meta-heuristic based computing numerical approaches along with the neural network's strength for solving the linear/non-linear mathematical models [17–24]. Some recent applications of heuristic computing are corneal models for eye surgery [25], the non-linear Riccati system [26], the Bagley-Torvik system [27], non-linear systems of Bratu type [17], prey-predator non-linear models [28], non-linear reactive transport models [29], non-linear optics models [30], non-linear singular functional differential models [31], singular non-linear systems arising in atomic physics [32], non-linear doubly singular systems [33], nanofluidic systems [34], micropolar fluid flow [35], the heartbeat model [36], the singular Lane-Emden equation based model [37], the heat conduction model of the human head [38], non-linear electric circuit models [39], finance [40], and mathematical models in Bioinformatics [41, 42]. These influences proved the value, worth and consequence of the stochastic solvers based on robustness, accuracy and convergence.

Keeping in view the value and worth of these applications, the authors worked to exploit the strength and significance of stochastic solvers for a reliable, efficient and stable approach to solve the NSP-BVPs. The present analysis for NSP-BVPs given in Equation (1) is performed via stochastic numerical solver along with utilization of the strength of artificial neural networks (ANNs) based on certain numbers of neurons, particle swarm optimization (PSO) and interior-point scheme, i.e., ANN-PSO-IPS. Some innovative influences of the presented solver are briefly summarized as:

- Novel neuro-swarm intelligent/soft computing heuristics ANN-PSO-IPS using different number of neurons are accessible for the numerical behavior of the second order NSP-BVPs.
- The overlapping outcomes of the designed ANN-PSO-IPS with the referenced exact solutions for two different variants of the second order non-linear NSP-BVPs establish the convergence, correctness and reliability.
- Authorization of accurate performance is validated through statistical observations on multiple runs of ANN-PSO-IPS in terms of Theil's Inequality Coefficient (TIC), Variance Account For (VAF), and semi-interquartile range (S-IR) and Nash Sutcliffe Efficiency (NSE) metrics.
- Besides practically accurate continuous outcomes on input training interval, ease in the concept, the smooth implementable procedure, robustness, extendibility, and stability are other worthy declarations for the proposed neuro-swarm intelligent computing heuristics.

The remaining parts of the paper are planned as: section Design Methodology defines the explanation of the proposed methodology for ANN-PSO-IPS, mathematical forms of the statistic based operators are provided in section Statistical Measures, the detailed results and discussions are given in section Results and Discussion, while the conclusions and future research plans are provided in section Conclusions.

DESIGN METHODOLOGY

The design approach of ANN-PSO-IPS is divided into two categories for a numerical solution of the non-linear second order NSP-BVPs. In category 1, the error-based fitness function is introduced, while in the second category, the combination of an optimization scheme PSO with IPS, i.e., PSO-IPS, is provided in the sense of introductory material, applications, and pseudocode.

ANN Modeling

Mathematical models for non-linear second order NSP-BVPs are assembled with the feed-forward ANNs strength, $\hat{\Psi}(x)$ shows the continuous mapping results, and its derivatives using the log-sigmoid $U(x) = \left(1 + \exp(-x)\right)^{-1}$ activation functions given as:

$$\begin{aligned} \hat{\Psi}(x) &= \sum_{i=1}^{k} a_i U(w_i x + b_i) = \sum_{i=1}^{k} \frac{a_i}{\left(1 + e^{-(w_i x + b_i)}\right)}, \\ \frac{d\hat{\Psi}}{dx} &= \sum_{i=1}^{k} a_i \frac{d}{dx} U(w_i x + b_i) = \sum_{i=1}^{k} \frac{a_i w_i e^{-(w_i t + b_i)}}{\left(1 + e^{-(w_i t + b_i)}\right)^2}, \\ \frac{d^2\hat{\Psi}}{dx^2} &= \sum_{i=1}^{k} a_i \frac{d^2}{dx^2} U(w_i x + b_i) \\ &= \sum_{i=1}^{k} a_i w_i^2 \left(\frac{2e^{-2(w_i x + b_i)}}{\left(1 + e^{-(w_i x + b_i)}\right)^3} - \frac{e^{-(w_i x + b_i)}}{\left(1 + e^{-(w_i x + b_i)}\right)^2} \right), \end{aligned} \tag{2}$$

where the weights are $\boldsymbol{a} = [a_1, a_2, a_3, ..., a_m]$, $\boldsymbol{w} = [w_1, w_2, w_3, ..., w_m]$ and $\boldsymbol{b} = [b_1, b_2, b_3, ..., b_m]$. In order to solve the non-linear second order NSP-BVPs given in the system (1), an error-based fitness formulation using the mean square error sense is written as:

$$E = E_1 + E_2, \tag{3}$$

where E_1 and E_2 are the error functions related to the differential system and the boundary conditions, respectively, written as:

$$E_1 = \frac{1}{N}\sum_{m=1}^{N}\left(\frac{d^2\hat{\Psi}_m}{dx_m^2} + \frac{p_m}{x_m^{\beta_1(1-x_m)^{\delta_1}}}\frac{d\hat{\Psi}_m}{dx_m} + \frac{q_m}{x_m^{\beta_2(1-x_m)^{\delta_2}}}\hat{\Psi}_m + N(\hat{\Psi}_m) - h_m\right), \quad 0 < x_m < 1, \tag{4}$$

$$E_2 = \frac{1}{2}\left(\hat{\Psi}_0 - \hat{\Psi}_N\right)^2 + \frac{1}{2}\left(\frac{d\hat{\Psi}_0}{dx_m} - \frac{d\hat{\Psi}_N}{dx_m}\right)^2, \tag{5}$$

where $Nh = 1$, $p_m = p(x_m)$, $q_m = q(x_m)$, $h_m = h(x_m)$, $\hat{\Psi}_m = \hat{\Psi}(x_m)$ and $x_m = mh.$, while $\hat{\Psi}$ is the approximate solution of Ψ of system represented in (1), N is total number of input grid points and h is the step size.

Optimization Process: PSO-IPS

The parameter optimization for second order non-linear NSP-BVPs is approved by the hybrid computing framework based on PSO and IPS.

The PSO approach [43] is applied as an effective alternative to the efficient global search mechanism of genetic algorithms [44] that is used as an optimization apparatus for the second order non-linear NSP-BVPs. Kennedy and Eberhart proposed PSO, which is a famous algorithm for the global search optimization strength, at the end of the 19th century. PSO is considered as an easy implementation process with low memory requirements [45]. This optimization algorithm exploits mathematical modeling inspired bythe swarm pattern of birds flocking as well as fish schooling. Recently, this global optimization procedure is used in different applications, like the fuel ignition model [46], non-linear physical models [47], parameter approximation systems of control auto regressive moving average models [48], balancing stochastic U-lines problems [49], operation scheduling of microgrids [50], and features classification [51].

In the search space theory, a single candidate solution is called a particle using the optimization process. For the PSO optimization approach, the prime swarms spread into the larger and for the adjustment of the parameters of PSO, the scheme delivers iteratively optimal outcomes $\boldsymbol{P}_{LB}^{\delta-1}$ and $\boldsymbol{P}_{GB}^{\delta-1}$ that indicate the swarm's position and velocity. The mathematical form is given as:

$$\boldsymbol{X}_i^{\delta} = \boldsymbol{X}_i^{\delta-1} + \boldsymbol{V}_i^{\delta-1}, \tag{6}$$

$$\boldsymbol{V}_i^{\delta} = \boldsymbol{\omega}\boldsymbol{V}_i^{\delta-1} + \delta_1(\boldsymbol{P}_{LB}^{\delta-1} - \boldsymbol{X}_i^{\delta-1})r_1 + \delta_2(\boldsymbol{P}_{GB}^{\delta-1} - \boldsymbol{X}_i^{\delta-1})\boldsymbol{r}_2, \tag{7}$$

where the position and velocity are $\mathbf{X}_i$ and $\boldsymbol{V_i}$, respectively, $\boldsymbol{r}_1$ and $\boldsymbol{r}_2$ are the pseudo random vectors between 0 and 1, while δ_1 and δ_2 are the acceleration constant values. The inertia weight vector is $\omega \in [0, 1]$. The scheme performance stops when the predefined flights are obtained.

The dynamic of the optimization PSO rapidly converges by the hybridization process with the suitable local search scheme by taking PSO global best values as an initial weight. Therefore, an efficient local search approach based on interior-point scheme (IPS) is used for quick fine-tuning of the outcomes achieved by the designed optimization approach. Some recent submissions of the IPS are mixed complementarity monotone systems [52], active noise control systems [53], simulation of aircraft parts riveting [54], the economic load dispatch model [55], and non-linear system identification [56].

The pseudocode based on the combination of PSO-IPS trains the ANN as well as the crucial setting of the parameters for both PSO and IPS are provided in **Table 1**. The optimization method become premature using a minor change in the parameter setting, thus, it requires several experiences, replications and information on essential optimization impressions of appropriate settings for the hybrid of PSO-IPS.

TABLE 1 | Pseudo code of the optimization tool PSO-IPS to find the weights of ANNs.

```
Start of PSO
  Step-1: Initialization: Randomly generate the
  initial swarm and adjust the parameters of [PSO] and
  [optimoptions] routine.
  Step-2: Fitness Calculation: Scrutinize the [fitness
  value] for every particle in Equation (3).
  Step-3: Ranking: Rank each particle of the minimum
  criteria of the [fitness function].
  Step-4: Stopping Criteria: Stop, if one of the below
  condition attained.
  • Selected flights/cycles
  • Level of Fitness
  When achieved the above standards, then move to Step-5
  Step-5: Renewal: For the position and velocity, use
  systems (6) and (7).
  Step-6: Improvement: Repeat the 2-6 steps, until the
  whole flights are achieved.
  Step-7: Storage: Store the achieved best fitness values
  and designate as the best global particle.
End of PSO
Start the PSO-IPS process
  Inputs : Best global values of the particle
  Output : W_PSO−IPS are the best vectors of PSO-IPS
  Initialize : Use [best global values] as a [start
  point]
  Termination : The process terminates, when [Fitness
  = E= 10^−20], [TolFun = TolCon = 10^−21], [Generation =
  700], [TolX = 10^−20] {MaxFunEvals = 270000}
  While: {Stop}
  Fitness Evaluation : For the fitness E by using the
  Equation (3).
  Adjustments: Invoke the routine [fmincon] for the IPS
  to modify the weight vector values.
Store to fitness step by using the simplified form of the
weight vector
  Store : Save W_PSO−IPS values, which are final adaptive
  weight values, function count, time, E, and generations
  for the present run.
End of the PSO-IPS
```

STATISTICAL MEASURES

The present study aims to present the statistical performance for solving both variants of second order non-linear NSP-BVPs. In this respect, three performance operators are implemented based on Theil's inequality coefficient (TIC), Nash Sutcliffe Efficiency (NSE), and Variance Account For (VAF). The mathematical notations of these operators are given as:

$$\text{TIC}=\frac{\sqrt{\frac{1}{n}\sum_{i=1}^{n}\left(\Psi_i-\hat{\Psi}_i\right)^2}}{\left(\sqrt{\frac{1}{n}\sum_{i=1}^{n}\Psi_i^2}+\sqrt{\frac{1}{n}\sum_{i=1}^{n}\hat{\Psi}_i^2}\right)} \tag{8}$$

$$\begin{cases}\text{NSE}=1-\dfrac{\sum_{i=1}^{n}\left(\Psi_i-\hat{\Psi}_i\right)^2}{\sum_{i=1}^{n}\left(\hat{\Psi}_i-\bar{\Psi}_i\right)^2},\ \bar{\Psi}_i=\dfrac{1}{n}\sum_{i=1}^{n}\Psi_i\\ \text{ENSE}=1-\text{NSE},\end{cases} \tag{9}$$

$$\begin{cases}VAF=\left(1-\dfrac{\text{var}\left(\Psi_i(x)-\hat{\Psi}_i(x)\right)}{\text{var}\left(\Psi_i(x)\right)}\right)*100,\\ EVAF=|100-VAF|.\end{cases} \tag{10}$$

$$\begin{cases}SIR=0.5\,(Q_3-Q_1),\\ Q_3=\ 3^{rd}\text{ quartile},\ Q_1=\ 1^{st}\text{ quartile}.\end{cases} \tag{11}$$

RESULTS AND DISCUSSION

In this section, the detailed results based on two variants of the second order NSP-BVPs are presented using the ANN-PSO-IPS and comparison of the proposed outcomes with the exact solutions will also be discussed.

Example 1: Consider the second order SPBVP is written as:

$$\begin{cases}\dfrac{d^2\Psi(x)}{dx^2}+\dfrac{2}{x^4(1-x)^{1.5}}\dfrac{d\Psi(x)}{dx}\\ \quad+\dfrac{1}{x^3(1-x)^{1.5}}\Psi(x)=h(x),\quad 0<x<1,\\ \Psi(0)=\Psi(1),\quad \dfrac{d\Psi(0)}{dx}=\dfrac{d\Psi(1)}{dx}.\end{cases} \tag{12}$$

The true solution of the Equation (12) is $e^{10(x-x^2)^2}$ and the fitness function is written as:

$$E=\frac{1}{N}\sum_{i=1}^{m}\left(\frac{d^2\hat{\Psi}_m}{dx_m^2}+\frac{2}{x_m^4(1-x_m)^{1.5}}\frac{d\hat{\Psi}_m}{dx_m}+\frac{1}{x_m^3(1-x_m)^{1.5}}\hat{\Psi}_m-h_m\right)^2+\frac{1}{2}\left(\left(\hat{\Psi}_0-\hat{\Psi}_N\right)^2+\left(\frac{d\hat{\Psi}_0}{dx_m}-\frac{d\hat{\Psi}_N}{dx_m}\right)^2\right), \tag{13}$$

Example 2: Consider the non-linear second order SPBVP is written as:

$$\begin{cases}\dfrac{d^2\Psi(x)}{dx^2}+\dfrac{2}{x^2(1-x)}\dfrac{d\Psi(x)}{dx}+\dfrac{1}{x(1-x)}\Psi(x)\\ \quad+\Psi^2(x)=h(x),\quad 0<x<1,\\ \Psi(0)=\Psi(1),\quad \dfrac{d\Psi(0)}{dx}=\dfrac{d\Psi(1)}{dx}.\end{cases} \tag{14}$$

The exact solution of the above equation is $e^{10(x-x^2)^2}$ and the fitness function is written as:

$$E=\frac{1}{N}\sum_{i=1}^{m}\left(\frac{d^2\hat{\Psi}_m}{dx_m^2}+\frac{2}{x_m^2(1-x_m)}\frac{d\hat{\Psi}_m}{dx_m}+\frac{1}{x_m(1-x_m)}\hat{\Psi}_m+\hat{\Psi}_m^2-h_m\right)^2+\frac{1}{2}\left(\left(\hat{\Psi}_0-\hat{\Psi}_N\right)^2+\left(\frac{d\hat{\Psi}_0}{dx_m}-\frac{d\hat{\Psi}_N}{dx_m}\right)^2\right). \tag{15}$$

In order to perform the solutions of the second order NSP-BVPs, the optimization is accomplished using the hybrid of global and local search capabilities, i.e., PSO-IPS. The process is repeated for sixty trials to generate a large dataset parameter using the ANNs. The best weight sets are provided to indicate the approximate numerical outcomes of the model (1) using 5 and 10 numbers of neurons. The mathematical formulations of the proposed numerical outcomes for 5 neurons are shown as:

$$\hat{\Psi}_1(\text{x})=\frac{5.8775}{1+e^{-(9.3350x-12.870)}}+\frac{7.3743}{1+e^{-(5.2745x-2.3623)}}+\frac{0.1197}{1+e^{-(\ -9.8796x+4.4603)}}+\frac{7.1505}{1+e^{-(\ -5.5221x+3.2724)}}-\frac{6.8433}{1+e^{-(\ 8.5033x+3.4988)}}, \tag{16}$$

$$\hat{\Psi}_2(x)=\frac{-7.2686}{1+e^{-(5.6952x-3.2662)}}+\frac{7.4887}{1+e^{-(6.7652x-9.3959)}}+\frac{11.9610}{1+e^{-(\ -5.7680x+3.3622)}}+\frac{9.0833}{1+e^{-(\ 4.5840x-2.2274)}}-\frac{4.0470}{1+e^{-(\ 3.2902x-4.1080)}}. \tag{17}$$

The mathematical formulations of the proposed numerical outcomes for 10 number of neurons are written as:

$$\hat{\Psi}_1(x)=\frac{-0.3444}{1+e^{-(0.1021x-1.9508)}}+\frac{1.6234}{1+e^{-(-0.2443x+2.2795)}}+\ldots+\frac{7.3336}{1+e^{-(\ 9.9170x-13.6069)}}, \tag{18}$$

$$\hat{\Psi}_2(x)=\frac{-3.4763}{1+e^{-(5.7313x-3.7465)}}+\frac{1.0055}{1+e^{-(-0.0494x-0.1392)}}+\ldots+\frac{0.8568}{1+e^{-(\ -0.7378x-2.2455)}}. \tag{19}$$

The optimization of the relations (13) and (15) is carried out with PSO-IPS for sixty trials and one set of trained weight of ANN based on 5 and 10 neurons is plotted in the **Figures 1A,B**, **2A,B**. The comparison of the best, mean and exact solutions are drawn in the **Figures 1C,D**, **2C,D** for 5 and 10 numbers of neurons. The best and mean results obtained by the designed approach ANN-PSO-IPS are overlapped to the exact results for both of the examples. This consistent overlapping of the results indicates the exactness and correctness of the designed scheme. The plots of absolute error (AE) for the 5 and 10 number of neurons are drawn in **Figures 1E,F**, **2E,F**. These AE values have been obtained

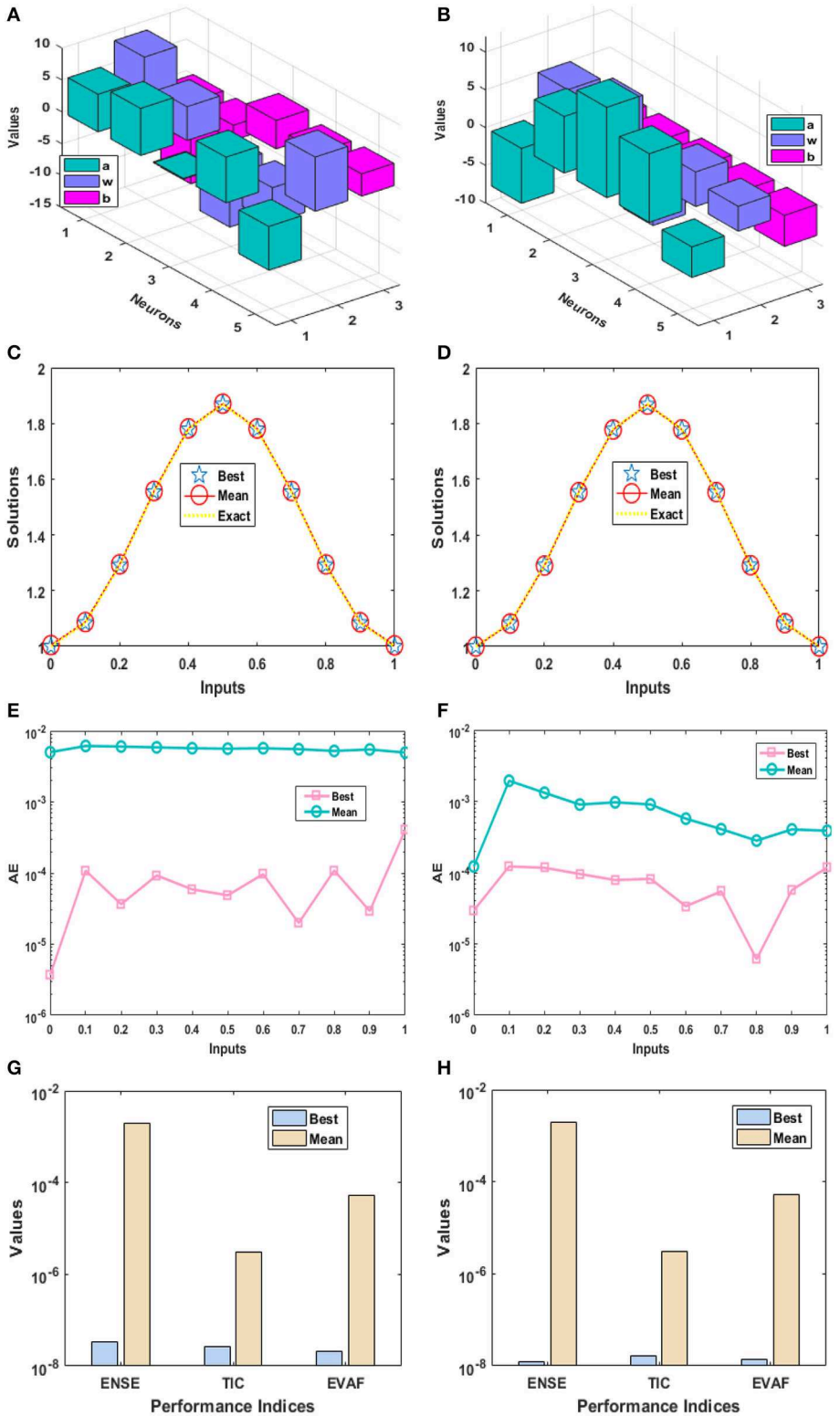

FIGURE 1 | Best weight, results of the designed methodology, values of the AE, and performance measures of Examples 1 and 2 for 5 numbers of neurons. **(A)** ANN best weights for Example 1. **(B)** ANN best weights for Example 2. **(C)** Result comparison for Example 1. **(D)** Result comparison for Example 2. **(E)** AE values for Example 1. **(F)** AE values of for Example 2. **(G)** Performance measures for Example 1. **(H)** Performance measures for Example 2.

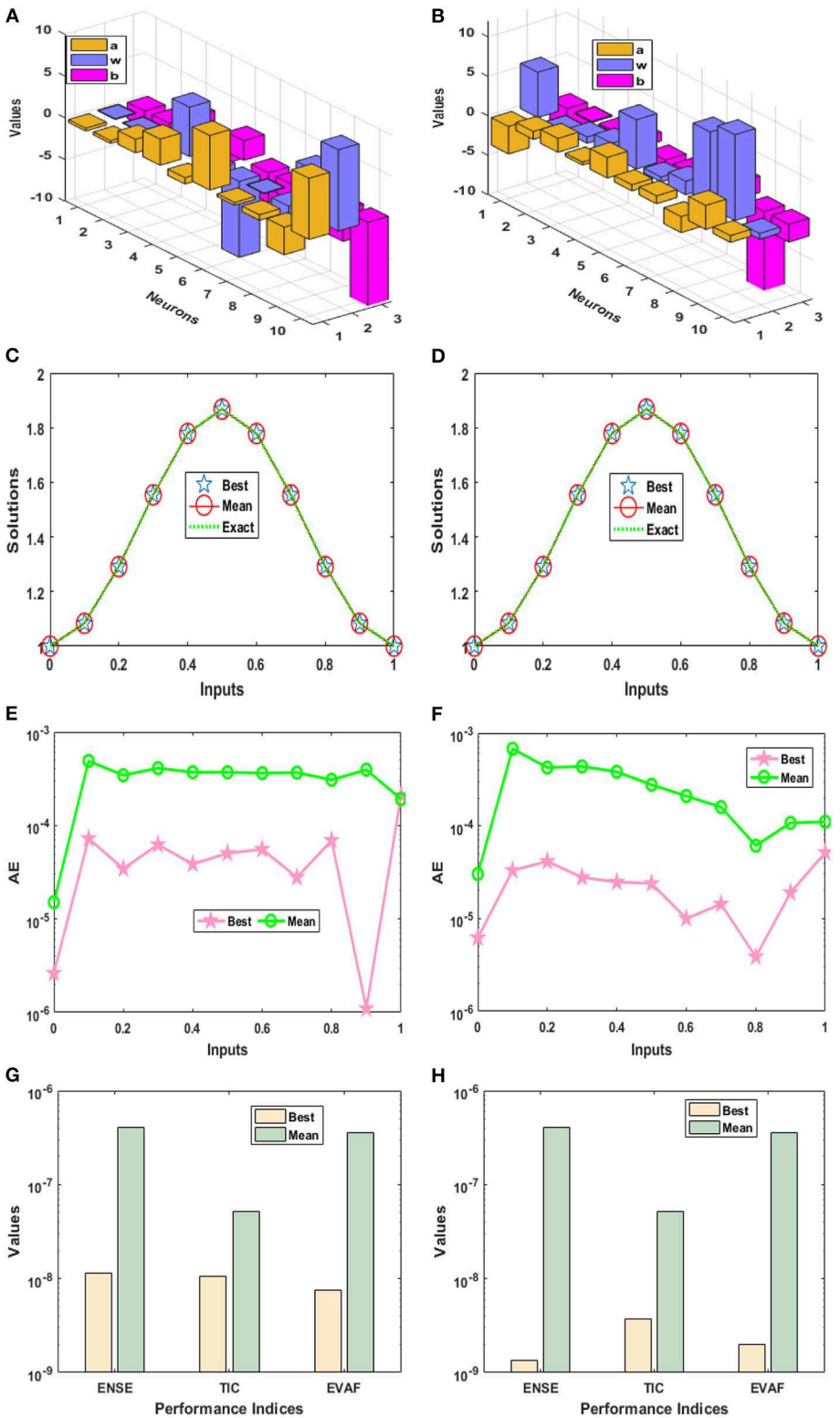

FIGURE 2 | Best weight, results of the designed methodology, values of the AE, and performance measures of Examples 1 and 2 for 10 numbers of neurons. **(A)** ANN best weights for Example 1. **(B)** ANN best weights for Example 2. **(C)** Result comparison for Example 1. **(D)** Result comparison for Example 2. **(E)** AE values of 10 neurons for Example 1. **(F)** AE values of 10 neurons for Example 2. **(G)** Performance measures for Example 1. **(H)** Performance measures for Example 2.

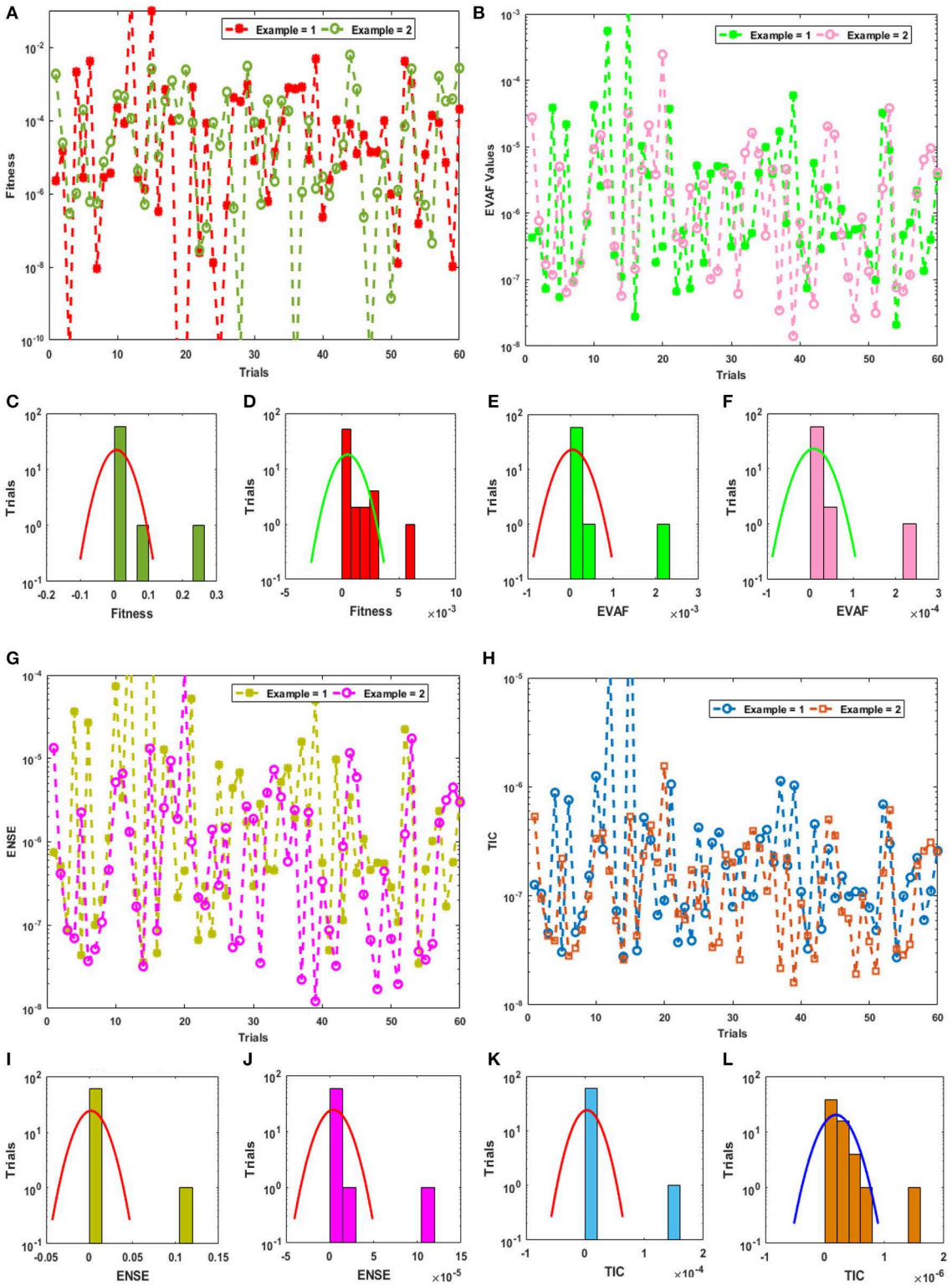

FIGURE 3 | Statistical analysis for Fitness, EVAF, ENSE, and TIC values along with the histograms for 5 numbers of neurons. **(A)** Analysis through Fitness values. **(B)** Analysis through EVAF values. **(C)** Fitness histogram for Example 1. **(D)** Fitness histogram for Example 2. **(E)** EVAF histogram for Example 1. **(F)** EVAF histogram for Example 2. **(G)** Analysis through ENSE values. **(H)** Analysis through TIC values. **(I)** ENSE histogram for Example 1. **(J)** ENSE histogram for Example 2. **(K)** TIC histogram for Example 1. **(L)** TIC histogram for Example 2.

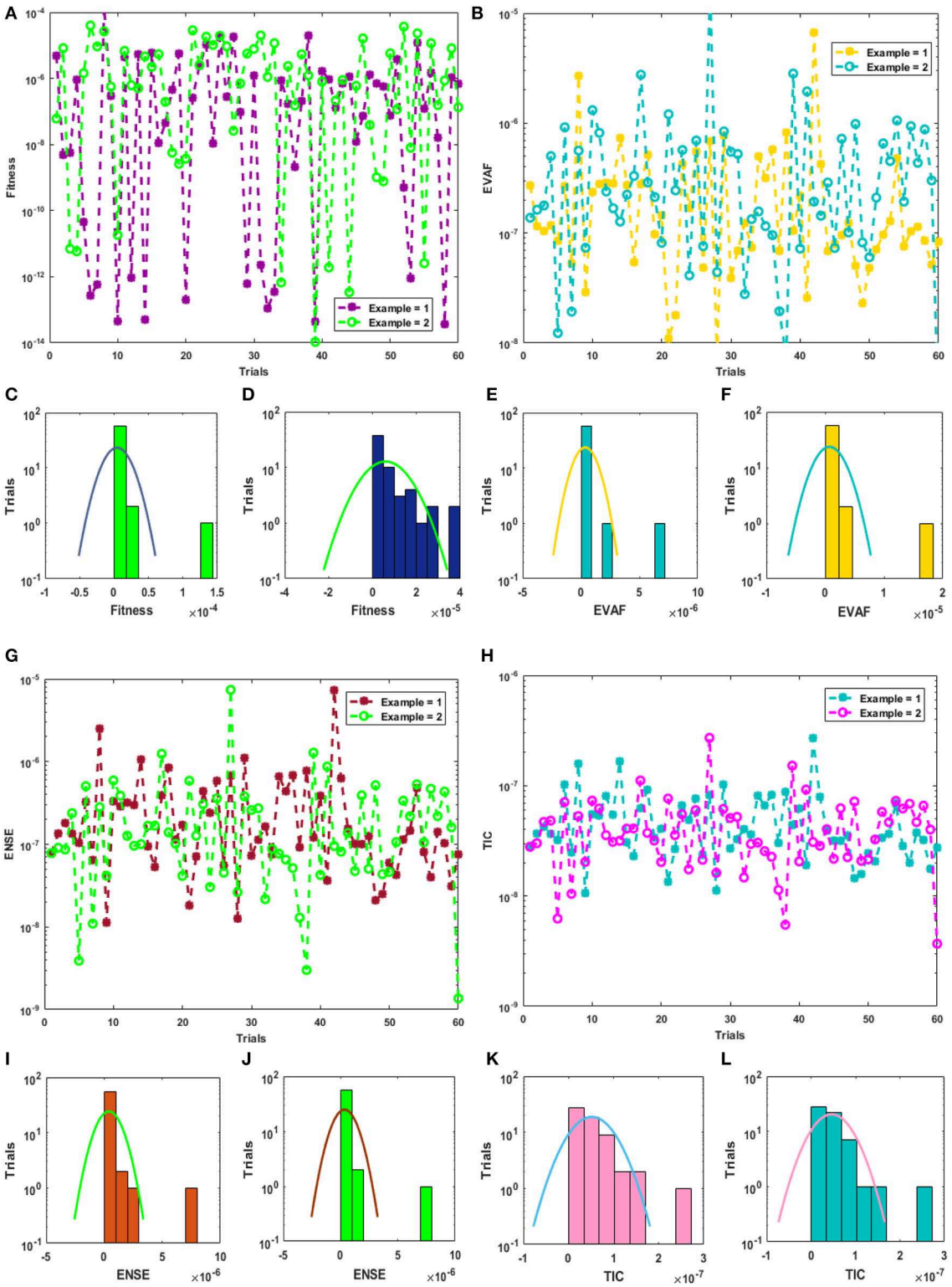

FIGURE 4 | Statistical analysis for Fitness, EVAF, ENSE, and TIC values along with the histograms for 10 numbers of neurons. **(A)** Analysis through Fitness values. **(B)** Analysis through EVAF values. **(C)** Fitness histogram for Example 1. **(D)** Fitness histogram for Example 2. **(E)** EVAF histogram for Example 1. **(F)** EVAF histogram for Example 2. **(G)** Analysis through ENSE values. **(H)** Analysis through TIC values. **(I)** ENSE histogram for Example 1. **(J)** ENSE histogram for Example 2. **(K)** TIC histogram for Example 1. **(L)** TIC histogram for Example 2.

TABLE 2 | Statistical measures of second order NSP-BVPs for 5 numbers of neurons.

x	Example 1			Example 2		
	Min	**Median**	**S-IR**	**Min**	**Median**	**S-IR**
0	4.3800E-10	2.4322E-05	5.8941E-05	4.1548E-09	2.7870E-05	4.0175E-05
0.1	1.0811E-04	7.7025E-04	8.6001E-04	1.2196E-04	1.0068E-03	1.0410E-03
0.2	3.6511E-05	5.6142E-04	6.2835E-04	1.1680E-04	7.2896E-04	6.7197E-04
0.3	8.7597E-05	6.4440E-04	5.9016E-04	8.0975E-05	5.2411E-04	3.5493E-04
0.4	2.9869E-05	6.4334E-04	7.4767E-04	7.8613E-05	5.7963E-04	6.0679E-04
0.5	4.8751E-05	5.6677E-04	6.4867E-04	8.1846E-05	4.9090E-04	4.7209E-04
0.6	6.9083E-05	6.0762E-04	7.6064E-04	3.3751E-05	2.7292E-04	3.2479E-04
0.7	1.9878E-05	5.8409E-04	5.8424E-04	5.4564E-05	2.6714E-04	2.3180E-04
0.8	3.2494E-05	5.0037E-04	6.1557E-04	1.4562E-08	8.5972E-05	1.0953E-04
0.9	1.2129E-05	6.6068E-04	8.2711E-04	1.9492E-05	1.8377E-04	2.5713E-04
1	6.2420E-06	3.2533E-04	2.7669E-04	3.7593E-05	1.6656E-04	2.0026E-04

TABLE 3 | Statistical measures of second order SPBVP for 10 numbers of neurons.

x	Example 1			Example 2		
	Min	**Median**	**S-IR**	**Min**	**Median**	**S-IR**
0	1.3750E-11	1.1115E-06	1.0015E-05	1.3497E-10	8.5111E-06	1.7554E-05
0.1	6.2531E-06	3.4802E-04	2.0725E-04	1.0887E-06	5.0029E-04	2.8479E-04
0.2	3.4460E-05	2.6909E-04	1.2230E-04	4.0212E-05	3.6106E-04	1.5219E-04
0.3	4.0693E-06	2.9278E-04	1.5321E-04	1.0086E-05	3.3328E-04	1.6158E-04
0.4	3.8667E-05	2.8024E-04	1.5726E-04	5.8796E-06	2.8468E-04	1.8934E-04
0.5	5.0393E-05	2.8371E-04	1.3840E-04	2.3541E-05	2.1966E-04	8.6765E-05
0.6	1.1706E-06	2.5999E-04	1.3755E-04	5.1929E-06	1.6256E-04	9.2463E-05
0.7	1.6981E-05	2.7881E-04	1.4362E-04	1.4313E-05	1.2823E-04	6.5314E-05
0.8	1.9865E-05	2.4636E-04	1.1779E-04	3.1422E-06	4.8243E-05	2.1416E-05
0.9	1.0978E-06	2.9394E-04	1.4451E-04	1.9040E-05	9.1881E-05	4.3721E-05
1	2.5240E-07	1.2135E-04	1.0572E-04	3.9770E-07	1.0216E-04	5.0242E-05

by using the proposed results obtained by ANN-PSO-IPS and the exact solutions. It is clear in **Figures 1E,F** that most of the best solutions lie around 10^{-04}–10^{-05} for both examples, while the mean values lie around 10^{-02}–10^{-03} and 10^{-03}–10^{-04} for examples 1 and 2, respectively. The best AE values for 10 neurons are plotted in **Figures 2E,F** lie around 10^{-04}–10^{-06}, while the mean values lie around 10^{-03}–10^{-04} for both examples. In order to find the best and mean values of the performance indices based on the VAF, ENSE, and TIC values, the **Figures 1G,H**, **2G,H** have been plotted using the 5 and 10 number of neurons for both examples. The best ENSE, TIC, and EVAF values for 5 neurons lie around 10^{-06}–10^{-08} for both examples. Whereas, for both examples using 5 numbers of neurons, the best ENSE values lie around 10^{-02}–10^{-04} and the best TIC and EVAF values lie around 10^{-04}–10^{-06}. Furthermore, for the 10 numbers of neurons, the best values of ENSE, TIC, and EVAF are close to 10^{-08} for example 1, while for example 2, these best values lie around 10^{-08}–10^{-09}. The mean ENSE and EVAF values for the example 1 and 2 lie around 10^{-06}–10^{-07}, while the mean TIC values lie around 10^{-07}–10^{-08} for both examples. It is noticed that the results of AE and the performance measures for 10 neurons are found to be better when compared to 5 neurons.

Statistical investigations of the present methodology for 60 independent trials using the 5 and 10 numbers of neurons for the examples 1 and 2 are provided in **Figures 3**, **4**. The Fitness, EVAF, ENSE, and TIC values along with the histogram are plotted in **Figures 3A,B,G,H**. These investigations show that around 70% of independent trials of the designed approach ANN-PSO-IPS achieved higher accuracy for all the statistical performances.

Statistics measures based on Minimum (Min), Median and S-IR gages for solving the second order SPBVP using the 5 and 10 numbers of neurons are tabulated in **Tables 2**, **3**. The statistical measures are provided in order to check the accuracy analysis of the presented scheme ANN-PSO-IPS. In **Table 2**, the Min values for example 1 and 2 lie around 10^{-04}–10^{-10} and 10^{-04}–10^{-09}, respectively, while the Median and S-IR values lie around 10^{-04}–10^{-05} for both examples. In **Table 3**, the Min values for the examples 1 and 2 lie around 10^{-05}–10^{-11} and 10^{-05}–10^{-10}, respectively, while

the Median and S-IR values lie around $10^{-04}-10^{-06}$ for both examples.

CONCLUSIONS

A novel application of a stochastic numerical solver based on neuro-swarm intelligent computing is presented to solve the singular non-linear second order periodic boundary value problems using different numbers of neurons based on the neural networks optimized with the global search capability of particle swarm optimization supported with quick fine tuning of decision variables by manipulating the strength of local search via interior-point scheme. The singular periodic model is efficiently evaluated by the designed computing solver with the layer structure based neural networks with 5 and 10 neurons and it is found that the accuracy of numerical outcomes is enhanced by large neurons-based networks. The precision of the stochastic designed approach is verified by obtaining identical outcomes with the exact solutions having 4–6 decimal places of accuracy for solving both the singular periodic non-linear models. From the plots of performance measures using the neuron analysis, one can also conclude that the calculated accuracy is better for 10 numbers of neurons. Statistical interpretation of findings through performance indices of TIC, EVAF, and ENSE based on 60 executions/trials of the solver for obtaining the solution of singular periodic non-linear model validate the trustworthiness, accurateness and robustness. Moreover, the values of the mean, median and semi interquartile range tabulated in **Tables 1**, **2** provide the precise and accurate values of the presented scheme ANN-PSO-IPS.

In future, the designed approach is a promising alternate solver to be exploited/explored to investigate the computational fluid dynamics problems, especially thin film flow, wire coating analysis, squeezing flow models, Jeffery Hamel flow, calendaring problems, stretching flow problems, food processing models, and related fields [57–62].

DATA AVAILABILITY STATEMENT

The original contributions presented in the study are included in the article/supplementary materials, further inquiries can be directed to the corresponding author/s.

AUTHOR CONTRIBUTIONS

All authors listed have made a substantial, direct and intellectual contribution to the work, and approved it for publication.

FUNDING

This paper has been partially supported by Ministerio de Ciencia, Innovacion y Universidades grant number PGC2018-0971-B-100 and Fundacion Seneca de la Region de Murcia grant number 20783/PI/18.

REFERENCES

1. Li F, Liang Z. Existence of positive periodic solutions to nonlinear second order differential equations. *Appl Math Lett.* (2005) **18:**1256–64. doi: 10.1016/j.aml.2005.02.014
2. Atici FM, Guseinov GS. On the existence of positive solutions for nonlinear differential equations with periodic boundary conditions. *J Comp Appl Math.* (2001) **132:**341–56. doi: 10.1016/S0377-0427(00)00438-6
3. Baslandze SR, Kiguradze IT. On the unique solvability of a periodic boundary value problem for third-order linear differential equations. *Differ Equat.* (2006) **42:**165–71. doi: 10.1134/S0012266106020029
4. Komashynska I, Al-Smadi M, Arqub OA, Momani S. An efficient analytical method for solving singular initial value problems of nonlinear systems. *Appl Math Inform Sci.* (2016) **10:**647–56. doi: 10.18576/amis/100224
5. Al-Smadi M, Arqub OA, Shawagfeh N, Momani S. Numerical investigations for systems of second-order periodic boundary value problems using reproducing kernel method. *Appl Math Comput.* (2016) **291:**137–48. doi: 10.1016/j.amc.2016.06.002
6. Agarwal RP, Filippakis ME, O'Regan D, Papageorgiou NS. Degree theoretic methods in the study of nonlinear periodic problems with nonsmooth potentials. *Differ Integral Equ.* (2006) **19:**279–96.
7. Agarwal RP. On periodic solutions of nonlinear second order differential systems. *J Comput Appl Math.* (1979) **5:**117–23. doi: 10.1016/0771-050X(79)90007-X
8. Geng F, Cui M. Solving singular nonlinear second-order periodic boundary value problems in the reproducing kernel space. *Appl Math Comput.* (2007) **192:**389–98. doi: 10.1016/j.amc.2007.03.016
9. Rachunková I. Existence of two positive solutions of a singular nonlinear periodic boundary value problem. *J Comput Appl Math.* (2000) **113:**27–34. doi: 10.1016/S0377-0427(99)00241-1
10. Jiang D, Chu J, O'Regan D, Agarwal RP. Multiple positive solutions to superlinear periodic boundary value problems with repulsive singular forces. *J Math Anal Appl.* (2003) **286:**563–76. doi: 10.1016/S0022-247X(03)00493-1
11. Zhang Z, Wang J. On existence and multiplicity of positive solutions to periodic boundary value problems for singular nonlinear second order differential equations. *J Math Anal Appl.* (2003) **281:**99–107. doi: 10.1016/S0022-247X(02)00538-3
12. Assadi R, Khuri SA, Sayfy A. Numerical solution of nonlinear second order singular BVPs based on green's functions and fixed-point iterative schemes. *Int J Appl Comp Math.* (2018) **4:**134. doi: 10.1007/s40819-018-0569-8
13. Xin L, Guo Y, Zhao J. Nontrivial solutions of second-order nonlinear boundary value problems. *Appl Math E-Notes.* (2019) **19:**668–74.
14. El-Sayed A, Gaafar FM. Existence of solutions for singular second-order ordinary differential equations with periodic and deviated nonlocal multipoint boundary conditions. *J Func Spaces.* (2018) **2018:**1–11. doi: 10.1155/2018/9726475
15. Wang Y, Li J, Cai Z. Positive solutions of periodic boundary value problems for the second-order differential equation with a parameter. *Bound Value Probl.* (2017) **2017:**1–11. doi: 10.1186/s13661-017-0776-y
16. Wang Y, Ru Y. On positive periodic solutions of second order singular equations. *Bound Value Probl.* (2018) 2018:114. doi: 10.1186/s13661-018-1036-5
17. Masood Z, Majeed K, Samar R, Raja MAZ. Design of Mexican hat wavelet neural networks for solving bratu type nonlinear systems. *Neurocomputing.* (2017) **221:**1–14. doi: 10.1016/j.neucom.2016.08.079
18. Raja MAZ, Niazi SA, Butt SA. An intelligent computing technique to analyze the vibrational dynamics of rotating electrical machine. *Neurocomputing.* (2017) **219:**280–99. doi: 10.1016/j.neucom.2016.09.032
19. Berg J, Nyström K. A unified deep artificial neural network approach to partial differential equations in complex geometries. *Neurocomputing.* (2018) **317:**28–41. doi: 10.1016/j.neucom.2018.06.056

20. Bukhari AH, Raja MAZ, Sulaiman M, Islam S, Shoaib M, Kumam P. Fractional neuro-sequential ARFIMA-LSTM for financial market forecasting. *IEEE Access*. (2020) **8:**71326–38. doi: 10.1109/ACCESS.2020.2985763
21. Pakdaman M, Ahmadian A, Effati S, Salahshour S, Baleanu D. Solving differential equations of fractional order using an optimization technique based on training artificial neural network. *Appl Math Comput.* (2017) **293:**81–95. doi: 10.1016/j.amc.2016.07.021
22. Raja MAZ, Manzar MA, Shah SM, Chen Y. Integrated intelligence of fractional neural networks and sequential quadratic programming for bagley–torvik systems arising in fluid mechanics. *J Comp Nonlinear Dynam.* (2020) **15:**051003. doi: 10.1115/1.4046496
23. Jafarian A, Nia SM, Golmankhaneh AK, Baleanu D. On artificial neural networks approach with new cost functions. *Appl Math Comput.* (2018) **339:**546–55. doi: 10.1016/j.amc.2018.07.053
24. Bukhari AH, Sulaiman M, Islam S, Shoaib M, Kumam P, Raja MAZ. Neuro-fuzzy modeling and prediction of summer precipitation with application to different meteorological stations. *Alex Eng J.* (2020) **59:**101–16. doi: 10.1016/j.aej.2019.12.011
25. Umar M, Amin F, Wahab HA, Baleanu D. Unsupervised constrained neural network modeling of boundary value corneal model for eye surgery. *Appl Soft Comput*. (2019) **85:**105826. doi: 10.1016/j.asoc.2019.105826
26. Raja MAZ, Manzar MA, Samar R. An efficient computational intelligence approach for solving fractional order Riccati equations using ANN and SQP. *Appl Math Model.* (2015) **39:**3075–93. doi: 10.1016/j.apm.2014.11.024
27. Raja MAZ, Samar R, Manzar MA, Shah SM. Design of unsupervised fractional neural network model optimized with interior point algorithm for solving Bagley–Torvik equation. *Math Comput Simul.* (2017) **132:**139–58. doi: 10.1016/j.matcom.2016.08.002
28. Umar M, Sabir Z, Raja MAZ. Intelligent computing for numerical treatment of nonlinear prey–predator models. *Appl Soft Comput.* (2019) **80:**506–24. doi: 10.1016/j.asoc.2019.04.022
29. Li R, Hu S, Wang Y, Yin M. A local search algorithm with tabu strategy and perturbation mechanism for generalized vertex cover problem. *Neural Comp Appl.* (2017) **28:**1775–85. doi: 10.1007/s00521-015-2172-9
30. Ahmad I, Ahmad S, Awais M, Ahmad SUI, Raja MAZ. Neuro-evolutionary computing paradigm for Painlevé equation-II in nonlinear optics. *Eur Phys J Plus*. (2018) **133:**184. doi: 10.1140/epjp/i2018-12013-3
31. Sabir Z, Wahab HA, Umar M, Erdogan F. Stochastic numerical approach for solving second order nonlinear singular functional differential equation. *Appl Math Comput*. (2019) **363:**124605 doi: 10.1016/j.amc.2019.124605
32. Sabir Z, Manzar MA, Raja MAZ, Sheraz M, Wazwaz AM. Neuro-heuristics for nonlinear singular Thomas-Fermi systems. *Appl Soft Comput*. (2018) **65:**152–69. doi: 10.1016/j.asoc.2018.01.009
33. Raja MAZ, Mehmood J, Sabir Z, Nasab AK, Manzar MA. Numerical solution of doubly singular nonlinear systems using neural networks-based integrated intelligent computing. *Neural Comp Appl.* (2019) **31:**793–812. doi: 10.1007/s00521-017-3110-9
34. Mehmood A, Zameer A, Ling SH, Raja MAZ. Design of neuro-computing paradigms for nonlinear nanofluidic systems of MHD Jeffery–Hamel flow. *J Taiw Inst Chem Eng.* (2018) **91:**57–85. doi: 10.1016/j.jtice.2018.05.046
35. Mehmood A, Afsar K, Zameer A, Awan SE, Raja MAZ. Integrated intelligent computing paradigm for the dynamics of micropolar fluid flow with heat transfer in a permeable walled channel. *Appl Soft Comput.* (2019) **79:**139–62. doi: 10.1016/j.asoc.2019.03.026
36. Raja MAZ, Shah FH, Alaidarous ES, Syam MI. Design of bio-inspired heuristic technique integrated with interior-point algorithm to analyze the dynamics of heartbeat model. *Appl Soft Comput.* (2017) 52**:**605–29. doi: 10.1016/j.asoc.2016.10.009
37. Sabir Z, Wahab HA, Umar M, Sakar MG, Raja MAZ. Novel design of Morlet wavelet neural network for solving second order Lane–Emden equation. *Math Comput Simul.* (2020) **172:**1–14. doi: 10.1016/j.matcom.2020.01.005
38. Raja MAZ, Umar M, Sabir Z, Khan JA, Baleanu D. A new stochastic computing paradigm for the dynamics of nonlinear singular heat conduction model of the human head. *Eur Phys J Plus.* (2018) **133:**364. doi: 10.1140/epjp/i2018-12153-4
39. Mehmood A, Zameer A, Ling SH, ur Rehman A, Raja MAZ. Integrated computational intelligent paradigm for nonlinear electric circuit models using neural networks, genetic algorithms and sequential quadratic programming. *Neural Comp Appl.* (2019) **32:**10337–57. doi: 10.1007/s00521-019-04573-3
40. Ara A, Khan NA, Razzaq OA, Hameed T, Raja MAZ. Wavelets optimization method for evaluation of fractional partial differential equations: an application to financial modelling. *Adv Differ Equ.* (2018) **2018:**8. doi: 10.1186/s13662-017-1461-2
41. Raja MAZ, Shah FH, Syam MI. Intelligent computing approach to solve the nonlinear Van der Pol system for heartbeat model. *Neural Comp Appl.* (2018) 30:3651–75. doi: 10.1007/s00521-017-2949-0
42. Raja MAZ, Asma K, Aslam MS. Bio-inspired computational heuristics to study models of hiv infection of CD4+ T-cell. *Int J Biomath.* (2018) **11:**1850019. doi: 10.1142/S1793524518500195
43. Shi Y, Eberhart RC. Empirical study of particle swarm optimization. In: *Proceedings of the 1999. Congress on Evolutionary Computation-CEC99.* Vol. 3. IEEE (1999). p. 1945–50.
44. Shi, Y. Particle swarm optimization: developments, applications and resources. In: *Proceedings of the 2001 Congress on Evolutionary Computation.* Vol. 1. IEEE (2001). p. 81–6.
45. Engelbrecht AP. *Computational Intelligence: An Introduction*. John Wiley and Sons (2007).
46. Raja MAZ. Solution of the one-dimensional Bratu equation arising in the fuel ignition model using ANN optimised with PSO and SQP. *Conn Sci.* (2014) **26:**195–214. doi: 10.1080/09540091.2014.907555
47. Raja MAZ, Zameer A, Kiani AK, Shehzad A, Khan MAR. Nature-inspired computational intelligence integration with Nelder–Mead method to solve nonlinear benchmark models. *Neural Comp Appl.* (2018) **29:**1169–93. doi: 10.1007/s00521-016-2523-1
48. Mehmood A, Zameer A, Raja MAZ, Bibi R, Chaudhary NI, Aslam MS. Nature-inspired heuristic paradigms for parameter estimation of control autoregressive moving average systems. *Neural Comp Appl.* (2019) **31:**5819–42. doi: 10.1007/s00521-018-3406-4
49. Aydogan EK, Delice Y, Özcan U, Gencer C, Bali Ö. Balancing stochastic U-lines using particle swarm optimization. *J Intell Manuf.* (2019) **30:**97–111. doi: 10.1007/s10845-016-1234-x
50. Takano H, Asano H, Gupta N. Application example of particle swarm optimization on operation scheduling of microgrids. In: *Frontier Applications of Nature Inspired Computation*. Springer (2020). p. 215–39. doi: 10.1007/978-981-15-2133-1
51. Ibrahim RA, Ewees AA, Oliva D, Elaziz MA, Lu S. Improved salp swarm algorithm based on particle swarm optimization for feature selection. *J Ambient Intell Humaniz Comput.* (2019) **10:**3155–69. doi: 10.1007/s12652-018-1031-9
52. Sicre MR, Svaiter BF. A $O(1/k^{3/2})$ hybrid proximal extragradient primal–dual interior point method for nonlinear monotone mixed complementarity problems. *Comp Appl Math.* (2018) **37:**1847–76. doi: 10.1007/s40314-017-0425-1
53. Raja MAZ, Aslam MS, Chaudhary NI, Khan WU. Bio-inspired heuristics hybrid with interior-point method for active noise control systems without identification of secondary path. *Front Inform Tech Electr Eng.* (2018) **19:**246–59. doi: 10.1631/FITEE.1601028
54. Stefanova M, Yakunin S, Petukhova M, Lupuleac S, Kokkolaras M. An interior-point method-based solver for simulation of aircraft parts riveting. *Eng Optimiz.* (2018) **50:**781–96. doi: 10.1080/0305215X.2017.1355367
55. Raja MAZ, Ahmed U, Zameer A, Kiani AK, Chaudhary NI. Bio-inspired heuristics hybrid with sequential quadratic programming and interior-point methods for reliable treatment of economic load dispatch problem. *Neural Comp Appl.* (2019) **31:**447–75. doi: 10.1007/s00521-017-3019-3
56. Umenberger J, Manchester IR. Specialized interior-point algorithm for stable nonlinear system identification. *IEEE Trans Automat Contr.* (2018) **64:**2442–56. doi: 10.1109/TAC.2018.2867358
57. de Assis RA, Pazim R, Malavazi MC, Petry PDC, de Assis LME, Venturino E. A mathematical model to describe the herd behaviour considering group defense. *Appl Math Nonlinear Sci.* (2020) **5:**11–24. doi: 10.2478/amns.2020.1.00002
58. Li T, Yang, W. Solution to chance constrained programming problem in swap trailer transport organisation based on improved simulated

annealing algorithm. *Appl Math Nonlinear Sci.* (2020) **5:**47–54. doi: 10.2478/amns.2020.1.00005
59. El-Borhamy M, Mosalam N. On the existence of periodic solution and the transition to chaos of Rayleigh-Duffing equation with application of gyro dynamic. *Appl Math Nonlinear Sci.* (2020) **5:**93–108. doi: 10.2478/amns.2020.1.00010
60. Evirgen F, Uçar S, Özdemir N. System analysis of HIV infection model with CD4+ T under non-singular kernel derivative. *Appl Math Nonlinear Sci.* (2020) **5:**139–46. doi: 10.2478/amns.2020.1.00013
61. Modanli M, Akgül A. On solutions of fractional order telegraph partial differential equation by crank-nicholson finite difference method. *Appl Math Nonlinear Sci.* (2020) **5:**163–70. doi: 10.2478/amns.2020.1.00015
62. Bicer E. An asymptotic result for neutral differential equations. *Appl Math Nonlinear Sci.* (2020) **5:**189–94. doi: 10.2478/amns.2020.1.00017

Conflict of Interest: The authors declare that the research was conducted in the absence of any commercial or financial relationships that could be construed as a potential conflict of interest.

frontiers in Physics

BRIEF RESEARCH REPORT
published: 14 August 2020
doi: 10.3389/fphy.2020.00258

Bifurcation and Numerical Simulations of Ca^{2+} Oscillatory Behavior in Astrocytes

Hongkun Zuo[1] *and Min Ye*[2]*

[1] *Department of Mathematics, Huainan Normal University, Huainan, China,* [2] *School of Education Science, Guangxi University for Nationalities, Nanning, China*

In this paper, the dynamical analysis of Ca^{2+} oscillations in astrocytes is theoretically investigated by the center manifold theorem and the stability theory of equilibrium point. The global structure of bifurcation and evoked Ca^{2+} dynamics are presented in a human astrocyte model from a mathematical perspective. Results show that the difference in appearance and disappearance of Ca^{2+} oscillations is partly due to two subcritical Hopf bifurcation points. In addition, the numerical simulations are performed to further verify the effectiveness of the proposed method.

Keywords: astrocyte, equilibrium, Hopf bifurcation, center manifold, stability

OPEN ACCESS

Edited by:
Jia-Bao Liu,
Anhui Jianzhu University, China

Reviewed by:
Junqiang Wei,
North China Electric Power University, China
Yong Zhao,
Henan Polytechnic University, China
Yong Lu,
Harbin Engineering University, China

***Correspondence:**
Min Ye
missye-2006@163.com

Specialty section:
This article was submitted to Mathematical and Statistical Physics, a section of the journal Frontiers in Physics

Received: *02 May 2020*
Accepted: *10 June 2020*
Published: *14 August 2020*

Citation:
Zuo H and Ye M (2020) Bifurcation and Numerical Simulations of Ca^{2+} Oscillatory Behavior in Astrocytes. Front. Phys. 8:258. doi: 10.3389/fphy.2020.00258

INTRODUCTION

Ca^{2+} as an important second messenger in the cytosol is critical for synaptic neurons and glia cells in the brain [1]. The oscillatory changes in concentration of Ca^{2+} are called Ca^{2+} oscillations and play an active part in the transmission of chemical and electrical signaling process [2]. Astrocytes comprise approximately 50% of the volume of human brain and exhibit not only neuron-dependent Ca^{2+} oscillations but also spontaneous Ca^{2+} waves [3]. It was demonstrated that the frequencies and amplitudes of Ca^{2+} oscillations play key roles in Ca^{2+} signal transduction in the nervous system [4]. Recent results from experiment calcium release-activated calcium channel (CRAC) have shown that it is effective for the control in inhibiting neuronal excitability by enhancing calcium release from astrocytes [5].

It was generally considered that Ca^{2+} oscillations in astrocyte take place in response to external stimuli, inducing the release of neuro-active chemicals [6, 7]. This view began to change as several lines of evidence indicate that these oscillations can also be formed spontaneously [8]. Nevertheless, the mechanism and functional role involved in these stochastic spontaneous Ca^{2+} waves are still not well-understood. Basically, Ca^{2+} signal transmission of astrocytes in the brain may vary owing to certain bifurcation principles, and different chemical information is typically characterized by frequency, amplitude, and spatial Ca^{2+} propagation [9]. Dynamical mechanisms that underlie the Ca^{2+} waves have been investigated from both theoretical and experimental points of view in recent years [10–18]. Therefore, the stability and bifurcation analysis are fundamental to investigate the appearance and disappearance of spontaneous Ca^{2+} oscillations in astrocytes. In the last decades, existing mathematical models helped explore the possible dynamical mechanism of these oscillatory activities in neuronal excitability [19–23].

STABILITY OF EQUILIBRIUM POINT AND BIFURCATION ANALYSIS

In the present work, we apply an extension of the one-pool model proposed by Lavrentovich and Hemkin as a specific example of the stability of equilibrium point and the bifurcation scenario. This model consists of three main variables: cytosol Ca^{2+} concentration (Ca_{cyt}), Ca^{2+} concentration in the endoplasmic reticulum (Ca_{er}), and IP_3 concentration in cell (IP_3). The equations and meanings of each expression in the model are given as follows:

$$\begin{cases} \frac{dCa_{\mathrm{cyt}}}{dt} = v_{in} - k_{\mathrm{out}} Ca_{\mathrm{cyt}} + v_{\mathrm{CICR}} - v_{\mathrm{serca}} + k_f \left(Ca_{\mathrm{er}} - Ca_{\mathrm{cyt}}\right), \\ \frac{dCa_{\mathrm{er}}}{dt} = v_{\mathrm{serca}} - v_{CICR} - k_f \left(Ca_{\mathrm{er}} - Ca_{\mathrm{cyt}}\right), \\ \frac{dIP_3}{dt} = v_{\mathrm{PLC}} - k_{\mathrm{deg}} IP_3, \end{cases} \tag{1}$$

where

$$\begin{aligned} v_{\mathrm{serca}} &= v_{M2}\left(\frac{Ca_{\mathrm{cyt}}^2}{Ca_{\mathrm{cyt}}^2 + k_2^2}\right), \\ V_{\mathrm{PLC}} &= v_p\left(\frac{Ca_{\mathrm{cyt}}^2}{Ca_{\mathrm{cyt}}^2 + k_p^2}\right), \\ v_{\mathrm{CICR}} &= 4v_{M3}\left(\frac{k_{\mathrm{CaA}}^n Ca_{\mathrm{cyt}}^n}{\left(Ca_{\mathrm{cyt}}^n + k_{\mathrm{CaA}}^n\right)\left(Ca_{\mathrm{cyt}}^n + k_{\mathrm{CaI}}^n\right)}\right) \\ &\quad \times \left(\frac{IP_3^m}{IP_3^m + k_{\mathrm{ip3}}^m}\right)\left(Ca_{\mathrm{er}} - Ca_{\mathrm{cyt}}\right). \end{aligned}$$

The details of each parameter can be found in **Table 1** and [4].

ANALYSIS OF STABILITY AND BIFURCATION OF EQUILIBRIA

In the following, v_{in} is chosen as the bifurcation parameter, corresponding to Ca^{2+} inflow into the cytosol through the astrocyte's membrane.

For convenience, let $x = Ca_{\mathrm{cyt}}$, $y = Ca_{\mathrm{er}}$, $z = \mathrm{IP}_3$, and $r = v_{\mathrm{in}}$, we first rewrite model (1) as the following form:

$$\begin{cases} \dot{x} = r - x + 0.5y - \frac{15x^2}{x^2+0.01} - \frac{3.466x^{2.02}z^{2.2}(x-y)}{(x^{2.02}+0.022)(z^{2.2}+0.0063)}, \\ \dot{y} = 0.5x - 0.5y + \frac{15x^2}{x^2+0.01} + \frac{3.466x^{2.02}z^{2.2}(x-y)}{(x^{2.02}+0.022)(z^{2.2}+0.0063)}, \\ \dot{z} = \frac{0.05x^2}{x^2+0.09} - 0.08z. \end{cases} \tag{2}$$

The equilibrium of system (2) meets the following equations:

$$\begin{cases} x = \frac{r}{k_{\mathrm{out}}} \\ z = \frac{v_{\mathrm{p}}x^2}{\left(x^2+k_{\mathrm{p}}^2\right)k_{\mathrm{deg}}} \\ y = \frac{v_{\mathrm{serca}} - v_{\mathrm{CICR}} + k_{\mathrm{f}}x}{k_{\mathrm{f}}} \end{cases} \tag{3}$$

TABLE 1 | Model parameters for which all results are computed unless otherwise stated.

v_{M2}	15 μM/s	v_{M3}	40.0 s^{-1}	k_{out}	0.5 s^{-1}
k_{deg}	0.08 s^{-1}	k_2	0.1 μM	m	2.2
k_{CaA}	0.15 μM	k_{CaI}	0.15 μM	n	2.02
k_{ip3}	0.1 μM	k_{p}	0.3 μM	k_{f}	0.5 s^{-1}

Let x_0, y_0, and z_0 be the roots of Equation (2) and $x_1 = x - x_0$, $y_1 = y - y_0$, and $z_1 = z - z_0$, we have the following representations:

$$\begin{cases} \dot{x}_1 = r - (x_1 + x_0) + 0.5\left(y_1 + y_0\right) - \frac{15(x_1+x_0)^2}{(x_1+x_0)^2+0.01} - \\ \qquad \frac{3.466(x_1+x_0)^{2.02}(z_1+z_0)^{2.2}\left(x_1+x_0-y_1-y_0\right)}{\left((x_1+x_0)^{2.02}+0.022\right)\left((z_1+z_0)^{2.2}+0.0063\right)}, \\ \dot{y}_1 = 0.5\left(x_1 + x_0\right) - 0.5\left(y_1 + y_0\right) + \frac{15(x_1+x_0)^2}{(x_1+x_0)^2+0.01} \\ \qquad + \frac{3.466(x_1+x_0)^{2.02}(z_1+z_0)^{2.2}\left(x_1+x_0-y_1-y_0\right)}{\left((x_1+x_0)^{2.02}+0.022\right)\left((z_1+z_0)^{2.2}+0.0063\right)}, \\ \dot{z}_1 = \frac{0.05(x_1+x_0)^2}{(x_1+x_0)^2+0.09} - 0.08\left(z_1 + z_0\right). \end{cases} \tag{4}$$

The corresponding equilibrium is (0, 0, 0), and system (4) has the same properties with the equilibrium of system (2). With simple calculation, it is easy to calculate the Jacobian matrix of system (4),

$$\mathrm{A} = (a_{ij})_{3\times 3} = \begin{pmatrix} a_{11} & a_{12} & a_{13} \\ a_{21} & a_{22} & a_{23} \\ a_{31} & a_{32} & a_{33} \end{pmatrix},$$

where

$$\begin{aligned} a_{11} &= \frac{30x^3}{\left(x^2+0.01\right)^2} - \frac{30}{x^2+0.01} - \frac{3.465966x^{2.02}z^{2.2}}{\sigma} \\ &\quad - \frac{7.0012517x^{1.02}z^{2.2}\left(x-y\right)}{\sigma} + \frac{14.002503x^{3.04}z^{2.2}\left(x-y\right)}{\sigma\left(x^{2.02}+0.021622\right)} - 1, \\ a_{12} &= \frac{3.465966x^{2.02}z^{2.2}}{\sigma} + 0.5, \\ a_{13} &= \frac{7.6251256x^{2.02}z^{3.4}\left(x-y\right)}{\sigma\left(z^{2.2}+0.00630957\right)} - \frac{7.625125x^{2.02}z^{1.2}\left(x-y\right)}{\sigma}, \\ a_{21} &= -\frac{30x^3}{\left(x^2+0.01\right)^2} + \frac{30}{x^2+0.01} + \frac{3.465966x^{2.02}z^{2.2}}{\sigma} \\ &\quad + \frac{7.0012517x^{1.02}z^{2.2}\left(x-y\right)}{\sigma} - \frac{14.002503x^{3.04}z^{2.2}\left(x-y\right)}{\sigma\left(x^{2.02}+0.021622\right)} + 0.5, \end{aligned}$$

$$
\begin{aligned}
a_{22} &= -\frac{3.465966x^{2.02}z^{2.2}}{\sigma} - 0.5,\\
a_{23} &= -\frac{7.6251256x^{2.02}z^{3.4}\left(x-y\right)}{\sigma\left(z^{2.2}+0.00630957\right)} + \frac{7.625125x^{2.02}z^{1.2}\left(x-y\right)}{\sigma},\\
a_{31} &= \frac{0.1x}{x^2+0.09} - \frac{0.1x^3}{\left(x^2+0.09\right)^2},\\
a_{32} &= 0,\\
a_{33} &= -0.8,\\
\sigma &= \left(x^{2.02}+0.02166228\right)^2\left(z^{2.2}+0.0063095\right).
\end{aligned}
$$

And one can easily obtain the following characteristic equation:

$$\lambda^3 + Q_3\lambda^2 + Q_2\lambda + Q_1 = 0,$$

where

$$
\begin{aligned}
Q_1 &= -\left(a_{11}+a_{22}+a_{33}\right),\\
Q_2 &= a_{11}a_{22} + a_{11}a_{33} + a_{22}a_{33} - a_{13}a_{31} - a_{12}a_{21} - a_{32}a_{23},\\
Q_3 &= a_{31}a_{13}a_{22} + a_{12}a_{21}a_{33} + a_{32}a_{23}a_{11} - a_{11}a_{22}a_{33}\\
&\quad - a_{12}a_{23}a_{31} - a_{13}a_{21}a_{32}.
\end{aligned}
$$

After a simple calculation, we have the following equations:

$$
\begin{aligned}
Q_1 &= \frac{30x}{x^2+0.01} - \frac{30x^3}{\left(x^2+0.01\right)^2} + \frac{6.93193x^{2.02}z^{2.2}}{\sigma_{11}}\\
&+\frac{7.00125x^{1.02}z^{2.2}\left(x-y\right)}{\sigma_{11}} - \frac{14.0025x^{3.04}z^{2.2}\left(x-y\right)}{\left(x^{2.02}+0.02166\right)^3\left(z^{2.2}+0.0063\right)},\\
Q_2 &= -\left(\frac{0.1x^3}{\left(x^2+0.09\right)^2} - \frac{0.1x}{x^2+0.09}\right)\left(\frac{7.62512x^{2.02}z^{1.2}\left(x-y\right)}{\sigma_{21}}\right.\\
&\left.-\frac{7.62512x^{2.02}z^{3.4}\left(x-y\right)}{\sigma_{22}\left(z^{2.2}+0.0063\right)^2}\right) - \frac{24x^3}{\sigma_{23}} + 0.5\left(\sigma_{22}+0.5\right)\\
&+\frac{0.55455x^{2.02}z^{2.2}}{\sigma_{21}} + \frac{0.5601x^{1.02}z^{2.2}\left(x-y\right)}{\sigma_{22}}\\
&-\frac{1.1202x^{3.04}z^{2.2}\left(x-y\right)}{\sigma_{24}} + \frac{2.4x}{x^2+0.01} + 0.12,\\
Q_3 &= 0.004\left(\frac{3.465966x^{2.02}z^{2.2}}{\left(x^{2.02}+0.02166\right)^2\left(z^{2.2}+0.0063\right)}\right),
\end{aligned}
$$

where

$$
\begin{aligned}
\sigma_{11} &= \left(x^{2.02}+0.02166\right)^2\left(z^{2.2}+0.0063\right),\\
Q_{21} &= \left(z^{2.2}+0.0063\right)\sigma_{22},\\
Q_{22} &= \left(x^{2.02}+0.02166\right)^2,\\
Q_{23} &= \left(x^2+0.01\right)^2,\\
Q_{24} &= \left(x^{2.02}+0.02166\right)^3\left(z^{2.2}+0.006309\right),
\end{aligned}
$$

Owing to the meaning of x, y, z and r, special conditions meet the needs whether there exists equilibrium of system (4) when $r \in [0.02, 0.06]$.

We consider the Hurwitz matrix using coefficients Q_i of the characteristic polynomial:

$$H_1 = (Q_1),\ H_2 = \begin{pmatrix} Q_1 & 1 \\ Q_3 & Q_2 \end{pmatrix},\ H_3 = \begin{pmatrix} Q_1 & 1 & 0 \\ Q_3 & Q_2 & 1 \\ 0 & 0 & Q_3 \end{pmatrix}.$$

It is easy to verify that the eigenvalues of the linearized system are negative or have a negative real part if the determinants of the three Hurwitz matrices are positive:

$$\det\left(H_i\right) > 0,\ i = 1, 2, 3,$$

Consider the stability and bifurcations of system (4) for varying parameter v_{in} in the case of the following Routh–Hurwitz criteria:

$$Q_1 > 0,\ Q_3 > 0,\ Q_1Q_2 > Q_3.$$

The corresponding two values can be obtained:

$$r_1 = 0.02383, r_2 = 0.05944.$$

After the computation based on the Routh–Hurwitz criteria, when we choose $r_1 = 0.02383$,

$$
\begin{aligned}
Q_1 &= 68.4381 > 0,\ Q_3 = 0.02838 > 0,\ Q_1Q_2\\
&- Q_3 = 0.775418 > 0.
\end{aligned}
$$

As $r_2 = 0.05944$,

$$
\begin{aligned}
Q_1 &= 60.5333804 > 0,\ Q_3 = 0.64149 > 0,\ Q_1Q_2\\
&- Q_3 = 0.027890411 > 0.
\end{aligned}
$$

It can be seen that all the two values satisfy the Routh–Hurwitz criteria. After using the normal form method, one can easily obtain the following conclusions:

(1) $r < 0.02383$, there is a stable node of system (4);
(2) $r = 0.02383$, and system (4) has a non-hyperbolic equilibrium $O_1 = (0.04766, 3.96096098, 0.0153858)$;
(3) $0.02383 < r < 0.05944$, system (4) has an equilibrium (saddle);
(4) $r = 0.05944$, and there exists a non-hyperbolic equilibrium $O_2 = (0.11886, 0.6665221778, 0.0847979)$;
(5) $r > 0.05944$, there is a stable node.

Let $r = r_0$, $x_1 = x - x_0$, $y_1 = y - y_0$, $z_1 = z - z_0$, and $r_1 = r - r_0$, the equilibrium of system (4) is (x_0, y_0, z_0). In order to apply the center manifold theorem with bifurcation parameter v_{in}, a new

variable r_1 is introduced in the original model. On the basis of $dr_1/dt = 0$, we have the following:

$$\begin{cases} \dot{x}_1 = (r_1 + r_0) - \frac{3.466(x_1+x_0)^{2.02}(z_1+z_0)^{2.2}(x_1+x_0-y_1-y_0)}{\left((x_1+x_0)^{2.02}+0.02166\right)\left((z_1+z_0)^{2.2}+0.00631\right)} \\ \qquad -\frac{15(x_1+x_0)^2}{(x_1+x_0)^2+0.01} - (x_1 + x_0) + 0.5\left(y_1 + y_0\right), \\ \dot{y}_1 = \frac{15(x_1+x_0)^2}{(x_1+x_0)^2+0.01} + \frac{3.466(x_1+x_0)^{2.02}(z_1+z_0)^{2.2}(x_1+x_0-y_1-y_0)}{\left((x_1+x_0)^{2.02}+0.02166\right)\left((z_1+z_0)^{2.2}+0.00631\right)} \\ \qquad +0.5\left(x_1 + x_0 - y_1 - y_0\right), \\ \dot{z}_1 = \frac{0.05(x_1+x_0)^2}{(x_1+x_0)^2+0.09} - 0.08\left(z_1 + z_0\right), \\ \dot{r}_1 = 0. \end{cases} \quad (5)$$

$r_1 = 0$, $O(x_1, y_1, z_1, r_1) = (0, 0, 0, 0)$ is the equilibrium of system (5), which has a same conclusion as the one of system (2) in stability and bifurcations.

For $r_0 = 0.02383$, the Jacobian matrix of system (4) has the following form:

$$\begin{pmatrix} -67.6083 & 0.71022 & 115.6304 & 1 \\ 67.1083 & -0.71022 & -115.6304 & 0 \\ 0.05041 & 0 & -0.08 & 0 \\ 0 & 0 & 0 & 0 \end{pmatrix}.$$

We have the eigenvalues of equilibrium point $O_1 = (0, 0, 0, 0)$ of system (5): $\xi_1 = -68.3987$, $\xi_2 = 0.0204i$, $\xi_3 = -0.0204i$, $\xi_4 = 0$, and the eigenvectors have met the following matrix:

$$\begin{pmatrix} -0.7097 & -0.0018 - 0.0406i & -0.0018 + 0.0406i & 0.1217 \\ 0.7045 & 0.9989 & 0.9989 & -0.9877 \\ 0.0005 & -0.0072 - 0.0238i & -0.0072 + 0.0238i & -0.0767 \\ 0 & 0 & 0 & 0.0608 \end{pmatrix}.$$

Suppose

$$\begin{pmatrix} x_1 \\ y_1 \\ z_1 \\ r_1 \end{pmatrix} = U \begin{pmatrix} u \\ v \\ w \\ s \end{pmatrix},$$

where

$$U = \begin{pmatrix} -0.7097 & -0.0018 & 0.0406 & 0.1217 \\ 0.7045 & 0.9989 & 0 & -0.9877 \\ 0.0005 & -0.0072 & 0.0238 & 0.0767 \\ 0 & 0 & 0 & 0.0608 \end{pmatrix}.$$

System (5) has the following form

$$\begin{pmatrix} \dot{u} \\ \dot{v} \\ \dot{w} \\ \dot{s} \end{pmatrix} = \begin{pmatrix} -68.3987 & 0 & 0 & 0 \\ 0 & 0 & -0.0204 & 0 \\ 0 & 0.0204 & 0 & 0 \\ 0 & 0 & 0 & 0 \end{pmatrix} \begin{pmatrix} u \\ v \\ w \\ s \end{pmatrix} + \begin{pmatrix} g_1 \\ g_2 \\ g_3 \\ g_4 \end{pmatrix}, \quad (6)$$

and

$$\begin{pmatrix} \dot{x}_1 \\ \dot{y}_1 \\ \dot{z}_1 \\ \dot{r}_1 \end{pmatrix} = U \begin{pmatrix} \dot{u} \\ \dot{v} \\ \dot{w} \\ \dot{s} \end{pmatrix} \Rightarrow \begin{pmatrix} \dot{u} \\ \dot{v} \\ \dot{w} \\ \dot{s} \end{pmatrix} = U^{-1} \begin{pmatrix} \dot{x}_1 \\ \dot{y}_1 \\ \dot{z}_1 \\ \dot{r}_1 \end{pmatrix} = U^{-1} \begin{pmatrix} f_1 \\ f_2 \\ f_3 \\ 0 \end{pmatrix},$$

where

$$\begin{aligned} f_1 &= g_{14} - 15g_{11}^2/\left(g_{11}^2 + 0.01\right) - g_{11} + 0.5g_{12} \\ &\quad - \left[3.465966222{g_{11}}^{2.02}{g_{13}}^{2.2}\left(g_{11} - g_{12}\right)\right] \\ &\quad / \left[\left({g_{11}}^{2.02} + 0.02166228889\right)^2\left({g_{13}}^{2.2} + 0.006309573445\right)\right], \\ f_2 &= 15g_{11}^2/\left(g_{11}^2 + 0.01\right) + 0.5\left(g_{11} - g_{12}\right) \\ &\quad + \left[3.465966222{g_{11}}^{2.02}{g_{13}}^{2.2}\left(g_{11} - g_{12}\right)\right] \\ &\quad / \left[\left({g_{11}}^{2.02} + 0.02166228889\right)^2\left({g_{13}}^{2.2} + 0.006309573445\right)\right], \\ f_3 &= 0.05g_{11}^2/\left(g_{11}^2 + 0.09\right) - 0.08g_{13}, \\ g_{11} &= x_1 + x_0 = -0.7097u - 0.0018v + 0.0406w + 0.1217s \\ &\quad + 0.04766, \\ g_{12} &= y_1 + y_0 = 0.7045u + 0.9989v - 0.9877s + 3.96096, \\ g_{13} &= z_1 + z_0 = 0.0005u - 0.0072v + 0.0238w + 0.0767s \\ &\quad + 0.01538, \\ g_{14} &= 0.0608s + 0.02383. \end{aligned}$$

Furthermore,

$$\begin{pmatrix} g_1 \\ g_2 \\ g_3 \\ g_4 \end{pmatrix} = U^{-1} \begin{pmatrix} f_1 \\ f_2 \\ f_3 \\ 0 \end{pmatrix} - \begin{pmatrix} -68.3987 & 0 & 0 & 0 \\ 0 & 0 & -0.0204 & 0 \\ 0 & 0.0204 & 0 & 0 \\ 0 & 0 & 0 & 0 \end{pmatrix} \begin{pmatrix} u \\ v \\ w \\ s \end{pmatrix},$$

where

$$U^{-1} = \begin{pmatrix} -1.3929 & 0.0146 & 2.3761 & 0.0280 \\ 0.9824 & 0.9908 & -1.6758 & 16.2432 \\ 0.3264 & 0.2994 & 41.4599 & -48.0914 \\ 0 & 0 & 0 & 16.4474 \end{pmatrix}.$$

Through calculation, we have the following equations:

$$\begin{aligned} g_1 &= -1.3928f_1 + 0.0146f_2 + 2.3761f_3 + 68.3987u, \\ g_2 &= 0.9823f_1 + 0.9907f_2 - 1.6757f_3 + 0.0204w, \\ g_3 &= 0.3264f_1 + 0.2994f_2 + 41.4599f_3 - 0.0204v, \\ g_4 &= 0. \end{aligned}$$

On the basis of the center manifold theory, one can conclude that there exists a center manifold of system (5), and its form can be expressed as

$$\begin{aligned} W_{loc}^{c}(O_1) &= \left\{(u,v,w,s) \in R^4 \middle| u \right. \\ &= \left. h^*(v,w,s), h^*(0,0,0) = 0, Dh^*(0,0,0) = 0 \right\}. \quad (7) \end{aligned}$$

Substituting Equation (7) into Equation (6), the following equations can be derived as:

$$\begin{pmatrix} h^*(\dot{v},w,s) \\ \dot{v} \\ \dot{w} \\ \dot{s} \end{pmatrix} = \begin{pmatrix} -68.3987 & 0 & 0 & 0 \\ 0 & 0 & -0.0204 & 0 \\ 0 & 0.0204 & 0 & 0 \\ 0 & 0 & 0 & 0 \end{pmatrix} \begin{pmatrix} h^*(v,w,s) \\ v \\ w \\ s \end{pmatrix} + \begin{pmatrix} g_1 \\ g_2 \\ g_3 \\ g_4 \end{pmatrix}.$$

Let $h(v,w,s) = av^2 + bw^2 + cs^2 + dvw + evs + fws + \ldots$, and the center manifold of system (5) is

$$N(h) = Dh \cdot \begin{bmatrix} \dot{v} \\ \dot{w} \\ \dot{s} \end{bmatrix} + 68.3987h - g_1 \equiv 0. \quad (8)$$

Using the method of high-order partial derivatives, one can obtain the following equations:

$$\begin{pmatrix} 136.79775 & 0 & 0 & 0.0406996 & 0 & 0 \\ 0 & 136.7975 & 0 & -0.04082 & 0 & 0 \\ 0 & 0 & 136.7973 & 0 & -0.000102 & -0.00002 \\ -0.040825 & 0.040699 & 0 & 68.39882 & 0 & 0 \\ -0.000102 & 0 & 0 & -0.000011 & 68.3987 & 0.020349 \\ 0 & -0.0000226 & 0 & -0.000051 & -0.02031 & 68.39873 \end{pmatrix} \begin{pmatrix} a \\ b \\ c \\ d \\ e \\ f \end{pmatrix} = 0.$$

Based on the center manifold theory, one can compute $a = -0.00094$, $b = -0.12224$, $c = -1.15703$, $d = 0.03634$, $e = 0.10863$, and $f = -0.75265$. So the system that is confined to this center manifold is as follows:

$$\begin{pmatrix} \dot{v} \\ \dot{w} \end{pmatrix} = \begin{pmatrix} 0 & -0.0204 \\ 0.0204 & 0 \end{pmatrix} \begin{pmatrix} v \\ w \end{pmatrix} + \begin{pmatrix} f^1(v,w) \\ f^2(v,w) \end{pmatrix}, \quad (9)$$

where

$$\begin{aligned} f^1(v,w) &= 0.014915s - 0.004304v + 0.00382w + 0.037228sv \\ &\quad - 0.257924sw + 0.012455vw + \cdots, \\ f^2(v,w) &= 0.017292v - 0.269399s - 0.086114w + 0.014479sv \\ &\quad - 0.100315sw + 0.004844vw + \cdots. \end{aligned}$$

Hence, it is easy to verify that

$$\begin{aligned} a &= \frac{1}{16}\left[f^1_{vvv} + f^1_{vww} + f^2_{vvw} + f^2_{www}\right]\Big|_{(0,0)} \\ &\quad + \frac{1}{16 \times 0.0204}[f^1_{vw}(f^1_{vv} + f^1_{ww}) \\ &\quad - f^2_{vw}(f^2_{vv} + f^2_{ww}) - f^1_{vv}f^2_{vv} + f^1_{ww}f^2_{ww})]\big|_{(v=0,w=0,s=0)} \\ &= 0.1014870557 > 0, \\ d &= \left.\frac{d(\mathrm{Re}(\xi(s)))}{ds}\right|_{(v=0,w=0,s=0)} = -0.0189 < 0. \end{aligned}$$

From the discussion above, we summarize the following conclusions.

Conclusion 1: A subcritical Hopf bifurcation occurs when r passes through $r_0 = 0.02383$ of system (2). $r < r_0$, and the equilibrium O_1 is stable. $r > r_0$, and the equilibrium loses its stability; meanwhile, a stable periodic solution occurs, and system (2) begins to oscillate.

$r_0 = 0.05944$, eigenvalues of equilibrium point $O_2 = (0, 0, 0, 0)$ of system (3) are $\xi_1 = -60.5573$, $\xi_2 = 0.1029i$, $\xi_3 = -0.1029i$, and $\xi_4 = 0$, respectively. System (5) has the following form:

$$\begin{pmatrix} \dot{u} \\ \dot{v} \\ \dot{w} \\ \dot{s} \end{pmatrix} = \begin{pmatrix} -60.5573 & 0 & 0 & 0 \\ 0 & 0 & -0.1029 & 0 \\ 0 & 0.1029 & 0 & 0 \\ 0 & 0 & 0 & 0 \end{pmatrix} \begin{pmatrix} u \\ v \\ w \\ s \end{pmatrix} + \begin{pmatrix} g_1 \\ g_2 \\ g_3 \\ g_4 \end{pmatrix}, \quad (10)$$

$$\begin{pmatrix} \dot{u} \\ \dot{v} \\ \dot{w} \\ \dot{s} \end{pmatrix} = U^{-1} \begin{pmatrix} f_1 \\ f_2 \\ f_3 \\ 0 \end{pmatrix},$$

where

$$U = \begin{pmatrix} -0.71 & 0.0393 & 0.1915 & 0.1341 \\ 0.7042 & -0.9695 & 0 & -0.9748 \\ 0.0012 & 0.1328 & 0.0654 & 0.1654 \\ 0 & 0 & 0 & 0.067 \end{pmatrix},$$

$$\begin{aligned} f_1 &= g_{14} - \frac{15g_{11}^2}{\left(g_{11}^2 + 0.01\right)} - g_{11} + 0.5g_{12} \\ &\quad - \frac{\left[3.465966222{g_{11}}^{2.02}{g_{13}}^{2.2}\left(g_{11} - g_{12}\right)\right]}{\left[\left({g_{11}}^{2.02} + 0.02166228889\right)^2\left({g_{13}}^{2.2} + 0.006309573445\right)\right]}, \end{aligned}$$

$$f_2 = \frac{15g_{11}^2}{\left(g_{11}^2+0.01\right)} + 0.5\left(g_{11}-g_{12}\right) + \frac{\left[3.465966222{g_{11}}^{2.02}{g_{13}}^{2.2}\left(g_{11}-g_{12}\right)\right]}{\left[\left({g_{11}}^{2.02}+0.02166228889\right)^2\left({g_{13}}^{2.2}+0.006309573445\right)\right]},$$

$$f_3 = \frac{0.05g_{11}^2}{\left(g_{11}^2+0.09\right)} - 0.08g_{13}.$$

And $g_{1j}\,(j=1,\ldots,4)$ have the following different formulae:

$$\begin{aligned} g_{11} &= x_1 + x_0 = -0.71u + 0.0393v + 0.1915w + 0.1341s + 0.1189,\\ g_{12} &= y_1 + y_0 = 0.7042u - 0.9695v - 0.9748s + 0.6664,\\ g_{13} &= z_1 + z_0 = 0.0012u + 0.1328v + 0.0654w + 0.1654s + 0.0848,\\ g_{14} &= 0.067s + 0.05944, \end{aligned}$$

$$\begin{pmatrix} g_1\\ g_2\\ g_3\\ g_4 \end{pmatrix} = U^{-1}\begin{pmatrix} f_1\\ f_2\\ f_3\\ 0 \end{pmatrix} - \begin{pmatrix} -60.5573 & 0 & 0 & 0\\ 0 & 0 & -0.1029 & 0\\ 0 & 0.1029 & 0 & 0\\ 0 & 0 & 0 & 0 \end{pmatrix}\begin{pmatrix} u\\ v\\ w\\ s \end{pmatrix}, \tag{11}$$

which reduce to the following equations:

$$\begin{aligned} g_1 &= -1.0337f_1 + 0.3727f_2 + 3.0268f_3 + 60.5573u,\\ g_2 &= -0.7508f_1 - 0.7607f_2 + 2.1985f_3 + 0.1029w,\\ g_3 &= 1.5436f_1 + 1.5379f_2 = 10.7708f_3 - 0.1029v,\\ g_4 &= 0. \end{aligned}$$

The center manifold of system (5) is

$$N(h) = Dh\cdot\begin{bmatrix}\dot{v}\\ \dot{w}\\ \dot{s}\end{bmatrix} + 60.5573h - g_1 \equiv 0,$$

where

$$u = h^*(v,w,s), h^*(0,0,0) = 0, Dh^*(0,0,0) = 0.$$

And thus, the following equation can be obtained:

$$\begin{pmatrix} 105.4628 & 0 & 0 & 0.04089 & 0 & 0\\ 0 & 105.462 & 0 & 0.04077 & 0 & 0\\ 0 & 0 & 105.4628 & 0 & 0.00001678 & -0.0001493\\ 0.040771 & -0.0408 & 0 & 52.7313 & 0 & 0\\ 0.000067 & 0 & 0 & -0.0000746 & 652.73142 & -0.02044\\ 0 & -0.00014 & 0 & 0.0000339 & 0.0203859 & 52.7313498 \end{pmatrix}\begin{pmatrix} a\\ b\\ c\\ d\\ e\\ f \end{pmatrix} = 0.$$

We compute $a = 1.073869652$, $b = 0.3254214051$, $c = 1.590904144$, $d = 0.8641549$, $e = 2.5838022$, and $f = 1.1901543$. So the system confined to the center manifold of system (5) is

$$\begin{pmatrix}\dot{v}\\ \dot{w}\end{pmatrix} = \begin{pmatrix} 0 & -0.1029\\ 0.1029 & 0\end{pmatrix}\begin{pmatrix} v\\ w\end{pmatrix} + \begin{pmatrix} f^1(v,w)\\ f^2(v,w)\end{pmatrix}, \tag{12}$$

where

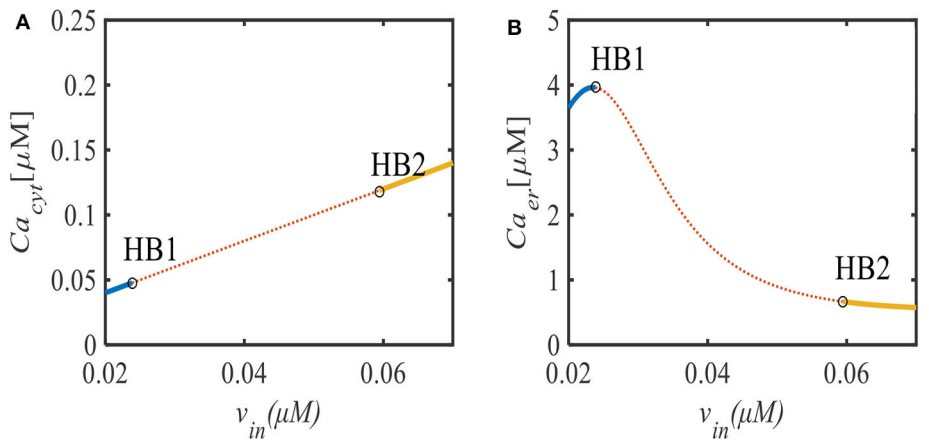

FIGURE 1 | (A) Bifurcation diagram of the equilibrium of system (2) in the (v_{in}, Ca_{cyt})-plane. **(B)** Bifurcation diagram of the equilibrium of system (2) in the (v_{in}, Ca_{er})-plane. Points HB1 and HB2 are the Hopf bifurcation points.

$$
\begin{aligned}
f^1(v,w) &= 0.079838w - 0.013612v - 0.034559\,\mathrm{s} - 0.671091sv \\
&\quad - 0.309119sw - 0.224447vw + \cdots, \\
f^2(v,w) &= 1.423469sv - 0.168005v - 0.204689w - 0.145723s \\
&\quad + 0.655680sw + 0.476081vw + \cdots.
\end{aligned}
$$

By computation, Conclusion 2 can be inferred as follows:

$$
\begin{aligned}
a &= \frac{1}{16}\left[f^1_{vvv} + f^1_{vww} + f^2_{vvw} + f^2_{www}\right]\Big|_{(0,0)} \\
&\quad + \frac{1}{16 \times 0.1029}[f^1_{vw}(f^1_{vv} + f^1_{ww}) \\
&\quad - f^2_{vw}(f^2_{vv} + f^2_{ww}) - f^1_{vv}f^2_{vv} + f^1_{ww}f^2_{ww})]\big|_{(v=0,w=0,s=0)} \\
&= 0.2483398204 > 0, \\
d &= \left.\frac{d(\mathrm{Re}(\xi(s))}{ds}\right|_{(v=0,w=0,s=0)} = -0.00069 < 0.
\end{aligned}
$$

Conclusion 2: A subcritical Hopf bifurcation occurs when r passes through $r_0 = 0.05944$ of system (2). $r < r_0$, the equilibrium O_2 is unstable, and system (2) begins to oscillate. $r > r_0$, the equilibrium O_2 is stable, and the global oscillations of system (2) vanish.

NUMERICAL SIMULATIONS

In order to investigate the bifurcation phenomenon in different Ca^{2+} oscillation patterns, we study the generation process with respect to the parameter v_{in}. The bifurcation diagram of the equilibrium of system (2) in the (Ca_{cyt}, v_{in})-plane [(Ca_{cyt}, v_{in})-plane)] is shown in **Figures 1A,B**. Each point of the curve (solid line) represents a stable equilibrium, and the dashed line represents an unstable equilibrium. The equilibrium undergoes the Hopf bifurcation twice, marked by points HB1 and HB2 with respect to the bifurcation parameter $v^1_{in} = 0.0238$ μM/s and $v^2_{in} = 0.0594$ μM/s. When $v_{in} < v^1_{in}$, there exists stable equilibrium of system (2). As v_{in} increases, the stable equilibrium loses its stability at the point HB1 and returns to being stable at HB2.

In **Figure 2**, we shall present the time evolutions of cytosol Ca^{2+} concentration in this model for different values of the parameter v_{in} by numerical simulation. The left panels represent time series of Ca_{cyt} comparison of parameter v_{in}, and the right panels are the corresponding Ca_{cyt}-Ca_{er}-IP_3 phase portrait. For example, there is a single peak in this type of oscillation for $v_{in} = 0.024$ μM/s in **Figure 2A**, and the corresponding 3D phase-space is shown in **Figure 2B**. Around $v_{in} = 0.033$ μM/s, it is seen that the number of peak counts and peak magnitude begin to increase, as shown in **Figures 2C,D**. Similarly, when $v_{in} = 0.052$ μM/s, five peaks were obtained (**Figures 2E,F**). Moreover, it should be mentioned in **Figures 2G,E**, although the results for peak magnitude look very similar and in agreement with the peak counts, that the oscillatory vibration is significantly different (**Figures 2G,H**).

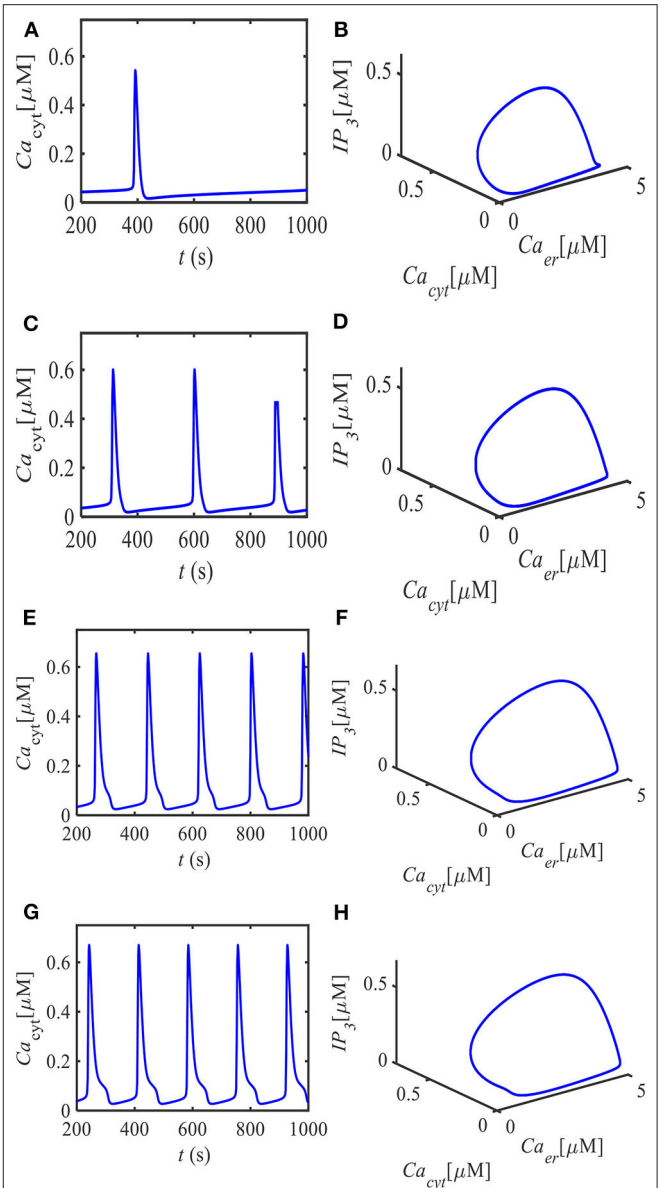

FIGURE 2 | Spontaneous Ca^{2+} oscillations in astrocytes emerged at different parts of the curve in **Figure 1** relative to points HB1 and HB2. The left panels denote the time evolution of Ca_{cyt} for different sets of parameter v_{in}, and the right panels denote the corresponding Ca_{cyt}-Ca_{er}-IP_3 phase portrait. **(A)** v_{in} = 0.024 μM/s, **(B)** portrait diagram as $v_{in} = 0.024$ μM/s, **(C)** $v_{in} = 0.033$ μM/s, **(D)** portrait diagram as $v_{in} = 0.033$ μM/s, **(E)** $v_{in} = 0.052$ μM/s, **(F)** portrait diagram as $v_{in} = 0.052$ μM/s, **(G)** $v_{in} = 0.0593$ μM/s, and **(H)** portrait diagram as $v_{in} = 0.0593$ μM/s.

CONCLUSION

In this paper, we have theoretically investigated the stability of equilibrium and bifurcation of spontaneous Ca^{2+} oscillations with a mathematical model in astrocytes. By choosing the flow of Ca^{2+} from the extracellular vesicles through the membrane and into the cytosol as the bifurcation parameter,

we conclude that two subcritical Hopf bifurcation points play an important role in the occurrence of Ca^{2+} oscillations. By combining the theoretical analysis results in this paper, we numerically gave the Hopf bifurcations, which agree with the theoretical results. Our results may be instructive for better understanding the role of spontaneous Ca^{2+} oscillations in astrocytes. Because synchronization of different oscillatory patterns may relate to bifurcation, we will give detailed research in future.

DATA AVAILABILITY STATEMENT

All datasets generated for this study are included in the article/supplementary material.

AUTHOR CONTRIBUTIONS

HZ and MY contributed to the conception and design of the study. HZ organized the literature and wrote the first draft of the manuscript. MY performed the design of figures. All authors contributed to the manuscript revision and read and approved the submitted version.

FUNDING

This work was supported by the Natural Science Foundation of China under Grant No. 11872084 and the Natural Science Foundation of the Anhui Higher Education Institutions of China under Grant Nos. KJ2016SD54 and KJ2017A460.

REFERENCES

1. Scemes E, Giaume C. Astrocyte calcium waves: what they are and what they do. *Glia*. (2006) **54**:716–25. doi: 10.1002/glia.20374
2. Nedergaard M, Ransom B, Goldman SA. New roles for astrocytes: redefining the functional architecture of the brain. *Trends Neurosci*. (2003) **26**:523–30. doi: 10.1016/j.tins.2003.08.008
3. Agulhon C, Petravicz J, McMullen AB, Sweger EJ, Minton SK, Taves SR, et al. What is the role of astrocyte calcium in neurophysiology? *Neuron*. (2008) **59**:932–46. doi: 10.1016/j.neuron.2008.09.004
4. Anwar H. Capturing intracellular Ca^{2+} dynamics in computational models of neurodegenerative diseases. *Drug Discov Today Dis Models*. (2016) **19**:37–42. doi: 10.1016/j.ddmod.2017.02.005
5. Toth AB, Hori K, Novakovic MM, Bernstein NG, Lambot L, Prakriya M. CRAC channels regulate astrocyte Ca^{2+} signaling and gliotransmitter release to modulate hippocampal GABAergic transmission. *Sci Signal*. (2019) **12**:eaaw5450. doi: 10.1126/scisignal.aaw5450
6. Volterra A, Meldolesi J. Astrocytes, from brain glue to communication elements: the revolution continues. *Nat Rev Neurosci*. (2005) **6**:626–40. doi: 10.1038/nrn1722
7. Halnes G, Østby I, Pettersen KH, Omholt SW, Einevoll GT. Electrodiffusive model for astrocytic and neuronal ion concentration dynamics. *PLoS Comput Biol*. (2013) **9**:e1003386. doi: 10.1371/journal.pcbi.1003386
8. Charles AC. Glia-neuron intercellular calcium signaling. *Dev Neurosci*. (1994) 16:196–206. doi: 10.1159/000112107
9. Matrosov VV, Kazantsev VB. Bifurcation mechanisms of regular and chaotic network signaling in brain astrocytes. *Chaos*. (2011) **21**:023103. doi: 10.1063/1.3574031
10. Ji Q, Lu Y. Bifurcations and continuous transitions in a nonlinear model of intracellular calcium oscillations. *Int J Bifurcat Chaos*. (2013) **23**:1350033. doi: 10.1142/S0218127413500338
11. Liu H, Pan Y, and Cao J. Composite learning adaptive dynamic surface control of fractional-order nonlinear systems. *IEEE Trans Syst Man Cybernetics*. (2019) **50**:2557–67. doi: 10.1109/tcyb.2019.2938754
12. Liu H, Wang H, Cao J, Alsaedi A, Hayat T. Composite learning adaptive sliding mode control of fractional-order nonlinear systems with actuator faults. *J Franklin Inst*. (2019) **36**:9580–99. doi: 10.1016/ j. franklin.2019. 02.042
13. Parri HR, Gould TM, Crunelli V. Spontaneous astrocytic Ca 2+ oscillations *in situ* drive NMDAR-mediated neuronal excitation. *Nat Neurosci*. (2001) **4**:803–12. doi: 10.1038/90507
14. Ding X, Zhang X, Ji L. Contribution of calcium fluxes to astrocyte spontaneous calcium oscillations in deterministic and stochastic models. *Appl Math Model*. (2018) **55**:371–82. doi: 10.1016/j.apm.2017.11.002
15. Li J, Tang J, Ma J, Du M, Wang R, Wu Y. Dynamic transition of neuronal firing induced by abnormal astrocytic glutamate oscillation. *Sci Rep*. (2016) **6**:32343. doi: 10.1038/srep32343
16. Ji Q, Zhou Y, Yang Z, Meng X. Evaluation of bifurcation phenomena in a modified Shen–Larter model for intracellular Ca^{2+} bursting oscillations. *Nonlinear Dyn*. (2016) **84**:1281–8. doi: 10.1007/s11071-015-2566-3
17. Oschmann F, Berry H, Obermayer K, Lenk K. From *in silico* astrocyte cell models to neuron-astrocyte network models: a review. *Brain Res Bull*. (2018) **136**:76–84. doi: 10.1016/j.brainresbull.2017.01.027
18. Matrosov V, Gordleeva S, Boldyreva N, Ben-Jacob E, Kazantsev V, de Pitta M, et al. Emergence of regular and complex calcium oscillations by inositol 1,4,5-Trisphosphate signaling in astrocytes. *Neurons Cogn*. (2019) 151–76. doi: 10.1007/978-3-030-00817-8_6
19. Zhou A, Liu X, Yu P. Bifurcation analysis on the effect of store-operated and receptor-operated calcium channels for calcium oscillations in astrocytes. *Nonlinear Dyn*. (2019) **97**:1–16. doi: 10.1007/s11071-019-05009-2
20. Engelborghs K, Luzyanina T, Roose D. Numerical bifurcation analysis of delay differential equations using DDE-BIFTOOL. *ACM Trans Math Softw*. (2002) **28**:1–21. doi: 10.1145/513001.513002
21. Yu P, Leung AY. The simplest normal form of Hopf bifurcation. *Nonlinearity*. (2003) **16**:277–300. doi: 10.1088/0951-7715/16/1/317
22. Yuan Y, Belair J. Stability and hopf bifurcation analysis for functional differential equation with distributed delay. *Siam J Appl Dyn Syst*. (2011) **10**:551–81. doi: 10.1137/100794493
23. Kopell N, Ermentrout GB, Whittington MA, Traub RD. Gamma rhythms and beta rhythms have different synchronization properties. *Proc Natl Acad Sci USA*. (2000) **97**:1867–72. doi: 10.1073/pnas.97.4.1867

Conflict of Interest: The authors declare that the research was conducted in the absence of any commercial or financial relationships that could be construed as a potential conflict of interest.

frontiers in Physics

ORIGINAL RESEARCH
published: 04 September 2020
doi: 10.3389/fphy.2020.00359

Computing Irregularity Indices for Probabilistic Neural Network

Shunguang Kang[1], *Yu-Ming Chu*[2,3]*, *Abaid ur Rehman Virk*[4], *Waqas Nazeer*[5] *and Jia Jia*[1]

[1] School of Tourism Data, Guilin Tourism University, Guilin, China, [2] Department of Mathematics, Huzhou University, Huzhou, China, [3] Hunan Provincial Key Laboratory of Mathematical Modeling and Analysis in Engineering, Changsha University of Science & Technology, Changsha, China, [4] Department of Mathematics, University of Management and Technology, Lahore, Pakistan, [5] Department of Mathematics, Government College University, Lahore, Pakistan

A topological index (TI) is a quantity expressed as a number that help us to catch symmetry of network. With the help of quantitative structure property relationship (QSPR), we can guess physical and chemical properties of several networks. A neural network is a computer system based on the nerve system. There are numerous uses of these systems in different fields of studies but their most critical use to date is in Neurochemistry. In this paper, we will discuss thirteen irregularity indices for probabilistic neural networks (PNN).

Keywords: irregularity indices, probabilistic neural network, graph, topological index, Zagreb index

OPEN ACCESS

Edited by:
Shaohui Wang,
Louisiana College, United States

Reviewed by:
Haidar Ali,
Government College University, Faisalabad, Pakistan
Darko Dimitrov,
Faculty of Information Studies Novo mesto, Slovenia

***Correspondence:**
Yu-Ming Chu
chuyuming@zjhu.edu.cn

Specialty section:
This article was submitted to Mathematical and Statistical Physics, a section of the journal Frontiers in Physics

Received: *25 March 2020*
Accepted: *28 July 2020*
Published: *04 September 2020*

Citation:
Kang S, Chu Y-M, Virk AuR, Nazeer W and Jia J (2020) Computing Irregularity Indices for Probabilistic Neural Network. Front. Phys. 8:359. doi: 10.3389/fphy.2020.00359

1. INTRODUCTION

PNN are likewise Parzen window pdf estimator. In last few years these networks are widely used in different problems. With the help of these networks, we can solve email security problems, also helpful in signature verification. A PNN network contain different sub networks. The input data is from the set of measurements. The Gaussian functions produce the second layer with the help of given set of data points. An average operation is perform by second layer which produce third layer.

Molecular structures can be studied by means of graph. A branch of mathematics thats deals with the study of molecular graphs is know as chemical graph theory. With the help of different tools of mathematics, we are able to identify the features that helps us in QSPR. Contaminate, TIs are arithmetic value link with graph of PNN and has utilization in different fields of study. TIs stay invariant of two isomorphic graphs and helpful to predict many properties of PNN [1–7]. Other growing field is Cheminformatics, in which QSAR and QSPR relationship is used to figure out properties of concerned network. In these investigation, a few Physico-chemical properties and TIs are helpful to examine the behavior of compound structures [8–17].

The other primeval TI is Randić index, introduced by Randić [18] in 1975. Due to huge applications of Randić index, the generalized Randić index was given in [12]. This variant develop intrust for both the mathematicians and chemists [19–24].

After Randić index, the most examined TIs are Zagreb indices [25–27]. The different variants of Zagreb index was studied in [28]. An other important topological invariant is a symmetric division index which is an excellent descriptor of the aggregate surface area for polychlorobiphenyls [29].

2. TOPOLOGICAL INDICES

A special number, in graph theoretical term, representing a molecular structure, is known as topological descriptor. A topological descriptor when correlates with a molecular property, it can be determine as graph-theoretic index or topological index. The First and second Zagreb indices are the oldest molecular descriptors invented in 1975 by Gutman [18] and their properties are extensively investigated. They are defined as:

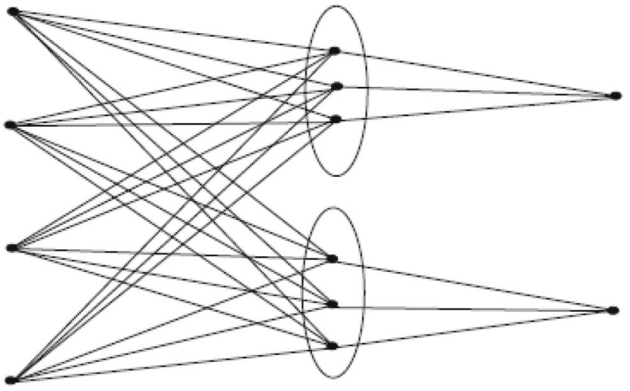

FIGURE 1 | *PNN*(4, 2, 3).

$$M_1(G) = \sum_{uv \in E(G)} (d_u + d_v).$$

$$M_2(G) = \sum_{uv \in E(G)} (d_u \times d_v).$$

The first genuine degree based TI was given by Randić in 1975 [18] as:

$$R(G) = \sum_{uv \in E(G)} \frac{1}{\sqrt{d_u.d_v}}.$$

The GRI known as General Randic Index [30] and is defined as:

$$GRI(G) = \sum_{uv \in E(G)} (d_u.d_v)^{\alpha}.$$

where α is an arbitrary real number.

The TI is known as Irregularity index [31], if TI of graph is greater equal to zero and TI of graph is equal to zero if and only if graph is regular. The Irregularity indices are given below. All these Irregularity indices are belong to degree based topological invariants excluding $IRM2(G)$. A simplified way of expressing the irregularity is a irregularity index.

- $VAR(G) = \sum_{u \epsilon V} (d_u - \frac{2m}{n})^2 = \frac{M_1(G)}{n} - (\frac{2m}{n})^2$
- $AL(G) = \sum_{uv \in E(G)} |d_u - d_v|$
- $IR1(G) = \sum_{u \in V} (d_u)^3 - \frac{2m}{n} \sum_{u \in V} (d_u)^2 = F(G) - \frac{2m}{n} M_1(G)$
- $IR2(G) = \sqrt{\frac{\sum_{uv \in E(G)} d_u d_v}{m}} - \frac{2m}{n} = \sqrt{\frac{M_2(G)}{m}} - \frac{2m}{n}$
- $IRF(G) = \sum_{uv \in E(G)} (d_u - d_v)^2 = F(G) - 2M_2(G)$
- $IRFW(G) = \frac{IRF(G)}{M_2(G)}$
- $IRA(G) = \sum_{uv \in E(G)} (d_u^{-1/2} - d_v^{-1/2})^2 = n - 2R(G)$
- $IRB(G) = \sum_{uv \in E(G)} (d_u^{1/2} - d_v^{1/2})^2 = M_1(G) - 2RR(G)$

TABLE 1 | E[*PNN*(*n*, *k*, *m*)].

(d_u, d_v)	Frequency
$(km, n+1)$	kmn
$(n+1, m)$	km

- $IRDIF(G) = \sum_{uv \in E(G)} |\frac{d_u}{d_v} - \frac{d_v}{d_u}| = \sum_{i<j} m_{i,j}(\frac{j}{i} - \frac{i}{j})$
- $IRLF(G) = \sum_{uv \in E(G)} \frac{|d_u - d_v|}{\sqrt{(d_u d_v)}} = \sum_{i<j} m_{i,j}(\frac{j-i}{\sqrt{ij}})$
- $IRLA(G) = 2 \sum_{uv \in E(G)} \frac{|d_u - d_v|}{(d_u + d_v)} = 2 \sum_{i<j} m_{i,j}(\frac{j-i}{i+j})$
- $IRD1(G) = \sum_{uv \in E(G)} ln1 + |d_u - d_v| = \sum_{i<j} m_{i,j} ln(i + j - 1)$
- $IRGA(G) \sum_{uv \in E(G)} ln(\frac{d_u + d_v}{2\sqrt{d_u d_v}}) \sum_{i<j} m_{i,j}(\frac{i+j}{2\sqrt{ij}})$

3. COMPUTATIONS OF PROBABILISTIC NEURAL NETWORK

In this section, we will discuss irregularity indices for probabilistic neural network. The molecular graph of $PNN(n, k, m)$ is given in **Figure 1**. The edge partition of $PNN(n, k, m)$ is given in **Table 1**. The total vertices in $PNN(n, k, m)$ are $n+k(m+1)$ and number of edges are $km(n+1)$.

Theorem 3.1. *Consider G as graph for probabilistic neural network PNN*$(n, k, m$*. Then,*

1. $VAR(G) = \frac{km(K^2m^2 - 4kmn^2 + k^2m + km^2 - 5kmn - km + 2kn + mn + 2n^2 + 2k + 2n)}{(km+k+n)^2}$
2. $AL(G) = k^2m^2n - kmn^2 - km^2 + 2kmn + km$
3. $IR1(G) = \frac{1}{km+k+n}(km(k^3m^3 + k^3m^2 + k^2m^2n + 2k^2mn + km^3 + 2k^2m + km^2 + 2kn^2 + m^2n + 2mn^2 + 2n^3 + 4kn + 2mn + 4n^2 + 2k + 2n))$
4. $IR2(G) = \frac{1}{km+k+n}(\sqrt{(k+1)m}km - 2kmn + \sqrt{(k+1)m}k + \sqrt{(k+1)mn} - 2km)$

Proof:

1. $$\begin{aligned} VAR(G) &= \sum_{u \in V} \left(d_u - \frac{2m}{n}\right)^2 = \frac{M_1(G)}{n} - \left(\frac{2m}{n}\right)^2 \\ &= \frac{k^2m^2 + km^2 + 2kmn + 2km}{km + k + n} - (\frac{kmn + km}{km + k + n})^2 \\ &= \frac{1}{(km + k + n)^2}\big(km(K^2m^2 - 4kmn^2 + k^2m + km^2 \\ &\quad -5kmn - km + 2kn + mn + 2n^2 + 2k + 2n))\end{aligned}$$

2. $$\begin{aligned} AL(G) &= \sum_{uv \in E(G)} |d_u - d_v| \\ &= |km - n - 1|(kmn) + |n + 1 - m|(km) \\ &= k^2m^2n - kmn^2 - km^2 + 2kmn + km.\end{aligned}$$

3. $$\begin{aligned} IR1(G) &= \sum_{u\in V} d_u^3 - \frac{2m}{n}\sum_{u\in V} d_u^2 = F(G) - \left(\frac{2m}{n}\right) M_1(G) \\ &= (k^3m^3 + 2k^2m^2n + 2k^2m^2 + km^3 + 2km^2n \\ &\quad +2kmn^2 + 2km^2 + 4kmn + 2km) \\ &\quad -\frac{2(kmn+km)}{(km+k+n)}(k^2m^2 + km^2 + 2kmn + 2km) \\ &= \frac{1}{km+k+n}(km(k^3m^3 + k^3m^2 \\ &\quad +k^2m^2n + 2k^2mn + km^3 + 2k^2m + km^2 + 2kn^2 \\ &\quad +m^2n + 2mn^2 + 2n^3 + 4kn + 2mn \\ &\quad +4n^2 + 2k + 2n)). \end{aligned}$$

4. $$\begin{aligned} IR2(G) &= \sqrt{\frac{\sum_{uv\in E(G)} d_u d_v}{m}} - \frac{2m}{n} = \sqrt{\frac{M_2(G)}{m}} - \frac{2m}{n} \\ &= \sqrt{\frac{(kmn+km)km + km(mn+m)}{kmn+km}} \\ &\quad -\left(\frac{2(kmn+km)}{km+k+n}\right) \\ &= \frac{1}{km+k+n}(\sqrt{(k+1)mkm} \\ &\quad -2kmn + \sqrt{(k+1)mk} \\ &\quad +\sqrt{(k+1)mn} - 2km). \end{aligned}$$

□

Theorem 3.2. *Consider G as graph for probabilistic neural network PNN(n, k, m. Then,*

1. $IRF(G) = k^3m^3 + km^3 + 2kmn^2 + 4kmn + 2km$
2. $IRFW(G) = \frac{k^2m^2+m^2+2n^2+4n+2}{m(kn+k+n+1)}$
3. $IRA(G) = \frac{1}{\sqrt{kmn+km}(mn+m)} km(n\sqrt{mn+m} + \sqrt{kmn+km})$
4. $IRB(G) = (-2k^2m^2n^2 - 2k^2m^2n + k^2m^2 - 2km^2n - km^2 + 2kmn + 2km)$

Proof:

1. $$\begin{aligned} IRF(G) &= \sum_{uv\in E(G)} (d_u - d_v)^2 \\ &= (km - n - 1)^2(kmn) + (n + 1 - m)^2(km) \\ &= k^3m^3 + km^3 + 2kmn^2 + 4kmn + 2km. \end{aligned}$$

2. $$\begin{aligned} IRFW(G) &= \frac{IRF(G)}{M_2(G)} \\ &= \frac{k^2m^2 + m^2 + 2n^2 + 4n + 2}{m(kn + k + n + 1)}. \end{aligned}$$

3. $$\begin{aligned} IRA(G) &= \sum_{uv\in E(G)} (d_u^{-1/2} - d_v^{-1/2})^2 \\ &= n - 2R(G) \\ &= \frac{1}{\sqrt{kmn+km}(mn+m)} \\ &\quad km(n\sqrt{mn+m} + \sqrt{kmn+km}). \end{aligned}$$

4. $$\begin{aligned} IRB(G) &= \sum_{uv\in E(G)} (d_u^{1/2} - d_v^{1/2})^2 \\ &= M_1(G) - 2RR(G) \\ &= (km + n + 1)km + km(m + n + 1) \\ &\quad -2k^2m^2n^2 - 2k^2m^2n - 2km^2n - 2km^2 \\ &= (-2k^2m^2n^2 - 2k^2m^2n \\ &\quad +k^2m^2 - 2km^2n - km^2 + 2kmn + 2km). \end{aligned}$$

□

Theorem 3.3. *Consider G as graph for probabilistic neural network PNN(n, k, m. Then,*

1. $IRDIF(G) = \frac{k^2m^2n - km^2 + kn^2 - n^3 + 2kn - 2n^2 + k - n}{n+1}$
2. $IRLF(G) = \frac{kmn(km-n-1)}{\sqrt{kmn+km}} + \frac{km(n-m+1)}{\sqrt{mn+m}}$
3. $IRLA(G) = \frac{km(km^2n + kmn^2 - km^2 + 2kmn - mn^2 - n^3 + km - 2mn - n^2 - m + n + 1)}{(km+n+1)(m+n+1)}$
4. $IRD1(G) = k^2m^2n - kmn^2 - km^2 + km$
5. $IRGA(G) = \frac{1}{\sqrt{(kmn+km)(mn+m)}}(km(0.71ln)km + n + 1)n\sqrt{mn+m} + 0.70ln(m + n + 1)\sqrt{kmn+km}$

Proof:

1. $$\begin{aligned} IRDIF(G) &= \sum_{uv\in E(G)} |\frac{d_u}{d_v} - \frac{d_v}{d_u}| \\ &= \left(\frac{km}{n+1} - \frac{n+1}{km}\right) kmn \\ &\quad +\left(\frac{n+1}{m} - \frac{n+1}{m} - \frac{m}{n+1}\right) km \\ &= \frac{k^2m^2n - km^2 + kn^2 - n^3 + 2kn - 2n^2 + k - n}{n+1}. \end{aligned}$$

2. $$\begin{aligned} IRLF(G) &= \sum_{uv\in E(G)} \frac{|d_u - d_v|}{\sqrt{d_u.d_v}} \\ &= \left(\frac{|km - n - 1|}{\sqrt{kmn}}\right)(kmn) + \left(\frac{|n + 1 - m|}{\sqrt{mn}}\right)(km) \\ &= \frac{kmn(km - n - 1)}{\sqrt{kmn + km}} + \frac{km(n - m + 1)}{\sqrt{mn + m}}. \end{aligned}$$

3 $$\begin{aligned} IRLA(G) &= \sum_{uv\in E(G)} 2\frac{|d_u - d_v|}{(d_u + d_v)} \\ &= 2\left(\frac{|km - n - 1|}{km + n + 1}\right)(kmn) \\ &\quad +2\left(\frac{|n + 1 - m|}{n + 1 + m}\right)(2km) \end{aligned}$$

$$= \frac{1}{(km+n+1)(m+n+1)}(km(km^2n+kmn^2 - km^2+2kmn-mn^2-n^3 + km-2mn-n^2-m+n+1).$$

4. $$IRD1(G) = \sum_{uv\in E(G)} ln\{1+|d_u-d_v|\} = ln\{1+|km-n-1|\}(kmn) + ln\{1+|n+1-m|\}(km) = k^2m^2n - kmn^2 - km^2 + km.$$

5. $$IRGA(G) = \sum_{uv\in E(G)} ln\left(\frac{d_u+d_v}{2\sqrt{d_ud_v}}\right) = ln\left(\frac{km+n+1}{2}\sqrt{km(n+1)}\right)(kmn) + ln\left(\frac{m+n+1}{2\sqrt{m(n+1)}}\right)(km) = \frac{1}{\sqrt{(kmn+km)(mn+m)}}(km(0.71ln)km+n+1) n\sqrt{mn+m} + 0.70ln(m+n+1)\sqrt{kmn+km}.$$

□

CONCLUSION

In this article, we have calculated degree-based irregularity indices of probabilistic neural network. Our outcomes are pertinent in material science and other applied sciences. It is demonstrated certainty that TIs help to anticipate numerous properties without setting off to the wet lab.

DATA AVAILABILITY STATEMENT

All datasets generated for this study are included in the article/supplementary material.

AUTHOR CONTRIBUTIONS

SK revised the introduction section and proofread the paper. Y-MC analyzed the results and arrange funding. AV proved the main results. WN proposed the problem and supervised this work. JJ improved the language and highlight the applications of the results. All authors listed approved it for publication.

FUNDING

The research was supported by the National Natural Science Foundation of China (Grant Nos. 11971142, 11871202, 61673169, 11701176, 11626101, and 11601485).

REFERENCES

1. Gao W, Younas M, Farooq A, Virk A, Nazeer W. Some reverse degree-based topological indices and polynomials of dendrimers. *Mathematics*. (2018) **6**:214. doi: 10.3390/math6100214
2. Gao W, Wang W, Dimitrov D, Wang Y. Nano properties analysis via fourth multiplicative ABC indicator calculating. *Arab J Chem.* (2018) **11**:793–801. doi: 10.1016/j.arabjc.2017.12.024
3. Gao W, Wu H, Siddiqui MK, Baig AQ. Study of biological networks using graph theory. *Saudi J Biol Sci.* (2018) **25**:1212–9. doi: 10.1016/j.sjbs.2017.11.022
4. Yang K, Yu Z, Luo Y, Yang Y, Zhao L, Zhou X. Spatial and temporal variations in the relationship between lake water surface temperatures and water quality-A case study of Dianchi Lake. *Sci Tot Environ.* (2018) **624**:859–71. doi: 10.1016/j.scitotenv.2017.12.119
5. Gao W, Guirao JLG, Abdel-Aty M, Xi W. An independent set degree condition for fractional critical deleted graphs. *Discr Contin Dyn Syst.* (2018) 12:877–86. doi: 10.3934/dcdss.2019058
6. Kang SM, Zahid MA, Virk AR, Nazeer W, Gao W. Calculating the degree-based topological indices of dendrimers. *Open Chem.* (2018) **16**:681–8. doi: 10.1515/chem-2018-0071
7. Shao Z, Virk AR, Javed MS, Rehman MA, Farahani MR. Degree based graph invariants for the molecular graph of Bismuth Tri-Iodide. *Eng Appl Sci Lett.* (2019) **2**:1–11. doi: 10.30538/psrp-easl2019.0011
8. Gao W, Wang W, Farahani MR. Topological indices study of molecular structure in anticancer drugs. *J Chem.* (2016) 2016. doi: 10.1155/2016/3216327
9. Naeem M, Siddiqui MK, Guirao JLG, Gao W. New and modified eccentric indices of octagonal grid omn. *Appl Math Nonlin Sci.* (2018) **3**:209–28. doi: 10.21042/AMNS.2018.1.00016
10. Gao W, Farahani MR, Shi L. Forgotten topological index of some drug structures. *Acta Med Mediter.* (2016) **32**:579–85. doi: 10.1155/2016/1053183
11. Ghorbani M, Ghazi M. Computing some topological indices of Triangular Benzenoid. *Digest J Nanomater Bios.* (2010) **5**:1107–11.
12. Amić D, Bešlo D, Luččić B, Nikolić S, Trinajstic N. The vertex-connectivity index revisited. *J Chem Inform Comput Sci.* (1998) **38**:819–22. doi: 10.1021/ci980039b
13. Gutman I. Some properties of the Wiener polynomial. *Graph Theory Notes NY.* (1993) **125**:13–8.
14. Ajmal M, Nazeer W, Munir M, Kang SM, Jung CY. The M-polynomials and topological indices of generalized prism network. *Int J Math Anal.* (2017) New York, NY **11**:293–303. doi: 10.12988/ijma.2017.7118
15. Munir M, Nazeer W, Shahzadi Z, Kang S. Some invariants of circulant graphs. *Symmetry.* (2016) **8**:134. doi: 10.3390/sym8110134
16. Dobrynin AA, Entringer R, Gutman I. Wiener index of trees: theory and applications. *Acta Appl Math.* (2001) **66**:211–49. doi: 10.1023/A:1010767517079
17. Gutman I, Polansky OE. *Mathematical Concepts in Organic Chemistry*. New York, NY: Springer Science & Business Media (2012).
18. Randić M. Characterization of molecular branching. *J Am Chem Soc.* (1975) **97**:6609–15. doi: 10.1021/ja00856a001
19. Hu Y, Li X, Shi Y, Xu T, Gutman I. On molecular graphs with smallest and greatest zeroth-order general Randić index. *MATCH Commun Math Comput Chem.* (2005) **54**:425–34.
20. Caporossi G, Gutman I, Hansen P, Pavlovic L. Graphs with maximum connectivity index. *Comput Biol Chem.* (2003) 27:85–90. doi: 10.1016/S0097-8485(02)00016-5
21. Li X, Gutman I. *Mathematical Chemistry Monographs No. 1*. Kragujevac: University of Kragujevac (2006).
22. Li X, Gutman I, Randić M. *Mathematical Aspects of Randić-type Molecular Structure Descriptors*. Kragujevac: University, Faculty of Science (2006).
23. Gutman I, Furtula B, Elphick C. Three new/old vertex-degree-based topological indices. *MATCH Commun Math Comput Chem.* (2014) **72**:617–32.
24. Li X, Shi Y. A survey on the Randić index. *MATCH Commun Math Comput Chem.* (2008) **59**:127–56.

25. Gutman I, Das KC. The first Zagreb index 30 years after. *MATCH Commun Math Comput Chem.* (2004) **50**:83–92.
26. Gao W, Wang Y, Wang W, Shi L. The first multiplication atom-bond connectivity index of molecular structures in drugs. *Saudi Pharm J.* (2017) **25**:548–55. doi: 10.1016/j.jsps.2017.04.021
27. Vukičević D, Graovac A. Valence connectivity versus Randić, Zagreb and modified Zagreb index: a linear algorithm to check discriminative properties of indices in acyclic molecular graphs. *Croat Chem Acta.* (2004) 77:501–8.
28. Miličević A, Nikolić S, Trinajstic N. On reformulated Zagreb indices. *Mol Divers.* (2004) 8:393–9. doi: 10.1023/B:MODI.0000047504.14261.2a
29. Gupta CK, Lokesha V, Shwetha SB, Ranjini PS. On the symmetric division deg index of graph. *Southeast Asian Bull Math.* (2016) **40**:59–80.
30. Kier L. *Molecular Connectivity in Chemistry and Drug Research.* Cambridge, MA: Elsevier (1999).
31. Réti T, Sharafdini R, Dregelyi-Kiss A, Haghbin H. Graph irregularity indices used as molecular descriptors in QSPR studies. *MATCH Commun Math Comput Chem.* (2018) **79**:509–24.

Conflict of Interest: The authors declare that the research was conducted in the absence of any commercial or financial relationships that could be construed as a potential conflict of interest.

frontiers in Physics

BRIEF RESEARCH REPORT
published: 09 September 2020
doi: 10.3389/fphy.2020.00368

Research on Improved Chaotic Particle Optimization Algorithm Based on Complex Function

Xiangli Xia[1] *and Shijin Li*[2]*

[1] Chongqing Key Laboratory of Spatial Data Mining and Big Data Integration for Ecology and Environment, Rongzhi College of Chongqing Technology and Business University, Chongqing, China, [2] Academic Affairs Office, Yunnan University of Finance and Economics, Kunming, China

In order to improve the performance of Particle Swarm Optimization (PSO) algorithm in solving continuous function optimization problems, a chaotic particle optimization algorithm for complex functions is proposed. Firstly, the algorithm uses qubit Bloch spherical coordinate coding scheme to initialize the initial position of the population. This coding method can expand the ergodicity of the search space, increase the diversity of the population, and further accelerate the convergence speed of the algorithm. Secondly, Logistic chaos is used to search the elite individuals of the population, which effectively prevents the PSO algorithm from falling into local optimization, thus obtaining higher quality optimal solution. Finally, complex functions are used to improve chaotic particles to further improve the convergence speed and optimization accuracy of PSO algorithm. Through the optimization tests of four complex high-dimensional functions, the simulation results show that the improved algorithm is more competitive and its overall performance is better, especially suitable for the optimization of complex high-dimensional functions.

Keywords: PSO algorithm, complex function, chaos search, convergence rate, improve chaotic particles

OPEN ACCESS

Edited by:
Jia-Bao Liu,
Anhui Jianzhu University, China

Reviewed by:
Ndolane Sene,
Cheikh Anta Diop University, Senegal
Hanliang Fu,
Illinois State University, United States

***Correspondence:**
Shijin Li
lee_shijin@sina.com

Specialty section:
This article was submitted to Mathematical and Statistical Physics, a section of the journal Frontiers in Physics

Received: *19 June 2020*
Accepted: *30 July 2020*
Published: *09 September 2020*

Citation:
Xia X and Li S (2020) Research on Improved Chaotic Particle Optimization Algorithm Based on Complex Function. Front. Phys. 8:368. doi: 10.3389/fphy.2020.00368

INTRODUCTION

Complex function optimization is an important research direction of optimization problems. Generally speaking, the solving methods of optimization problems can be divided into analytical method and numerical calculation [1]. The analytical method solves the problem according to the relationship between the derivative of the objective function and the extreme value of the function. This method is only suitable for optimization problems with relatively simple objective function. According to the variation rule of objective function value, In appropriate steps along the direction that optimizes the value of the objective function, An approximate calculation method that approaches the optimal point of the objective function step by step, This method is good at solving continuous differentiated convex optimization problems, With the continuous expansion of engineering optimization problems, most of the objective functions are non-convex optimization problems. The emergence of group intelligent optimization algorithms provides a limited way for complex function optimization problems [2, 3].

Particle Swarm Optimization (PSO) algorithm is a kind of bionic intelligent optimization algorithm based on population, which is proposed by Kennedy et al. [4]. Each particle in the PSO algorithm represents a feasible solution; the location of food source is the global optimal location point. PSO has strong search diversity, simple operation and few adjustment parameters. As soon as it was proposed, it was widely used [5, 6], especially PSO has shown excellent optimization ability

in complex optimization problems [7]. In reference [8], Eberhart and Shi found that when the maximum velocity of the particle is not too small ($v_{\max} > 3$), The inertia weight ω=0.8 is best. In addition, this conclusion has been confirmed on many subsequent issues. Clert [9] when carefully studying a general PSO system, the change of speed can be controlled by controlling ϕ_1 and ϕ_2. In order to improve the calculation speed of particle motion trajectory, Clert introduced contraction factor χ to improve the basic model of PSO algorithm. PSO algorithm has the following advantages:

First, the algorithm is easy to describe.
Second, there are few parameters to be adjusted in the algorithm.
Third, the number of functions to be evaluated in the algorithm is small.
Fourth, the number of populations required by the algorithm in the process of solving the problem is small.
Fifth, the algorithm converges quickly.

Because there are few parameters in PSO, PSO is easy to Realize , there is also less demand for computing resources, the gradient information of fitness function is not needed, only the value of fitness function is needed. Although PSO algorithm has various advantages, but the PSO algorithm itself also has several limitations, its performance is as follows. First, PSO is a probabilistic algorithm, without systematic and standardized theoretical support, It is still difficult to verify the correctness of PSO algorithm from a mathematical point of view so far. Moreover, based on the theory of random events, it is an extremely difficult task to analyze the particle trajectory quantitatively in the search process of PSO algorithm. However, this is also related to the key issues of convergence and parameter selection of PSO algorithm. Although most scholars are currently verifying the convergence of its improved PSO algorithm, But none of them has produced a set of mature and universal theories. Second, the behavior and characteristics of complex systems are the emergence of behaviors that are continuously superimposed through interaction between individual individuals in the system. Although the control of individual behaviors is relatively simple, however, this does not mean that the control of the whole system is an easy task. Third, as far as the whole algorithm is concerned, due to the lack of balance mechanism, when solving some complex or special problems, the algorithm is easy to lose population diversity and fall into local extreme. The structure and contents of the paper are as follows: (1) Introduce the basic particle swarm optimization algorithm and the algorithm flow; (2) Introduce the quantum chaotic adaptive particle swarm optimization algorithm, explaining the quantum Bloch coordinate coding, chaos optimization method, quantum particle swarm optimization algorithm, adaptive inertia weight and the improved algorithm flow, respectively; (3) Comparing the convergence test through experiments.

BASIC PSO

The mathematical description of PSO algorithm is follow that the population with dimension D and scale N can be expressed as $X = \{X_1, X_2, ..., X_D\}$, then at time t, the position of the i$^{\text{th}}$ particle is $X_i(t) = \{X_{i1}(t), X_{i2}(t), ..., X_{iD}(t)\}$ and its velocity is $V_i(t) = \{V_{i1}(t), V_{i2}(t), ..., V_{iD}(t)\}$. The algorithm always maintains two optimal positions: evolution process, the individual best position $pbest_i(t)$ of particle i, expressed as $p_i(t) = \{p_{i1}(t), p_{i1}(t), ..., p_{iD}(t)\}$, and $gbest$ (t) of population a best location, expressed as $p_g(t) = \{p_{g1}(t), p_{g1}(t), ..., p_{gD}(t)\}$. If the optimization model is $max\, f(X)$, the update formulas of $p_i(t)$ and $p_g(t)$ are as follows:

$$P_i^{(t+1)} = \begin{cases} X_i^{(t+1)} & f(X_i^{(t+1)}) > f(P_i^{(t)}); \\ P_i^{(t)} & f(X_i^{(t+1)}) \le f(P_i^{(t)}) \end{cases} \quad (1)$$

$$p_g^{(t+1)} = \max_{1 \le i \le N} p_i^{(t+1)} \quad (2)$$

In the t-th iteration, p_{best} and g_{best} represent historical and global optimal positions. Then the calculation formula for particle flight update is expressed as follows:

$$v_{i,d}^{t+1} = w v_{i,d}^t + c_1 r_1 (pbest_{i,d}^t - x_{i,d}^t) + c_2 r_2 (gbest_d^t - x_{i,d}^t) \quad (3)$$

$$x_{i,d}^{t+1} = x_{i,d}^t + v_{i,d}^{t+1} \quad (4)$$

Where $v_{i,d}^{t+1}$ represents the flight speed of i^{th} particle iterations $t + 1$; XID represents the position of i^{th} particle with iterations t. w represents the inertia weight, which is taken here as 0.6; c_1 and c_2 represent learning factors, generally taking$c_1 = 2, c_2 = 2$; $r_1 \in [0, 1]$ $r_2 \in [0, 1]$.

The flow of the basic PSO algorithm is as follows:

(1) Set the parameters of PSO algorithm, such as population size, problem dimension, inertia weight, maximum range and maximum speed, etc. Randomly initialize group position and speed.

(2) Judge whether the particle is beyond the search range, and correct the position if it is beyond the range.

(3) According to the state of each particle, calculate the corresponding fitness value.

(4) Update *pbest* according to the current fitness value.

(5) Update *gbest* according to the current fitness value.

(6) According to formulas (3) and (4), update the speed and position.

(7) Judge the termination condition, and return to (2) if it is not terminated, otherwise it will end.

QUANTUM CHAOS ADAPTIVE PSO ALGORITHM

Initial Population of Quantum Bloch Coordinate Coding

In quantum computation, the smallest information unit is expressed by qubits, which are also called qubits. The state of a qubit can be expressed as [10]:

$$|\varphi\rangle = \cos(\theta/2)\,|0\rangle + e^{i\varphi}\,\sin(\theta/2)\,|1\rangle \tag{5}$$

In Equation (5), numbers φ and θ define a point, Qubits establish correlation with Bloch spherical points, and the conversion formula is as follows:

$$|\varphi\rangle = \left[\cos\varphi\sin\theta \;\; \sin\varphi\sin\theta \;\; \cos\theta\right]^T \tag{6}$$

Let p_i be the i-th candidate solution in the group, and its coding scheme is as follows:

$$p_i = \begin{vmatrix} \cos\varphi_{i1}\sin\theta_{i1} & \cdots & \cos\varphi_{in}\sin\theta_{id} \\ \sin\varphi_{i1}\sin\theta_{i1} & \cdots & \sin\varphi_{in}\sin\theta_{id} \\ \cos\theta_{i1} & \cdots & \cos\theta_{id} \end{vmatrix} \tag{7}$$

Where $\varphi_{ij} = 2\pi \times rnd$, $\theta_{ij} = \pi \times rnd$ and $rnd \in [0,1]$; Each candidate solution occupies three positions in the space, i.e., represents the following three optimization solutions:

$$\begin{aligned} P_{ix} &= (\cos\varphi_{i1}\sin\theta_{i1}, \cdots, \cos\varphi_{id}\sin\theta_{id})\,; \\ P_{iy} &= (\sin\varphi_{i1}\sin\theta_{i1}, \cdots, \sin\varphi_{id}\sin\theta_{id})\,; \\ P_{iz} &= (\cos\theta_{i1}, \cdots, \cos\theta_{id}) \end{aligned} \tag{8}$$

Note that the feasible solutions corresponding to P_{ix},P_{iy} and P_{iz} are as follows:

$$\begin{aligned} x_{ix} &= (x_{i1}^1, x_{i2}^1, \ldots, x_{in}^1); \\ x_{iy} &= (x_{i1}^2, x_{i2}^2, \ldots, x_{in}^2); \\ x_{iz} &= (x_{i1}^3, x_{i2}^3, \ldots, x_{in}^3) \end{aligned} \tag{9}$$

Transformation of solution space: Bloch coordinates of the i-th qubit on candidate solution p_i are $\left[x_{ix}, x_{iy}, x_{iz}\right]^T$, and the value of solution space is $\left[a_j, b_j\right]$, then the transformation formula mapping $I^d = [-1,1]^d$ is follow:

$$\begin{aligned} x_{ij}^1 &= \tfrac{1}{2}\left[b_j\,(1 + x_{ix}) + a_j\,(1 - x_{ix})\right]; \\ x_{ij}^2 &= \tfrac{1}{2}\left[b_j\left(1 + x_{iy}\right) + a_j\left(1 - x_{iy}\right)\right]; \\ x_{ij}^3 &= \tfrac{1}{2}\left[b_j\,(1 + x_{iz}) + a_j\,(1 - x_{iz})\right] \end{aligned} \tag{10}$$

Therefore, individuals with smaller fitness values are selected as the initial population among all candidate solutions. Bloch coding can enhance the ergodicity of the optimization space, improve the population, and further improve the optimization performance.

Chaos Optimization Method

Chaos has the characteristics of randomness, ergodicity and regularity. In the field of optimization design, the ergodicity of chaos phenomenon can be used as an optimization mechanism to avoid falling into local minima in the search process. Chaotic variables are used to search and this method is applied to the optimization of continuous complex objects. The steps of chaos optimization algorithm using Logistic mapping are as follows:

(1) Let $k = 0, x_j^k, j = 1, 2, ..., n$ to chaotic variables $x_j^k \in [0,1]$.

$$s_j^k = \frac{x_j^k - x_{\min,j}}{x_{\max,j} - x_{\min,j}} \;\; j = 1, 2, ..., n \tag{11}$$

In the formula, $x_{\max,j}$ is max bounds and $x_{\min,j}$ is the search min bounds of the j-dimensional variable, respectively.

(2) Calculate next value s_j^{k+1}.

$$S_j^{k=1} = 4s_j^k(1 - s_j^k) \tag{12}$$

(3) The chaotic variable s_j^k is transformed into the decision variable x_j^{k+1}. Using a certain chaotic mapping structure to generate chaotic sequences, m is the length of chaotic sequences. These sequences are inversely transformed to the original search space through equation (13).

$$x_j^{k+1} = x_{\min,j} + s_j^{k+1}(x_{\max,j} - x_{\min,j}) \tag{13}$$

The new solution is taken as the result of chaotic optimization K=K+1, otherwise, the new solution is transferred to (2) and the iteration is continued.

(4) Calculate the fitness value $F(X_i)$ of X_i and compare it with the fitness value $F(X_i)$ of X_i to retain the best solution;

(5) Updating Chaotic Search Space $(x_{\min,j}, x_{\max,j})$.

Quantum PSO Algorithm

In 2004, Sun studied the convergence behavior of absorption-related particles and proposed a quantum PSO algorithm based on the model of quantum mechanics. In quantum mechanics, when each particle moves in the search space, there is a DELTA potential well-centered on p. The properties of particles in quantum space satisfying aggregated states are completely different from those in classical mechanics. The particle with quantum behavior has no definite trajectory when moving, i.e., The velocity and position are uncertain, and this uncertainty makes the possible position of the particle "everywhere" (i.e., In the whole feasible solution region) full of possibilities, and the particle has the possibility to get rid of the local optimal value point with large interference. It can ensure the global convergence of the algorithm and has only position vector, no speed vector, few control parameters and strong optimization ability in the optimization model.

Quantum PSO algorithm is described as follows: in D-dimensional space, there are m particles, the individual extreme point is$pBest_i = (pBest_{i1}, pBest_{i2}, ..., pBest_{iD})$, and the potential center point is p; The current global extreme point searched by the whole particle swarm is $gBest=(gBest_1, gBest_2, .., gBest_D)$. Then, The position update operation for this particle is as follows:

$$p = \frac{rand1() \times pBest_{id} + rand2() \times gBest_d}{rand1() + rand2()} \tag{14}$$

$$l = z \times |X_{id}(t) - p| \ \ 0 < z < \ln\sqrt{2} \tag{15}$$

$$X_{id}(t+1) \begin{cases} p - l \times \ln[1/rand3()] & rand3() > 0.5; \\ p + l \times \ln[1/rand3()] & rand3() \leq 0.5 \end{cases} \tag{16}$$

Where $i = 1, 2, ..., m$ and $Z \leq \ln\sqrt{2}$, usually 0.5–1.0; The range are (0, 1).

Adaptive Inertia Weights

The global exploration ability and local mining ability of PSO algorithm are contradictory to each other, and it is hard to seek a balance point. To balance the global exploration and local development capabilities of PSO algorithm, an improved chaotic particle optimization Algorithm is proposed to further modify the optimization algorithm effect.

Accord to the particle position update formula (3), two adaptive inertia weights w_j and w'_j are introduced. Among them, w_j is used to control the influence degree of the original particle position on the new particle position, and w'_j is used to balance the influence weight of the particle flight speed on the new position. The improved particle position update formula is expressed as follows:

$$x_{i,d}^{t+1} = w_j x_{i,d}^{t} + w'_j v_{i,d}^{t+1} \tag{17}$$

From above formula 17, w_j and w'_j can keep the fault tolerance of particle population, and enhance robustness of the algorithm to quit the local optimization in the optimization process.

The mathematical expressions for w_j and w'_j are as follows:

$$w_j = 1/(1 + \exp(-f(j)/u)^{iter}) \tag{18}$$

$$w_j^{'} = 1 - w_j \tag{19}$$

In the formula, $f(j)$ express adaptive value of the j-th particle, u express the best value in the particle population in the first iteration calculation, and *iter* represents the current iteration number.

Quantum Chaos Adaptive PSO Algorithm Steps

The specific steps of QCPSO algorithm search are as follows:

(1) Initialize all parameters including N, c_1, c_2, M,v,D, $t = 0$;

(2) The current fitness value of each particle is calculated by the optimization function and compared with the fitness value corresponding to the individual historical optimal solution. If the current fitness value is better than the fitness value corresponding to the individual historical optimal solution, the current solution is replaced by the individual optimal solution *pbest*, otherwise it is not replaced.

(3)The optimal solution *gbest* of the current population is determined by comparing the optimal fitness values of all particles;

(4) Updating the flight speed of particles;

(5) Updating the weights w_j and w'_j;

(6) Updating the position of particles;

(7) If $t < M$ and not converge

$t = t + 1$

Go to step (3);

Otherwise

Find the global optimal solution and go to step (8);

(8) Output the best value.

CONVERGENCE TEST COMPARISONS

The PSO algorithm is improved by parameter adjustment strategy, and the search process is optimized by re-search and reverse learning. In order to embody the effectiveness of the improved PSO algorithm put forward in the research of test case generation, it is relative to other algorithms, and has the best effect. Based on existing problems that need to be studied, this paper uses Matlab 2016a programming to implement the above-mentioned algorithm, and evaluates the advantages and disadvantages through fitness value, average coverage rate and iteration times. To ensure the fairness and scientificity of the performance comparison of all algorithms, each group of experiments is run 100 times to obtain the average value.

The basic parameters of the whole experiment are seen as follows: $M = 1{,}000$, $N = 30$, $D = 30$, and the range of values is [0.4, 0.9]. To verify the superiority of QCPSO algorithm put forward, four typical test functions Sphere, Rosenbrock, Rastrigrin and Griewank are compared and tested. These four functions include unimodal function, multimodal function and trigonometric function, which are relatively comprehensive. The specific formulas of the test functions are as follows.

$$f_1(x) = \sum_{i=1}^{n} x_i^2 \ \ x \in [-100, 100] \tag{20}$$

$$f_2(x) = \sum_{i=1}^{n-1} (100(x_{i+1} - x_i^2)^2 + (1 - x_i)^2) \ \ x \in [-30, 30] \tag{21}$$

$$f_3(x) = \sum_{i=1}^{n} (x_i^2 - 10\cos(2\pi x_i) + 10) \ \ x \in [-5, 5] \tag{22}$$

$$f_4(x) = (\sum_{i=1}^{n} x_i^2 - \prod_{i=1}^{n} \cos(x_i/\sqrt{i}) + 1)/4000 \ \ x \in [-600, 600] \tag{23}$$

In order to verify the performance advantages of the improved PSO algorithm, it is necessary to judge the fitness values of four typical test functions and compare them with the results of other

TABLE 1 | Value for three Algorithms.

Algorithm	Value	$D = 30$, Iteration = 100				$D = 50$, Iteration = 100			
		F1	F2	F3	F4	F1	F2	F3	F4
PSO	Optimal	2.397	5.761	1.986	1.238	1.987	4.679	1.658	0.832
	Average	3.537	6.231	2.421	2.179	2.589	4.998	2.821	1.998
	S.D	4.176	7.876	3.876	3.459	3.765	5.452	3.239	2.987
GA	Optimal	2.568	6.324	2.451	1.591	2.512	5.311	1.981	1.287
	Average	3.679	6.981	3.318	2.993	2.991	5.688	3.003	2.342
	S.D	4.876	9.546	4.584	3.987	4.327	7.444	4.176	3.561
QCPSO	Optimal	0.112	2.346	0	0	0.021	0.114	0	0
	Average	1.543	3.378	1.2×10^{-3}	1.6×10^{-9}	1.221	1.557	1.1×10^{-18}	1.2×10^{-25}
	S.D	2.129	4.127	0.0334	0.0564	1.967	2.227	0	0

The optimization experiments are carried out under the test (F1, F2, F3, and F4) functions from the PSO, GA, and QCPSO algorithm, and the experimental results are analyzed and compared.

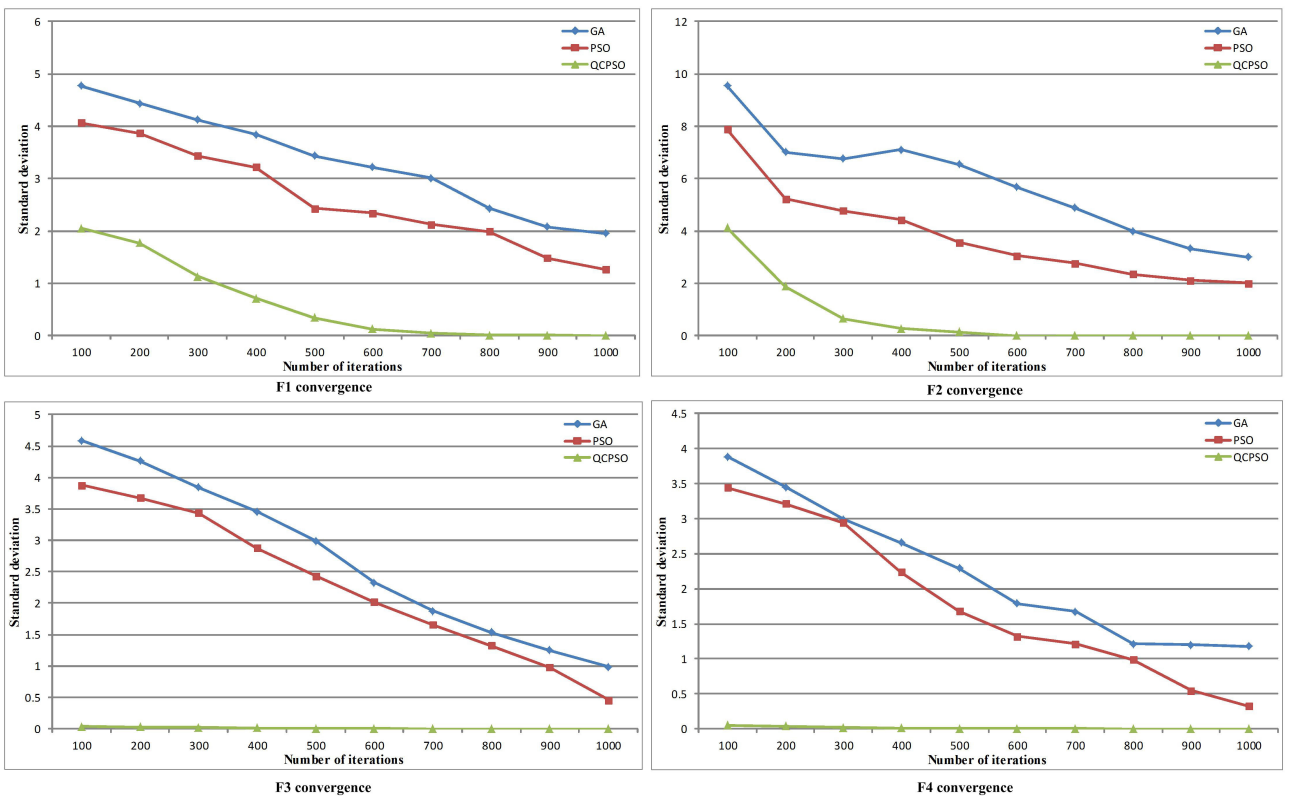

FIGURE 1 | Convergence Comparison of *four* Functions ($D = 30$).

algorithms. First of all, the inertia weight is used to improve the learning factor. The relationship between the two can be divided into three types: linear, non-linear and trigonometric functions. In this paper, the non-linear relationship is used to carry out the relationship of learning factors, so that the learning factor changes non-linearly and gradually with the inertia weight, and the equation is expressed as $c = A\omega^2 + B\omega + C$; $c_2 + c_1 = 2$, and the inertia weight adopts the commonly used exponential function decreasing method, taking $A = 0.45$, $B = 0.9$, $C = 0.45$, $\omega_{max} = 0.9$,$\omega_{\min} = 0.4$. Secondly, the optimal solution and suboptimal solution in the current iteration are searched again, and the particles outside the tabu region are optimized by chaos. The improved algorithm is compared with PSO, GA and QCPSO through four typical test functions. The comparison of four typical test functions in four algorithms is shown in **Table 1**.

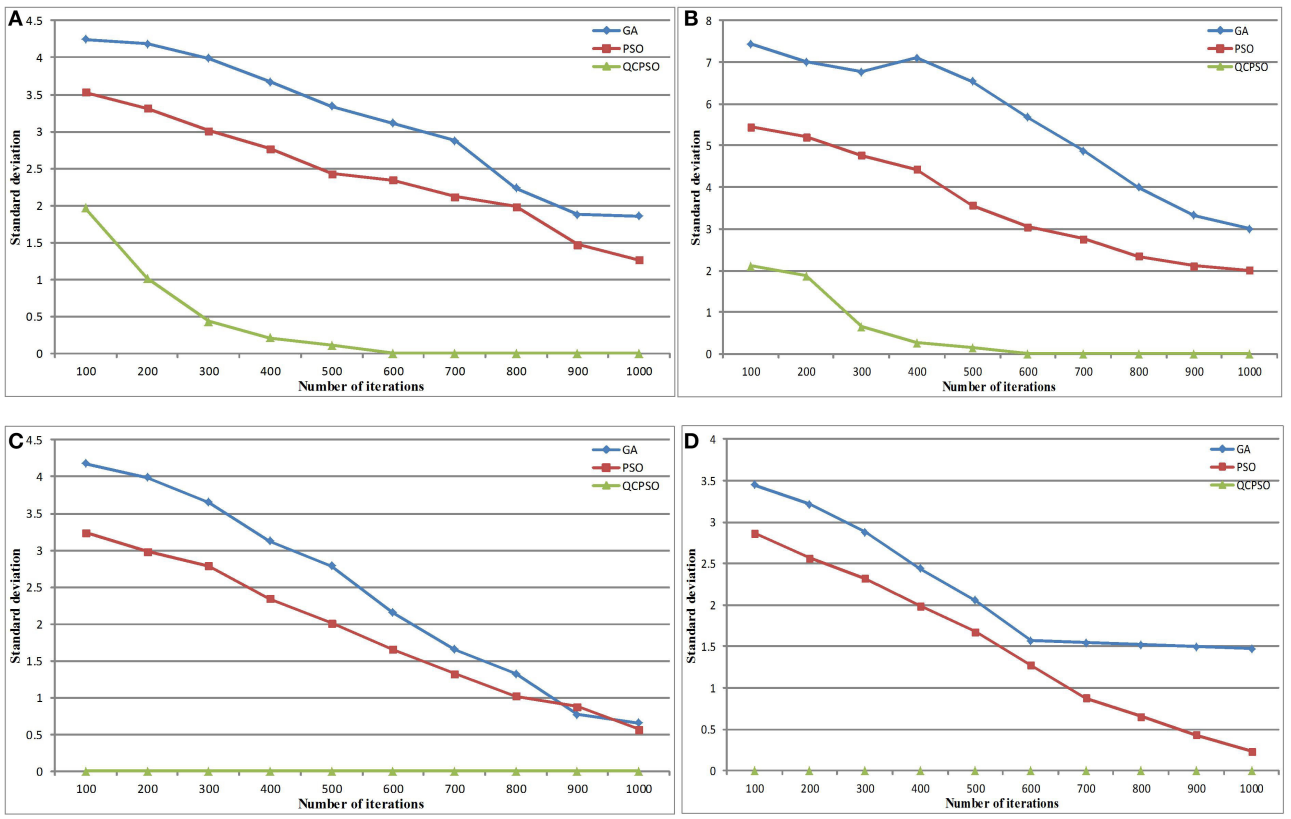

FIGURE 2 | Convergence Comparison of *four* Functions ($D = 50$). **(A)** F1 convergence, **(B)** F2 convergence, **(C)** F3 convergence, **(D)** F4 convergence.

For a variable dimension of 20, As can be seen from **Table 1**: In 20 independent repetitions, For the test functions F3 and F4, QCPSO algorithm result the best value, but for average value and standard deviation of these two test functions, QCPSO is best again, and QCPSO are obviously better than PSO algorithm and GA algorithm. Accord to four functions, QCPSO is significantly better than PSO and GA, accord to the average value, standard deviation and the optimal value.

For the variable dimension of 50, it can be seen from **Table 1** that for the test functions F1, F2, F3, and F4, the average value and standard deviation of the optimal value of QCPSO are significantly better than those of PS0 algorithm and GA algorithm, and when the corresponding value ratio dimension is 20, it is smaller as a whole.

In order to verify the convergence, the following is verified by iterations of the algorithm. The standard deviation value increases with the number of iterations. The specific effect is shown in **Figures 1**, **2**.

Figures 1, **2** is a 30-dimensional optimization curve of 4 benchmark test functions in QCPSO, PSO, and GA (semi-logarithmic curve, and the optimization curve is drawn by semilogy function). The 30-and 50-dimensional optimization curves obtained in the experiment are similar to those in **Figure 2** and will not be given here due to limited space.

As can be seen from **Figures 1**, **2**, when QCPSO algorithm optimizes F2 and F4 functions, there are many inflection points, indicating that QCPSO's ability to jump out of local optimization is enhanced. As can be seen intuitively from **Figure 1**, QCPSO algorithm is more effective than the PSO and GA algorithms for most of the four functions in **Table 1** with dimension 30. Among them, QCPSO algorithm obtains the optimal values in four test functions (F1, F2, F3, F4). The convergence speed of QCPSO is best than other three algorithms. As can be seen from **Figures 1**, **2**, QCPSO quickly searches for satisfactory solutions for most optimization problems.

In short, QCPSO algorithm has greatly improved its optimization capability compared with standard PSO. For most optimization problems, QCPSO algorithm is better than GA and standard PSO algorithms.

CONCLUSION

In our research, an improved chaotic PSO algorithm based on complex functions are proposed. By comparing the convergence of four complex functions, the proposed QCPSO algorithm has high convergence and stable performance. The convergence of complexity functions is verified to illustrate the advantages of the algorithm, and more complexity functions are used to verify the advantages of the algorithm in the later period. It is proved in different dimensions that the reliability of the algorithm is verified by

the population of higher dimensions, and the universality of the algorithm is better explained. In the future research work, the improved particle swarm optimization algorithm for complex functions will be applied in other fields to improve the actual effect of the existing work [11–14]. For example, geographic location prediction, GPS trajectory prediction, flow prediction, etc.

DATA AVAILABILITY STATEMENT

The original contributions presented in the study are included in the article/supplementary material, further inquiries can be directed to the corresponding author/s.

AUTHOR CONTRIBUTIONS

XX and SL participated in the preparation and presentation of the manuscript.

FUNDING

This work was supported by the Science and Technology Research Program of Chongqing Municipal Education Commission (Grant No. KJQN201902103) and the Open Fund of Chongqing Key Laboratory of Spatial Data Mining and Big Data Integration for Ecology and Environment (No. ZKPT0120193007).

REFERENCES

1. Liu H, Niu P. Enhanced shuffled frog-leaping algorithm for solving numerical function optimization problems. *J Intell Manufact.* (2015) **29**:1133–53. doi: 10.1007/s10845-015-1164-z
2. Chen Z, Zhou S, Luo J. A robust ant colony optimization for continuous functions. *Exp Syst App.* (2017) **81**:309–20. doi: 10.1016/j.eswa.2017.03.036
3. Li G, Cui L, Fu X, Wen Z, Lu N, Lu J. Artificial bee colony algorithm with gene recombination for numerical function optimization. *Appl Soft Comput.* (2017) **52**:146–59. doi: 10.1016/j.asoc.2016.12.017
4. Margreitter C, Oostenbrink C. Correction to optimization of protein backbone dihedral angles by means of hamiltonian reweighting. *J Chem Inform Model.* (2018) **58**:1716–20. doi: 10.1021/acs.jcim.8b00470
5. Palma LB, Coito FV, Ferreira BG. PSO based on-line optimization for DC motor speed control. In: *2015 9th International Conference on Compatibility and Power Electronics (CPE)*. Costa da Caparica (2015).
6. Sheng-Feng C, Xiao-Hua C, Lu Y. Application of wavelet neural network with improved PSO algorithm in power transformer fault diagnosis. *Pow Syst Protect Control.* (2014) **42**:37–42. Available online at: https://www.researchgate.net/publication/286059512_Application_of_wavelet_neural_network_with_improved_particle_swarm_optimization_algorithm_in_power_transformer_fault_diagnosis
7. Prativa A, Sumitra M. Efficient player selection strategy based diversified PSO algorithm for global optimization. *Inform Sci.* (2017) **397–8**:69–90. doi: 10.1016/j.ins.2017.02.027
8. Jiang X, Ling H. A new multi-objective particle swarm optimizer with fuzzy learning sub-swarms and self-adaptive parameters. *Adv Sci Lett.* (2012) **7**:696–9. doi: 10.1166/asl.2012.2720
9. Clerc M. The swarm and the queen: towards a deterministic and adaptive PSO.//congress on evolutionary computation-cec. *IEEE.* (2002) **3**:1951–7. doi: 10.1109/cec.1999.785513
10. Tsubouchi M, Momose T. Rovibrational wave-packet manipulation using shaped mid-infrared femtosecond pulses toward quantum computation: optimization of pulse shape by a genetic algorithm. *Phys Rev A.* (2008) **77**:052326. doi: 10.1103/PhysRevA.77.052326
11. Jiang W, Carter DR, Fu HL, Jacobson MG, Zipp KY, Jin J, et al. The impact of the biomass crop assistance program on the United States forest products market: an application of the global forest products model. *Forests.* (2019) **10**:1–12. doi: 10.3390/f10030215
12. Liu JB, Zhao J, Zhu ZX. On the number of spanning trees and normalized laplacian of linear octagonal-quadrilateral networks. *Int J Quant Chem.* (2019) **119**:1–21. doi: 10.1002/qua.25971
13. Liu JB, Zhao J, Cai Z. "On the generalized adjacency, laplacian and signless laplacian spectra of the weighted edge corona networks. *Phys A.* (2020) **540**:1–11. doi: 10.1016/j.physa.2019.123073
14. Liu W, Li J, Ren L, Xu J, Li C, Li S. Exploring livelihood resilience and its impact on livelihood strategy in rural China. *Soc Indicat Res.* (2020) **150**:977–98. doi: 10.1007/s11205-020-02347-2

Conflict of Interest: The authors declare that the research was conducted in the absence of any commercial or financial relationships that could be construed as a potential conflict of interest.

frontiers in Physics

BRIEF RESEARCH REPORT
published: 18 September 2020
doi: 10.3389/fphy.2020.00350

Exact Values for Some Size Ramsey Numbers of Paths and Cycles

Xiangmei Li[1], *Asfand Fahad*[2*], *Xiaoqing Zhou*[3] *and Hong Yang*[3]

[1] School of Cybersecurity, Chengdu University of Information Technology, Chengdu, China, [2] Department of Mathematics, COMSATS University Islamabad, Vehari, Pakistan, [3] School of Information Science and Engineering, Chengdu University, Chengdu, China

For the graphs G_1, G_2, and G, if every 2-coloring (*red* and *blue*) of the edges of G results in either a copy of *blue* G_1 or a copy of *red* G_2, we write $G \to (G_1, G_2)$. The size Ramsey number $\hat{R}(G_1, G_2)$ is the smallest number e such that there is a graph G with size e satisfying $G \to (G_1, G_2)$, i.e., $\hat{R}(G_1, G_2) = \min\{|E(G)| : G \to (G_1, G_2)\}$. In this paper, by developing the procedure and algorithm, we determine exact values of the size Ramsey numbers of some paths and cycles. More precisely, we obtain that $\hat{R}(C_4, C_5) = 19$, $\hat{R}(C_6, C_6) = 26$, $\hat{R}(P_4, C_5) = 14$, $\hat{R}(P_4, P_5) = 10$, $\hat{R}(P_4, P_6) = 14$, $\hat{R}(P_5, P_5) = 11$, $\hat{R}(P_3, P_5) = 7$ and $\hat{R}(P_3, P_6) = 8$.

Keywords: size Ramsey number, 2-coloring, connected graphs, connectivity, paths, cycles

OPEN ACCESS

Edited by:
Muhammad Javaid, University of Management and Technology, Lahore, Pakistan

Reviewed by:
Kashif Ali, COMSATS Institute of Information Technology, Pakistan
Yilun Shang, Northumbria University, United Kingdom

***Correspondence:**
Asfand Fahad
asfandfahad1@yahoo.com

Specialty section:
This article was submitted to Mathematical and Statistical Physics, a section of the journal Frontiers in Physics

Received: *01 May 2020*
Accepted: *23 July 2020*
Published: *18 September 2020*

Citation:
Li X, Fahad A, Zhou X and Yang H (2020) Exact Values for Some Size Ramsey Numbers of Paths and Cycles. Front. Phys. 8:350. doi: 10.3389/fphy.2020.00350

1. INTRODUCTION

We use standard notions and symbols from the field of graph theory, see [1]. By $G = G(V, E)$, we denote a simple graph with vertex and edge sets V and E having cardinalities $|V(G)|$ and $|E(G)|$, respectively. For $S_1, S_2 \subseteq V(G)$, we denote $E(S_1) = \{uv \in E(G) | v, u \in S_1\}$ and $E(S_1, S_2) = \{uv \in E(G) | u \in S_1, v \in S_2\}$. Moreover, we denote: the degree of a vertex v in G by $d(v|G)$ (or $d(v)$), the minimum degree among the vertices of G by $\delta(G)$, a path and a cycle having i vertices by P_i and C_i, respectively. For the graphs G_1, G_2, and G, if every 2-coloring (*red* and *blue*) of the edges of G results in either a copy of *blue* G_1 or a copy of *red* G_2, we call it Ramsey property of G and write $G \to (G_1, G_2)$. The size Ramsey number $\hat{R}(G_1, G_2)$ is the smallest number e such that there is a graph G with size e satisfying $G \to (G_1, G_2)$, i.e., $\hat{R}(G_1, G_2) = \min\{|E(G)| : G \to (G_1, G_2)\}$. For $k \in \mathbb{N}$, a non-complete graph G is called k-connected if $|V(G)| > k$ and $G - X$ is connected for every set $X \subseteq V$ with $|X| < k$. The greatest integer k such that G is k-connected is the connectivity $\kappa(G)$ of G. For the complete graph K_n, we define $\kappa(K_n) = n - 1$.

In 1978, Erdös et al. initiated the study of the size Ramsey number, and later it was continued by Faudree [2, 3], Lortz and Mengersen [4], and Pikhurko [5]. From these studies, we can see that the size Ramsey number $\hat{R}(G_1, G_2)$ exists for the graphs G_1 and G_2. Su and Shao applied a backtracking algorithm to find some upper bounds for the size Ramsey numbers. The study of the size Ramsey numbers based on the graph coloring is implicitly connected to several branches of science, such as: the energies of the status level "fully functional nodes," "partially functional nodes," and "non-functional nodes" can be interpreted by the way of graph coloring [6], frequency channel assignment [7, 8], time tabling [9], and CAD problems [10, 11]. For more literature regarding the Ramsey numbers, we refer [12–16] to the readers. This paper is devoted to study the properties of the graphs G with the smallest size for which $G \to (G_1, G_2)$ for given graphs G_1 and G_2. Moreover, by developing the procedure and algorithm, we determined size Ramsey numbers of some paths and cycles.

2. THE APPROACH

Lemma 1. *Let G be a graph with the smallest size for which $G \to (G_1, G_2)$. Then any G', obtained by removing all the isolated vertices of G, is connected.*

Proof: By the definition of G', we have $G' \to (G_1, G_2)$. Suppose to the contrary that there are at least two components H_1, H_2 in G'. Let $G' = H_1 \cup H_2 \cup \ldots \cup H_n$ with $n \geq 2$. Since H_i is not an isolated vertex for any i, we have $|E(H_i)| < |E(G')|$ for any i. Then there is a 2-coloring (red and blue) f_i of the edges of H_i such that H_i contains neither red G_1 nor blue G_2. Now, consider a 2-edge coloring f of the edges of G' with $f(e) = f_i(e)$ for any $e \in H_i$ for $i = 1, 2, \cdots, n$. Then G contains neither red G_1 nor blue G_2 under f, and so $G' \nrightarrow (G_1, G_2)$, a contradiction.

Remark 1: Given the graphs G, G_1, G_2 with $G \to (G_1, G_2)$, by the Lemma 1, we only need to consider the connected graphs for G.

Lemma 2. *If G is a graph with the smallest size for which $G \to (G_1, G_2)$, and G is a connected graph, then $\kappa(G) \geq \min\{\kappa(G_1), \kappa(G_2)\}$.*

Proof: Assume on contrary that we have $\kappa(G) < \min\{\kappa(G_1), \kappa(G_2)\}$. Let $S \subseteq V(G)$ such that $|S| = \kappa(G)$ and $G - S$ is disconnected and assume $G - S = H_1 \cup H_2 \cup \ldots \cup H_n$ with $n \geq 2$. Let $V(T_i) = V(H_i) \cup S$ and $E(T_i) = E(H_i) \cup E(H_i, S)$. Since G is a graph with the smallest size for which $G \to (G_1, G_2)$, there is a red-blue coloring f_i of the edges of T_i such that T_i contains neither red G_1 nor blue G_2 for any i. Let $E(S) = \{e_1, e_2, \cdots, e_k\}$ for some k. Now consider a 2-edge coloring f of the edges of G with $f(e) = f_i(e)$ for any $e \in H_i$ for $i = 1, 2, \cdots, n$, $f(e_1) = red$, $f(e_i) = blue$ for any $i = 2, 3, \cdots, k$. Then G contains neither red G_1 nor blue G_2 under f, and so $G' \nrightarrow (G_1, G_2)$. Now, we consider the following two cases:

Case 1: If there is a *red* copy of G_1 as a subgraph of G.

Subcase 1.1: $E(G_1) \subseteq E(T_i) \cup E(S)$ with $i \in \{1, \ldots, n\}$.

Since f_i is a *red-blue* coloring of the edges of T_i such that T_i contains no red G_1. Then $E(G_1) \cap E(S) \neq \emptyset$. Since $G_1[E(G_1) \cap E(S)]$ is not a clique with $|S|$ vertices, there is a cut-set S_1 of G_1 with $S_1 \subseteq S$. Then $|S_1| \leq |S| < \kappa(G_1)$ by the assumption, a contraction.

Subcase 1.2: $E(G_1) \cap E(H_i) \neq \emptyset, E(G_1) \cap E(H_j) \neq \emptyset$ with $i \neq j$.

Then S is a cut-set of G_1 with $|S| < \kappa(G_1)$ by the assumption, a contraction.

Case 2: If there is a *blue* copy of G_2 as a subgraph of G.

Subcase 2.1: $E(G_2) \subseteq E(T_i) \cup E(S)$ with $i \in \{1, \ldots, n\}$.

Since f_i is a red-blue coloring of the edges of T_i such that T_i contains no blue G_2. Then $E(G_2) \cap E(S) \neq \emptyset$. Since $G_2[E(G_2) \cap E(S)]$ is not a clique with $|S|$ vertices, there is a cut-set S_2 of G_2 with $S_2 \subseteq S$. Then $|S_2| \leq |S| < \kappa(G_2)$ by the assumption, a contraction.

Subcase 2.2: $E(G_2) \cap E(H_i) \neq \emptyset, E(G_2) \cap E(H_j) \neq \emptyset$ with $i \neq j$.

Then S is a cut-set of G_2 with $|S| < \kappa(G_2)$ by the assumption, a contraction.

Lemma 3. *For the graphs G, G_1 and G_2, if there exist vertices $v_1, \ldots, v_t$ for some $1 \leq t \leq |V(G)|$ satisfying that $d(v_i|G^{i-1}) < \delta(G_1) + \delta(G_2) - 1$ for any $i = 1, 2, \cdots, t$ and $G_t \nrightarrow (G_1, G_2)$, where $G^i = G - \{v_1, \ldots, v_i\}$ and $G^0 = G$. Then $G \nrightarrow (G_1, G_2)$.*

Proof: We apply induction on t to prove it. Firstly, it is clear that the lemma holds if $t = 1$. Now, we suppose the stated result holds for $t = i$, we need to prove it for $t = i + 1$. Since the lemma holds if $t = i$, we have $G^1 \nrightarrow (G_1, G_2)$. Then there is a *red-blue* coloring g of the edges of G^1 such that there is neither a *red* copy of G_1 nor a *blue* copy of G_2 in G^1. Let $E(w) = \{uv \in E(G) | u = w \text{ or } v = w\}$. Since $d(v_1|G^0) < \delta(G_1) + \delta(G_2) - 1$, we can divide $E(v_1)$ into E_1, E_2 with $|E_1| < \delta(G_1), |E_2| < \delta(G_2)$. Let f be a coloring of G obtained by assigning *red* to E_1, *blue* to E_1 based on g.

Case 1: If there is a *red* copy of G_1 as a subgraph of G under f, then $v_1 \in V(G_1)$. Since $|E_1| < \delta(G_1)$, then $d(v_1|G_1) < \delta(G_1)$, a contraction.

Case 2: If there is a *blue* copy of G_2 as a subgraph of G under f, then $v_1 \in V(G_2)$. Since $|E_2| < \delta(G_2)$, then $d(v_1|G_2) < \delta(G_2)$, a contraction.

There is neither a *red* copy of G_1 nor a *blue* copy of G_2 in G under f. Therefore, $G \nrightarrow (G_1, G_2)$.

The contrapositive of the Lemma 3 for $t = 1$ produces the following corollary:

Corollary 1. *For any graphs G_1 and G_2, if G is any graph with the smallest size for which $G \to (G_1, G_2)$, then $\delta(G) \geq \delta(G_1) + \delta(G_2) - 1$.*

Lemma 4. *For any graphs G_1 and G_2, if G is any graph with order n and size m such that $G \not\to (G_1, G_2)$, then for any graph G' with order at most n and size $m - 1 < \frac{n(n-1)}{2}$, we have $G' \not\to (G_1, G_2)$.*

Proof: First, we have G' is not a complete graph, then there are two vertices u, v with $uv \notin E(G')$. Now, we insert the edge uv to obtain a graph G'' based on G'. Then G'' is a graph with m edges and n vertices and so $G'' \not\to (G_1, G_2)$. Therefore, there is a $red - blue$ coloring f of G'' such that there is neither a *red* copy of G_1 nor a *blue* copy of G_2 in G'' under f. Then, there is also neither a *red* copy of G_1 nor a *blue* copy of G_2 in G' under $f|_{G'}$. Then $G' \not\to (G_1, G_2)$.

By applying the Lemma 1 and the Corollary 1, we only need to consider the connected graphs, and then propose the following algorithm (*FindSizeRamseynumber*) to find the size Ramsey number of G_1 and G_2. We will use the software *nauty* [17] to generate non-isomorphic graphs with necessary properties. If G_1 and G_2 are k-connected graphs, we further apply the Lemma 2 to reduces the number of graphs needed to be processed. For testing if $G \to (G_1, G_2)$, we applying the backtracking procedure proposed in [18].

Procedure Find(m,n,G_1,G_2);
input: m, n be integers;
graphs G_1 and G_2.

TABLE 1 | Exact values $\hat{R}(G_1, G_2)$ of the size Ramsey numbers of some paths and cycles.

G_1	G_2	(n, m)	$\#A(n, m)$	$\#B(n, m)$	result
C_4	C_5	(7,19)	2	1	$\hat{R}(C_4, C_5) = 19$
C_6	C_6	(8,26)	2	1	$\hat{R}(C_6, C_6) = 26$
P_4	C_5	(7,14)	59	1	$\hat{R}(P_4, C_5) = 14$
P_4	P_5	(6,10)	14	4	$\hat{R}(P_4, P_5) = 10$
P_4	P_6	(7,14)	64	30	$\hat{R}(P_4, P_6) = 14$
P_5	P_5	(6,11)	9	3	$\hat{R}(P_5, P_5) = 11$
P_3	P_5	(5,7)	4	2	$\hat{R}(P_3, P_5) = 7$
P_3	P_6	(6,8)	22	1	$\hat{R}(P_3, P_6) = 8$

begin
generate the family $\mathcal{G}$ of all the non-isomorphic connected graphs with size m and
order n with minimum degree $\delta(G_1) + \delta(G_2) - 1$; (Apply Lemma 1 and Corollary 1);
foreach G in $\mathcal{G}$
if $(G \to (G_1, G_2))$
return true;
end if
end for
return true;
end.
Algorithm FindSizeRamseynumber(G_1,G_2);

input: graphs G_1 and G_2.
begin
1 : Find a graph G such $G \to (G_1, G_2)$;
2 : $m = |E(G)| - 1$;
3 : $n = \min\{\lfloor \frac{2m}{\delta(G_1)+\delta(G_2)-1} \rfloor, m + 1\}$;
4 : **while Find**(m, n, G_1, G_2) **do**;
5 : $n = n - 1$;
6 : **if** $m > \frac{n(n-1)}{2}$ **do**
7 : $m = m - 1$;
8 : $n = \min\{\lfloor \frac{2m}{\delta(G_1)+\delta(G_2)-1} \rfloor, m + 1\}$;
9 : **end if**
10: **end while**
11: **return** $m + 1$.
end.

3. RESULTS

Example 1. $\hat{R}(C_4, C_5) = 19$.

Proof: Consider $G_1 = C_4$, $G_2 = C_5$. By Algorithm *FindSizeRamseynumber*, we first find the graph H satisfying $H \to (C_4, C_5)$ (line 1). Therefore, $\hat{R}(C_4, C_5) \leq 19$. Then, we consider the edge number less than 19 (i.e., $m \leq 18$, by line 2), and the order of graph at most $\min\{\lfloor \frac{2m}{\delta(G_1)+\delta(G_2)-1} \rfloor, m + 1\} \leq 12$. Now, the procedure will check if there is no graph G with minimum degree 3, size at most and order from 7 to 12 satisfying $G \to (C_4, C_5)$ (line 3-10). In this case, by applying Procedure *Find*, we find that there is no such graph. Therefore, $\hat{R}(C_4, C_5) \geq 19$.

By applying Algorithm *FindSizeRamseynumber*, we obtain many size Ramsey numbers presented in **Table 1**, where $\#A(n, m)$ denote the number of non-isomorphic connected graphs with minimum degree $\delta(G_1) + \delta(G_2) - 1$ with size m and order n, and $\#B(n, m)$ denote the number of such graphs G with $G \to (G_1, G_2)$. An application of the algorithm can be used in some other graph problems, see [19].

4. CONCLUSION

It is a very hard task to determine the size Ramsey number even for small graphs. Faudree and Sheehan gave a table of the size Ramsey numbers for graphs with order not more than four [3]. Su and Shao [18] provide upper bounds for the size Ramsey numbers of some paths and cycles. Until now, very limited results on the size Ramsey numbers are known. In this paper, we have developed some computational techniques to determine many of those size Ramsey numbers. There are numerous variants of the Ramsey numbers such as ordered Ramsey numbers, size Ramsey numbers and zero-sum Ramsey numbers, see [20]. It is also very difficult to compute each variant of these Ramsey numbers. In order to compute some possible Ramsey numbers, we need to obtain the structure of the graphs by studying their mathematical properties. So, the approach of this paper may be considered to compute some challenging Ramsey numbers.

AUTHOR CONTRIBUTIONS

All authors contributed equally in completing the current work.

REFERENCES

1. Bondy JA, Murty USR. *Graph Theory with Applications.* London; Basingstoke: The Macmillan Press Ltd. (1976).
2. Faudree RJ, Rousseau CC, Sheehan J. A class of size Ramsey problems involving stars. In: Bollobas B, editor. *Graph Theory and Combinatorics.* Cambridge: Cambridge Univ Press (1983). p. 273–81.
3. Faudree RJ, Sheehan J. Size Ramsey Numbers for small-order graphs. *J Graph Theory.* (1983) **7**:53–5.
4. Lortz R, Mengersen I. Size Ramsey results for paths versus stars. *Australas J Comb.* (1998) **18**:3–12.
5. Pikhurko O. Asymptotic size Ramsey results for bipartite graphs. *SIAM J Discr Math.* (2002) **16**:99–113. doi: 10.1137/S0895480101384086
6. Shang Y. Vulnerability of networks: fractional percolation on random graphs. *Phys Rev E.* (2014) **89**:12813. doi: 10.1103/PhysRevE.89.012813
7. Ramanathan S, Lloyd EL. Scheduling broadcasts inmultihop radio networks. *IEEE/ACM Trans Network.* (1993) **1**:166–72.
8. Smith K, Palaniswami M. Static and dynamic channel assignment using neural networks. *IEEE J Select Areas Commun.* (1997) **15**:238–49.
9. de Werra D. An introduction to timetabling. *Eur J Oper Res.* (1985) **19**:151–62.
10. De Micheli G. *Synthesis and Optimization of Digital Circuits.* New York, NY: McGraw Hill (1994).

11. Gajski D, Dutt N, Wu A, Lin S. *High-Level Synthesis: Introduction to Chip and System Design*. Boston, MA: Kluwer (1992).
12. Erdös P, Rousseau CC, Faudree RJ, Schelp RH. The size Ramsey number. *Period Math Hung.* (1978) **9**:145–61.
13. Shao Z, Xu X, Bao Q. On the Ramsey Numbers $R(C_m, B_n)$. *Ars Combinatoria.* (2010) **94**:265–71.
14. Pikhurko O. Size Ramsey numbers of stars versus 3-chromatic graphs. *Combinatorica.* (2001) **21**:403–12. doi: 10.1007/s004930100004
15. Shao Z, Shi X, Xu X, Pan L. Some three-color Ramsey numbers $R(P_4, P_5, C_k)$ and $R(P_4, P_6, C_k)$. *Eur J Combinatorics.* (2009) **30**:396–403. doi: 10.1016/j.ejc.2008.05.008
16. Shao Z, Xu J, Pan L. Lower bounds on Ramsey numbers $R(6, 8)$, $R(7, 9)$ and $R(8, 17)$. *Ars Combinatoria.* (2010) **94**:55–59.
17. McKay BD. *Nauty User Guide (version 26)*. Australian National University. Available online at: http://userscecsanueduau/~bdm/
18. Shao Z, Su C. On upper bounds for some size Ramsey numbers. *J Chongqing Univers Posts Telecommun.* (2011) **23**:770–2.
19. Shang Y. On the number of spanning trees, the Laplacian eigenvalues, and the Laplacian Estrada index of subdivided-line graphs. *Open Math.* (2016) **14**:641–8. doi: 10.1515/math-2016-0055
20. Radziszowski S. Small Ramsey Numbers. *Electron. J. Comb.* (2017). doi: 10.37236/21

Conflict of Interest: The authors declare that the research was conducted in the absence of any commercial or financial relationships that could be construed as a potential conflict of interest.

frontiers in Computational Neuroscience

ORIGINAL RESEARCH
published: 15 October 2020
doi: 10.3389/fncom.2020.556628

Reconfigurable Filtering of Neuro-Spike Communications Using Synthetically Engineered Logic Circuits

Geoflly L. Adonias[1], Harun Siljak[2], Michael Taynnan Barros[3,4], Nicola Marchetti[2], Mark White[5] and Sasitharan Balasubramaniam[1]*

[1] Telecommunications Software & Systems Group, Waterford Institute of Technology, Waterford, Ireland, [2] CONNECT Centre, Trinity College Dublin, Dublin, Ireland, [3] CBIG at Biomeditech, Faculty of Medicine and Health Technology, Tampere University, Tampere, Finland, [4] School of Computer Science and Electronic Engineering, University of Essex, Colchester, United Kingdom, [5] Research, Innovation & Graduate Studies, Waterford Institute of Technology, Waterford, Ireland

High-frequency firing activity can be induced either naturally in a healthy brain as a result of the processing of sensory stimuli or as an uncontrolled synchronous activity characterizing epileptic seizures. As part of this work, we investigate how logic circuits that are engineered in neurons can be used to design spike filters, attenuating high-frequency activity in a neuronal network that can be used to minimize the effects of neurodegenerative disorders such as epilepsy. We propose a reconfigurable filter design built from small neuronal networks that behave as digital logic circuits. We developed a mathematical framework to obtain a transfer function derived from a linearization process of the Hodgkin-Huxley model. Our results suggest that individual gates working as the output of the logic circuits can be used as a reconfigurable filtering technique. Also, as part of the analysis, the analytical model showed similar levels of attenuation in the frequency domain when compared to computational simulations by fine-tuning the synaptic weight. The proposed approach can potentially lead to precise and tunable treatments for neurological conditions that are inspired by communication theory.

Keywords: neuron, Hodgkin-Huxley, linear model, transfer function, systems theory, epilepsy, filter

OPEN ACCESS

Edited by:
Shaohui Wang,
Louisiana College, United States

Reviewed by:
Daya Shankar Gupta,
Camden County College, United States
Keke Wang,
Embry-Riddle Aeronautical University, Prescott, United States

****Correspondence:***
Geoflly L. Adonias
gadonias@tssg.org

Received: *28 April 2020*
Accepted: *28 August 2020*
Published: *15 October 2020*

Citation:
Adonias GL, Siljak H, Barros MT, Marchetti N, White M and Balasubramaniam S (2020) Reconfigurable Filtering of Neuro-Spike Communications Using Synthetically Engineered Logic Circuits. Front. Comput. Neurosci. 14:556628. doi: 10.3389/fncom.2020.556628

1. INTRODUCTION

Seizure dynamics with either spontaneous and recurrent profiles can occur even in healthy patients during the processing of sensory stimuli or it could manifest itself as an uncontrolled synchronous neural activity in large areas of the brain (Jirsa et al., 2014). Any disruption to the mechanisms that inhibit action potential initiation or the stimulation of processes that facilitate membrane excitation, can prompt seizures. Tackling this disease efficiently is an existing clinical issue where new approaches are constantly being investigated in order to provide precise and reliable strategies in inhibiting or disrupting seizure-triggering populations of neurons. For example, controlling neuron firing threshold can most likely prevent seizure activity, which can often be achieved at a single neuron level (Scharfman, 2007).

The development of techniques for the treatment of this type of neurodegenerative disorder is challenging not only due to the complexity of the brain function and structure but also as a result of the invasiveness and discomfort caused by today's most common neurostimulation or surgery approaches (Rolston et al., 2012). However, due to the lack of success in non-invasive approaches,

the immediate future epilepsy treatment will still see invasive methods. This approach must achieve population-level control with state-of-the-art technology in not only neuroengineering but must also integrate other disciplines. Recent advancements in nanotechnology, for instance, have been enabling the development of novel devices at the nano-scale that are capable of improving bio-compatibility. Nanotechnology-based treatment also includes advantages in the treatment precision, patient comfort as well as longer treatment lifetime. However, there still remain numerous challenges in the use of nanotechnology. For example, the passage of chemicals through the blood-brain barrier (BBB) is among the many challenges that disrupt the efficiency of nanoparticles-mediated drug delivery functioning. Challenges still remain as to how nanoparticles that pass through the BBB will diffuse toward specific neural populations. However, if the drug-loaded nanoparticles can be delivered at sufficient concentrations and accurately to a specific location, this can influence neural activities (Bennewitz and Saltzman, 2009; Veletić et al., 2019). As an example, drug delivery targets specific neurodegeneration promoting factors (Feng et al., 2019) by performing a drug-induced control over intracellular, extracellular and synaptic properties that regulate spiking activity (Blier and De Montigny, 1987).

Previous studies on the firing response of neurons have investigated the filtering capabilities either due to realistic synaptic dynamics (Brunel et al., 2001; Moreno-Bote and Parga, 2004) or by naturally manipulating the resting potential of voltage-dependent active conductances of a neuron enhancing its temporal filtering properties (Fortune and Rose, 1997; Motanis et al., 2018). On the other hand, existing analyses do not account for the many molecular control mechanisms that may influence the synaptic activity, e.g., drug. In the case of seizures, the understanding of the drug-induced firing response may allow further analysis on the impact of high-frequency firing on the neural tissue as well as how to desynchronize or slow it down. Frequency-domain analysis has been performed on top of linear models of the Hodgkin-Huxley (HH) formalism to investigate not only the transmission of information through the use of subthreshold electrical stimulation (Khodaei and Pierobon, 2016) but also the influence of axonal demyelination on the propagation of action potentials (Chaubey and Goodwin, 2016). Although Hodgkin-Huxley is not the only neuron model available in the literature, it is one of the most plausible models for computational neuroscience (Long and Fang, 2010). Other proposed models are, for example, integrate-and-fire, Izhikevich and Fitzhugh-Nagumo models (Mishra and Majhi, 2019).

The manipulation of cellular activity, such as neuronal spiking activity, using molecules complexes to mimic logic gates and transistors has also been proposed in the literature. One example is the work of Vogels and Abbott (2005), in which the propagation of neuronal signals in networks of integrate-and-fire models of neurons was investigated and they found that different types of logic gates may arise within the network by either strengthening or weakening specific synapses. Goldental et al. (2014) used identical neurons to propose dynamic logic gates that work based on their historical activities, interconnection profiles, as well as the frequency of stimulation at their input terminals. In our previous works (Adonias et al., 2019; Adonias et al., 2020), we developed several logic gates arranged in groups of three heterogeneous models of neurons, with two working as inputs and one as the output, and performed a queueing-theoretical analysis aiming at the study of such a complex network as a single element behaving as the collective of those cells. Irrespective of the tremendous efforts from the scientific community, these works do not provide a framework of reconfigurable circuits that could pave the way for more sophisticated approaches for neuron control. Further investigation of novel neuronal electronic components constructions is needed to develop bio-compatible and reliable solutions that can address defective neuronal networks. While the scientific community has been witnessing remarkable progress in the manipulation and engineering of the behavior of mammalian cells (Lienert et al., 2014), the existing models do not yield analytical expressions that could be used to model drug-induced filtering capabilities of a neuron and, in particular, incorporating computing paradigms. The main focus of this work is to lay the ground-work of analytical models for digital filters that are designed and engineered into neurons, potentially leading to the development of novel epilepsy treatments.

In this work, we propose a mathematical framework aiming at the interpretation of the filtering capabilities in small populations of neurons that are engineered into a logic circuit (**Figure 1**). The circuit aims to reduce the firing rates from its inputs by performing the binary logic as well as integrating reconfigurability, where the different logic circuit arrangements, as well as logic gate types, can be tuned to change the filtering properties. To achieve that in our mathematical framework, we modify parameters on the logic circuit transfer function, derived from the linear interpretation of the Hodgkin-Huxley neuronal model. These parameters are related to neuronal and synaptic properties of a neuro-spike communication, such as conductances and weight, and can potentially be achieved

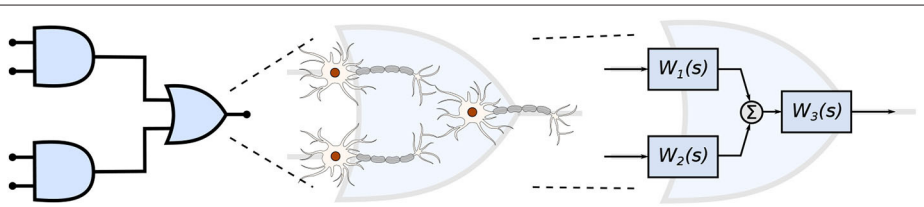

FIGURE 1 | Engineered neuronal digital logic circuit, where each gate is composed of three neurons and each block $W_i(s)$ represents one neuron as a transfer function to enable communication metric analysis.

through the sustained administration of a specific drug. Our mathematical framework is, from an application point-of-view, a design platform for neuroscientists in creating filtering solutions for smoothing out the effects of neurological diseases that require the minimization of firing activity. The framework models the effects of drug-induced molecular changes in models of neurons aiming to control the neuronal activity of a synthetic engineered cell, however, the fabrication and specifications of such a drug are out of the scope of this paper. The contributions of this paper are as follows:

- **Neuronal logic circuits are built** using computational models of neurons and this arrangement is expected to be capable of acting as digital filters, converging four inputs into one output with a shift in attenuation driven by modifications to the synaptic weight.
- **A mathematical framework is proposed** paving the way for the design of neuronal digital filters to help suppress the destructive effects of neurodegenerative diseases. This framework should enable the relationship between biophysical models and drug design, facilitating scientists control over the behavior of the filters.
- **Analysis of the performance of the neuronal filters** in terms of accuracy and of signal power attenuated by the circuit. This analysis gives an insight into how parameters such as weight or frequency at the input would affect the performance of such filters.

The remainder of this paper is as follows, section 2.1 briefly describes how neurons differ between each other and how they communicate with one another. In section 2.2, we explain how neurons can function as non-linear electronic circuits based on the seminal work of Hodgkin and Huxley (1952) and we also describe the process of linearization aiming to derive a transfer function of the filter model. The filter design is explained in section 2.3 which also covers how neurons are represented as compartments and connected to form logic gates and, consequently, to form logic circuits. In section 3, we present the results that are discussed in section 4 and, finally, the conclusions are presented in section 5.

2. MATERIALS AND METHODS

2.1. Neuronal Communication

To be able to synthetically implement complex functions inside the brain, we must control how the neurons exchange information using the propagation of action potentials inside a network of neurons. The number of excitatory and inhibitory connections between neurons determines the spatio-temporal dynamics of the action potentials propagation (Zhou et al., 2018). Efficient coding and modulation of neuronal information have been used to implement bio-computational approaches in our previous work (Adonias et al., 2020). Bio-computing can be created from neuronal networks that are engineered to function as logic circuits through controlling the neuro-spike communication and curbing the signal propagation dynamics between the neurons.

We aim to investigate the neuronal and synaptic properties in constructing logic circuits that perform the filtering of spikes in small populations from the somatosensory cortex. The cortex is responsible for most of the signal processing performed by the brain and comprises a rich variety of morpho-electrical types of neuronal and non-neuronal cells. We will take into account these characteristics in the construction of our mathematical framework that is used to design the circuits.

2.1.1. Properties of a Neuron

Neurons are divided into three main parts: dendrites, soma, and axon. Dendrites receive stimuli from other cells and the way these dendritic trees are projected onto neighboring neurons in a network helps to classify neuron morphological types. The axon passes stimuli forward to cells connected down the network through its axon terminals and the soma is the main body of the neuron. Each neuron's response to a stimulus will dictate the electrophysiological neuron type. The soma is where most proteins and genes are produced and where stimuli are generated and fired down the axon.

Besides the way dendrites are projected, the proteins and genes that neurons express and their morphological and electrophysiological characteristics are important for the classification of different types of neurons. One of the most comprehensive works on neuronal modeling, by Markram et al. (2015), classifies the neurons from the rat's somatosensory cortex based on their morpho-electrical properties (morphological and electrical characteristics) as well as the cortical layer they belong (columnar and laminar organization).

2.1.1.1. Morpho-electrical characteristics

Even though all neurons used in this work can assume different morphological structure, it is exactly by analyzing their axonal and dendritic ramification that we can have a good enough categorization of their respective morphological types. Regardless of their types, neurons in the cortical layer are considered of small sizes (8 - 16 μm). Furthermore, inhibitory neurons can be better identified by their axonal features while excitatory neurons can be more easily classified based on their dendritic features (Markram et al., 2015). Each morphological type (m-type) can fire different spiking patterns and this may affect the gating capabilities of neurons due to the fluctuations on precise spike timing. Markram et al. (2015) categorized 11 different electrical types (e-types) of neurons, hence, 11 different ways of firing a spike train generated in response to an injected step current.

2.1.1.2. Cortical organization

The cerebral cortex comprises six distinguished horizontal layers of neurons, with each layer having particular characteristics such as cell density and type, layer size, and thickness. This horizontal configuration is also known as a "laminar" organization, where the layers are identified as (1) Molecular layer, which contains only a few scattered neurons and consists mostly of glial cells and axonal and dendritic connections of neurons from other layers; (2) External granular layer, containing several stellate and small pyramidal neurons; (3) Pyramidal layer, contains non-pyramidal and pyramidal cells of small and medium sizes;

(4) Inner granular layer, predominantly populated with stellate and pyramidal cells, this is the target of thalamic inputs; (5) Ganglionic layer, containing large pyramidal cells that establish connections with subcortical structures; and (6) Multiform layer, populated by just a few large pyramidal neurons and a good amount of multiform neurons, which sends information back to the thalamus. All layers may contain inter-neurons bridging two different brain regions.

The neurons are not just stacked one on top of another suggesting a horizontal organization, indeed vertical connections are also found in between the neurons from either the same or different layers. This allows another type of classification known as mini-columns (also called, micro-columns) with a diameter of 30–50 μm and when activated by peripheral stimuli, they are seen as macro-columns, with a diameter of 0.4–0.5 mm (Peters, 2010). This will create network topologies with intrinsic characteristics, e.g., connection probabilities between neurons, that influence the signal propagation to converge into either a specific pattern or flow.

2.1.2. Neuron-to-Neuron Communication

The communication between a pair of neurons is done through the diffusion of neurotransmitters in the synaptic cleft; this process is triggered by an electrical impulse reaching the axon terminals of the transmitting cell characterizing an electrochemical signaling process known as the *synapse*. Action potentials propagate down the axon of the pre-synaptic cell, which is the sender cell, and when reaching the axon terminals also known as pre-synaptic terminals, it triggers the release of vesicles containing neurotransmitters into the synaptic cleft, which is the gap between a pre- and a post-synaptic terminal, as illustrated in **Figure 2**. Those neurotransmitters

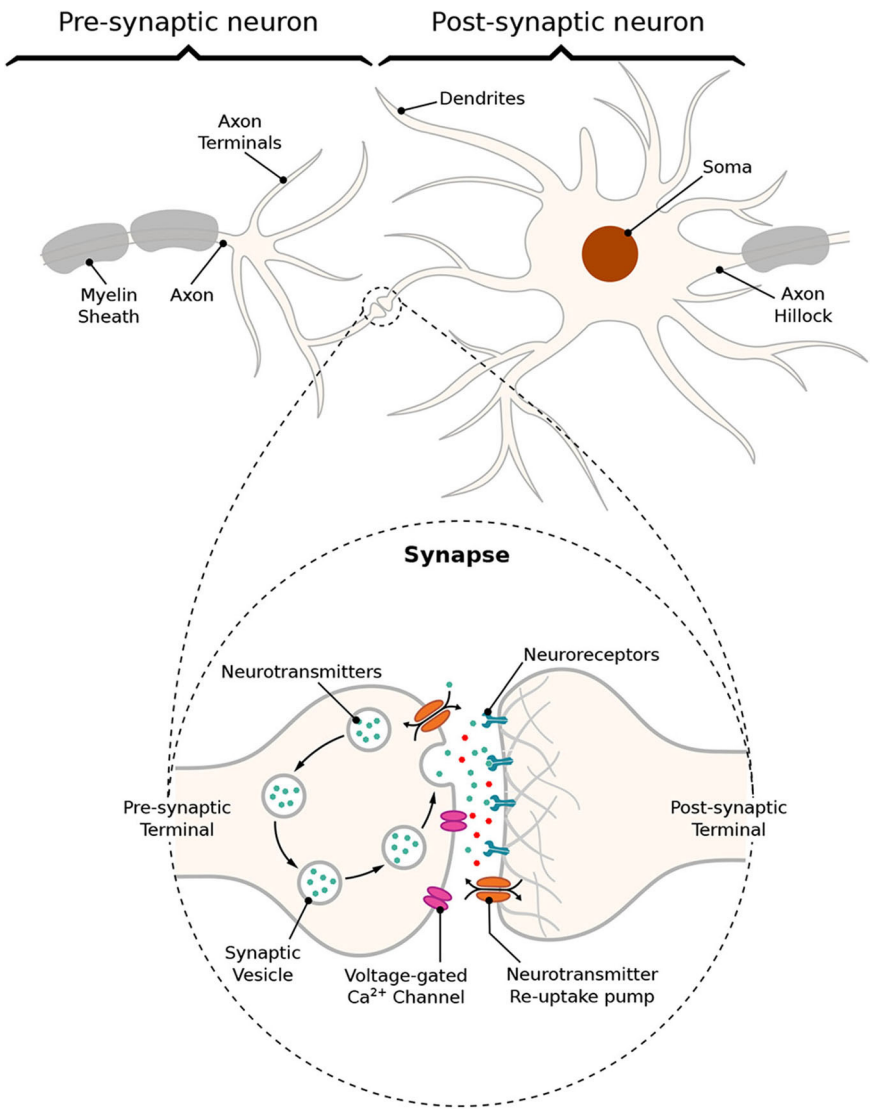

FIGURE 2 | Schematic of a *synapse*; action potentials traveling down the axon trigger the release of neurotransmitters into the cleft between pre- and post-synaptic terminals, traveling toward neuroreceptors on the other end leading to changes on membrane conductance that can either excite or inhibit the post-synaptic neuron.

will probabilistically bind to neuro-receptors located at the post-synaptic terminals, i.e., dendrites (Balevi and Akan, 2013), triggering the exchange of ions through the membrane that can either excite or inhibit the cell, depending on the type of neurotransmitters that were received. In our work, we focus on the synaptic weight between the pre- and post-synaptic terminals. The synaptic weight is a measure of how much influence the pre-synaptic stimuli have on the post-synaptic cell and it is known to have its value best approximated to the time integral of the synaptic conductance (Gardner, 1989). Furthermore, the value of synaptic conductance in the post-synaptic terminal is driven by the number of neurotransmitters bound to neuroreceptors (Guillamon et al., 2006). We illustrate the synaptic weight, in **Figure 2**, as red neurotransmitters which should have their release from the pre-synaptic terminals induced by the administration of a specific drug.

In an excitatory synapse, the membrane potential of the post-synaptic cell, which rests at approximately −65 mV, will start depolarizing itself until it reaches a threshold, *th*, for action potential initiation. On the other hand, if the synapse is inhibitory, the membrane should get even more polarized making it nearly impossible for the cell to fire a spike and not allowing the propagation of any signal down the network from the inhibited cell. After reaching *th*, the membrane potential should increase toward a maximum peak of depolarization, and then the cell will start the process of repolarization toward its resting potential. For a brief moment, the potential inside the cell will cross the level of potential when at rest making the membrane hyperpolarized, which is a period known as the *refractory period* and it can be further subdivided as *absolute* and *relative*. The absolute refractory period (ARP) lasts around 1–2 ms during which the neuron is unable to fire again regardless of the strength of the stimuli; then, it is followed by the relative refractory period (RRP) during which a response in the potential of the cell may be evoked depending on the strength of the stimuli (Mishra and Majhi, 2019).

2.2. Electronic Interpretation of a Neuron Model

The main structures of a neuron, previously mentioned in section 2.1.1, can assume different shapes and spatial structures that play an important role in determining its input and output relationship. By sectioning the neuron into several compartment models, we are able to account for the influence that individual compartments have on the communication process of the neuron. Even though we consider the same value of resting potential for all compartments of the cell, there is some discussion on whether different compartments have different potentials when at rest (Hu and Bean, 2018).

We aim to develop a transfer function for the neuron-spike response, or output $[V(s)]$, to a particular spike input $[I(s)]$. Using a transfer function for each neuron which is represented as a single compartment, we are able to efficiently associate the configuration of the filters with the structure of the neural network as well as the individual characteristics of each neuron. On top of that, we also are able to focus on frequency domain for an effective spike firing filtering. We rely on the electronic interpretation of the Hodgkin-Huxley model of neuron action potentials, which is made based on the neuronal cable theory assumptions on the static ionic channels conductance. In this section, we provide the details of the development of the transfer function, which is built on the linearization process of the Hodgkin-Huxley neuron model.

2.2.1. Hodgkin-Huxley Formalism

As aforementioned in section 1, neurons can perform spike filtering tasks either by manipulating ionic conductances, such as sodium and potassium conductances, from within the cell (Fortune and Rose, 1997) or by working on the extracellular environment where the synapse occurs (Brunel et al., 2001; Moreno-Bote and Parga, 2004). Furthermore, filtering capabilities may vary according to the non-linearities of the neuron's activity and action potential propagation. In order to design an efficient filtering process, we will need to eliminate the non-linearities so we can directly link neurons properties to the filtering behavior and adjust these properties according to a desired filtering performance level. We consider the Hodgkin and Huxley non-linear model (Pospischil et al., 2008) as our basic model since it perfectly describes the influence of ionic conductance and synaptic conductance in the propagation of the action potentials. We assume that parts of the neuron will constitute a compartment, which results in the electric

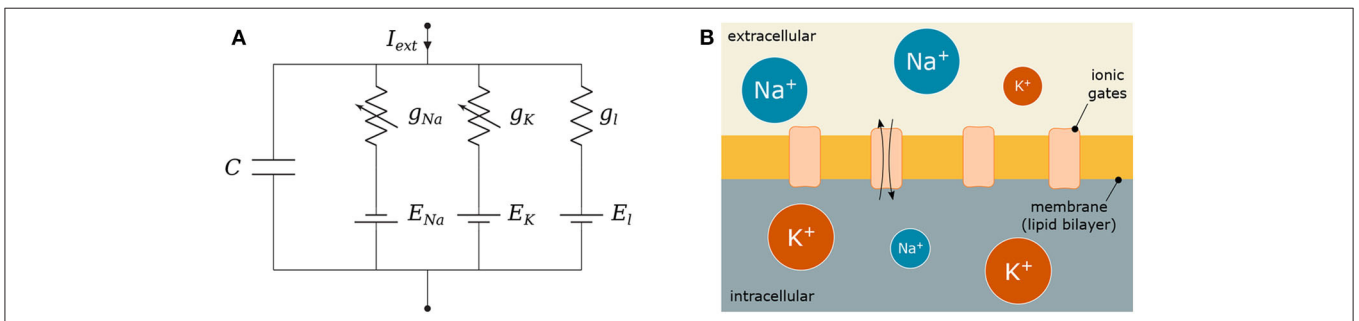

FIGURE 3 | Hodgkin-Huxley (HH) model: **(A)** Electronic circuit representation and **(B)** Equivalent biological HH compartment; the lipid bilayer is modeled as *C*, the conductances *g* represent how open or close the ionic gates are and the gradient of ions between the intra- and extra-cellular space define the reversal potentials *E*.

circuit in **Figure 3A** when applying the conventional neural cable theory.

Figure 3 depicts C as the membrane capacitance, each voltage-gated ionic channel represented by its respective conductances g_{Na} and g_K and the leak channel by the linear conductance g_l. The membrane capacitance is proportional to the surface area of the neuron and, along with its resistance, dictates how fast its potential responds to the ionic flow. The ratio between intra- and extra-cellular ions define the reversal potentials $E_{Na,K,l}$ establishing a gradient that will drive the flow of ions (Barreto and Cressman, 2011).

When an external stimulus, I_{ext}, is presented, it triggers either the activation or inactivation of the ionic channels that allow the exchange of ions that result in depolarization (or hyperpolarization when inhibitory) of the membrane of the cell. These dynamics are modeled as

$$C\frac{\mathrm{d}V}{\mathrm{d}t} = -I_l - I_{Na} - I_K + I_{ext}, \tag{1}$$

where V is the membrane potential and I_x are the ionic currents where x represents either a specific ion (Na, K) or the leak channel (l). Those currents are described as

$$I_l = g_l(V - E_l), \tag{2}$$

$$I_{Na} = g_{Na}m^3h(V - E_{Na}), \tag{3}$$

$$I_K = g_K n^4(V - E_K), \tag{4}$$

where m and h are the activation and inactivation variables of the sodium channel, respectively, and n is the activation variable of the potassium channel, following the conventional approach described by Hodgkin and Huxley (1952) and stated as

$$\frac{\mathrm{d}m}{\mathrm{d}t} = \alpha_m(V)(1 - m) - \beta_m(V)m, \tag{5}$$

$$\frac{\mathrm{d}h}{\mathrm{d}t} = \alpha_h(V)(1 - h) - \beta_h(V)h, \tag{6}$$

$$\frac{\mathrm{d}n}{\mathrm{d}t} = \alpha_n(V)(1 - n) - \beta_n(V)n, \tag{7}$$

in which the values of the rate constants α_i and β_i for the i-th ionic channel can be defined as

$$\alpha_m = \frac{0.1(V + 40)}{1 + e^{-(V+40)/10}}, \tag{8}$$

$$\beta_m = 4e^{-(V+65)/20}, \tag{9}$$

$$\alpha_h = 0.07e^{-(V+65)/20}, \tag{10}$$

$$\beta_h = \frac{1}{1 + e^{-(V+35)/10}}, \tag{11}$$

$$\alpha_n = \frac{0.01(V + 55)}{1 - e^{-(V+55)/10}}, \tag{12}$$

$$\beta_n = 0.125e^{-(V+65)/80}. \tag{13}$$

The membrane capacitance is proportional to the size of the cell, and on the other hand, the bigger the cell diameter, the lower the spontaneous firing rate (Sengupta et al., 2013). Furthermore, each ionic channel can be studied as containing one or more physical gates which can assume either a permissive or a non-permissive state when controlling the flow of ions. The channel is open when all gates are in the permissive state, and it is closed when all of them are in the non-permissive state (Baxter and Byrne, 2014).

2.2.2. Hodgkin-Huxley Linear Model

In order to derive a transfer function for the Hodgkin-Huxley model, we must consider each neuron as a system that is linear and time-invariant (LTI). If the system is non-linear, then a linearization process should be done before any frequency analysis is performed. For a more detailed analysis on the procedures for linearization of the Hodgkin-Huxley model, the reader is referred to Koch (2004), Mauro et al. (1970), Sabah and Leibovic (1969), and Chandler et al. (1962).

The linearization process requires that we reconsider the electronic components in each neuron compartment to adequately eliminate trivial relationships. Membranes with specific types of voltage- and time-dependent conductances can behave as if they had inductances even though neurobiology does not possess any coil-like elements. This modification will transform the behavior of non-linear components toward linearization, resulting in a proportional relationship between the voltage and current changes (Koch, 2004).

Every linearization process is performed for small variations around a fixed point, hereafter denominated by δ, and in the case of the Hodgkin-Huxley model, this fixed point should be the steady-state (resting state) of the system. Because the sodium activation generates a current component that flows in an opposite direction compared to that of a passive current, the branch concerning the sodium activation should have components with negative values while the branches regarding potassium activation and sodium inactivation should have components with positive values (Sabah and Leibovic, 1969). The linear version of the circuit of **Figure 3A** is illustrated in **Figure 4**, where C is the membrane capacitance, g_n, g_m, and g_h are the conductances of the inductive branches connected in series with

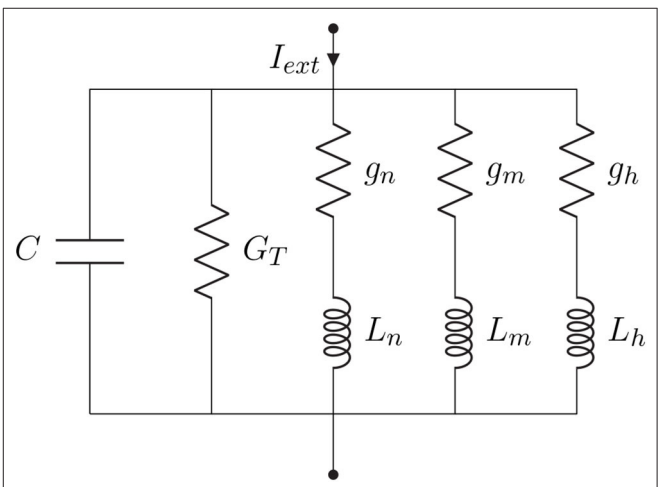

FIGURE 4 | Hodgkin-Huxley linear circuit model representation.

their respective inductances L_n, L_m, and L_h derived from the linearization process and $G_T = G_L + G_K + G_{Na}$ is the total pure membrane conductance.

Let us consider the membrane potential deviation, δV, around some fixed potential. Thus, we can express the response of the circuit to small-signal inputs as

$$C\frac{d\delta V}{dt} = I_{ext} - \delta I_l - \delta I_K - \delta I_{Na}, \tag{14}$$

where $\delta I_{l,Na,K}$ are current variations at any given steady-state and can be defined as

$$\delta I_l = g_l \delta V, \tag{15}$$

$$\delta I_K = G_K \delta V + 4g_K n_\infty^3 (V - E_K)\delta n, \tag{16}$$

$$\delta I_{Na} = G_{Na}\delta V + 3g_{Na} m_\infty^2 h_\infty (V - E_{Na})\delta m + g_{Na} m_\infty^3 (V - E_{Na})\delta h, \tag{17}$$

where $G_{K,Na}$ are pure conductances of potassium and sodium and G_L the pure leak conductance expressed as

$$G_L = \bar{g}_l, \tag{18}$$

$$G_K = \bar{g}_K n_\infty^4, \tag{19}$$

$$G_{Na} = \bar{g}_{Na} m_\infty^3 h_\infty, \tag{20}$$

where $\bar{g}_{K,Na}$ are the maximum attainable conductances, and δn, δm, and δh are small variations around the steady-state of the activation and inactivation variables n, m, and h which are written as

$$\frac{d\delta n}{dt} = \frac{d\alpha_n}{dV}\delta V - (\alpha_n + \beta_n)\delta V - n_\infty \left(\frac{d\alpha_n}{dt} - \frac{d\beta_n}{dt}\right)\delta V, \tag{21}$$

$$\frac{d\delta m}{dt} = \frac{d\alpha_m}{dV}\delta V - (\alpha_m + \beta_m)\delta V - m_\infty \left(\frac{d\alpha_m}{dt} - \frac{d\beta_m}{dt}\right)\delta V, \tag{22}$$

$$\frac{d\delta h}{dt} = \frac{d\alpha_h}{dV}\delta V - (\alpha_h + \beta_h)\delta V - h_\infty \left(\frac{d\alpha_h}{dt} - \frac{d\beta_h}{dt}\right)\delta V, \tag{23}$$

as a function of the derivative of the rate constants $\alpha_{n,m,h}$ and $\beta_{n,m,h}$, and n_∞, m_∞, and h_∞ are the steady-state values of m, n, and h defined as

$$n_\infty = \frac{\alpha_n}{\alpha_n + \beta_n}, \tag{24}$$

$$m_\infty = \frac{\alpha_m}{\alpha_m + \beta_m}, \tag{25}$$

$$h_\infty = \frac{\alpha_h}{\alpha_h + \beta_h}, \tag{26}$$

and the conductances, $g_{n,m,h}$, and inductances, $L_{n,m,h}$, of the inductive branches are defined as

$$g_n = \frac{4\bar{g}_K n_\infty^3 (V - E_K)\left[\left.\frac{d\alpha_n}{dV}\right|_r - n_\infty \left.\frac{d(\alpha_n + \beta_n)}{dV}\right|_r\right]}{\alpha_n + \beta_n}, \tag{27}$$

$$L_n = \frac{1}{g_n(\alpha_n + \beta_n)}, \tag{28}$$

$$g_m = \frac{3\bar{g}_{Na} m_\infty^2 h_\infty (V - E_{Na})\left[\left.\frac{d\alpha_m}{dV}\right|_r - m_\infty \left.\frac{d(\alpha_m + \beta_m)}{dV}\right|_r\right]}{\alpha_m + \beta_m}, \tag{29}$$

$$L_m = \frac{1}{g_m(\alpha_m + \beta_m)}, \tag{30}$$

$$g_h = \frac{\bar{g}_{Na} m_\infty^3 (V - E_{Na})\left[\left.\frac{d\alpha_h}{dV}\right|_r - h_\infty \left.\frac{d(\alpha_h + \beta_h)}{dV}\right|_r\right]}{\alpha_h + \beta_h}, \tag{31}$$

$$L_h = \frac{1}{g_h(\alpha_h + \beta_h)}. \tag{32}$$

Each channel has a probability of being open which represents the fraction of gates in that channel that are in the permissive state (Gerstner et al., 2014). The gating variables are described by the coupling of the conductances $g_{n,m,h}$ and their respective inductances $L_{n,m,h}$ which are functions of the rate constants representing the transition from permissive to non-permissive state, $\alpha(V)$, and vice-versa, $\beta(V)$ which should take a short period of time, $\tau = [\alpha(V) + \beta(V)]^{-1}$, to eventually reach a steady-state value, α_∞ and β_∞ (Koslow and Subramaniam, 2005).

Borrowing concepts from systems theory such as frequency analysis of LTI systems, as a standard procedure for the analysis of linear differential equations as simpler algebraic expressions (see Nise, 2015), and the linearization of non-linear systems for the reason previously mentioned at the beginning of this section, we derived a transfer function in the *Laplace* domain for the linear system from **Figure 4**. The relationship between the different elements of the circuit and their respective impedance and admittance values from the *Laplace* transforms are depicted in **Table 1**.

Therefore, the relationship between the output and the input of the system in the frequency domain is expressed as

TABLE 1 | Impedance relationships for capacitors, resistors, and inductors.

Component	Impedance	Admittance
Capacitor	$\frac{1}{Cs}$	Cs
Resistor	R	$G = \frac{1}{R}$
Inductor	Ls	$\frac{1}{Ls}$

$$\frac{V(s)}{I(s)} = \frac{s^3 L_n L_m L_h}{\{L_n L_m L_h[s^4 C + s^3(G_T + g_n + g_m + g_h)] + s^2(L_m L_h + L_n L_h + L_m L_h)\}} \quad (33)$$

where $s = \sigma + j\omega$ is a complex variable; $j = \sqrt{-1}$ and $\omega = 2\pi f$, where f is the frequency in Hertz. Let us rewrite Equation (33) as

$$W(s) = C^{-1}\frac{s}{s^2 + sC^{-1}(G_T + g_n + g_m + g_h) + C^{-1}(L_m^{-1} + L_n^{-1} + L_h^{-1})}. \quad (34)$$

Now, denoting $\gamma = G_T + g_n + g_m + g_h$ and $\lambda^{-1} = L_n^{-1} + L_m^{-1} + L_h^{-1}$ and performing a few algebraic manipulations, we end up with the following transfer function for the filter model

$$W(s) = \gamma^{-1}\frac{C^{-1}\gamma s}{s^2 + C^{-1}\gamma s + \lambda^{-1}C^{-1}}. \quad (35)$$

For frequency response analysis, we observe the behavior of $W(j\omega)$, i.e., substitute $s = j\omega$. For $\omega \to 0$, $W(j\omega)$ behaves like ω; for $\omega \to \infty$ it behaves like $\frac{1}{\omega+1}$, i.e., in both cases it tends to zero, and hence demonstrates the behavior of a second-order band-pass filter (BPF). It corresponds to the canonical form $\frac{K(\omega_0/Q)s}{s^2+(\omega_0/Q)s+\omega_0^2}$ where $K = \gamma^{-1}$ is the gain, $Q = \gamma^{-1}\sqrt{C\lambda^{-1}}$ is the selectivity and $\omega_0 = \sqrt{\lambda^{-1}C^{-1}}$ is the peak frequency of the filter. This agrees with findings from previous literature on the matter (Plesser and Geisel, 1999) that concluded the periodicity of a stimulus is optimally encoded by a neuron only in a specific spectral window.

2.3. Transfer Function Filter Design

Given the transfer function for a neural compartment in the previous section, we now progress toward a transfer function for the spike filter. The filter is comprised of neurons that are particularly chosen to have a network that will behave as a digital gate and a small population that will behave as a circuit that implements the filter. Our aim is to capture the relationship between compartments as well as neuron connections so we can build a transfer function for the filter while considering neuron connection variables (synaptic conductance and synaptic weight) that allow easy reconfiguration of the filtering process. The linearization process combined with the analysis of the neuron communications is the driver of the filtering process, which also allows the derivation of a filter transfer function which is detailed below.

2.3.1. Biological Logic Gates and Circuits

Synthetic biology is the technology that allows the control of the neurons' internal process in order to construct non-natural activity and functioning of neurons, e.g., logic gates (Larouche and Aguilar, 2018). Synthetic logic operations inspire scientists to address the challenges posed by novel synthetic biomedical systems, such as biocompatibility and long-term use.

Figure 5A shows the three types of the circuit we have built and analyzed in this work. From circuits A to C, the number of OR gates is decreased; when compared to AND gates, OR gates are quite permissive. In our previous study (Adonias et al., 2020), we present an analysis on how signals from two input neurons will need to be close to each other to amplify the action potential of the output neuron in order to achieve maximum AND-gating accuracy. The transformation from a purely OR-formed logic circuit to a purely AND-formed one leads to the confirmation of what the truth-tables suggest, i.e., fewer states evoke spikes in the output and, consequently, the attenuation of higher frequencies in the inputs. **Figure 5B** shows the connection of AND gates in cascade, and this analysis is further discussed in the section 4. Each of the circuits was analyzed with one and two AND's in cascade, hence the nomenclature of a letter followed by a number, the letter refers to the type of circuit and the number accounts for how many AND gates are connected in cascade. Only two types of logic gates were used to build the circuits, an AND composed of the cells L23-MC (Layer 2/3 Martinotti Cell), L23-NBC (Layer 2/3 Nest Basket Cell), and L1-HAC (Layer 1 Horizontal Axon Cell); and an OR composed of the cells L23-MC, L23-NBC, and L1-DAC (Layer 1 Descending Axon Cell). These cells were picked because they showed the best performance in our previous analysis on their individual gating capabilities.

Given that several factors such as connection probability, type of cell, and different numbers of compartments (as discussed in section 2.3.2) among different types of neurons may influence its gating capabilities. This variation on the quantity of compartments could also lead to variations on periods for the action potential to reach the post-synaptic terminals and start the synapse process. Furthermore, cells with bigger sizes of soma may take more time and amount of stimuli to reach threshold for action potential initiation (Sengupta et al., 2013), thus, also

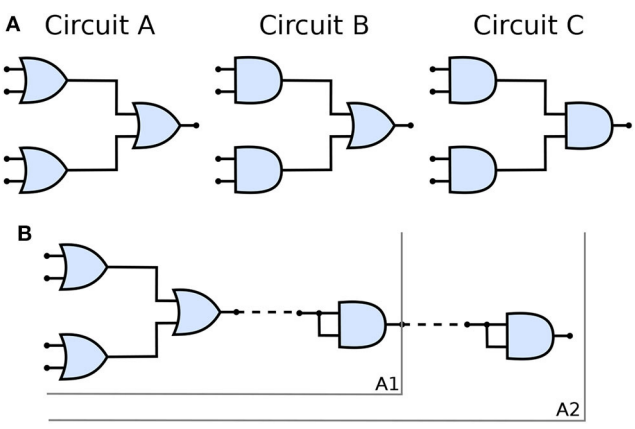

FIGURE 5 | (A) Schematic of circuits A, B, and C and **(B)** The connection of AND gates in cascade to circuit A. *A*1 refers to the arrangement described by a single AND gate connected to the output of the circuit A and *A*2 refers to another AND gate connected to the output of *A*1 arrangement, i.e., two AND gates in cascade with circuit A. Analogous nomenclature is employed for both circuits B, as in B1/B2 and C, as in C1/C2.

affecting the way a neuronal logic gate would work regarding a specific morphological neuronal type. For that reason, it is safe to keep two cells fixed as inputs (as illustrated in **Figure 1**) and then deploy an arrangement with which its performance has been previously assessed, allowing us to be fairly certain about how the synthetic gate or circuit should behave. Each neuron is represented by a block, $W_i(s)$ for the i-th neuron, and its representation in the frequency domain is proposed in Equation (35) and further detailed in section 2.3.2.

2.3.2. Compartmental Modeling

Neurons are very complex structures with numerous ramifications and several factors that contribute to their highly non-linear dynamism. Aiming to make the comprehension of such a complex electrical behavior easier, one employs a widely used technique called "compartmental modeling." Since different neurons have different morphologies, the mechanism of determining the number of compartments will be based on estimating the length of a specific neuronal structure. For instance, a varying length of axon, which will reflect in different quantities of compartment in series, where we will have a fixed size for each segment of the axon representing one compartment. This is a very natural and elegant way to model dynamic systems as multiple interconnected compartments where each compartment is described by its own set of equations, carrying the influence of one compartment to the next reproducing the behavior of the whole neuron.

Observing the neuron as a set of compartments described by transfer functions equivalent to that of (35), the neuronal morphology of a pyramidal cell, as illustrated in **Figure 6A**, (or any cell for that matter) can be modeled as an electrical circuit as shown in the topology of **Figure 6B**; the dendritic ramifications are modeled as a combination of serial and parallel connections terminating in the soma which is connected to the axon modeled as a series of compartments; its interpretation in terms of filtering is given in **Figure 6C**. The effect of a serial connection of two compartments is one of set-intersection when observed in the frequency domain: two bandpass filters in series pass only the frequencies that exist in both of their passbands. On the other hand, a parallel connection has a set-union effect, a parallel connection of filters will pass all the frequencies in both their passbands. As such, a large network (tree) of such compartments with similar bands combined in a cell, and cells combined in a group of cells will exhibit asymptotic bandpass behavior as well.

Every single compartment, each represented by one transfer function, is grouped in trees of three cells (**Figure 1**) forming a logic gate; the three gates are connected into a tree of their own, as illustrated in **Figure 5A**, forming a logic circuit. All of the cells are represented with the same form of the transfer function,

$$W_i(s) = \zeta_i \gamma_i^{-1} \frac{C_i^{-1}\gamma_i s}{s^2 + C_i^{-1}\gamma_i s + \lambda_i^{-1} C_i^{-1}},\ i = 1, \ldots, 9 \qquad (36)$$

with symbols defined previously, and a new parameter ζ_i describing the synaptic weight for the ith cell; ζ_i acts as a tunable gain for the neurons.

Using the parameters from (Mauro et al., 1970) aiming to keep them within the physically sensible orders of magnitude, we obtain the reference values of $\bar{\gamma} = 0.0024$, $\bar{\lambda} = 119$, $\bar{C} = 1$ and $\bar{\zeta} = 1$, and the values for 9 cells were generated multiplying these reference values by a uniformly distributed random variable in the range $(0, 1)$. This kind of distribution is widely used to describe experiments where an arbitrary result should lie between certain boundaries, and in our case boundaries are defined by reasonable orders of magnitude around values made available by previous studies; keeping exactly the same parameters for all cells in the cascade is not realistic. The total transfer function of this system is

$$W = ((W_1 + W_2)W_3W_7 + (W_4 + W_5)W_6W_8)W_9, \qquad (37)$$

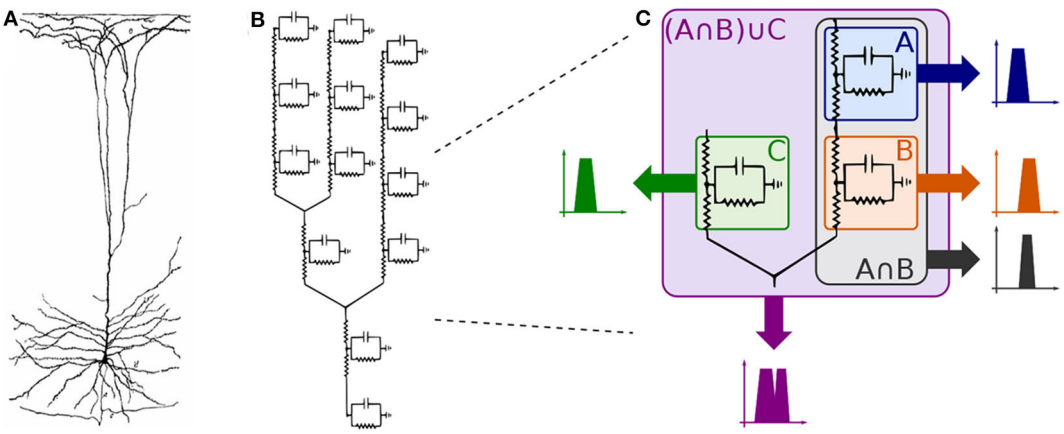

FIGURE 6 | Compartmental neuron representation: **(A)** Natural topology of a pyramidal cell, **(B)** Electronic circuit compartments, and **(C)** Effects of serial and parallel connections between compartments.

and its frequency response (Bode plot) for the relevant range of frequencies in our applications (Wilson et al., 2004) is shown in **Figure 7B**.

Let us now observe three cases concerning the choice of ζ_i values. In the first case, we keep all of them at unity and consider it our base case for this part of the analysis (and to keep it aligned with the rest of the paper, we call it *Circuit B*). In the second case, we double the values of ζ_3 and ζ_6, which corresponds to the manipulation of the output cell for the two input gates in *Circuit A*. In our linear model, this is equivalent to doubling ζ_9 and leaving everything else intact. Finally, in the third case, we manipulate the output cell of the last gate by halving its synaptic conductance (*Circuit C*). This effectively means that the three cases are $\zeta_{9B} = 1$, $\zeta_{9A} = 2$, and $\zeta_{9C} = 1/2$, respectively. Since the tunable gain ζ_9 of the gate W_9, is the tunable gain of the whole system W according to (37), its change would offset the frequency response along the ordinate axis, i.e., lower gains (lower conductance) would suppress the unwanted frequencies in a better way, while higher gains would do the opposite. This is demonstrated in **Figure 7A**. The process of the analysis is summarized in **Algorithm 1** and a summary with all elements from both the original and linearized versions of the Hodgkin-Huxley as well as the transfer function model is presented in **Table 2**.

Alternatively, as we suggested earlier, a single transfer function of a compartment serves as an approximation of the entire system due to the effects of repeated bandpass filtering in **Figure 6C**. In such case, we observe 20 dB/decade slope in the Bode plot shown in **Figure 7A** (as compared to 80 dB/decade slope in **Figure 7B**) and the same offset of $20 \cdot \log_{10} 2 \approx 6$ dB in case of halving/doubling the synaptic weight. Since the filter is of a band-passing nature, it is only natural that, around the resonant frequency, lower and higher frequency amplitudes should be ideally attenuated toward zero. Thus, it is worth mentioning that in both cases depicted here, the part of the frequency response with the cusp is at very low frequencies, so it is not visible in the relevant part of the spectrum. As such, the filter behaves as a low pass filter for all practical considerations.

3. RESULTS

In this section, we discuss the simulation results concerning the reconfigurable logic gates as well as the circuits. For all simulations, intrinsic parameters of the cell were kept at their default values (such as the length and diameter of each of their compartments) meaning that nothing concerning their morphological properties was changed, the spike trains fed to the input of the circuits followed a *Poisson* process and the threshold for spike detection and data analysis was 0 mV where any potential higher than that in a specific time slot would be considered a bit "1," characterizing the use of a simple *On-Off Keying (OOK)* modulation which was implemented where a spike is considered as a bit "1" and its absence a bit "0" in each time slot. The cell models and information on their respective connection probabilities between different pair of

Algorithm 1 | Linear model filter analysis

Initialize:

$\Gamma = \{\gamma_1, \ldots, \gamma_9\} \in (0, \bar{\gamma})$

$\Lambda = \{\lambda_1, \ldots, \lambda_9\} \in (0, \bar{\lambda})$

$\mathcal{C} = \{C_1, \ldots, C_9\} \in (0, \bar{C})$

$Z = \{\zeta_1, \ldots, \zeta_9\} \in (0, \bar{\zeta})$

for $1 \leq i \leq 9$ **do**

$W_i \leftarrow \zeta_i \gamma_i^{-1} \frac{C_i^{-1}\gamma_i s}{s^2 + C_i^{-1}\gamma_i s + \lambda_i^{-1} C_i^{-1}}$

end

$W_B \leftarrow ((W_1 + W_2)W_3 W_7 + (W_4 + W_5)W_6 W_8)W_9$

$W_A \leftarrow 2W_B$

$W_C \leftarrow 0.5W_B$

Plot frequency response: W_A, W_B, W_C

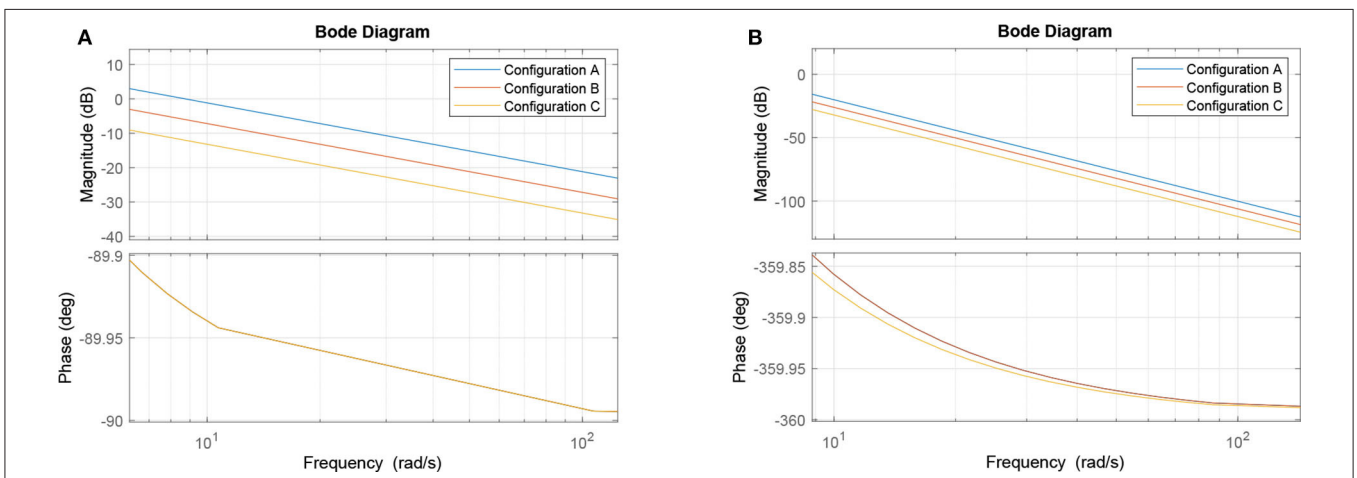

FIGURE 7 | Bode plots: **(A)** Single second-order bandpass filter approximation and **(B)** Filter structure from Equation (37).

TABLE 2 | Summary of elements described in the proposed model.

Element	Description
C	Membrane capacitance
g_{Na}, g_K, g_l	Sodium, potassium, and leak conductances
E_{Na}, E_K, E_l	Sodium, potassium, and leak reversal potentials
I_{ext}	External stimulus
I_{Na}, I_K, I_l	Ionic current for the sodium, potassium, and leak channels
V	Membrane potential
m, h	Sodium activation and inactivation variables
n	Potassium activation variable
α, β	Rate constants for m, h, and n from permissive to non-permissive state and vice-versa
δ	Small variation around the steady-state
G_T	Total pure conductance
G_{Na}, G_K, G_L	Sodium, potassium, and leak pure conductances
$\bar{g}_{Na}, \bar{g}_K, \bar{g}_l$	Maximum attainable sodium, potassium and leak conductances
$m_\infty, h_\infty, n_\infty$	Steady-state values of m, h, and n
g_m, g_h, g_n	Conductances of the inductive branches
L_m, L_h, L_n	Inductances of the ionic paths
W	Transfer function of the filter
K, Q, ω_0	Gain, selectivity, and peak frequency of the filter
ζ	Synaptic weight

neurons were obtained from the work of Markram et al. (2015), and then we used NEURON and Python for simulation and data analysis (Carnevale and Hines, 2009; Hines et al., 2009). The source-code of our simulations is publicly available on a GitHub repository[1].

3.1. Reconfigurable Logic Gates

In this work, we call "reconfigurable" logic gates, the gates that work by changing the synaptic weight between the connections of both input cells with the output cell in a neuronal logic gate structure. Aiming to measure individual gate accuracy, the spike trains in the inputs were randomly produced but we control their frequency variation, in other words, for each simulation, the frequency at all inputs was the same and any change in the frequency was performed for all inputs of the gates meaning that none of the simulations account for different frequency values between different inputs in a single simulation. The accuracy is a simple but powerful measure for the performance of the gates, with which we intend to analyze the effects of the dynamics of the cell on the output of the circuit when comparing this output with the ideal response of the circuit derived from its truth-table. The accuracy is calculated according to the following equation (Hanisch and Pierobon, 2017):

$$A(E[Y];\, Y) = \frac{P_{1,1} + P_{0,0}}{\sum_{Y} \sum_{E[Y]} P_{Y,E[Y]}}, \tag{38}$$

where $P_{Y,E[Y]}$ is the probability of Y given $E[Y]$ in which Y is the actual output and $E[Y]$ is the expected output and $Y \,\&\, E[Y] \in \{0, 1\}$. $P_{Y,E[Y]}$ resembles the conditional probabilities in a binary symmetric channel (BSC). Thus, $P_{0,0} = 1 - P_{1,0}$, and $P_{0,1} = 1 - P_{1,1}$. It is possible to calculate $P_{1,1}$, for instance, by counting the number of bits there are for each input-output combination. In other words, considering $\#B_{i,j}$ the number of times a bit i was received when bit j was sent knowing that $i \,\&\, j \in \{0, 1\}$, then $P_{1,1} = \#B_{1,1}/(\#B_{1,1} + \#B_{0,1})$.

Given the objective of obtaining a behavior similar to an OR gate, the synaptic weight should be set to 0.06 μS, meaning that the pre-synaptic stimuli will drive a higher influence on the depolarization of the post-synaptic cell. On the other hand, for an AND behavior, the weight is set to 0.03 μS, which reduces the influence of a single spike and look to a response of the post-synaptic neuron only when two spikes arrive very close to each other in terms of time. This is conducted so we have acceptable levels of accuracy when compared to the expected outputs of the gate.

Figure 8 show similar responses when gates originally built to be of a specific kind. This means either OR or AND gates can change their configurations that drives their gating capabilities by modifying the synaptic weight between the connections of the input cells and the output cell. Although there is quite a visible difference between the performance of AND and OR gates, even at high frequencies (150 Hz), the accuracy of the reconfigurable logic gates remains above 80%.

3.2. Neuronal Logic Circuits

Once the reconfigurable behavior of the gates is assessed, they are connected to other gates to form a logic circuit. The performance is measured employing a ratio (frequency response), i.e., the number of spikes (bits "1") in the output divided by the nominal input frequency, in Hertz. This ratio is also known as the magnitude, or gain when evaluating the data in decibels. Following the approach for individual gates, the inputs are random and the frequency is increased uniformly. Since the gates showed similar accuracy when increasing the input frequency, we picked the one analyzed in **Figure 8A** for our circuit analysis with a reconfigurable logic gate, modifying only the output gate's synaptic properties.

Figure 9A show the results for the circuits in **Figure 5A**. As expected, Circuit C has a stronger attenuation of the signals passing through it, and this is mainly due to the fact it is an arrangement with three AND gates and, based on the truth table, an AND gate only responds to stimuli if all its inputs are active at the same time. The magnitude in decibels shown in **Figure 9B** follow a standard presentation of the response of digital filters.

In the non-linear case of the system, the filtering is even better than what the linear model would promise, i.e., the suppression of unwanted frequencies is better due to superexponential decay. Let us compare **Figures 7B**, **9B**. The linear model suggests that a constant difference of 6 dB is to be expected if the synaptic weight of the output cell is halved (or doubled), and a linear, constant amplitude drop. In the nonlinear model, we do observe a 20 dB/decade drop and 6 dB difference at relevant frequencies, but instead of a linear trend, we observe a convex response, which

[1]https://github.com/gladonias/neuronal-filters

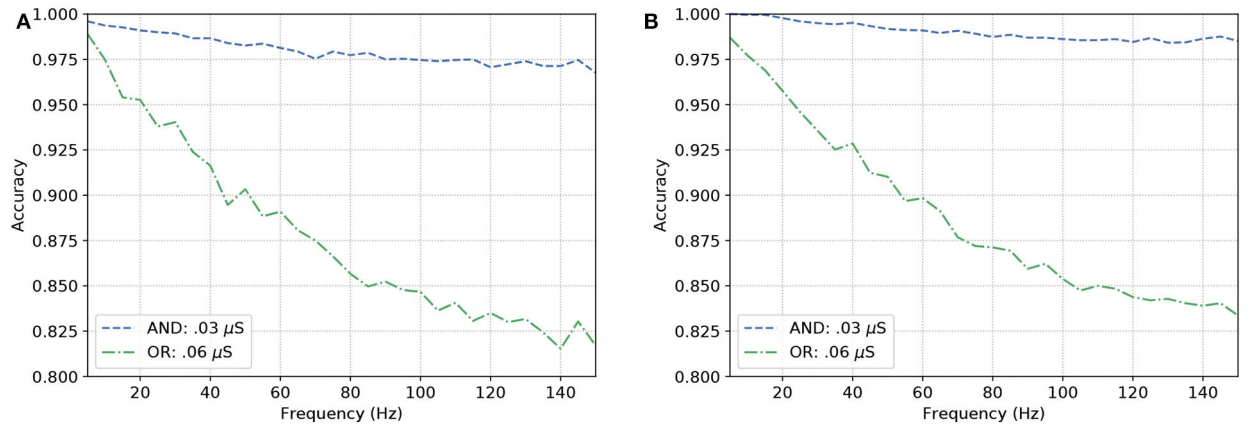

FIGURE 8 | Analysis on reconfigurable logic gates with neurons of types **(A)** L23-MC, L23-NBC, and L1-DAC and **(B)** L23-MC, L23-NBC, and L1-HAC.

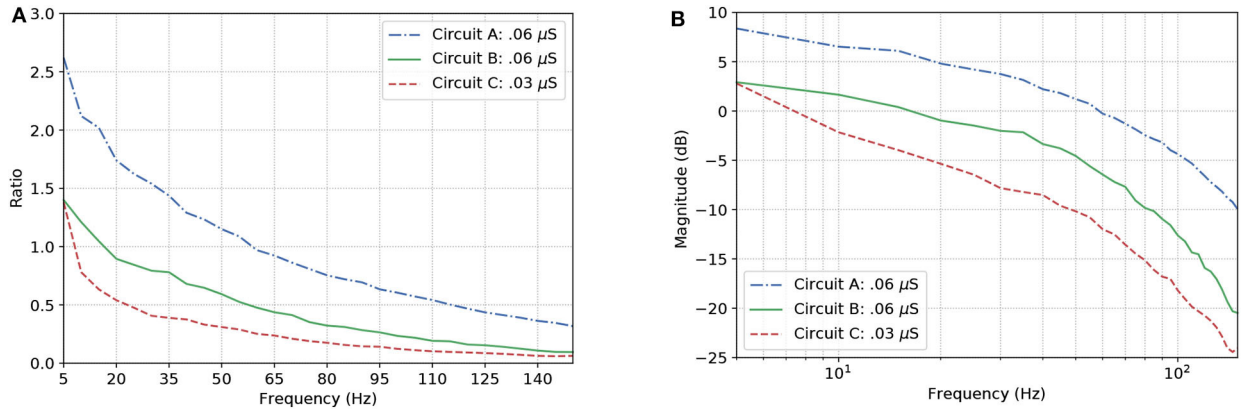

FIGURE 9 | Effects of dynamic changes to the synaptic weight in circuits A, B, and C; **(A)** Frequency response and **(B)** Magnitude in decibels.

helps in attenuating high frequencies faster than we would expect from the linear model. This is because the linear model is accurate in a neighborhood of the point at which it was linearized.

Now, let us consider $H(\nu)$ as the response of an ideal low-pass filter, and $W(\nu)$ the response of the proposed neuronal filter, the counter-efficiency of W given H is calculated as

$$\psi(W|H) = \int_0^{\nu_c} |W(\nu) - H(\nu)|\, d\nu + \int_{\nu_c}^{\nu_f} |W(\nu)|\, d\nu \qquad (39)$$

where ν_c is the cut-off frequency and ν_f is the last evaluated frequency (in this relationship, the lower the value, the more efficient the filter is). Since, in terms of magnitude, a frequency band when cut by an ideal filter should be attenuated toward negative infinity ($-\infty$), we have to pick a limit for the calculation of the area under the curves. In our case, after a visual inspection, the baseline for calculation chosen was -25 dB, because this is the closest integer value to the lowest values of magnitude.

Figure 10 depicts the counter-efficiency analysis performed for the three circuits. As it is shown, for different frequency bands we have some circuits performing better than others. Also, each circuit has a preferable frequency band for achieving maximum efficiency. For frequencies lower than or equal to 80 Hz, Circuit C seems the most efficient, especially at 60 Hz, while frequencies around 100 Hz show Circuit B as the most efficient which is also the band where it performs the best. Circuit A, on the other hand, has its best performance for 120 Hz, and probably for higher frequencies as well if the trend continues.

This shift in performance may allow us to control which type of circuit we want to activate inside the brain depending on which activity the subject is performing at the time, e.g., being awake or being asleep. These changes may be induced by the intake of specific drugs that alter synaptic properties in a neuronal connection.

Figure 11 shows a parallel analysis between the magnitude in dB and the accuracy of the filters with AND gates in cascade. Each circuit is identified by a pair of characters, the first is the letter referring to the circuit analyzed, the second is how many AND gates were connected in cascade. For example, *A*2 means Circuit A with two AND gates in cascade, as illustrated in **Figure 5B**.

The results suggest that, by increasing the number of gates in cascade, we have to deal with attenuation in the network due to

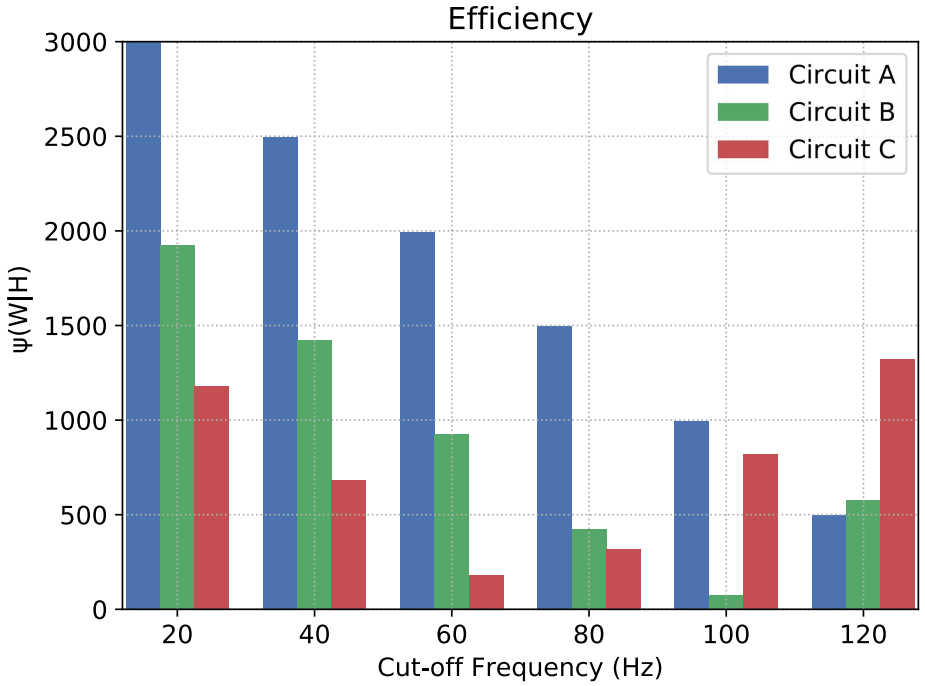

FIGURE 10 | Counter-efficiency of the circuits when compared to ideal filters (the lower the value, the better the filter's performance).

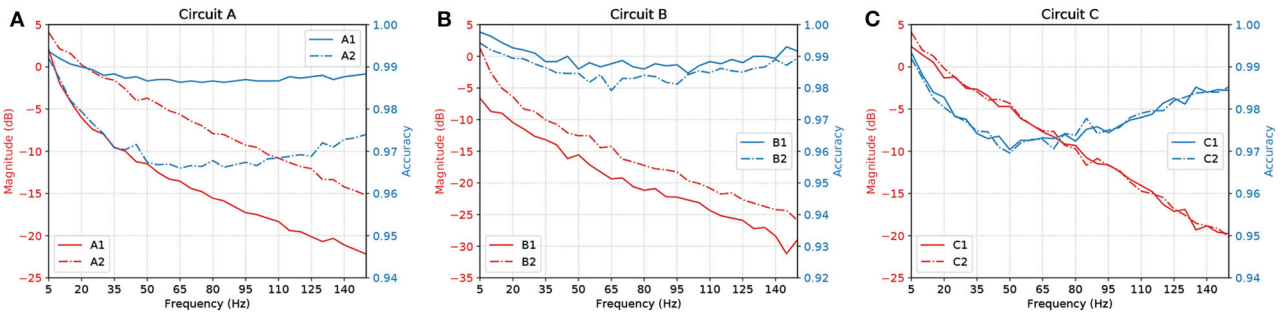

FIGURE 11 | Parallel between Magnitude (dB) and accuracy of circuits **(A)** A, **(B)** B, and **(C)** C, with AND gates in cascade.

propagation caused by specific characteristics of the cell, such as the connection probability; hence, the more gates in cascade the worse the performance of the circuit. Also, even though the ratio keeps going downwards, at some point, the accuracy will start to shoot up. With careful evaluation, the dip in the accuracy along mid-range frequencies is very low in terms of scale, showing a difference of only around 0.03 on the values of accuracy.

4. DISCUSSION

Synaptic weight plays a role in the influence of the pre-synaptic stimuli and its impact on the post-synaptic neuron and has a value proportional to the synaptic conductance (Gardner, 1989) which is driven by the amount and type of neurotransmitters that are being bound to the post-synaptic terminals. The higher the connection probability between pairs of neurons, the stronger the influence of a specific synaptic weight. This is due to the proportional relationship that the weight has with each synaptic connection that individually releases a certain amount of neurotransmitters, hence, different neuron types may affect the influence of a fixed value of synaptic weight. This explains how the accuracy values fluctuate between different types of gates and circuits as shown in **Figure 11**. Within a larger network spatial dimension, the types of neurons may drive a higher accuracy fluctuation since the network connection exhibits different synaptic weights between each other.

With our model, we have mainly investigated the attenuation on the spiking frequency for three different types of circuits in which we decrease the number of OR gates by replacing them with AND gates. We were also able to have the fine-tuning synaptic properties showing a difference of around 5 dB in performance between the curves in **Figure 9B**. Changes in the

synapse are also considered (Vogels and Abbott, 2005), either by strengthening or weakening specific synaptic connections, logic gates were built within a homogeneous network of integrate-and-fire neurons. Moreover, the experiments conducted by Goldental et al. (2014) followed a procedure that enforced stimulations on neuronal circuits within a network of cortical cells *in-vitro* and they do propose other types of gates such as XOR and NOT. Furthermore, we increased the number of AND gates in a cascade-like manner in order to confirm that the longer the line of cascade gates, the more attenuated the signal should be if none of those elements receives any kind of external stimuli despite the spike coming from the circuit, and this result is depicted in **Figure 11**. A peak value in the difference of around 8 dB occurs in Circuit A, decreasing to around 5 dB in Circuit B and there is a small difference in Circuit C. The transfer function derived from the Hodgkin-Huxley linear model suggests a band-pass behavior of the system (Plesser and Geisel, 1999) for very low frequencies leaving us with a low-pass filter acting on higher frequencies ranging from 5 to 150 Hz. Considering the time for a spike to be fired that comprises depolarization, repolarization, and refractory period, higher frequencies will lead to saturation and non-realistic behavior of neuronal firing.

Our results, therefore, suggest that neuronal logic circuits can be used to construct also digital filters, filtering abnormal high-frequency activity which can have many sources including neurodegenerative diseases. A metric of counter-efficiency was also proposed, which should show how far apart the real results are from the ideal cases. We found that frequency bands were found to be of optimal value for different types of circuits such as 60 Hz for circuit C, 100 Hz for circuit B, and 120 Hz for circuit A, as shown in **Figure 10**. Based on the presented results, we demonstrate that by reconfiguring the gates inside the digital filters we can shift the intensity with how we attenuate the spiking frequency allowing an on-the-fly adaptation of the filtering tasks depending on the activity that is being performed by the subject where, for instance, circuit C should outperform both A and B for frequencies lower than or equal to 80 Hz.

The envisioned application of the proposed mathematical framework is for *in-silico* pharmacology and how it can be used to provide advanced prediction supporting computational strategies to test drugs. Since drug design and discovery in neuroscience are very challenging, especially due to the complexity of the brain and the significant impediment of the blood-brain barrier (BBB) imposes on the delivery of therapeutic agents to the brain. The success rate for approval by competent authorities of such drugs is $<$10%. Such a low rate is attributed not only to factors related to the disease itself, such as complexity, slow development, and gradual onset but also, to the limited availability of animal models with good predictive validity and the limited understanding of the biological side of the brain (Geerts et al., 2020). The system model derived from a set of coupled neuron compartments can help push forward the design of these neuronal filters and provide a platform for *in silico* drug-induced treatments on top of engineered biological models of neurons. A platform that could lead to cost-effective drug development and analysis of potential bio-computational units capable of enhancing signal processing in the brain, as well as predicting long-term effects of using a specific drug are potential uses of the proposed mathematical framework.

5. CONCLUSION

In this work, we proposed a reconfigurable spike filtering design using neuronal networks that behave as a digital logic circuit. This approach requires the cells to be sensitive to modifications through chemicals delivered through several proposed methods available in the literature. From the Hodgkin-Huxley action potential model we developed a mathematical framework to obtain the transfer function of the filter. This required a linearization of the Hodgkin-Huxley model that changes the cable theory simplification for each cell compartment. To evaluate the system, we have used our transfer function as well as the NEURON simulator to show how the frequency of operation, logic circuit configuration as well as logic circuit size can affect the accuracy and efficiency of the signal propagation. We observed that all-ANDs circuit produces more accurate results concerning their truth-table when compared to all-ORs. In addition, the results show that each digital logic circuit is also reconfigurable in terms of cut-off frequency of the filter, by manipulating the types of gates in the last layer of the circuit.

We believe the proposed filter design and its mathematical framework will contribute to synthetic biology approaches for neurodegenerative disorders such as epilepsy, by showing how the control of cellular communication inside a small population can affect the propagation of signals. For future work, we plan the use of non-neuronal cells, e.g. astrocytes, for the control of gating operations and the assessment of neuronal filtering capabilities at a network level. Treatment techniques based on this method can be a radical new approach to reaching precision and adaptable outcomes, inspired from electronic engineering as well as communication engineering. Such techniques could tackle at a single-cell level, neurons affected by seizure-induced high-frequency firing or bypass neurons that have been affected by a disease-induced neuronal death and degeneration, thus keeping the neuronal pathway working at a performance as optimal as possible.

DATA AVAILABILITY STATEMENT

The original contributions presented in the study are included in the article/supplementary material, further inquiries can be directed to the corresponding author/s.

AUTHOR CONTRIBUTIONS

GA performed the simulations and wrote the manuscript. HS performed the control-theoretic analysis. GA, HS, and MB performed the data analysis. SB, NM, MB, and MW led the work development. All authors contributed to manuscript writing and revision. All authors also have read and approved the submitted version.

FUNDING

This publication has emanated from research conducted with the financial support of Science Foundation Ireland (SFI) and is co-funded under the European Regional Development Fund for the CONNECT Research Centre (13/RC/2077) and the FutureNeuro Research Centre (16/RC/3948). The work of MB was supported by the European Union's Horizon 2020 Research and Innovation Programme through the Marie Skłodowska-Curie Grant under Agreement 839553.

REFERENCES

Adonias, G. L., Yastrebova, A., Barros, M. T., Balasubramaniam, S., and Koucheryavy, Y. (2019). "A logic gate model based on neuronal molecular communication engineering," in *Proceedings of the 4th Workshop on Molecular Communications* (Linz), 15–16.

Adonias, G. L., Yastrebova, A., Barros, M. T., Koucheryavy, Y., Cleary, F., and Balasubramaniam, S. (2020). Utilizing neurons for digital logic circuits: a molecular communications analysis. *IEEE Trans. NanoBiosci.* 19, 224–236. doi: 10.1109/TNB.2020.2975942

Balevi, E., and Akan, O. B. (2013). A physical channel model for nanoscale neuro-spike communications. *IEEE Trans. Commun.* 61, 1178–1187. doi: 10.1109/TCOMM.2012.010213.110093

Barreto, E., and Cressman, J. R. (2011). Ion concentration dynamics as a mechanism for neuronal bursting. *J. Biol. Phys.* 37, 361–373. doi: 10.1007/s10867-010-9212-6

Baxter, D. A., and Byrne, J. H. (2014). "Chapter 14: Dynamical properties of excitable membranes," in *From Molecules to Networks, 3rd Edn*, eds J. H. Byrne, R. Heidelberger, and M. N. Waxham (Boston, MA: Academic Press), 409–442. doi: 10.1016/B978-0-12-397179-1.00014-2

Bennewitz, M. F., and Saltzman, W. M. (2009). Nanotechnology for delivery of drugs to the brain for epilepsy. *Neurotherapeutics* 6, 323–336. doi: 10.1016/j.nurt.2009.01.018

Blier, P., and De Montigny, C. (1987). Modification of 5-HT neuron properties by sustained administration of the 5-HT1A agonist gepirone: electrophysiological studies in the rat brain. *Synapse* 1, 470–480. doi: 10.1002/syn.890010511

Brunel, N., Chance, F. S., Fourcaud, N., and Abbott, L. F. (2001). Effects of synaptic noise and filtering on the frequency response of spiking neurons. *Phys. Rev. Lett.* 86, 2186–2189. doi: 10.1103/PhysRevLett.86.2186

Carnevale, N. T., and Hines, M. L. (2009). *The NEURON Book, 1st Edn*. New York, NY: Cambridge University Press.

Chandler, W., Fitzhugh, R., and Cole, K. S. (1962). Theoretical stability properties of a space-clamped axon. *Biophys. J.* 2(Pt 1), 105–127. doi: 10.1016/S0006-3495(62)86844-1

Chaubey, S., and Goodwin, S. J. (2016). A unified frequency domain model to study the effect of demyelination on axonal conduction. *Biomed. Eng. Comput. Biol.* 7:BECB.S38554. doi: 10.4137/BECB.S38554

Feng, T., Huang, X., Ni, R., Suen, W. L. L., and Chau, Y. (2019). "Nanoparticles for drug delivery targeting neurodegeneration in brain and eye," in *Nanomaterials for Drug Delivery and Therapy*, ed A. M. Grumezescu (Norwich, NY: William Andrew Publishing), 149–183. doi: 10.1016/B978-0-12-816505-8.00006-0

Fortune, E. S., and Rose, G. J. (1997). Passive and active membrane properties contribute to the temporal filtering properties of midbrain neurons *in vivo*. *J. Neurosci.* 17, 3815–3825. doi: 10.1523/JNEUROSCI.17-10-03815.1997

Gardner, D. (1989). Noise modulation of synaptic weights in a biological neural network. *Neural Netw.* 2, 69–76. doi: 10.1016/0893-6080(89)90016-6

Geerts, H., Wikswo, J., van der Graaf, P. H., Bai, J. P., Gaiteri, C., Bennett, D., et al. (2020). Quantitative systems pharmacology for neuroscience drug discovery and development: current status, opportunities, and challenges. *Pharmacometr. Syst. Pharmacol.* 9, 5–20. doi: 10.1002/psp4.12478

Gerstner, W., Kistler, W. M., Naud, R., and Paninski, L. (2014). *Neuronal Dynamics: From Single Neurons to Networks and Models of Cognition and Beyond*. Cambridge, UK: Cambridge University Press. doi: 10.1017/CBO9781107447615

Goldental, A., Guberman, S., Vardi, R., and Kanter, I. (2014). A computational paradigm for dynamic logic-gates in neuronal activity. *Front. Comput. Neurosci.* 8:52. doi: 10.3389/fncom.2014.00052

Guillamon, A., McLaughlin, D. W., and Rinzel, J. (2006). Estimation of synaptic conductances. *J. Physiol.* 100, 31–42. doi: 10.1016/j.jphysparis.2006.09.010

Hanisch, N., and Pierobon, M. (2017). "Digital modulation and achievable information rates of thru-body haptic communications," in *Disruptive Technologies in Sensors and Sensor Systems, Vol. 10206* (Anaheim, CA: International Society for Optics and Photonics), 1020603. doi: 10.1117/12.2262842

Hines, M., Davison, A., and Muller, E. (2009). NEURON and python. *Front. Neuroinform.* 3:1. doi: 10.3389/neuro.11.001.2009

Hodgkin, A. L., and Huxley, A. F. (1952). A quantitative description of membrane current and its application to conduction and excitation in nerve. *J. Physiol.* 117, 500–544. doi: 10.1113/jphysiol.1952.sp004764

Hu, W., and Bean, B. P. (2018). Differential control of axonal and somatic resting potential by voltage-dependent conductances in cortical layer 5 pyramidal neurons. *Neuron* 97, 1315–1326.e3. doi: 10.1016/j.neuron.2018.02.016

Jirsa, V. K., Stacey, W. C., Quilichini, P. P., Ivanov, A. I., and Bernard, C. (2014). On the nature of seizure dynamics. *Brain* 137, 2210–2230. doi: 10.1093/brain/awu133

Khodaei, A., and Pierobon, M. (2016). "An intra-body linear channel model based on neuronal subthreshold stimulation," in *2016 IEEE International Conference on Communications (ICC)* (Kuala Lumpur), 1–7. doi: 10.1109/ICC.2016.7511483

Koch, C. (2004). "Linearizing voltage-dependent currents," in *Biophysics of Computation: Information Processing in Single Neurons, Computational Neuroscience*, ed M. Stryker (New York, NY: Oxford University Press), 232–247.

Koslow, S., and Subramaniam, S. (2005). *Databasing the Brain: From Data to Knowledge (Neuroinformatics)*. Hoboken, NJ: Wiley.

Larouche, J., and Aguilar, C. A. (2018). New technologies to enhance in vivo reprogramming for regenerative medicine. *Trends Biotechnol.* 37, 604–617. doi: 10.1016/j.tibtech.2018.11.003

Lienert, F., Lohmueller, J. J., Garg, A., and Silver, P. A. (2014). Synthetic biology in mammalian cells: next generation research tools and therapeutics. *Nat. Rev. Mol. Cell Biol.* 15, 95–107. doi: 10.1038/nrm3738

Long, L. and Fang, G. (2010). "A review of biologically plausible neuron models for spiking neural networks," in *AIAA Infotech@Aerospace 2010* (Atlanta, GA: America Institute of Aeronautics and Astronautics), 1–14. doi: 10.2514/6.2010-3540

Markram, H., Muller, E., Ramaswamy, S., Reimann, M. W., Abdellah, M., Sanchez, C. A., et al. (2015). Reconstruction and simulation of neocortical microcircuitry. *Cell* 163, 456–492. doi: 10.1016/j.cell.2015.09.029

Mauro, A., Conti, F., Dodge, F., and Schor, R. (1970). Subthreshold behavior and phenomenological impedance of the squid giant axon. *J. Gen. Physiol.* 55, 497–523. doi: 10.1085/jgp.55.4.497

Mishra, A., and Majhi, S. K. (2019). A comprehensive survey of recent developments in neuronal communication and computational neuroscience. *J. Indus. Inform. Integr.* 13, 40–54. doi: 10.1016/j.jii.2018.11.005

Moreno-Bote, R., and Parga, N. (2004). Role of synaptic filtering on the firing response of simple model neurons. *Phys. Rev. Lett. 92:028102.* doi: 10.1103/PhysRevLett.92.028102

Motanis, H., Seay, M. J., and Buonomano, D. V. (2018). Short-term synaptic plasticity as a mechanism for sensory timing. *Trends Neurosci.* 41, 701–711. doi: 10.1016/j.tins.2018.08.001

Nise, N. S. (2015). *Control Systems Engineering, 7th Edn*. Pomona, CA: Wiley; California State Politechnic University.

Peters, A. (2010). "Chapter 4: The morphology of minicolumns," in *The Neurochemical Basis of Autism: From Molecules to Minicolumns*, ed G. J. Blatt (Boston, MA: Springer US), 45–68. doi: 10.1007/978-1-4419-1272-5_4

Plesser, H. E., and Geisel, T. (1999). Bandpass properties of integrate-fire neurons. *Neurocomputing* 26–27, 229–235. doi: 10.1016/S0925-2312(99)00076-4

Pospischil, M., Toledo-Rodriguez, M., Monier, C., Piwkowska, Z., Bal, T., Frégnac, Y., et al. (2008). Minimal Hodgkin-Huxley type models for

different classes of cortical and thalamic neurons. *Biol. Cybern*. 99, 427–441. doi: 10.1007/s00422-008-0263-8

Rolston, J. D., Englot, D. J., Wang, D. D., Shih, T., and Chang, E. F. (2012). Comparison of seizure control outcomes and the safety of vagus nerve, thalamic deep brain, and responsive neurostimulation: evidence from randomized controlled trials. *Neurosurg. Focus FOC* 32:E14. doi: 10.3171/2012.1.FOCUS11335

Sabah, N., and Leibovic, K. (1969). Subthreshold oscillatory responses of the Hodgkin-Huxley cable model for the squid giant axon. *Biophys. J.* 9, 1206–1222. doi: 10.1016/S0006-3495(69)86446-5

Scharfman, H. E. (2007). The neurobiology of epilepsy. *Curr. Neurol. Neurosci. Rep*. 7, 348–354. doi: 10.1007/s11910-007-0053-z

Sengupta, B., Faisal, A. A., Laughlin, S. B., and Niven, J. E. (2013). The effect of cell size and channel density on neuronal information encoding and energy efficiency. *J. Cereb. Blood Flow Metab*. 33, 1465–1473. doi: 10.1038/jcbfm.2013.103

Veletić, M., Barros, M. T., Balasingham, I., and Balasubramaniam, S. (2019). "A molecular communication model of exosome-mediated brain drug delivery," in *Proceedings of the Sixth Annual ACM International Conference on Nanoscale Computing and Communication, NANOCOM'19* (New York, NY: Association for Computing Machinery), 1–7. doi: 10.1145/3345312.3345478

Vogels, T. P., and Abbott, L. F. (2005). Signal propagation and logic gating in networks of integrate-and-fire neurons. *J. Neurosci*. 25, 10786–10795. doi: 10.1523/JNEUROSCI.3508-05.2005

Wilson, C. J., Weyrick, A., Terman, D., Hallworth, N. E., and Bevan, M. D. (2004). A model of reverse spike frequency adaptation and repetitive firing of subthalamic nucleus neurons. *J. Neurophysiol*. 91, 1963–1980. doi: 10.1152/jn.00924.2003

Zhou, Y., Peng, Z., Seven, E. S., and Leblanc, R. M. (2018). Crossing the blood-brain barrier with nanoparticles. *J. Controll. Release* 270, 290–303. doi: 10.1016/j.jconrel.2017.12.015

Conflict of Interest: The authors declare that the research was conducted in the absence of any commercial or financial relationships that could be construed as a potential conflict of interest.

frontiers in Physics

BRIEF RESEARCH REPORT
published: 16 October 2020
doi: 10.3389/fphy.2020.571507

Synchronizability of Multilayer Networks With K-nearest-neighbor Topologies

Li Zhang[1] *and Yongqing Wu*[2]*

[1] Department of Mathematics, College of Science, Liaoning Technical University, Fuxin, China, [2] Basic Teaching Department, Liaoning Technical University, Huludao, China

In this paper, the synchronizability of multilayer K-nearest-neighbor networks is studied by using the master stability function method. The analytical expressions for the eigenvalues of the supra-Laplacian matrix are given for two-layer and multilayer K-nearest-neighbor networks. In addition, the impacts of various topological parameters (such as the network size, the node degree, the number of layers, the intra-layer and the inter-layer coupling strengths) on the network synchronizability are discussed. Finally, the theoretical results are verified through numerical simulation.

Keywords: multilayer network, K-nearest-neighbor topology, synchronizability, master stability function method, supra-Laplacian matrix

OPEN ACCESS

Edited by:
Jia-Bao Liu,
Anhui Jianzhu University, China

Reviewed by:
Anouar Ben Mabrouk,
University of Kairouan, Tunisia
Song Zheng,
Zhejiang University of Finance and Economics, China
Xiaoyang Liu,
Jiangsu Normal University, China

***Correspondence:**
Yongqing Wu
yqwuyywu@163.com

Specialty section:
This article was submitted to Mathematical and Statistical Physics, a section of the journal Frontiers in Physics

Received: *11 June 2020*
Accepted: *08 September 2020*
Published: *16 October 2020*

Citation:
Zhang L and Wu Y (2020) Synchronizability of Multilayer Networks With K-nearest-neighbor Topologies. Front. Phys. 8:571507. doi: 10.3389/fphy.2020.571507

1. INTRODUCTION

Since the appearance of small-world networks and scale-free networks [1, 2], complex networks have attracted much attention due to their pervading through various scientific fields. Till now, complex networks have been applied in nature and society, such as scientific cooperation networks, information networks, biological networks, power grids, social networks, and so on [3, 4]. Recently, a new description of the complex network called the multilayer network, where nodes interact with more than one type of links, was put forward and gradually became an important branch of complex networks [5–8].

Synchronization, as a significative collective behavior on complex networks, has been widely and extensively discussed during the past two decades [9–14]. Further, there has been an increasing interest focusing on the finite-time synchronization, especially when the synchronization is required to be realized in finite time because of practical need [15, 16]. On the other hand, scholars have done a lot of work to analyze the synchronization of multilayer networks. A general framework for studying the diffusion processes on multiplex networks was proposed in [17, 18]. In 2014, Aguirre et al. revealed that the connector nodes between layers play an important role in the synchronizability of interconnected networks [19]. Further, intra-layer synchronization, inter-layer synchronization, counterpart synchronization, and generalized synchronization in multiplex networks have been investigated [20–24]. Tang et al. proposed three necessary regions to describe the different types of coherent behaviors (such as complete synchronization, intra-layer synchronization, and inter-layer synchronization) in multiplex networks based on the master stability function method [25].

However, most of the existing works focused on the effects of network structures on the synchronizability of multilayer networks through numerical simulation. To better understand the relationships between topological parameters and synchronizability, it is necessary to give a more rigorous theoretical analysis. Recently, the analytical expressions for the eigenvalues of multilayer

fully-connected networks, star networks, chain networks, and star-ring networks were derived to analyze the synchronizability [26–30]. To the best of our knowledge, very little work has been devoted to studying the synchronizability of multilayer K-nearest-neighbor networks. Due to the complexity of the multilayer networks, it is still a real challenge to derive the analytical expressions for the eigenvalue spectrum of the supra-Laplacian matrix.

Motivated by the above discussion, we study the synchronizability of multilayer networks with K-nearest-neighbor topologies. The present study uses the master stability function method to investigate the relationships between various topological parameters and network synchronizability. With this framework, we strictly derive the analytical expressions for the eigenvalues of two-layer and multilayer K-nearest-neighbor networks. Analytical and numerical results show that the network size, the node degree, the number of layers, the intra-layer and the inter-layer coupling strengths can have important effects on the synchronizability of multilayer K-nearest-neighbor networks.

The structure of this paper is organized as follows. The model of multilayer networks and some preliminaries are given in section 2. Section 3 studies the synchronizability of two-layer and multilayer K-nearest-neighbor networks. Numerical examples in section 4 illustrate the effectiveness of theoretical results. The conclusion is finally drawn in section 5.

2. PROBLEM FORMULATION AND PRELIMINARIES

The dynamics of multilayer networks consisting of M layers are described as follows [25]:

$$\frac{dX_i^{\alpha}}{dt} = f\left(X_i^{\alpha}\right) - a\sum_{j=1}^{N} w_{ij}^{\alpha} H\left(X_j^{\alpha}\right) - d\sum_{\beta=1}^{M} d_i^{\alpha\beta}\Gamma\left(X_i^{\beta}\right), \quad (1)$$

where $X_i^{\alpha} \in R^n$ is the state of the *i-th* node in the α*-th* layer, $1 \le i \le N$, $1 \le \alpha \le M$. $f : R^n \to R^n$ is a smooth nonlinear vector function. The continuous function $H : R^n \to R^n$ and a are the intra-layer coupling function and coupling strength, respectively. $\Gamma : R^n \to R^n$ and d are the inter-layer coupling function and coupling strength, respectively. For simplicity, let $H(X_j^{\alpha}) = HX_j^{\alpha}$, $\Gamma(X_i^{\alpha}) = \Gamma X_i^{\alpha}$ and $H = \Gamma$. In the α*-th* layer, if the *i-th* node is connected with the *j-th* ($j \ne i$) node, $w_{ij}^{\alpha} = -1$, otherwise, $w_{ij}^{\alpha} = 0$, and $w_{ii}^{\alpha} = -\sum_{j=1, j\ne i}^{N} w_{ij}^{\alpha}$ ($i, j = 1, 2, ..., N$ and $\alpha = 1, 2, ..., M$). $L^{(\alpha)} = (aw_{ij}^{\alpha}) \in R^{N\times N}$ is the Laplacian matrix of the α*-th* layer. Similarly, if the *i-th* node, in the α*-th* layer, is connected with its replica in the β*-th* ($\alpha \ne \beta$) layer, $d_i^{\alpha\beta} = -1$, otherwise $d_i^{\alpha\beta} = 0$, and $d_i^{\alpha\alpha} = -\sum_{k=1, k\ne\alpha}^{M} d_i^{\alpha k}$ ($\alpha, \beta = 1, 2, ..., M$ ($\alpha \ne \beta$)). It is obvious that $L^I = (dd_i^{\alpha\beta}) \in R^{M\times M}$ is the interlayer Laplacian matrix.

Denote

$$X^{(\alpha)} = \begin{pmatrix} X_1^{\alpha} \\ X_2^{\alpha} \\ \vdots \\ X_N^{\alpha} \end{pmatrix}, X = \begin{pmatrix} X^{(1)} \\ X^{(2)} \\ \vdots \\ X^{(M)} \end{pmatrix},$$

$$\tilde{f}(X^{(\alpha)}) = \begin{pmatrix} f(X_1^{\alpha}) \\ f(X_2^{\alpha}) \\ \vdots \\ f(X_N^{\alpha}) \end{pmatrix}, F(X) = \begin{pmatrix} \tilde{f}(X^{(1)}) \\ \tilde{f}(X^{(2)}) \\ \vdots \\ \tilde{f}(X^{(M)}) \end{pmatrix},$$

then we can rewrite the evolution of the multilayer network (1) as following form:

$$\frac{dX}{dt} = F(X) - \left(\left(\mathcal{L}^L + \mathcal{L}^I\right) \otimes \Gamma\right) X, \quad (2)$$

where

$$\mathcal{L}^L = \begin{pmatrix} L^{(1)} & 0 & \cdots & 0 \\ 0 & L^{(2)} & \cdots & 0 \\ \vdots & \vdots & \ddots & \vdots \\ 0 & 0 & \cdots & L^{(M)} \end{pmatrix} = \bigoplus_{\alpha=1}^{M} L^{(\alpha)}, \quad (3)$$

$$\mathcal{L}^I = L^I \otimes I_N. \quad (4)$$

Here, $\otimes$ is the Kronecker product, $\oplus$ is the direct sum operation, I_N is the $N \times N$ identity matrix. Then we can get the supra-Laplacian matrix of multilayer networks (1),

$$\mathcal{L} = \mathcal{L}^L + \mathcal{L}^I. \quad (5)$$

The decomposition of the supra-Laplacian matrix given in Equation (5) is fundamental for the discovery of several spectral performances of the multilayer networks [17]. According to the master stability function (MSF) framework [31], the synchronized regions of dynamical systems can be classified into four classes: empty, bounded, unbounded and the union of some bounded and unbounded regions. Here, we only focus on the bounded and unbounded synchronized regions. If the synchronized region is unbounded, the network synchronizability is positively correlated to the non-zero minimum eigenvalue (λ_2) of the supra-Laplacian matrix. On the other hand, if the synchronized region is bounded, the eigenratio of the maximum eigenvalue and the non-zero minimum eigenvalue ($r = \lambda_{max}/\lambda_2$) characterizes the network synchronizability. A smaller r value means that there is a stronger synchronizability of the network.

Throughout the rest of this paper, a useful lemma is presented as follows.

Lemma 1. *(see [28]) Let A and B are two square matrices with the same size, then*

$$\begin{vmatrix} A & B & \cdots & B \\ B & A & \cdots & B \\ \vdots & \vdots & \ddots & \vdots \\ B & B & \cdots & A \end{vmatrix}_{M\times M} = |A - B|^{M-1} \cdot |A + (M-1)B|, \quad (6)$$

where M is a positive integer greater than 1.

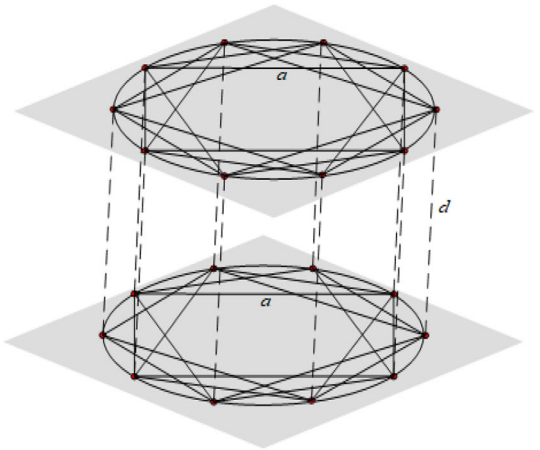

FIGURE 1 | Two-layer networks with K-nearest-neighbor topologies, where d is the inter-layer coupling strength and a is the intra-layer coupling strength.

3. SYNCHRONIZABILITY OF MULTILAYER NETWORKS

In this section, analytical results are presented for the synchronizability of multilayer networks with K-nearest-neighbor topologies.

3.1. Two-Layer K-nearest-neighbor Networks

We consider a two-layer model, each layer is a K-nearest-neighbor network with N nodes (K is an even number) and every node in one layer is connecting with its counterpart in the other layer. The corresponding structure can be shown in **Figure 1**.

So the supra-Laplacian matrix can be written as follows:

$$\mathcal{L} = \begin{pmatrix} A + dI_N & -dI_N \\ -dI_N & A + dI_N \end{pmatrix}, \tag{7}$$

where

$$A = \begin{pmatrix} Ka & \overbrace{-a\cdots-a}^{\frac{K}{2}} & 0 & \cdots & 0 & \overbrace{-a\cdots-a}^{\frac{K}{2}} \\ -a & Ka & \overbrace{-a\cdots-a}^{\frac{K}{2}} & 0 & \cdots 0 & \overbrace{-a\cdots-a}^{\frac{K}{2}-1} \\ -a & -a & Ka & \overbrace{-a\cdots-a}^{\frac{K}{2}} & 0\cdots 0 & \overbrace{-a\cdots-a}^{\frac{K}{2}-2} \\ \vdots & \ddots & \ddots & \ddots & \ddots & \vdots \\ \overbrace{-a\cdots-a}^{\frac{K}{2}-1} & 0\cdots & 0 & \overbrace{-a\cdots-a}^{\frac{K}{2}} & Ka & -a \\ \overbrace{-a\cdots-a}^{\frac{K}{2}} & 0 & \cdots & 0 & \overbrace{-a\cdots-a}^{\frac{K}{2}} & Ka \end{pmatrix}.$$

TABLE 1 | Change of a, d, K, N for λ_2, $r = \lambda_{max}/\lambda_2$ of two-layer K-nearest-neighbor networks.

		Increase of	a	d	K	N
λ_2	$d < \frac{a\pi^2K(K+1)(K+2)}{12N^2}$	$\lambda_2 \approx 2d$	—	↑	—	—
	$d > \frac{a\pi^2K(K+1)(K+2)}{12N^2}$	$\lambda_2 \approx \frac{a\pi^2K(K+1)(K+2)}{6N^2}$	↑	—	↑	↓
$r = \frac{\lambda_{max}}{\lambda_2}$	$d < \frac{a\pi^2K(K+1)(K+2)}{12N^2}$	$r \approx \frac{a(K+1)(3\pi+2)+6\pi d}{6\pi d}$	↑	↓	↑	—
	$d > \frac{a\pi^2K(K+1)(K+2)}{12N^2}$	$r \approx \frac{2aN^2(K+1)(3\pi+2)+12\pi dN^2}{a\pi^3K(K+1)(K+2)}$	↓	↑	↓	↑

↑, *increase*; ↓, *decrease*; —, *unchange*.

According to Lemma 1, we can get the characteristic polynomial of $\mathcal{L}$:

$$\begin{aligned} |\lambda I_{2N} - \mathcal{L}| &= \begin{vmatrix} \lambda I_N - (A + dI_N) & dI_N \\ dI_N & \lambda I_N - (A + dI_N) \end{vmatrix} \\ &= |(\lambda - 2d)I_N - A| \cdot |\lambda I_N - A| . \end{aligned} \tag{8}$$

Let $|\lambda I_N - A| = 0$, the eigenvalues of the K-nearest neighbor network can be written as [32]:

$$\lambda_l = Ka - 2a\sum_{j=1}^{K/2} \cos\left(\frac{2\pi\left(l-1\right)j}{N}\right), \quad l = 1, 2, ..., N.$$

Let $|(\lambda - 2d)I_N - A| = 0$, it follows that

$$\lambda_l - 2d = Ka - 2a\sum_{j=1}^{K/2} \cos\left(\frac{2\pi\left(l-1\right)j}{N}\right), \quad l = 1, 2, ..., N.$$

Then, the eigenvalues of $\mathcal{L}$ are

$$\begin{aligned} 0, Ka - 2a\sum_{j=1}^{K/2} \cos\left(\frac{2\pi\left(l-1\right)j}{N}\right), 2d, Ka \\ + 2d - 2a\sum_{j=1}^{K/2} \cos\left(\frac{2\pi\left(l-1\right)j}{N}\right), \\ l = 2, 3, ..., N. \end{aligned} \tag{9}$$

When $1 \ll K \ll N$, we can obtain the smallest non-zero eigenvalue λ_2 and the largest eigenvalue λ_{max} based on the series expansion,

$$\lambda_2 \approx \min\left\{\frac{a\pi^2K\left(K+1\right)\left(K+2\right)}{6N^2}, 2d\right\}, \tag{10}$$

$$\lambda_{max} \approx a\left(K+1\right)\left(1+\frac{2}{3\pi}\right) + 2d. \tag{11}$$

The relationships between λ_2, $r = \lambda_{max}/\lambda_2$ and the network parameters are shown in **Table 1**.

Remark 1. *When $K = 2$, the eigenvalues of single networks are $\lambda_l = 2a - 2a\cos\left(\frac{2\pi(l-1)}{N}\right) = 4a\sin^2\left(\frac{(l-1)\pi}{N}\right), l = 1, 2, ..., N$. Then, the eigenvalues of supra-Laplacian matrix $\mathcal{L}$ are $4a\sin^2\left(\frac{(l-1)\pi}{N}\right), 2d + 4a\sin^2\left(\frac{(l-1)\pi}{N}\right), l = 1, 2, ..., N$. In [26], synchronizability of duplex ring networks was investigated. Obviously, the network model of this paper is more general.*

3.2. Multilayer K-nearest-neighbor Networks

Similarly, we consider the multilayer network with M layers, the corresponding structure is shown in **Supplementary Figure 1**.

We obtain the supra-Laplacian matrix $\mathcal{L}$,

$$\mathcal{L} = \begin{pmatrix} A+(M-1)dI_N & -dI_N & \cdots & -dI_N \\ -dI_N & A+(M-1)dI_N & \cdots & -dI_N \\ \vdots & \vdots & \ddots & \vdots \\ -dI_N & -dI_N & \cdots & A+(M-1)dI_N \end{pmatrix}_{M\times M}, \tag{12}$$

where A is given in section 3.1.

According to Lemma 1, the characteristic polynomial of $\mathcal{L}$ is:

$$\begin{aligned} &|\lambda I_{MN} - \mathcal{L}| \\ &= \begin{vmatrix} (\lambda-(M-1)d)I_N - A & dI_N & \cdots & dI_N \\ dI_N & (\lambda-(M-1)d)I_N - A & \cdots & dI_N \\ \vdots & \vdots & \ddots & \vdots \\ dI_N & dI_N & \cdots & (\lambda-(M-1)d)I_N - A \end{vmatrix} \\ &= |(\lambda - Md)I_N - A|^{M-1} \cdot |\lambda I_N - A| \,. \end{aligned} \tag{13}$$

Then, the eigenvalues of $\mathcal{L}$ are

$$\begin{aligned} &0, Ka - 2a\sum_{j=1}^{K/2}\cos\left(\frac{2\pi\,(l-1)\,j}{N}\right), \underbrace{Md, ..., Md}_{M-1}, \\ &\underbrace{\begin{matrix} Ka + Md - 2a\sum_{j=1}^{K/2}\cos\left(\frac{2\pi(l-1)j}{N}\right), ..., Ka + Md \\ -2a\sum_{j=1}^{K/2}\cos\left(\frac{2\pi(l-1)j}{N}\right) \end{matrix}}_{M-1}, \\ &l = 2, 3, ..., N. \end{aligned} \tag{14}$$

When $1 \ll K \ll N$, we can obtain the smallest non-zero eigenvalue λ_2 and the largest eigenvalue λ_{max} based on the series expansion,

$$\lambda_2 \approx \min\left\{\frac{a\pi^2 K\,(K+1)\,(K+2)}{6N^2}, Md\right\}, \tag{15}$$

$$\lambda_{max} \approx a\,(K+1)\left(1+\frac{2}{3\pi}\right) + Md. \tag{16}$$

The relationships between λ_2, $r = \lambda_{max}/\lambda_2$ and the network parameters are shown in **Supplementary Table 1**.

Remark 2. *When $M = 2$, the smallest non-zero eigenvalue $\lambda_2 \approx \min\left\{\frac{a\pi^2K(K+1)(K+2)}{6N^2}, 2d\right\}$ and the largest eigenvalue $\lambda_{max} \approx a\,(K+1)\left(1+\frac{2}{3\pi}\right) + 2d$, which are equal to the eigenvalues in Equations (10) and (11). Actually, the two-layer network is a special case of the multilayer network.*

4. NUMERICAL SIMULATIONS

In this section, numerical examples are presented to study the synchronizability of the multilayer K-nearest-neighbor networks.

4.1. The Synchronizability of Two-Layer Networks

(1) Let $N = 200$, $K = 50$, $d = 1$, the impact of the intra-layer coupling strength a on network synchronizability is shown in **Figures 2A,B**. When the synchronized region is unbounded, **Figure 2A** displays that λ_2 increases with small a ($a < a_0 = \frac{12N^2d}{\pi^2K(K+1)(K+2)} \approx 0.3668$), and then reaches a certain value $\lambda_2 = 2d = 2$. This implies that the synchronizability of two-layer networks is first enhanced with small values of increasing a and then held constant with ever-increasing a. When the synchronized region is bounded, it can be observed from **Figure 2B** that the eigenratio $r = \lambda_{max}/\lambda_2$ first decreases with small a ($a < a_0$) and then increases monotonically. It means that the synchronizability is enhanced firstly, then gets weakened after reaching the maximum. The synchronizability of two-layer networks is maximized at $a_0 = \frac{12N^2d}{\pi^2K(K+1)(K+2)}$.

(2) Let $N = 200$, $K = 50$, $a = 0.5$, the impact of the inter-layer coupling strength d on network synchronizability is shown in **Figures 2C,D**. When $0.5 < d < d_0 = \frac{a\pi^2K(K+1)(K+2)}{12N^2} \approx 1.3632$, **Figure 2C** depicts that λ_2 increases linearly with small d. When $d > d_0$, it reaches a certain value $\lambda_2 = 2d_0$. This implies that, with an unbounded synchronized region, the synchronizability is first enhanced with small d and then kept invariant. In **Figure 2D**, it can be observed that the eigenratio $r = \lambda_{max}/\lambda_2$ first decreases with small d ($d < d_0$) and then increases slowly. It means that, with a bounded synchronized region, the synchronizability is enhanced firstly and then slowly gets weakened after reaching the maximum. The synchronizability of two-layer networks is maximized at $d_0 = \frac{a\pi^2K(K+1)(K+2)}{12N^2}$.

(3) Let $N = 200$, $d = 5$, $a = 0.5$, the relationship between the synchronizability and the node degree K is shown in **Figures 3A,B**. When the synchronized region is unbounded, as shown in **Figure 3A**, λ_2 increases sharply with increasing K ($50 < K < K_0 = 77$), and then reaches a $\lambda_2 = 2d = 10$. This implies that the synchronizability of two-layer networks is first enhanced and enhanced and then kept invariant. When the synchronized region is bounded, it can be observed from from **Figure 3B** that the eigenratio $r = \lambda_{max}/\lambda_2$ first decreases with increasing K ($50 < K < K_0 = 77$) and then increases monotonically. It means that the synchronizability is enhanced sharply with increasing K, then reaches its maximum, and finally gets weakened. The two-layer networks is maximized at $K_0 = 77$.

(4) Let $K = 50$, $a = d = 1$, the relationship between the synchronizability and the network size N is shown in **Figures 3C,D**. When $300 < N < 330$, it depicts that λ_2 and the eigenratio $r = \lambda_{max}/\lambda_2$ remain invariant with increasing N. When $N > 330$, λ_2 decreases with increasing N, and the eigenratio $r = \lambda_{max}/\lambda_2$ increases with increasing N. This implies that, with unbounded or bounded synchronized regions, the synchronizability is first kept invariant and then gets weakened with increasing the network size N.

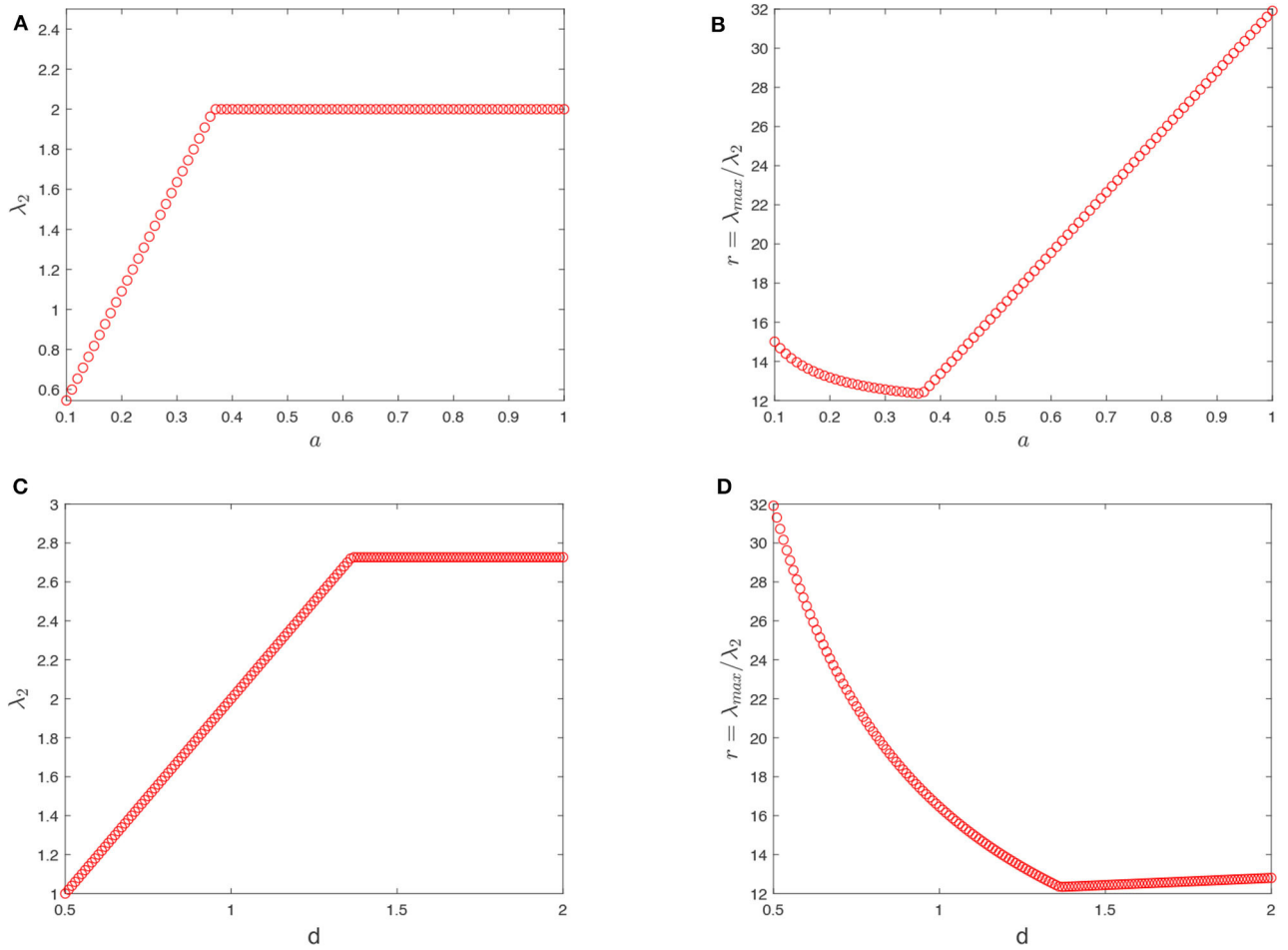

FIGURE 2 | Synchronizability of two-layer K-nearest-neighbor networks. Panels **(A,B)** display λ_2 and $r = \lambda_{max}/\lambda_2$ vs. the intra-layer coupling strength a ($N = 200$, $K = 50$, $d = 1$). Panels **(C,D)** display λ_2 and $r = \lambda_{max}/\lambda_2$ vs. the inter-layer coupling strength d ($N = 200$, $K = 50$, $a = 0.5$).

4.2. The Synchronizability of Multilayer Networks

Here, we investigate the synchronizability of multilayer K-nearest-neighbor networks. As shown in **Supplementary Figures 2,3**, the impact of the intra-layer coupling strength a, the inter-layer coupling strength d, the node degree K and the network size N on network synchronizability are similar to the two-layer K-nearest-neighbor networks.

It can be seen from **Supplementary Figure 2** that λ_2 increases nearly linearly at the beginning and then reaches a upper bounded value, the eigenratio $r = \lambda_{max}/\lambda_2$ first decreases and then increases monotonically. It reveals that the synchronizability is enhanced firstly, and then reaches its maximum. Furthermore, the optimal parameters $a_0 = \frac{6MN^2d}{\pi^2K(K+1)(K+2)} \approx 1.8339$, $d_0 = \frac{a\pi^2K(K+1)(K+2)}{6MN^2} \approx 0.2726$ and $K_0 = 133$ are obtained to maximize the synchronizability of multilayer networks. **Supplementary Figures 3A,B** depict that λ_2 and the eigenratio $r = \lambda_{max}/\lambda_2$ remain invariant with increasing N ($100 < N < 147$). When $N > 147$, λ_2 decreases and the eigenratio $r = \lambda_{max}/\lambda_2$ increases with increasing N. This implies that, the synchronizability is first kept invariant and then gets weakened with increasing the network size N. Let $N = 200$, $K = 50$, $a = d = 0.5$, **Supplementary Figures 3C,D** show that λ_2 increases at the beginning and then keeps invariant, the eigenratio $r = \lambda_{max}/\lambda_2$ first decreases and then increases slowly with increasing the number of layers M. The observation reveals that the synchronizability of multilayer networks is maximized at $M_0 = 6$.

5. CONCLUSION

This paper aims to investigate the synchronizability of multilayer networks with K-nearest-neighbor topologies. The master stability function method allows one to analyze how various topological parameters influence network synchronizability. Here, the analytical expressions for the eigenvalues of two-layer and multilayer K-nearest-neighbor networks have been obtained. Further, we have discussed the impacts of the network size, the node degree, the number of layers, the intra-layer

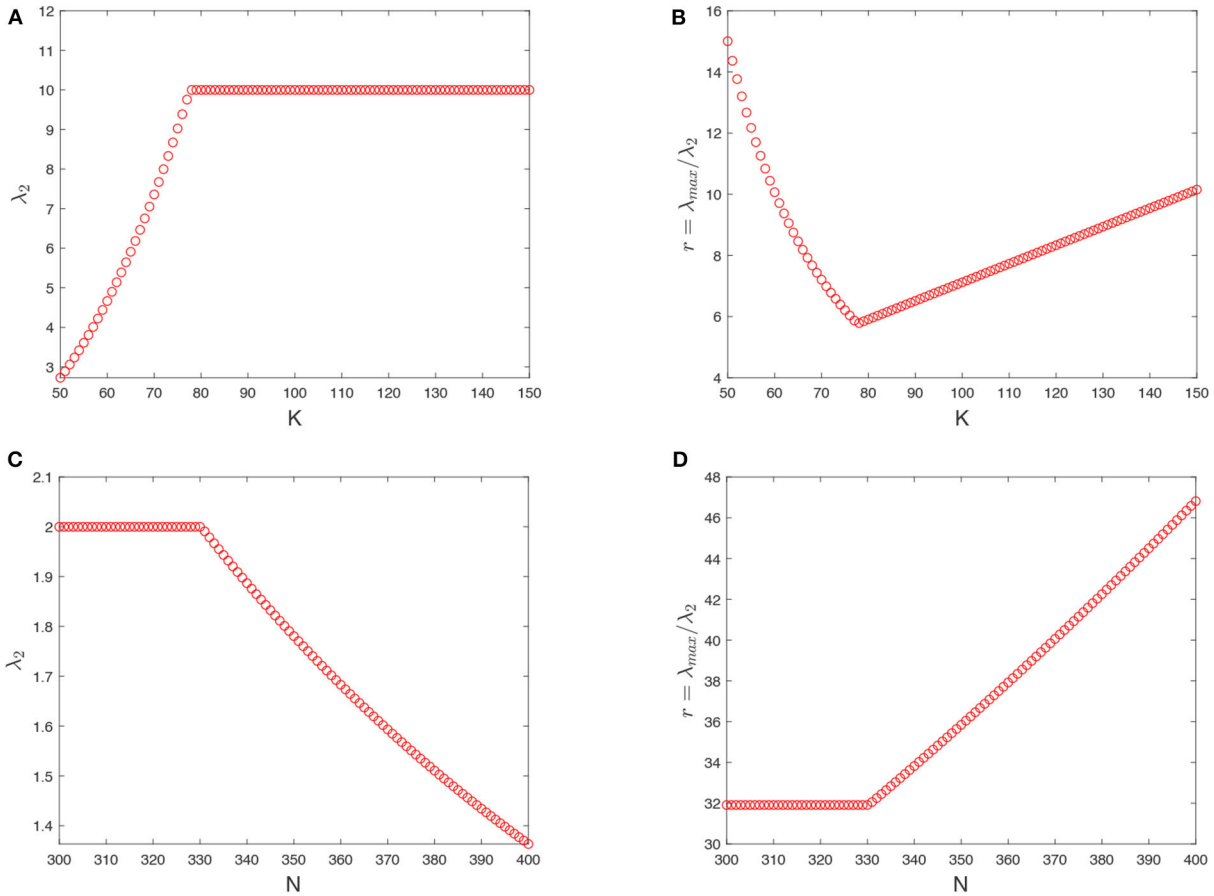

FIGURE 3 | Synchronizability of two-layer K-nearest-neighbor networks. Panels **(A,B)** display λ_2 and $r = \lambda_{max}/\lambda_2$ vs. the node degree K ($N = 200$, $d = 5$, $a = 0.5$). Panels **(C,D)** display λ_2 and $r = \lambda_{max}/\lambda_2$ vs. the network size N ($K = 50$, $a = d = 1$).

and the inter-layer coupling strengths on the synchronizability of multilayer K-nearest-neighbor networks. Recently, network coherence [33, 34] is an interesting but challenging topic, and coherence analysis of multilayer networks is a part of our future work.

DATA AVAILABILITY STATEMENT

All datasets generated for this study are included in the article/**Supplementary Material**.

AUTHOR CONTRIBUTIONS

LZ and YW contributed to the conception and design of the study. YW organized the literature. LZ performed the design of figures and wrote the first draft of the manuscript. All authors contributed to the manuscript revision and read and approved the submitted version.

FUNDING

This work was supported by the National Natural Science Foundation of China (Grant No. 61304173), and Foundation of Liaoning Educational Committee (Grant No. LJ2017QL021).

SUPPLEMENTARY MATERIAL

The Supplementary Material for this article can be found online at: https://www.frontiersin.org/articles/10.3389/fphy.2020.571507/full#supplementary-material

REFERENCES

1. Watts DJ, Strogatz SH. Collective dynamics of 'small-world' networks. *Nature*. (1998) **393**:440–2. doi: 10.1038/30918
2. Barabási AL, Albert R. Emergence of scaling in random networks. *Science*. (1999) **286**:509–12. doi: 10.1126/science.286.5439.509
3. Boccaletti S, Latora V, Moreno Y, Chavez M, Hwang DU. Complex networks: structure and dynamics. *Phys Rep*. (2006) **424**:175–308. doi: 10.1016/j.physrep.2005.10.009

4. Newman MEJ. *Networks: An Introduction*. Oxford: Oxford University Press (2010).
5. Mucha PJ, Richardson T, Macon K, Porter MA, Onnela JP. Community structure in time-dependent, multiscale, and multiplex networks. *Science*. (2010) **328**:876–8. doi: 10.1126/science.1184819
6. Lee K, Kim JY, Lee S, Goh K. Multiplex networks. In: D'Agostino G, Scala A, editors. *Networks of Networks: The Last Frontier of Complexity*. Berlin: Springer International Publishing (2014). p.53–72.
7. Kivelä M, Arenas A, Barthelemy M, Gleeson JP, Moreno Y, Porter MA. Multilayer networks. *J Complex Netw*. (2014) **2**:203–71. doi: 10.1093/comnet/cnu016
8. Boccaletti S, Bianconi G, Criado R, del Genio CI, Gómez-Gardeñes J, Romance M, et al. The structure and dynamics of multilayer networks. *Physics Reports*. (2014) **544**:1-C122. doi: 10.1016/j.physrep.2014.07.001
9. Wang XF, Chen GR. Synchronization in small-world dynamical networks. *Int J Bifurcat Chaos*. (2002) **12**:187–92. doi: 10.1142/S0218127402004292
10. Wang XF, Chen GR. Synchronization in scale-free dynamical networks: robustness and fragility. *IEEE Trans Circ Syst I Fundament Theory Appl*. (2002) **49**:54–62. doi: 10.1109/81.974874
11. Arenas A, Díaz-Guilera A, Kurths J, Moreno Y, Zhou CS. Synchronization in complex networks. *Phys Rep*. (2008) **469**:93–153. doi: 10.1016/j.physrep.2008.09.002
12. Li CP, Sun WG, Kurths J. Synchronization between two coupled complex networks. *Physical Review E*. (2007) **76**:046204. doi: 10.1103/PhysRevE.76.046204
13. Yu WW, Chen GR, Lü JH, Kurths J. Synchronization via pinning control on general complex networks. *SIAM J Control Optimizat*. (2013) **51**:1395–416. doi: 10.1137/100781699
14. Xu J, Li N, Zhang XL, Qin XL. Fuzzy synchronization control for fractional-order chaotic systems with different structures. *Front Phys*. (2020) **8**:155. doi: 10.3389/fphy.2020.00155
15. Liu XY, Lam J, Yu WW, Chen GR. Finite-time consensus of multiagent systems with a switching protocol. *IEEE Trans Neural Netw Learn Syst*. (2016) **27**:853–62. doi: 10.1109/TNNLS.2015.2425933
16. Liu XY, Su HS, Chen MZQ. A switching approach to designing finite-time synchronization controllers of coupled neural networks. *IEEE Trans Neural Netw Learn Syst*. (2016) **27**:471–82. doi: 10.1109/TNNLS.2015.2448549
17. Gómez S, Diaz-Guilera A, Gómez-Gardeñes J, Perez-Vicente CJ. Diffusion dynamics on multiplex networks. *Phys Rev Lett*. (2013) **110**:028701. doi: 10.1103/PhysRevLett.110.028701
18. Solé-Ribalta A, De Domenico M, Kouvaris NE, Diaz-Guilera A, Gomez S, Arenas A. Spectral properties of the Laplacian of multiplex networks. *Phys Rev E*. (2013) **88**:032807. doi: 10.1103/PhysRevE.88.032807
19. Aguirre J, Sevilla-Escoboza R, Gutiérrez R, Papo D, Buldú JM. Synchronization of interconnected networks: the role of connector nodes. *Phys Rev Lett*. (2014) **112**:248701. doi: 10.1103/PhysRevLett.112.248701
20. Gambuzza LV, Frasca M, Gómez-Gardeñes J. Intra-layer synchronization in multiplex networks. *Europhys Lett*. (2015) **110**:20010. doi: 10.1209/0295-5075/110/20010
21. Sevilla-Escoboza R, Sendiña-Nadal I, Leyva I, Gutierrez R, Buldu JM, Boccaletti S. Inter-layer synchronization in multiplex networks of identical layers. *Chaos*. (2016) **26**:065304. doi: 10.1063/1.4952967
22. Leyva I, Sevilla-Escoboza R, Sendiña-Nadal I, Gutierrez R, Buldu JM, Boccaletti S. Inter-layer synchronization in non-identical multi-layer networks. *Sci Rep*. (2017) **7**:45475. doi: 10.1038/srep45475
23. Wei X, Wu XQ, Lu JA, Zhao JC. Counterpart synchronization of duplex networks with delayed nodes and noise perturbation. *J Stat Mech Theory Exp*. (2015) **2015**:P11021. doi: 10.1088/1742-5468/2015/11/P11021
24. Ning D, Wu XQ, Lu JA, Lü JH. Driving-based generalized synchronization in two-layer networks via pinning control. *Chaos*. (2015) **25**:113104. doi: 10.1063/1.4935069
25. Tang LK, Wu XQ, Lü JH, Lu JA, D'Souza RM. Master stability functions for complete, intralayer, and interlayer synchronization in multiplex networks of coupled Rössler oscillators. *Phys Rev E*. (2019) **99**:012304. doi: 10.1103/PhysRevE.99.012304
26. Wei J, Wu XQ, Lu JA, Wei X. Synchronizability of duplex regular networks. *Europhys Lett*. (2017) **120**:20005. doi: 10.1209/0295-5075/120/20005
27. Xu MM, Lu JA, Zhou J. Synchronizability and eigenvalues of two-layer star networks. *Acta Phys Sin*. (2016) **65**:028902. doi: 10.7498/aps.65.028902
28. Sun J, Li XX, Zhang JH, Shen YZ, Li YY. Synchronizability and eigenvalues of multilayer star networks through unidirectionally coupling. *Acta Phys Sin*. (2017) **66**:188901 (in Chinese). doi: 10.7498/aps.66.188901
29. Deng Y, Jia Z, Deng GM, Zhang QF. Eigenvalue spectrum and synchronizability of multiplex chain networks. *Phys A*. (2020) **537**:122631. doi: 10.1016/j.physa.2019.122631
30. Deng Y, Jia Z, Yang FM. Synchronizability of multilayer star and star-ring networks. *Discrete Dyn Nat Soc*. (2020) **2020**:9143917. doi: 10.1155/2020/9143917
31. Pecora LM, Carroll TL. Master stability functions for synchronized coupled systems. *Phys Rev Lett*. (1998) **80**:2109. doi: 10.1103/PhysRevLett.80.2109
32. Wang XF, Li X, Chen GR. *Network Science: An Introduction*. Beijing: High Education Press (2012) (in Chinese).
33. Hong MD, Sun WG, Liu SY, Xuan TF. Coherence analysis and Laplacian energy of recursive trees with controlled initial states. *Front Inf Technol Electron Eng*. (2020) **21**:931-8. doi: 10.1631/FITEE.1900133
34. Sun WG, Sun MT, Guan JB, Jia Q. Robustness of coherence in noisy scale-free networks and applications to identification of influential spreaders. *IEEE Trans Circ Syst II Express Briefs*. (2020) **67**:1274–8. doi: 10.1109/TCSII.2019.2929139

Conflict of Interest: The authors declare that the research was conducted in the absence of any commercial or financial relationships that could be construed as a potential conflict of interest.

frontiers in Physics

BRIEF RESEARCH REPORT
published: 16 October 2020
doi: 10.3389/fphy.2020.583603

Network Coherence in a Family of Book Graphs

Jing Chen[1], *Yifan Li*[2] *and Weigang Sun*[2]*

[1] School of Information Technology, Zhejiang Yuying College of Vocational Technology, Hangzhou, China, [2] School of Sciences, Hangzhou Dianzi University, Hangzhou, China

In this paper, we study network coherence characterizing the consensus behaviors with additive noise in a family of book graphs. It is shown that the network coherence is determined by the eigenvalues of the Laplacian matrix. Using the topological structures of book graphs, we obtain recursive relationships for the Laplacian matrix and Laplacian eigenvalues and further derive exact expressions of the network coherence. Finally, we illustrate the robustness of network coherence under the graph parameters and show that the parameters have distinct effects on the coherence.

Keywords: consensus, coherence, book graph, Laplacian spectra, recursive

OPEN ACCESS

Edited by:
Jia-Bao Liu,
Anhui Jianzhu University, China

Reviewed by:
Junhao Peng,
Guangzhou University, China
Zhongjun Ma,
Guilin University of Electronic Technology, China
Yu Sun,
Jiangsu University, China

***Correspondence:**
Weigang Sun
qdswg@163.com

Specialty section:
This article was submitted to Mathematical and Statistical Physics, a section of the journal Frontiers in Physics

Received: *15 July 2020*
Accepted: *08 September 2020*
Published: *16 October 2020*

Citation:
Chen J, Li Y and Sun W (2020) Network Coherence in a Family of Book Graphs. Front. Phys. 8:583603. doi: 10.3389/fphy.2020.583603

1. INTRODUCTION

With the discovery of deterministic small-world [1] and scale-free [2] networks, deterministically growing network models have gained increasing attention because they can provide exact results for topology and dynamics. As a special type of deterministic networks, fractal networks constructed by fractal structures, such as Koch fractals [3], Sierpinski fractals [4], and Vicsek fractals [5], have been widely studied. Presently the main issues that require consideration in fractal networks include random walks [6–9], consensus dynamics [10, 11] and percolation [12]. It is proved that fractal networks are good candidate network models for verifying the results of random graphs.

Calculating the Laplacian spectrum of a network plays an important role in the study of network characteristics. For example, the Kirchhoff index and global mean first-passage time of a network are related to the sum of reciprocals of non-zero eigenvalues [13–15]. The synchronizability [16] of a network refers to the ratio of the second smallest eigenvalue to the largest eigenvalue of the Laplacian matrix. In addition, the effective graph resistance is connected with the Laplacian spectrum [17]. Recently, network coherence [10] was introduced to characterize the extent of consensus of coupled agents under the noisy circumstance and was determined by the Laplacian spectrum in an H_2 norm. This concept of the network coherence helps to study the relationship between the Laplacian eigenvalues and network consistency. Great progress has been made for some special networks such as Vicsek fractals [10], tree-like networks [11], Sierpiński graphs [18] and weighted networks [19]. Many works have been devoted to studying the network coherence. Hong et al. studied the role of Laplacian energy on the coherence in a family of tree-like networks with controlled initial states [20]. Patterson and Bamieh investigated the leader-follower coherence and proposed optimal algorithms to select the leaders [21]. Later, Sun et al. proposed a leader centrality to identify more influential spreaders using the optimal coherence [22].

It is known that the topology of a graph dominates the Laplacian eigenvalues [23]. Thus, calculating the Laplacian eigenvalues is a technical challenge and it is theoretical and practical interest to find new ways to calculate them. In this paper, a family of book graphs is chosen as our network models. The topological indices, e.g., randic index, sum connectivity index, geometric-arithmetic index, fourth atom-bond connectivity index, and edge labeling, have been analytically

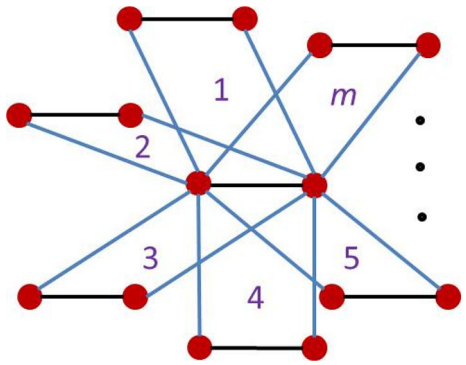

FIGURE 1 | Book graphs B_m.

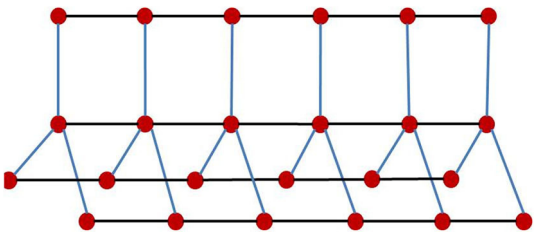

FIGURE 2 | Stacked book graphs $B_{m,n}$ with $m = 3, n = 6$.

obtained [24, 25]. However, the dynamics of the book graphs remains less understood, in spite of the facts that studying the dynamical processes leads to a better understanding of how the underlying systems work.

The rest of this paper is organized as follows. Book graphs and network coherence are presented in section 2. Section 3 gives detailed calculations of network coherence. Conclusions are given in section 4.

2. MODEL PRESENTATION AND NETWORK COHERENCE

2.1. Book Graphs

Book graphs B_m are defined as the graph Cartesian product [26], i.e., $B_m = S_{m+1} \square P_2$, where $S_m (m \geq 1)$ is a star graph and P_2 is the path graph on two nodes, see **Figure 1**. The stacked book graphs $B_{m,n}$ of order (m, n) are $B_{m,n} = S_{m+1} \square P_n$, where $P_n (n \geq 2)$ is the path graph on n nodes, see **Figure 2**.

2.2. Network Coherence

The network coherence was introduced to characterize the steady-state variance of the deviation from consensus. The relationship [10] between network coherence and Laplacian eigenvalues was established. The consensus dynamics with the additive noise are given by

$$\dot{x}_i(t) = -\sum_{j \in \Omega_i} L_{ij} x_j(t) + \eta_i(t),$$

where $x_i(t)$ is the state of node i and subject to the stochastic noise $\eta_i(t)$. L is the Laplacian matrix. Ω_i is the neighboring node set of node i, and $\eta_i(t)$ is a delta-correlated Gaussian noise.

Then, the first-order network coherence is defined as the mean, steady-state variance of the deviation from the average of all node values, i.e.,

$$H := \frac{1}{N} \sum_{i=1}^{N} \lim_{t \to \infty} \mathbf{var} \left\{ x_i(t) - \frac{1}{N} \sum_{j=1}^{N} x_j(t) \right\},$$

where **var** is the expectation of the squared deviation of a random variable from its mean.

Let $0 = \lambda_1 < \lambda_2 \leq \ldots \leq \lambda_N$ be the Laplacian eigenvalues. The network coherence is given by

$$H = \frac{1}{2N} \sum_{i=2}^{N} \frac{1}{\lambda_i}. \tag{1}$$

When the network has a smaller variance, it has a higher network coherence, meaning that it is more robust to the noise.

3. CALCULATIONS OF NETWORK COHERENCE

In this section, we present the detailed calculations of the sum of reciprocals of the Laplacian eigenvalues and obtain exact expressions of network coherence. According to the structure of $B_{m,n}$, its Laplacian matrix reads as

$$L_{m,n} = \begin{pmatrix} L_m + I_{m+1} & -I_{m+1} & 0 & \cdots & 0 & 0 \\ -I_{m+1} & L_m + 2I_{m+1} & -I_{m+1} & \cdots & 0 & 0 \\ 0 & -I_{m+1} & L_m + 2I_{m+1} & \cdots & 0 & 0 \\ \vdots & \vdots & \vdots & \vdots & \vdots & \vdots \\ 0 & 0 & 0 & \cdots & L_m + 2I_{m+1} & -I_{m+1} \\ 0 & 0 & 0 & \cdots & -I_{m+1} & L_m + I_{m+1} \end{pmatrix},$$

where L_m is the Laplacian matrix of a star graph S_m, that is,

$$L_m = \begin{pmatrix} m & -1 & \cdots & -1 \\ -1 & 1 & \cdots & 0 \\ \vdots & \vdots & \vdots & \vdots \\ -1 & 0 & \cdots & 1 \end{pmatrix}.$$

Then, we need to solve the characteristic equation $L_{m,n} x = \lambda x$, which is given by

$$\begin{aligned} (L_m + I_{m+1}) x_1 - I_{m+1} x_2 &= \lambda x_1, \\ -I_{m+1} x_1 + (L_m + 2I_{m+1}) x_2 - I_{m+1} x_3 &= \lambda x_2, \\ \vdots \qquad\qquad\qquad\qquad\quad \vdots \quad &\vdots \\ -I_{m+1} x_{n-1} + (L_m + I_{m+1}) x_n &= \lambda x_n, \end{aligned} \tag{2}$$

where $x = (x_1^{\mathrm{T}}, x_2^{\mathrm{T}}, \ldots, x_n^{\mathrm{T}})^{\mathrm{T}}$ and the dimension of $x_i (1 \leq i \leq n)$ is $m + 1$.

Suppose $L_m x_i = \lambda_j x_i, i = 1, 2, \ldots, n$, where $\lambda_j (j = 1, 2, \ldots, m+1)$ are the eigenvalues of L_m. Then, Equation (2) becomes

$$\begin{array}{rl} \left(\lambda_j + 1\right) x_1 - x_2 & = \lambda x_1, \\ -x_1 + \left(\lambda_j + 2\right) x_2 - x_3 & = \lambda x_2, \\ \vdots \quad \vdots \quad \vdots & \\ -x_{n-1} + (\lambda_j + 1) x_n & = \lambda x_n. \end{array} \tag{3}$$

We then rewrite Equation (3) as

$$\left(R_n^j(\lambda) - \lambda_j\right) x_1 = 0, n \geq 2,$$

where

$$R_n^j(\lambda) = \lambda - 1 - \cfrac{1}{\lambda - \left(\lambda_j + 2\right) - \cfrac{1}{\lambda - \left(\lambda_j + 2\right) - \cfrac{1}{\cdots \lambda - \left(\lambda_j + 2\right) - \cfrac{1}{\lambda - \left(\lambda_j + 1\right)}}}}.$$

Further, we have

$$R_n^j(\lambda) = \lambda_j, j = 1, 2, \ldots, m+1. \tag{4}$$

We rewrite $R_n^j(\lambda)$ in a recursive form as

$$\begin{cases} R_n^j(\lambda) = \lambda - 1 - \dfrac{1}{R_{n-1}^j(\lambda) - \left(\lambda_j + 1\right)}, \\ R_2^j(\lambda) = \lambda - 1 - \dfrac{1}{\lambda - \left(\lambda_j + 1\right)} = \dfrac{\lambda^2 - (2 + \lambda_j)\lambda + \lambda_j}{\lambda - \left(\lambda_j + 1\right)}. \end{cases}$$

From Equation (4), each eigenvalue λ_j produces to n eigenvalues and $B_{m,n}$ has $n(m+1)$ eigenvalues, denoted by $\Lambda_n = \{\lambda_i^n | 1 \leq i \leq n(m+1)\} = \Lambda_n^1 \cup \Lambda_n^2 \ldots \cup \Lambda_n^{m+1}$. For convenient calculations, we denote the smallest eigenvalues $\lambda_1^n = 0$. In the following subsections, we divide λ_j into two cases: $\lambda_j \neq 0$ and $\lambda_j = 0$ to obtain the network coherence.

3.1. When $\lambda_j \neq 0, j = 2, \ldots, m+1$

Let $R_n^j(\lambda) = T_n^j(\lambda)/P_n^j(\lambda)$, where $T_n^j(\lambda)$ and $P_n^j(\lambda)$ are two polynomials satisfying $\gcd[T_n^j(\lambda), P_n^j(\lambda)] = 1$, the term **gcd** is the greatest common divisor. Then, we obtain the following recursive relationships as

$$\begin{aligned} T_n^j(\lambda) &= [T_{n-1}^j(\lambda) - \left(\lambda_j + 1\right) P_{n-1}^j(\lambda)]\lambda - T_{n-1}^j(\lambda) + \lambda_j P_{n-1}^j(\lambda), \\ P_n^j(\lambda) &= T_{n-1}^j(\lambda) - \left(\lambda_j + 1\right) P_{n-1}^j(\lambda), \end{aligned} \tag{5}$$

where the initial conditions are

$$\begin{aligned} T_2^j(\lambda) &= \lambda^2 - (2 + \lambda_j)\lambda + \lambda_j, \\ P_2^j(\lambda) &= \lambda - (\lambda_j + 1). \end{aligned}$$

From Equation (5), we have

$$\begin{cases} t_n^j(0) = -t_{n-1}^j(0) + \lambda_j p_{n-1}^j(0), \\ p_n^j(0) = t_{n-1}^j(0) - \left(\lambda_j + 1\right) p_{n-1}^j(0). \end{cases} \tag{6}$$

where $t_n^j(0)$ and $p_n^j(0)$ are the constant terms of $T_n^j(\lambda)$ and $P_n^j(\lambda)$.

It follows from Equation (6) that

$$p_n^j(0) + \left(\lambda_j + 2\right) p_{n-1}^j(0) + p_{n-2}^j(0) = 0. \tag{7}$$

Solving Equation (7) with initial conditions of $p_2^j(0) = -(\lambda_j + 1)$ and $p_3^j(0) = \lambda_j^2 + 3\lambda_j + 1$ yields

$$p_n^j(0) = c_1^j (r_1^j)^g + c_2^j (r_2^j)^g, \tag{8}$$

where r_1^j and r_2^j are the roots of the characteristic equation $\lambda^2 + (\lambda_j + 2)\lambda + 1 = 0$. The constants r_1^j, r_2^j, c_1^j and c_2^j are

$$\begin{cases} r_1^j = \frac{-(\lambda_j+2)+\sqrt{\lambda_j(\lambda_j+4)}}{2}, \\ r_2^j = \frac{-(\lambda_j+2)-\sqrt{\lambda_j(\lambda_j+4)}}{2}, \\ c_1^j = \frac{1}{(r_1^j)^2-1}\left[(\lambda_j)^2 + 3\lambda_j + 1 + (\lambda_j + 1) r_2^j\right], \\ c_2^j = \frac{1}{(r_2^j)^2-1}\left[(\lambda_j)^2 + 3\lambda_j + 1 + (\lambda_j + 1) r_1^j\right]. \end{cases}$$

Substituting Equation (8) into Equation (6) yields

$$t_n^j(0) = -\left[c_1^j (r_1^j)^{n-2}\left(1 + r_1^j\right) + c_2^j (r_2^j)^{n-2}\left(1 + r_2^j\right)\right].$$

Next, we need to calculate the first-order terms $t_n^j(1), p_n^j(1)$ of $T_n^j(\lambda)$ and $P_n^j(\lambda)$. Using the relationship between $T_n^j(\lambda)$ and $P_n^j(\lambda)$ of Equation (5) gives

$$\begin{aligned} t_n^j(1) &= t_{n-1}^j(0) - \left(\lambda_j + 1\right) p_{n-1}^j(0) - t_{n-1}^j(1) + \lambda_j p_{n-1}^j(1), \\ p_n^j(1) &= t_{n-1}^j(1) - \left(\lambda_j + 1\right) p_{n-1}^j(1), \end{aligned}$$

where the initial values are $t_2^j(1) = -(\lambda_j + 2), p_2^j(1) = 1, p_3^j(1) = -(2\lambda_j + 3)$. Then, we obtain

$$\begin{aligned} t_n^j(1) &= \left\{e_j (r_1^j)^2 + \left[n g_j + \left(\lambda_j + 1\right) e_j\right] r_1^j \right. \\ &+ (n-1)\left(\lambda_j + 1\right) g_j \left.\right\} (r_1^j)^{n-2} \\ &+ \left\{f_j (r_2^j)^2 + \left[n h_j + \left(\lambda_j + 1\right) f_j\right] r_2^j \right. \\ &+ (n-1)\left(\lambda_j + 1\right) h_j \left.\right\} (r_2^j)^{n-2}, \\ p_n^j(1) &= e_j (r_1^j)^{n-1} + f_j (r_2^j)^{n-1} + (n-1)\left[g_j (r_1^j)^{n-2} + h_j (r_2^j)^{n-2}\right], \end{aligned}$$

where

$$\begin{cases} g_j &= -\frac{c_1^j\left[(\lambda_j+2)r_1^j+1\right]}{2(r_1^j)^2+(\lambda_j+2)r_1^j}, \\ h_j &= -\frac{c_2^j\left[(\lambda_j+2)r_2^j+1\right]}{2(r_2^j)^2+(\lambda_j+2)r_2^j}, \\ e_j &= \frac{[1-(g_j+h_j)]r_2^j+2(g_jr_1^j+h_jr_2^j)+(2\lambda_j+3)}{1-(r_1^j)^2}, \\ f_j &= \frac{[1-(g_j+h_j)]r_1^j+2(g_jr_1^j+h_jr_2^j)+(2\lambda_j+3)}{1-(r_2^j)^2}. \end{cases}$$

We introduce a new polynomial as

$$\begin{aligned} D_n^j(\lambda) &= T_n^j(\lambda)-\lambda_jP_n^j(\lambda), \\ &= \left(\lambda-\lambda_{(j-1)n+1}^n\right)\left(\lambda-\lambda_{(j-1)n+2}^n\right)\ldots\left(\lambda-\lambda_{jn}^n\right). \end{aligned} \quad (9)$$

Using the Vieta's formula [26, 27] for $D_n^j(\lambda)=0$, we obtain its constant and first-order terms, denoted by $d_n^j(0), d_n^j(1)$, that is,

$$\begin{cases} d_n^j(0) &= t_n^j(0)-\lambda_jp_n^j(0) \\ &= -c_1^j(r_1^j)^{n-2}\left[1+\left(1+\lambda_j\right)r_1^j\right] \\ &- c_2^j(r_2^j)^{n-2}\left[1+\left(1+\lambda_j\right)r_2^j\right], \\ d_n^j(1) &= t_n^j(1)-\lambda_jp_g^j(1) \\ &= (r_1^j)^{n-2}\left[e_j(r_1^j)^2+\left(ng_j+e_j\right)r_1^j+(n-1)g_j\right] \\ &+(r_2^j)^{n-2}\left[f_j(r_2^j)^2+\left(nh_j+f_j\right)r_2^j+(n-1)h_j\right]. \end{cases} \quad (10)$$

3.2. When $\lambda_j = 0$

When $\lambda_j = 0$, $R_n^1(\lambda)=0$ has only one root $\lambda_1^n=0$. To obtain all the non-zero roots of $R_n^j(\lambda)=0$, we introduce a new polynomial, i.e.,

$$Z_n^1(\lambda)=\frac{1}{\lambda}R_n^1(\lambda).$$

Further,

$$\begin{aligned} T_n^1(\lambda) &= (\lambda-1)T_{n-1}^1(\lambda)-P_{n-1}^1(\lambda), \\ P_n^1(\lambda) &= \lambda T_{n-1}^1(\lambda)-P_{n-1}^1(\lambda), \end{aligned}$$

where the initial conditions are $T_2^1(\lambda)=\lambda-2, P_2^1(\lambda)=\lambda-1$. In the same way, we obtain the following coefficients, which are given by

$$\begin{cases} t_n^1(0)=(-1)^{n-1}n, \\ t_n^1(1)=(-1)^{n-2}\cdot\frac{n(n^2-1)}{6}, \end{cases}$$

$$\begin{cases} p_n^1(0)=(-1)^{n-2}, \\ p_n^1(1)=(-1)^{n-2}\cdot\frac{n(n-1)}{2}, \end{cases}$$

It follows from Equation (9) that

$$\begin{cases} d_n^1(0) &= (-1)^{n-1}\lambda_2^n\lambda_3^n\ldots\lambda_n^n, \\ &= (-1)^{n-1}n, \\ d_n^1(1) &= (-1)^{n-2}\left[\lambda_3^n\lambda_4^n\ldots\lambda_n^n+\lambda_2^n\lambda_4^n\ldots\lambda_n^n+\ldots\right. \\ &+ \left.\lambda_2^n\lambda_3^n\ldots\lambda_{n-1}^n\right], \\ &= (-1)^{n-2}\cdot\frac{n(n^2-1)}{6}. \end{cases} \quad (11)$$

3.3. Exact Solution of Network Coherence for $B_{m,n}$

We introduce a polynomial $D_n(\lambda)$ to obtain the exact solution of the network coherence, i.e.,

$$D_n(\lambda)=\prod_{j=1}^{m+1}D_n^j(\lambda)=\prod_{i=2}^{n(m+1)}(\lambda-\lambda_i^n).$$

According to Equations (10) and (11), the constant and first-order terms of $D_n(\lambda)$ are

$$\begin{aligned} d_n(0) &= \prod_{j=1}^{m+1}d_n^j(0), \\ d_n(1) &= \underbrace{d_n^1(1)d_n^2(0)\ldots d_n^{m+1}(0)}_{m+1} \\ &+\underbrace{d_n^1(0)d_n^2(1)\ldots d_n^{m+1}(0)}_{m+1}+\ldots+\underbrace{d_n^1(0)d_n^2(0)\ldots d_n^{m+1}(1)}_{m+1}. \end{aligned}$$

Based on the Vieta's theorem [26, 27], the network coherence reads as

$$H=\frac{1}{2N}\sum_{i=2}^{N}\frac{1}{\lambda_i}=-\frac{1}{2N}\frac{d_n(1)}{d_n(0)}.$$

When $m=3$, the Laplacian matrix L_m has four eigenvalues, that is, $\lambda_1=0, \lambda_2=\lambda_3=1, \lambda_4=4$. Using the above-mentioned calculations, we obtain the analytical expression of network coherence, i.e.,

$$\begin{aligned} H_{(n)} = \frac{1}{8n}\Big\{ &\frac{n^2-1}{6} \\ &-20\frac{[\alpha_1+g_2(nr_1^2+n-1)](r_1^2)^{n-2}+[\alpha_2+h_2(nr_2^2+n-1)](r_2^2)^{n-2}}{\beta_1(r_1^2)^{n-2}+\beta_2(r_2^2)^{n-2}} \\ &-2\frac{[\theta_1+g_4(nr_1^4+n-1)](r_1^4)^{n-2}+[\theta_2+h_4(nr_2^4+n-1)](r_2^4)^{n-2}}{\eta_1(r_1^4)^{n-2}+\eta_2(r_2^4)^{n-2}}\Big\}, \end{aligned} \quad (12)$$

where $\alpha_1=-\frac{5-2\sqrt{5}}{25}$, $\alpha_2=-\frac{5+2\sqrt{5}}{25}$, $\beta_1=15-7\sqrt{5}$,$\beta_2=15+7\sqrt{5}$, $\theta_1=-\frac{10-7\sqrt{2}}{32}$, $\theta_2=-\frac{10+7\sqrt{2}}{32}$, $\eta_1=24-17\sqrt{2}$, $\eta_2=24+17\sqrt{2}$, $g_2=-\frac{(5-\sqrt{5})(3r_1^2+1))}{10r_1^2(2r_1^2+3)}$, $h_2=-\frac{(5+\sqrt{5})(3r_2^2+1))}{10r_2^2(2r_2^2+3)}$, $g_4=-\frac{(2-\sqrt{2})(6r_1^4+1))}{8r_1^4(r_1^4+3)}$, $h_4=-\frac{(2+\sqrt{2})(6r_2^4+1))}{8r_2^4(r_2^4+3)}$, $r_1^2=\frac{-3+\sqrt{5}}{2}$, $r_2^2=\frac{-3-\sqrt{5}}{2}$, $r_1^4=-3+2\sqrt{2}$, $r_2^4=-3-2\sqrt{2}$.

3.4. Exact Solution of Network Coherence for B_m

To investigate the effect of the parameters m on the network coherence, we propose another method to obtain the solution regarding the parameters m. When $n=2$, the Laplacian matrix is

$$L_{m,2}=\begin{pmatrix} L_m & -I_{m+1} \\ -I_{m+1} & L_m \end{pmatrix}.$$

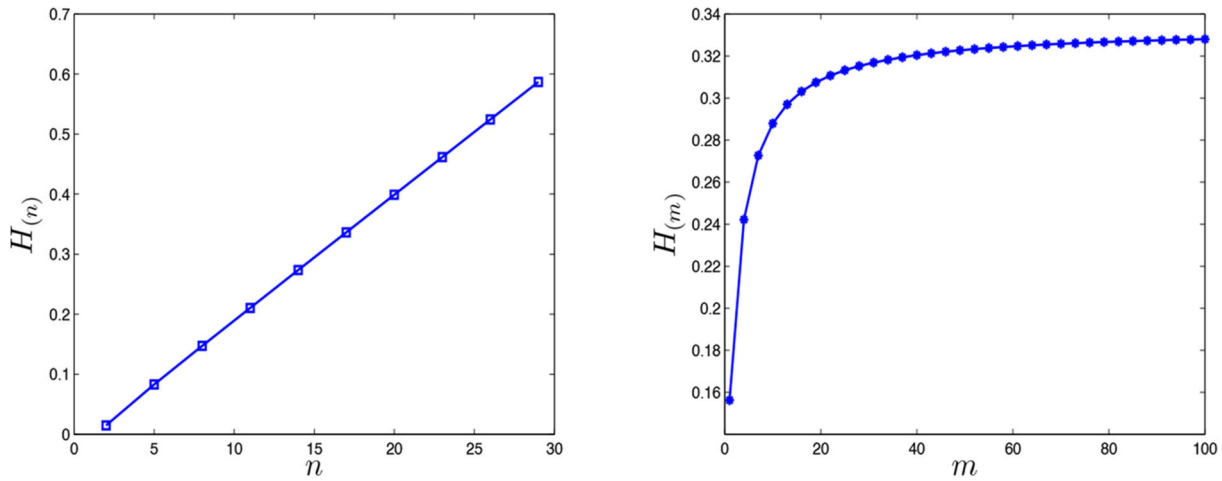

FIGURE 3 | Network coherence regarding the parameters n and m.

Then, the characteristic polynomial $P(\lambda)$ of $L_{m,2}$ is

$$\begin{aligned} P(\lambda) &= \begin{vmatrix} L_m - \lambda I_{m+1} & -I_{m+1} \\ -I_{m+1} & L_m - \lambda I_{m+1} \end{vmatrix} \\ &= \left|L_m - (\lambda+1)I\right| \cdot \left|L_m - (\lambda-1)I\right| \\ &= \lambda(\lambda-2)(\lambda-m-1)(\lambda-m-3)(\lambda-1)^{m-1}(\lambda-3)^{m-1}. \end{aligned}$$

The roots of this polynomial $P(\lambda)$ are as follows,

$$\left\{0, 2, m+1, m+3, \underbrace{1, \ldots, 1}_{m-1}, \underbrace{3, \ldots, 3}_{m-1}\right\}.$$

By the definition (1), we finally obtain the network coherence with regard to the parameters m, which is given by

$$H_{(m)} = \frac{1}{4m+4}\left[\frac{1}{2} + \frac{1}{m+1} + \frac{1}{m+3} + \frac{4(m-1)}{3}\right]. \quad (13)$$

From the expressions (12) and (13), we plot the relationships between network coherence and the parameters m and n, see **Figure 3**. It shows that the values of network coherence linearly increase with n, while the network coherence will achieve a steady constant state for a large m, i.e., $H_{(m)} \to \frac{1}{3}$, meaning that the consensus displays worse with increasing values of n. In a word, the number of nodes n in the path graph has more influence than the number of nodes m in the star graph.

4. CONCLUSIONS

In this paper, we have studied the consensus problems in noisy book graphs. Using the graph's constructions, we have obtained the recursive relationships for the Laplacian matrix and Laplacian eigenvalues and proposed a method to derive exact expressions of the sum of reciprocals of these eigenvalues. We then have presented exact solutions of network coherence with regard to graph parameters and investigated their effects on the coherence. It is shown that the larger size of star graphs results in better consensus, while the larger size of path graphs leads to worse consensus. The obtained results showed that the structure difference produces distinct performance on the coherence. Our method for the book graphs could be applied to study their random walks and Kirchhoff index.

DATA AVAILABILITY STATEMENT

The raw data supporting the conclusions of this article will be made available by the authors, without undue reservation.

AUTHOR CONTRIBUTIONS

JC, YL, and WS contributed to the conception and design of the study. JC and YL performed the analytical and numerical results. JC and WS wrote the manuscript. All authors contributed to the manuscript revision, read, and approved the submitted version. All authors contributed to the article and approved the submitted version.

FUNDING

This work was supported by the Zhejiang Provincial Natural Science Foundation of China (No. LY20F030007).

REFERENCES

1. Comellas F, Ozon J, Peters JG. Deterministic small-world communication networks. *Inf Process Lett.* (2000) **76**:83–90. doi: 10.1016/S0020-0190(00)00118-6
2. Barabási AL, Ravasz E, Vicsek T. Deterministic scale-free networks. *Phys A.* (2001) **299**:559–64. doi: 10.1016/S0378-4371(01)00369-7
3. Dai MF, Li XY, Xi LF. Random walks on non-homogenous weighted Koch networks. *Chaos.* (2013) **23**:033106. doi: 10.1063/1.4810927

4. Wang SJ, Yu ZY, Xi LF. Average geodesic distance of Sierpinski gasket and Sierpinski networks. *Fractals*. (2017) **25**:1750044. doi: 10.1142/S0218348X1750044X
5. Zhang ZZ, Wu B, Zhang HJ, Zhou SG, Guan JH, Wang ZG. Determining global mean-first-passage time of random walks on Vicsek fractals using eigenvalues of Laplacian matrices. *Phys Rev E*. (2010) **81**:031118. doi: 10.1103/PhysRevE.81.031118
6. Condamin S, Bénichou O, Tejedor V, Voituriez R, Klafter J. First-passage times in complex scale-invariant media. *Nature*. (2007) **450**: 77–80. doi: 10.1038/nature06201
7. Wu ZK, Hou BY, Zhang HJ, Jin F. Scaling of average weighted shortest path and average receiving time on weighted expanded Koch networks. *Int J Mod Phys B*. (2014) **28**:1450111. doi: 10.1142/S0217979214501112
8. Peng JH, Agliari E, Zhang, ZZ. Exact calculations of first-passage properties on the pseudofractal scale-free web. *Chaos*. (2015) **25**:073118. doi: 10.1063/1.4927085
9. Peng JH, Agliari E. Exact results for the first-passage properties in a class of fractal networks. *Chaos*. (2019) **29**:023105. doi: 10.1063/1.5080481
10. Patterson S, Bamieh B. Consensus and coherence in fractal networks. *IEEE Trans Control Netw Syst*. (2014) **1**:338–48. doi: 10.1109/TCNS.2014.2357552
11. Sun WG, Ding QY, Zhang JY, Chen FY. Coherence in a family of tree networks with an application of Laplacian spectrum. *Chaos*. (2014) **24**:043112. doi: 10.1063/1.4897568
12. Balankin AS, Martinez-Cruz MA, Susarrey-Huerta O, Adame LD. Percolation on infinitely ramified fractal networks. *Phys Lett A*. (2018) **382**:12–9. doi: 10.1016/j.physleta.2017.10.035
13. Klein DJ and Randić M. Resistance distance. *J Math Chem*. (1993) **13**:81–95. doi: 10.1007/BF01164627
14. Bonchev D, Balaban AT, Liu X, Klein DJ. Molecular cyclicity and centricity of polycyclic graphs. I. Cyclicity based on resistance distances or reciprocal distances. *Int J Quant Chem*. (1994) **50**:1–20. doi: 10.1002/qua.560500102
15. Wang XQ, Dai MF, Chen YF, Zong Y, Sun Y, Su, WY. Determining entire mean first-passage time for Cayley networks. *Int J Mod Phys C*. (2018) **29**:1850009. doi: 10.1142/S0129183118500092
16. Duan ZS, Chen GR, Huang L. Complex network synchronizability: analysis and control. *Phys Rev E*. (2007) **76**:056103. doi: 10.1103/PhysRevE.76.056103
17. Ellens W, Spieksma FM, Van Mieghem P, Jamakovic A, Kooij RE. Effective graph resistance. *Linear Algebra Appl*. (2011) **435**:2491–506. doi: 10.1016/j.laa.2011.02.024
18. Qi Y, Zhang ZZ, Yi Y, Li H. Consensus in self-similar hierarchical graphs and Sierpiński graphs: Convergence speed, delay robustness, and coherence. *IEEE Trans Cybern*. (2019) **49**:592–603. doi: 10.1109/TCYB.2017.2781714
19. Dai MF, He JJ, Zong Y, Ju TT, Sun Y, Su WY. Coherence analysis of a class of weighted networks. *Chaos*. (2018) **28**:043110. doi: 10.1063/1.4997059
20. Hong MD, Sun WG, Liu SY, Xuan TF. Coherence analysis and Laplacian energy of recursive trees with controlled initial states. *Front Inform Technol Elect Eng*. (2020) **21**:931–8. doi: 10.1631/FITEE.1900133
21. Patterson S, Bamieh B. Leader selection for optimal network coherence. In: *Proceedings of the 49th IEEE Conference on Decision and Control*. Atlanta, GA (2010). p. 2692–7. doi: 10.1109/CDC.2010.5718151
22. Sun WG, Sun MT, Guan JB, Jia Q. Robustness of coherence in noisy scale-free network and applications to identification of influential spreaders. *IEEE Trans Circuits Syst II*. (2020) **67**:1274–8. doi: 10.1109/TCSII.2019.2929139
23. Grone R, Merris R, Sunder VS. The Laplacian spectrum of a graph. *SIAM J Matrix Anal Appl*. (1990) **11**:218–38. doi: 10.1137/0611016
24. Khalid R, Idrees N, Saif MJ. Topological characterization of book graph and stacked book graph. *Comput Mater Con*. (2019) **60**:41–54. doi: 10.32604/cmc.2019.06554
25. Daoud SN, Elsawy AN. Edge even graceful labelling of some book graphs. *J Taibah Univ Sci*. (2018) **12**: 315–30. doi: 10.1080/16583655.2018.1469292
26. Beineke LW, Wilson RJ, Cameron PJ. *Topics in Algebraic Graph Theory*. New York, NY: Cambridge University Press (2004).
27. Comellas F, Miralles A. Mean first-passage time for random walks on generalized deterministic recursive trees. *Phys Rev E*. (2010) **81**:061103. doi: 10.1103/PhysRevE.81.061103

Conflict of Interest: The authors declare that the research was conducted in the absence of any commercial or financial relationships that could be construed as a potential conflict of interest.

frontiers in Physics

BRIEF RESEARCH REPORT
published: 27 October 2020
doi: 10.3389/fphy.2020.553261

Third Smallest Wiener Polarity Index of Unicyclic Graphs

Wei Fang[1,2], *Muhan Ma*[3], *FuYuan Chen*[4,5]* and *Hufeng Dong*[5]

[1]Anhui Province Key Laboratory of Animal Nutritional Regulation and Health, Anhui Science and Technology University, Fengyang, China, [2]School of Mathematical Sciences, Anhui University, Hefei, China, [3]Mathematics and Applied Mathematics, Reading Academy Nanjing University of Information Science and Technology, Nanjing, China, [4]Department of Applied Mathematics, Northwestern Polytechnical University, Xi'an, China, [5]Institute of Statistics and Applied Mathematics, Anhui University of Finance and Economics, Bengbu, China

The Wiener polarity index $W_P(G)$ of a graph G is the number of unordered pairs of vertices $\{u, v\}$ where the distance between u and v is 3. In this paper, we determine the third smallest Wiener polarity index of unicyclic graphs. Moreover, the corresponding extremal graphs are characterized.

Keywords: wiener polarity index, minimum, unicyclic graph, extremal graph, electrical networks

OPEN ACCESS

Edited by:
Muhammad Javaid,
University of Management and Technology, Pakistan

Reviewed by:
YaJing Wang,
North University of China, China
Akbar Ali,
University of Hail, Saudi Arabia

***Correspondence:**
Fuyuan Chen
chen_fuyuan@sina.com

Specialty section:
This article was submitted to Mathematical and Statistical Physics, a section of the journal Frontiers in Physics

Received: *18 April 2020*
Accepted: *09 September 2020*
Published: *27 October 2020*

Citation:
Fang W, Ma M, Chen F and Dong H (2020) Third Smallest Wiener Polarity Index of Unicyclic Graphs. Front. Phys. 8:553261. doi: 10.3389/fphy.2020.553261

1. INTRODUCTION

Graph theory is one of the most special and unique branches of mathematics. Recently, it has attained much attention among researchers because of its wide range of applications in computer science, electrical networks, interconnected networks, biological networks, chemistry, etc.

The chemical graph theory (CGT) is a fast-growing area among researchers. It helps in understanding the structural properties of a molecular graph. There are many chemical compounds that possess a variety of applications in the fields of commercial, industrial, and pharmaceutical chemistry and daily life and in the laboratory.

In a chemical graph, the vertices represent atoms and edges refer to the chemical bonds in the underlying chemical structure. A topological index is a numerical value that is computed mathematically from the molecular graph. It is associated with the chemical constitution indicating the correlation of the chemical structure with many physical and chemical properties and biological activities [1–3].

Let G be a simple and connected graph with $|V(G)| = n$ and $|E(G)| = m$. Sometimes we refer to G as a (n, m) graph. For any $u, v \in V(G)$, the *distance* $d_G(u, v)$ between the vertices u and v of G is equal to the length of (number of edges in) the shortest path that connects u and v. $N_G^i(u) = \{v \in V(G) | d_G(u, v) = i\}$ is called the ith neighbor vertex set of u. Especially, if $i = 1$, then $N_G^1(u)$(or $N_G(u)$ for short) be the *neighbor vertex set* of u, and $d_G(u) = |N_G(u)|$ is called the *degree* of G. If $d_G(u) = 1$, then we call u a *pendant vertex* of G.

A unicyclic graph of order n is a connected graph with n vertices and m edges. It is well-known that every unicyclic graph has exactly one cycle. Let $\mathcal{U}_n$ denote the class of unicyclic graphs on n vertices. As usual, let $K_{1,n-1}$, C_n, and P_n be the star, cycle, and path of order n, respectively.

Let $\gamma(G, k)$ denote the number of unordered vertices pairs of G, each of whose distance is equal to k. The Wiener polarity index, denoted by $W_P(G)$, is defined to be the number of unordered vertices pairs of distance 3, i.e., $W_P(G) = \gamma(G, 3)$.

There is another important graph-based structure descriptor, called Wiener index, based on distances in a graph. The *Wiener index* $W(G)$ is denoted by [4]

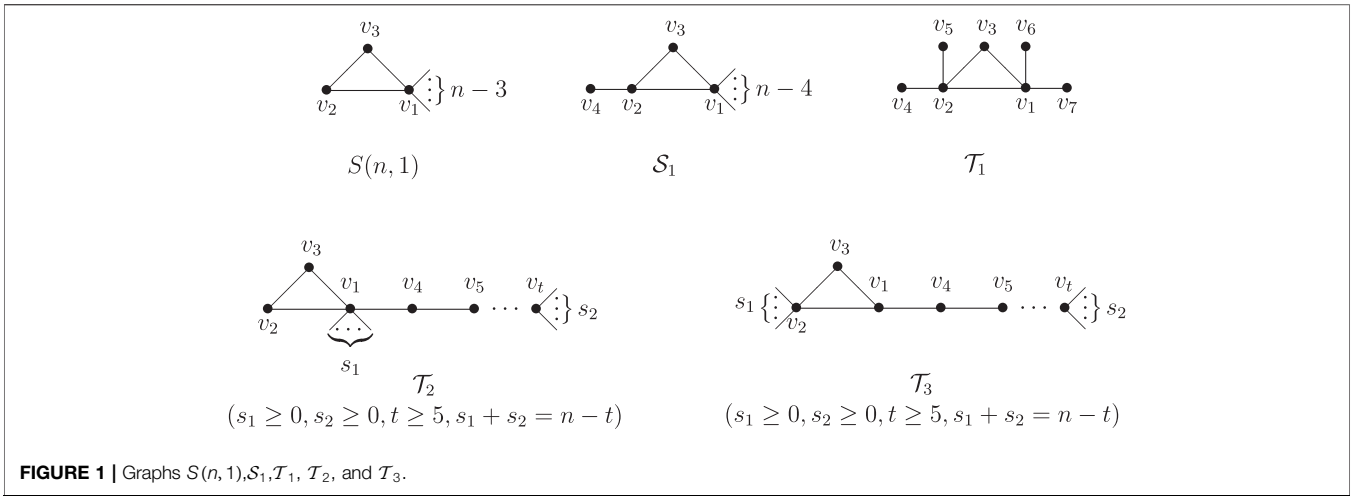

FIGURE 1 | Graphs $S(n,1)$,$\mathcal{S}_1$,$\mathcal{T}_1$, $\mathcal{T}_2$, and $\mathcal{T}_3$.

$$W(G) = \frac{1}{2}\sum_{u,v \in V(G)} d(u,v) = \sum_{k \geq 1} \gamma(G,k).$$

The name Wiener polarity index is introduced by Harold Wiener [4] in 1947. In Ref. [4], Wiener used a linear formula of $W(G)$ and $W_P(G)$ to calculate the boiling points t_B of the paraffins, i.e.,

$$t_B = aW(G) + bW_P(G) + c,$$

where a, b, and c are constants for a given isomeric group.

If $G_1, \cdots, G_t$ are the connected components of a graph G, then $W_P(G) = \sum_{i=1}^{t} W_P(G_i)$. Therefore, it will suffice to consider the Wiener polarity index of connected graphs.

In 1998, Lukovits and Linert [5] demonstrated quantitative structure-property relationships in a series of acyclic and cycle-containing hydrocarbons by using the Wiener polarity index. In 2002, Hosoya [6] found a physicochemical interpretation of $W_P(G)$. Du et al. [7] obtained the smallest and largest Wiener polarity indices together with the corresponding graphs among all trees on n vertices, respectively. Deng [8] characterized the extremal Wiener polarity indices among all chemical trees of order n. Hou [9] determined the maximum Wiener polarity index of unicyclic graphs and characterized the corresponding extremal graphs. Lei [8] determined the extremal trees with the given degree sequence with respect to the Wiener polarity index. In a previous study [10], the authors obtained the first and second smallest Wiener polarity indexes of unicyclic graphs. In this paper, we determine the third smallest Wiener polarity index of unicyclic graphs. Moreover, all the corresponding extremal graphs are characterized.

2. THE THIRD SMALLEST WIENER POLARITY INDEX OF UNICYCLIC GRAPHS

The girth $g(G)$ of a connected graph G is the length of a shortest cycle in G. Let $S(n,1)$ be the unicyclic graph obtained from $K_{1,n-1}$ by adding one edge to two pendant vertices of $K_{1,n-1}$.

A *non – pendant vertex* of G is a vertex of G which is not a pendant vertex. Suppose U is a unicyclic graph with unique cycle C_t, in the sequel, we agree that $V(C_t) = \{v_1, v_2, \ldots, v_t\}$ and $E(C_t) = \{v_1v_2, v_2v_3, \ldots, v_{t-1}v_t, v_1v_t\}$. For $1 \leq i \leq t$, let $l_i = \max\{d(v_i, x)$, where w is a non-pendant vertex and there is exactly one path connecting v_i with $x\}$.

Lemma 2.1. [10] Let $U \in \mathcal{U}_n$, then $W_P(G) \geq 0$, where equality holds if and only if $U \in S(n,1)$ *or* $U \cong C_4$ *or* $U \cong C_5$ ($S(n,1)$ is shown in **Figure 1**).

Lemma 2.2. Let $G \in \mathcal{U}_n$ and $\left|N_G^2(u)\right| \geq k$ for any $u \in V(G)$. $G + w$ be the new graph obtained from G by adding one vertex w and one edge adjacent to u in G. Then, $W_P(G + w) \geq W_P(G) + k$.

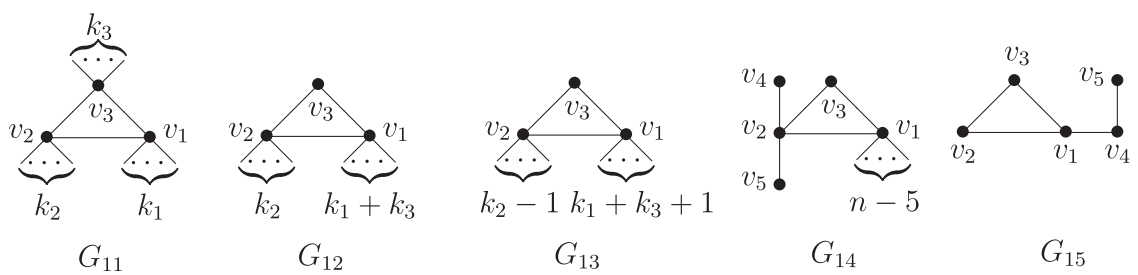

FIGURE 2 | Graphs G_{1i} $(1 \leq i \leq 4)$.

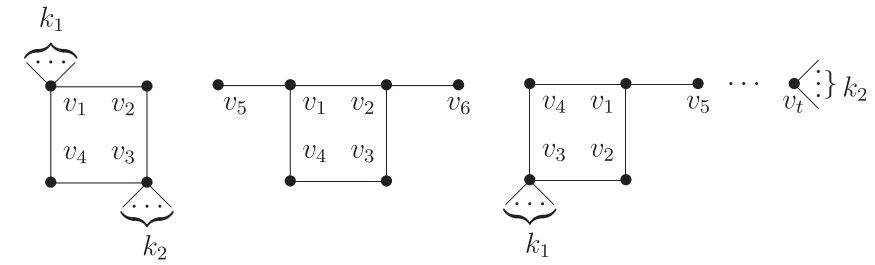

$\mathcal{S}_3$ $\mathcal{T}_4$ $\mathcal{T}_5$

$(k_1, k_2 \geq 0,$ $(6 \leq t \leq n, k_1, k_2 \geq 0,$

$k_1 + k_2 = n - 4)$ $k_1 + k_2 = n - t)$

FIGURE 3 | Graphs $\mathcal{S}_2$, $\mathcal{T}_4$, and $\mathcal{T}_5$.

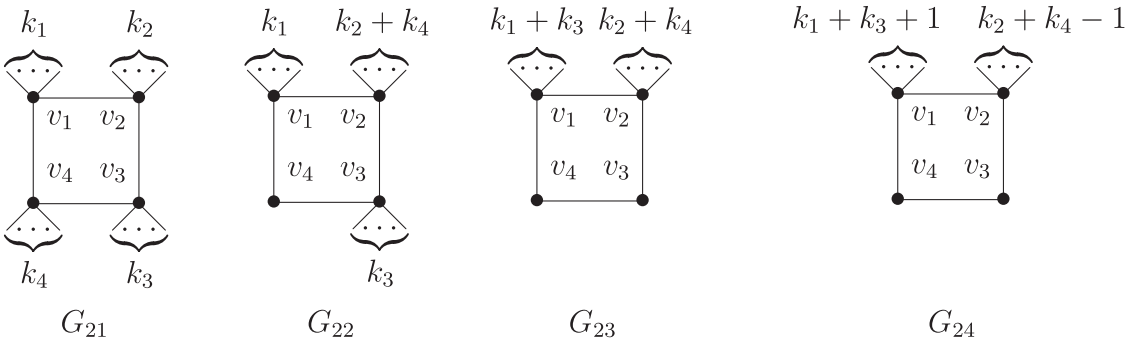

G_{21} G_{22} G_{23} G_{24}

FIGURE 4 | Graphs $G_{2i}\,(1 \leq i \leq 4)$.

Proof. Since $N_{G+w}(w) = \{u\}$ and $\left|N_G^2(u)\right| \geq k$, then $W_P(G + w) = W_P(G) + \left|N_G^3(w)\right| = W_P(G) + \left|N_G^2(u)\right| \geq W_P(G) + k$.

Lemma 2.3 [10]. Suppose $U \in \mathcal{U}_n \backslash \{S(n, 1)\}$. If $g(U) = 3$ and $n \geq 5$, then $W_P(U) \geq n - 4$, where equality holds if and only if $U \cong \mathcal{S}_1$ ($\mathcal{S}_1$ is shown in **Figure 1**).

Lemma 2.4. Let $U \in \mathcal{U}_n$. If $g(U) = 3$, then the third smallest Wiener polarity index $W_P(U) = n - 3$, the equality holds if and only if $U \cong \mathcal{T}_i, 1 \leq i \leq 3$ ($\mathcal{T}_1, \mathcal{T}_2$, and $\mathcal{T}_3$ are shown in **Figure 1**).

Proof. Let $C_3 = \{v_1, v_2, v_3\}$; we consider the next cases.

Case 1. $\max\{l_1, l_2, l_3\} = 0$.

This implies that U is a unicyclic graph obtained by attaching $k_i \geq 0$ pendant vertices to v_i, where $1 \leq i \leq 3$. Without loss of generality, let $k_1 + k_3 \geq k_2$. The graph $G_{1i}\,(1 \leq i \leq 4)$ is shown in **Figure 2**; by the definition of Wiener polarity index, we have

$$\begin{aligned} W_P(G_{11}) &= k_1k_2 + k_2k_3 + k_1k_3; \\ W_P(G_{12}) &= k_1k_2 + k_2k_3; \\ W_P(G_{13}) &= (k_1 + k_3 + 1)(k_2 - 1) \\ &= k_1k_2 + k_2k_3 - (k_1 + k_3 + 1 - k_2); \\ W_P(G_{14}) &= 2(n - 5) \geq n - 4\,(n \geq 6); \\ W_P(\mathcal{S}_1) &= n - 4\,(n \geq 5). \end{aligned}$$

Obviously, $W_P(G_{11}) \geq W_P(G_{12}) > W_P(G_{13})$; the equality holds if and only if $G_{11} \cong G_{12}$. Then the third smallest Wiener polarity index is $W_P(\mathcal{T}_1) = 4 = n - 3$.

Case 2. $\max\{l_1, l_2, l_3\} \geq 1$.

G_{15} is the subgraph of U and $W_P(G_{15}) = 2, \left|N_{G_{15}}^2(u)\right| \geq 1$, the equality holds if and only if $u \neq v_4$ by Lemma 2.2; we have

$$W_P(U) \geq W_P(G_{15}) + n - 5 = n - 3,$$

the equality holds if and only if $\mathcal{T}_2$ or $\mathcal{T}_3$.

By combining the above arguments, the result follows.

Lemma 2.5 *Let $U \in \mathcal{U}_n$. If $g(U) = 4$, then the third smallest Wiener polarity index $W_P(U) = n - 3$, the equality holds if and only if $U \cong \mathcal{T}_4$ or $\mathcal{T}_5$ ($\mathcal{T}_4$ and $\mathcal{T}_5$ are shown in* **Figure 3**).

Proof. Let $C_4 = \{v_1, v_2, v_3, v_4\}$, we consider the next cases.

Case 1. $\max\{l_1, l_2, l_3, l_4\} = 0$.

This implies that U is a unicyclic graph obtained by attaching $k_i \geq 0$ pendant vertices to v_i, where $1 \leq i \leq 4$. Without loss of generality, let $k_1 + k_3 \geq k_2 + k_4$. The graph $G_{2i}\,(1 \leq i \leq 4)$ is shown in **Figure 4**; by the definition of Wiener polarity index, we have

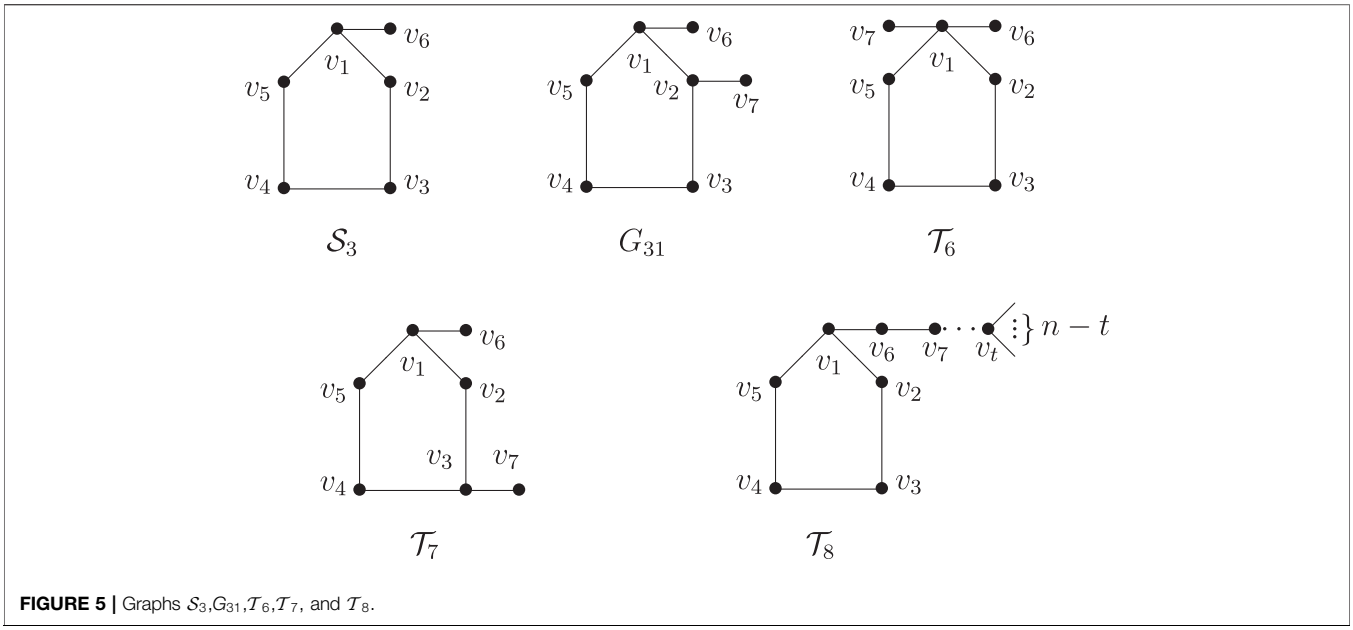

FIGURE 5 | Graphs $\mathcal{S}_3$,G_{31},$\mathcal{T}_6$,$\mathcal{T}_7$, and $\mathcal{T}_8$.

$$W_P(G_{21}) = k_1k_2 + k_2k_3 + k_3k_4 + k_1k_4 + \sum_{i=1}^{4} k_i,$$
$$W_P(G_{22}) = k_1k_2 + k_2k_3 + k_3k_4 + k_1k_4 + \sum_{i=1}^{4} k_i,$$
$$W_P(G_{23}) = k_1k_2 + k_2k_3 + k_3k_4 + k_1k_4 + \sum_{i=1}^{4} k_i,$$
$$W_P(G_{24}) = (k_1 + k_3 + 1)(k_2 + k_4 - 1) + \sum_{i=1}^{4} k_i.$$

Obviously, $W_P(G_{21}) = W_P(G_{22}) = W_P(G_{23}) > W_P(G_{24}) \geq n-3$; the equality holds if and only if $G_{24} \cong \mathcal{T}_4$. Then the third smallest Wiener polarity index is $W_P(\mathcal{T}_4) = 3 = n-3$.

Case 2. $\max\{l_1, l_2, l_3, v_4\} \geq 1$.

$\mathcal{S}_2$ ($k_1 = 1$ and $k_2 = 0$) is the subgraph of U and $W_P(\mathcal{S}_2) = 1$ ($k_1 = 1$ and $k_2 = 0$), by Lemma 2.2, we have

$$W_P(U) \geq 1 + n - 5 = n - 4,$$

the equality holds if and only if $U \cong \mathcal{S}_2$ ($k_1 = 1, k_2 = 1$). If $\mathcal{S}_2$ ($k_1 = 1, k_2 = 1$) is the induced subgraph of U, by Lemma 2.2, we have

$$W_P(U) \geq 2 + n - 5 = n - 3,$$

the equality holds if and only if $U \cong \mathcal{T}_5$.

By combining the above arguments, the result follows.

Lemma 2.6 *Let $U \in \mathcal{U}_n$. If $g(U) = 5$, then the third smallest Wiener polarity index $W_P(U) = n-3$, the equality holds if and only if $U \cong \mathcal{T}_i$, $(i = 6, 7, 8)$ ($\mathcal{T}_6$, $\mathcal{T}_7$, and $\mathcal{T}_8$ are shown in* **Figure 5**).

Proof. Let $C_5 = \{v_1, v_2, v_3, v_4, v_5\}$, we consider the next cases.

Case 1. $\max\{l_1, l_2, l_3, l_4, l_5\} = 0$.

This implies that U is a unicyclic graph obtained by attaching $k_i \geq 0$ pendant vertices to v_i, where $1 \leq i \leq 5$.

If $n = 5$, then there exists only one graph C_5 and $W_P(C_5) = 0$.

If $n = 6$, then there exists only one graph $\mathcal{S}_3$ and $W_P(\mathcal{S}_3) = 2 = n-4$.

If $n = 7$, then there exists three graphs G_{31}, $\mathcal{T}_6$, and $\mathcal{T}_7$, $W_P(G_{31}) = 5 = n-2$, $W_P(\mathcal{T}_6) = W_P(\mathcal{T}_7) = 4 = n-3$.

If $n > 7$, then G_{31} or $\mathcal{T}_6$ or $\mathcal{T}_7$ is the subgraph of U and $\min\{|N^2_{G_{31}}(u)|, |N^2_{\mathcal{T}_6}(u)|, |N^2_{\mathcal{T}_7}(u)|\} \geq 2$. By Lemma 2.2, we have $W_P(U) \geq 4 + 2 + n - 8 = n - 2$.

Case 2. $\max\{l_1, l_2, l_3, l_4, l_5\} \geq 1$. $\mathcal{T}_8$ ($n = t = 7$) is the subgraph of U and $W_P(\mathcal{T}_8) = 4$ ($n = t = 7$); meanwhile, $|N^2_{\mathcal{T}_8}(u)| \geq 1$, the equality holds if and only if $u = v_7$. By Lemma 2.2, we have $W_P(U) \geq 4 + n - 7 = n - 3$, the equality holds if and only if $U = \mathcal{T}_8$.

By combining the above arguments, the result follows.

Lemma 2.7 *Let $U \in \mathcal{U}_n$ and $g(U) = 6$. If $n = 6$, then $W_P(C_6) = n-3$; if $n > 7$, then $W_P(U) \geq n-2$.*

Proof. When $g(U) = 6$ and $n = 6$, then there exists only one graph C_6 and $W_P(C_6) = 3 = n-3$.

When $n \geq 7$, C_6 is the subgraph of U and $|N^2_{C_6}(u)| \geq 2$, by Lemma 2.2, we have $W_P(U) \geq 3 + 2 + n - 7 = n - 2$.

Lemma 2.8 Let $U \in \mathcal{U}_n$, if $g(U) = s \geq 7$, then $W_P(U) \geq n$, the equality holds if and only if $U \cong C_s$.

Proof. If $U \cong C_s$, then by the definition of Wiener polarity index, we have $W_P(U) = n$.

If $U \ncong C_s$, then C_s ($s \geq 7$) is the subgraph of U and $|N^2_{C_s}(u)| \geq 2$. By Lemma 2.2, we have $W_P(U) \geq W_P(C_s) + 2 + (n-s-1) = n+1$.

By combining the above arguments, the result follows.

Theorem 2.9. Let $U \in \mathcal{U}_n$; then the third smallest Wiener polarity index $W_P(U) = n-3$, the equality holds if and only if $U \cong C_6$ or $\mathcal{T}_i$, $1 \leq i \leq 8$ ($\mathcal{T}_1$,$\mathcal{T}_2$, and $\mathcal{T}_3$ are shown in **Figure 1**; $\mathcal{T}_4$ and $\mathcal{T}_5$ are shown in **Figure 3**; $\mathcal{T}_6$,$\mathcal{T}_7$, and $\mathcal{T}_8$ are shown in **Figure 5**).

Proof. By Lemma 2.4–2.8, the result follows.

3. CONCLUSIONS

Chemical graph theory is an important area of research in mathematical chemistry which deals with topology of molecular structure such as the mathematical study of isomerism and the development of topological descriptors or indices. In this paper, we first introduce some useful graph transformations and determine the third smallest Wiener polarity index of unicyclic graphs. In addition, all the corresponding extremal graphs are characterized.

DATA AVAILABILITY STATEMENT

All datasets presented in this study are included in the article.

AUTHOR CONTRIBUTIONS

WF performed conceptualization. FC and HD were responsible for methodology. WF and MM wrote the original manuscript. WF and FC reviewed and edited the article.

FUNDING

This work was supported by open project of Anhui University (No. KF2019A01), Natural Science Research Foundation of Department of Education of Anhui Province (No. KJ2019A0817, No. KJ2020A0061), and National Science Foundation of China under grant (No. 11601001).

REFERENCES

1. Liu J-B, Wang C, Wang S, Wei B. Zagreb indices and multiplicative zagreb indices of eulerian graphs. *Bull. Malays. Math. Sci. Soc* (2019) **42**:67–78. doi:10.1007/s40840-017-0463-2
2. Liu J-B, Pan X-F, Hu F-T, Hu F-F. Asymptotic Laplacian-energy-like invariant of lattices. *Appl Math Comput* (2015) **253**:205–14. doi:10.1016/j.amc.2014.12.035
3. Liu J-B, Pan X-F. Minimizing Kirchhoff index among graphs with a given vertex bipartiteness. *Appl Math Comput* (2016) **291**:84–8. doi:10.1016/j.amc.2016.06.017
4. Wiener H. Structural determination of paraffin boiling points. *J Am Chem Soc* (1947) **69**:17–20. doi:10.1021/ja01193a005
5. Lukovits I, Linert W. Polarity-numbers of cycle-containing structures. *J Chem Inf Comput Sci* (1998) **38**:715–9. doi:10.1021/ci970122j
6. Hosoya H. Mathematical and chemical analysis of Wieners polarity number. In: Rouvray DH, King RB, editors *Topology in chemistry-discrete mathematics of molecules*. **Vol. 57**. Chichester: Horwood (2002).
7. Du W, Li X, Shi Y. Algorithms and extremal problem on Wiener polarity index. *MATCH Commun. Math. Comput. Chem* (2009) **62**:235–44.
8. Lei H, Li T, Shi Y, Wang H. Wiener polarity index and its generalization in trees. *MATCH Commun. Math. Comput. Chem* (2017) **78**:199–212.
9. Hou H, Liu B, Huang Y. The maximum Wiener polarity index of unicyclic graphs. *Appl Math Comput* (2011) **218**:10149–57. doi:10.1016/j.amc.2012.03.090
10. Liu M, Liu B. On the wiener polarity index. *MATCH Commum. Math. Comput. Chem* (2011) **66**:293–304.

Conflict of Interest: The authors declare that the research was conducted in the absence of any commercial or financial relationships that could be construed as a potential conflict of interest.

frontiers in Physics

BRIEF RESEARCH REPORT
published: 05 November 2020
doi: 10.3389/fphy.2020.555573

Some Properties of Relative Bi-(Int-)Γ-Hyperideals in Ordered Γ-Semihypergroups

Yongsheng Rao[1], *Peng Xu*[1,2], *Zehui Shao*[1], *Saeed Kosari*[1]* *and Saber Omidi*[3]

[1]*Institute of Computing Science and Technology, Guangzhou University, Guangzhou, China,* [2]*School of Computer Science of Information Technology, Qiannan Normal University for Nationalities, Duyun, China,* [3]*Department of Education in Tehran, Tehran, Iran*

In this article, we study the concept of relative bi-r-hyperideals ($\mathcal{J}$-bi-r-hyperideals) in ordered r-semihypergroups and present some related examples of this concept. Especially, characterization of $\mathcal{J}$-simple ordered r-semihypergroups in terms of $\mathcal{J}$-bi-r-hyperideals is given. Furthermore, we define the notion of $\mathcal{J}$-(bi-)int-r-hyperideals in ordered r-semihypergroups and investigate its related properties. We show that $\mathcal{J}$-int-r-hyperideals and $\mathcal{J}$-r-hyperideals coincide in a $\mathcal{J}$-regular ordered r-semihypergroup.

Keywords: ordered Γ-semihypergroup, $\mathcal{J}$-bi-Γ-hyperideal, $\mathcal{J}$-(bi-)int-Γ-hyperideal, $\mathcal{J}$-regular AMS mathematics subject classification: 16Y99, 20N20, 06F99

OPEN ACCESS

Edited by:
Muhammad Javaid, University of Management and Technology, Lahore, Pakistan

Reviewed by:
Kazuharu Bamba, Fukushima University, Japan
Naveed Yaqoob, Majmaah University, Saudi Arabia

***Correspondence:**
S. Kosari
saeedkosari38@yahoo.com

Specialty section:
This article was submitted to Mathematical and Statistical Physics, a section of the journal Frontiers in Physics

Received: *25 April 2020*
Accepted: *24 August 2020*
Published: *05 November 2020*

Citation:
Rao Y, Xu P, Shao Z, Kosari S and Omidi S (2020) Some Properties of Relative Bi-(Int-)Γ-Hyperideals in Ordered Γ-Semihypergroups. Front. Phys. 8:555573. doi: 10.3389/fphy.2020.555573

1. INTRODUCTION

One of the motivations for the study of hyperstructures comes from biological inheritance and physical phenomenon as the nuclear fission. Another motivation for the study of hyperstructures comes from chemical reactions and redox reactions. Dehghan Nezhad et al. [1] provided a physical example of hyperstructures associated with the elementary particle physics: leptons. As we know, the Higgs boson is an elementary particle in the standard model of particle physics. In [2], it is shown that the leptons and gauge bosons along with the interactions between their members construct an H_v-structure. Yaqoob et al. [3] studied some properties of (fuzzy) r-hyperideals in involution r-semihypergroups. In [4], the concepts of uni-soft r-hyperideals and uni-soft interior r-hyperideals of ordered r-semihypergroups are investigated.

Algebraic hyperstructures are a suitable generalization of classical algebraic structures. In a classical algebraic structure, the composition of two elements is an element, while in an algebraic hyperstructure, the composition of two elements is a set. The concept of hyperstructures was first introduced by Marty [5] at the eighth congress of Scandinavian Mathematicians in 1934. Nowadays, we can easily find well-written books for the introduction to hyperstructures, which include Corsini [6], Corsini and Leoreanu [7], Davvaz [8], Davvaz and Leoreanu-Fotea [9], Davvaz and Vougiouklis [10], and Vougiouklis [11]. For the information about hyper rings, we refer the reader to Ref. 9.

The study of ordered semihypergroups began with the work of Heidari and Davvaz [12]. In 2015, Davvaz et al. [13] discussed the notion of a pseudo-order in an ordered semihypergroup. The focus of the study was to find out if there is a relationship between ordered semihypergroups and ordered semigroups by using pseudo-orders. In 2016, Gu and Tang [14] answered to the open problem given by Davvaz et al. [13]. In [15], Tipachot and Pibaljommee introduced the concept of fuzzy interior hyperideals on ordered semihypergroups. Recently, Mahboob et al. [16] studied the concept of (m, n)-hyperideals on ordered semihypergroups. Recall, from Ref. 12, that an ordered semihypergroup $(S, \circ, \leq)$ is a semihypergroup (S) together with a (partial) order relation $\leq$ that is compatible with the hyperoperation $\circ$, meaning that, for any $x, y, z \in S$,

$$x \leq y \Rightarrow z \circ x \leq z \circ y \text{ and } x \circ z \leq y \circ z.$$

Here, $A \leq B$ means that for any $a \in A$, there exists $b \in B$ such that $a \leq b$, for all nonempty subsets A and B of S.

Good and Hughes [17] introduced the notion of bi-ideals of a semigroup as early as 1952. In 1962, Wallace [18] introduced the notion of relative ideals ($\mathcal{J}$-ideals) on semigroups. In 1967, Hrmová [19] generalized the notion of $\mathcal{J}$-ideal by introducing the notion of a $(\mathcal{J}_1, \mathcal{J}_2)$-ideal of a semigroup S. Recently, Khan and Ali [20] introduced the concept of relative bi-ideals in ordered semigroups. The notion of Γ-semigroup was introduced by Sen and Saha [21] in 1986, which is a generalization of semigroups. In 2011, Anvariyeh et al. [22] introduced the notion of Γ-hyperideal of a Γ-semihypergroup. Later on, Yaqoob and Aslam [23] studied prime (m, n) bi-Γ-hyperideals of Γ-semihypergroups. Omidi et al. [24, 25] discussed some important properties of bi-Γ-hyperideals of an ordered Γ-semihypergroup. Bi-Γ-hyperideal is a special case of (m, n)-Γ-hyperideal [26]. In 2017, Tang et al. [27] considered and proved some theorems on fuzzy interior Γ-hyperideals in ordered Γ-semihypergroups. Pseudo-orders are the bridge between ordered Γ-semigroups and ordered Γ-semihypergroups, see Ref. 28.

After an introduction, in **Section 2**, we introduce some notation and terminologies. **Section 2** aims for summarizing the fundamental materials on ordered Γ-semihypergroups. **Section 3** is devoted to the study of relative Γ-hyperideals ($\mathcal{J}$-Γ-hyperideals) and relative bi-Γ-hyperideals ($\mathcal{J}$-bi-Γ-hyperideals) of an ordered Γ-semihypergroup. In this section, our main results are stated and proved. $\mathcal{J}$-simple ordered Γ-semihypergroups are characterized by using the notions of $\mathcal{J}$-Γ-hyperideals and $\mathcal{J}$-bi-Γ-hyperideals. Finally, in **Section 4**, the notion of $\mathcal{J}$-(bi-)int-Γ-hyperideals ($\mathcal{J}$-(bi-)interior-Γ-hyperideals) are studied and their related properties are discussed. It is shown that, in $\mathcal{J}$-regular ordered Γ-semihypergroups the $\mathcal{J}$-Γ-hyperideals and the $\mathcal{J}$-int-Γ-hyperideals coincide.

2. PRELIMINARIES

Let S and Γ be two nonempty sets. Then, S is called a Γ-semihypergroup [22] if every $\gamma \in \Gamma$ is a hyperoperation on S, i.e., $x\gamma y \subseteq S$, for every $x, y \in S$, $\alpha, \beta \in \Gamma$, and $x, y, z \in S$, we have

$$x\alpha(y\beta z) = (x\alpha y)\beta z.$$

If every $\gamma \in \Gamma$ is an operation, then S is a Γ-semigroup. Let A and B be two nonempty subsets of S. We define

$$A\gamma B = \cup\{a\gamma b \mid a \in A, b \in B\}.$$

Also,

$$A\Gamma B = \cup\{a\gamma b \mid a \in A, b \in B \text{ and } \gamma \in \Gamma\} = \bigcup_{\gamma \in \Gamma} A\gamma B.$$

In the following, we recall the notion of an ordered Γ-semihypergroup, and then we present basic definitions and notations, which we will need in this article. Throughout this article, unless otherwise specified, S is always an ordered Γ-semihypergroup $(S, \Gamma, \leq)$.

Definition 2.1 (see [29]). An algebraic hyperstructure $(S, \Gamma, \leq)$ is called an ordered Γ-semihypergroup if (S, Γ) is a Γ-semihypergroup and (S) is a partially ordered set such that for any $x, y, z \in S$ and $\gamma \in \Gamma$, $x \leq y$ implies $z\gamma x \leq z\gamma y$ and $x\gamma z \leq y\gamma z$. Here, if A and B are two nonempty subsets of S, then we say that $A \leq B$ if, for every $a \in A$, there exists $b \in B$ such that $a \leq b$.

Let S be an ordered Γ-semihypergroup. By a sub Γ-semihypergroup of S, we mean a nonempty subset A of S such that $a\gamma b \subseteq A$ for all $a, b \in A$ and $\gamma \in \Gamma$. A nonempty subset A of S is called idempotent if $A = (A\Gamma A]$.

Example 1. (See Ref. 25.) Let $(S, \circ, \leq)$ be an ordered semihypergroup and Γ a nonempty set. We define $a\gamma b = a \circ b$ for every $a, b \in S$ and $\gamma \in \Gamma$. Then, $(S, \Gamma, \leq)$ is an ordered Γ-semihypergroup.

Let $\mathcal{J}$ be a nonempty subset of an ordered Γ-semihypergroup $(S, \Gamma, \leq)$. If H is a nonempty subset of $\mathcal{J}$, then we define

$$(H]_{\mathcal{J}} := \{j \in \mathcal{J} \mid j \leq h \text{ for some } h \in H\}.$$

Note that if $\mathcal{J} = S$, then we define

$$(H] := \{x \in S \mid x \leq h \text{ for some } h \in H\}.$$

If A and B are nonempty subsets of S, then we have

(1) $A \subseteq (A]_{\mathcal{J}}$ for all $A \subseteq \mathcal{J}$
(2) $((A]_{\mathcal{J}}]_{\mathcal{J}} = (A]_{\mathcal{J}}$
(3) If $A \subseteq B \subseteq \mathcal{J}$, then $(A]_{\mathcal{J}} \subseteq (B]_{\mathcal{J}}$
(4) $(A]_{\mathcal{J}}\Gamma(B]_{\mathcal{J}} \subseteq (A\Gamma B]_{\mathcal{J}}$

An element a of an ordered Γ-semihypergroup $(S, \Gamma, \leq)$ is regular [25] if there exist $x \in S$ and $\alpha, \beta \in \Gamma$ such that $a \leq a\alpha x\beta a$. This is equivalent to saying that $a \in (a\Gamma S\Gamma a]$, for each $a \in S$. An ordered Γ-semihypergroup S is said to be regular if every element of S is a regular element.

Definition 2.2. Let $(S, \Gamma, \leq)$ be an ordered Γ-semihypergroup. A nonempty subset A of S is called a left (resp. right) Γ-hyperideal [24] of S if it satisfies the following conditions:

(1) $S\Gamma A \subseteq A$ (resp. $A\Gamma S \subseteq A$)
(2) If $x \in A$, $y \in S$, and $y \leq x$, then $y \in A$

If A is both a left Γ-hyperideal and a right Γ-hyperideal of S, then it is called a Γ-hyperideal (or two-sided Γ-hyperideal) of S.

3. BASIC PROPERTIES OF RELATIVE BI-Γ-HYPERIDEALS ($\mathcal{J}$-BI-Γ-HYPERIDEALS)

Let $(S, \Gamma, \leq)$ be an ordered Γ-semihypergroup and $\mathcal{I}$ and $\mathcal{J}$ be the nonempty subsets of S. Then, $\mathcal{I}$ is called a left $\mathcal{J}$-Γ-hyperideal of S if it satisfies the following conditions:

(1) $\mathcal{J}\Gamma\mathcal{I} \subseteq \mathcal{I}$
(2) When $x \in \mathcal{J}$ and $y \in \mathcal{I}$ such that $x \leq y$, it implies that $x \in \mathcal{I}$

A right $\mathcal{J}$-Γ-hyperideal of an ordered Γ-semihypergroup S is defined in a similar way. By two-sided $\mathcal{J}$-Γ-hyperideal or simply $\mathcal{J}$-Γ-hyperideal, we mean a nonempty subset of S which is both left and right $\mathcal{J}$-Γ-hyperideal of S.

Definition 3.1. Let $\mathcal{J}_1$ and $\mathcal{J}_2$ be the nonempty subsets of S. A nonempty subset $\mathcal{I}$ of S is said to be an $(\mathcal{J}_1, \mathcal{J}_2)$-Γ-hyperideal of S if it satisfies the following conditions:

(1) $\mathcal{J}_1\Gamma\mathcal{I} \subseteq \mathcal{I}$ and $\mathcal{I}\Gamma\mathcal{J}_2 \subseteq \mathcal{I}$
(2) When $x \in \mathcal{J}_1 \cup \mathcal{J}_2$ and $y \in \mathcal{I}$ such that $x \leq y$, it implies that $x \in \mathcal{I}$

Example 2. Let $S = \{a, b, c, d, e, f\}$ and $\Gamma = \{\gamma, \beta\}$ be the sets of binary hyperoperations defined as follows:

γ	a	b	c	d	e	f
a	a	b	a	a	a	a
b	b	b	b	b	b	b
c	a	b	$\{a, c\}$	a	a	$\{a, f\}$
d	a	b	$\{a, e\}$	a	a	$\{a, d\}$
e	a	b	$\{a, e\}$	a	a	$\{a, d\}$
f	a	b	$\{a, c\}$	a	a	$\{a, f\}$

β	a	b	c	d	e	f
a	a	b	a	a	a	a
b	b	b	b	b	b	b
c	a	b	a	a	a	a
d	a	b	a	$\{a, d\}$	$\{a, e\}$	a
e	a	b	a	a	a	a
f	a	b	a	$\{a, f\}$	$\{a, c\}$	a

Then, S is a Γ-semihypergroup [23]. We have $(S, \Gamma, \leq)$ as an ordered Γ-semihypergroup, where the order relation $\leq$ is defined by

$$\leq := \{(a, a), (b, a), (b, b), (b, c), (b, f), (c, c), (d, d), (e, e), (f, f)\}.$$

The covering relation and the figure of S are given by

$$\prec = \{(b, a), (b, c), (b, f)\}.$$

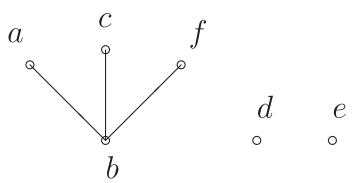

Let $\mathcal{J}_1 = \{a, b, c\}$, $\mathcal{J}_2 = \{b, d, f\}$, and $\mathcal{I} = \{a, b, f\}$. One can check that $\mathcal{I}$ is a $(\mathcal{J}_1, \mathcal{J}_2)$-Γ-hyperideal of S.Here are some elementary properties of these concepts.

Lemma 3.2. Let $(S, \Gamma, \leq)$ be an ordered Γ-semihypergroup. If $\mathcal{J}$ is a sub Γ-semihypergroup of S, then $(\mathcal{J}\Gamma a\Gamma\mathcal{J}]_{\mathcal{J}}$ is a $\mathcal{J}$-Γ-hyperideal of S for each $a \in S$.

Proof. Let $a \in S$. We show that $(\mathcal{J}\Gamma a\Gamma\mathcal{J}]_{\mathcal{J}}$ is a $\mathcal{J}$-Γ-hyperideal of S. We have

$$\begin{aligned} \mathcal{J}\Gamma(\mathcal{J}\Gamma a\Gamma\mathcal{J}]_{\mathcal{J}} &= (\mathcal{J}]_{\mathcal{J}}\Gamma(\mathcal{J}\Gamma a\Gamma\mathcal{J}]_{\mathcal{J}} \\ &\subseteq (\mathcal{J}\Gamma(\mathcal{J}\Gamma a\Gamma\mathcal{J})]_{\mathcal{J}} \\ &= (\mathcal{J}\Gamma\mathcal{J}(\Gamma a\Gamma\mathcal{J})]_{\mathcal{J}} \\ &\subseteq (\mathcal{J}\Gamma a\Gamma\mathcal{J}]_{\mathcal{J}}. \end{aligned}$$

Similarly, we have $(\mathcal{J}\Gamma a\Gamma\mathcal{J}]_{\mathcal{J}}\Gamma\mathcal{J} \subseteq (\mathcal{J}\Gamma a\Gamma\mathcal{J}]_{\mathcal{J}}$. Now, let $x \in \mathcal{J}$ and $y \in (\mathcal{J}\Gamma a\Gamma\mathcal{J}]_{\mathcal{J}}$ such that $x \leq y$. Then, $x \leq y \leq z$ for some $z \in \mathcal{J}\Gamma a\Gamma\mathcal{J}$. Hence, $x \leq z$ and so $x \in (\mathcal{J}\Gamma a\Gamma\mathcal{J}]_{\mathcal{J}}$. Therefore, $(\mathcal{J}\Gamma a\Gamma\mathcal{J}]_{\mathcal{J}}$ is a $\mathcal{J}$-Γ-hyperideal of S.

Theorem 3.3. Let I be a left Γ-hyperideal of an ordered Γ-semihypergroup $(S, \Gamma, \leq)$ and $\varnothing \neq \mathcal{J} \subseteq S$ such that $I \subseteq \mathcal{J}$. If M is an idempotent left $\mathcal{J}$-Γ-hyperideal of I, then M is a left Γ-hyperideal of S.

Proof. Clearly, I is an ordered sub-Γ-semihypergroup of S. We have

$$\begin{aligned} S\Gamma M &= S\Gamma(M\Gamma M] \\ &= (S]\Gamma(M\Gamma M] \\ &\subseteq (S\Gamma(M\Gamma M)] \\ &= ((S\Gamma M)\Gamma M] \\ &\subseteq ((S\Gamma I)\Gamma M] \\ &\subseteq (I\Gamma M] \\ &\subseteq (\mathcal{J}\Gamma M] \\ &\subseteq (M]_{\mathcal{J}} \\ &= M. \end{aligned}$$

If $m \in M \subseteq I$ and $x \in S$ such that $x \leq m$, then we have $x \in I \subseteq \mathcal{J}$. Since M is a left $\mathcal{J}$-Γ-hyperideal of I, it follows that $x \in M$. Hence, M is a left Γ-hyperideal of S. ∎

Theorem 3.4. Let I be a Γ-hyperideal of a regular ordered Γ-semihypergroup $(S, \Gamma, \leq)$ and $\mathcal{J}_1$, $\mathcal{J}_2 \subseteq S$ such that $I \subseteq \mathcal{J}_1 \cap \mathcal{J}_2$. Then, any $(\mathcal{J}_1, \mathcal{J}_2)$-Γ-hyperideal of I is a Γ-hyperideal of S.

Proof. Let I be a Γ-hyperideal of S. Then, $I\Gamma I \subseteq S\Gamma I \subseteq I$. So, I is an ordered sub-Γ-semihypergroup of S. Let A $(A \subseteq I)$ be a $(\mathcal{J}_1, \mathcal{J}_2)$-Γ-hyperideal of I. We prove that A is a Γ-hyperideal of S. Let $i \in I \subseteq S$. Then, there exist $x \in S$ and $\alpha, \beta \in \Gamma$ such that

$$i \leq i\alpha x\beta i \leq i\alpha x\beta(i\alpha x\beta i) = i\alpha(x\beta i\alpha x)\beta i.$$

Since I is a Γ-hyperideal of S, it follows that

$$x\beta i\alpha x \subseteq (S\Gamma I)\Gamma S \subseteq I\Gamma S \subseteq I.$$

Hence, $i \leq t$, for some $t \in i_\alpha(x\beta i\alpha x)\beta i \subseteq i\Gamma I\Gamma i$. This means that $i \in (i\Gamma I\Gamma i]_I$. Therefore, I is a regular ordered sub-Γ-semihypergroup of S.

Let $a \in A$ $(A \subseteq I)$ and $s \in S$. Then, $a_\gamma s \subseteq I$ where $\gamma \in \Gamma$. Now, suppose that $v \in a_\gamma s \subseteq I$. Then, there exist $y \in I$ and $\lambda, \mu \in \Gamma$ such that

$$\begin{aligned} v \leq v\lambda y\mu v &\subseteq (a\gamma s)\lambda y\mu(a\gamma s) \\ &\subseteq A\Gamma(S\Gamma I\Gamma I)\Gamma S \\ &\subseteq A\Gamma I\Gamma S \\ &\subseteq A\Gamma I \\ &\subseteq A\Gamma(\mathcal{J}_1 \cap \mathcal{J}_2) \\ &\subseteq A\Gamma\mathcal{J}_2 \\ &\subseteq A. \end{aligned}$$

Similarly, we have $s\gamma a \subseteq A$.

If $u \in A \subseteq I$ and $v \in S$ such that $v \leq u$, then we have $u \in I \subseteq \mathcal{J}_1 \cap \mathcal{J}_2 \subseteq \mathcal{J}_1 \subseteq \mathcal{J}_1 \cup \mathcal{J}_2$. Since A is a $(\mathcal{J}_1, \mathcal{J}_2)$-Γ-hyperideal of I, it follows that $v \in A$. Hence, A is a Γ-hyperideal of S.

Let a be an element of an ordered Γ-semihypergroup $(S, \Gamma, \leq)$. We denote by $L_1(a)$ (resp. $R_2(a)$, $I_{\mathcal{J}}(a)$) the left (resp. right, two-sided) relative Γ-hyperideal of S generated by a. The intersection of all $(\mathcal{J}_1, \mathcal{J}_2)$-Γ-hyperideals of S containing the element a is denoted by $I_{\mathcal{J}}(a)$, where $\mathcal{J} = \mathcal{J}_1 \cup \mathcal{J}_2$.

Lemma 3.5. Let a be an element of an ordered Γ-semihypergroup $(S, \Gamma, \leq)$ and $\mathcal{J}_1$ and $\mathcal{J}_2$ be two sub-Γ-semihypergroups of S. Then,

(1) $L_1(a) = (a \cup \mathcal{J}_1 \Gamma a]_{\mathcal{J}_1}$
(2) $R_2(a) = (a \cup a \Gamma \mathcal{J}_2]_{\mathcal{J}_2}$
(3) $I_{\mathcal{J}}(a) = (a \cup \mathcal{J}_1 \Gamma a \cup a \Gamma \mathcal{J}_2 \cup \mathcal{J}_1 \Gamma a \Gamma \mathcal{J}_2]_{\mathcal{J}}$, where $\mathcal{J} = \mathcal{J}_1 \cup \mathcal{J}_2$

Proof. Since $a \in L_1(a)$ and $\mathcal{J}_1 \Gamma a \subseteq L_1(a)$, it follows that $(a \cup \mathcal{J}_1 \Gamma a]_{\mathcal{J}_1} \subseteq L_1(a)$. We have

$$\begin{aligned} \mathcal{J}_1 \Gamma (a \cup \mathcal{J}_1 \Gamma a]_{\mathcal{J}_1} &\subseteq (\mathcal{J}_1]_{\mathcal{J}_1} \Gamma (a \cup \mathcal{J}_1 \Gamma a]_{\mathcal{J}_1} \\ &\subseteq (\mathcal{J}_1 \Gamma (a \cup \mathcal{J}_1 \Gamma a)]_{\mathcal{J}_1} \\ &\subseteq (\mathcal{J}_1 \Gamma a]_{\mathcal{J}_1} \\ &\subseteq (a \cup \mathcal{J}_1 \Gamma a]_{\mathcal{J}_1}. \end{aligned}$$

On the contrary, we have $(L_1(a)]_{\mathcal{J}_1} = L_1(a)$. Thus, $L_1(a) = (a \cup \mathcal{J}_1 \Gamma a]_{\mathcal{J}_1}$ is a left $\mathcal{J}_1$-Γ-hyperideal of S containing a. This means that $L_1(a) \subseteq (a \cup \mathcal{J}_1 \Gamma a]_{\mathcal{J}_1}$.

Now, we show that $L_1(a)$ is the smallest left $\mathcal{J}_1$-Γ-hyperideal of S containing a. Suppose that A is a left $\mathcal{J}_1$-Γ-hyperideal of S containing a. We have

$$L_1(a) = (a \cup \mathcal{J}_1 \Gamma a]_{\mathcal{J}_1} \subseteq (A \cup \mathcal{J}_1 \Gamma A]_{\mathcal{J}_1} \subseteq (A]_{\mathcal{J}_1} \subseteq A.$$

This proves that (1) holds. Conditions (2) and (3) are proved similarly.

Let $(S, \Gamma, \leq)$ be an ordered Γ-semihypergroup and $\mathcal{J}_1$ and $\mathcal{J}_2$ be nonempty subsets of S. Then, S is said to be left $\mathcal{J}_1$-simple if it has no proper left $\mathcal{J}_1$-Γ-hyperideal. In the same way, we can define a right $\mathcal{J}_2$-simple ordered Γ-semihypergroup. If S is a left $\mathcal{J}_1$-simple and right $\mathcal{J}_2$-simple) ordered Γ-semihypergroup, then S is a $(\mathcal{J}_1, \mathcal{J}_2)$-simple ordered Γ-semihypergroup.

Lemma 3.6. Let $(S, \Gamma, \leq)$ be an ordered Γ-semihypergroup and $\mathcal{J}_1$ and $\mathcal{J}_2$ be sub-Γ-semihypergroups of S such that $\mathcal{J} = \mathcal{J}_1 \cup \mathcal{J}_2$. Then, the following assertions hold:

(1) S is left $\mathcal{J}_1$-simple if and only if $(\mathcal{J}_1 \Gamma a]_{\mathcal{J}} = S$ for each $a \in S$
(2) S is right $\mathcal{J}_2$-simple if and only if $(a \Gamma \mathcal{J}_2]_{\mathcal{J}} = S$ for each $a \in S$
(3) S is $(\mathcal{J}_1, \mathcal{J}_2)$-simple if and only if $(\mathcal{J}_1 \Gamma a \Gamma \mathcal{J}_2]_{\mathcal{J}} = S$ for each $a \in S$

Proof. The proof is straightforward.

We continue this section with the following definition.

Definition 3.7. Let $(S, \Gamma, \leq)$ be an ordered Γ-semihypergroup and $\mathcal{J}$ a nonempty subset of S. A sub-Γ-semihypergroup $\mathcal{B}$ of S is called a relative bi-Γ-hyperideal ($\mathcal{J}$-bi-Γ-hyperideal) of S if the following conditions hold:

(1) $\mathcal{B} \Gamma \mathcal{J} \Gamma \mathcal{B} \subseteq \mathcal{B}$
(2) When $a \in \mathcal{J}$ and $b \in \mathcal{B}$ such that $a \leq b$, it implies that $a \in \mathcal{B}$

Example 3. We come back to **Example 2** and consider ordered Γ-semihypergroup $(S, \Gamma, \leq)$. Let $\mathcal{B} = \{a, b, c\}$ and $\mathcal{J} = \{b, f\}$. It is a routine matter to verify that $\mathcal{B}$ is a $\mathcal{J}$-bi-Γ-hyperideal of S.

Lemma 3.8. The intersection of any family of $\mathcal{J}$-bi-Γ-hyperideals of an ordered Γ-semihypergroup $(S, \Gamma, \leq)$ is a $\mathcal{J}$-bi-Γ-hyperideal of S.

Proof. This proof is straightforward.

Let $(S, \Gamma, \leq)$ be an ordered Γ-semihypergroup and $\mathcal{J}$ be any nonempty subset of S. Then, S is said to be $\mathcal{J}$-regular if, for each $j \in \mathcal{J}$, there exist $x \in \mathcal{J}$ and $\alpha, \beta \in \Gamma$ such that $j \leq j \alpha x \beta j$.

Theorem 3.9. Let $(S, \Gamma, \leq)$ be an ordered Γ-semihypergroup and $\mathcal{J}$ a sub-Γ-semihypergroup of S. Then, the following assertions are equivalent:

(1) S is $\mathcal{J}$-regular
(2) $\mathcal{B} = (\mathcal{B} \Gamma \mathcal{J} \Gamma \mathcal{B}]_{\mathcal{J}}$ for every $\mathcal{J}$-bi-Γ-hyperideal $\mathcal{B}$ $(\subseteq \mathcal{J})$ of S

Proof. (1) $\Rightarrow$ (2) Assume that (1) holds. Since $\mathcal{B}$ is a $\mathcal{J}$-bi-Γ-hyperideal of S, we get $\mathcal{B} \Gamma \mathcal{J} \Gamma \mathcal{B} \subseteq \mathcal{B}$. Thus, $(\mathcal{B} \Gamma \mathcal{J} \Gamma \mathcal{B}]_{\mathcal{J}} \subseteq (\mathcal{B}]_{\mathcal{J}} = \mathcal{B}$. Now, let $b \in \mathcal{B}$ $(\subseteq \mathcal{J})$. Since S is $\mathcal{J}$-regular, there exist $x \in \mathcal{J}$ and $\alpha, \beta \in \Gamma$ such that

$$b \leq b \alpha x \beta b \subseteq \mathcal{B} \Gamma \mathcal{J} \Gamma \mathcal{B}.$$

Hence, $b \in (\mathcal{B} \Gamma \mathcal{J} \Gamma \mathcal{B}]_{\mathcal{J}}$ and so $\mathcal{B} \subseteq (\mathcal{B} \Gamma \mathcal{J} \Gamma \mathcal{B}]_{\mathcal{J}}$. Therefore, $\mathcal{B} = (\mathcal{B} \Gamma \mathcal{J} \Gamma \mathcal{B}]_{\mathcal{J}}$. (2) $\Rightarrow$ (1) Let $\mathcal{R}$ be a right $\mathcal{J}$-Γ-hyperideal and $\mathcal{L}$ a left $\mathcal{J}$-Γ-hyperideal of S. By routine checking, we can easily verify that $\mathcal{R}$ and $\mathcal{L}$ are $\mathcal{J}$-bi-Γ-hyperideals of S. By **Lemma 3.8**, $\mathcal{R} \cap \mathcal{L}$ is a $\mathcal{J}$-bi-Γ-hyperideal of S. By hypothesis, we have

$$\begin{aligned} \mathcal{R} \cup \mathcal{L} &= ((\mathcal{R} \cup \mathcal{L}) \Gamma \mathcal{J} \Gamma (\mathcal{R} \cup \mathcal{L})]_{\mathcal{J}} \\ &\subseteq (\mathcal{R} \Gamma \mathcal{J} \Gamma \mathcal{L}]_{\mathcal{J}} \\ &\subseteq (\mathcal{R} \Gamma \mathcal{L}]_{\mathcal{J}}. \end{aligned}$$

Let $a \in \mathcal{J}$. Since $a \in R_2(a)$ and $a \in L_1(a)$, it follows that $a \in R_2(a) \cup L_1(a)$. By (1) and (2) of **Lemma 3.5**, we have

$$\begin{aligned} a \in (R_2(a) \Gamma L_1(a)]_{\mathcal{J}} &= ((a \cup a \Gamma \mathcal{J}]_{\mathcal{J}} \Gamma (a \cup \mathcal{J} \Gamma a]_{\mathcal{J}}]_{\mathcal{J}} \\ &= ((a \cup a \Gamma \mathcal{J}) \Gamma (a \cup \mathcal{J} \Gamma a)]_{\mathcal{J}} \\ &\subseteq (a \Gamma a \cup a \Gamma \mathcal{J} \Gamma a]_{\mathcal{J}}. \end{aligned}$$

Then, $a \leq w$, for some $w \in a \Gamma a \cup a \Gamma \mathcal{J} \Gamma a$. If $w \in a \Gamma a$, then $a \leq a \gamma a \leq a \gamma (a \gamma a)$. So, $a \in (a \Gamma \mathcal{J} \Gamma a]_{\mathcal{J}}$. Therefore, S is $\mathcal{J}$-regular. If $w \in a \Gamma \mathcal{J} \Gamma a$, then $a \leq a \delta x \lambda a$, for some $x \in \mathcal{J}$ and $\delta, \lambda \in \Gamma$. Thus, $a \in (a \Gamma \mathcal{J} \Gamma a]_{\mathcal{J}}$. Therefore, S is $\mathcal{J}$-regular.

Definition 3.10. Let $(S, \Gamma, \leq)$ be an ordered Γ-semihypergroup and $\mathcal{J}_1$ and $\mathcal{J}_2$ be the nonempty subsets of S. A sub-Γ-semihypergroup $\mathcal{B}$ of S is said to be a $(\mathcal{J}_1, \mathcal{J}_2)$-bi-Γ-hyperideal of S if it satisfies the following conditions:

(1) $\mathcal{B} \Gamma (\mathcal{J}_1 \cup \mathcal{J}_2) \Gamma \mathcal{B} \subseteq \mathcal{B}$
(2) When $a \in \mathcal{J}_1 \cup \mathcal{J}_2$ and $b \in \mathcal{B}$ such that $a \leq b$, it implies that $a \in \mathcal{B}$

Example 4. Let $S = \{e, a, b, c, d\}$ and $\Gamma = \{\gamma, \beta\}$ be the sets of binary hyperoperations defined as follows:

γ	e	a	b	c	d
e	e	e	e	e	e
a	e	$\{a,b\}$	b	b	b
b	e	b	b	b	b
c	e	c	c	c	c
d	e	d	d	d	d

β	e	a	b	c	d
e	e	e	e	e	e
a	e	a	a	a	a
b	e	a	$\{a,b\}$	a	a
c	e	c	c	c	c
d	e	d	d	d	d

Then, S is a Γ-semihypergroup [23]. We have $(S, \Gamma, \leq)$ as an ordered Γ-semihypergroup, where the order relation $\leq$ is defined by

$$\leq := \{(a,a), (b,a), (b,b), (c,c), (d,c), (d,d), (e,e)\}.$$

The covering relation and the figure of S are given by

$$\prec = \{(b,a), (d,c)\}.$$

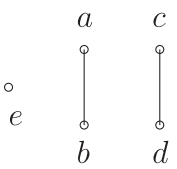

Let $\mathscr{B} = \{e,a,b\}$, $\mathcal{J}_1 = \{c\}$, and $\mathcal{J}_2 = \{d\}$. It is easy to see that $\mathscr{B}$ is a $(\mathcal{J}_1, \mathcal{J}_2)$-bi-Γ-hyperideal of S.

The concept of $\mathcal{J}$-bi-Γ-hyperideals of an ordered Γ-semihypergroup is a generalization of the concept of $\mathcal{J}$-Γ-hyperideals (left $\mathcal{J}$-Γ-hyperideals and right $\mathcal{J}$-Γ-hyperideals) of an ordered Γ-semihypergroup. Obviously, every left (right) $\mathcal{J}$-Γ-hyperideal of an ordered Γ-semihypergroup S is a $\mathcal{J}$-bi-Γ-hyperideal of S, but the following example shows that the converse is not true in the general case.

Example 5. Consider the ordered Γ-semihypergroup $(S, \Gamma, \leq)$ given in **Example 2.** It is easy to check that $\mathscr{B} = \{a,b,c\}$ is a $\mathcal{J}$-bi-Γ-hyperideal on S, where $\mathcal{J} = \{b,f\}$, but it is not a right $\mathcal{J}$-Γ-hyperideal on S. Since $c \in \mathscr{B}$ and $f \in \mathcal{J}$, but $c\gamma f = \{a,f\} \not\subseteq \{a,b,c\}$ which implies that $\mathscr{B}\Gamma\mathcal{J} \subseteq \mathscr{B}$ does not hold.

Theorem 3.11. Let $(S, \Gamma, \leq)$ be an ordered Γ-semihypergroup and $\mathcal{J}_1$ and $\mathcal{J}_2$ be two sub-Γ-semihypergroups of S. Then, S is left $\mathcal{J}_1$-simple and right $\mathcal{J}_2$-simple if and only if S does not contain proper $(\mathcal{J}_1, \mathcal{J}_2)$-bi-Γ-hyperideals.

Proof. Let S be a left $\mathcal{J}_1$-simple and right $\mathcal{J}_2$-simple ordered Γ-semihypergroup and B a $(\mathcal{J}_1, \mathcal{J}_2)$-bi-Γ-hyperideal of S. It is sufficient to prove that $S \subseteq B$. Consider $s \in S$ and $b \in B$. Since S is left $\mathcal{J}_1$-simple, we obtain

$$S = L_1(b) = (b \cup \mathcal{J}_1 \Gamma b]_{\mathcal{J}_1},$$

by **Lemma 3.5**. We need to consider only two cases:

Case 1. Let $s \leq b$. As B is $(\mathcal{J}_1, \mathcal{J}_2)$-bi-Γ-hyperideal, we have $s \in B$.

Case 2. Let $s \leq j_1 \gamma b$, for some $j_1 \in \mathcal{J}_1$ and $\gamma \in \Gamma$. By assumption, S is a right $\mathcal{J}_2$-simple ordered Γ-semihypergroup. Therefore,

$$S = R_2(b) = (b \cup b\Gamma\mathcal{J}_2]_{\mathcal{J}_2},$$

by **Lemma 3.5**. Since $j_1 \in \mathcal{J}_1 \subseteq S$, we have $j_1 \leq b$ or $j_1 \in (b\lambda j_2]_{\mathcal{J}_2}$ for some $j_2 \in \mathcal{J}_2$ and $\lambda \in \Gamma$. By **Lemma 3.6**, we have

$$S = (b\Gamma\mathcal{J}_2]_{\mathcal{J}} = (\mathcal{J}_1\Gamma b]_{\mathcal{J}},$$

and so

$$\begin{aligned} b \in (b\Gamma\mathcal{J}_2]_{\mathcal{J}} &\subseteq b\Gamma(\mathcal{J}_1\Gamma b]_{\mathcal{J}}]_{\mathcal{J}} \\ &\subseteq (b\Gamma\mathcal{J}_1\Gamma b]_{\mathcal{J}} \\ &\subseteq (b\Gamma\mathcal{J}\Gamma b]_{\mathcal{J}}, \end{aligned}$$

where $\mathcal{J} = \mathcal{J}_1 \cup \mathcal{J}_2$. Hence, S is a $\mathcal{J}$-regular ordered Γ-semihypergroup. So, there exist $x \in \mathcal{J}$ and $\alpha, \beta \in \Gamma$ such that $b \leq b\alpha x\beta b$. We now turn to the case $j_1 \leq b$. From this, we conclude that $j_1\gamma b \leq b\gamma b$. So, we obtain

$$\begin{aligned} (j_1\gamma b]_{\mathcal{J}} &\subseteq (b\gamma b]_{\mathcal{J}} \\ &\subseteq (b\gamma(b\alpha x\beta b)]_{\mathcal{J}} \\ &\subseteq (b\gamma b\alpha(x\beta b)]_{\mathcal{J}} \\ &\subseteq (B\Gamma\mathcal{J}\Gamma B]_{\mathcal{J}} \\ &\subseteq (B]_{\mathcal{J}} \\ &= B. \end{aligned}$$

Since $s \leq j_1\gamma b$, it follows that $s \in B$. This gives $S \subseteq B$. If $j_1 \in (b\lambda j_2]_{\mathcal{J}_2}$, then

$$\begin{aligned} (j_1\gamma b]_{\mathcal{J}} &\subseteq ((b\lambda j_2]_{\mathcal{J}_2}\gamma b]_{\mathcal{J}} \\ &\subseteq (B\Gamma\mathcal{J}\Gamma B]_{\mathcal{J}} \\ &\subseteq (B]_{\mathcal{J}} \\ &= B, \end{aligned}$$

and so $s \in B$. We thus get $S \subseteq B$.

Conversely, suppose that S does not contain proper $(\mathcal{J}_1, \mathcal{J}_2)$-bi-Γ-hyperideals. Let M be a left $\mathcal{J}_1$-Γ-hyperideal and right $\mathcal{J}_2$-Γ-hyperideal of S. We have

$$\begin{aligned} M\Gamma(\mathcal{J}_1 \cup \mathcal{J}_2)\Gamma M &= M\Gamma\mathcal{J}_1\Gamma M \cup M\Gamma\mathcal{J}_2\Gamma M \\ &\subseteq M\Gamma M \\ &\subseteq M. \end{aligned}$$

Hence, M is a $(\mathcal{J}_1, \mathcal{J}_2)$-bi-Γ-hyperideal of S. By assumption, we have $S = M$. Therefore, S is a left $\mathcal{J}_1$-simple and right $\mathcal{J}_2$-simple ordered Γ-semihypergroup.

4. RELATIVE (BI)-INT-Γ-HYPERIDEALS ($\mathcal{J}$-(BI)-INT-Γ-HYPERIDEALS)

Definition 4.1. Let $(S, \Gamma, \leq)$ be an ordered Γ-semihypergroup and $\mathcal{J}$ a nonempty subset of S. A sub-Γ-semihypergroup $\mathcal{C}_I$ of S is called a $\mathcal{J}$-int-Γ-hyperideal of S if the following conditions hold:

(1) $\mathcal{J}\Gamma\mathcal{C}_I\Gamma\mathcal{J} \subseteq \mathcal{C}_I$
(2) If $x \in \mathcal{J}$, $y \in \mathcal{C}_I$, and $x \leq y$, then $x \in \mathcal{C}_I$

It is not difficult to see that every $\mathcal{J}$-Γ-hyperideal of an ordered Γ-semihypergroup S is a $\mathcal{J}$-int-Γ-hyperideal of S. The following example shows that the converse is not true in general.

Example 6. Let $S = \{a, b, c, d\}$ and $\Gamma = \{\gamma\}$. We define

γ	a	b	c	d
a	a	a	a	a
b	a	a	a	a
c	a	a	a	$\{a, b\}$
d	a	a	$\{a, b\}$	$\{a, b, c\}$

Then, S is a Γ-semihypergroup. We have $(S, \Gamma, \leq)$ is an ordered Γ-semihypergroup, where the order relation $\leq$ is defined by

$$\leq \; := \{(a, a), (a, b), (a, c), (a, d), (b, b), (c, c), (d, d)\}.$$

The covering relation and the figure of S are given by

$$\prec = \{(a, b), (a, c), (a, d)\}.$$

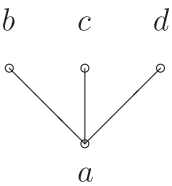

Let $\mathcal{C}_I = \{a, c\}$ and $\mathcal{J} = \{b, d\}$. Here, $\mathcal{C}_I$ is a $\mathcal{J}$-int-Γ-hyperideal of S, but not a $\mathcal{J}$-Γ-hyperideal of S. Indeed, since $\mathcal{J}\Gamma\mathcal{C}_I = \{a, b\} \not\subseteq \mathcal{C}_I$, it follows that $\mathcal{C}_I$ is not a $\mathcal{J}$-Γ-hyperideal of S.The following example shows that a $\mathcal{J}$-regular ordered Γ-semihypergroup is not regular in general.

Example 7. Consider the Γ-semihypergroup (S, Γ) given in **Example 6**. Let $\leq$ be the relation on S defined as follows:

$$\leq \; := \{(a, a), (b, a), (b, b), (b, c), (c, c), (d, d)\}.$$

Then, $(S, \Gamma, \leq)$ is an ordered Γ-semihypergroup. The covering relation and the figure of S are given by:

$$\prec = \{(b, a), (b, c)\}.$$

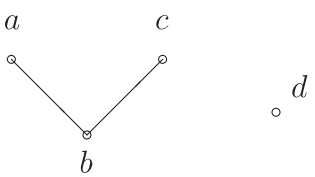

Let $\mathcal{J} = \{a, b\} \subset S$. An easy computation shows that S is a $\mathcal{J}$-regular ordered Γ-semihypergroup, but it is clearly not regular.

Theorem 4.2. Let $(S, \Gamma, \leq)$ be a $\mathcal{J}$-regular ordered Γ-semihypergroup, where $\mathcal{J}$ is a nonempty subset of S. Then, every $\mathcal{J}$-int-Γ-hyperideal $\mathcal{C}_I$ $(\mathcal{C}_I \subseteq \mathcal{J})$ of S is a $\mathcal{J}$-Γ-hyperideal of S.

Proof. Let $\mathcal{C}_I$ be a $\mathcal{J}$-int-Γ-hyperideal of S. Then, $\mathcal{C}_I$ is a sub-Γ-semihypergroup of S and $(\mathcal{C}_I]_{\mathcal{J}} = \mathcal{C}_I$. Let $a \in \mathcal{C}_I \subseteq \mathcal{J}$. Since S is $\mathcal{J}$-regular, there exist $x \in \mathcal{J}$ and $\alpha, \beta \in \Gamma$ such that $a \leq a\alpha x\beta a$. Now, let $j \in \mathcal{J}$ and $\gamma \in \Gamma$. Then,

$$\begin{aligned} j\gamma a &\leq j\gamma(a\alpha x\beta a) \\ &= (j\gamma a\alpha x)\beta a \\ &\subseteq (\mathcal{J}\Gamma\mathcal{C}_I\Gamma\mathcal{J})\Gamma\mathcal{C}_I \\ &\subseteq \mathcal{C}_I\Gamma\mathcal{C}_I \\ &\subseteq \mathcal{C}_I. \end{aligned}$$

Thus, $\mathcal{J}\Gamma\mathcal{C}_I \subseteq (\mathcal{C}_I]_{\mathcal{J}} = \mathcal{C}_I$. By a similar argument, we have $\mathcal{C}_I\Gamma\mathcal{J} \subseteq \mathcal{C}_I$. Hence, the result follows.In the following, we introduce the notion of $\mathcal{J}$-bi-int-Γ-hyperideals as a generalization of $\mathcal{J}$-Γ-hyperideals, $\mathcal{J}$-bi-Γ-hyperideals, and $\mathcal{J}$-int-Γ-hyperideals of ordered Γ-semihypergroups.

Definition 4.3. Let $(S, \Gamma, \leq)$ be an ordered Γ-semihypergroup and $\mathcal{J}$ a nonempty subset of S. A sub-Γ-semihypergroup $\mathcal{D}_{b-i}$ of S is called a $\mathcal{J}$-bi-int-Γ-hyperideal of S if the following conditions hold:

(1) $\mathcal{J}\Gamma\mathcal{D}_{b-i}\Gamma\mathcal{J} \cap \mathcal{D}_{b-i}\Gamma\mathcal{J}\Gamma\mathcal{D}_{b-i} \subseteq \mathcal{D}_{b-i}$
(2) If $x \in \mathcal{J}$, $y \in \mathcal{D}_{b-i}$, and $x \leq y$, then $x \in \mathcal{D}_{b-i}$

Lemma 4.4. Let $(S, \Gamma, \leq)$ be an ordered Γ-semihypergroup and $\mathcal{J}$ a nonempty subset of S. Then, the following statements hold:

(1) Every $\mathcal{J}$-Γ-hyperideal of S is a $\mathcal{J}$-bi-int-Γ-hyperideal of S
(2) The intersection of $\mathcal{J}$-bi-int-Γ-hyperideals of S is a $\mathcal{J}$-bi-int-Γ-hyperideal of S
(3) If B is a $\mathcal{J}$-bi-Γ-hyperideal and C a $\mathcal{J}$-int-Γ-hyperideal of S, then $\mathcal{D}_{b-i} = B \cap C$ is a $\mathcal{J}$-bi-int-Γ-hyperideal of S

Proof. (1) Let A be a $\mathcal{J}$-Γ-hyperideal of S. Then, $\mathcal{J}\Gamma A \subseteq A$ and $A\Gamma\mathcal{J} \subseteq A$. We have

$$\begin{aligned} \mathcal{J}\Gamma A\Gamma\mathcal{J} \cup A\Gamma\mathcal{J}\Gamma A &\subseteq A\Gamma\mathcal{J}\Gamma A \\ &\subseteq A\Gamma A \\ &\subseteq A, \end{aligned}$$

and

$$\begin{aligned} \mathcal{J}\Gamma A\Gamma\mathcal{J} \cup A\Gamma\mathcal{J}\Gamma A &\subseteq \mathcal{J}\Gamma A\Gamma\mathcal{J} \\ &\subseteq A\Gamma\mathcal{J} \\ &\subseteq A. \end{aligned}$$

Therefore, A is a $\mathcal{J}$-bi-int-Γ-hyperideal of S.

(2) The proof is similar to the proof of **Lemma 3.8**.

(3) Clearly, $\mathcal{D}_{b-i} = B \cap C$ is a sub-Γ-semihypergroup of S. We have

$$\begin{aligned} \mathcal{D}_{b-i}\Gamma\mathcal{J}\Gamma\mathcal{D}_{b-i} &= (B \cap C)\Gamma\mathcal{J}\Gamma(B \cap C) \\ &\subseteq B\Gamma\mathcal{J}\Gamma B \\ &\subseteq B, \end{aligned}$$

and

$$\begin{aligned} \mathcal{J}\Gamma\mathcal{D}_{b-i}\Gamma\mathcal{J} &= \mathcal{J}\Gamma(B \cap C)\Gamma\mathcal{J} \\ &\subseteq \mathcal{J}\Gamma C\Gamma\mathcal{J} \\ &\subseteq C. \end{aligned}$$

Hence, $\mathcal{J}\Gamma\mathcal{D}_{b-i}\Gamma\mathcal{J}\cap\mathcal{D}_{b-i}\Gamma\mathcal{J}\Gamma\mathcal{D}_{b-i}\subseteq B\cap C=\mathcal{D}_{b-i}$. Therefore, $\mathcal{D}_{b-i}=B\cap C$ is a $\mathcal{J}$-bi-int-Γ-hyperideal of S.

Example 8. Let $S=\{a,b,c,d,e\}$ and $\Gamma=\{\gamma\}$. We define

γ	a	b	c	d	e
a	a	$\{a,b\}$	$\{a,c\}$	$\{a,d\}$	e
b	a	$\{a,b\}$	$\{a,c\}$	$\{a,d\}$	e
c	a	$\{a,b\}$	$\{a,c\}$	$\{a,d\}$	e
d	a	$\{a,b\}$	$\{a,c\}$	$\{a,d\}$	e
e	a	$\{a,b\}$	$\{a,c\}$	$\{a,d\}$	e

Then, S is a Γ-semihypergroup. We have $(S,\Gamma,\leq)$ as an ordered Γ-semihypergroup [29], where the order relation $\leq$ is defined by

$$\leq := \{(a,a),(b,b),(c,c),(d,d),(e,e),(a,c),(b,a),(b,c),(d,a),(d,c),(e,a),(e,c)\}.$$

The covering relation and the figure of S are given by

$$\prec=\{(a,c),(b,a),(d,a),(e,a)\}.$$

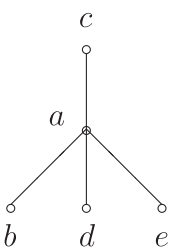

Let $\mathcal{D}_{b-i}=\{a,b,d\}$ and $\mathcal{J}=\{c,d\}$. Then, $\mathcal{J}\Gamma\mathcal{D}_{b-i}\Gamma\mathcal{J}=\{a,c,d\}$ and $\mathcal{D}_{b-i}\Gamma\mathcal{J}\Gamma\mathcal{D}_{b-i}=\{a,b,d\}$, so $\{a,c,d\}\cap\{a,b,d\}=\{a,d\}\subseteq\mathcal{D}_{b-i}$. Hence, $\mathcal{D}_{b-i}$ is a $\mathcal{J}$-bi-int-Γ-hyperideal of S. It is easy to see that $\mathcal{D}_{b-i}$ ($\mathcal{D}_{b-i}\Gamma\mathcal{J}\nsubseteq\mathcal{D}_{b-i}$) is not a $\mathcal{J}$-Γ-hyperideal of S.

5. CONCLUSION

In this article, we studied some properties of $\mathcal{J}$-(bi-)Γ-hyperideals of ordered Γ-semihypergroups. In particular, we introduced and studied $\mathcal{J}$-int-Γ-hyperideals and $\mathcal{J}$-bi-int-Γ-hyperideals. Furthermore, we proved that $\mathcal{J}$-int-Γ-hyperideals and $\mathcal{J}$-Γ-hyperideals coincide in $\mathcal{J}$-regular ordered Γ-semihypergroups. When we deal with $\mathcal{J}$-(bi-)Γ-hyperideals of ordered Γ-semihypergroups, it is natural to talk about fuzzy $\mathcal{J}$-(bi-)Γ-hyperideal. According to the research results, it is suggested to define and investigate some properties of fuzzy $\mathcal{J}$-(bi-)Γ-hyperideals, rough prime $\mathcal{J}$-bi-Γ-hyperideals, fuzzy prime $\mathcal{J}$-bi-Γ-hyperideals, and uni-soft $\mathcal{J}$-int-Γ-hyperideals in ordered Γ-semihypergroups. As an application of the results of this article, the corresponding results of ordered semihypergroups can be also obtained by moderate modification.

DATA AVAILABILITY STATEMENT

All datasets presented in this study are included in the article/supplementary material.

AUTHOR CONTRIBUTIONS

All authors have made a substantial, direct, and intellectual contribution to the work and approved it for publication.

FUNDING

This work was supported by the National Key R&D Program of China (Grant no. 2019YFA0706402), the Natural Science Foundation of Guangdong Province (Grant no. 2018A0303130115), and Guangzhou Academician and Expert Workstation (Grant no. 20200115-9).

REFERENCES

1. Dehghan Nezhad A, Moosavi Nejad SM, Nadjafikhah M, Davvaz B. A physical example of algebraic hyperstructures: leptons. *Indian J Phys* (2012) **86**(11): 1027–32. doi:10.1007/s12648-012-0151-x
2. Davvaz B, Nezhad AD, Nejad SMM. Algebraic hyperstructure of observable elementary particles including the Higgs boson. *Proc Natl Acad Sci, India, Sect A Phys Sci* (2020). **90**:169–76. doi:10.1007/s40010-018-0553-z
3. Yaqoob N, Tang J, Chinram R. Structures of involution Γ-semihypergroups. *Honam Mathematical J* (2018) **40**(1):109–24. doi:10.5831/HMJ.2018.40.1.109
4. Khan A, Farooq M, Yaqoob N. Uni-soft structures applied to ordered Γ-semihypergroups. *Proc Natl Acad Sci, India, Sect A Phys Sci* (2020) **90**: 457. doi:10.1007/s40010-019-00602-x
5. Marty F. Sur une generalization de la notion de groupe. In: Proceedings of the 8th Congress Math. Scandinaves, Stockholm, Sweden; Stockholm, Sweden (1934). p. 45–49.
6. Corsini P. *Prolegomena of hypergroup theory*. 2nd ed. Udine, Italy: Aviani Editore (1993).
7. Corsini P, Leoreanu V. Applications of hyperstructure theory. In: *Advances in mathematics*. Dordrecht, Netherlands: Kluwer Academic Publishers (2003).
8. Davvaz B. *Semihypergroup theory*. New York, NY: Elsevier (2016).
9. Davvaz B, Leoreanu-Fotea V. *Hyperring theory and applications*. Palm Harbor, FL: International Academic Press (2007).
10. Davvaz B, Vougiouklis T. *A walk through weak hyperstructures-H_v-structures*. Hackensack, NJ: World Scientific Publishing Co. Pte. Ltd. (2019).
11. Vougiouklis T. *Hyperstructures and their representations*. Palm Harbor, FL: Hadronic Press Inc. (1994).
12. Heidari D, Davvaz B. On ordered hyperstructures. *Politehn Univ Bucharest Sci Bull Ser A Appl Math Phys* (2011) **73**(2):85–96.
13. Davvaz B, Corsini P, Changphas T. Relationship between ordered semihypergroups and ordered semigroups by using pseudoorder. *Eur J Combinator* (2015) **44**:208–17. doi:10.1016/j.ejc.2014.08.006
14. Gu Z, Tang X. Ordered regular equivalence relations on ordered semihypergroups. *J Algebra* (2016) **450**:384–97. doi:10.1016/j.jalgebra.2015.11.026
15. Tipachot N, Pibaljommee B. Fuzzy interior hyperideals in ordered semihypergroups. *Ital J Pure Appl Math* (2016) **36**:859–70.
16. Mahboob A, Khan NM, Davvaz B. (m,n)-hyperideals in ordered semihypergroups. *Categ General Alg Structures Appl* (2020) **12**(1):43–67. doi:10.29252/cgasa.12.1.43
17. Good RA, Hughes DR. Associated groups for a semigroup. *Bull Am Math Soc* (1952) **58**:624–5.
18. Wallace A. Relative ideals in semigroups, I (Faucett's theorem). *Colloq Math* (1962). **9**:55–61. doi:10.4064/cm-9-1-55-61.
19. Hrmová R. Relative ideals in semigroups. *Matematický časopis* (1967) **17**(3): 206–23.

20. Khan NM, Ali MF. Relative bi-ideals and relative quasi ideals in ordered semigroups. *Hacet J Math Stat* (2020) **49**(3):950–61. doi:10.15672/hujms.624046
21. Sen MK, Saha NK. On Γ-semigroup I. *Bull Calcutta Math Soc* (1986). **78**:180–6.
22. Anvariyeh SM, Mirvakili S, Davvaz B. On Γ-hyperideals in Γ-semihypergroups. *Carpathian J Math* (2010) **26**(1):11–23.
23. Yaqoob N, Aslam M. Prime (*m*, *n*) Bi-Γ -hyperideals in Γ-semihypergroups. *Appl Math Inf Sci* (2014) **8**(5):2243–9. doi:10.12785/amis/080519
24. Omidi S, Davvaz B. Bi-Γ-hyperideals and Green's relations in ordered Γ-semihypergroups. *Eurasian Mathematical J* (2017) **8**(4):63–73.
25. Omidi S, Davvaz B, Hila K. Characterizations of regular and intra-regular ordered Γ-semihypergroups in terms of bi-Γ-hyperideals. *Carpathian Math Publ* (2019) **11**(1):136–51. doi:10.15330/cmp.11.1.136-151
26. Basar A, Abbasi MY, Bhavanari S. On generalized Γ-hyperideals in ordered Γ-semihypergroups. *Fundam J Math Appl* (2019) **2**(1):18–23. doi:10.33401/fujma.543712
27. Tang J, Davvaz B, Xie X-Y, Yaqoob N. On fuzzy interior Γ-hyperideals in ordered Γ-semihypergroups. *J Intell Fuzzy Syst* (2017). **32**:2447–60. doi:10.3233/jifs-16431
28. Omidi S, Davvaz B, Abdiogluv C. Some properties of quasi-Γ-hyperideals and hyperfilters in ordered Γ-semihypergroups. *Southeast Asian Bull Math* (2018) **42**(2):223–42.
29. Omidi S, Davvaz B. Convex ordered Gamma-semihypergroups associated to strongly regular relations. *Matematika* (2017) **33**(2):227–40. doi:10.11113/matematika.v33.n2.838

Conflict of Interest: The authors declare that the research was conducted in the absence of any commercial or financial relationships that could be construed as a potential conflict of interest.

frontiers in Physics

BRIEF RESEARCH REPORT
published: 11 November 2020
doi: 10.3389/fphy.2020.00381

Research on the Theory of Optical Transmission for Bragg Fiber With High-Index-Core

*Daojun Liu and Ji Zhang**

Department of General Education, AnHui XinHua University, Hefei, China

The paper analyzes the two theories of conducted light signal for Bragg fiber with high-index core, namely total internal reflection and photonic bandgap. From the perspective of the wave equation, the distribution of the electromagnetic field and the conditions for forming the guided mode when the optical signal is transmitted in the core of fiber are explained. The analysis of photonic bandgap adopts the band structure principle of natural crystals for analogy. Then, the formation process of the photonic bandgap is elaborated on.

Keywords: optical communication, fiber mode, wave theory, photonic band-gap, finite difference time domain, Bragg fiber

OPEN ACCESS

Edited by:
Jinde Cao,
Southeast University, China

Reviewed by:
Yujun Yang,
Yantai University, China
Zhongxun Zhu,
South-Central University for Nationalities, China

****Correspondence:***
Ji Zhang
coolfall123@126.com

Specialty section:
This article was submitted to Mathematical and Statistical Physics, a section of the journal Frontiers in Physics

Received: *24 April 2020*
Accepted: *07 August 2020*
Published: *11 November 2020*

Citation:
Liu D and Zhang J (2020) Research on the Theory of Optical Transmission for Bragg Fiber With High-Index-Core. Front. Phys. 8:381. doi: 10.3389/fphy.2020.00381

INTRODUCTION

The concept of Bragg fiber has been proposed for a long time. With a periodic refractive index distribution along the radial direction, it belongs to a one-dimensional bandgap photonic crystal fiber. Generally speaking, Bragg fiber is of a cylindrical hollow structure, which is difficult in production and practical application, so the application of this fiber is slow after being proposed for many years. In recent years, it has been proposed to fill the hollow structure of Bragg fiber with a high refractive dielectric material to make it the Bragg fiber with high-index core [1–3]. **Figures 1**, **2** show the schematic diagram of the sectional drawing and refractive index of Bragg fiber with high-index core, respectively. It combines ordinary hollow Bragg fiber with traditional fiber. In this way, the problem in processing is solved. More importantly, two binding mechanisms for fiber transmission are provided, namely total internal reflection and photonic bandgap effect. Besides, more controllable structural parameters in the design can be obtained, making it free to choose to strengthen or weaken certain non-linear optical effects. Also, dispersion flattened of the specific band, and the extremely high non-linear coefficient can be obtained [2, 4–6].

ANALYSIS OF WAVE THEORY FOR BRAGG FIBER WITH HIGH-INDEX CORE

The optical signal should satisfy the wave equation derived from Maxwell's equations [7]

$$\nabla^2 E + \left(\frac{n\omega}{c}\right)^2 E = 0. \tag{1}$$

$$\nabla^2 H + \left(\frac{n\omega}{c}\right)^2 H = 0. \tag{2}$$

Generally speaking, the vector solution to the earlier mentioned vector wave equation is very complicated. Therefore, the scalar effective index method is adopted for the solution of fiber in most

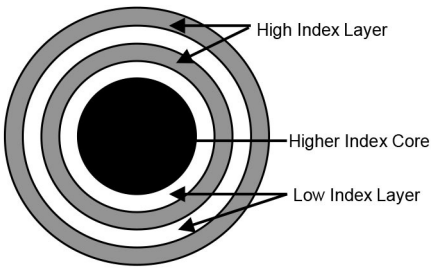

FIGURE 1 | Sectional drawing of Bragg fiber with high-index core.

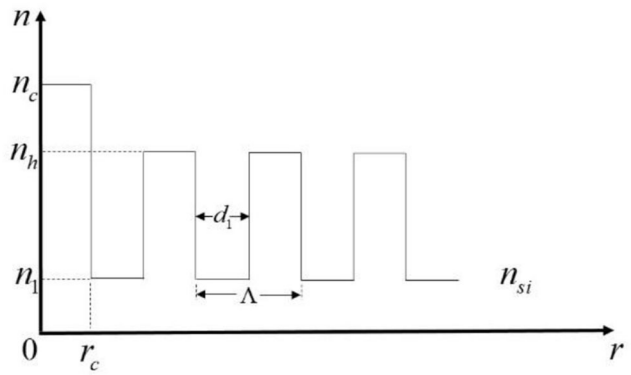

FIGURE 2 | Refractive index of Bragg fiber with high-index core.

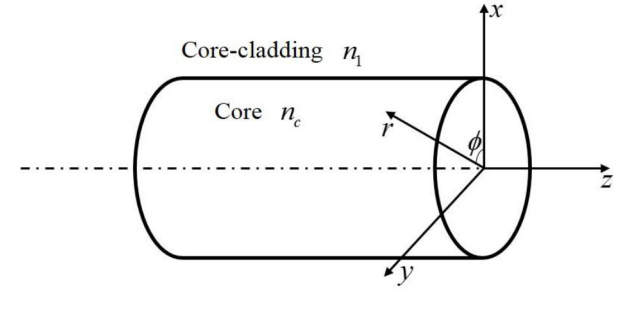

FIGURE 3 | Schematic diagram of the coordinates of the fiber in the cylindrical coordinate system.

cases [8]. Our concern is the optical power distribution of the optical field in the cross-section of the optical fiber during the transmission of an optical signal in optical fiber. To know the distribution, it is necessary to find the solution for the scalar field of the optical fibers of Equations (1) and (2) that satisfy the core-cladding boundary conditions. In the cylindrical coordinate system (r, ϕ, z) shown in **Figure 3**, Equation (1) can be expanded into a wave equation [5, 6, 9].

$$\frac{\partial^2 E_Z}{\partial r^2}+\frac{1}{r}\frac{\partial E_Z}{\partial r}+\frac{1}{r^2}\frac{\partial^2 E_Z}{\partial \phi^2}+\frac{\partial^2 E_Z}{\partial z^2}+(\frac{n\omega}{c})^2 E_Z=0 \qquad (3)$$

The following parameters can generally be provided in the field of optical fiber communication $k=2\pi/\lambda=2\pi f/c=\omega/c$. λ and f are wavelength and frequency, β is propagation constant. As it is shown in **Figure 3**, core ($0 \le r \le a$) refractive index $n(r)=n_c$, cladding ($r \ge a$) refractive index $n(r)=n_1$.

$E_z(z)$ in Equation (3) is set as $E_z(r, \phi, z)=E_z(r)E_z(\phi)E_z(z)$ with the method of separation of variables. The optical signal transmitted along the z-axis $E_z(z)$ is of the form of $\exp(-j\beta z)$. As optical fiber is of circular symmetry, $E_z(\phi)$ is the periodic function for ϕ. As a result, it can be set as $\exp(jm\phi)$ in which m is an integer. Because $E_z(r)$ is unknown, it can be expressed as

$$E_z(r,\phi,z)=E_z(r)e^{j(m\phi-\beta z)}. \qquad (4)$$

In the core and cladding, substituting Equation (4) into Equation (3) yields two m-order Bessel equations

$$\frac{d^2E_z(r)}{dr^2}+\frac{1}{r}\frac{dE_Z(r)}{dr}+(\frac{u^2}{a^2}-\frac{m^2}{r^2})E_Z(r)=0(r\le a). \qquad (5)$$

$$\frac{d^2E_z(r)}{dr^2}+\frac{1}{r}\frac{dE_Z(r)}{dr}-(\frac{w^2}{a^2}-\frac{m^2}{r^2})E_Z(r)=0(r\ge a). \qquad (6)$$

Among them, u, v, and w are three dimensionless variables namely

$$\left.\begin{aligned} u^2 &= a^2(n_c^2k^2-\beta^2).\\ w^2 &= a^2(\beta^2-n_1^2k^2).\\ v^2 &= u^2+w^2=a^2k^2(n_c^2-n_1^2). \end{aligned}\right\} \qquad (7)$$

Therefore, the specific distribution of the electromagnetic in the fiber can be obtained through analysis of the solution to Equations (5) and (6) [5, 6].

In the core ($r \le a$), the light wave produces total internal reflection, so the transmission of the light wave in the Z direction is slower than the transmission of a plane wave in the medium n_c, namely $\beta < kn_c$. Where r = 0, the electromagnetic field should be a finite real number. According to these characteristics, the solution to Equation (5) should be m order Bessel function $J_m(ur/a)$, so the expression of the electric field $E_z(r, \phi, z)$ and the magnetic field $H_z(r, \phi, z)$ in the core is as follows

$$\left.\begin{aligned} E_{zc}(r,\phi,z) &= A\frac{J_m(ur/a)}{J_m(u)}e^{j(m\Phi-\beta z)}(0\le r\le a).\\ H_{zc}(r,\phi,z) &= B\frac{J_m(ur/a)}{J_m(u)}e^{j(m\Phi-\beta z)}(0\le r\le a). \end{aligned}\right\} \qquad (8)$$

In the cladding ($r \ge a$), the light wave decays in the r direction. Where $r \to \infty$, the electromagnetic field should decay to zero, namely $\beta > kn_1$. The solution to Equation (6) should take the m-order-corrected Bessel function $K_m(ur/a)$, so the expression of the electric field $E_z(r, \phi, z)$ and the magnetic field $H_z(r, \phi, z)$ in the cladding is as follows

$$\left.\begin{aligned} E_{z1}(r,\phi,z) &= A\frac{K_m(wr/a)}{k_m(w)}e^{j(m\Phi-\beta z)}(r\ge a).\\ H_{z1}(r,\phi,z) &= B\frac{K_m(wr/a)}{k_m(w)}e^{j(m\Phi-\beta z)}(r\ge a). \end{aligned}\right\} \qquad (9)$$

In the equation, A and B are constants determined by the excitation conditions. It can be concluded from two types

of Bessel function curves of the principle of optical fiber communication that $J_m(u)$ is similar to a sine curve with analogous amplitude attenuation, and $K_m(w)$ is similar to an index curve of attenuation. It can be learned from Equation (7) that where such parameters as n_c, n_1, a, and k are determined, u and w are only determined by β. Therefore, deriving the characteristic equation, satisfying β can obtain the value of β and u,w. The boundary condition of the electromagnetic in the core-cladding surface is as follows

$$\left.\begin{array}{l} E_{zc} = E_{z1} H_{zc} = H_{z1}. \\ E_{\phi c} = E_{\phi 1} H_{\phi c} = H_{\phi 1}. \end{array}\right\} \tag{10}$$

It can be learned from Equations (8) and (9) that E_z and H_z satisfy the requirement of the boundary condition. The boundary condition satisfied by E_ϕ and H_ϕ can derive the characteristics equation satisfied by β

$$\begin{aligned} &[\tfrac{J'_m(u)}{uJ_m(u)} + \tfrac{K'_m(w)}{wK_m(w)}][\tfrac{n_c^2}{n_1^2}\tfrac{J'_m(u)}{uJ_m(u)} + \tfrac{K'_m(w)}{wK(w)}] \\ &= (\tfrac{\beta}{nk})^2 m^2 (\tfrac{1}{u^2} + \tfrac{1}{w^2})(\tfrac{n_c^2}{n_1^2}\tfrac{1}{u^2} + \tfrac{1}{w^2}). \end{aligned} \tag{11}$$

The equation is combined with the characteristic parameters v defined by Equation (7); the value of β can be obtained with the numerical solution and thus determine the electromagnetic field distribution of light wave in the core.

ANALYSIS OF PHOTONIC BANDGAP THEORY FOR BRAGG FIBER WITH HIGH-INDEX CORE

A photonic crystal is a new type of optical material that emerged in recent years. The regular microstructure is introduced onto ordinary optical material artificially to form the microstructural material with a periodically changing refractive index. Generally speaking, the size of the microstructure is sub-micron and of the same order of magnitude to the wavelength of the light wave. This material with a periodical distribution of refractive index shows the special optical property for selecting different wavelengths of light. In other words, the light of some wavelengths could not exist or be transmitted in the photonic crystal but be reflected. For these wavelengths, photonic crystal is like a mirror to stop and reflect the incident light. This phenomenon is similar to the energy band structure of semiconductor physics [7, 10–12].

According to solid-state physics, the motion of electrons in its periodic potential field satisfies the Schrödinger equation in natural crystal

$$\left.\begin{array}{l} \left[-\frac{\hbar^2}{2m}\nabla^2 + V(\vec{r})\right]\psi = E\psi. \\ V(\vec{r}) = V(\vec{r} + \vec{R}). \end{array}\right\} \tag{12}$$

In Equation (12), $V(\vec{r})$ represents the potential energy, and $\vec{R}$ represents the lattice constant in the crystal. The electron wave can exhibit the energy band structure in the periodic potential field and form a forbidden band due to the scattering of atoms of the crystal [11]. The formation mechanism of the energy band in the photonic crystal is similar to the earlier mentioned process. The propagation of the electromagnetic wave in medium satisfies Maxwell equation [13–16]

$$\left.\begin{array}{l} \nabla \cdot \vec{D} = \rho. \\ \nabla \cdot \vec{B} = 0. \\ \nabla \times \vec{E} = -\frac{\partial \vec{B}}{\partial t}. \\ \nabla \times \vec{H} = \vec{J} + \frac{\partial \vec{D}}{\partial t}. \end{array}\right\} \tag{13}$$

In Equation (13) $\vec{J} = \sigma\vec{E}$ $\vec{D} = \varepsilon\vec{E}$ $\vec{B} = \mu\vec{H}$. Among them, σ, ε, andμ represent conductivity, permittivity, and permeability, respectively. If there is no free charge and current while the medium is also a non-magnetic and isotropic material, $\varepsilon = \varepsilon(\vec{r})$ should be a periodic function considering the periodicity of the photonic crystal [14, 15]. $\varepsilon(\vec{r}) = \varepsilon_0\varepsilon_r(\vec{r})$, $\mu = \mu_0$, where $\varepsilon_r(\vec{r})$ is the relative permittivity of the medium. It can be obtained through substituting the discussed parameters into Equation (13)

$$\left.\begin{array}{l} \nabla \cdot \varepsilon_0\varepsilon_r(\vec{r})\vec{E} = 0. \\ \nabla \cdot \mu_0\vec{H} = 0. \\ \nabla \times \vec{E} + \mu_0\frac{\partial \vec{H}}{\partial t} = 0. \\ \nabla \times \vec{H} - \varepsilon_0\varepsilon_r(\vec{r})\frac{\partial \vec{E}}{\partial t} = 0. \end{array}\right\} \tag{14}$$

Considering that the incident light signal is a harmonic electromagnetic wave, if $\vec{E} = \vec{E}(\vec{r})e^{j\omega t}$, $\vec{H} = \vec{H}(\vec{r})e^{j\omega t}$, then it can be obtained through substituting into Equation (14)

$$\left.\begin{array}{l} \nabla \cdot \varepsilon_0\varepsilon_r(\vec{r})\vec{E}(\vec{r}) = 0. \\ \nabla \cdot \mu_0\vec{H}(\vec{r}) = 0. \\ \nabla \times \vec{E}(\vec{r}) + j\omega\mu_0\vec{H}(\vec{r}) = 0. \\ \nabla \times \vec{H}(\vec{r}) - j\omega\varepsilon_0\varepsilon_r(\vec{r})\vec{E}(\vec{r}) = 0. \end{array}\right\} \tag{15}$$

After simplifying Equation (15), it can be obtained for TE mode ($H_x = H_y = E_z = 0$) [2, 5, 6]

$$\nabla \times \left[\frac{1}{\varepsilon(\vec{r})}\nabla \times \vec{H}(\vec{r})\right] = \left(\frac{\omega}{c}\right)^2 \vec{H}(\vec{r}). \tag{16}$$

It can be obtained for TM mode ($E_x = E_y = H_z = 0$)

$$\nabla \times \nabla \times \vec{E}(\vec{r}) = \left(\frac{\omega}{c}\right)^2 \varepsilon(\vec{r})\vec{E}(\vec{r}). \tag{17}$$

In Equations (16) and (17), $c = \frac{1}{\sqrt{\varepsilon_0\mu_0}}$ is the velocity of light in vacuum. Equations (16) and (17) are the Helmholtz equations obtained through Maxwell's equations. The permittivity in photonic crystal shows a periodical change. The permittivity is set as the sum of two parts $\varepsilon(\vec{r})$=$\varepsilon'(\vec{r})$+$\bar{\varepsilon}$, where $\varepsilon'(\vec{r})$ is the

changing permittivity and $\bar{\varepsilon}$ is the average permittivity. It can be obtained through substituting the discussed parameter in respect to Equation (17)

$$\left.\begin{array}{l}\left[-\nabla^2-\left(\frac{\omega}{c}\right)^2\varepsilon'(\vec{r})\right]\vec{E}(\vec{r})+\nabla\left[\nabla\vec{E}(\vec{r})\right]\\=\left(\frac{\omega}{c}\right)^2\bar{\varepsilon}\vec{E}(\vec{r}).\\\\\varepsilon'(\vec{r})=\varepsilon'(\vec{r}+\vec{R}).\end{array}\right\} \quad (18)$$

Where $\vec{R}$ is the lattice constant of the photonic crystal. If we use Equations (18) and (12) to make the following analogy [17–19]

$$\left.\begin{array}{l}-\left(\frac{\omega}{c}\right)^2\varepsilon'(\vec{r})\sim V(\vec{r}).\\\qquad\qquad\left(\frac{\omega}{c}\right)^2\bar{\varepsilon}\sim E.\end{array}\right\} \quad (19)$$

The two are extremely similar. It is discovered in further comparison that Equation (18) has one more item $\nabla\left[\nabla\vec{E}(\vec{r})\right]$ and is a vector, whereas Equation (12) is scalar. However, if vertical incidence or one-dimensional conditions are considered, then$\nabla\left[\nabla\vec{E}(\vec{r})\right]=0$. In this way, there is almost no difference between the two. As a result, Equation (18) can also use the Bloch theorem to calculate the energy band or bandgap. It can be seen from the previous analysis that the movement of a photon in a photonic crystal is similar to the movement of electrons in a periodic potential field, which could cause energy band structure with bandgap. The solution to Equations (16) and (17) show that there is no solution in some frequency bands. It means that photonic crystal stops the transmission of an electromagnetic wave in these frequency bands, resulting in the photonic bandgap. This method to constrain optical transmission is sometimes more efficient than total reflection [6, 20–23]. Because photonic crystal has the special property to control light, researchers introduced this microstructure into the cladding of fiber in the 1990s to form a forbidden band to stop light signal from entering the cladding and constrain it in the core to form a guided mode.

CONCLUSION

Bragg fiber with high-index core can provide two kinds of light-guiding modes for optical signal transmission, namely full reflection effect and photonic bandgap effect. The specific process of optical signal transmission in optical fiber is analyzed and calculated from the wave equation. The transmission constant is obtained by numerical solution to the equations β, and the distribution of the electromagnetic field and the conditions for forming the guided mode when the optical signal is transmitted in the core of fiber are determined [24, 25]. The photonic bandgap is a kind of special structure obtained by the analogy of photonic crystal and natural crystal, which is similar to the energy band structure of the natural crystal. By analogy with the equation established in the transmission of optical signals in photonic crystal and the Schrodinger equation of solid-state physics, it is learned that the optical signals of certain frequency bands in photonic crystals cannot be transmitted, thus forming the forbidden band, that is, the principle of photonic bandgap effect.

DATA AVAILABILITY STATEMENT

The original contributions presented in the study are included in the article/supplementary material, further inquiries can be directed to the corresponding author.

AUTHOR CONTRIBUTIONS

DL and JZ contributed to the conception and design of the study. JZ organized the literature. DL performed the design of figures and wrote the first draft of the manuscript. All authors contributed to the manuscript revision, read, and approved the submitted version.

FUNDING

This work was supported by the Natural Science Foundation of Anhui Province of China (Grant Nos. KJ2019A0879 and KJ2018A0588).

ACKNOWLEDGMENTS

The authors would like to express their sincere gratitude to the reviewers and the editors for their careful reviews and constructive recommendations.

REFERENCES

1. Zhang WD, Li X, Bai JH, Zhang L, Zhao JL. Generation and application of fiber-based structured light field. *Acta Optica Sin.* (2019) 39:51–69. doi: 10.3788/AOS201939.0126003
2. Niu J. *Research on the band-Gap properties of two-dimensional double-layer photonic crystals* (M.S. thesis). Dept. Communication, Henan Polytechnic University, Jiaozuo, China (2014).
3. Zheng Y, Hwa-Yaw T. Industrial and medical applications of fiber Bragg gratings (Invited Paper). *Chin Optics Lett.* (2016) 14:25–9. doi: 10.3788/COL201614.120007
4. Meng Y, Su XM, Pan Y. Characteristics of Fabry-Perot cavity based on dynamic grating in Er-doped fiber and fiber Bragg grating. *Acta Optica Sin.* (2018) 38:78–86. doi: 10.3788/AOS201838.1006003
5. Yue YL. *Studies on the band-Gap structures of photonic crystal fiber and properties of directional coupling waveguides* (M.S. thesis). Dept. Communication, Nanchang University, Nanchang, China (2008).
6. Tang C. *Research on photonic crystal fibers* (M.S. thesis). Dept. Communication, University of Electronic Science and Technology of China, Chengdu, China (2005).
7. Zhang M, Sun X. *Optical Fiber in Principle and System of Optical Fiber Communication*. Nanjing: Southeast University Press (2009). p. 24–32.
8. Xu XN, Chen YJ. Curvature sensing measurement based on seven-core fiber and few-mode fiber splicing structure. *Acta Optica Sin.* (2019) 39:03060011–7. doi: 10.3788/AOS201939.0306001
9. Zhang H, Wu Z, Shum P, Wang R, Dinh X, Fu S, et al. Fiber Bragg gratings in heterogeneous multicore fiber for directional bending sensing. *J Optics.* (2016) 18:085705–10. doi: 10.1088/2040-8978/18/8/085705

10. Ertman S, Lesiak P, Woliński TR. Optofluidic photonic crystal fiber-based sensors. *J Lightwave Technol.* (2017) 35:3399–405. doi: 10.1109/JLT.2016.2596540
11. Li Y, Tian J, Fu Q, Sun Y, Yao Y. A multi-point switchable and self-adaptive ultrasonic sensor using fiber Bragg gratings in a fiber ring laser. *J Lightwave Technol.* (2019) 37:1160–7. doi: 10.1109/JLT.2018.2888756
12. Dong Y, Xiao S, Wu B, Xiao H, Jian S. Refractive index and temperature sensor based on D-shaped fiber combined with a fiber Bragg grating. *IEEE Sens J.* (2019) 19:1362–7. doi: 10.1109/JSEN.2018.2880305
13. Chang M, Li B, Chen N, Lu X, Zhang X, Xu J. A compact and broadband photonic crystal fiber polarization filter based on a plasmonic resonant thin gold film. *IEEE Photonics J.* (2019) 11:1–12. doi: 10.1109/JPHOT.2019.2899117
14. Rifat A, Mahdiraji GA, Ahmed R, Desmond MC, Sua YM, Shee YG, et al. Copper-graphene-based photonic crystal fiber plasmonic biosensor. *IEEE Photonics J.* (2016) 8:4800408–15. doi: 10.1109/JPHOT.2015.2510632
15. Huq Arif MF, Ahmed K, Asaduzzaman S, Azad MAK. Design and optimization of photonic crystal fiber for liquid sensing applications. *Photonic Sens.* (2016) 6:279–88. doi: 10.1007/s13320-016-0323-y
16. Tao C, Wei H, Feng W. Photonic crystal fiber in-line Mach-Zehnder interferometer for explosive detection. *Optics Express.* (2016) 24:2806–17. doi: 10.1364/OE.24.002806
17. Belli F, Abdolvand A, Travers JC, Russell SJ. Control of ultrafast pulses in a hydrogen-filled hollow-core photonic-crystal fiber by Raman coherence. *Phys Rev A.* (2018) 97:013814–22. doi: 10.1103/PhysRevA.97.013814
18. Chen H, Yan H, Shan G. Design of two-dimensional bending vector sensor based on selective infiltration of photonic crystal fiber. *Chin J Lasers.* (2016) 43:0105003–11. doi: 10.3788/CJL201643.0105003
19. Zhang SH, Li JS, Li SG. Surface plasmon resonance sensor based on D-shaped photonic crystal fiber with two micro-openings. *Optical Fiber Technol.* (2018) 46:311–7. doi: 10.1088/1361-6463/aace72
20. Chen X, Xia L, Li C. Surface plasmon resonance sensor based on a novel D-shaped photonic crystal fiber for low refractive index detection. *IEEE Photonics J.* (2018) 10:1–9. doi: 10.1109/JPHOT.2018.2790424
21. Wu T, Shao Y, Wang Y, Cao S, Wang Y. Surface plasmon resonance biosensor based on gold-coated side-polished hexagonal structure photonic crystal fiber. *Optics Express.* (2017) 25:20313–22. doi: 10.1364/OE.25.020313
22. Chen D, Shen L. Ultrahigh Birefringent photonic crystal fiber with ultralow confinement loss. *IEEE Photonics Technol Lett.* (2014) 4:185–7. doi: 10.1109/LPT.2006.890040
23. Xi X, Wong G, Frosz M, Babic F, Ahmed G, Jiang X, et al. Orbital-angular-momentum-preserving helical Bloch modes in twisted photonic crystal fiber. *Optica.* (2014) 1:00165–9. doi: 10.1364/OPTICA.1.000165
24. Morshed M, Imran HM, Roy TK, Uddin MS, Abdur RSM. Microstructure core photonic crystal fiber for gas sensing applications. *Appl Opt.* (2015) 54:8637–43. doi: 10.1364/AO.54.008637
25. Roussel N, Magne S, Martinez C, Ferdinand P. Measurement of index modulation along fiber bragg gratings by side scattering and local heating techniques. *Optical Fiber Technol Mater Dev Syst.* (2018) 5:119–32. doi: 10.1006/ofte.1998.0277

Conflict of Interest: The authors declare that the research was conducted in the absence of any commercial or financial relationships that could be construed as a potential conflict of interest.

frontiers in Physics

ORIGINAL RESEARCH
published: 11 November 2020
doi: 10.3389/fphy.2020.00357

Certain Concepts of Vague Graphs With Applications to Medical Diagnosis

Zehui Shao[1], *Saeed Kosari*[1]*, *Muhammad Shoaib*[2] *and Hossein Rashmanlou*[3]

[1] *Institute of Computing Science and Technology, Guangzhou University, Guangzhou, China,* [2] *Department of Mathematics, University of the Punjab, New Campus, Lahore, Pakistan,* [3] *Mazandaran Adib Institute of Higher Education, Sari, Iran*

The purpose of this research study is to present and explore the key properties of some new operations on vague graphs, including rejection, maximal product, symmetric difference, and residue product. This article introduces the notions of degree of a vertex and total degree of a vertex in a vague graph. As well, this study outlines the specific conditions required for obtaining the degrees of vertices in vague graphs under the operations of maximal product, symmetric difference, and rejection. The article also discusses applications of vague sets in medical diagnosis.

Keywords: vague set, maximal product, rejection, symmetric difference, residue product, application

OPEN ACCESS

Edited by:
Muhammad Javaid, University of Management and Technology, Pakistan

Reviewed by:
Anouar Ben Mabrouk, University of Kairouan, Tunisia
Ndolane Sene, Cheikh Anta Diop University, Senegal

***Correspondence:**
Saeed Kosari
saeedkosari38@yahoo.com

Specialty section:
This article was submitted to Mathematical and Statistical Physics, a section of the journal Frontiers in Physics

Received: *17 May 2020*
Accepted: *27 July 2020*
Published: *11 November 2020*

Citation:
Shao Z, Kosari S, Shoaib M and Rashmanlou H (2020) Certain Concepts of Vague Graphs With Applications to Medical Diagnosis. Front. Phys. 8:357. doi: 10.3389/fphy.2020.00357

1. INTRODUCTION

Graph theory is an extremely useful tool for solving combinatorial problems in a wide range of fields, including geometry, algebra, number theory, topology, operations research, biology, and social systems. Graph theory also has many applications of great scope, such as in networking, image capture, clustering, handling uncertainty, image segmentation, finding communities in networks, bioscience, information technology, operations research, and social science networks consisting of points connected by lines. In fact, graph theory studies connections between objects, such as vertices and edges and the various relations between them. Fuzzy graph theory is finding an increasing number of applications in modeling real-time systems, where the amount of information inherent in the system varies with different levels of precision. In 1965, Zadeh [1] first proposed the theory of fuzzy sets. The fuzzy graph, with the approximate reasoning, enables many combinatorial problems in fields, such as topology and algebra to be solved more easily. The concept of fuzzy graphs is discussed by Rosenfeld [2] as well as by Bhattacharya [3, 4]. Fuzzy graphs date back to the nineteenth century, and their use has grown tremendously in recent years [5, 6]. Gau and Buehrer [7] proposed the concept of vague set in 1993, which replaces the value of an element in a set with a subinterval of $[0, 1]$. Specifically, a true-membership function $t_v(x)$ and a false-membership function $f_v(x)$ are used to describe the boundaries of the membership degree. Descriptions of real-world problems can be improved by using the theory of vague sets. Researchers have applied this theory to several real-world situations, such as decision-making and fuzzy control. The theory of vague sets is also helpful for fault diagnosis and knowledge discovery. Interval-valued fuzzy sets have a case vague set, which has been applied in different fields of mathematics. Ramakrishna [8] introduced the concept of vague graph and also studied related properties. Vague graphs have numerous applications in geometry and operations research and are also useful in many areas of computer science. Rashmanlou and Borzooei [9] studied new concepts relating to vague graphs, product vague graphs [10], regularity of vague graphs [11], and vague competition graphs [12]. Krishna and Lavanya [13] developed new concepts of coloring in vague graphs. Besides the

membership degree, the non-membership degree has been introduced as well, which is presented by Atanassove [14] in an intuitionistic fuzzy set, a type of extension of a fuzzy set. Parvathi and Karunambigai [15] discussed intuitionistic fuzzy graphs. Devi et al. [16] presented new concepts regarding intuitionistic fuzzy labeling graphs.

In this study we outline and explore the key properties of some new operations on vague graphs, including rejection, maximal product, symmetric difference, and residue product. We introduce new notions, such as degree of a vertex and total degree of a vertex in a vague graph. We also outline specific conditions for obtaining the degrees of vertices in vague graphs under the operations of maximal product, symmetric difference, and rejection. Furthermore, we explore applications of vague sets in medical diagnosis.

2. PRELIMINARIES

In this section we introduce the key preliminary notions and definitions that are used in this study.

Definition 2.1 ([17]). A graph is an ordered pair $G = (V, E)$, where V is the set of vertices of G and E is the set of all edges, arcs, or lines, which are two-element subsets of V (that is, an edge is related to two vertices and the relation is represented as an unordered pair $\{m, n\}$ of those vertices).

Note that for an edge $\{m, n\}$, graph theorists usually use the somewhat shorter notation mn. Two vertices m and n in an undirected graph G are said to be adjacent in G if mn is an edge of G. An edge whose endpoints are the same is called a loop. A graph without loops is called a simple graph.

Definition 2.2 ([7]). A vague set M is a pair $(T_M; F_M)$ of functions on a set V, where T_M and F_M are real-valued $V \to [0, 1]$ functions such that $T_M(m) + F_M(m) < 1$ for all $m \in V$. The interval $[T_M(m), 1 - F_M(m)]$ is known as the vague value of m in M.

In this definition, for m in M, $T_M(m)$ is the lower bound for the degree of membership and $F_M(m)$ is the lower bound for the negative of the degree of membership. Therefore, the degree of membership of $m \in M$ is given by the interval $[T_M(m), 1 - F_M(m)]$.

Definition 2.3 ([8]). Let $G = (V, E)$ be a crisp graph. A pair $\mathbf{G} = (M, N)$ is called a vague graph defined on the crisp graph $G = (V, E)$ if $M = (T_M, F_M)$ is a vague set on V and $N = (T_N, F_N)$ is vague set on $E \subseteq V \times V$ such that $T_N(mn) \leq \min(T_M(m), T_M(n))$ and $F_N(mn) \geq \max(F_M(m), F_M(n))$ for each edge mn in E.

Definition 2.4 ([9]). A vague graph $\mathbf{G}$ is said to be strong if $T_N(mn) = \min(T_M(m), T_M(n))$ and $F_N(mn) = \max(F_M(m), F_M(n))$ for all $m, n \in V$.

Definition 2.5 ([9]). A vague graph $\mathbf{G}$ is said to be complete if $T_N(mn) = \min(T_M(m), T_M(n))$ and $F_N(mn) = \max(F_M(m), F_M(n))$ for all $mn \in E$.

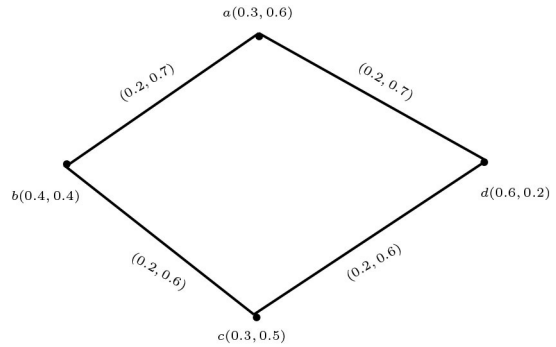

FIGURE 1 | The vague graph **G** in Example 2.7.

Definition 2.6 ([11]). A vague graph $\mathbf{G}$ is said to be connected if $T_N^\infty(m_i m_j) > 0$ and $F_N^\infty(m_i m_j) < 1$ for all $m_i, m_j \in V$. Also, we have

$$T_N^\infty(mn) = \sup\{T_N(mn_1) \wedge T_N(n_1n_2) \wedge T_N(n_2n_3) \wedge \ldots \wedge T_N(n_{k-1}n) \mid m, n_1, n_2, \ldots, n_{k-1}, n \in V\}$$

and

$$F_N^\infty(mn) = \inf\{F_N(mn_1) \vee F_N(n_1n_2) \vee F_N(n_2n_3) \vee \ldots \vee F_N(n_{k-1}n) \mid m, n_1, n_2, \ldots, n_{k-1}, n \in V\}.$$

Example 2.7. Consider a vague graph $\mathbf{G}$ such that $V = \{a, b, c\}$, $E = \{ab, bc, cd, ad\}$, $M = \langle(\frac{a}{0.3}, \frac{b}{0.4}, \frac{c}{0.3}, \frac{d}{0.6}), (\frac{a}{0.6}, \frac{b}{0.4}, \frac{c}{0.5}, \frac{a}{0.2})\rangle$, and $N = \langle(\frac{ab}{0.2}, \frac{bc}{0.2}, \frac{cd}{0.2}, \frac{ad}{0.2}), (\frac{ab}{0.7}, \frac{bc}{0.6}, \frac{cd}{0.6}, \frac{ad}{0.7})\rangle$.

By routine computations, it is easy to show that $\mathbf{G}$ is a vague graph (**Figure 1**).

3. OPERATIONS ON VAGUE GRAPHS

In this section we define four new kinds of operations on vague graphs: the maximal product, residue product, rejection, and symmetric difference. We show that the maximal product, residue product, or rejection of two vague graphs is again a vague graph.

Definition 3.1. The maximal product $\mathbf{G}_1 * \mathbf{G}_2 = (M_1 * M_2, N_1 * N_2)$ of two vague graphs $\mathbf{G}_1 = (M_1, N_1)$ and $\mathbf{G}_2 = (M_2, N_2)$ is defined by

(i) $$(T_{M_1} * T_{M_2})((m_1, m_2)) = \max\{T_{M_1}(m_1), T_{M_2}(m_2)\},$$
$$(F_{M_1} * F_{M_2})((m_1, m_2)) = \min\{F_{M_1}(m_1), F_{M_2}(m_2)\}$$
$$\forall\, (m_1, m_2) \in (V_1 \times V_2);$$

(ii) $$(T_{M_1} * T_{M_2})((m, m_2)(m, n_2)) = \max\{T_{M_1}(m), T_{N_2}(m_2n_2)\},$$
$$(F_{M_1} * F_{M_2})((m, m_2)(m, n_2)) = \min\{F_{M_1}(m), F_{N_2}(m_2n_2)\}$$
$$\forall\, m \in V_1 \text{ and } m_2n_2 \in E_2;$$

(iii) $$(T_{M_1} * T_{M_2})((m_1, z)(n_1, z)) = \max\{T_{N_1}(m_1n_1), T_{M_2}(z)\},$$
$$(F_{M_1} * F_{M_2})((m_1, z)(n_1, z)) = \min\{F_{N_1}(m_1n_1), F_{M_2}(z)\}$$
$$\forall\, z \in V_2 \text{ and } m_1n_1 \in E_1.$$

Example 3.2. Consider the two vague graphs $\mathbf{G}_1$ and $\mathbf{G}_2$ shown in **Figures 2**, **3**. Their maximal product $\mathbf{G}_1 * \mathbf{G}_2$ is shown in **Figure 4**.

For the vertex (a, d), we find the membership and non-membership values as follows:

$$\begin{aligned}(T_{M_1} * T_{M_2})((a,d)) &= \max\{T_{M_1}(a), T_{M_2}(d)\}\\ &= \max\{0.4, 0.1\} = 0.4,\\ (F_{M_1} * F_{M_2})((a,d)) &= \min\{F_{M_1}(a), F_{M_2}(d)\}\\ &= \min\{0.5, 0.3\} = 0.3,\\ &\text{for } a \in V_1 \text{ and } d \in V_2.\end{aligned}$$

For the edge $(a, d)(a, e)$, we find the following membership and non-membership values:

$$\begin{aligned}(T_{M_1} * T_{M_2})((a,d)(a,e)) &= \max\{T_{M_1}(a), T_{N_2}(de)\}\\ &= \max\{0.4, 0.1\} = 0.4,\\ (F_{M_1} * F_{M_2})((a,d)(a,e)) &= \min\{F_{M_1}(a), F_{N_2}(de)\}\\ &= \min\{0.5, 0.6\} = 0.5,\\ &\text{for } a \in V_1 \text{ and } de \in E_2.\end{aligned}$$

Now, for edge $(a, g)(b, g)$ we have

$$\begin{aligned}(T_{M_1} * T_{M_2})((a,g)(b,g)) &= \max\{T_{N_1}(ab), T_{M_2}(g)\}\\ &= \max\{0.2, 0.3\} = 0.3,\\ (F_{M_1} * F_{M_2})((a,g)(b,g)) &= \min\{F_{N_1}(ab), F_{M_2}(g)\}\\ &= \min\{0.7, 0.4\} = 0.4,\\ &\text{for } g \in V_2 \text{ and } ab \in E_1.\end{aligned}$$

Similarly, we can find the membership and non-membership values for all the remaining vertices and edges.

Proposition 3.3. The maximal product of two vague graphs $\mathbf{G}_1$ and $\mathbf{G}_2$ is a vague graph.

Proof: Let $\mathbf{G}_1 = (M_1, N_1)$ and $\mathbf{G}_2 = (M_2, N_2)$ be two vague graphs on crisp graphs $G_1 = (V_1, E_1)$ and $G_2 = (V_2, E_2)$, respectively, and let $((m_1, m_2)(n_1, n_2)) \in E_1 \times E_2$. Then by Definition 3.1 we have two cases:

(i) If $m_1 = n_1 = m$, then

$$\begin{aligned}&(T_{N_1} * T_{N_2})((m,m_2)(m,n_2)) = \max\{T_{M_1}(m), T_{N_2}(m_2n_2)\}\\ &\le \max\{T_{M_1}(m), \min\{T_{M_2}(m_2), T_{M_2}(n_2)\}\}\\ &= \min\{\max\{\{T_{M_1}(m), T_{M_2}(m_2)\}, \max\{\{T_{M_1}(m), T_{M_2}(n_2)\}\}\\ &= \min\{(T_{M_1} * T_{M_2})(m,m_2), (T_{M_1} * T_{M_2})(m,n_2)\},\\ &(F_{N_1} * F_{N_2})((m,m_2)(m,n_2)) = \min\{F_{M_1}(m), F_{N_2}(m_2n_2)\}\\ &\ge \min\{F_{M_1}(m), \max\{F_{M_2}(m_2), F_{M_2}(n_2)\}\}\\ &= \max\{\min\{\{F_{M_1}(m), F_{M_2}(m_2)\}, \min\{\{F_{M_1}(m), F_{M_2}(n_2)\}\}\\ &= \max\{(F_{M_1} * F_{M_2})(m,m_2), (F_{M_1} * F_{M_2})(m,n_2)\}.\end{aligned}$$

(ii) If $m_2 = n_2 = z$, then

$$\begin{aligned}&(T_{N_1} * T_{N_2})((m_1,z)(n_1,z)) = \max\{T_{N_1}(m_1n_1), T_{M_2}(z)\}\\ &\le \max\{\min\{T_{N_1}(m_1n_1), T_{M_2}(z)\}\\ &= \min\{\max\{\{T_{N_1}(m_1), T_{M_2}(z)\}, \max\{\{T_{M_1}(n_1), T_{M_2}(z)\}\}\\ &= \min\{(T_{M_1} * T_{M_2})(m_1,z), (T_{M_1} * T_{M_2})(n_1,z)\},\\ &(F_{N_1} * F_{N_2})((m_1,z)(n_1,z)) = \min\{F_{N_1}(m_1n_1), F_{M_2}(z)\}\\ &\ge \min\{\max\{F_{N_1}(m_1n_1), F_{M_2}(z)\}\\ &= \max\{\min\{\{F_{M_1}(m_1), F_{M_2}(z)\}, \min\{\{F_{M_1}(n_1), F_{M_2}(z)\}\}\\ &= \max\{(F_{M_1} * F_{M_2})(m_1,z), (F_{M_1} * F_{M_2})(n_1,z)\}.\end{aligned}$$

Therefore, $\mathbf{G}_1 * \mathbf{G}_2$ is a vague graph. □

Theorem 3.4. The maximal product of two strong vague graphs $\mathbf{G}_1$ and $\mathbf{G}_2$ is a strong vague graph.

Proof: Let $\mathbf{G}_1 = (M_1, N_1)$ and $\mathbf{G}_2 = (M_2, N_2)$ be two strong vague graphs on crisp graphs $G_1 = (V_1, E_1)$ and $G_2 = (V_2, E_2)$, respectively, and let $((m_1, m_2)(n_1, n_2)) \in E_1 \times E_2$. Then, by Proposition 3.3, $\mathbf{G}_1 * \mathbf{G}_2$ is a vague graph. Now we have two cases:

(i) If $m_1 = n_1 = m$, then

$$\begin{aligned}&(T_{N_1} * T_{N_2})((m,m_2)(m,n_2)) = \max\{T_{M_1}(m), T_{N_2}(m_2n_2)\}\\ &= \max\{T_{M_1}(m), \min\{T_{M_2}(m_2), T_{M_2}(n_2)\}\}\\ &= \min\{\max\{\{T_{M_1}(m), T_{M_2}(m_2)\}, \max\{\{T_{M_1}(m), T_{M_2}(n_2)\}\}\\ &= \min\{(T_{M_1} * T_{M_2})(m,m_2), (T_{M_1} * T_{M_2})(m,n_2)\},\\ &(F_{N_1} * F_{N_2})((m,m_2)(m,n_2)) = \min\{F_{M_1}(m), F_{N_2}(m_2n_2)\}\\ &= \min\{F_{M_1}(m), \max\{F_{M_2}(m_2), F_{M_2}(n_2)\}\}\\ &= \max\{\min\{\{F_{M_1}(m), F_{M_2}(m_2)\}, \min\{\{F_{M_1}(m), F_{M_2}(n_2)\}\}\\ &= \max\{(F_{M_1} * F_{M_2})(m,m_2), (F_{M_1} * F_{M_2})(m,n_2)\}.\end{aligned}$$

(ii) If $m_2 = n_2 = z$, then

$$\begin{aligned}&(T_{N_1} * T_{N_2})((m_1,z)(n_1,z)) = \max\{T_{N_1}(m_1n_1), T_{M_2}(z)\}\\ &= \max\{\min\{T_{N_1}(m_1n_1), T_{M_2}(z)\}\\ &= \min\{\max\{\{T_{N_1}(m_1), T_{M_2}(z)\}, \max\{\{T_{M_1}(n_1), T_{M_2}(z)\}\}\\ &= \min\{(T_{M_1} * T_{M_2})(m_1,z), (T_{M_1} * T_{M_2})(n_1,z)\},\\ &(F_{N_1} * F_{N_2})((m_1,z)(n_1,z)) = \min\{F_{N_1}(m_1n_1), F_{M_2}(z)\}\\ &= \min\{\max\{F_{N_1}(m_1n_1), F_{M_2}(z)\}\\ &= \max\{\min\{\{F_{M_1}(m_1), F_{M_2}(z)\}, \min\{\{F_{M_1}(n_1), F_{M_2}(z)\}\}\\ &= \max\{(F_{M_1} * F_{M_2})(m_1,z), (F_{M_1} * F_{M_2})(n_1,z)\}.\end{aligned}$$

Therefore, $\mathbf{G}_1 * \mathbf{G}_2$ is a strong vague graph. □

Example 3.5. Consider the strong vague graphs $\mathbf{G}_1$ and $\mathbf{G}_2$ as in **Figure 5**.

It is easy to see that $\mathbf{G}_1 * \mathbf{G}_2$ is a strong vague graph too.

Remark 3.1. If the maximal product of two vague graphs $\mathbf{G}_1 = (M_1, N_1)$ and $\mathbf{G}_2 = (M_2, N_2)$ is a strong vague graph, $\mathbf{G}_1$ and $\mathbf{G}_2$ need not be strong in general.

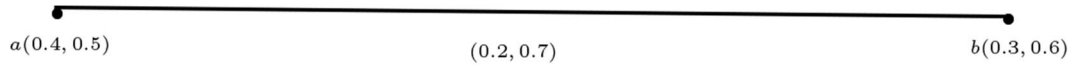

FIGURE 2 | G_1.

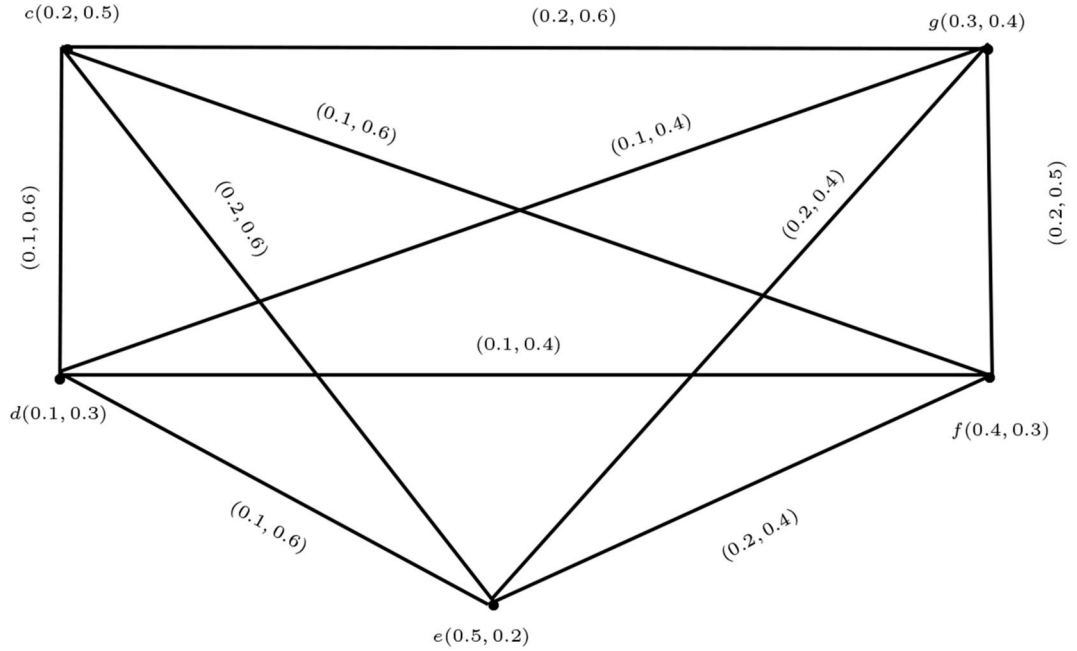

FIGURE 3 | G_2.

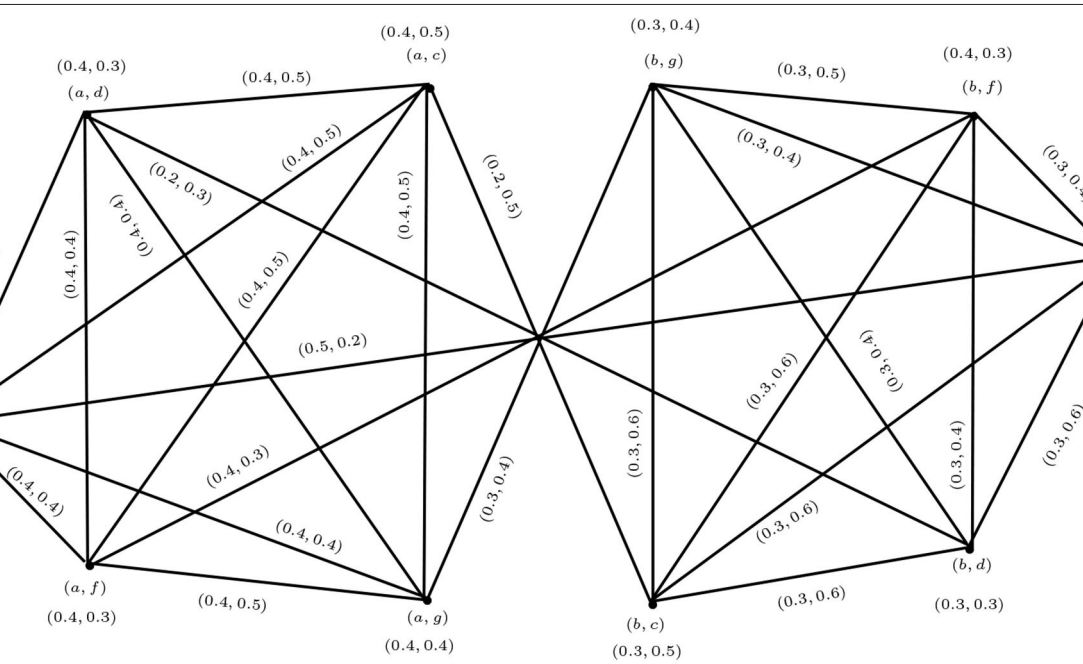

FIGURE 4 | $G_1{}^*G_2$.

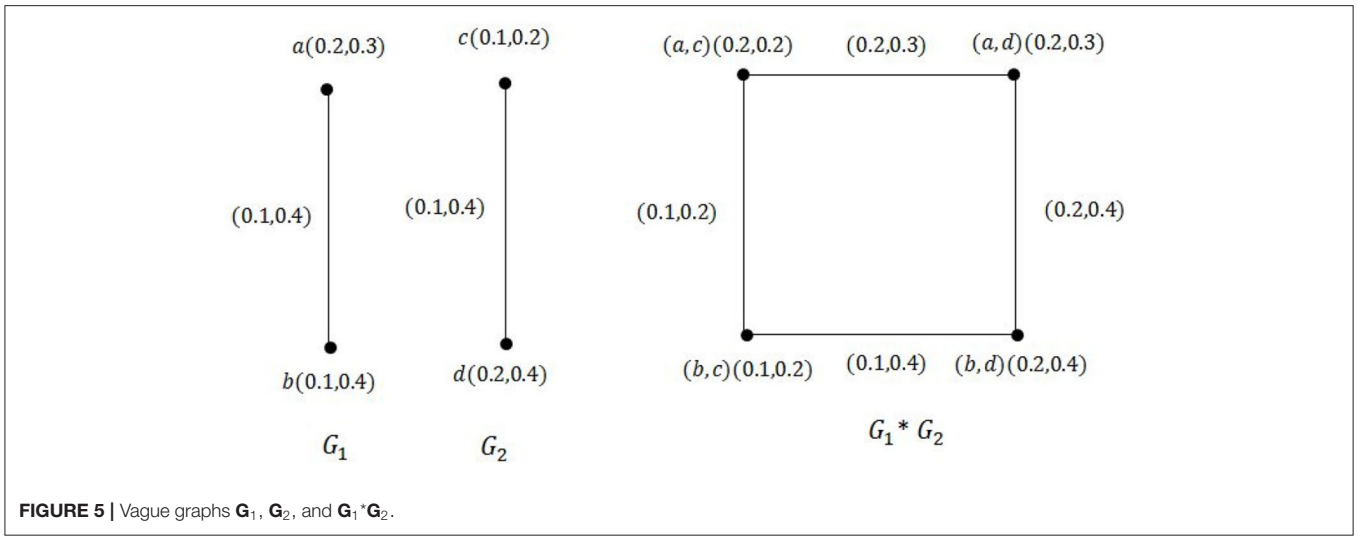

FIGURE 5 | Vague graphs $\mathbf{G}_1$, $\mathbf{G}_2$, and $\mathbf{G}_1{}^*\mathbf{G}_2$.

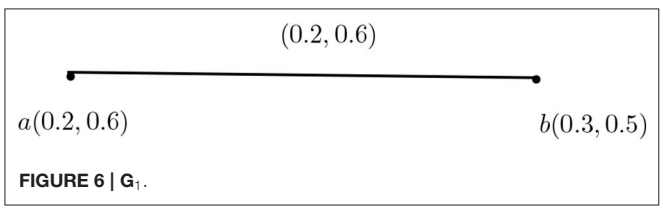

FIGURE 6 | $\mathbf{G}_1$.

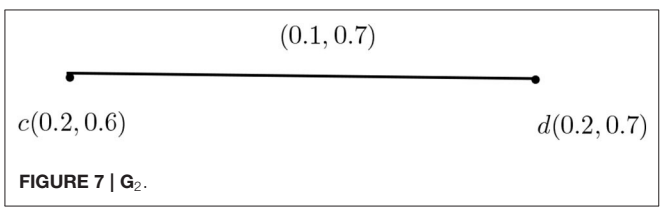

FIGURE 7 | $\mathbf{G}_2$.

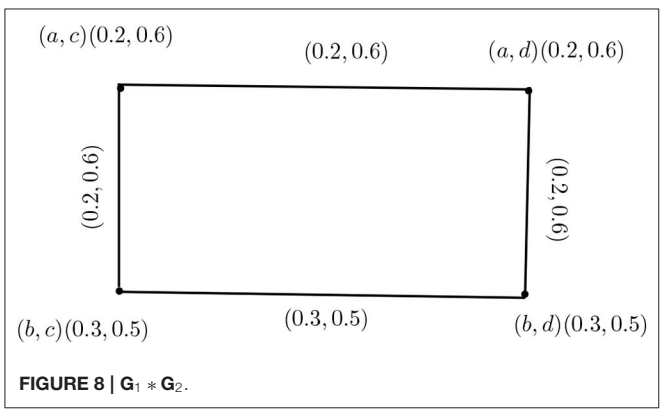

FIGURE 8 | $\mathbf{G}_1 * \mathbf{G}_2$.

Example 3.6. Consider the vague graphs $\mathbf{G}_1$ and $\mathbf{G}_2$ as in **Figures 6**, **7**. The maximal product of $\mathbf{G}_1$ and $\mathbf{G}_2$ is $\mathbf{G}_1 * \mathbf{G}_2$ shown in **Figure 8**.

We can see that $\mathbf{G}_1$ and $\mathbf{G}_1 * \mathbf{G}_2$ are strong vague graphs, but $\mathbf{G}_2$ is not strong: since $T_{N_2}(m_2, n_2) = 0.1$ but $\min\{T_{M_2}(m_2), T_{M_2}(n_2\} = \min\{0.2, 0.2\} = 0.2$, we have $T_{N_2}(m_2, n_2) \neq \min\{T_{M_2}(m_2), T_{M_2}(n_2\}$.

Theorem 3.7. The maximal product of two connected vague graphs is a connected vague graph.

Proof: Let $\mathbf{G}_1 = (M_1, N_1)$ and $\mathbf{G}_2 = (M_2, N_2)$ be two connected vague graphs on crisp graphs $G_1 = (V_1, E_1)$ and $G_2 = (V_2, E_2)$, respectively, where $V_1 = \{m_1, m_2, \ldots, m_k\}$ and $V_2 = \{n_1, n_2, \ldots, n_s\}$. Then $T^{\infty}_{N_1}(m_i m_j) > 0$ for all $m_i, m_j \in V_1$ and $T^{\infty}_{N_2}(n_i n_j) > 0$ for all $n_i, n_j \in V_2$ (or $F^{\infty}_{N_1}(m_i m_j) < 1$ for all $m_i, m_j \in V_1$ and $F^{\infty}_{N_2}(n_i n_j) < 1$ for all $n_i, n_j \in V_2$). The maximal product of $\mathbf{G}_1 = (M_1, N_1)$ and $\mathbf{G}_2 = (M_2, N_2)$ can be taken as $\mathbf{G} = (M, N)$. Now, consider the k subgraphs of $\mathbf{G}$ with the vertex set $\{(m_i, n_1), (m_i, n_2), \ldots, (m_i, n_s)\}$ for $i = 1, 2, \ldots, k$. Each of these subgraphs of $\mathbf{G}$ is connected, since the m_i's are the same and $\mathbf{G}_2$ is connected, so that each n_i is adjacent to at least one of the vertices in V_2. Also, since $\mathbf{G}_1$ is connected, each x_i is adjacent to at least one of the vertices in V_1.

Hence, there exists at least one edge between any pair of the above k subgraphs. Thus, we have $T^{\infty}_{N}((m_i, n_j)(m_m, n_n)) > 0$ (or $F^{\infty}_{N}((m_i, n_j)(m_m, n_n)) < 1$) for all $((m_i, n_j)(m_m, n_n)) \in E$. Therefore, G is a connected vague graph. □

Remark 3.2. The maximal product of two complete vague graphs is not a complete vague graph in general. This is because we do not include the case where $(m_1, m_2) \in E_1$ and $(n_1, n_2) \in E_2$ in the definition of the maximal product of two vague graphs.

Remark 3.3. The maximal product of two complete vague graphs is a strong vague graph.

Example 3.8. Consider the complete vague graphs $\mathbf{G}_1$ and $\mathbf{G}_2$ in **Figure 5**. A simple calculation yields that $\mathbf{G}_1 * \mathbf{G}_2$ is a strong vague graph.

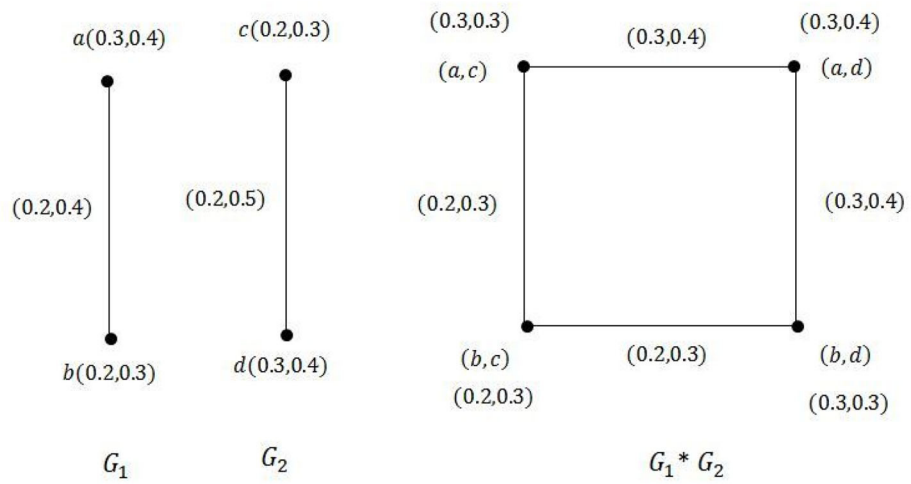

FIGURE 9 | Vague graphs $\mathbf{G}_1$, $\mathbf{G}_2$, and $\mathbf{G}_1 * \mathbf{G}_2$.

Definition 3.9. Let $\mathbf{G}_1 = (M_1, N_1)$ and $\mathbf{G}_2 = (M_2, N_2)$ be two vague graphs. For any vertex $(m_1, m_2) \in V_1 \times V_2$ we define

$$\begin{aligned}(d_T)_{\mathbf{G}_1*\mathbf{G}_2}(m_1,m_2) &= \sum_{(m_1,m_2)(n_1,n_2)\in E_1\times E_2} (T_{N_1} * T_{N_2})((m_1,m_2)(n_1,n_2))\\ &= \sum_{m_1=n_1,\, m_2n_2\in E_2} \max\{T_{M_1}(m_1), T_{N_2}(m_2n_2)\}\\ &\quad + \sum_{m_1n_1\in E_1,\, m_2=n_2} \max\{T_{N_1}(m_1n_1), T_{M_2}(m_2)\},\\ (d_F)_{\mathbf{G}_1*\mathbf{G}_2}(m_1,m_2) &= \sum_{(m_1,m_2)(n_1,n_2)\in E_1\times E_2} (F_{N_1} * F_{N_2})((m_1,m_2)(n_1,n_2))\\ &= \sum_{m_1=n_1,\, m_2n_2\in E_2} \min\{F_{M_1}(m_1), F_{N_2}(m_2n_2)\}\\ &\quad + \sum_{m_1n_1\in E_1,\, m_2=n_2} \min\{F_{N_1}(m_1n_1), F_{M_2}(m_2)\}.\end{aligned}$$

Theorem 3.10. Let $\mathbf{G}_1 = (M_1, N_1)$ and $\mathbf{G}_2 = (M_2, N_2)$ be two vague graphs. If $T_{M_1} \geq T_{N_2}$, $F_{M_1} \leq F_{N_2}$, $T_{M_2} \geq T_{N_1}$, and $F_{M_2} \leq F_{N_1}$, then $(d_T)_{\mathbf{G}_1*\mathbf{G}_2}(m_1, m_2) = (d)_{G_2}(m_2)T_{M_1}(m_1) + (d)_{G_1}(m_1)T_{M_2}(m_2)$ and $(d_F)_{\mathbf{G}_1*\mathbf{G}_2}(m_1, m_2) = (d)_{G_2}(m_2)F_{M_1}(m_1) + (d)_{G_1}(m_1)F_{M_2}(m_2)$.

Proof: From the definition of a vertex in the cartesian product, we have

$$\begin{aligned}(d_T)_{\mathbf{G}_1*\mathbf{G}_2}(m_1,m_2) &= \sum_{(m_1,m_2)(n_1,n_2)\in E_1\times E_2} (T_{N_1} * T_{N_2})((m_1,m_2)(n_1,n_2))\\ &= \sum_{m_1=n_1,\, m_2n_2\in E_2} \max\{T_{M_1}(m_1), T_{N_2}(m_2n_2)\}\\ &\quad + \sum_{m_1n_1\in E_1,\, m_2=n_2} \max\{T_{N_1}(m_1n_1), T_{M_2}(m_2)\}\\ &= \sum_{m_2n_2\in E_2,\, m_1=n_1} T_{N_2}(m_2n_2) + \sum_{m_1n_1\in E_1, m_2=n_2} T_{N_1}(m_1n_1)\\ &= (d)_{G_2}(m_2)T_{M_1}(m_1) + (d)_{G_1}(m_1)T_{M_2}(m_2),\end{aligned}$$

$$\begin{aligned}(d_F)_{\mathbf{G}_1*\mathbf{G}_2}(m_1,m_2) &= \sum_{(m_1,m_2)(n_1,n_2)\in E_1\times E_2} (F_{N_1} * F_{N_2})((m_1,m_2)(n_1,n_2))\\ &= \sum_{m_1=n_1,\, m_2n_2\in E_2} \min\{F_{M_1}(m_1), F_{N_2}(m_2n_2)\}\\ &\quad + \sum_{m_1n_1\in E_1,\, m_2=n_2} \min\{F_{N_1}(m_1n_1), F_{M_2}(m_2)\}\\ &= \sum_{m_2n_2\in E_2,\, m_1=n_1} F_{N_2}(m_2n_2) + \sum_{m_1n_1\in E_1, m_2=n_2} F_{N_1}(m_1n_1)\\ &= (d)_{G_2}(m_2)F_{M_1}(m_1) + (d)_{G_1}(m_1)F_{M_2}(m_2),\end{aligned}$$

as claimed. □

Example 3.11. Consider the vague graphs $\mathbf{G}_1$, $\mathbf{G}_2$, and $\mathbf{G}_1 * \mathbf{G}_2$ as in **Figure 9**. Since $T_{M_1} \geq T_{N_2}$, $F_{M_1} \leq F_{N_2}$, $T_{M_2} \geq T_{N_1}$, and $F_{M_2} \leq F_{N_1}$, by Theorem 3.10 we have

$$\begin{aligned}&(d_T)_{\mathbf{G}_1*\mathbf{G}_2}(a,c) = (d)_{G_2}(c)T_{M_1}(a) + (d)_{G_1}(a)T_{M_2}(c) = 1\cdot(0.3)\\ &+ 1\cdot(0.2) = 0.5,\\ &(d_F)_{\mathbf{G}_1*\mathbf{G}_2}(a,c) = (d)_{G_2}(c)F_{M_1}(a) + (d)_{G_1}(a)F_{M_2}(c) = 1\cdot(0.4)\\ &+ 1\cdot(0.3) = 0.7.\end{aligned}$$

$$\begin{aligned}&(d_T)_{\mathbf{G}_1*\mathbf{G}_2}(a,d) = (d)_{G_2}(d)T_{M_1}(a) + (d)_{G_1}(a)T_{M_2}(d) = 1\cdot(0.3)\\ &+ 1\cdot(0.3) = 0.6,\\ &(d_F)_{\mathbf{G}_1*\mathbf{G}_2}(a,d) = (d)_{G_2}(d)F_{M_1}(a) + (d)_{G_1}(a)F_{M_2}(d) = 1\cdot(0.4)\\ &+ 1\cdot(0.4) = 0.8.\end{aligned}$$

$$\begin{aligned}&(d_T)_{\mathbf{G}_1*\mathbf{G}_2}(b,c) = (d)_{G_2}(c)T_{M_1}(b) + (d)_{G_1}(b)T_{M_2}(c) = 1\cdot(0.2)\\ &+ 1\cdot(0.2) = 0.4,\\ &(d_F)_{\mathbf{G}_1*\mathbf{G}_2}(b,c) = (d)_{G_2}(c)F_{M_1}(b) + (d)_{G_1}(b)F_{M_2}(c) = 1\cdot(0.3)\\ &+ 1\cdot(0.3) = 0.6.\end{aligned}$$

$(d_T)_{\mathbf{G}_1*\mathbf{G}_2}(b,d) = (d)_{G_2}(d)T_{M_1}(b) + (d)_{G_1}(b)T_{M_2}(d) = 1\cdot(0.2) + 1\cdot(0.3) = 0.5,$
$(d_F)_{\mathbf{G}_1*\mathbf{G}_2}(b,d) = (d)_{G_2}(d)F_{M_1}(b) + (d)_{G_1}(b)F_{M_2}(d) = 1\cdot(0.3) + 1\cdot(0.4) = 0.7.$

By direct calculations we obtain

$$\begin{aligned}
(d_T)_{\mathbf{G}_1*\mathbf{G}_2}(a,c) &= 0.3+0.2 = 0.5,\\
(d_F)_{\mathbf{G}_1*\mathbf{G}_2}(a,c) &= 0.4+0.3 = 0.7,\\
(d_T)_{\mathbf{G}_1*\mathbf{G}_2}(a,d) &= 0.3+0.3 = 0.6,\\
(d_F)_{\mathbf{G}_1*\mathbf{G}_2}(a,d) &= 0.4+0.4 = 0.8,\\
(d_T)_{\mathbf{G}_1*\mathbf{G}_2}(b,c) &= 0.2+0.2 = 0.4,\\
(d_F)_{\mathbf{G}_1*\mathbf{G}_2}(b,c) &= 0.3+0.3 = 0.6,\\
(d_T)_{\mathbf{G}_1*\mathbf{G}_2}(b,d) &= 0.3+0.2 = 0.5,\\
(d_F)_{\mathbf{G}_1*\mathbf{G}_2}(b,d) &= 0.3+0.4 = 0.7.
\end{aligned}$$

It is clear that the degrees of vertices calculated using the formula in Theorem 3.10 and by the direct method are the same.

Definition 3.12. Let $\mathbf{G}_1 = (M_1, N_1)$ and $\mathbf{G}_2 = (M_2, N_2)$ be two vague graphs. For any vertex $(m_1, m_2) \in V_1 \times V_2$ we define

$$\begin{aligned}
(td_T)_{\mathbf{G}_1*\mathbf{G}_2}(m_1,m_2) &= \sum_{(m_1,m_2)(n_1,n_2)\in E_1\times E_2} (T_{N_1} * T_{N_2})((m_1,m_2)(n_1,n_2))\\
&\quad + (T_{M_1} * T_{M_2})(m_1,m_2)\\
&= \sum_{m_1=n_1,\, m_2n_2\in E_2} \max\{T_{M_1}(m_1), T_{N_2}(m_2n_2)\}\\
&\quad + \sum_{m_1n_1\in E_1,\, m_2=n_2} \max\{T_{N_1}(m_1n_1), T_{M_2}(m_2)\}\\
&\quad + \max\{T_{M_1}(m_1), T_{M_2}(m_2)\},
\end{aligned}$$

$$\begin{aligned}
(td_F)_{\mathbf{G}_1*\mathbf{G}_2}(m_1,m_2) &= \sum_{(m_1,m_2)(n_1,n_2)\in E_1\times E_2} (F_{N_1} * F_{N_2})((m_1,m_2)(n_1,n_2))\\
&\quad + (F_{M_1} * F_{M_2})(m_1,m_2)\\
&= \sum_{m_1=n_1,\, m_2n_2\in E_2} \min\{F_{M_1}(m_1), F_{N_2}(m_2n_2)\}\\
&\quad + \sum_{m_1n_1\in E_1,\, m_2=n_2} \min\{F_{N_1}(m_1n_1), F_{M_2}(m_2)\}\\
&\quad + \min\{F_{M_1}(m_1), F_{M_2}(m_2)\}.
\end{aligned}$$

Example 3.13. In this example we find the degree and the total degree of vertices (a, c) and (a, d) in Example 3.2:

$$\begin{aligned}
(d_T)_{\mathbf{G}_1*\mathbf{G}_2}(a,c) &= (d)_{G_2}(a)T_{M_1}(c) + (d)_{G_1}(c)T_{M_2}(a)\\
&= 1(0.2) + 4(0.4) = 0.2 + 1.6 = 1.8,\\
(d_F)_{\mathbf{G}_1*\mathbf{G}_2}(a,c) &= (d)_{G_2}(a)F_{M_1}(c) + (d)_{G_1}(c)F_{M_2}(a)\\
&= 1(0.5) + 4(0.5) = 0.3 + 1.2 = 1.5.
\end{aligned}$$

Therefore, $d_{\mathbf{G}_1*\mathbf{G}_2}(a,c) = (1.8, 1.5)$. In addition, by the definition of the total vertex degree in the maximal product,

$$\begin{aligned}
(td_T)_{\mathbf{G}_1*\mathbf{G}_2}(a,c) &= (d)_{G_2}(a)T_{M_1}(c) + (d)_{G_1}(c)T_{M_2}(a)\\
&\quad + \max\{T_{M_1}(a), T_{M_2}(c)\}\\
&= 1(0.2) + 4(0.4) + \max(0.2, 0.4) = 2.2,\\
(td_F)_{\mathbf{G}_1*\mathbf{G}_2}(a,c) &= (d)_{G_2}(a)F_{M_1}(c) + (d)_{G_1}(c)F_{M_2}(a)\\
&\quad + \min\{F_{M_1}(a), F_{M_2}(c)\}\\
&= 1(0.5) + 4(0.5) + \min(0.3, 0.4) = 1.8.
\end{aligned}$$

Therefore, $td_{\mathbf{G}_1*\mathbf{G}_2}(a,c) = (2.2, 1.8)$.

We also have

$$\begin{aligned}
(d_T)_{\mathbf{G}_1*\mathbf{G}_2}(a,d) &= (d)_{G_2}(a)T_{M_1}(d) + (d)_{G_1}(d)T_{M_2}(a)\\
&= 1(0.1) + 4(0.4) = 0.1 + 1.6 = 1.7,\\
(d_F)_{\mathbf{G}_1*\mathbf{G}_2}(a,d) &= (d)_{G_2}(a)F_{M_1}(d) + (d)_{G_1}(d)F_{M_2}(a)\\
&= 1(0.3) + 4(0.5) = 0.3 + 2 = 2.3,
\end{aligned}$$

$$\begin{aligned}
(td_T)_{\mathbf{G}_1*\mathbf{G}_2}(a,d) &= (d)_{G_2}(a)T_{M_1}(d) + (d)_{G_1}(d)T_{M_2}(a)\\
&\quad + \max\{T_{M_1}(a), T_{M_2}(d)\}\\
&= 1(0.1) + 4(0.4) + \max(0.4, 0.1) = 2.1,\\
(td_F)_{\mathbf{G}_1*\mathbf{G}_2}(a,d) &= (d)_{G_2}(a)F_{M_1}(d) + (d)_{G_1}(d)F_{M_2}(a)\\
&\quad + \min\{F_{M_1}(a), F_{M_2}(d)\}\\
&= 1(0.3) + 4(0.5) + \min(0.5, 0.3) = 2.6.
\end{aligned}$$

Hence, $d_{\mathbf{G}_1*\mathbf{G}_2}(a,d) = (1.7, 2.3)$ and $td_{\mathbf{G}_1*\mathbf{G}_2}(a,d) = (2.1, 2.6)$.

Similarly, we can find the degree and the total degree of all vertices in $\mathbf{G}_1 * \mathbf{G}_2$.

Theorem 3.14. Let $\mathbf{G}_1 = (M_1, N_1)$ and $\mathbf{G}_2 = (M_2, N_2)$ be two vague graphs. If $T_{M_1} \geq T_{N_2}$, $F_{M_1} \leq F_{N_2}$, $T_{M_2} \geq T_{N_1}$, and $F_{M_2} \leq F_{N_1}$, then $(td_T)_{\mathbf{G}_1*\mathbf{G}_2}(m_1,m_2) = (d)_{G_2}(m_2)T_{M_1}(m_1) + (d)_{G_1}(m_1)T_{M_2}(m_2) + \max\{T_{M_1}(m_1), T_{M_2}(m_2)\}$ and $(td_F)_{\mathbf{G}_1*\mathbf{G}_2}(m_1,m_2) = (d)_{G_2}(m_2)F_{M_1}(m_1) + (d)_{G_1}(m_1)F_{M_2}(m_2) + \min\{F_{M_1}(m_1), F_{M_2}(m_2)\}$.

Proof: From Definition 3.12 we have

$$\begin{aligned}
(td_T)_{\mathbf{G}_1*\mathbf{G}_2}(m_1,m_2) &= \sum_{(m_1,m_2)(n_1,n_2)\in E_1\times E_2} (T_{N_1} * T_{N_2})((m_1,m_2)(n_1,n_2))\\
&\quad + (T_{M_1} * T_{M_2})(m_1,m_2)\\
&= \sum_{m_1=n_1,\, m_2n_2\in E_2} \max\{T_{M_1}(m_1), T_{N_2}(m_2n_2)\}\\
&\quad + \sum_{m_1n_1\in E_1,\, m_2=n_2} \max\{T_{N_1}(m_1n_1), T_{M_2}(m_2)\}\\
&\quad + \max\{T_{M_1}(m_1), T_{M_2}(m_2)\}\\
&= \sum_{m_2n_2\in E_2,\, m_1=n_1} T_{N_2}(m_2n_2) + \sum_{m_1n_1\in E_1,\, m_2=n_2} T_{N_1}(m_1n_1)\\
&\quad + \max\{T_{M_1}(m_1), T_{M_2}(m_2)\}\\
&= (d)_{G_2}(m_2)T_{M_1}(m_1) + (d)_{G_1}(m_1)T_{M_2}(m_2)\\
&\quad + \max\{T_{M_1}(m_1), T_{M_2}(m_2)\}
\end{aligned}$$

and

$$\begin{aligned}(td_F)_{\mathbf{G}_1*\mathbf{G}_2}(m_1,m_2) &= \sum_{(m_1,m_2)(n_1,n_2)\in E_1\times E_2}(F_{N_1}*F_{N_2})((m_1,m_2)(n_1,n_2))\\ &\quad+(F_{M_1}*F_{M_2})(m_1,m_2)\\ &= \sum_{m_1=n_1,\, m_2n_2\in E_2}\min\{F_{M_1}(m_1),F_{N_2}(m_2n_2)\}\\ &\quad+\sum_{m_1n_1\in E_1,\, m_2=n_2}\min\{F_{N_1}(m_1n_1),F_{M_2}(m_2)\}\\ &\quad+\min\{F_{M_1}(m_1),F_{M_2}(m_2)\}\\ &= \sum_{m_2n_2\in E_2,\, m_1=n_1}F_{N_2}(m_2n_2)+\sum_{m_1n_1\in E_1,\, m_2=n_2}F_{N_1}(m_1n_1)\\ &\quad+\min\{F_{M_1}(m_1),F_{M_2}(m_2)\}\\ &= (d)_{G_2}(m_2)F_{M_1}(m_1)+(d)_{G_1}(m_1)F_{M_2}(m_2)\\ &\quad+\min\{F_{M_1}(m_1),F_{M_2}(m_2)\},\end{aligned}$$

as asserted. □

Example 3.15. Consider the vague graphs $\mathbf{G}_1$, $\mathbf{G}_2$, and $\mathbf{G}_1*\mathbf{G}_2$ in **Figure 9**. The total degree of the vertex in the maximal product is calculated by the following formula:

$$\begin{aligned}(td_T)_{\mathbf{G}_1*\mathbf{G}_2}(m_1,m_2) &= (d)_{G_2}(m_2)T_{M_1}(m_1)+(d)_{G_1}(m_1)T_{M_2}(m_2)\\ &\quad+\max\{T_{M_1}(m_1),T_{M_2}(m_2)\},\\ (td_F)_{\mathbf{G}_1*\mathbf{G}_2}(m_1,m_2) &= (d)_{G_2}(m_2)F_{M_1}(m_1)+(d)_{G_1}(m_1)F_{M_2}(m_2)\\ &\quad+\min\{F_{M_1}(m_1),F_{M_2}(m_2)\}.\end{aligned}$$

Using the formula we find that

$$\begin{aligned}(td_T)_{\mathbf{G}_1*\mathbf{G}_2}(a,c) &= (d)_{G_2}(c)T_{M_1}(a)+(d)_{G_1}(a)T_{M_2}(c)\\ &\quad+\max\{T_{M_1}(a),T_{M_2}(c)\}\\ &= 1\cdot(0.3)+1\cdot(0.2)+\max\{0.2,0.3\}\\ &= 0.3+0.2+0.3=0.8,\\ (td_F)_{\mathbf{G}_1*\mathbf{G}_2}(a,c) &= (d)_{G_2}(c)F_{M_1}(a)+(d)_{G_1}(a)F_{M_2}(c)\\ &\quad+\min\{F_{M_1}(a),F_{M_2}(c)\}\\ &= 1\cdot(0.4)+1\cdot(0.3)+\min\{0.3,0.4\}\\ &= 0.4+0.3+0.3=1.\end{aligned}$$

$$\begin{aligned}(td_T)_{\mathbf{G}_1*\mathbf{G}_2}(a,d) &= (d)_{G_2}(d)T_{M_1}(a)+(d)_{G_1}(a)T_{M_2}(d)\\ &\quad+\max\{T_{M_1}(a),T_{M_2}(d)\}\\ &= 1\cdot(0.3)+1\cdot(0.3)+\max\{0.3,0.3\}\\ &= 0.3+0.3+0.3=0.9,\\ (td_F)_{\mathbf{G}_1*\mathbf{G}_2}(a,d) &= (d)_{G_2}(d)F_{M_1}(a)+(d)_{G_1}(a)F_{M_2}(d)\\ &\quad+\min\{F_{M_1}(a),F_{M_2}(d)\}\\ &= 1\cdot(0.4)+1\cdot(0.4)+\min\{0.4,0.4\}\\ &= 0.4+0.4+0.4=1.2.\end{aligned}$$

$$\begin{aligned}(td_T)_{\mathbf{G}_1*\mathbf{G}_2}(b,c) &= (d)_{G_2}(c)T_{M_1}(b)+(d)_{G_1}(b)T_{M_2}(c)\\ &\quad+\max\{T_{M_1}(b),T_{M_2}(c)\}\\ &= 1\cdot(0.2)+1\cdot(0.2)+\max\{0.2,0.2\}\\ &= 0.2+0.2+0.2=0.6,\\ (td_F)_{\mathbf{G}_1*\mathbf{G}_2}(b,c) &= (d)_{G_2}(c)F_{M_1}(b)+(d)_{G_1}(b)F_{M_2}(c)\\ &\quad+\min\{F_{M_1}(b),F_{M_2}(c)\}\\ &= 1\cdot(0.3)+1\cdot(0.3)+\min\{0.3,0.3\}\\ &= 0.3+0.3+0.3=0.9.\end{aligned}$$

$$\begin{aligned}(td_T)_{\mathbf{G}_1*\mathbf{G}_2}(b,d) &= (d)_{G_2}(d)T_{M_1}(b)+(d)_{G_1}(b)T_{M_2}(d)\\ &\quad+\max\{T_{M_1}(b),T_{M_2}(d)\}\\ &= 1\cdot(0.2)+1\cdot(0.3)+\max\{0.2,0.3\}\\ &= 0.2+0.3+0.3=0.8,\\ (td_F)_{\mathbf{G}_1*\mathbf{G}_2}(b,d) &= (d)_{G_2}(d)F_{M_1}(b)+(d)_{G_1}(b)F_{M_2}(d)\\ &\quad+\min\{F_{M_1}(b),F_{M_2}(d)\}\\ &= 1\cdot(0.3)+1\cdot(0.4)+\min\{0.3,0.4\}\\ &= 0.3+0.4+0.3=1.\end{aligned}$$

On the other hand, by direct calculations we obtain

$$\begin{aligned}(td_T)_{\mathbf{G}_1*\mathbf{G}_2}(a,c) &= 0.3+0.2+0.3=0.8,\\ (td_F)_{\mathbf{G}_1*\mathbf{G}_2}(a,c) &= 0.4+0.3+0.3=1,\\ (td_T)_{\mathbf{G}_1*\mathbf{G}_2}(a,d) &= 0.3+0.3+0.3=0.9,\\ (td_F)_{\mathbf{G}_1*\mathbf{G}_2}(a,d) &= 0.4+0.4+0.4=1.2,\\ (td_T)_{\mathbf{G}_1*\mathbf{G}_2}(b,c) &= 0.2+0.2+0.2=0.6,\\ (td_F)_{\mathbf{G}_1*\mathbf{G}_2}(b,c) &= 0.3+0.3+0.3=0.9,\\ (td_T)_{\mathbf{G}_1*\mathbf{G}_2}(b,d) &= 0.3+0.2+0.3=0.8,\\ (td_F)_{\mathbf{G}_1*\mathbf{G}_2}(b,d) &= 0.4+0.3+0.3=1.\end{aligned}$$

It is thus clear that the total degrees of vertices calculated using the formula and by the direct method are the same.

Definition 3.16. The rejection $\mathbf{G}_1|\mathbf{G}_2=(M_1|M_2,N_1|N_2)$ of two vague graphs $\mathbf{G}_1=(M_1,N_1)$ and $\mathbf{G}_2=(M_2,N_2)$ is defined as follows:

(i) $$\begin{aligned}(T_{M_1}|T_{M_2})((m_1,m_2)) &= \min\{T_{M_1}(m_1),T_{M_2}(m_2)\},\\ (F_{M_1}|F_{M_2})((m_1,m_2)) &= \max\{F_{M_1}(m_1),F_{M_2}(m_2)\}\\ &\quad\forall\,(m_1,m_2)\in(V_1\times V_2);\end{aligned}$$

(ii) $$\begin{aligned}(T_{N_1}|T_{N_2})((m,m_2)(m,n_2)) &= \min\{T_{M_1}(m),T_{M_2}(m_2),T_{M_2}(n_2)\},\\ (F_{N_1}|F_{N_2})((m,m_2)(m,n_2)) &= \max\{F_{M_1}(m),F_{M_2}(m_2),F_{M_2}(n_2)\}\\ &\quad\forall\, m\in V_2 \text{ and } m_2n_2\notin E_2;\end{aligned}$$

(iii) $$\begin{aligned}(T_{N_1}|T_{N_2})((m,m_2)(m,n_2)) &= \min\{T_{M_1}(m),T_{M_2}(m_2),T_{M_2}(n_2)\}\\ (F_{N_1}|F_{N_2})((m,m_2)(m,n_2)) &= \max\{F_{M_1}(m),F_{M_2}(m_2),F_{M_2}(n_2)\}\\ &\quad\forall\, m\in V_2 \text{ and } m_1n_1\notin E_1;\end{aligned}$$

(iv) $$\begin{aligned}(T_{N_1}|T_{N_2})((m_1,m_2)(n_1,n_2)) &= \min\{T_{M_1}(m_1),T_{M_1}(n_1),T_{M_2}(m_2),T_{M_2}(n_2)\},\\ (F_{N_1}|F_{N_2})((m_1,m_2)(n_1,n_2)) &= \max\{F_{M_1}(m_1),F_{M_1}(n_1),F_{M_2}(m_2),F_{N_2}(n_2)\}\\ &\quad\forall\, m_1n_1\notin E_1 \text{ and } m_2n_2\notin E_2.\end{aligned}$$

Example 3.17. Consider the vague graphs $\mathbf{G}_1$ and $\mathbf{G}_2$ in **Figures 10**, **11**. The rejection of $\mathbf{G}_1$ and $\mathbf{G}_2$, i.e., $\mathbf{G}_1|\mathbf{G}_2$, is shown in **Figure 12**.

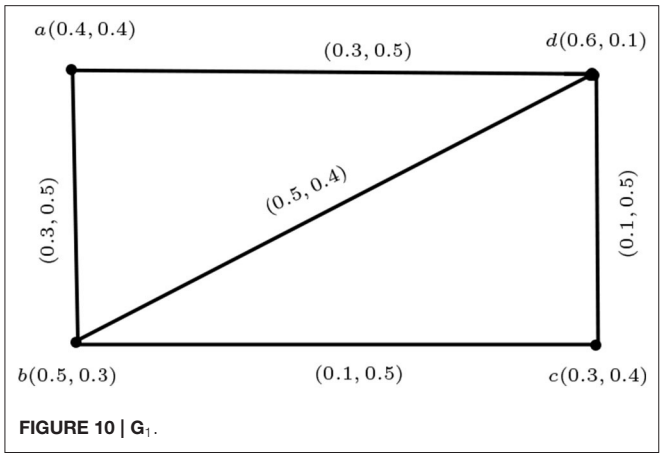

FIGURE 10 | $\mathbf{G}_1$.

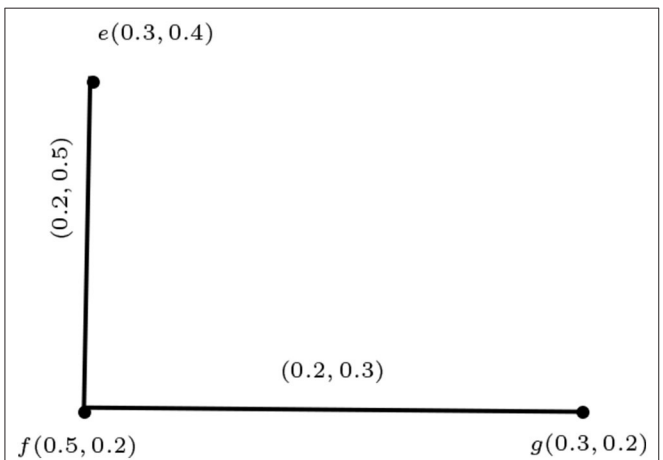

FIGURE 11 | $\mathbf{G}_2$.

For the vertex (a, e), we find the membership and non-membership values as follows:

$$\begin{aligned}(T_{M_1}|T_{M_2})((a,e)) &= \min\{T_{M_1}(a), T_{M_2}(e)\}\\ &= \min\{0.4, 0.3\} = 0.3,\\ (F_{M_1}|F_{M_2})((a,e)) &= \max\{F_{M_1}(a), F_{M_2}(e)\}\\ &= \max\{0.4, 0.4\} = 0.4\end{aligned}$$

for $a \in V_1$ and $e \in V_2$.

For the edge $(e, c)(e, a)$, the membership and non-membership values are given by

$$\begin{aligned}(T_{N_1}|T_{N_2})((e,c)(e,a)) &= \min\{T_{M_1}(e), T_{M_2}(c), T_{M_2}(a)\}\\ &= \min\{0.3, 0.3, 0.4\} = 0.3,\\ (F_{N_1}|F_{N_2})((e,c)(e,a)) &= \max\{F_{M_1}(e), F_{M_2}(c), F_{M_2}(a)\}\\ &= \max\{0.4, 0.4, 0.4\} = 0.4\end{aligned}$$

for $e \in V_2$ and $ac \notin E_1$.

For the edge $(e, c)(e, g)$ we have

$$\begin{aligned}(T_{N_1}|T_{N_2})((e,c)(e,g)) &= \min\{T_{M_1}(e), T_{M_2}(c), T_{M_2}(g)\}\\ &= \min\{0.3, 0.3, 0.3\} = 0.3,\\ (F_{N_1}|F_{N_2})((e,c)(e,g)) &= \max\{F_{M_1}(e), F_{M_2}(c), F_{M_2}(g)\}\\ &= \max\{0.4, 0.4, 0.2\} = 0.4\end{aligned}$$

for $e \in V_2$ and $cg \notin E_2$.

Similarly, we can find the membership and non-membership values for all the remaining vertices and edges.

Proposition 3.18. The rejection of two vague graphs $\mathbf{G}_1$ and $\mathbf{G}_2$ is a vague graph.

Proof: Let $\mathbf{G}_1 = (M_1, N_1)$ and $\mathbf{G}_2 = (M_2, N_2)$ be two vague graphs on crisp graphs $G_1 = (V_1, E_1)$ and $G_2 = (V_2, E_2)$, respectively, and let $((m_1, m_2)(n_1, n_2)) \in E_1 \times E_2$. Then by Definition 3.16 we have the following:
(i) If $m_1 = n_1$ and $m_2 n_2 \notin E_2$, then

$$\begin{aligned}&(T_{N_1}|T_{N_2})((m_1,m_2)(n_1,n_2)) = \min\{T_{M_1}(m_1), T_{M_2}(m_2), T_{M_2}(n_2)\}\\ &= \min\{\min\{T_{M_1}(m_1), T_{M_2}(m_2)\}, \min\{T_{M_1}(n_1), T_{M_2}(n_2)\}\}\\ &= \min\{(T_{M_1}|T_{M_2})(m_1,m_2), (T_{M_1}|T_{M_2})(n_1,n_2)\},\end{aligned}$$

$$\begin{aligned}&(F_{N_1}|F_{N_2})((m_1,m_2)(n_1,n_2)) = \max\{F_{M_1}(m_1), F_{M_2}(m_2), F_{M_2}(n_2)\}\\ &= \max\{\max\{F_{M_1}(m_1), F_{M_2}(m_2)\}, \max\{F_{M_1}(n_1), F_{M_2}(n_2)\}\}\\ &= \max\{(F_{M_1}|F_{M_2})(m_1,m_2), (F_{M_1}|F_{M_2})(n_1,n_2)\}.\end{aligned}$$

(ii) If $m_2 = n_2$ and $m_1 n_1 \notin E_1$, then

$$\begin{aligned}&(T_{N_1}|T_{N_2})((m_1,m_2)(n_1,n_2)) = \min\{T_{M_1}(m_1), T_{M_1}(n_1), T_{M_2}(m_2)\}\\ &= \min\{\min\{T_{M_1}(m_1), T_{M_2}(m_2)\}, \min\{T_{M_1}(n_1), T_{M_2}(n_2)\}\}\\ &= \min\{(T_{M_1}|T_{M_2})(m_1,m_2), (T_{M_1}|T_{M_2})(n_1,n_2)\},\end{aligned}$$

$$\begin{aligned}&(F_{N_1}|F_{N_2})((m_1,m_2)(n_1,n_2)) = \max\{F_{M_1}(m_1), F_{M_1}(n_1), F_{M_2}(m_2)\}\\ &= \max\{\max\{F_{M_1}(m_1), F_{M_2}(m_2)\}, \max\{F_{M_1}(n_1), F_{M_2}(n_2)\}\}\\ &= \max\{(F_{M_1}|F_{M_2})(m_1,m_2), (F_{M_1}|F_{M_2})(n_1,n_2)\}.\end{aligned}$$

(iii) If $m_1 n_1 \notin E_1$ and $m_2 n_2 \notin E_2$, then

$$\begin{aligned}&(T_{N_1}|T_{N_2})((m_1,m_2)(n_1,n_2)) = \min\{T_{M_1}(m_1), T_{M_1}(n_1), T_{M_2}(m_2), T_{M_2}(n_2)\}\\ &= \min\{\min\{T_{M_1}(m_1), T_{M_2}(m_2)\}, \min\{T_{M_1}(n_1), T_{M_2}(n_2)\}\}\\ &= \min\{(T_{M_1}|T_{M_2})(m_1,m_2), (T_{M_1}|T_{M_2})(n_1,n_2)\},\end{aligned}$$

$$\begin{aligned}&(F_{N_1}|F_{N_2})((m_1,m_2)(n_1,n_2)) = \max\{F_{M_1}(m_1), F_{M_1}(n_1), F_{M_2}(m_2), T_{M_2}(n_2)\}\\ &= \max\{\max\{F_{M_1}(m_1), F_{M_2}(m_2)\}, \max\{F_{M_1}(n_1), F_{M_2}(n_2)\}\}\\ &= \max\{(F_{M_1}|F_{M_2})(m_1,m_2), (F_{M_1}|F_{M_2})(n_1,n_2)\}.\end{aligned}$$

Therefore, $\mathbf{G}_1|\mathbf{G}_2 = (M_1|M_2, N_1|N_2)$ is a vague graph. □

Remark 3.4. *The rejection of two complete vague graphs* $\mathbf{G}_1 = (M_1, N_1)$ *and* $\mathbf{G}_2 = (M_2, N_2)$ *is a complete vague graph.*

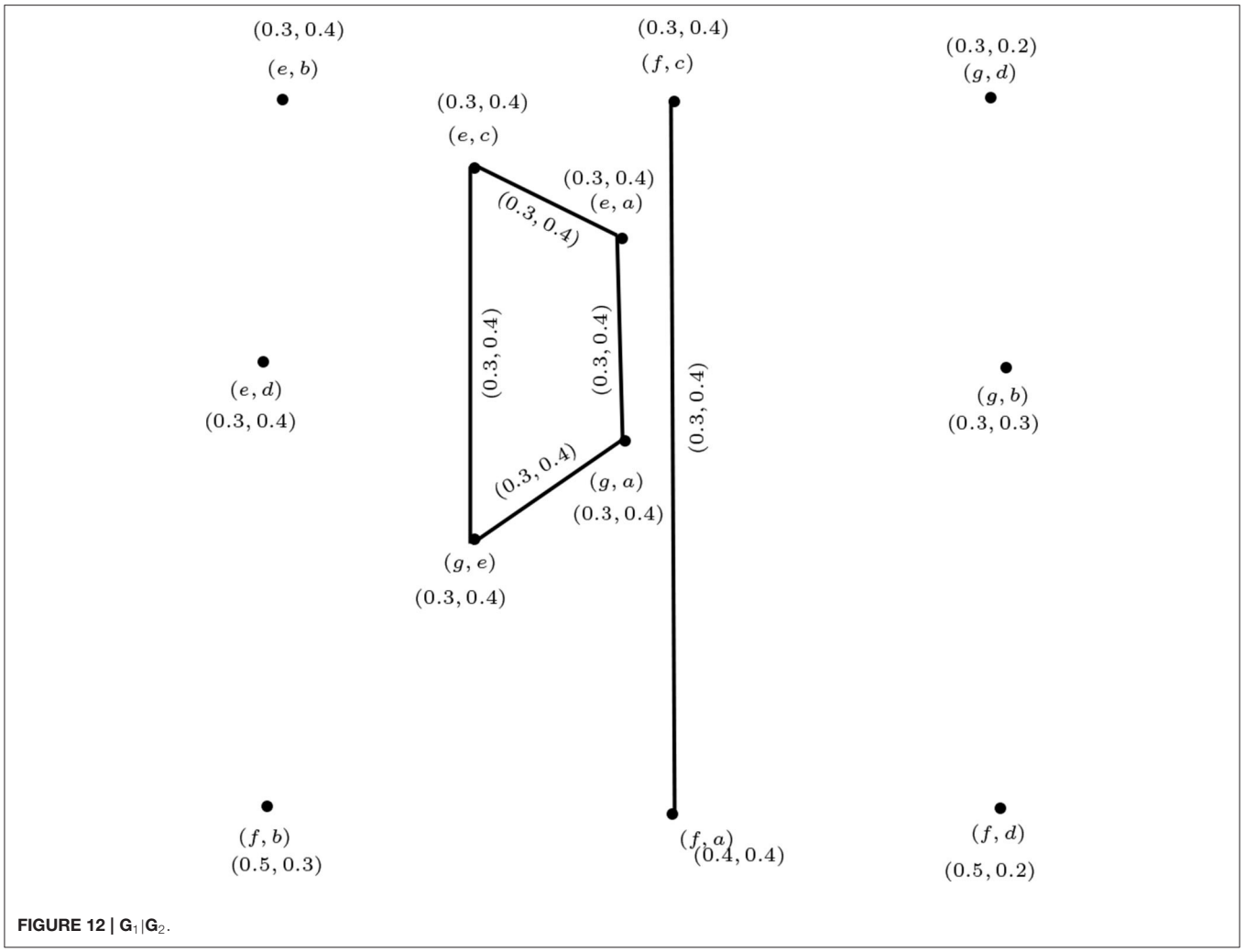

FIGURE 12 | $\mathbf{G}_1|\mathbf{G}_2$.

Definition 3.19. Let $\mathbf{G}_1 = (M_1, N_1)$ and $\mathbf{G}_2 = (M_2, N_2)$ be two vague graphs. For any vertex $(m_1, m_2) \in V_1 \times V_2$ we define

$$
\begin{aligned}
(d_T)_{\mathbf{G}_1|\mathbf{G}_2}(m_1, m_2) &= \sum_{(m_1,m_2)(n_1,n_2)\in E_1\times E_2} (T_{N_1}|T_{N_2})((m_1, m_2)(n_1, n_2)) \\
&= \sum_{m_1=n_1,\, m_2n_2\notin E_2} \min\{T_{M_1}(m_1), T_{M_2}(m_2), T_{M_2}(n_2)\} \\
&+ \sum_{m_2=n_2,\, m_1n_1\notin E_1} \min\{T_{M_1}(m_1), T_{M_1}(n_1), T_{M_2}(m_2)\} \\
&+ \sum_{m_1n_1\notin E_1 \text{ and } m_2n_2\notin E_2} \min\{T_{M_1}(m_1), T_{M_1}(n_1), T_{M_2}(m_2), T_{M_2}(n_2)\},
\end{aligned}
$$

$$
\begin{aligned}
(d_F)_{\mathbf{G}_1|\mathbf{G}_2}(m_1, m_2) &= \sum_{(m_1,m_2)(n_1,n_2)\in E_1\times E_2} (F_{N_1}|F_{N_2})((m_1, m_2)(n_1, n_2)) \\
&= \sum_{m_1=n_1,\, m_2n_2\notin E_2} \max\{F_{M_1}(m_1), F_{M_2}(m_2), F_{M_2}(n_2)\} \\
&+ \sum_{m_2=n_2,\, m_1n_1\notin E_1} \max\{F_{M_1}(m_1), F_{M_1}(n_1), F_{M_2}(m_2)\} \\
&+ \sum_{m_1n_1\notin E_1 \text{ and } m_2n_2\notin E_2} \max\{F_{M_1}(m_1), F_{M_1}(n_1), F_{M_2}(m_2), F_{M_2}(n_2)\}.
\end{aligned}
$$

Definition 3.20. Let $\mathbf{G}_1 = (M_1, N_1)$ and $\mathbf{G}_2 = (M_2, N_2)$ be two vague graphs. For any vertex $(m_1, m_2) \in V_1 \times V_2$ we define

$$
\begin{aligned}
(td_T)_{\mathbf{G}_1|\mathbf{G}_2}(m_1, m_2) &= \sum_{(m_1,m_2)(n_1,n_2)\in E_1\times E_2} (T_{N_1}|T_{N_2})((m_1, m_2)(n_1, n_2)) \\
&+ (T_{M_1}|T_{M_2})(m_1, m_2) \\
&= \sum_{m_1=n_1,\, m_2n_2\notin E_2} \min\{T_{M_1}(m_1), T_{M_2}(m_2), T_{M_2}(n_2)\} \\
&+ \sum_{m_2=n_2,\, m_1n_1\notin E_1} \min\{T_{M_1}(m_1), T_{M_1}(n_1), T_{M_2}(m_2)\} \\
&+ \sum_{m_1n_1\notin E_1 \text{ and } m_2n_2\notin E_2} \min\{T_{M_1}(m_1), T_{M_1}(n_1), T_{M_2}(m_2), T_{M_2}(n_2)\},
\end{aligned}
$$

$$
\begin{aligned}
(td_F)_{\mathbf{G}_1|\mathbf{G}_2}(m_1, m_2) &= \sum_{(m_1,m_2)(n_1,n_2)\in E_1\times E_2} (F_{N_1}|F_{N_2})((m_1, m_2)(n_1, n_2)) \\
&+ (F_{M_1}|F_{M_2})(m_1, m_2) \\
&= \sum_{m_1=n_1,\, m_2n_2\notin E_2} \max\{F_{M_1}(m_1), F_{M_2}(m_2), F_{M_2}(n_2)\} \\
&+ \sum_{m_2=n_2,\, m_1n_1\notin E_1} \max\{F_{M_1}(m_1), F_{M_1}(n_1), F_{M_2}(m_2)\} \\
&+ \sum_{m_1n_1\notin E_1 \text{ and } m_2n_2\notin E_2} \max\{F_{M_1}(m_1), F_{M_1}(n_1), F_{M_2}(m_2), F_{M_2}(n_2)\}.
\end{aligned}
$$

Example 3.21. In this example we find the degree and total degree of the vertex (e, a) in Example 3.17:

$$\begin{aligned}(d_T)_{\mathbf{G}_1|\mathbf{G}_2}(e,a) &= \min\{T_{M_2}(e), T_{M_1}(a), T_{M_1}(c)\} \\ &+ \min\{T_{M_2}(e), T_{M_1}(a), T_{M_2}(g)\} \\ &= \min\{0.3, 0.4, 0.3\} + \min\{0.3, 0.4, 0.3\} \\ &= 0.3 + 0.3 \\ &= 0.6,\end{aligned}$$

$$\begin{aligned}(d_F)_{\mathbf{G}_1|\mathbf{G}_2}(e,a) &= \max\{F_{M_2}(e), F_{M_1}(a), F_{M_1}(c)\} \\ &+ \max\{F_{M_2}(e), F_{M_1}(a), F_{M_2}(g) \\ &= \max\{0.4, 0.4, 0.4\} + \max\{0.4, 0.4, 0.2\} \\ &= 0.4 + 0.4 \\ &= 0.8.\end{aligned}$$

Therefore, $d_{\mathbf{G}_1|\mathbf{G}_2}(a, c)$= (0.6,0.8).

In addition, by the definition of the total vertex degree in the maximal product,

$$\begin{aligned}(td_T)_{\mathbf{G}_1|\mathbf{G}_2}(e,a) &= \min\{T_{M_2}(e), T_{M_1}(a), T_{M_1}(c)\} \\ &+ \min\{T_{M_2}(e), T_{M_1}(a), T_{M_2}(g)\} \\ &\quad + \min\{T_{M_2}(e), T_{M_1}(a)\} \\ &= \min\{0.3, 0.4, 0.3\} + \min\{0.3, 0.4, 0.3\} \\ &+ \min\{0.3, 0.4\} \\ &= 0.3 + 0.3 + 0.3 \\ &= 0.9,\end{aligned}$$

$$\begin{aligned}(td_F)_{\mathbf{G}_1|\mathbf{G}_2}(e,a) &= \max\{F_{M_2}(e), F_{M_1}(a), F_{M_1}(c)\} \\ &+ \max\{F_{M_2}(e), F_{M_1}(a), F_{M_2}(g)\} \\ &\quad + \max\{F_{M_2}(e), F_{M_1}(a)\} \\ &= \max\{0.4, 0.4, 0.4\} + \max\{0.4, 0.4, 0.2\} \\ &+ \max\{0.3, 0.4\} \\ &= 0.4 + 0.4 + 0.4 \\ &= 1.2.\end{aligned}$$

Therefore, $td_{\mathbf{G}_1|\mathbf{G}_2}(a, c)$= (0.9,1.2).

Similarly, we can find the degree and the total degree of all vertices in $\mathbf{G}_1|\mathbf{G}_2$.

Definition 3.22. The symmetric difference $\mathbf{G}_1 \oplus \mathbf{G}_2 = (M_1 \oplus M_2, N_1 \oplus N_2)$ of two vague graphs $\mathbf{G}_1 = (M_1, N_1)$ and $\mathbf{G}_2 = (M_2, N_2)$ is defined as follows:

(i) $$\begin{aligned}(T_{M_1} \oplus T_{M_2})((m_1,m_2)) &= \min\{T_{M_1}(m_1), T_{M_2}(m_2)\}, \\ (F_{M_1} \oplus F_{M_2})((m_1,m_2)) &= \max\{F_{M_1}(m_1), F_{M_2}(m_2)\} \\ &\forall (m_1,m_2) \in (V_1 \times V_2);\end{aligned}$$

(ii) $$\begin{aligned}(T_{N_1} \oplus T_{N_2})((m,m_2)(m,n_2)) &= \min\{T_{M_1}(m), T_{N_2}(m_2n_2)\}, \\ (F_{N_1} \oplus F_{N_2})((m,m_2)(m,n_2)) &= \max\{F_{M_1}(m), F_{N_2}(m_2n_2)\} \\ &\forall\, m \in V_1 \text{ and } m_2n_2 \in E_2;\end{aligned}$$

(iii) $$\begin{aligned}(T_{N_1} \oplus T_{N_2})((m_1,z)(n_1,z)) &= \min\{T_{N_1}(m_1n_1), T_{M_2}(z)\}, \\ (F_{N_1} \oplus F_{N_2})((m_1,z)(n_1,z)) &= \max\{F_{N_1}(m_1n_1), F_{M_2}(z)\} \\ &\forall\, z \in V_2 \text{ and } m_1n_1 \in E_1;\end{aligned}$$

(iv) $$(T_{N_1} \oplus T_{N_2})((m_1,m_2)(n_1,n_2)) = \begin{cases} \min\{T_{M_1}(m_1), T_{M_1}(n_1), T_{N_2}(m_2n_2)\} \\ \qquad \forall\, m_1n_1 \notin E_1 \text{ and } m_2n_2 \in E_2, \\ \min\{T_{M_2}(m_2), T_{M_2}(n_2), T_{N_1}(m_1n_1)\} \\ \qquad \forall\, m_1n_1 \in E_1 \text{ and } m_2n_2 \notin E_2, \end{cases}$$

$$(F_{N_1} \oplus F_{N_2})((m_1,m_2)(n_1,n_2)) = \begin{cases} \max\{F_{M_1}(m_1), F_{M_1}(n_1), F_{N_2}(m_2n_2)\} \\ \qquad \forall\, m_1n_1 \notin E_1 \text{ and } m_2n_2 \in E_2, \\ \max\{F_{M_2}(m_2), F_{M_2}(n_2), F_{N_1}(m_1n_1)\} \\ \qquad \forall\, m_1n_1 \in E_1 \text{ and } m_2n_2 \notin E_2. \end{cases}$$

Example 3.23. Consider the vague graphs $\mathbf{G}_1$ and $\mathbf{G}_2$ as in **Figures 13**, **14**. The symmetric difference of $\mathbf{G}_1$ and $\mathbf{G}_2$, i.e., $\mathbf{G}_1 \oplus \mathbf{G}_2$, is shown in **Figure 15**.

For the vertex (a,f), we find the membership and non-membership values as follows:

$$\begin{aligned}(T_{M_1} \oplus T_{M_2})((a,f)) &= \min\{T_{M_1}(a), T_{M_2}(f)\} \\ &= \min\{0.2, 0.3\} = 0.2, \\ (F_{M_1} \oplus F_{M_2})((a,f)) &= \max\{F_{M_1}(a), F_{M_2}(f)\} \\ &= \max\{0.4, 0.3\} = 0.4\end{aligned}$$

for $a \in V_1$ and $f \in V_2$.

For the edge $(a,d)(a,e)$, the membership and non-membership values are given by

$$\begin{aligned}(T_{N_1} \oplus T_{N_2})((a,d)(a,e)) &= \min\{T_{M_1}(a), T_{N_2}(de)\} \\ &= \min\{0.2, 0.1\} = 0.1, \\ (F_{N_1} \oplus F_{N_2})((a,d)(a,e)) &= \max\{F_{M_1}(a), F_{N_2}(de)\} \\ &= \max\{0.4, 0.6\} = 0.6\end{aligned}$$

for $a \in V_1$ and $de \in E_2$.

For the edge $(a,d)(b,d)$ we have

$$\begin{aligned}(T_{N_1} \oplus T_{N_2})((a,d)(b,d)) &= \min\{T_{N_1}(ab), T_{M_2}(d)\} \\ &= \min\{0.2, 0.2\} = 0.2, \\ (F_{N_1} \oplus F_{N_2})((a,d)(b,d)) &= \max\{F_{N_1}(ab), F_{M_2}(d)\} \\ &= \max\{0.7, 0.4\} = 0.7\end{aligned}$$

for $ab \in E_1$ and $d \in V_2$.

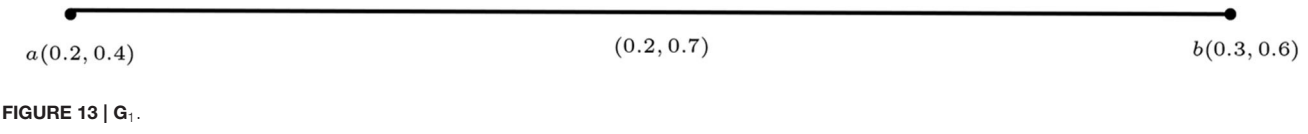

FIGURE 13 | $\mathbf{G}_1$.

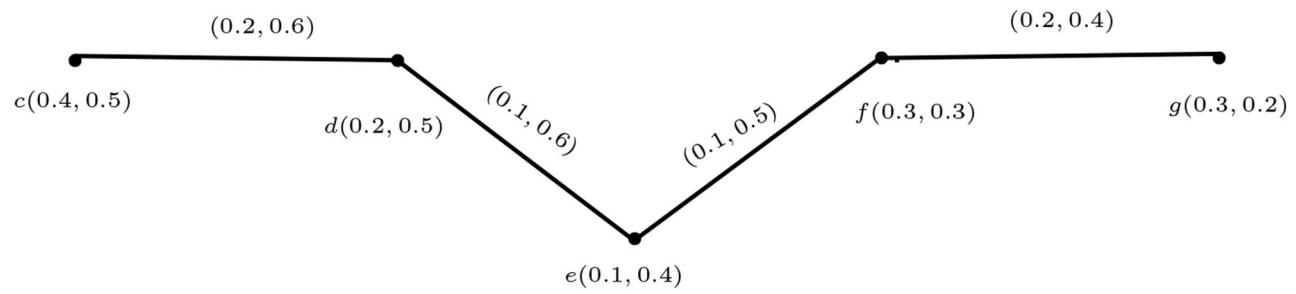

FIGURE 14 | $\mathbf{G}_2$.

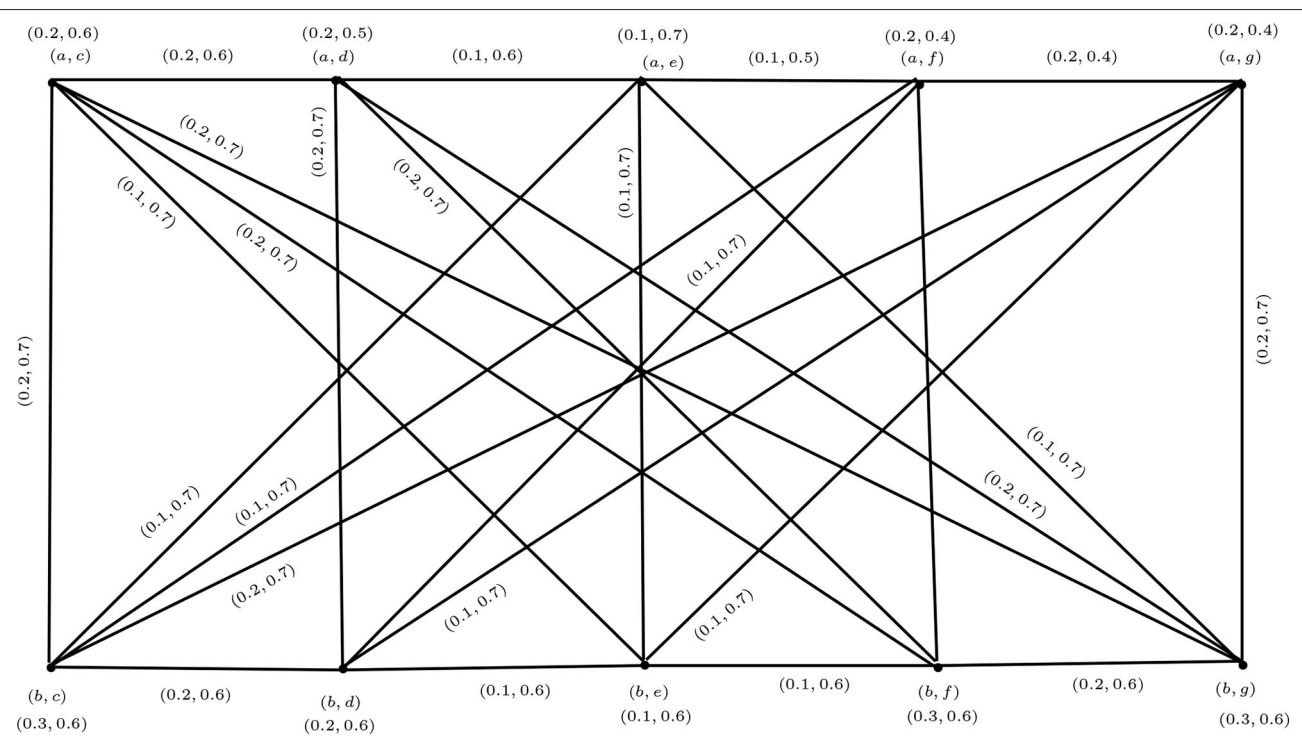

FIGURE 15 | $\mathbf{G}_1 \oplus \mathbf{G}_2$.

For the edge $(a,c)(b,f)$, the membership and non-membership values are

$$\begin{aligned}(T_{N_1} \oplus T_{N_2})((a,c)(b,f)) &= \min\{T_{M_2}(c), T_{M_2}(f), T_{N_1}(ab)\}\\ &= \min\{0.4, 0.3, 0.2\} = 0.2,\\ (F_{N_1} \oplus F_{N_2})((a,c)(b,f)) &= \max\{F_{M_2}(c), F_{M_2}(f), F_{N_1}(ab)\}\\ &= \max\{0.5, 0.3, 0.7\} = 0.7\end{aligned}$$

for $ab \in E_1$ and $cf \notin E_2$.

In the same way, we can find the membership and non-membership values for all remaining vertices and edges.

Proposition 3.24. The symmetric difference of two vague graphs $\mathbf{G}_1$ and $\mathbf{G}_2$ is a vague graph.

Proof: Let $\mathbf{G}_1 = (M_1, N_1)$ and $\mathbf{G}_2 = (M_2, N_2)$ be two vague graphs on crisp graphs $G_1 = (V_1, E_1)$ and $G_2 = (V_2, E_2)$, respectively, and let $((m_1, m_2)(n_1, n_2)) \in E_1 \times E_2$. Then by Definition 3.22 we have the following cases:

(i) If $m_1 = n_1 = m$, then

$$\begin{aligned}
&(T_{N_1} \oplus T_{N_2})((m, m_2)(m, n_2)) = \min\{T_{M_1}(m), T_{N_2}(m_2 n_2)\} \\
&\leq \min\{T_{M_1}(m), \min\{T_{M_2}(m_2), T_{M_2}(n_2)\}\} \\
&= \min\{\min\{T_{M_1}(m), T_{M_2}(m_2)\}, \min\{T_{M_1}(m), T_{M_2}(n_2)\}\} \\
&= \min\{(T_{M_1} \oplus T_{M_2})(m, m_2), (T_{M_1} \oplus T_{M_2})(m, n_2)\},
\end{aligned}$$

$$\begin{aligned}
&(F_{N_1} \oplus F_{N_2})((m, m_2)(m, n_2)) = \max\{F_{M_1}(m), F_{N_2}(m_2 n_2)\} \\
&\geq \max\{F_{M_1}(m), \max\{F_{M_2}(m_2), F_{M_2}(n_2)\}\} \\
&= \max\{\max\{F_{M_1}(m), F_{M_2}(m_2)\}, \max\{F_{M_1}(m), F_{M_2}(n_2)\}\} \\
&= \max\{(F_{M_1} \oplus F_{M_2})(m, m_2), (F_{M_1} \oplus F_{M_2})(m, n_2)\}.
\end{aligned}$$

(ii) If $m_2 = n_2 = z$, then

$$\begin{aligned}
&(T_{N_1} \oplus T_{N_2})((m_1, z)(n_1, z)) = \min\{T_{N_1}(m_1 n_1), T_{M_2}(z)\} \\
&\leq \min\{\min\{T_{N_1}(m_1 n_1), T_{M_2}(z)\} \\
&= \min\{\min\{T_{M_1}(m_1), T_{M_2}(z)\}, \min\{T_{M_1}(n_1), T_{M_2}(z)\}\} \\
&= \min\{(T_{M_1} \oplus T_{M_2})(m_1, z), (T_{M_1} \oplus T_{M_2})(n_1, z)\},
\end{aligned}$$

$$\begin{aligned}
&(F_{N_1} \oplus F_{N_2})((m_1, z)(n_1, z)) = \max\{F_{N_1}(m_1 n_1), F_{M_2}(z)\} \\
&\geq \max\{\max\{F_{N_1}(m_1 n_1), F_{M_2}(z)\} \\
&= \max\{\max\{F_{M_1}(m_1), F_{M_2}(z)\}, \max\{F_{M_1}(n_1), F_{M_2}(z)\}\} \\
&= \max\{(F_{M_1} \oplus F_{M_2})(m_1, z), (F_{M_1} \oplus F_{M_2})(n_1, z)\}.
\end{aligned}$$

(iii) If $m_1 n_1 \notin E_1$ and $m_2 n_2 \in E_2$, then

$$\begin{aligned}
&(T_{N_1} \oplus T_{N_2})((m_1, m_2)(n_1, n_2)) = \min\{T_{M_1}(m_1), T_{M_1}(n_1), T_{N_2}(m_2 n_2)\} \\
&\leq \min\{T_{M_1}(m_1), T_{M_1}(n_1), min\{T_{M_2}(m_2) T_{M_2}(n_2)\}\} \\
&= \min\{\min\{T_{M_1}(m_1), T_{M_2}(m_2)\}, \{T_{M_1}(m_1), T_{M_2}(n_2)\}\} \\
&= \min\{(T_{M_1} \oplus T_{M_2})(m_1, m_2), (T_{M_1} \oplus T_{M_2})(n_1, n_2)\},
\end{aligned}$$

$$\begin{aligned}
&(F_{N_1} \oplus F_{N_2})((m_1, m_2)(n_1, n_2)) = \max\{F_{M_1}(m_1), F_{M_1}(n_1), F_{N_2}(m_2 n_2)\} \\
&\geq \max\{F_{M_1}(m_1), F_{M_1}(n_1), \max\{F_{M_2}(m_2) F_{M_2}(n_2)\}\} \\
&= \max\{\max\{F_{M_1}(m_1), F_{M_2}(m_2)\}, \{F_{M_1}(m_1), F_{M_2}(n_2)\}\} \\
&= \max\{(F_{M_1} \oplus F_{M_2})(m_1, m_2), (F_{M_1} \oplus F_{M_2})(n_1, n_2)\}.
\end{aligned}$$

(iv) If $m_1 n_1 \in E_1$ and $m_2 n_2 \notin E_2$, then

$$\begin{aligned}
&(T_{N_1} \oplus T_{N_2})((m_1, m_2)(n_1, n_2)) = \min\{T_{M_2}(m_2), T_{M_2}(n_2), T_{N_1}(m_1 n_1)\} \\
&\leq \min\{T_{M_2}(m_2), T_{M_2}(n_2), \min\{T_{M_1}(m_1) T_{M_1}(n_1)\}\} \\
&= \min\{\min\{T_{M_1}(m_1), T_{M_2}(m_2)\}, \{T_{M_1}(n_1), T_{M_2}(n_2)\} \\
&= \min\{(T_{M_1} \oplus T_{M_2})(m_1, m_2), (T_{M_1} \oplus T_{M_2})(n_1, n_2)\},
\end{aligned}$$

$$\begin{aligned}
&(F_{N_1} \oplus F_{N_2})((m_1, m_2)(n_1, n_2)) = \max\{F_{M_2}(m_2), F_{M_2}(n_2), F_{N_1}(m_1 n_1)\} \\
&\geq \max\{F_{M_2}(m_2), F_{M_2}(n_2), \max\{F_{M_1}(m_1) F_{M_1}(n_1)\}\} \\
&= \max\{\max\{F_{M_2}(m_2), F_{M_1}(m_1)\}, \{F_{M_2}(m_2), F_{M_1}(n_1)\} \\
&= \max\{(F_{M_1} \oplus F_{M_2})(m_1, m_2), (F_{M_1} \oplus F_{M_2})(n_1, n_2)\}.
\end{aligned}$$

Hence $\mathbf{G}_1 \oplus \mathbf{G}_2$ is a vague graph. □

Remark 3.5. The symmetric difference of two connected vague graphs $\mathbf{G}_1 = (M_1, N_1)$ and $\mathbf{G}_2 = (M_2, N_2)$ is connected, because we include the case where $(m_1, m_2) \in E_1$ and $(n_1, n_2) \in E_2$ in the definition of the symmetric difference of two vague graphs.

Definition 3.25. Let $\mathbf{G}_1 = (M_1, N_1)$ and $\mathbf{G}_2 = (M_2, N_2)$ be two vague graphs. For any vertex $(m_1, m_2) \in V_1 \times V_2$ we define

$$\begin{aligned}
(d_T)_{\mathbf{G}_1 \oplus \mathbf{G}_2}(m_1, m_2) &= \sum_{(m_1, m_2)(n_1, n_2) \in E_1 \times E_2} (T_{N_1} \oplus T_{N_2})((m_1, m_2)(n_1, n_2)) \\
&= \sum_{m_1 = n_1,\, m_2 n_2 \in E_2} \min\{T_{M_1}(m_1), T_{N_2}(m_2 n_2)\} \\
&\quad + \sum_{m_1 n_1 \in E_1,\, m_2 = n_2} \min\{T_{N_1}(m_1 n_1), T_{M_2}(m_2)\} \\
&\quad + \sum_{m_1 n_1 \notin E_1 \text{ and } m_2 n_2 \in E_2} \min\{T_{M_1}(m_1), T_{M_1}(n_1), T_{N_2}(m_2 n_2)\} \\
&\quad + \sum_{m_1 n_1 \in E_1 \text{ and } m_2 n_2 \notin E_2} \min\{T_{N_1}(m_1 n_1), T_{M_2}(m_2), T_{M_2}(n_2)\}
\end{aligned}$$

and

$$\begin{aligned}
(d_F)_{\mathbf{G}_1 \oplus \mathbf{G}_2}(m_1, m_2) &= \sum_{(m_1, m_2)(n_1, n_2) \in E_1 \times E_2} (F_{N_1} \oplus F_{N_2})((m_1, m_2)(n_1, n_2)) \\
&= \sum_{m_1 = n_1,\, m_2 n_2 \in E_2} \max\{F_{M_1}(m_1), F_{N_2}(m_2 n_2)\} \\
&\quad + \sum_{m_1 n_1 \in E_1,\, m_2 = n_2} \max\{F_{N_1}(m_1 n_1), F_{M_2}(m_2)\} \\
&\quad + \sum_{m_1 n_1 \notin E_1 \text{ and } m_2 n_2 \in E_2} \max\{F_{M_1}(m_1), F_{M_1}(n_1), F_{N_2}(m_2 n_2)\} \\
&\quad + \sum_{m_1 n_1 \in E_1 \text{ and } m_2 n_2 \notin E_2} \max\{F_{N_1}(m_1 n_1), F_{M_2}(m_2), F_{M_2}(n_2)\}.
\end{aligned}$$

Theorem 3.26. Let $\mathbf{G}_1 = (M_1, N_1)$ and $\mathbf{G}_2 = (M_2, N_2)$ be two vague graphs. If $T_{M_1} \geq T_{N_2}$, $F_{M_1} \leq F_{N_2}$, $T_{M_2} \geq T_{N_1}$, and $F_{M_2} \leq F_{N_1}$, then for every $(m_1, m_2) \in V_1 \times V_2$ we have $(d)_{\mathbf{G}_1 \oplus \mathbf{G}_2}(m_1, m_2) = q(d)_{\mathbf{G}_1}(m_1) + s(d)_{\mathbf{G}_2}(m_2)$, where $s = |V_1| - (d)_{G_1}(m_1)$ and $q = |V_2| - (d)_{G_2}(m_2)$.

Proof: Using Definition 3.25,

$$\begin{aligned}
(d_T)_{\mathbf{G}_1 \oplus \mathbf{G}_2}(m_1, m_2) &= \sum_{(m_1, m_2)(n_1, n_2) \in E_1 \times E_2} (T_{N_1} \oplus T_{N_2})((m_1, m_2)(n_1, n_2)) \\
&= \sum_{m_1 = n_1,\, m_2 n_2 \in E_2} \min\{T_{M_1}(m_1), T_{N_2}(m_2 n_2)\} \\
&\quad + \sum_{m_1 n_1 \in E_1,\, m_2 = n_2} \min\{T_{N_1}(m_1 n_1), T_{M_2}(m_2)\} \\
&\quad + \sum_{m_1 n_1 \notin E_1 \text{ and } m_2 n_2 \in E_2} \min\{T_{M_1}(m_1), T_{M_1}(n_1), T_{N_2}(m_2 n_2)\} \\
&\quad + \sum_{m_1 n_1 \in E_1 \text{ and } m_2 n_2 \notin E_2} \min\{T_{N_1}(m_1 n_1), T_{M_2}(m_2), T_{M_2}(n_2)\} \\
&= \sum_{m_2 n_2 \in E_2} T_{N_2}(m_2 n_2) + \sum_{m_1 n_1 \in E_1} T_{N_1}(m_1 n_1) \\
&\quad + \sum_{m_1 n_1 \notin E_1 \text{ and } m_2 n_2 \in E_2} T_{N_2}(m_2 n_2)\} + \sum_{m_1 n_1 \in E_1 \text{ and } m_2 n_2 \notin E_2} T_{N_1}(m_1 n_1) \\
&= q(d_T)_{\mathbf{G}_1}(m_1) + s(d_T)_{\mathbf{G}_2}(m_2),
\end{aligned}$$

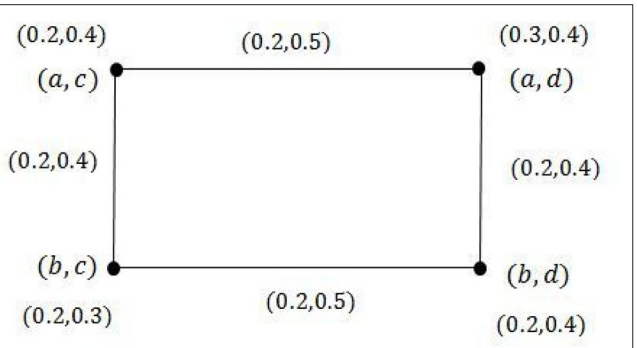

FIGURE 16 | $\mathbf{G}_1 \oplus \mathbf{G}_2$ of the vague graphs in **Figure 9**.

$$
\begin{aligned}
(d_F)_{\mathbf{G}_1\oplus\mathbf{G}_2}(m_1,m_2) &= \sum_{(m_1,m_2)(n_1,n_2)\in E_1\times E_2} (F_{N_1}\oplus F_{N_2})((m_1,m_2)(n_1,n_2)) \\
&= \sum_{m_1=n_1,\, m_2n_2\in E_2} \max\{F_{M_1}(m_1), F_{N_2}(m_2n_2)\} \\
&\quad + \sum_{m_1n_1\in E_1,\, m_2=n_2} \max\{F_{N_1}(m_1n_1), F_{M_2}(m_2)\} \\
&\quad + \sum_{m_1n_1\notin E_1 \text{ and } m_2n_2\in E_2} \max\{F_{M_1}(m_1), F_{M_1}(n_1), F_{N_2}(m_2n_2)\} \\
&\quad + \sum_{m_1n_1\in E_1 \text{ and } m_2n_2\notin E_2} \max\{F_{N_1}(m_1n_1), F_{M_2}(m_2), F_{M_2}(n_2)\} \\
&= \sum_{m_2n_2\in E_2} F_{N_2}(m_2n_2) + \sum_{m_1n_1\in E_1} F_{N_1}(m_1n_1) \\
&\quad + \sum_{m_1n_1\notin E_1 \text{ and } m_2n_2\in E_2} F_{N_2}(m_2n_2)\} + \sum_{m_1n_1\in E_1 \text{ and } m_2n_2\notin E_2} F_{N_1}(m_1n_1) \\
&= q(d_F)_{\mathbf{G}_1}(m_1) + s(d_F)_{\mathbf{G}_2}(m_2),
\end{aligned}
$$

and hence the result is proved. □

Example 3.27. Consider the two vague graphs $\mathbf{G}_1$ and $\mathbf{G}_2$ in **Figure 9** and their symmetric difference in **Figure 16**. In **Figure 9**, $T_{M_1} \geq T_{N_2}$, $F_{M_1} \leq F_{N_2}$, $T_{M_2} \geq T_{N_1}$, and $F_{M_2} \leq F_{N_1}$. Then, the total degree of a vertex in the symmetric difference is calculated by the following formula:

$$
\begin{aligned}
(d_T)_{\mathbf{G}_1\oplus\mathbf{G}_2}(m_1,m_2) &= q(d_T)_{\mathbf{G}_1}(m_1) + s(d_T)_{\mathbf{G}_2}(m_2), \\
(d_F)_{\mathbf{G}_1\oplus\mathbf{G}_2}(m_1,m_2) &= q(d_F)_{\mathbf{G}_1}(m_1) + s(d_F)_{\mathbf{G}_2}(m_2).
\end{aligned}
$$

Using the formula we find that

$$
\begin{aligned}
(d_T)_{\mathbf{G}_1\oplus\mathbf{G}_2}(a,c) &= 1\cdot(0.2) + 1\cdot(0.2) = 0.4, \\
(d_F)_{\mathbf{G}_1\oplus\mathbf{G}_2}(a,c) &= 1\cdot(0.4) + 1\cdot(0.5) = 0.9, \\
(d_T)_{\mathbf{G}_1\oplus\mathbf{G}_2}(a,d) &= 1\cdot(0.2) + 1\cdot(0.2) = 0.4, \\
(d_F)_{\mathbf{G}_1\oplus\mathbf{G}_2}(a,d) &= 1\cdot(0.4) + 1\cdot(0.5) = 0.9.
\end{aligned}
$$

Hence, $(d)_{\mathbf{G}_1\oplus\mathbf{G}_2}(a,c) = (0.4, 0.9)$ and $(d)_{\mathbf{G}_1\oplus\mathbf{G}_2}(a,d) = (0.4, 0.9)$.

In the same way, we can show that $(d)_{\mathbf{G}_1\oplus\mathbf{G}_2}(b,c) = (d)_{\mathbf{G}_1\oplus\mathbf{G}_2}(b,d) = (0.4, 0.9)$. Direct calculations give

$$
\begin{aligned}
(d_T)_{\mathbf{G}_1\oplus\mathbf{G}_2}(a,c) &= 0.2 + 0.2 = 0.4, \\
(d_F)_{\mathbf{G}_1\oplus\mathbf{G}_2}(a,c) &= 0.4 + 0.5 = 0.9, \\
(d_T)_{\mathbf{G}_1\oplus\mathbf{G}_2}(a,d) &= 0.2 + 0.2 = 0.4, \\
(d_F)_{\mathbf{G}_1\oplus\mathbf{G}_2}(a,d) &= 0.4 + 0.5 = 0.9, \\
(d_T)_{\mathbf{G}_1\oplus\mathbf{G}_2}(b,c) &= 0.2 + 0.2 = 0.4, \\
(d_F)_{\mathbf{G}_1\oplus\mathbf{G}_2}(b,c) &= 0.4 + 0.5 = 0.9, \\
(d_T)_{\mathbf{G}_1\oplus\mathbf{G}_2}(b,d) &= 0.2 + 0.2 = 0.4, \\
(d_F)_{\mathbf{G}_1\oplus\mathbf{G}_2}(b,d) &= 0.4 + 0.5 = 0.9.
\end{aligned}
$$

It is obvious from the above that the degrees of vertices calculated using the formula and by the direct method are the same.

Definition 3.28. Let $\mathbf{G}_1 = (M_1, N_1)$ and $\mathbf{G}_2 = (M_2, N_2)$ be two vague graphs. For any vertex $(m_1, m_2) \in V_1 \times V_2$ we define

$$
\begin{aligned}
(td_T)_{\mathbf{G}_1\oplus\mathbf{G}_2}(m_1,m_2) &= \sum_{(m_1,m_2)(n_1,n_2)\in E_1\times E_2} (T_{N_1}\oplus T_{N_2})((m_1,m_2)(n_1,n_2)) \\
&\quad + (T_{M_1}\oplus T_{M_2}(m_1,m_2) \\
&= \sum_{m_1=n_1,\, m_2n_2\in E_2} \min\{T_{M_1}(m_1), T_{N_2}(m_2n_2)\} \\
&\quad + \sum_{m_1n_1\in E_1,\, m_2=n_2} \min\{T_{N_1}(m_1n_1), T_{M_2}(m_2)\} \\
&\quad + \sum_{m_1n_1\notin E_1 \text{ and } m_2n_2\in E_2} \min\{T_{M_1}(m_1), T_{M_1}(n_1), T_{N_2}(m_2n_2)\} \\
&\quad + \sum_{m_1n_1\in E_1 \text{ and } m_2n_2\notin E_2} \min\{T_{N_1}(m_1n_1), T_{M_2}(m_2), T_{M_2}(n_2)\} \\
&\quad + \min\{T_{M_1}(m_1), T_{M_2}(m_2)\}
\end{aligned}
$$

and

$$
\begin{aligned}
(td_F)_{\mathbf{G}_1\oplus\mathbf{G}_2}(m_1,m_2) &= \sum_{(m_1,m_2)(n_1,n_2)\in E_1\times E_2} (F_{N_1}\oplus F_{N_2})((m_1,m_2)(n_1,n_2)) \\
&\quad + (F_{M_1}\oplus F_{M_2}(m_1,m_2) \\
&= \sum_{m_1=n_1,\, m_2n_2\in E_2} \max\{F_{M_1}(m_1), F_{N_2}(m_2n_2)\} \\
&\quad + \sum_{m_1n_1\in E_1,\, m_2=n_2} \max\{F_{N_1}(m_1n_1), F_{M_2}(m_2)\} \\
&\quad + \sum_{m_1n_1\notin E_1 \text{ and } m_2n_2\in E_2} \max\{F_{M_1}(m_1), F_{M_1}(n_1), F_{N_2}(m_2n_2)\} \\
&\quad + \sum_{m_1n_1\in E_1 \text{ and } m_2n_2\notin E_2} \max\{F_{N_1}(m_1n_1), F_{M_2}(m_2), F_{M_2}(n_2)\} \\
&\quad + \max\{F_{M_1}(m_1), F_{M_2}(m_2)\}.
\end{aligned}
$$

Example 3.29. In this example we find the degree and total degree of the vertex (a, e) in Example 3.23. We have

$$
\begin{aligned}
s &= |V_1| - (d)_{G_1}(a) \\
&= 2 - 1 = 1
\end{aligned}
$$

and, similarly,

$$q = |V_2| - (d)_{G_2}(e) = 5 - 2 = 3.$$

Therefore

$$(d_T)_{\mathbf{G}_1\oplus\mathbf{G}_2}(a,e) = q(d_T)_{\mathbf{G}_1}(a) + s(d_T)_{\mathbf{G}_2}(e) = 3(0.2) + 1(0.1 + 0.1) = 0.6 + 0.2 = 0.8,$$

$$(d_F)_{\mathbf{G}_1\oplus\mathbf{G}_2}(a,e) = q(d_F)_{\mathbf{G}_1}(a) + s(d_F)_{\mathbf{G}_2}(e) = 3(0.4) + 1(0.6 + 0.5) = 1.2 + 1.1 = 2.3.$$

So

$$(d)_{\mathbf{G}_1\oplus\mathbf{G}_2}(a,e) = (0.8, 2.3).$$

In addition, by Definition 3.28 we have

$$\begin{aligned}(td_T)_{\mathbf{G}_1\oplus\mathbf{G}_2}(a,e) &= q(td_T)_{\mathbf{G}_1}(a) + s(td_T)_{\mathbf{G}_2}(e) \\ &\quad - (s-1)T_{\mathbf{G}_2}(e) - (q-1)T_{\mathbf{G}_1}(a) \\ &\quad - \max\{T_{\mathbf{G}_1}(a), T_{\mathbf{G}_2}(e)\} \\ &= 3(0.2 + 0.2) + 1(0.1 + 0.1 + 0.1) \\ &\quad - (1-1)(0.1) - (3-1)(0.2) - \max\{0.2, 0.1\} \\ &= 3(0.4) + 0.3 - 0.4 - 0.2 = 0.9,\end{aligned}$$

$$\begin{aligned}(td_F)_{\mathbf{G}_1\oplus\mathbf{G}_2}(a,e) &= q(td_F)_{\mathbf{G}_1}(a) + s(td_F)_{\mathbf{G}_2}(e) \\ &\quad - (s-1)F_{\mathbf{G}_2}(e) - (q-1)F_{\mathbf{G}_1}(a) \\ &\quad - \min\{F_{\mathbf{G}_1}(a), F_{\mathbf{G}_2}(e)\} \\ &= 3(0.2 + 0.2) + 1(0.4 + 0.5 + 0.6) \\ &\quad - (1-1)(0.4) - (3-1)(0.4) - \min\{0.4, 0.4\} \\ &= 3(0.4) + 1.5 - 0.8 - 0.4 = 1.5.\end{aligned}$$

Therefore,

$$(td)_{\mathbf{G}_1\oplus\mathbf{G}_2}(a,e) = (0.9, 1.5).$$

Similarly, we can find the degree and total degree of all vertices in $\mathbf{G}_1 \oplus \mathbf{G}_2$.

Theorem 3.30. Let $\mathbf{G}_1 = (M_1, N_1)$ and $\mathbf{G}_2 = (M_2, N_2)$ be two vague graphs.

(i) If $T_{M_1} \geq T_{N_2}$ and $T_{M_2} \geq T_{N_1}$, then for all $(m_1, m_2) \in V_1 \times V_2$,

$$(td_T)_{\mathbf{G}_1\oplus\mathbf{G}_2}(m_1,m_2) = q(td_T)_{\mathbf{G}_1}(m_1) + s(td_T)_{\mathbf{G}_2}(m_2) - (q-1)T_{\mathbf{G}_1}(m_1) - \max\{T_{\mathbf{G}_1}(m_1), T_{\mathbf{G}_2}(m_2)\}.$$

(ii) If $F_{M_1} \leq F_{N_2}$ and $F_{M_2} \leq F_{N_1}$, then for all $(m_1, m_2) \in V_1 \times V_2$,

$$(td_F)_{\mathbf{G}_1\oplus\mathbf{G}_2}(m_1,m_2) = q(td_F)_{\mathbf{G}_1}(m_1) + s(td_F)_{\mathbf{G}_2}(m_2) - (q-1)F_{\mathbf{G}_1}(m_1) - \min\{F_{\mathbf{G}_1}(m_1), F_{\mathbf{G}_2}(m_2)\}.$$

Here $s = |V_1| - (d)_{G_1}(m_1)$ and $q = |V_2| - (d)_{G_2}(m_2)$.

Proof: For all $(m_1, m_2) \in V_1 \times V_2$ we have

$$\begin{aligned}(td_T)_{\mathbf{G}_1\oplus\mathbf{G}_2}(m_1,m_2) &= \sum_{(m_1,m_2)(n_1,n_2)\in E_1\times E_2} (T_{N_1} \oplus T_{N_2})((m_1,m_2)(n_1,n_2)) \\ &\quad + (T_{M_1} \oplus T_{M_2})(m_1,m_2) \\ &= \sum_{m_1=n_1,\, m_2n_2\in E_2} \min\{T_{M_1}(m_1), T_{N_2}(m_2n_2)\} \\ &\quad + \sum_{m_1n_1\in E_1,\, m_2=n_2} \min\{T_{N_1}(m_1n_1), T_{M_2}(m_2)\} \\ &\quad + \sum_{m_1n_1\notin E_1 \text{ and } m_2n_2\in E_2} \min\{T_{M_1}(m_1), T_{M_1}(n_1), T_{N_2}(m_2n_2)\} \\ &\quad + \sum_{m_1n_1\in E_1 \text{ and } m_2n_2\notin E_2} \min\{T_{N_1}(m_1n_1), T_{M_2}(m_2), T_{M_2}(n_2)\} \\ &\quad + \max\{T_{M_1}(m_1), T_{M_2}(m_2)\} \\ &= \sum_{m_2n_2\in E_2} T_{N_2}(m_2n_2) + \sum_{m_1n_1\in E_1} T_{N_1}(m_1n_1) \\ &\quad + \sum_{m_1n_1\notin E_1 \text{ and } m_2n_2\in E_2} T_{N_2}(m_2n_2)\} + \sum_{m_1n_1\in E_1 \text{ and } m_2n_2\notin E_2} T_{N_1}(m_1n_1) \\ &\quad + \max\{T_{M_1}(m_1), T_{M_2}(m_2)\} \\ &= \sum_{m_2n_2\in E_2} T_{N_2}(m_2n_2) + \sum_{m_1n_1\in E_1} T_{N_1}(m_1n_1) \\ &\quad + \sum_{m_1n_1\notin E_1 \text{ and } m_2n_2\in E_2} T_{N_2}(m_2n_2)\} \\ &\quad + \sum_{m_1n_1\in E_1 \text{ and } m_2n_2\notin E_2} T_{N_1}(m_1n_1) + T_{M_1}(m_1) + T_{M_2}(m_2) \\ &\quad - \max\{T_{M_1}(m_1), T_{M_2}(m_2)\} \\ &= q(td_T)_{\mathbf{G}_1}(m_1) + s(td_T)_{\mathbf{G}_2}(m_2) \\ &\quad - (q-1)T_{\mathbf{G}_1}(m_1) - \max\{T_{\mathbf{G}_1}(m_1), T_{\mathbf{G}_2}(m_2)\},\end{aligned}$$

$$\begin{aligned}(td_F)_{\mathbf{G}_1\oplus\mathbf{G}_2}(m_1,m_2) &= \sum_{(m_1,m_2)(n_1,n_2)\in E_1\times E_2} (F_{N_1} \oplus F_{N_2})((m_1,m_2)(n_1,n_2)) \\ &\quad + (F_{M_1} \oplus F_{M_2})(m_1,m_2) \\ &= \sum_{m_1=n_1,\, m_2n_2\in E_2} \max\{F_{M_1}(m_1), F_{N_2}(m_2n_2)\} \\ &\quad + \sum_{m_1n_1\in E_1,\, m_2=n_2} \max\{F_{N_1}(m_1n_1), F_{M_2}(m_2)\} \\ &\quad + \sum_{m_1n_1\notin E_1 \text{ and } m_2n_2\in E_2} \max\{F_{M_1}(m_1), F_{M_1}(n_1), F_{N_2}(m_2n_2)\} \\ &\quad + \sum_{m_1n_1\in E_1 \text{ and } m_2n_2\notin E_2} \max\{F_{N_1}(m_1n_1), F_{M_2}(m_2), F_{M_2}(n_2)\} \\ &\quad + \min\{F_{M_1}(m_1), F_{M_2}(m_2)\} \\ &= \sum_{m_2n_2\in E_2} F_{N_2}(m_2n_2) + \sum_{m_1n_1\in E_1} F_{N_1}(m_1n_1) \\ &\quad + \sum_{m_1n_1\notin E_1 \text{ and } m_2n_2\in E_2} F_{N_2}(m_2n_2)\}\end{aligned}$$

$$
\begin{aligned}
&+ \sum_{m_1n_1\in E_1 \text{ and } m_2n_2\notin E_2} F_{N_1}(m_1n_1)\\
&\quad + \min\{F_{M_1}(m_1), F_{M_2}(m_2)\}\\
&= \sum_{m_2n_2\in E_2} F_{N_2}(m_2n_2) + \sum_{m_1n_1\in E_1} F_{N_1}(m_1n_1)\\
&\quad + \sum_{m_1n_1\notin E_1 \text{ and } m_2n_2\in E_2} F_{N_2}(m_2n_2)\}\\
&\quad + \sum_{m_1n_1\in E_1 \text{ and } m_2n_2\notin E_2} F_{N_1}(m_1n_1) + F_{M_1}(m_1) + F_{M_2}(m_2)\\
&\qquad\qquad - \min\{F_{M_1}(m_1), F_{M_2}(m_2)\}\\
&= q(td_F)_{\mathbf{G}_1}(m_1) + s(td_F)_{\mathbf{G}_2}(m_2)\\
&\quad - (q-1)F_{\mathbf{G}_1}(m_1) - \min\{F_{\mathbf{G}_1}(m_1), F_{\mathbf{G}_2}(m_2)\},
\end{aligned}
$$

where $s = |V_1| - (d)_{G_1}(m_1)$ and $q = |V_2| - (d)_{G_2}(m_2)$. □

Example 3.31. In this example, we calculate the total degree of the vertices in Example 3.27.

The total degree of a vertex in the symmetric difference is given by

$$
\begin{aligned}
&(td_T)_{\mathbf{G}_1\oplus\mathbf{G}_2}(m_1,m_2) = q(td_T)_{\mathbf{G}_1}(m_1) + s(td_T)_{\mathbf{G}_2}(m_2)\\
&- (q-1)T_{\mathbf{G}_1}(m_1) - \max\{T_{\mathbf{G}_1}(m_1), T_{\mathbf{G}_2}(m_2)\},\\
&(td_F)_{\mathbf{G}_1\oplus\mathbf{G}_2}(m_1,m_2) = q(td_F)_{\mathbf{G}_1}(m_1) + s(td_F)_{\mathbf{G}_2}(m_2)\\
&- (q-1)F_{\mathbf{G}_1}(m_1) - \min\{F_{\mathbf{G}_1}(m_1), F_{\mathbf{G}_2}(m_2)\}.
\end{aligned}
$$

Using the above formula, we calculate

$$
\begin{aligned}
(td_T)_{\mathbf{G}_1\oplus\mathbf{G}_2}(a,c) &= 1\cdot(0.5) + 1\cdot(0.4) - (1-1)\cdot(0.3)\\
&\quad - \max\{0.2, 0.3\} = 0.6,\\
(td_F)_{\mathbf{G}_1\oplus\mathbf{G}_2}(a,c) &= 1\cdot(0.8) + 1\cdot(0.8) - (1-1)\cdot(0.4)\\
&\quad - \min\{0.3, 0.4\} = 1.3,\\
(td_T)_{\mathbf{G}_1\oplus\mathbf{G}_2}(a,d) &= 1\cdot(0.5) + 1\cdot(0.5) - (1-1)\cdot(0.3)\\
&\quad - \max\{0.3, 0.3\} = 0.7,\\
(td_F)_{\mathbf{G}_1\oplus\mathbf{G}_2}(a,d) &= 1\cdot(0.8) + 1\cdot(0.9) - (1-1)\cdot(0.4)\\
&\quad - \min\{0.4, 0.4\} = 1.3,\\
(td_T)_{\mathbf{G}_1\oplus\mathbf{G}_2}(b,c) &= 1\cdot(0.4) + 1\cdot(0.4) - (1-1)\cdot(0.2)\\
&\quad - \max\{0.2, 0.2\} = 0.6,\\
(td_F)_{\mathbf{G}_1\oplus\mathbf{G}_2}(b,c) &= 1\cdot(0.7) + 1\cdot(0.8) - (1-1)\cdot(0.2)\\
&\quad - \min\{0.3, 0.3\} = 1.2,\\
(td_T)_{\mathbf{G}_1\oplus\mathbf{G}_2}(b,d) &= 1\cdot(0.4) + 1\cdot(0.5) - (1-1)\cdot(0.2)\\
&\quad - \max\{0.2, 0.3\} = 0.6,\\
(td_F)_{\mathbf{G}_1\oplus\mathbf{G}_2}(b,d) &= 1\cdot(0.7) + 1\cdot(0.9) - (1-1)\cdot(0.2)\\
&\quad - \min\{0.3, 0.4\} = 1.3.
\end{aligned}
$$

By direct calculations, we find

$$
\begin{aligned}
(td_T)_{\mathbf{G}_1\oplus\mathbf{G}_2}(a,c) &= 0.2 + 0.2 + 0.2 = 0.6,\\
(td_F)_{\mathbf{G}_1\oplus\mathbf{G}_2}(a,c) &= 0.4 + 0.5 + 0.4 = 1.3,\\
(td_T)_{\mathbf{G}_1\oplus\mathbf{G}_2}(a,d) &= 0.2 + 0.2 + 0.3 = 0.7,\\
(td_F)_{\mathbf{G}_1\oplus\mathbf{G}_2}(a,d) &= 0.4 + 0.5 + 0.4 = 1.3,\\
(td_T)_{\mathbf{G}_1\oplus\mathbf{G}_2}(b,c) &= 0.2 + 0.2 + 0.2 = 0.6,\\
(td_F)_{\mathbf{G}_1\oplus\mathbf{G}_2}(b,c) &= 0.4 + 0.5 + 0.3 = 1.2,\\
(td_T)_{\mathbf{G}_1\oplus\mathbf{G}_2}(b,d) &= 0.2 + 0.2 + 0.2 = 0.6,\\
(td_F)_{\mathbf{G}_1\oplus\mathbf{G}_2}(b,d) &= 0.4 + 0.5 + 0.4 = 1.3.
\end{aligned}
$$

It is clear that the total degrees of vertices calculated using the formula and by the direct method are the same.

Definition 3.32. The residue product $\mathbf{G}_1 \bullet \mathbf{G}_2 = (M_1 \bullet M_2, N_1 \bullet N_2)$ of two vague graphs $\mathbf{G}_1 = (M_1, N_1)$ and $\mathbf{G}_2 = (M_2, N_2)$ is defined as follows:

(i)
$$
\begin{aligned}
(T_{M_1} \bullet T_{M_2})((m_1,m_2)) &= \max\{T_{M_1}(m_1), T_{M_2}(m_2)\},\\
(F_{M_1} \bullet F_{M_2})((m_1,m_2)) &= \min\{F_{M_1}(m_1), F_{M_2}(m_2)\}\\
&\qquad \forall\, (m_1,m_2) \in (V_1 \times V_2);
\end{aligned}
$$

(ii)
$$
\begin{aligned}
(T_{N_1} \bullet T_{N_2})((m_1,m_2)(n_1,n_2)) &= T_{N_1}(m_1n_1),\\
(F_{N_1} \bullet F_{N_2})((m_1,m_2)(n_1,n_2)) &= F_{N_1}(m_1n_1)\\
&\qquad \forall\, m_1n_1 \in E_1,\ m_2 \neq n_2.
\end{aligned}
$$

Example 3.33. Consider the vague graphs $\mathbf{G}_1$ and $\mathbf{G}_2$ in **Figures 17**, **18**. The residue product of $\mathbf{G}_1$ and $\mathbf{G}_2$, i.e., $\mathbf{G}_1 \bullet \mathbf{G}_2$, is shown in **Figure 19**.

For the vertex (b, e), we find the membership and non-membership values as follows:

$$
\begin{aligned}
(T_{M_1} \bullet T_{M_2})((b,e)) &= \max\{T_{M_1}(b), T_{M_2}(e)\}\\
&= \max\{0.2, 0.2\} = 0.2,\\
(F_{M_1} \bullet F_{M_2})((b,e)) &= \min\{F_{M_1}(b), F_{M_2}(e)\}\\
&= \min\{0.7, 0.6\} = 0.6
\end{aligned}
$$

for $b \in V_1$ and $e \in V_2$.

For the edge $(a,c)(b,d)$, we calculate the membership and non-membership values to be

$$
\begin{aligned}
(T_{N_1} \bullet T_{N_2})((a,c)(b,d)) &= T_{N_1}(ab) = 0.1,\\
(F_{N_1} \bullet F_{N_2})((a,c)(b,d)) &= F_{N_1}(ab) = 0.8
\end{aligned}
$$

for $ab \in E_1$ and $c \neq d$.

Similarly, we can find the membership and non-membership values for all the remaining vertices and edges.

Proposition 3.34. The residue product of two vague graphs $\mathbf{G}_1$ and $\mathbf{G}_2$ is a vague graph.

Proof: Let $\mathbf{G}_1 = (M_1, N_1)$ and $\mathbf{G}_2 = (M_2, N_2)$ be two vague graphs on crisp graphs $G_1 = (V_1, E_1)$ and $G_2 = (V_2, E_2)$,

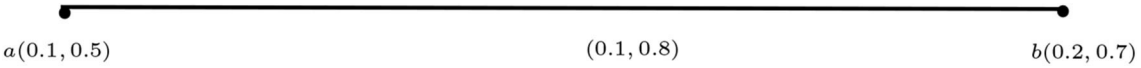

FIGURE 17 | $\mathbf{G}_1$.

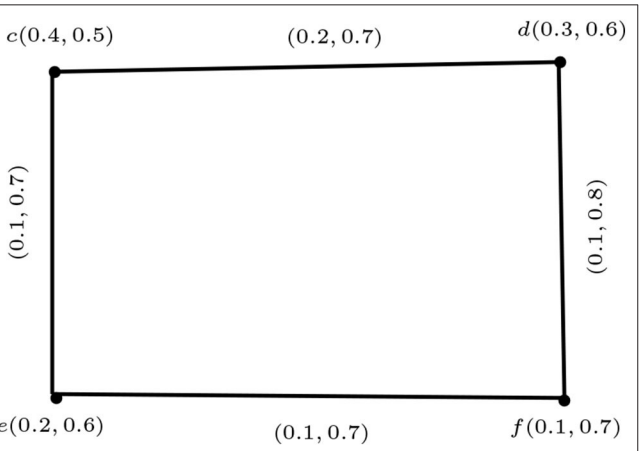

FIGURE 18 | $\mathbf{G}_2$.

respectively, and let $((m_1, m_2)(n_1, n_2)) \in E_1 \times E_2$. If $m_1n_1 \in E_1$ and $m_2 \neq n_2$, then

$$
\begin{aligned}
&(T_{N_1} \bullet T_{N_2})((m_1, m_2)(n_1, n_2)) = T_{N_1}(m_1n_1)\\
&\leq \min\{T_{M_1}(m_1), T_{M_1}(n_1)\}\\
&\leq \max\{\min\{T_{M_1}(m_1), T_{M_1}(n_1)\}, \min\{T_{M_2}(m_2), T_{M_2}(n_2)\}\}\\
&= \min\{\max\{T_{M_1}(m_1), T_{M_1}(n_1)\}, \max\{T_{M_2}(m_2), T_{M_2}(n_2)\}\}\\
&= \min\{(T_{M_1} \bullet T_{M_2})(m_1, m_2), (T_{M_1} \bullet T_{M_2})(n_1, n_2)\},\\
&(F_{N_1} \bullet F_{N_2})((m_1, m_2)(n_1, n_2)) = F_{N_1}(m_1n_1)\\
&\geq \max\{F_{M_1}(m_1), F_{M_1}(n_1)\}\\
&\geq \min\{\max\{F_{M_1}(m_1), F_{M_1}(n_1)\}, \max\{F_{M_2}(m_2), F_{M_2}(n_2)\}\}\\
&= \max\{\min\{F_{M_1}(m_1), F_{M_1}(n_1)\}, \min\{F_{M_2}(m_2), F_{M_2}(n_2)\}\}\\
&= \max\{(F_{M_1} \bullet F_{M_2})(m_1, m_2), (F_{M_1} \bullet F_{M_2})(n_1, n_2)\},
\end{aligned}
$$

which completes the proof. □

Definition 3.35. Let $\mathbf{G}_1 = (M_1, N_1)$ and $\mathbf{G}_2 = (M_2, N_2)$ be two vague graphs. For any vertex $(m_1, m_2) \in V_1 \times V_2$ we define

$$
\begin{aligned}
(d_T)_{\mathbf{G}_1 \bullet \mathbf{G}_2}(m_1, m_2) &= \sum_{(m_1,m_2)(n_1,n_2) \in E_1 \times E_2} (T_{N_1} \bullet T_{N_2})((m_1, m_2)(n_1, n_2))\\
&= \sum_{m_1n_1 \in E_1,\, m_2 \neq n_2} T_{N_1}(m_1n_1)\\
&= (d_T)_{\mathbf{G}_1}(m_1),
\end{aligned}
$$

$$
\begin{aligned}
(d_F)_{\mathbf{G}_1 \bullet \mathbf{G}_2}(m_1, m_2) &= \sum_{(m_1,m_2)(n_1,n_2) \in E_1 \times E_2} (F_{N_1} \bullet F_{N_2})((m_1, m_2)(n_1, n_2))\\
&= \sum_{m_1n_1 \in E_1,\, m_2 \neq n_2} F_{N_1}(m_1n_1)\\
&= (d_F)_{\mathbf{G}_1}(m_1).
\end{aligned}
$$

Definition 3.36. Let $\mathbf{G}_1 = (M_1, N_1)$ and $\mathbf{G}_2 = (M_2, N_2)$ be two vague graphs. For any vertex $(m_1, m_2) \in V_1 \times V_2$ we define

$$
\begin{aligned}
(td_T)_{\mathbf{G}_1 \bullet \mathbf{G}_2}(m_1, m_2) &= \sum_{(m_1,m_2)(n_1,n_2) \in E_1 \times E_2} (T_{N_1} \bullet T_{N_2})((m_1, m_2)(n_1, n_2))\\
&+ (T_{M_1} \bullet T_{M_2})(m_1, m_2)\\
&= \sum_{m_1n_1 \in E_1,\, m_2 \neq n_2} T_{N_1}(m_1n_1) + \min\{T_{M_1}(m_1), T_{M_2}(m_2)\}\\
&= \sum_{m_1n_1 \in E_1,\, m_2 \neq n_2} T_{N_1}(m_1n_1) + T_{M_1}(m_1) + T_{M_2}(m_2)\\
&\quad - \max\{T_{M_1}(m_1), T_{M_2}(m_2)\}\\
&= (td_T)_{\mathbf{G}_1}(m_1) + T_{M_2}(m_2) - \max\{T_{M_1}(m_1), T_{M_2}(m_2)\},
\end{aligned}
$$

$$
\begin{aligned}
(td_F)_{\mathbf{G}_1 \bullet \mathbf{G}_2}(m_1, m_2) &= \sum_{(m_1,m_2)(n_1,n_2) \in E_1 \times E_2} (F_{N_1} \bullet F_{N_2})((m_1, m_2)(n_1, n_2))\\
&+ (F_{M_1} \bullet F_{M_2})(m_1, m_2)\\
&= \sum_{m_1n_1 \in E_1,\, m_2 \neq n_2} F_{N_1}(m_1n_1) + \max\{F_{M_1}(m_1), F_{M_2}(m_2)\}\\
&= \sum_{m_1n_1 \in E_1,\, m_2 \neq n_2} F_{N_1}(m_1n_1) + F_{M_1}(m_1) + F_{M_2}(m_2)\\
&\quad - \min\{F_{M_1}(m_1), F_{M_2}(m_2)\}\\
&= (td_F)_{\mathbf{G}_1}(m_1) + F_{M_2}(m_2) - \min\{F_{M_1}(m_1), F_{M_2}(m_2)\}.
\end{aligned}
$$

Example 3.37. In this example we find the degree and total degree of the vertex (b, e) in Example 3.33:

$$
\begin{aligned}
(d_T)_{\mathbf{G}_1 \bullet \mathbf{G}_2}(b, e) &= (d_T)_{\mathbf{G}_1}(b)\\
&= 0.1 + 0.1 = 0.2,\\
(d_F)_{\mathbf{G}_1 \bullet \mathbf{G}_2}(b, e) &= (d_F)_{\mathbf{G}_1}(b)\\
&= 0.8 + 0.8 = 1.6.
\end{aligned}
$$

Therefore,

$$
(d)_{\mathbf{G}_1 \bullet \mathbf{G}_2}(b, e) = (0.2, 1.6).
$$

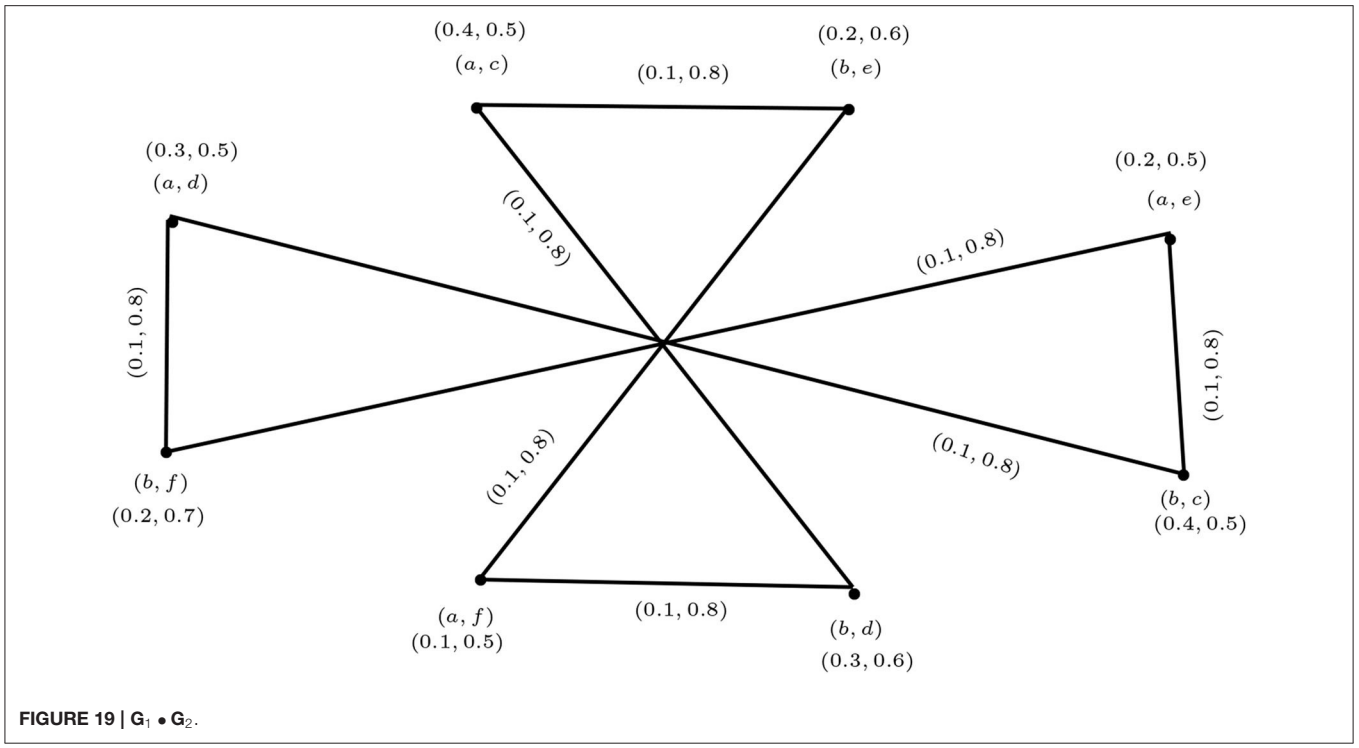

FIGURE 19 | $\mathbf{G}_1 \bullet \mathbf{G}_2$.

TABLE 1 | The vague relation $L(P \to S)$.

L	Heartburn	Coughing	Pain during swallowing	Weight loss
Shahbaz	(0.8, 0)	(0.6, 0.2)	(0.2, 0.3)	(0.1, 0.6)
Faisal	(0.3, 0.1)	(0.3, 0.5)	(0.3, 0.6)	(0.2, 0.6)
Shoaib	(0.5, 0.2)	(0.1, 0.2)	(0.1, 0.8)	(0.3, 0.4)
Danish	(0.4, 0.4)	(0, 0.3)	(0.5, 0.4)	(0.5, 0.3)

TABLE 2 | The vague relation $R(S \to D)$.

R	Cancer of kidney	Cancer of colon	Cancer of breast	Cancer of bladder
Heartburn	(0.1, 0.3)	(0.6, 0.1)	(0.2, 0.3)	(0.7, 0.1)
Coughing	(0.5, 0.4)	(0.3, 0.4)	(0.3, 0.5)	(0.2, 0.6)
Pain during swallowing	(0.3, 0.6)	(0.5, 0.2)	(0.6, 0.1)	(0.7, 0.1)
Weight loss	(0.2, 0.3)	(0.6, 0.3)	(0.5, 0.2)	(0.7, 0.1)

The total degree of (b, e) is given by

$$\begin{aligned}(td_T)_{\mathbf{G}_1\bullet\mathbf{G}_2}(b,e) &= (td_T)_{\mathbf{G}_1}(b) + T_{M_2}(e) - \max\{T_{M_1}(b), T_{M_2}(e)\}\\ &= (0.2+0.2)+0.2-\max(0.2,0.2)\\ &= 0.4,\end{aligned}$$

$$\begin{aligned}(td_F)_{\mathbf{G}_1\bullet\mathbf{G}_2}(b,e) &= (td_F)_{\mathbf{G}_1}(b) + F_{M_2}(e) - \min\{F_{M_1}(b), F_{M_2}(e)\}\\ &= (0.8+0.8)+0.6-\min(0.7,0.6)\\ &= 1.6.\end{aligned}$$

Therefore,

$$(td)_{\mathbf{G}_1\bullet\mathbf{G}_2}(b,e) = (0.4, 1.6).$$

Similarly, we can find the degree and total degree of all vertices in $\mathbf{G}_1 \bullet \mathbf{G}_2$.

4. APPLICATION OF VAGUE SETS TO MEDICAL DIAGNOSIS

Following the approach outlined by De et al. [18], we will apply vague sets to medical diagnosis by using a max-min-max composition in terms of vague relations. First, we use vague sets to define the disease symptoms. Then, we describe medical knowledge in terms of vague relations. Finally, we determine a diagnosis on the basis of vague relations. Consider four patients named Shahbaz, Shoaib, Faisal, and Danish, and define the set of patients $P = \{\text{Shahbaz, Shoaib, Faisal, Danish}\}$. Let the set of symptoms under consideration be $S = \{\text{heartburn, coughing, pain during swallowing, weight loss}\}$. A vague relation L is available from set P to set S, and this is summarized in **Table 1**.

Cancer is a group of dangerous and prevalent diseases, and represents one of humankind's greatest medical challenges. Many people are diagnosed with late-stage cancer that is difficult or

TABLE 3 | The composition $M(P \rightarrow D)$ of vague relations L and R.

M	Cancer of kidney	Cancer of colon	Cancer of breast	Cancer of bladder
Shahbaz	(0.5, 0.3)	(0.6, 0.1)	(0.2, 0.3)	(0.7, 0.1)
Faisal	(0.3, 0.3)	(0.3, 0.1)	(0.3, 0.3)	(0.3, 0.1)
Shoaib	(0.2, 0.3)	(0.5, 0.2)	(0.3, 0.3)	(0.5, 0.2)
Danish	(0.5, 0.3)	(0.5, 0.3)	(0.5, 0.3)	(0.5, 0.3)

TABLE 4 | S_R, the best version of R determined by the formula $S_R = T_R - F_R\pi_R$.

S_R	Cancer of kidney	Cancer of colon	Cancer of breast	Cancer of bladder
Shahbaz	0.44	0.57	0.05	0.68
Faisal	0.18	0.24	0.18	0.24
Shoaib	0.05	0.44	0.18	0.44
Danish	0.44	0.44	0.44	0.44

impossible to treat because of a lack of awareness of the disease symptoms. Mathematical models involving vague sets can be used to determine the most likely diagnosis given a set of symptoms that a patient presents with.

There are many different types of cancers; here we focus on a few of the more life-threatening kinds: (1) kidney cancer, (2) colon cancer, (3) breast cancer, and (4) bladder cancer. We define the set of diagnoses to be $D = \{$cancer of kidney, cancer of colon, cancer of breast, cancer of bladder$\}$. The vague relation $R(S \rightarrow D)$ from the set of symptoms to the set of diagnoses is given in **Table 2**. The composition $M(P \rightarrow D)$ of the vague relations L and R is shown in **Table 3**; it gives the diagnosis for each patient via the formulas

$$T_M(p_i, d_k) = \bigvee_{s \in S} [T_L(p_i, s) \wedge T_R(s, d_k)],$$
$$F_M(p_i, d_k) = \bigwedge_{s \in S} [F_L(p_i, s) \vee F_R(s, d_k)],$$

where p_i denotes the patients, d_k denotes the different diagnoses, $\wedge = \min$, and $\vee = \max$.

Shown in **Table 4** is S_R, the best version of diagnosis for this set of patients, which is determined by the formula $S_R = T_R - F_R\pi_R$. It is very important because the max-min-max rule alone fails to provide exact information.

5. CONCLUSION

Compared with fuzzy models, vague models offer greater compatibility and flexibility. A vague graph is a type of extension of a fuzzy graph, and is used widely in the field of computer science. We have defined four new operations of a vague graph, called the maximal product, rejection, symmetric difference, and residue product. We have discussed their properties and provided examples on finding the degree of a vertex and the total degree of vertices of graphs that meet specific conditions. We have formulated and proved theorems for these graphs by using the concept of degree of a vertex and total degree of a vertex of a graph. Furthermore, we have presented an application of vague sets to the medical diagnosis of four types of cancer. In future work we will explore further properties relating to vague graphs and bipolar vague graphs.

DATA AVAILABILITY STATEMENT

All datasets generated for this study are included in the article/supplementary material.

AUTHOR CONTRIBUTIONS

All authors listed have made a substantial, direct and intellectual contribution to the work, and approved it for publication.

FUNDING

This work was supported by the National Key R&D Program of China (grant no. 2019YFA0706402), the Natural Science Foundation of Guangdong Province (grant no. 2018A0303130115), and the Guangzhou Academician and Expert Workstation (no. 20200115-9).

REFERENCES

1. Zadeh L. Fuzzy sets. *Inform Control*. (1965) 8:338–53.
2. Rosenfeld A. Fuzzy graphs. In: Zadeh LA, Fu KS, Shimura M, editors. *Fuzzy Sets and Their Application*. New York, NY: Academic Press (2006). p. 77–95.
3. Bhattacharya P. Some remarks on fuzzy graphs. *Pattern Recogn Lett*. (1987) 6:297–302.
4. Bhattacharya P, Suraweera F. An Algorithm to compute the max-min powers and a property of fuzzy graphs. *Pattern Recogn Lett*. (1991) 12:413–20.
5. Nagoor Gani A, Latha SR. On irregular fuzzy graphs. *Appl Math Sci*. (2012) 6:517–23.
6. Nagoor Gani A, Basheer Ahamed M. Order and size in fuzzy graphs. *Bull Pure Appl Sci*. (2003) 22:145–8.
7. Gau WL, Buehrer DJ. Vague sets. *IEEE Trans Syst Man Cybernet*. (1993) 23:610–4.
8. Ramakrishna N. Vague graphs. *Int J Comput Cogn*. (2009) 7:51–8.
9. Borzooei RA, Rashmanlou H. New concepts of vague graphs. *Int J Mach Learn Cybernet*. (2015) 8:1081–92. doi: 10.1007/s13042-015-0475-x
10. Rashmanlou H, Borzooei RA. Product vague graphs and its applications. *J Intell Fuzzy Syst*. (2016) 30:371–82. doi: 10.3233/IFS-151762
11. Boorzooei RA, Rashmanlou H, Samanta S, Pal M. Regularity of vague graphs. *J Intell Fuzzy Syst*. (2016) 30:3681–9. doi: 10.3233/IFS-162114
12. Borzooei RA, Rashmanlou H, Samanta S, Pal M. New concepts of vague competition graphs. *J Intell Fuzzy Syst*. (2016) 31:69–75. doi: 10.3233/IFS-162121
13. Kumar K, Lavanya S, Broumi S, Rashmanlou H. New concepts of coloring in vague graphs with application. *J Intell Fuzzy Syst*. (2017) 33:1715–21. doi: 10.3233/JIFS-17489
14. Atanassov K. Intuitionistic fuzzy sets. *Fuzzy Sets Syst*. (1986) 20:87–96.

15. Parvathi R, Karunambigai MG. Intuitionistic fuzzy graphs, computational intelligence, theory and applications. In: *International Conference in Germany*. Berlin (2006). p. 18–20.
16. Devi M, Ameenal Bibi K, Rashmanlou H. New concepts in intuitionistic fuzzy labeling graphs. *Int J Adv Intell Paradigms*. (2020).
17. Berge C. *Graphs and Hyper Graphs*. Amsterdam: North-Holland Publishing Company (1973).
18. De SK, Biswas R, Roy AR. An application of intuitionistic fuzzy sets in medical diagnosis. *Fuzzy Sets Syst*. (2001) 117:209–13. doi: 10.1016/S0165-0114(98)00235-8

Conflict of Interest: The authors declare that the research was conducted in the absence of any commercial or financial relationships that could be construed as a potential conflict of interest.

frontiers in Physics

BRIEF RESEARCH REPORT
published: 24 November 2020
doi: 10.3389/fphy.2020.580554

The Maximum Principle for Variable-Order Fractional Diffusion Equations and the Estimates of Higher Variable-Order Fractional Derivatives

Guangming Xue[1,2], *Funing Lin*[1,2] *and Guangwang Su*[1,2]*

[1] College of Information and Statistics, Guangxi University of Finance and Economics, Nanning, China, [2] Guangxi Key Laboratory Cultivation Base of Cross-Border E-Commerce Intelligent Information Processing, Nanning, China

In this paper, the maximum principle of variable-order fractional diffusion equations and the estimates of fractional derivatives with higher variable order are investigated. Firstly, we deduce the fractional derivative of a function of higher variable order at an arbitrary point. We also give an estimate of the error. Some important inequalities for fractional derivatives of variable order at arbitrary points and extreme points are presented. Then, the maximum principles of Riesz-Caputo fractional differential equations in terms of the multi-term space-time variable order are proved. Finally, under the initial-boundary value conditions, it is verified via the proposed principle that the solutions are unique, and their continuous dependance holds.

Keywords: maximum principle, fractional diffusion equation, fractional derivative with variable order, extreme point, boundary value problem

OPEN ACCESS

Edited by:
Jia-Bao Liu, Anhui Jianzhu University, China

Reviewed by:
Dongyan Li, Xi'an Polytechnic University, China
Lin Wang, Anhui University of Science and Technology, China

***Correspondence:**
Guangwang Su
617326891@qq.com

Specialty section:
This article was submitted to Mathematical and Statistical Physics, a section of the journal Frontiers in Physics

Received: *06 July 2020*
Accepted: *12 August 2020*
Published: *24 November 2020*

Citation:
Xue G, Lin F and Su G (2020) The Maximum Principle for Variable-Order Fractional Diffusion Equations and the Estimates of Higher Variable-Order Fractional Derivatives. Front. Phys. 8:580554. doi: 10.3389/fphy.2020.580554

1. INTRODUCTION

Fractional calculus Podlubny [1]; as a natural extension of traditional integer calculus, has become a classical and essential branch of mathematics through a long historical development. Recently Al-Refai and Baleanu [2], obtained the estimates of fractional derivatives with higher order for extreme points, providing an approach to the establishment of the maximum principles, as well as the results of the existence and uniqueness of solutions for the fractional differential equations (FDEs). As a kind of well-known technique for handling FDEs, the maximum principle may facilitate to acquire the key access to the solutions in the absence of any prior detailed knowledge about the solutions Protter and Weinberger [3]. Liu et al. [4] derived a maximum principle for fractional differential equations (VOFDEs, for short) with multi-term time variable order $0<\alpha(\zeta,\tau)\le 1$ and space variable orders $0<\gamma(\zeta,\tau)\le 1$ and $1<\beta(\zeta,\tau)\le 2$ in the sense of Riesz-Caputo, and showed the uniqueness of solutions as well as continuous of VOFDEs via the dependance. Ye et al. [5] investigated the solutions maximum principle. More researches in this area can be consulted in Luchko [6–8]; Li et al. [9]; Al-Refai and Luchko [10]; Yang et al. [11]; Coronelescamilla et al. [12]; Hajipour et al. [13].

However, the restriction for most of the aforesaid fractional diffusion equations is that their orders are constant. Such a restriction was relaxed by Samko and Ross [14] via a proposed variable-order (VO) operator to describe the diffusion process. In fact, VOFDEs are widely used as powerful tools in many research topics, such as visco-elasticity Coimbra [15]; oscillation Ingman and Suzdalnitsky [16]; anomalous diffusion Sun et al. [17]; etc. For more applications of fractional differential equations, please refer to Cooper and Cowan [18]; Liu [19]; Sun et al. [20]; Liu and Li [21]; Yang [22], etc.

The contributions of this paper can be summarized as follows:

(1) The higher derivative of fractional function with variable order is given. On the basis of it, three useful theorems are given, which provide theoretical guarantee for the applications.
(2) The maximum principle for one-dimensional multi-term space-time higher VOFDEs is given.
(3) Based on the proposed method, a concrete example is given for the practical applications.

The paper is structured as the following. In **Section 2**, we recall some fundamental definitions that will be used in this paper. In **Section 3**, we derive some equalities and inequalities of the higher VOFDEs at arbitrary points and extreme points. We also give an estimate of the error. In **Section 4**, by virtue of these important inequalities, we establish the maximum principle for Riesz-Caputo FDEs with multi-term time variable order and space variable orders. In **Section 5**, based on the given principle, the uniqueness of solutions with their continuous dependance in the present of initial-boundary value conditions are strictly proved.

Notations: Throughout this paper, ζ denotes the space variable and τ denotes the time variable. $\Omega_T := (0, L) \times (0, T]$, $\overline{\Omega}_T$ and $\partial\Omega_T$ are the closure and the boundary of Ω_T, respectively. $\alpha(\cdot,\cdot)$, $\gamma(\cdot,\cdot)$ and $\beta(\cdot,\cdot)$ represent binary VO functions. It is supposed that the VO functions $\alpha, \alpha_1, \ldots, \alpha_n$, β and γ satisfy that

$$1 < \alpha_n(\zeta,\tau) < \cdots < \alpha_1(\zeta,\tau) < \alpha(\zeta,\tau) \le 2, \quad (\zeta,\tau) \in \overline{\Omega}_T,$$

where $(\zeta,\tau) \in \overline{\Omega}_T$, $\beta(\zeta,\tau) \in (1,2]$ and $\gamma(\zeta,\tau) \in (0,1]$. Also, the functions $e(\zeta,\tau)$, $m(\zeta,\tau)$, $n(\zeta,\tau)$ and $a_i(\zeta,\tau), i = 1,2,\ldots,n$ are supposed to be all continuous on $\overline{\Omega}_T$ with $m(\zeta,\tau) > 0$, $n(\zeta,\tau) \ge 0$ and $e(\zeta,\tau) \le 0$.

2. PRELIMINARIES

Throughout this paper, $\mathbb{R}_+$ denotes the set of all positive real numbers. Let $C^n[0,T] = \{f : f^{(n)} \in C[0,T]\}$ be a Banach space with the norm $f_{C^n} = \max_{t\in[0,T]}[|f(t)|, |f'(t)|, \ldots, |f^{(n)}(t)|]$. For more details about the relevant concepts and results, please see Podlubny [1]; Liu et al. [4]; Kilbas et al. [23].

Definition 1. Let $f \in C[0,T]$ and $\alpha : (0,L) \times (0,T) \to \mathbb{R}_+$ be a VO function. The Riemann-Liouville fractional integrals of left-side VO and right-side VO are defined as

$$I_{0,\tau}^{\alpha(\zeta,\tau)} f(\tau) = \begin{cases} \dfrac{1}{\Gamma[\alpha(\zeta,\tau)]} \displaystyle\int_0^\tau (\tau - \vartheta)^{\alpha(\zeta,\tau)-1} f(\vartheta)\, d\vartheta, & \alpha(\zeta,\tau) > 0, \\ f(\tau), & \alpha(\zeta,\tau) = 0, \end{cases}$$

$$I_{\tau,T}^{\alpha(\zeta,\tau)} f(\tau) = \begin{cases} \dfrac{(-1)^{[\alpha(\zeta,\tau)]}}{\Gamma[\alpha(\zeta,\tau)]} \displaystyle\int_0^\tau (\tau - \vartheta)^{\alpha(\zeta,\tau)-1} f(\vartheta)\, d\vartheta, & \alpha(\zeta,\tau) > 0, \\ f(\tau), & \alpha(\zeta,\tau) = 0, \end{cases}$$

respectively, where $\Gamma[\alpha(\zeta,\tau)] = \int_0^\infty \theta^{\alpha(\zeta,\tau)-1} e^{-\theta} d\theta$ and $[\alpha(\zeta,\tau)]$ is the smallest integer not less than $\alpha(\zeta,\tau)$.

Definition 2. Let $f \in C^n[0,T]$ and $\alpha : [0,L] \times [0,T] \to \mathbb{R}_+$ be a VO function. The Caputo fractional derivatives of left-side VO and right-side VO are defined respectively as

$$\begin{aligned} {}^C D_{0,\tau}^{\alpha(\zeta,\tau)} f(\tau) &= I_{0,\tau}^{n-\alpha(\zeta,\tau)} \frac{d^n}{d\tau^n} f(\tau) \\ &= \begin{cases} \dfrac{1}{\Gamma[n-\alpha(\zeta,\tau)]} \displaystyle\int_0^\tau (\tau-\vartheta)^{n-\alpha(\zeta,\tau)-1} f^{(n)}(\vartheta) d\vartheta, & n-1 < \alpha(\zeta,\tau) < n, \\ f^{(n)}(\tau), & \alpha(\zeta,\tau) = n, \end{cases} \\ {}^C D_{\tau,T}^{\alpha(\zeta,\tau)} f(\tau) &= I_{\tau,T}^{n-\alpha(\zeta,\tau)} \frac{d^n}{d\tau^n} f(\tau) \\ &= \begin{cases} \dfrac{(-1)^n}{\Gamma[n-\alpha(\zeta,\tau)]} \displaystyle\int_0^\tau (\tau-\vartheta)^{n-\alpha(\zeta,\tau)-1} f^{(n)}(\vartheta) d\vartheta, & n-1 < \alpha(\zeta,\tau) < n, \\ f^{(n)}(\tau), & \alpha(\zeta,\tau) = n. \end{cases} \end{aligned}$$

Definition 3. The VO Riesz-Caputo fractional operator ${}^C R_\zeta^{\beta(\zeta,\tau)}$ of VO $\beta(\zeta,\tau)$ with $n-1 < \beta(\zeta,\tau) \le n$ and $0 \le \zeta \le L$ is defined as

$${}^C R_\zeta^{\beta(\zeta,\tau)} w(\zeta,\tau) := -\rho_{\beta(\zeta,\tau)} \left({}^C D_{0,\zeta}^{\beta(\zeta,\tau)} + {}^C D_{\zeta,L}^{\beta(\zeta,\tau)} \right) w(\zeta,\tau),$$

where $\Gamma[\alpha(\zeta,\tau)] = \int_0^\infty \theta^{\alpha(\zeta,\tau)-1} e^{-\theta} d\theta$, $\rho_{\beta(\zeta,\tau)} = 2^{-1}\cos^{-1}[\beta(\zeta,\tau)\pi/2]$ is the coefficient with $\beta(\zeta,\tau) \ne 1, 2, 3, \ldots$, and

$${}^C D_{0,\zeta}^{\beta(\zeta,\tau)} w(\zeta,\tau) = \frac{1}{\Gamma(n-\beta(\zeta,\tau))} \int_0^\zeta (\zeta-\vartheta)^{n-\beta(\zeta,\tau)-1} \frac{\partial^n w(\vartheta,\tau)}{\partial\vartheta^n} d\vartheta,$$

$${}^C D_{\zeta,L}^{\beta(\zeta,\tau)} w(\zeta,\tau) = \frac{(-1)^n}{\Gamma(n-\beta(\zeta,\tau))} \int_\zeta^L (\vartheta-\zeta)^{n-\beta(\zeta,\tau)-1} \frac{\partial^n w(\vartheta,\tau)}{\partial\vartheta^n} d\vartheta.$$

Moreover, if $\beta(\zeta,\tau) = n$, ${}^C R_\zeta^{\beta(\zeta,\tau)} w(\zeta,\tau) = [\partial^n w(\zeta,\tau)/\partial\zeta^n]$.

In this paper, we are interested in the following VOFDEs:

$$\begin{aligned} P_{\alpha,\alpha_1,\ldots,\alpha_n}({}_0^C D_\tau) w(\zeta,\tau) = -\Big[& m(\zeta,\tau) {}^C R_\zeta^{\beta(\zeta,\tau)} w(\zeta,\tau) \\ & + n(\zeta,\tau) {}^C R_\zeta^{\gamma(\zeta,\tau)} w(\zeta,\tau) \\ & + e(\zeta,\tau) w(\zeta,\tau) \Big] \\ & + F(\zeta,\tau,w), (\zeta,\tau) \in \Omega_T, \end{aligned} \tag{1}$$

where $P_{\alpha,\alpha_1,\ldots,\alpha_n}({}_0^C D_\tau)$ denotes the multi-term time VO Caputo fractional derivative operator, i.e.,

$$\begin{aligned} P_{\alpha,\alpha_1,\ldots,\alpha_n}({}_0^C D_t) w(\zeta,\tau) = {} & {}_0^C D_t^{\alpha(\zeta,\tau)} w(\zeta,\tau) \\ & + \sum_{i=1}^n a_i(\zeta,\tau) {}_0^C D_t^{\alpha_i(\zeta,\tau)} w(\zeta,\tau). \end{aligned} \tag{2}$$

3. THE VARABLE-ORDER FRACTIONAL DERIVTIVES AT ARBITRARY POINTS AND EXTREME POINTS

In this section, we are in position to give some basic results.

Theorem 1. Let $f \in C^n[0,T]$. and $\eta_n(\cdot,\cdot)$ be a VO function. If η_n satisfies

$$n-1 < \eta_n(\zeta,\tau) < n, \quad \forall (\zeta,\tau) \in \overline{\Omega}_T,$$

then for any arbitrary point $\tau_0 \in (0, T)$, the following equation holds

$$
{}^{C}D^{\eta_n(\zeta,\tau_0)}_{0,\tau_0} f(\tau_0) = -\sum_{k=0}^{n-1} \frac{1}{\Gamma[k+1-\eta_n(\zeta,\tau_0)]} \tau_0^{k-\eta_n(\zeta,\tau_0)} h^{(k)}_{n-1}(0) + \frac{1}{\Gamma[-\eta_n(\zeta,\tau_0)]} \int_0^{\tau_0} (\tau_0 - s)^{-\eta_n(\zeta,\tau_0)-1} h_{n-1}(s)ds,
$$

where $h_{n-1}(\tau) = f(\tau) - \sum_{k=0}^{n-1} [f^{(k)}(\tau_0)(\tau - \tau_0)^k/k!]$.

Proof. We shall prove this by induction argument. If $0 < \eta_1(\zeta, \tau_0) < 1$, the result has been obtained in Liu et al. [4]. Assume that this is true for $n-1 < \eta_n(\zeta, \tau_0) < n$. Now we check that it still holds whenever $n < \eta_{n+1}(\zeta, \tau_0) < n+1$.

Let $\eta_{n+1}(\zeta, \tau_0) = \delta(\zeta, \tau_0) + n$, where $0 < \delta(\zeta, \tau_0) < 1$. Then $n - 1 < n - 1 + \delta(\zeta, \tau_0) < n$. Define $\eta_n(\zeta, \tau_0) = n - 1 + \delta(\zeta, \tau_0)$. Then. $n - 1 < \eta_n(\zeta, \tau_0) < n$.

By the induction hypothesis, one obtains

$$
{}^{C}D^{n-1+\delta(\zeta,\tau_0)}_{0,\tau_0} f(\tau_0) = -\sum_{k=0}^{n-1} \frac{1}{\Gamma[k+2-n-\delta(\zeta,\tau_0)]} \tau_0^{k+1-n-\delta(\zeta,\tau_0)} h^{(k)}_{n-1}(0) + \frac{1}{\Gamma[1-n-\delta(\zeta,\tau_0)]} \int_0^{\tau_0} (\tau_0 - s)^{-n-\delta(\zeta,\tau_0)} h_{n-1}(s)ds.
$$

Substituting $f'(\tau)$ for $f(\tau)$ in the preceding equation, one has

$$
{}^{C}D^{n-1+\delta(\zeta,\tau_0)}_{0,\tau_0} f'(\tau_0) = -\sum_{k=0}^{n-1} \frac{1}{\Gamma[k+2-n-\delta(\zeta,\tau_0)]} \tau_0^{k+1-n-\delta(\zeta,\tau_0)} z^{(k)}_{n-1}(0) + \frac{1}{\Gamma[1-n-\delta(\zeta,\tau_0)]} \int_0^{\tau_0} (\tau_0 - s)^{-n-\delta(\zeta,\tau_0)} z_{n-1}(s)ds,
$$

where $z_{n-1}(\tau) = f'(\tau) - \sum_{k=0}^{n-1} [f^{(k+1)}(\tau_0)(\tau - \tau_0)^k/k!]$.

Obviously, we have:

(1) $h_n'(\tau) = z_{n-1}(\tau)$,
(2) $h_n(\tau_0) = h_n'(\tau_0) = h_n''(\tau_0) = \cdots = h_n^{(n)}(\tau_0) = 0$.

Hence,

$$
h_n(\tau) = (\tau_0 - \tau)^{n+1} \mu_n(\tau),
$$

where $\mu_n(\tau) \in C[0, T]$ and $h_n^{(k+1)}(0) = z_{n-1}^{(k)}(0)$.

Integrating by parts, we have

$$
\int_0^{\tau_0} (\tau_0 - s)^{-n-\delta(\zeta,\tau_0)} z_{n-1}(s)ds = (\tau_0 - s)^{-n-\delta(\zeta,\tau_0)} h_n(s)|_0^{\tau_0} - (n + \delta(\zeta, \tau_0)) \times \int_0^{\tau_0} (\tau_0 - s)^{-1-n-\delta(\zeta,\tau_0)} h_n(s)ds.
$$

So

$$
\lim_{s \to \tau_0} \frac{h_n(s)}{(\tau_0 - s)^{n+\delta(\zeta,\tau_0)}} = \lim_{s \to \tau_0} (\tau_0 - s)^{1-\delta(\zeta,\tau_0)} \mu_n(\tau) = 0, \quad \forall \zeta \in [0, L],
$$

and

$$
\begin{aligned}
&\frac{1}{\Gamma(1-n-\delta(\zeta,\tau_0))} \int_0^{\tau_0} (\tau_0 - s)^{-n-\delta(\zeta,\tau_0)} z_{n-1}(s)ds \\
&= -\frac{\tau_0^{-n-\delta(\zeta,\tau_0)} h_n(0)}{\Gamma(1-n-\delta(\zeta,\tau_0))} - \frac{n+\delta(\zeta,\tau_0)}{\Gamma(1-n-\delta(\zeta,\tau_0))} \int_0^{\tau_0} (\tau_0 - s)^{-n-\delta(\zeta,\tau_0)-1} h_n(s)ds \\
&= -\frac{\tau_0^{-n-\delta(\zeta,\tau_0)} h_n(0)}{\Gamma(1-n-\delta(\zeta,\tau_0))} + \frac{1}{\Gamma(-n-\delta(\zeta,\tau_0))} \int_0^{\tau_0} (\tau_0 - s)^{-n-\delta(\zeta,\tau_0)-1} h_n(s)ds.
\end{aligned}
$$

Thus,

$$
\begin{aligned}
{}^{C}D^{n-1+\delta(\zeta,\tau_0)}_{0,\tau_0} f'(\tau_0) &= -\sum_{k=0}^{n-1} \frac{1}{\Gamma(k+2-n-\delta(\zeta,\tau_0))} \tau_0^{k+1-n-\delta(\zeta,\tau_0)} h_n^{(k+1)}(0) - \frac{\tau_0^{-n-\delta(\zeta,\tau_0)} h_n(0)}{\Gamma(1-n-\delta(\zeta,\tau_0))} \\
&\quad + \frac{1}{\Gamma(-n-\delta(\zeta,\tau_0))} \int_0^{\tau_0} (\tau_0 - s)^{-n-\delta(\zeta,\tau_0)-1} h_n(s)ds \\
&= -\sum_{k=1}^{n} \frac{1}{\Gamma(k+1-n-\delta(\zeta,\tau_0))} \tau_0^{k-n-\delta(\zeta,\tau_0)} h_n^{(k)}(0) - \frac{\tau_0^{-n-\delta(\zeta,\tau_0)} h_n(0)}{\Gamma(1-n-\delta(\zeta,\tau_0))} \\
&\quad + \frac{1}{\Gamma(-n-\delta(\zeta,\tau_0))} \int_0^{\tau_0} (\tau_0 - s)^{-n-\delta(\zeta,\tau_0)-1} h_n(s)ds \\
&= -\sum_{k=0}^{n} \frac{1}{\Gamma(k+1-n-\delta(\zeta,\tau_0))} \tau_0^{k-n-\delta(\zeta,\tau_0)} h_n^{(k)}(0) \\
&\quad + \frac{1}{\Gamma(-n-\delta(\zeta,\tau_0))} \int_0^{\tau_0} (\tau_0 - s)^{-n-\delta(\zeta,\tau_0)-1} h_n(s)ds \\
&= -\sum_{k=0}^{n-1} \frac{1}{\Gamma(k+1-\eta_{n+1}(\zeta,\tau_0))} \tau_0^{k-\eta_{n+1}(\zeta,\tau_0)} h_n^{(k)}(0) \\
&\quad + \frac{1}{\Gamma(-\eta_{n+1}(\zeta,\tau_0))} \int_0^{\tau_0} (\tau_0 - s)^{-\eta_{n+1}(\zeta,\tau_0)-1} h_n(s)ds.
\end{aligned}
$$

Hence ${}^{C}D^{n-1+\delta(\zeta,\tau_0)}_{0,\tau_0} f'(\tau_0) = {}^{C}D^{n+\delta(\zeta,\tau_0)}_{0,\tau_0} f(\tau_0) = {}^{C}D^{\eta_{n+1}(\zeta,\tau_0)}_{0,\tau_0} f(\tau_0)$. This complete the proof.

Remark 1. If $\eta_n(\zeta, \tau) \equiv \overline{\alpha}$ in $\overline{\Omega}_T$ $(n-1 < \overline{\alpha} \leq n)$ and τ_0 is an extreme point, then Theorem 1 coincides with Al-Refai and Baleanu [2]'s result. Thus, our result generalizes AL-Refai and Baleanu's original idea.

Theorem 2.

Let $f \in C^n[0, T]$. Suppose that the VO function $\eta_n(\zeta, \tau)$ satisfies

$$n-1<\eta_n(\zeta,\tau)<n,\quad \forall(\zeta,\tau)\in\overline{\Omega}_T.$$

For any arbitrary point $\tau_0\in(0,T)$, one gets

(1) For any nonnegative $f^{(n)}(\tau)$ with $\tau\in[0,\tau_0]$, then

$${}^{C}D^{\eta_n(\zeta,\tau_0)}_{0,\tau_0}f(\tau_0)\geq-\sum_{k=0}^{n-1}\frac{1}{\Gamma\left(k+1-\eta_n(\zeta,\tau_0)\right)}\tau_0^{k-\eta_n(\zeta,\tau_0)}h^{(k)}_{n-1}(0)$$

(2) For any non-positive $f^{(n)}(\tau)$ with $\tau\in[0,\tau_0]$, then

$${}^{C}D^{\eta_n(\zeta,\tau_0)}_{0,\tau_0}f(\tau_0)\leq-\sum_{k=0}^{n-1}\frac{1}{\Gamma\left(k+1-\eta_n(\zeta,\tau_0)\right)}\tau_0^{k-\eta_n(\zeta,\tau_0)}h^{(k)}_{n-1}(0)$$

where $h_{n-1}(\tau)=f(\tau)-\sum_{k=0}^{n-1}\left(f^{(k)}(\tau_0)(\tau-\tau_0)^k/k!\right)$.

Proof. Employing the Taylor series expansion, we know that there is some τ_0 with $\tau<\vartheta_n(\tau)<\tau_0$ such that

$$h_{n-1}(\tau)=f(\tau)-\sum_{k=0}^{n-1}\frac{f^{(k)}(\tau_0)(\tau-\tau_0)^k}{k!}=\frac{f^{(n)}(\vartheta_n(\tau))(\tau-\tau_0)^n}{n!}$$

So, we have

$$\begin{aligned}m_n&=\frac{1}{\Gamma\left(-\eta_n(\zeta,\tau_0)\right)}\int_0^{\tau_0}(\tau_0-s)^{-\eta_n(\zeta,\tau_0)-1}h_{n-1}(s)ds.\\&=\frac{1}{\Gamma\left(-\eta_n(\zeta,\tau_0)\right)}\int_0^{\tau_0}(\tau_0-s)^{-\eta_n(\zeta,\tau_0)-1}\frac{f^{(n)}(\vartheta_n(\tau))(\tau-\tau_0)^n}{n!}ds.\\&=\frac{(-1)^n}{n!\Gamma\left(-\eta_n(\zeta,\tau_0)\right)}\int_0^{\tau_0}(\tau_0-s)^{n-\eta_n(\zeta,\tau_0)-1}f^{(n)}(\vartheta_n(s))ds.\end{aligned}\tag{3}$$

Note that $n-1<\eta_n(\zeta,\tau_0)<n$, and

$$\Gamma\left(-\eta_n(\zeta,\tau_0)\right)\begin{cases}>0, & \text{if } n \text{ is even},\\ <0, & \text{otherwise.}\end{cases}$$

Therefore, we get $\left((-1)^n/\Gamma(-\eta_n(\zeta,\tau_0))\right)>0$, and

$$m_n=\begin{cases}\geq0, & \text{if } f^{(n)}(\tau)\geq0,\\ <0, & \text{otherwise.}\end{cases}$$

Theorem 3. Let $f\in C^n[0,T]$, and $\left|f^{(n)}(\tau)\right|\leq M$, for all $\tau\in[0,T]$. If the VO function $\eta_n(\zeta,\tau)$ satisfies

$$n-1<\eta_n(\zeta,\tau)<n,\quad \forall(\zeta,\tau)\in\overline{\Omega}_T,$$

then for any arbitrary point $\tau_0\in(0,T)$, the following equation holds:

$${}^{C}D^{\eta_n(\zeta,\tau_0)}_{0,\tau_0}f(\tau_0)=-\sum_{k=0}^{n-1}\frac{1}{\Gamma\left(k+1-\eta_n(\zeta,\tau_0)\right)}\tau_0^{k-\eta_n(\zeta,\tau_0)}h^{(k)}_{n-1}(0)+m_n,$$

where $h_{n-1}(\tau)=f(\tau)-\sum_{k=0}^{n-1}\left(f^{(k)}(\tau_0)(\tau-\tau_0)^k/k!\right)$, and

$$|m_n|\leq\frac{Mt_0^{n-\eta_n(\zeta,\tau_0)}}{n!\left(n-\eta_n(\zeta,\tau_0)\right)\left|\Gamma\left(-\eta_n(\zeta,\tau_0)\right)\right|}.$$

Proof. According to **Eq. 3**, one has

$$m_n=\frac{(-1)^n}{n!\Gamma\left(-\eta_n(\zeta,\tau_0)\right)}\int_0^{\tau_0}(\tau_0-s)^{n-\eta_n(\zeta,\tau_0)-1}f^{(n)}(\vartheta_n(s))ds.$$

As a result,

$$\begin{aligned}|m_n|&\leq\frac{M}{n!\left|\Gamma\left(-\eta_n(\zeta,\tau_0)\right)\right|}\int_0^{\tau_0}(\tau_0-s)^{n-\eta_n(\zeta,\tau_0)-1}ds\\&=\frac{Mt_0^{n-\eta_n(\zeta,\tau_0)}}{n!\left(n-\eta_n(\zeta,\tau_0)\right)\left|\Gamma\left(-\eta_n(\zeta,\tau_0)\right)\right|}.\end{aligned}$$

Theorem 4. Given a VO function $\alpha:[0,L]\times[0,T]\to\mathbb{R}_+$ with $1<\alpha(\zeta,\tau)<2$ for all $(\zeta,\tau)\in\overline{\Omega}_T$. If $f\in C^2[0,T]$ attains its maximum at $\tau_0\in(0,T)$, then it holds that

$${}^{C}D^{\alpha(\zeta,\tau_0)}_{0,\tau_0}f(\tau_0)\leq\frac{\alpha(\zeta,\tau_0)-1}{\Gamma(2-\alpha(\zeta,\tau_0))}\tau_0^{-\alpha(\zeta,\tau_0)}\left[f(0)-f(\tau_0)\right]-\frac{\tau_0^{1-\alpha(\zeta,\tau_0)}}{\Gamma(2-\alpha(\zeta,\tau_0))}f'(0).$$

Moreover, if $f'(0)\geq0$, then ${}^{C}_{0}D^{\alpha(\zeta,\tau_0)}_{0,\tau_0}f(\tau_0)\leq0,\forall\zeta\in[0,L]$.

Proof. Let $\phi(\tau):=f(\tau)-f(\tau_0)\in C^2[0,T]$. Obviously, we have

(1) $\phi(\tau)\leq0,\tau\in[0,T]$;
(2) $\phi(\tau_0)=\phi'(\tau_0)=0$ and $\phi''(\tau_0)\leq0$;
(3) $\phi(\tau)=(\tau_0-\tau)^2\cdot\nu(\tau)$ where $\nu\in C[0,T]$ and $\nu(\tau)\leq0$, $\forall\tau\in[0,T]$.

It can be easily verified that

$${}^{C}D^{\alpha(\zeta,\tau)}_{0,\tau}\phi(\tau)={}^{C}D^{\alpha(\zeta,\tau)}_{0,\tau}f(\tau),\forall(\zeta,\tau)\in\overline{\Omega}$$

By Theorem 1, we obtain

$$\begin{aligned}{}^{C}D^{\alpha(\zeta,\tau_0)}_{0,\tau_0}\phi(\tau_0)&=-\frac{\tau_0^{1-\alpha(\zeta,\tau_0)}}{\Gamma(2-\alpha(\zeta,\tau_0))}\phi'(0)\\&+\frac{\alpha(\zeta,\tau_0)-1}{\Gamma(2-\alpha(\zeta,\tau_0))}\tau_0^{-\alpha(\zeta,\tau_0)}\phi(0)\\&+\frac{(\alpha(\zeta,\tau_0)-1)\cdot\alpha(\zeta,\tau_0)}{\Gamma(2-\alpha(\zeta,\tau_0))}\int_0^{\tau_0}(\tau_0-s)^{-\alpha(\zeta,\tau_0)-1}\phi(s)ds\end{aligned}$$

Since for all $\tau\in[0,\tau_0],\phi(\tau)\leq0$ and $\phi(\tau)=(\tau_0-\tau)^2\nu(\tau)$, it follows that $M:=\max_{\tau\in[0,\tau_0]}\nu(\tau)\leq0$.

Hence,

$$\begin{aligned}&\int_0^{\tau_0}(\tau_0-s)^{-\alpha(\zeta,\tau_0)-1}\phi(s)ds\\&=\int_0^{\tau_0}(\tau_0-s)^{1-\alpha(\zeta,\tau_0)}\nu(s)ds\\&\leq M\int_0^{\tau_0}(\tau_0-s)^{1-\alpha(\zeta,\tau_0)}ds\\&=M\frac{-1}{2-\alpha(\zeta,\tau_0)}(\tau_0-s)^{2-\alpha(\zeta,\tau_0)}\Big|_0^{\tau_0}\\&=M\frac{\tau_0^{2-\alpha(\zeta,\tau_0)}}{2-\alpha(\zeta,\tau_0)}\leq0,\forall\zeta\in[0,L].\end{aligned}$$

Therefore

$$
\begin{aligned}
&{}^{C}D^{\alpha(\zeta,\tau_0)}_{0,\tau_0} f(\tau_0) = -\frac{\tau_0^{1-\alpha(\zeta,\tau_0)}}{\Gamma(2-\alpha(\zeta,\tau_0))}\phi'(0)\\
&+\frac{\alpha(\zeta,\tau_0)-1}{\Gamma(2-\alpha(\zeta,\tau_0))}\tau_0^{-\alpha(\zeta,\tau_0)}\phi(0)\\
&+\frac{(\alpha(\zeta,\tau_0)-1)\cdot\alpha(\zeta,\tau_0)}{\Gamma(2-\alpha(\zeta,\tau_0))}\int_0^{\tau_0}(\tau_0-s)^{-1-\alpha(\zeta,\tau_0)}\nu(s)ds\\
&\le -\frac{\tau_0^{1-\alpha(\zeta,\tau_0)}}{\Gamma(2-\alpha(\zeta,\tau_0))}\phi'(0)+\frac{\alpha(\zeta,\tau_0)-1}{\Gamma(2-\alpha(\zeta,\tau_0))}\tau_0^{-\alpha(\zeta,\tau_0)}\phi(0)\\
&=\frac{\alpha(\zeta,\tau_0)-1}{\Gamma(2-\alpha(\zeta,\tau_0))}\tau_0^{-\alpha(\zeta,\tau_0)}\left[f(0)-f(\tau_0)\right]-\frac{\tau_0^{1-\alpha(\zeta,\tau_0)}}{\Gamma(2-\alpha(\zeta,\tau_0))}f'(0).
\end{aligned}
$$

Consequently, ${}^{C}D^{\alpha(\zeta,\tau_0)}_{0,\tau_0} f(\tau_0)\le 0$ for all $\zeta\in[0,L]$ whenever $f'(0)\ge 0$,

4. THE MAXIMUM PRINCIPLE

In this section, we will display and show the maximum principle for one-dimensional multi-term space-time higher VOFDEs.

For convenience, the symbol $Q_{\beta,\gamma}$ is used to denote the operator given by

$$
\begin{aligned}
Q_{\beta,\gamma}w(\zeta,\tau) = m(\zeta,\tau)\,{}^{C}R^{\beta(\zeta,\tau)}_{\zeta}w(\zeta,\tau) + n(\zeta,\tau)\,{}^{C}R^{\gamma(\zeta,\tau)}_{\zeta}w(\zeta,\tau)\\
+ e(\zeta,\tau)w(\zeta,\tau).
\end{aligned}
$$

It is easy to see that $Q_{\beta,\gamma}$ is a space VO operator on ζ.

Theorem 5. Suppose $w(\zeta,\tau)\in C^{2,2}(\overline{\Omega}_T)$ and

$$
P_{\alpha,\alpha_1,\ldots,\alpha_n}\left({}^{C}D_{0,t}\right)w(\zeta,\tau)+Q_{\beta,\gamma}w(\zeta,\tau)\ge 0,\quad \forall(\zeta,\tau)\in\Omega_T.
$$

If $(\partial w/\partial\zeta)|_{\zeta=0}\ge 0$ but $(\partial w/\partial\zeta)|_{\zeta=L}\le 0$ whenever $0\le\tau\le T$, then

$$
\max_{(\zeta,\tau)\in\overline{\Omega}_T} w(\zeta,\tau)\le\max\left\{\max_{(\zeta,\tau)\in\partial\Omega_T} w(\zeta,\tau),0\right\},
$$

Proof. We prove this by contradiction. Assume that there exits $(\zeta_0,\tau_0)\in\Omega_T$ such that

$$
w(\zeta_0,\tau_0)>\max\left\{\max_{(\zeta,\tau)\in\partial\Omega_T} w(\zeta,\tau),0\right\}=M\ge 0.
$$

Let $w^*(\zeta,\tau)=w(\zeta,\tau)+(\epsilon/2)\left((T-\tau)/T\right)^2$ for all $(\zeta,\tau)\in\overline{\Omega}_T$, where $\varepsilon=w(\zeta_0,\tau_0)-M>0$.

Precisely, we have

$$
\begin{cases}
{}^{C}D^{\alpha(\zeta,\tau)}_{0,\tau}w^*(\zeta,\tau) = {}^{C}D^{\alpha(\zeta,\tau)}_{0,\tau}w(\zeta,\tau)+\dfrac{\varepsilon}{T^2}\dfrac{\tau^{2-\alpha(\zeta,\tau)}}{\Gamma(3-\alpha(\zeta,\tau))},\\
{}^{C}D^{\alpha_i(\zeta,\tau)}_{0,\tau}w^*(\zeta,\tau) = {}^{C}D^{\alpha_i(\zeta,\tau)}_{0,\tau}w(\zeta,\tau)+\dfrac{\varepsilon}{T^2}\dfrac{\tau^{2-\alpha_i(\zeta,\tau)}}{\Gamma(3-\alpha_i(\zeta,\tau))},\quad i=1,2,\ldots,n,
\end{cases}
$$

and

$$
\begin{cases}
{}^{C}R^{\gamma(\zeta,\tau)}_{\zeta}w^*(\zeta,\tau) = {}^{C}R^{\gamma(\zeta,\tau)}_{\zeta}w(\zeta,\tau),\\
{}^{C}R^{\beta(\zeta,\tau)}_{x}w^*(\zeta,\tau) = {}^{C}R^{\beta(\zeta,\tau)}_{\zeta}w(\zeta,\tau).
\end{cases}
$$

This implies that

$$
w^*(\zeta,\tau)=w(\zeta,\tau)+\frac{\varepsilon}{2}\left(\frac{T-\tau}{T}\right)^2\le w(\zeta,\tau)+\frac{\varepsilon}{2},\quad(\zeta,\tau)\in\overline{\Omega}_T,
$$

Thus,

$$
\begin{aligned}
&w^*(\zeta_0,\tau_0)>w(\zeta_0,\tau_0)=M+\varepsilon\ge\varepsilon+w(\zeta,\tau)\ge w^*(\zeta,\tau)+\frac{\varepsilon}{2},\\
&(\zeta,\tau)\in\partial\Omega_T.
\end{aligned}
$$

This means w^* fails to reach the maximum value on the boundary $\partial\Omega_T$. Assume that w^* obtains the maximum value at $(\zeta_1,\tau_1)\in\Omega_T$. It follows that

$$
w^*(\zeta_1,\tau_1)\ge w^*(\zeta_0,\tau_0)>\varepsilon+M\ge\varepsilon>0.
$$

Trivially, one has

$$
\begin{aligned}
P_{\alpha,\alpha_1,\ldots,\alpha_n}\left({}^{C}D_{0,\tau}\right)w^*(\zeta,\tau) &= P_{\alpha,\alpha_1,\ldots,\alpha_n}\left({}^{C}D_{0,\tau}\right)w(\zeta,\tau)\\
&+\frac{\varepsilon}{T^2}\left[\frac{\tau^{2-\alpha(\zeta,\tau)}}{\Gamma(3-\alpha(\zeta,\tau))}+\sum_{i=1}^{n}\frac{a_i(\zeta,\tau)\cdot\tau^{2-\alpha_i(\zeta,\tau)}}{\Gamma(3-\alpha_i(\zeta,\tau))}\right].
\end{aligned}
\tag{4}
$$

and

$$
\begin{aligned}
&Q_{\beta,\gamma}w^*(\zeta_1,\tau_1) = p(\zeta_1,\tau_1)\,{}^{C}R^{\beta(\zeta_1,\tau_1)}_{x}w^*(\zeta_1,\tau_1)\\
&+q(\zeta_1,\tau_1)\,{}^{C}R^{\gamma(\zeta_1,\tau_1)}_{x}w^*(\zeta_1,\tau_1)+e(\zeta_1,\tau_1)w^*(\zeta,\tau)\\
&=p(\zeta_1,\tau_1)\,{}^{C}R^{\beta(\zeta_1,\tau_1)}_{x}w(\zeta_1,\tau_1)+q(\zeta_1,\tau_1)\,{}^{C}R^{\gamma(\zeta_1,\tau_1)}_{x}w(\zeta_1,\tau_1)\\
&+e(\zeta_1,\tau_1)w^*(\zeta_1,\tau_1)=Q_{\beta,\gamma}w(\zeta_1,\tau_1)-e(\zeta_1,\tau_1)w(\zeta_1,\tau_1)\\
&+e(\zeta_1,\tau_1)w^*(\zeta_1,\tau_1)=Q_{\beta,\gamma}w(\zeta_1,\tau_1)+e(\zeta_1,\tau_1)\frac{\varepsilon}{2}\left(\frac{T-t_1}{T}\right)^2.
\end{aligned}
\tag{5}
$$

Note that $q(\zeta_1,\tau_1)\ge 0$ and $p(\zeta_1,\tau_1)>0$, which follow by applying Theorem four in this paper along with Theorems 3.2 and 3.3 in Liu et al. [4]. By virtue of **Eqs 4** and **5**, we have

$$
\begin{aligned}
&P_{\alpha,\alpha_1,\ldots,\alpha_n}\left({}^{C}D_{0,\tau}\right)w(\zeta_1,\tau_1)+Q_{\beta,\gamma}w(\zeta_1,\tau_1)\\
&=P_{\alpha,\alpha_1,\ldots,\alpha_n}\left({}^{C}D_{0,\tau}\right)w^*(\zeta_1,\tau_1)-e(\zeta_1,\tau_1)\frac{\varepsilon}{2}\left(\frac{T-\tau_1}{T}\right)^2\\
&-\frac{\varepsilon}{T^2}\left[\frac{\tau_1^{2-\alpha(\zeta_1,\tau_1)}}{\Gamma(3-\alpha(\zeta_1,\tau_1))}+\sum_{i=1}^{n}\frac{a_i(\zeta_1,\tau_1)\cdot\tau_1^{2-\alpha_i(\zeta_1,\tau_1)}}{\Gamma(3-\alpha_i(\zeta_1,\tau_1))}\right]\\
&+Q_{\beta,\gamma}w^*(\zeta_1,\tau_1)\le-\frac{\varepsilon}{T^2}\left[\frac{\tau_1^{2-\alpha(\zeta_1,\tau_1)}}{\Gamma(3-\alpha(\zeta_1,\tau_1))}\right.\\
&\left.+\sum_{i=1}^{n}\frac{a_i(\zeta_1,\tau_1)\cdot\tau_1^{2-\alpha_i(\zeta_1,\tau_1)}}{\Gamma(3-\alpha_i(\zeta_1,\tau_1))}\right]+e(\zeta_1,\tau_1)\varepsilon\left[1-\frac{1}{2}\left(\frac{T-\tau_1}{T}\right)^2\right]<0.
\end{aligned}
$$

This is a contradiction to our assumption that

$$
P_{\alpha,\alpha_1,\ldots,\alpha_n}\left({}^{C}D_{0,\tau}\right)w(\zeta,\tau)+Q_{\beta,\gamma}w(\zeta,\tau)\ge 0,\quad\forall(\zeta,\tau)\in\Omega_T.
$$

This completes the proof.

If we substitute $-w$ for w in Theorem 5, the minimum principle is obtained as follows.

Theorem 6. Suppose $w(\zeta,\tau) \in C^{2,2}(\overline{\Omega}_T)$, and

$$P_{\alpha,\alpha_1,\ldots,\alpha_n}({}^{C}D_{0,\tau})w(\zeta,\tau) + Q_{\beta,\gamma}w(\zeta,\tau) \le 0, \quad \forall (\zeta,\tau) \in \Omega_T. \tag{6}$$

If $(\partial w/\partial\zeta)|_{\zeta=0} \le 0$ and $(\partial w/\partial\zeta)|_{\zeta=L} \ge 0$, for all $\tau \in [0,T]$, then

$$\min_{(\zeta,\tau)\in\overline{\Omega}_T} w(\zeta,\tau) \ge \min\left\{\min_{(\zeta,\tau)\in\partial\Omega_T} w(\zeta,\tau), 0\right\},$$

where $\partial\Omega_T$ is the boundary of Ω_T.

5. APPLICATIONS

In this section, we discuss multi-term space-time higer VOFDEs in the one-dimensional case:

$$P_{\alpha,\alpha_1,\ldots,\alpha_n}({}^{C}_{0}D_{\tau})w(\zeta,\tau) + Q_{\beta,\gamma}w(\zeta,\tau) = f(\zeta,\tau), \quad (\zeta,\tau) \in \Omega_T, \tag{7}$$

with the initial conditions

$$w(\zeta,0) = \Theta(\zeta), \zeta \in [0,L]. \tag{8}$$

The boundary conditions are taken into consideration as below:

$$\begin{cases} w(0,\tau) = k_1(\tau), & \tau \in [0,T], \\ w(L,\tau) = k_2(\tau), & \tau \in [0,T]. \end{cases} \tag{9}$$

By Theorems 5 and 6, we can get the following theorems.

Theorem 7. Suppose $f(\zeta,\tau) \ge 0$, $(\zeta,\tau) \in \Omega_T$; $\Theta(\zeta) \le 0, \zeta \in [0,L]$; $k_1(\tau) \le 0, k_2(\tau) \le 0, \tau \in [0,T]$. If $w(\zeta,\tau) \in C^{2,2}(\overline{\Omega}_T)$ is a solution of the problem **Eqs 7–9** with $(\partial w/\partial\zeta)|_{\zeta=0} \ge 0$ and $(\partial w/\partial\zeta)|_{\zeta=L} \le 0$ for all $\tau \in [0,T]$, then $w(\zeta,\tau) \le 0$, $(\zeta,\tau) \in \overline{\Omega}_T$.

Theorem 8. Suppose $f(\zeta,\tau) \le 0$, $(\zeta,\tau) \in \Omega_T$; $\Theta(\zeta) \ge 0, \zeta \in [0,L]$; $k_1(\tau) \ge 0, k_2(\tau) \ge 0, \tau \in [0,T]$. If $w(\zeta,\tau) \in C^{2,2}(\overline{\Omega}_T)$ is a solution of the problem **Eqs 7–9** with $(\partial w/\partial\zeta)|_{\zeta=0} \le 0$ and $(\partial w/\partial\zeta)|_{\zeta=L} \ge 0$ for all $\tau \in [0,T]$, then $w(\zeta,\tau) \ge 0$, $(\zeta,\tau) \in \overline{\Omega}_T$,.

Remark 2. If $f(\zeta,\tau) = 0$, then, according to Theorem 7 and 8, we know that the diffusion problem **Eqs 7–9** with zero initial and boundary conditions permits only zero solution in $C^{2,2}(\overline{\Omega}_T)$.

Consider the next nonlinear diffusion equation

$$\begin{aligned} &P_{\alpha,\alpha_1,\ldots,\alpha_n}({}^{C}_{0}D_{0,\tau})w(\zeta,\tau) = -\big[m(\zeta,\tau)\,{}^{C}R^{\beta(\zeta,\tau)}_{\zeta}w(\zeta,\tau) \\ &+ n(\zeta,\tau)\,{}^{C}R^{\gamma(\zeta,\tau)}_{\zeta}w(\zeta,\tau) + e(\zeta,\tau)w(\zeta,\tau)] \\ &+ F(\zeta,\tau,w), (\zeta,\tau) \in \Omega_T. \end{aligned} \tag{10}$$

Theorem 9. Assume that the partial derivative $\partial_w F = \partial_w F(\zeta,\tau,w)$ exists and satisfies $\partial_w F(\zeta,\tau,w) - e(\zeta,\tau) \le 0$ for all $(\zeta,\tau,w) \in \Omega_T \times \mathbb{R}$. If $(\partial w/\partial\zeta)|_{\zeta=0} = 0$ and $(\partial w/\partial\zeta)|_{\zeta=L} = 0$ for all $\tau \in [0,T]$, then the problem **Eqs 8–10** has at most one solution $w = w(\zeta,\tau)$, $(\zeta,\tau) \in \overline{\Omega}_T$ in $C^{2,2}(\overline{\Omega}_T)$.

Proof. Suppose that $w_1, w_2 \in C^{2,2}(\overline{\Omega}_T)$ are two solutions of the problem **Eqs 8–10**. Let $w = w_1 - w_2$. Then

$$\begin{aligned} &P_{\alpha,\alpha_1,\ldots,\alpha_n}({}^{C}D_{0,\tau})w(\zeta,\tau) = -\big[m(\zeta,\tau)\,{}^{C}R^{\beta(\zeta,\tau)}_{x}w(\zeta,\tau) \\ &+ n(\zeta,\tau)\,{}^{C}R^{\gamma(\zeta,\tau)}_{x}w(\zeta,\tau) + e(\zeta,\tau)w(\zeta,\tau)] + F(\zeta,\tau,w_1) \\ &- F(\zeta,\tau,w_2). \end{aligned}$$

Since the homogeneous initial and boundary conditions are fulfilled by w, one has

$$w(\zeta,\tau) = 0, (\zeta,\tau) \in \partial\Omega_T.$$

Owing to the existence of $\partial_w F = \partial_w F(\zeta,\tau,w)$, it holds that

$$F(\zeta,\tau,w_1) - F(\zeta,\tau,w_2) = \frac{\partial F}{\partial w}(w^*)(w_1(\zeta,\tau) - w_2(\zeta,\tau))$$

for all $(\zeta,\tau) \in \Omega_T$, where $w^* = (1-\varrho)w_1 + \varrho w_2$ for some $0 \le \varrho \le 1$.

Consequently,

$$\begin{cases} P_{\alpha,\alpha_1,\ldots,\alpha_n}({}^{C}D_{0,\tau})w(\zeta,\tau) = -\big[m(\zeta,\tau)\,{}^{C}R^{\beta(\zeta,\tau)}_{\zeta}w(\zeta,\tau) + \\ +n(\zeta,\tau)\,{}^{C}R^{\gamma(\zeta,\tau)}_{\zeta}w(\zeta,\tau)\big] + h(\zeta,\tau)w(\zeta,\tau), \\ w(\zeta,\tau) = 0, (\zeta,\tau) \in \partial\Omega_T, \end{cases} \tag{11}$$

where $h(\zeta,\tau) = (\partial F/\partial w)(w^*) - e(\zeta,\tau) \le 0$ for all $(\zeta,\tau) \in \Omega_T$.

By Theorem 7, $w(\zeta,\tau) \le 0$ holds for all $(\zeta,\tau) \in \overline{\Omega}_T$. Conversely, $w(\zeta,\tau) \ge 0$ is also true by using Theorem 8. So, $w(\zeta,\tau) = 0$, i.e.,

$$w_1(\zeta,\tau) = w_2(\zeta,\tau), \quad \forall (\zeta,\tau) \in \overline{\Omega}_T.$$

This completes the proof.

6. CONCLUSIONS

This paper serves as a survey on the maximum principle and the estimates of time higher VOFDEs. The proposed maximum principle contributes to verify some important properties of solutions, including the uniqueness and the continuous dependance with initial-boundary value conditions being taken account. In the future, we will put attention to the solutions for problem **Eq. 1** in more general forms, and investigate the numerical solutions with their applications.

DATA AVAILABILITY STATEMENT

All datasets presented in this study are included in the article.

AUTHOR CONTRIBUTIONS

GX, FL, and GS contributed conception and layout of the research; GX organized the literature; FL completed the initial draft of the paper; GS carried out the proof; The main idea of this paper was proposed by GX; All authors approved the submitted paper.

FUNDING

The authors would like to express their thanks to the reviewers and the editors for their insightful recommendations. This work is supported by the Young and Middle-aged Researchers' Basic Ability Promotion Project of Guangxi Colleges and Universities (Grant No. 2019KY0669).

REFERENCES

1. Podlubny I. *Fractional differential equations.* San Diego, CA: Academic Press (1999)
2. Al-Refai M, Baleanu D. Estimates of higher order fractional derivatives at extreme points. *J Nonlinear Sci Appl* (2017) 10:5174–81. doi:10.22436/jnsa.010.10.05
3. Protter MH, Weinberger HF. Parabolic equations. In: *Maximum principles in differential equations*. New York, NY: Springer (1984) p. 159–94.
4. Liu Z, Zeng S, Bai Y. Maximum principles for multi-term space-time variable-order fractional diffusion equations and their applications. *Fractional Calculus and Applied Analysis.* (2016) 19:188–211. doi:10.1515/fca-2016-0011
5. Ye H, Liu F, Anh V, Turner I. Maximum principle and numerical method for the multi-term time-space Riesz-Caputo fractional differential equations. *Appl Math Comput.* (2014) 227:531–40. doi:10.1016/j.amc.2013.11.015
6. Luchko Y. Boundary value problems for the generalized time-fractional diffusion equation of distributed order. *Fract. Calc. Appl. Anal.* (2009) 12:409–22.
7. Luchko Y. Maximum principle for the generalized time-fractional diffusion equation. *J Math Anal Appl.* (2009) 351:218–23. doi:10.1016/j.jmaa.2008.10.018
8. Luchko Y. Some uniqueness and existence results for the initial-boundary-value problems for the generalized time-fractional diffusion equation. *Comput Math Appl.* (2010) 59:1766–72. doi:10.1016/j.camwa.2009.08.015
9. Li Z, Luchko Y, Yamamoto M. Asymptotic estimates of solutions to initial-boundary-value problems for distributed order time-fractional diffusion equations. *Fractional Calculus and Applied Analysis.* (2014) 17:1114–36. doi:10.2478/s13540-014-0217-x
10. Al-Refai M, Luchko Y. Maximum principle for the multi-term time-fractional diffusion equations with the Riemann-Liouville fractional derivatives. *Appl Math Comput.* (2015) 257:40–51. doi:10.1016/j.amc.2014.12.127
11. Yang J, Yao H, Wu B. An efficient numerical method for variable order fractional functional differential equation. *Appl Math Lett.* (2018) 76:221–6. doi:10.1016/j.aml.2017.08.020
12. Coronel-Escamilla A, Gómez-Aguilar JF, Torres L, Escobar-Jiménez RF. A numerical solution for a variable-order reaction-diffusion model by using fractional derivatives with non-local and non-singular kernel. *Phys Stat Mech Appl.* (2018) 491:406–24. doi:10.1016/j.physa.2017.09.014
13. Hajipour M, Jajarmi A, Baleanu D, Sun H. On an accurate discretization of a variable-order fractional reaction-diffusion equation. *Commun Nonlinear Sci Numer Simulat.* (2019) 69:119–33. doi:10.1016/j.cnsns.2018.09.004
14. Samko SG, Ross B. Integration and differentiation to a variable fractional order. *Integr Transforms Special Funct.* (1993) 1:277–300. doi:10.1080/10652469308819027
15. Coimbra CFM. Mechanics with variable-order differential operators. *Ann Phys.* (2003) 12:692–703. doi:10.1002/andp.200310032
16. Ingman D, Suzdalnitsky J. Control of damping oscillations by fractional differential operator with time-dependent order. *Comput Methods Appl Mech Eng.* (2004) 193:5585–95. doi:10.1016/j.cma.2004.06.029
17. Sun H, Chen W, Chen Y. Variable-order fractional differential operators in anomalous diffusion modeling. *Phys Stat Mech Appl.* (2009) 388:4586–92. doi:10.1016/j.physa.2009.07.024
18. Cooper GRJ, Cowan DR. Filtering using variable order vertical derivatives. *Comput Geosci.* (2004) 30:455–9. doi:10.1016/j.cageo.2004.03.001
19. Liu Z. Existence results for quasilinear parabolic hemivariational inequalities. *J Differ Equ.* (2008) 244:1395–409. doi:10.1016/j.jde.2007.09.001
20. Sun H, Zhang Y, Chen W, Reeves DM. Use of a variable-index fractional-derivative model to capture transient dispersion in heterogeneous media. *J Contam Hydrol* (2014) 157:47–58. doi:10.1016/j.jconhyd.2013.11.002
21. Liu Z, Li X. Approximate controllability for a class of hemivariational inequalities. *Nonlinear Anal R World Appl.* (2015) 22 581–91. doi:10.1016/j.nonrwa.2014.08.010
22. Yang X-J. Fractional derivatives of constant and variable orders applied to anomalous relaxation models in heat-transfer problems. (2016) arXiv preprint arXiv:1612.03202.
23. Kilbas AAA, Srivastava HM, Trujillo JJ. *Theory and applications of fractional differential equations*. Vol. 204. Amsterdam, Netherlands: Elsevier Science Limited (2006)

Conflict of Interest: The authors declare that the research was conducted in the absence of any commercial or financial relationships that could be construed as a potential conflict of interest.

frontiers in Physics

BRIEF RESEARCH REPORT
published: 12 January 2021
doi: 10.3389/fphy.2020.600960

Resistance Distances in Linear Polyacene Graphs

Dayong Wang[1] *and Yujun Yang*[2]*

[1]Business School, Hohai University, Nanjing, China, [2]School of Mathematics and Information Sciences, Yantai University, Yantai, China

The resistance distance between any two vertices of a connected graph is defined as the net effective resistance between them in the electrical network constructed from the graph by replacing each edge with a unit resistor. In this article, using electric network approach and combinatorial approach, we derive exact expression for resistance distances between any two vertices of polyacene graphs.

Keywords: hexagonal lattice, local rules, polyacene graph, resistance distance, circuit reduction

1 INTRODUCTION

Let $G = (V(G), E(G))$ be a connected graph. It is interesting to consider distance functions on G. The most natural and best-known distance function is the shortest path distance. For any two vertices $i, j \in V(G)$, the *shortest path distance* between i and j, denoted by $d_G(i, j)$, is defined as the length of a shortest path connecting i and j. Two decays ago, another novel distance function, named resistance distance, was identified by Klein and Randić [1]. The concept of resistance distance originates from electrical circuit theory. If we view G as an electrical network N by replacing each edge of G with a unit resistor, then the *resistance distance* [1] between i and j, denoted by $\Omega_G(i, j)$, is defined as the net effective resistance between the corresponding nodes in the electrical network N. In contrast to the shortest path distance, the resistance distance has a notable feature that if i and j are connected by more than one path, then they are closer than they are connected by the only shortest path. So it is suggested that resistance distance is more appropriate to deal with wave-like motion in the network, like the communication in chemical molecules. In addition, it turns out that the resistance distance has some pure mathematical interpretations, which could be expressed in terms of the generalized inverse of the Laplacian matrix [1], the number of spanning trees and spanning bi-trees [2], and random walks on graphs [3, 4].

Besides being an intrinsic graph metric and an important component of electrical circuit theory, resistance distance also turns out to have important applications in chemistry. For this reason, resistance distance has been widely studied in the mathematical, chemical, and physical literature. In the study of resistance distance, the main focus is placed on the problem of computation of resistance distance. This problem has been a classical problem in electrical network theory studied by numerous researchers for a long time. Besides, it is also relevant to a wide range of problems ranging from random walks, the theory of harmonic functions, to lattice Green's functions. Consequently, this problem has attracted much attention, and many researchers have devoted themselves to it. Up to now, resistance distances have been computed for many interesting (classes of) graphs, with emphasis being placed on some highly concerned electrical networks and chemical interesting graphs. For example, resistance distances have been computed for Platonic solids [5], and for some fullerene graphs including buckminsterfullerene [6], circulant graphs [7], distance-regular graphs [8, 9], pseudo–distance-regular graphs [10], wheels and fans [11], Cayley graphs over finite abelian groups [12], complete graph minus N edges [13], resistor network embedded on a globe [14], Möbius ladder [15], $m \times n$ cobweb network [16], complete n-partite graphs [17], $m \times n$ resistor network [18],

OPEN ACCESS

Edited by:
Andre P. Vieira,
University of São Paulo, Brazil

Reviewed by:
Zhibin Du,
South China Normal University, China
Mohammad Reza Farahani,
Iran University of Science and Technology, Iran

***Correspondence:**
Yujun Yang
yangyj@yahoo.com

Specialty section:
This article was submitted to Mathematical and Statistical Physics, a section of the journal Frontiers in Physics

Received: *31 August 2020*
Accepted: *24 November 2020*
Published: *12 January 2021*

Citation:
Wang D and Yang Y (2021) Resistance Distances in Linear Polyacene Graphs. Front. Phys. 8:600960. doi: 10.3389/fphy.2020.600960

ladder graph [19], n-step network [20], Cayley graphs on symmetric groups [21], Apollonian network [22], Sierpinski Gasket Network [23], generalized decorated square and simple cubic network lattices [24], self-similar (x, y) -flower networks [25], almost complete bipartite graphs [26], straight linear 2-trees [27], and path networks [28].

It is interesting to note that a good deal of attention has been paid on resistance distances in plane networks, such as Platonic solids, fullerene graphs, wheels, fans, ladder graphs, Apollonian network, Sierpinski Gasket Network, $m \times n$ resistor network, and straight linear 2-tree. Motivated by this fact, we are devoted to considering other interesting plane networks. In this article, we take the linear polyacene graphs into consideration. It is well known that the linear polyacene graphs are graph representations of an important class of benzenoid hydrocarbons, and it is an interesting class of plane hexagonal networks. We use L_n to denote the linear polyacene graph with $n-1$ benzenoid rings (i.e., hexagons), as shown in **Figure 1**. Using electrical network approach and resistance distance local rules, we derive exact expression for resistance distances between any two vertices of L_n.

2 RESISTANCE DISTANCES IN LINEAR POLYACENE GRAPHS

Let L_n be the linear polyacene graph with $n-1$ benzenoid rings. Obviously, L_n has $4n-2$ vertices and $5n-4$ edges. For convenience, we label the vertices in L_n as in **Figure 1**. We partite the vertex set of L_n into two classes: $V_1 = \{p_1, p_2, \ldots, p_n, q_1, q_2, \ldots, q_n\}$ and $V_2 = \{s_1, s_2, \ldots, s_{n-1}, t_1, t_2, \ldots, t_{n-1}\}$. To compute resistance distances between any two vertices of L_n, we take two steps. In the first step, we compute resistance distances between vertices in V_1. To this end, we first view L_n as a weighted ladder graph L_n^* by simply replacing all the paths $p_i s_i p_{i+1}$ and $q_i t_i q_{i+1}$ $(1 \le i \le n-1)$ by edges of resistance 2. Then, by making use of the electric network approach as inspired in [19], we obtain resistance distances between vertices in V_1. Next, for the second step, using the results obtained in the first step together with resistance distance local rules, we derive expressions for resistance distances between the remaining pairs of vertices.

Before stating the main result, we introduce the elegant resistance distance local rules, which will be frequently used later. For any vertex $a \in V(G)$, we use $n_G(a)$ to denote the set of neighbors of a. Then, we have the following sum rules for resistance distances.

Lemma 2.1 [29]. Let $G = (V(G), E(G))$ be a connected graph with $n\,(n \ge 2)$ vertices. Then,

1) For any $a, b \in V(G)$ $(a \ne b)$ $(a \ne b)$

$$\Delta_a \Omega_G(a,b) + \sum_{i \in n_G(a)} (\Omega_G(i,a) - \Omega_G(i,b)) = 2, \tag{1}$$

where Δ_a denotes the degree of the vertex a.

2) For any three different vertices $a, b, c \in V$,

$$\Delta_c (\Omega_G(c,a) - \Omega_G(c,b)) + \sum_{i \in n_G(c)} (\Omega_G(i,b) - \Omega_G(i,a)) = 0. \tag{2}$$

Now, we are ready for the main theorem. For simplicity, we let $\alpha = 3 - 2\sqrt{2}$, and define $f(x,y)$ and $g(x,y)$ as follows:

$$f(x,y) = (1-\alpha^{x-y})\left(2 - \alpha^{x+y-1} + \alpha^{2y-1} + \alpha^{2n-2x+1}\left(1 - \alpha^{x-y} - 2\alpha^{x+y-1}\right)\right),$$
$$g(x,y) = (1+\alpha^{x-y})\left(2 + \alpha^{x+y-1} + \alpha^{2y-1} + \alpha^{2n-2x+1}\left(1 + \alpha^{x-y} + 2\alpha^{x+y-1}\right)\right).$$

Then, the main result is given in the following.

Theorem 2.2. The resistance distances between any two vertices in the linear polyacene graph L_n can be computed as follows.

$$\Omega_{L_n}(p_i, p_j) = i - j + \frac{f(i,j)}{4\sqrt{2}(1-\alpha^{2n})}, \tag{2.1}$$

$$\Omega_{L_n}(q_i, p_j) = i - j + \frac{g(i,j)}{4\sqrt{2}(1-\alpha^{2n})}, \tag{2.2}$$

$$\Omega_{L_n}(s_i, p_j) = i - j + \frac{3}{4} - \frac{f(i+1,i)}{16\sqrt{2}(1-\alpha^{2n})} + \frac{f(i,j)+f(i+1,j)}{8\sqrt{2}(1-\alpha^{2n})}, \tag{2.3}$$

$$\Omega_{L_n}(s_i, q_j) = j - i - \frac{1}{4} + \frac{f(j+1,j)}{16\sqrt{2}(1-\alpha^{2n})} + \frac{g(j,i)+g(j,i+1)}{8\sqrt{2}(1-\alpha^{2n})}, \tag{2.4}$$

$$\Omega_{L_n}(s_i, s_j) = \frac{1}{2} - i + j - \frac{f(i+1,i)+f(j+1,j)+f(j,i)+f(j+1,i)+f(j,i+1)+f(j+1,i+1)}{16\sqrt{2}(1-\alpha^{2n})}, \tag{2.5}$$

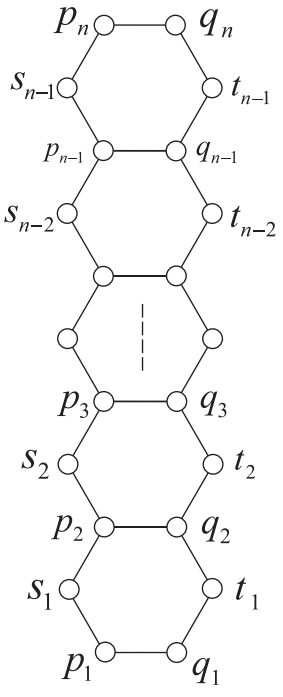

FIGURE 1 | Linear polyacne graph L_n and its vertex labeling.

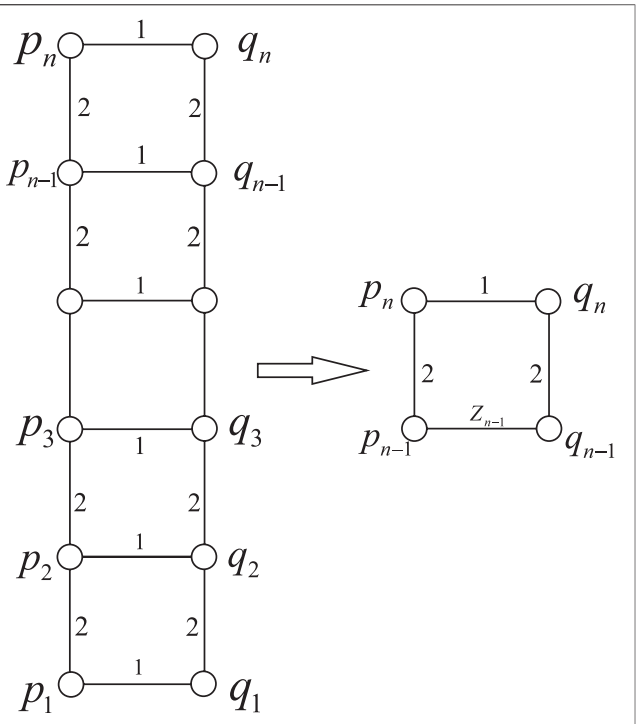

FIGURE 2 | Weighted ladder graph L_n^* (left) and the circuit reduction of L_{n-1}^* with respect to p_{n-1} and q_{n-1} (right).

$$\Omega_{L_n}(s_i,t_j)=\frac{1}{2}+i-j+\frac{g(i,j)+g(i,j+1)+g(i+1,j)+g(i+1,j+1)-f(i+1,i)}{16\sqrt{2}(1-\alpha^{2n})}-\frac{f(i+1,i)+f(i+2,i+1)}{32\sqrt{2}(1-\alpha^{2n})}. \tag{2.6}$$

Proof. We divide the proof into two steps.

Step 1. Computation of resistance distances between any two vertices in V_1.

To compute resistance distances between vertices in V_1, we view L_n as a weighted ladder graph L_n^* by simply replacing all the paths $p_is_ip_{i+1}$ and $q_it_iq_{i+1}$ $(1\le i\le n-1)$ by edges of resistance 2, see **Figure 2** (left). Clearly, $\Omega_{L_n^*}(p,q)=\Omega_{L_n}(p,q)$ holds for all $p,q\in V(L_n^*)$.

First, we compute resistance distances between the end vertices p_1, p_n, q_1, and q_n. let $x_n:=\Omega_{L_n^*}(p_n,p_1)$, $y_n:=\Omega_{L_n^*}(p_n,q_1)$, and $z_n:=\Omega_{L_n^*}(p_n,q_n)$. Clearly, L_n^* can be obtained from L_{n-1}^* by adding two vertices p_n and q_n, and the three edges with end vertices $\{p_{n-1},p_n\}$, $\{p_n,q_n\}$, and $\{q_n,q_{n-1}\}$, as shown in **Figure 2** (right). Hence, according to rules for series and parallel circuits, z_n could be expressed in term of z_{n-1} as

$$z_n=\frac{z_{n-1}+4}{z_{n-1}+5},\quad \forall n\ge 2, \tag{2.7}$$

with initial condition $z_1=1$. Solving the recurrence relation by Mathematica [30], we obtain

$$z_n=-2\left(1+\sqrt{2}\right)+\frac{4\sqrt{2}}{1-\left(3-2\sqrt{2}\right)^{2n}},\quad n\ge 1. \tag{2.8}$$

Specially, we have $z_1=1$, $z_2=\frac{5}{6}$, $z_3=\frac{29}{35}$, and $z_4=\frac{169}{204}$. It is easily checked that z_n can also be expressed as

$$z_n=-2\left(1+\sqrt{2}\right)+\frac{4\sqrt{2}\left(3+2\sqrt{2}\right)^n}{\left(3+2\sqrt{2}\right)^n-\left(3-2\sqrt{2}\right)^n},\quad n\ge 1. \tag{2.9}$$

We proceed to use z_n to find explicit formulas for x_n and y_n. To this end, we make circuit reduction to the subgraph L_n^* of L_{n+1}^* with respect to p_n, q_n, and p_1, where $n\ge 1$. Precisely speaking, we reduce L_n^* to a Y-shaped graph which has outer vertices p_n, q_n, and p_1. We use A, B, and C to denote the effective resistances between end vertices of those edges of the Y-shaped graph. Then, we have $B+C=y_n$, $A+C=x_n$, and $A+B=z_n$. Solving these equations, we get

$$A=\frac{x_n-y_n+z_n}{2},B=\frac{-x_n+y_n+z_n}{2},C=\frac{x_n+y_n-z_n}{2}.$$

On the other hand, by parallel and series connection rules, we have $x_{n+1}=\frac{(A+2)(B+3)}{z_n+5}+C$ and $y_{n+1}=\frac{(B+2)(A+3)}{z_n+5}+C$. So, it follows that

$$x_{n+1}=\frac{(x_n-y_n+z_n+4)(-x_n+y_n+z_n+6)}{4(z_n+5)}+\frac{x_n+y_n-z_n}{2},\quad n\ge 1, \tag{2.10}$$

$$y_{n+1}=\frac{(-x_n+y_n+z_n+4)(x_n-y_n+z_n+6)}{4(z_n+5)}+\frac{x_n+y_n-z_n}{2},\quad n\ge 1, \tag{2.11}$$

with initial conditions $x_1=0$ and $y_1=1$. **Eq. 2.10** minus **Eq. 2.11** yields

$$x_{n+1}-y_{n+1}=\frac{x_n-y_n}{z_n+5}.$$

Set $t_n:=x_n-y_n$. It follows that

$$t_{n+1}=\frac{t_n}{z_n+5},\quad n\ge 1 \text{ and } t_1=-1. \tag{2.12}$$

Thus, we have

$$t_{n+1}=-\prod_{k=1}^{n}\frac{1}{z_k+5}. \tag{2.13}$$

Since $\frac{1}{z_k+5}=\frac{(3+2\sqrt{2})^k-(3-2\sqrt{2})^k}{(3+2\sqrt{2})^{k+1}-(3-2\sqrt{2})^{k+1}}$, using **Eq. 2.9** and doing some algebraic calculations, we get

$$t_n=\frac{-4\sqrt{2}}{\left(3+2\sqrt{2}\right)^n-\left(3-2\sqrt{2}\right)^n},\quad n\ge 1. \tag{2.14}$$

This could also be rewritten as $t_n=\frac{-4\sqrt{2}(3-2\sqrt{2})^n}{1-(3-2\sqrt{2})^{2n}}$, for all $n\ge 1$. Now, we come back to solve x_n and y_n. By using $x_n=t_n+y_n$, **Eqs 2.8–2.14** and doing some algebra, **Eq. 2.11** becomes

$$y_{n+1} = y_n + \frac{2\sqrt{2}}{1-\left(3-2\sqrt{2}\right)^{n+1}} - \frac{2\sqrt{2}}{1-\left(3-2\sqrt{2}\right)^{n}} + 1, \quad n \geq 1 \text{ and } y_1 = 1. \tag{2.15}$$

Solving the recursion relation, we get

$$y_n = n - 2 - \sqrt{2} + \frac{2\sqrt{2}}{1-\left(3-2\sqrt{2}\right)^{n}}, \quad n \geq 1. \tag{2.16}$$

Now, by **Eqs 2.14–2.16**, together with the relation $x_n = t_n + y_n$, we get

$$x_n = n - 2 - \sqrt{2} + \frac{2\sqrt{2}}{1+\left(3-2\sqrt{2}\right)^{n}}, \quad n \geq 1. \tag{2.17}$$

Next, we proceed to compute $\Omega_{L_n^*}(p_n, p_i)$, $\Omega_{L_n^*}(p_n, q_i)$, and $\Omega_{L_n^*}(p_i, q_i)$, where $n > i > 1$. To achieve our goal, we consider L_n^* as the union of three graphs: the upper part of p_{i+1} and q_{i+1}, the lower part of p_i and q_i, and the middle part consisting of p_{i+1}, q_{i+1}, p_i, and q_i, as shown in **Figure 3**. Note that the upper and the lower graphs are corresponding to the graphs L_{n-i}^* and L_i^*, respectively. We make circuit reductions as illustrated in **Figure 3**. First, make the circuit reduction of the upper part with respect to p_n, p_{i+1}, and q_{i+1} to obtain a Y-shaped graph, and assume that resistances along its edges are M, N, and K. Then, reduce the lower part of p_i and q_i to be edge with resistance $\Omega_{L_n^*}(p_i, q_i) = z_i$. We could find that

$$M + N = x_{n-i}, M + K = y_{n-i}, N + K = z_{n-i}. \tag{2.18}$$

Note that

$$\begin{aligned} x_n + y_n - z_n &= 2n - 2, \\ x_n - y_n + z_n &= -2 - 2\sqrt{2} + \frac{4\sqrt{2}}{1+\left(3-2\sqrt{2}\right)^{n}}, \\ -x_n + y_n + z_n &= -2 - 2\sqrt{2} + \frac{4\sqrt{2}}{1-\left(3-2\sqrt{2}\right)^{n}}. \end{aligned} \tag{2.19}$$

Solving M, N, and K, we obtain

$$\begin{aligned} M &= \frac{x_{n-i} + y_{n-i} - z_{n-i}}{2} = n - i - 1, \\ N &= \frac{x_{n-i} - y_{n-i} + z_{n-i}}{2} = -1 - \sqrt{2} + \frac{2\sqrt{2}}{1+\left(3-2\sqrt{2}\right)^{n-i}}, \\ K &= \frac{-x_{n-i} + y_{n-i} + z_{n-i}}{2} = -1 - \sqrt{2} + \frac{2\sqrt{2}}{1-\left(3-2\sqrt{2}\right)^{n-i}}. \end{aligned} \tag{2.20}$$

Then, applying parallel and series connection rules to the reduced circuit in **Figure 3**, we obtain

$$\begin{aligned} \Omega_{L_n^*}(p_n, p_i) &= \frac{(N+2)(K+z_i+2)}{z_{n-i}+z_i+4} + M, \\ \Omega_{L_n^*}(p_n, q_i) &= \frac{(K+2)(N+z_i+2)}{z_{n-i}+z_i+4} + M, \\ \Omega_{L_n^*}(p_i, q_i) &= \frac{z_i(z_{n-i}+4)}{z_{n-i}+z_i+4}. \end{aligned} \tag{2.21}$$

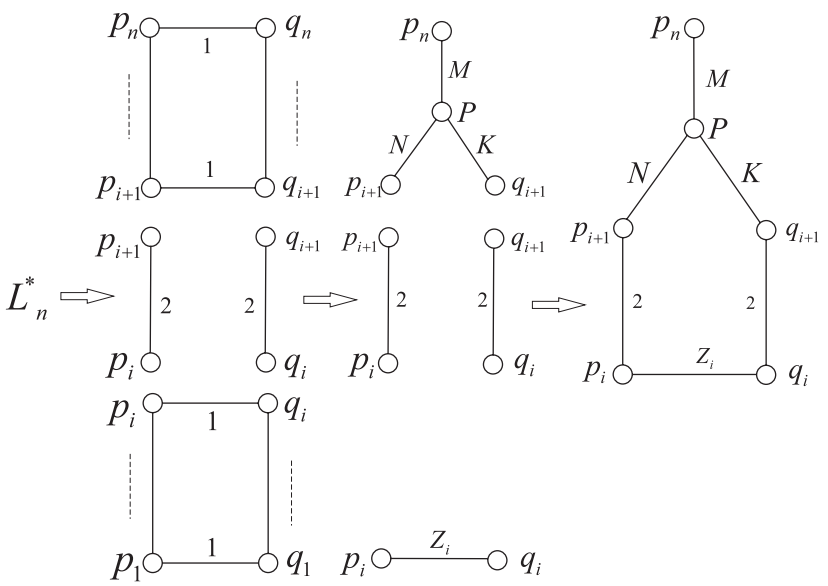

FIGURE 3 | L_n^* and circuit reduction to find $\Omega_{L_n^*}(p_n, p_i)$, $\Omega_{L_n^*}(q_n, p_i)$, and $\Omega_{L_n^*}(p_i, q_i)$.

Substituting **Eqs 2.8–2.20** into **Eq. 2.21**, we have

$$\Omega_{L_n^*}(p_n,p_i) = n-i + \frac{(1-\alpha^{n-i})(2-2\alpha^{n+i}-\alpha^{n+i-1}-\alpha^{n-i+1}+\alpha^{2i-1}+\alpha)}{4\sqrt{2}(1-\alpha^{2n})},$$
$$\Omega_{L_n^*}(p_n,q_i) = n-i + \frac{(1+\alpha^{n-i})(2+2\alpha^{n+i}+\alpha^{n+i-1}+\alpha^{n-i+1}+\alpha^{2i-1}+\alpha)}{4\sqrt{2}(1-\alpha^{2n})},$$
$$\Omega_{L_n^*}(p_i,q_i) = \frac{1+\alpha^{2i-1}+\alpha^{2n-2i+1}+\alpha^{2n}}{\sqrt{2}(1-\alpha^{2n})}. \quad (2.22)$$

Finally, we compute $\Omega_{L_n^*}(p_i,p_j)$ and $\Omega_{L_n^*}(q_i,p_j)$ $(n>i\geq j\geq 1)$. To this end, we consider L_n^* as the union of two graphs: the upper part and the lower part with respect to p_i and q_i, as illustrated in **Figure 4**. Note the lower part is the graph L_i^*, and the upper part is the graph L_{n-i}^*. Next, we make circuit reduction to L_{n-i}^* so that it is reduced to an edge $p_{i+1}q_{i+1}$ with resistance z_{n-i}. Then, we reduce L_i^* to a Y-shaped graph with end vertices p_i, q_i, and p_j, and resistances D, E, and F along its edges. These reductions are illustrated in **Figure 4**. Then, we have

$$D+E=\Omega_{L_i^*}(p_i,p_j), D+F=\Omega_{L_i^*}(p_i,q_i)=z_i, E+F=\Omega_{L_i^*}(q_i,p_j). \quad (2.23)$$

It follows that

$$D=\frac{\Omega_{L_i^*}(p_i,p_j)+z_i-\Omega_{L_i^*}(q_i,p_j)}{2},$$
$$E=\frac{\Omega_{L_i^*}(p_i,p_j)-z_i+\Omega_{L_i^*}(q_i,p_j)}{2}, \quad (2.24)$$
$$F=\frac{-\Omega_{L_i^*}(p_i,p_j)+z_i+\Omega_{L_i^*}(q_i,p_j)}{2}.$$

On the other hand, by the series and parallel connection rules, we have

$$\Omega_{L_n^*}(p_i,p_j)=\frac{D(z_{n-i}+F+4)}{z_{n-i}+z_i+4}+E,$$
$$\Omega_{L_n^*}(q_i,p_j)=\frac{F(z_{n-i}+D+4)}{z_{n-i}+z_i+4}+E. \quad (2.25)$$

By **Eqs. (2.8)**, **Eqs 2.22–2.25**, and doing some algebra using Mathematica [30], we obtain

$$\Omega_{L_n^*}(p_i,p_j) = i-j + \frac{(1-\alpha^{i-j})(2-\alpha^{i+j-1}+\alpha^{2j-1}+\alpha^{2n-2i+1}(1-\alpha^{i-j}-2\alpha^{i+j-1}))}{4\sqrt{2}(1-\alpha^{2n})}, \quad (2.26)$$

$$\Omega_{L_n^*}(q_i,p_j) = i-j + \frac{(1+\alpha^{i-j})(2+\alpha^{i+j-1}+\alpha^{2j-1}+\alpha^{2n-2i+1}(1+\alpha^{i-j}+2\alpha^{i+j-1}))}{4\sqrt{2}(1-\alpha^{2n})}. \quad (2.27)$$

It is easily verified that **Eq. 2.27** is valid for $i=j$.

Step 2. Computation of resistance distances between $p,q\in V_2$ and between $p\in V_1$ and $q\in V_2$.

First, we compute $\Omega_{L_n}(s_i,p_i)$ and $\Omega_{L_n}(s_i,p_{i+1})$. Applying Lemma 2.1 to pairs of vertices $\{s_i,p_i\}$ and $\{s_i,p_{i+1}\}$, we obtain

$$2\Omega_{L_n}(s_i,p_i)+\Omega_{L_n}(p_i,s_i)-\Omega_{L_n}(p_i,p_i)+\Omega_{L_n}(p_{i+1},s_i) - \Omega_{L_n}(p_{i+1},p_i)=2, \quad (2.28)$$

$$2\Omega_{L_n}(s_i,p_{i+1})+\Omega_{L_n}(p_i,s_i)-\Omega_{L_n}(p_i,p_{i+1})+\Omega_{L_n}(p_{i+1},s_i) - \Omega_{L_n}(p_{i+1},p_{i+1})=2. \quad (2.29)$$

Multiplying **Eq. 2.28** by 3 and then minus **Eq. 2.29**, we get

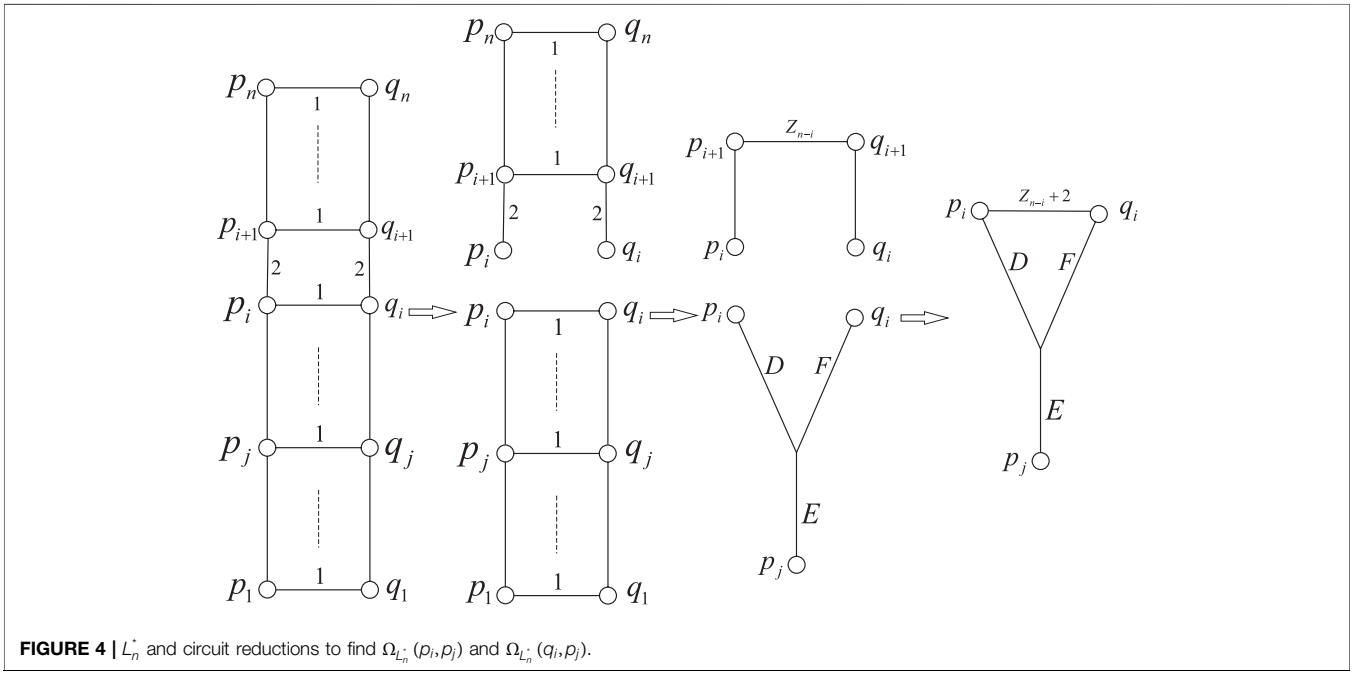

FIGURE 4 | L_n^* and circuit reductions to find $\Omega_{L_n^*}(p_i,p_j)$ and $\Omega_{L_n^*}(q_i,p_j)$.

$$\Omega_{L_n}(s_i,p_i)=\frac{1}{8}\left(4+2\Omega_{L_n}(p_i,p_{i+1})\right). \tag{2.30}$$

Then, substituting the value of $\Omega_{L_n}(p_i,p_{i+1})$ as obtained in Step 1 into **Eq. 2.30**, we could obtain

$$\Omega_{L_n}(p_{i+1},p_i)=1+\frac{(1-\alpha)\left(2-\alpha^{2i}+\alpha^{2i-1}+\alpha^{2n-2i-1}\left(1-\alpha-2\alpha^{2i}\right)\right)}{4\sqrt{2}\left(1-\alpha^{2n}\right)}. \tag{2.31}$$

Substituting **Eq. 2.31** into **Eq. 2.30**, we have

$$\Omega_{L_n}(s_i,p_i)=\frac{3}{4}+\frac{(1-\alpha)\left(2-\alpha^{2i}+\alpha^{2i-1}+\alpha^{2n-2i-1}\left(1-\alpha-2\alpha^{2i}\right)\right)}{16\sqrt{2}\left(1-\alpha^{2n}\right)}. \tag{2.32}$$

In the same way, we could obtain that

$$\Omega_{L_n}(s_i,p_{i+1})=\frac{3}{4}+\frac{(1-\alpha)\left(2-\alpha^{2i}+\alpha^{2i-1}+\alpha^{2n-2i-1}\left(1-\alpha-2\alpha^{2i}\right)\right)}{16\sqrt{2}\left(1-\alpha^{2n}\right)}. \tag{2.33}$$

Second, we calculate the resistance distance between s_i and p_j. Again, applying Lemma 2.1 to $\{s_i,p_j\}$, we obtain

$$2\Omega_{L_n}(s_i,p_j)+\Omega_{L_n}(p_i,s_i)-\Omega_{L_n}(p_i,p_j)+\Omega_{L_n}(p_{i+1},s_i)-\Omega_{L_n}(p_{i+1},p_j)=2. \tag{2.34}$$

By **Eqs 2.32**, **2.33**, it follows that

$$\Omega_{L_n}(p_i,s_i)+\Omega_{L_n}(p_{i+1},s_i)=\frac{3}{2}+\frac{(1-\alpha)\left(2-\alpha^{2i}+\alpha^{2i-1}+\alpha^{2n-2i-1}\left(1-\alpha-2\alpha^{2i}\right)\right)}{8\sqrt{2}\left(1-\alpha^{2n}\right)}. \tag{2.35}$$

For the sake of simplicity, we define

$$f(x,y)=(1-\alpha^{x-y})\left(2-\alpha^{x+y-1}+\alpha^{2y-1}+\alpha^{2n-2x+1}\left(1-\alpha^{x-y}-2\alpha^{x+y-1}\right)\right). \tag{2.36}$$

Then, **Eq. 2.35** can be rewritten as

$$\Omega_{L_n}(p_i,s_i)+\Omega_{L_n}(p_{i+1},s_i)=\frac{3}{2}+\frac{f(i+1,i)}{8\sqrt{2}\left(1-\alpha^{2n}\right)}. \tag{2.37}$$

On the other hand, by **Eq. 2.26**, we have

$$\Omega_{L_n}(p_i,p_j)+\Omega_{L_n}(p_{i+1},p_j)=2i-2j+1+\frac{f(i,j)+f(i+1,j)}{4\sqrt{2}\left(1-\alpha^{2n}\right)}. \tag{2.38}$$

Substituting **Eqs. 2.37**, **2.38** into **Eq. 2.34**, we draw the conclusion that

$$\Omega_{L_n}(s_i,p_j)=i-j+\frac{3}{4}-\frac{f(i+1,i)}{16\sqrt{2}\left(1-\alpha^{2n}\right)}+\frac{f(i,j)+f(i+1,j)}{8\sqrt{2}\left(1-\alpha^{2n}\right)}. \tag{2.39}$$

Third, we calculate the resistance distance between s_j and q_i. Apply Lemma 2.1 to $\{s_j,q_i\}$ to obtain

$$2\Omega_{L_n}(s_j,q_i)+\Omega_{L_n}(p_j,s_j)-\Omega_{L_n}(p_j,q_i)+\Omega_{L_n}(p_{j+1},s_j)-\Omega_{L_n}(p_{j+1},q_i)=2. \tag{2.40}$$

By **Eq. 2.37**, we have

$$\Omega_{L_n}(p_j,s_j)+\Omega_{L_n}(p_{j+1},s_j)=\frac{3}{2}+\frac{f(j+1,j)}{8\sqrt{2}\left(1-\alpha^{2n}\right)}. \tag{2.41}$$

For simplicity, we define

$$g(x,y)=(1+\alpha^{x-y})\left(2+\alpha^{x+y-1}+\alpha^{2y-1}+\alpha^{2n-2x+1}\left(1+\alpha^{x-y}+2\alpha^{x+y-1}\right)\right). \tag{2.42}$$

On the other hand, by **Eq. 2.27**, we have

$$\Omega_{L_n}(q_i,p_j)+\Omega_{L_n}(q_i,p_{j+1})=2i-2j-1+\frac{g(i,j)+g(i,j+1)}{4\sqrt{2}\left(1-\alpha^{2n}\right)}. \tag{2.43}$$

Substituting **Eqs. 2.41**–**2.43** into **Eq. 2.40**, we get

$$\Omega_{L_n}(s_j,q_i)=i-j-\frac{1}{4}+\frac{f(i+1,i)}{16\sqrt{2}\left(1-\alpha^{2n}\right)}+\frac{g(i,j)+g(i,j+1)}{8\sqrt{2}\left(1-\alpha^{2n}\right)}. \tag{2.44}$$

Fourth, we calculate the resistance distance between s_i and s_j. Applying Lemma 2.1 to $\{s_i,s_j\}$, we have

$$2\Omega_{L_n}(s_i,s_j)+\Omega_{L_n}(p_i,s_i)-\Omega_{L_n}(p_i,s_j)+\Omega_{L_n}(p_{i+1},s_i)-\Omega_{L_n}(p_{i+1},s_j)=2. \tag{2.45}$$

As $\Omega_{L_n}(p_i,s_i)$, $\Omega_{L_n}(p_i,s_j)$, $\Omega_{L_n}(p_{i+1},s_i)$, and $\Omega_{L_n}(p_{i+1},s_j)$ have been given by **Eq. 2.39**, simple calculation leads to

$$\Omega_{L_n}(s_i,s_j)=\frac{1}{2}-i+j-\frac{f(i+1,i)+f(j+1,j)+f(j,i)+f(j+1,i)+f(j,i+1)+f(j+1,i+1)}{16\sqrt{2}\left(1-\alpha^{2n}\right)}.$$

Fifth and finally, we calculate the resistance between s_i and t_j. Applying Lemma 2.1 to $\{s_i,t_j\}$, we have

$$2\Omega_{L_n}(s_i,t_j)+\Omega_{L_n}(p_i,s_i)-\Omega_{L_n}(p_i,t_j)+\Omega_{L_n}(p_{i+1},s_i)-\Omega_{L_n}(p_{i+1},t_j)=2 \tag{2.46}$$

Note by the symmetry of L_n that we have $\Omega_{L_n}(p_i,t_j)=\Omega_{L_n}(q_i,s_j)$ and $\Omega_{L_n}(p_{i+1},t_j)=\Omega_{L_n}(q_{i+1},s_j)$. Using the results obtained in **Eqs. 2.39**–**2.44**, simple algebraic calculation yields

$$\Omega_{L_n}(s_i, t_j) = \frac{1}{2} + i - j + \frac{g(i,j) + g(i,j+1) + g(i+1,j) + g(i+1,j+1) - f(i+1,i)}{16\sqrt{2}(1-\alpha^{2n})} - \frac{f(i+1,i) + f(i+2,i+1)}{32\sqrt{2}(1-\alpha^{2n})}. \quad (2.47)$$

3 CONCLUSION

The computation of resistance distances is a classical problem in electrical circuit theory, which has attracted much attention. It is of special interest to investigate resistance distances in plane networks. Along this line, we have considered the linear polyacene network, with exact expression for resistance distances in this network being given. It is a primary attempt for the computation of resistance distances in plane hexagonal lattice. Resistance distances in more and more plane hexagonal lattices are greatly anticipated.

DATA AVAILABILITY STATEMENT

The original contributions presented in the study are included in the article/Supplementary Material; further inquiries can be directed to the corresponding author.

AUTHOR CONTRIBUTIONS

All authors listed have made a substantial, direct, and intellectual contribution to the work and approved it for publication.

FUNDING

This research was funded by the National Natural Science Foundation of China through grant number 116711347, and project ZR2019YQ02 by Shandong Provincial Natural Science Foundation.

ACKNOWLEDGMENTS

We would like to thank the anonymous reviewers for their useful comments.

REFERENCES

1. Klein DJ, Randić M. Resistance distance. *J Math Chem* (1993) 12:81–95. doi:10.1007/BF01164627
2. Shapiro LW. An electrical lemma. *Math Mag* (1987) 60:36–8.
3. Nash Williams JAC, St. Random walks and electric currents in networks. *Proc. Cambridge Phil Soc* (1959) 55:181–94. 10.1017/S0305004100033879
4. Doyle PG, Snell JL. *Random walks and electric networks*. Washington, DC: The Mathematical Association of America (1984) 118 p.
5. Lukovits I, Nikolić S, Trinajstić N. Resistance distance in regular graphs. *Int J Quant Chem* (1999) 71:217–25. 10.1002/(SICI)1097-461X(1999)71:3<217::AID-QUA1>3.0.CO;2-C
6. Fowler PW. Resistance distances in fullerene graphs. *Croat Chem Acta* (2002) 75:401–8.
7. Zhang H, Yang Y. Resistance distance and Kirchhoff index in circulant graphs. *Int J Quant Chem* (2007) 107:330–9. 10.1002/qua.21068
8. Palacios JL. Closed-form formulas for Kirchhoff index. *Int J Quant Chem* (2001) 81:135–40. 10.1002/1097-461X(2001)81:2%3C135::AID-QUA4%3E3.0.CO;2-G
9. Jafarizadeh MA, Sufiani R, Jafarizadeh S. Recursive calculation of effective resistances in distance-regular networks based on Bose-Mesner algebra and Christoffel-Darboux identity. *J Math Phys* (2009) 50:023302. doi:10.1063/1.3077145
10. Jafarizadeh S, Sufiani R, Jafarizadeh MA. Evaluation of effective resistances in pseudo-distance-regular resistor networks. *J Stat Phys* (2010) 139:177–99. doi:10.1007/s10955-009-9909-8
11. Bapat RB, Gupta S. Resistance distance in wheels and fans. *Indian J Pure Appl Math* (2010) 41:1–13. doi:10.1007/s13226-010-0004-2
12. Gao X, Luo Y, Liu W. Resistance distances and the Kirchhoff index in Cayley graphs. *Discrete Appl Math* (2011) 159:2050–7. doi:10.1016/j.dam.2011.06.027
13. Chair N. Exact two-point resistance, and the simple random walk on the complete graph minus *N* edges. *Ann Phys* (2012) 327:3116–29. doi:10.1016/j.aop.2012.09.002
14. Tan Z, Essam JW, Wu FY. Two-point resistance of a resistor network embedded on a globe. *Phys Rev E Stat Nonlinear Soft Matter Phys* (2014) 90:012130. doi:10.1103/PhysRevE.90.012130
15. Chair N, Ali Dannoun EM. Two-point resistance of the Möbius ladder. *Phys Scripta* (2015) 90:035206. doi:10.1088/0031-8949/90/3/035206
16. Tan Z. Theory on resistance of *m*×*n* cobweb network and its application. *Int J Circ Theor Appl* (2015) 43:1687–702. doi:10.1002/cta.2035
17. Gervacio SV. Resistance distance in complete *n*-partite graphs. *Discrete Appl Math* (2016) 203:53–61. doi:10.1016/j.dam.2015.09.017
18. Tan Z. Two-point resistance of an *m*×*n* resistor network with an arbitrary boundary and its application in RLC network. *Chin Phys B* (2016) 25:050504. doi:10.1088/1674-1056/25/5/050504
19. Cinkir Z. Effective resistances and Kirchhoff index of a ladder graph. *J Math Chem* (2016) 54:955–66. doi:10.1007/s10910-016-0597-8
20. Tan Z, Asad JH, Owaidat MQ. Resistance formulae of a multipurpose ?-step network and its application in LC network. *Int J Circuit Theor Appl* (2017) 45:1942–57. doi:10.1002/cta.2366
21. Vaskouski M, Zadorozhnyuk A. Resistance distances in Cayley graphs on symmetric groups. *Discrete Appl Math* (2017) 227:121–35. doi:10.1016/j.dam.2017.04.044
22. Shangguan Y, Chen H. Two-point resistances in an Apollonian network. *Phys Rev E* (2017) 96:062140. doi:10.1103/PhysRevE.96.062140
23. Jiang Z, Yan W. Some two-point resistances of the Sierpinski gasket network. *J Stat Phys* (2018) 172:824–32. doi:10.1007/s10955-018-2067-0
24. Owaidat MQ, Asad JH, Tan Z. Resistance computation of generalized decorated square and simple cubic network lattices. *Results Phys* (2019) 12:1621–7. doi:10.1016/j.rinp.2019.01.070
25. Shangguan Y, Chen H. Two-point resistances in a family of self-similar (x,y)-flower networks. *Physica A* (2019) 523:382–91. doi:10.1016/j.physa.2019.02.008
26. Ye L, Yan W. Resistance between two vertices of almost complete bipartite graphs. *Discrete Appl Math* (2019) 257:299–305. doi:10.1016/j.dam.2018.08.030
27. Barrett W, Evans EJ, Francis AE. Resistance distance in straight linear 2-trees. *Discrete Appl Math* (2019) 258:13–34. doi:10.1016/j.dam.2018.10.043
28. Jiang Z, Yan W. Resistances between two nodes of a path network. *Appl Math Comput* (2019) 361:42–6. doi:10.1016/j.amc.2019.05.006
29. Chen H, Zhang F. Resistance distance local rules. *J Math Chem* (2008) 44:405–17. 10.1007/s10910-007-9317-8
30. Wolfram Research, Inc. *Mathematica*. version 9.0. Champaign, IL: Wolfram research Inc. (2012).

Conflict of Interest: The authors declare that the research was conducted in the absence of any commercial or financial relationships that could be construed as a potential conflict of interest.

Advantages of publishing in Frontiers

OPEN ACCESS
Articles are free to read for greatest visibility and readership

FAST PUBLICATION
Around 90 days from submission to decision

HIGH QUALITY PEER-REVIEW
Rigorous, collaborative, and constructive peer-review

TRANSPARENT PEER-REVIEW
Editors and reviewers acknowledged by name on published articles

Frontiers
Avenue du Tribunal-Fédéral 34
1005 Lausanne | Switzerland

Visit us: www.frontiersin.org
Contact us: frontiersin.org/about/contact

REPRODUCIBILITY OF RESEARCH
Support open data and methods to enhance research reproducibility

DIGITAL PUBLISHING
Articles designed for optimal readership across devices

FOLLOW US
@frontiersin

IMPACT METRICS
Advanced article metrics track visibility across digital media

EXTENSIVE PROMOTION
Marketing and promotion of impactful research

LOOP RESEARCH NETWORK
Our network increases your article's readership